

LINEAR STABILITY ANALYSIS OF NONAXISYMMETRIC INSTABILITIES IN
SELF-GRAVITATING POLYTROPIC DISKS

by

KATHRYN Z. HADLEY

A DISSERTATION

Presented to the Department of Physics
and the Graduate School of the University of Oregon
in partial fulfillment of the requirements
for the degree of
Doctor of Philosophy

March 2011

DISSERTATION APPROVAL PAGE

Student: Kathryn Z. Hadley

Title: Linear Stability Analysis of Nonaxisymmetric Instabilities in Self-gravitating
Polytropic Disks

This dissertation has been accepted and approved in partial fulfillment of the
requirements for the Doctor of Philosophy degree in the Department of Physics by:

Raymond Frey	Chairperson
James Imamura	Advisor
Robert Zimmerman	Member
Paul Csonka	Member
Alan Rempel	Outside Member

and

Richard Linton	Vice President for Research and Graduate Studies/Dean of the Graduate School
----------------	---

Original approval signatures are on file with the University of Oregon Graduate School.

Degree awarded March 2011

© 2011 Kathryn Z. Hadley

DISSERTATION ABSTRACT

Kathryn Z. Hadley

Doctor of Philosophy

Department of Physics

March 2011

Title: Linear Stability Analysis of Nonaxisymmetric Instabilities in Self-gravitating Polytropic Disks

Approved: _____
Dr. James N. Imamura

An important problem in astrophysics involves understanding the formation of planetary systems. When a star-forming cloud collapses under gravity its rotation causes it to flatten into a disk. Only a small percentage of the matter near the rotation axis falls inward to create the central object, yet our Sun contains over 99% of the matter of our Solar System. We examine how global hydrodynamic instabilities transport angular momentum through the disk causing material to accrete onto the central star.

We analyze the stability of polytropic disks in the linear regime. A power law angular velocity of power q is imposed, and the equilibrium disk structure is found through solution of the time-independent hydrodynamic equations via the Hachisu self-consistent field method. The disk is perturbed, and the time-dependent linearized hydrodynamic equations are used to evolve it. If the system is unstable, the characteristic growth rate and frequency of the perturbation are calculated. We consider modes with azimuthal $e^{im\phi}$ dependence, where m is an integer and ϕ is the azimuthal angle. We map trends across a wide parameter space by varying m , q and the ratios of the star-to-disk mass M_*/M_d and inner-to-outer disk radius r_-/r_+ .

We find that low m modes dominate for small $r./r_+$, increasing to higher $r./r_+$ as M_*/M_d increases, independent of q . Three main realms of behavior are identified, for $M_* \ll M_d$, $M_* \approx M_d$ and $M_* \gg M_d$, and analyzed with respect to the I, J and P mode types as discussed in the literature. Analysis shows that for $M_* \ll M_d$, small $r./r_+$ disks are dominated by low m I modes, which give way to high m J modes at high $r./r_+$. Low m J modes dominate $M_* \approx M_d$ disks for small $r./r_+$, while higher m I modes dominate for high $r./r_+$. Behavior diverges with q for $M_* \gg M_d$ systems with high q models approximating $M_* \approx M_d$ characteristics, while low q models exhibit $m = 2$ I modes dominating where $r./r_+ < 0.60$.

CURRICULUM VITAE

NAME OF AUTHOR: Kathryn Z. Hadley

PLACE OF BIRTH: Racine, Wisconsin

DATE OF BIRTH: October 25, 1955

GRADUATE AND UNDERGRADUATE SCHOOLS ATTENDED:

University of Oregon, Eugene
Central Washington University, Ellensburg
Yakima Valley Community College, Yakima Washington
Weber State College, Ogden, Utah

DEGREES AWARDED:

Doctor of Philosophy, Physics, 2011, University of Oregon
Master of Science, Physics, 2005, University of Oregon
Bachelor of Science, Physics, 2003, Central Washington University
Associate of Science, Physics, 2000, Yakima Valley Community College

AREAS OF SPECIAL INTEREST:

Theoretical Astrophysics

PROFESSIONAL EXPERIENCE:

Teaching assistant, Department of Physics, University of Oregon, Eugene,
Oregon, 2003 - 2011

GK-12 fellow, Department of Physics, University of Oregon, Eugene, Oregon,
2005 - 2008

Undergraduate Catalytic Outreach and Research Experience Pod leader,
Department of Physics, University of Oregon, 2008 - 2009

Instructor, Lane Community College, Eugene, Oregon, 2006 - 2011

GRANTS, AWARDS, AND HONORS:

Outstanding Teaching Assistant of the Year, University of Oregon, 2004

PUBLICATIONS:

Hadley, K. Z., & Imamura, J.N., 2010, Nonaxisymmetric Instabilities of Self-gravitating disks I. Toroids, *Ap&SS*, submitted

ACKNOWLEDGMENTS

I would like to thank Jim Imamura for the countless hours he has spent teaching me. Some of my best memories are of sitting in his office, watching the afternoon light fade into dusk until he became a silhouette against the window, still excited to delve into whatever tangent of theory arose. His insight and depth of knowledge made this work possible. I would also like to thank the members of our research group, a convergence of several remarkable and unique individuals. Paul Fernandez was of tremendous help in handling the mountains of data generated, and richly contributed to the flow of conversation and discovery that permeated our group meetings. Scott Ernst worked tirelessly to develop the Imogen code which was not used in the computations presented in this dissertation but represents a future direction, allowing us to add magnetic fields to our nonlinear calculations. Erik Kever, our wildcat virtuoso programmer, is amazing and inspiring. Each person in the group has developed a unique internal landscape in the realm of physics, and the taking part in the infused collection of these viewpoints is like putting on 3-D glasses. William Dumas tended to listen quietly, assembling every facet until some thread of convergence triggered an insight that he would share. Rebecka Tumblin was a relative newcomer at the time of this writing, with infectious enthusiasm.

I also want to thank the University of Oregon Physics Department and the National Science Foundation for support during my years as a graduate student. Dean Livelybrooks has encouraged me and included me in the GK-12 Fellowship and Undergraduate Catalytic Outreach Research Experience (UCORE), which allowed me to focus on the fundamental nature of physics in the universe in a time when funding is hard to come by for research of this nature.

I dedicate this dissertation to my husband Jay. I will be forever grateful for his belief in me.

TABLE OF CONTENTS

Chapter	Page
I. INTRODUCTION	1
1.1. Background of Astrophysical Disks	1
1.2. Present Work	5
1.3. Organization of Dissertation	6
II. THE PHYSICAL PROBLEM	8
2.1. Disks and Disk Formation in Protostellar Systems	8
2.2. Hydrodynamic Instabilities	9
III. METHODS	13
3.1. Equilibrium Methods	13
3.2. Methods for Time Dependent Calculations	19
3.3. Work Integrals	29
3.4. Quasi-linear Theory	34
IV. RESULTS	38
4.1. Equilibrium Results	38
4.2. Linear Results	46

Chapter	Page
4.2.1. Convergence Test.....	62
4.2.2. Results for $q = 1.5$ Models.....	63
4.2.3. Results for $q = 1.75$ Models.....	85
4.2.4. Results for $q = 2.0$ Models.....	97
V. DISCUSSION AND CONCLUSION.....	112
5.1. Comparison with Earlier Work.....	112
5.1.1. Comparison with Andalib, Tohline and Christodoulou.....	112
5.1.2. Comparison with Kojima.....	115
5.1.3. Star Motion for $m = 1$ Modes.....	117
5.1.4. Comparison with Woodward, Tohline and Hachisu.....	123
5.2. Applications of Quasi-linear Torque Calculations	130
5.3. Conclusions.....	138
APPENDICES	141
A. PLOTS FOR SELECTED $q = 1.5$ MODELS	141
B. PLOTS FOR SELECTED $q = 1.75$ MODELS	218
C. PLOTS FOR SELECTED $q = 2.0$ MODELS	294

Chapter	Page
REFERENCES CITED.....	370

LIST OF FIGURES

Figure	Page
2.1. Kelvin-Helmholtz instability diagram	10
3.1.1. Qualitative grid layout	16
3.1.2. Mass density contours for varying M_*/M_d	17
3.1.3. Mass density contours for varying r/r_+	18
3.1.4. Mass density contours for varying q	19
3.2.1. Temporally evolving mass density perturbation.....	22
3.2.2. Temporally evolving phase angle	22
3.2.3. W and $ \delta\rho/\rho_0$ phases for representative models	26
3.2.4. W and $ \delta\rho/\rho_0$ amplitudes for representative models	28
3.2.5. Mass density contours for representative models	29
3.3.1. Work integral plots for representative models.....	32
3.3.2. Stress plots for representative models.....	33
3.4.1. Torque and δj for representative models.....	36
4.1.1. Virial error and MIRP	39
4.1.2. Total angular momentum	40
4.1.3. Location of R_0	41
4.1.4. Maximum density ρ_0	41
4.1.5. $T/ W $ for $q = 1.5, 1.75$ and 2.0	42
4.1.6. Q_- and Q_+ for $q = 1.5$ and 1.75	43
4.1.7. $Q_+ - Q_-$ for $q = 1.5$ and 1.75	44

Figure	Page
4.1.8. Self-gravity parameter p	45
4.1.9. Self-gravity parameter η	45
4.2.3. Characteristic plot for $M_* < M_d$	50
4.2.4. Characteristic plot for $M_* \approx M_d$	51
4.2.5. Characteristic plot for $M_* > M_d$	51
4.2.6. y_2 eigenvalues for $q = 1.5, 1.75$ and 2.0	53
4.2.7. y_1 eigenvalues for $q = 1.5, 1.75$ and 2.0	54
4.2.8. Parameter space map for $m = 1$	56
4.2.9. Parameter space map for $m = 2$	57
4.2.10. Parameter space map for $m = 3$	58
4.2.11. Parameter space map for $m = 4$	59
4.2.12. $M_*/M_d = 0.0$ models run for $q = 1.5, 1.75$ and 2.0	60
4.2.13. $M_*/M_d > 0.0$ models run for $q = 1.5$	60
4.2.14. $M_*/M_d > 0.0$ models run for $q = 1.75$ and 2.0	61
4.2.1.1. Convergence test results	63
4.2.2.1. Analysis plots for $M_*/M_d = 0.0, q = 1.5, m = 2$	66
4.2.2.2. Parameter space map for $q = 1.5, m = 1$	71
4.2.2.3. Parameter space map for $q = 1.5, m = 2$	73
4.2.2.4. Parameter space map for $q = 1.5, m = 3$	77
4.2.2.5. Parameter space map for $q = 1.5, m = 4$	78
4.2.2.6. Parameter space map for $q = 1.5, m = 1, 2, 3$ and 4	79
4.2.2.7. Parameter space map overlaid on p , for $q = 1.5$	80

Figure	Page
4.2.2.8. Parameter space map overlaid on η for $q = 1.5$	81
4.2.2.9. y_1 eigenvalues and corotation radii for $q = 1.5$	83
4.2.2.10. y_2 eigenvalues for $q = 1.5$	84
4.2.3.1. Parameter space map for $q = 1.75, m = 1$	87
4.2.3.2. Parameter space map for $q = 1.75, m = 2$	88
4.2.3.3. Parameter space map for $q = 1.75, m = 3$	89
4.2.3.4. Parameter space map for $q = 1.75, m = 4$	90
4.2.3.5. Parameter space map for $q = 1.75, m = 1, 2, 3$ and 4	91
4.2.3.6. Parameter space map overlaid on p for $q = 1.75$	92
4.2.3.7. Parameter space map overlaid on η for $q = 1.75$	93
4.2.3.8. y_1 eigenvalues and corotation radii for $q = 1.75$	95
4.2.3.9. y_2 eigenvalues for $q = 1.75$	96
4.2.4.1. Plots for $q = 2.0, m = 2, M_*/M_d = 50.0, r/r_+ = 0.40$	99
4.2.4.2. Plots for $q = 2.0, m = 2, M_*/M_d = 5.0, r/r_+ = 0.40$	100
4.2.4.3. Parameter space map for $q = 2.0, m = 1$	102
4.2.4.4. Parameter space map for $q = 2.0, m = 2$	103
4.2.4.5. Parameter space map for $q = 2.0, m = 3$	104
4.2.4.6. Parameter space map for $q = 2.0, m = 4$	105
4.2.4.7. Parameter space map for $q = 2.0, m = 1, 2, 3$ and 4	106
4.2.4.8. Parameter space map overlaid on p for $q = 2.0$	107
4.2.4.9. Parameter space map overlaid on η for $q = 2.0$	108
4.2.4.10. y_1 eigenvalues and corotation radii for $q = 2.0$	110

Figure	Page
4.2.4.11. y_2 eigenvalues for $q = 2.0$	111
5.1.1.1. I mode threshold comparison with ATC	114
5.1.1.2. J mode threshold comparison with ATC	115
5.1.2.1. Comparison with Kojima	116
5.1.2.2. Models illustrating edge vs. P mode	117
5.1.3.1. Transmission and reflection waves	119
5.1.3.2. Phase plots for $m = 1$ sequence	121
5.1.3.3. Growth rates vs. M_*/M_d for $m = 1$	123
5.1.4.1. Comparison with WTH for $m = 1$	125
5.1.4.2. Comparison of A mode and edge mode.....	126
5.1.4.3. Comparison with WTH for $m = 2$	128
5.2.1. Mass density contours, angular momentum, torque, and angular momentum transport time for I and J modes	133
5.2.2. Mass density contours, angular momentum, torque, and angular momentum transport time for P, edge and A modes	135
5.2.3. Evolution of angular momentum	136
5.2.4. Evolution of angular velocity	137

LIST OF TABLES

Table	Page
4.2.1. Modal dominance for $q = 1.5$	47
4.2.2. Modal dominance for $q = 1.75$ and $q = 2.0$	49
4.2.2.1. Characteristic radii, $y_1(m)$ and $y_2(m)$ for selected $q = 1.5$ models.....	82
4.2.3.1. Characteristic radii, $y_1(m)$ and $y_2(m)$ for selected $q = 1.75$ models	94
4.2.4.1. Characteristic radii, $y_1(m)$ and $y_2(m)$ for selected $q = 2.0$ models.....	109
5.1.4.1. WTH comparison models, $y_1(m)$ and $y_2(m)$ eigenvalues	129

CHAPTER I

INTRODUCTION

1.1. Background of Astrophysical Disks

Disks play important roles in the structure and evolution of a variety of astrophysical systems including spiral galaxies (*e.g.*, Binney & Tremaine 1994), accretion disks about white dwarfs, neutron stars and black holes (*e.g.*, Shapiro & Teukolsky 1983) as well as protostellar and protoplanetary systems (Stone, Gammie, Balbus & Hawley 2000). Star formation begins when a dense pocket in a Giant Molecular Cloud contracts, triggered by an external stimulus such as a shock wave. Without some overall spin, a protostellar system would collapse under gravity into a spherical object. However, typical cloud cores are known to rotate. This rotation, coupled with the large dynamic range of the collapse, leads to a strong enhancement of the spin rate. Centrifugal force works against gravitational force and the collapsing object tends to form into a flattened disk. Material near the spin axis, however, suffers little rotational support and falls inward to form a small central object, typically a few percent of the matter of the system. However, in a Solar System like ours, up to 99% of the original mass ends up forming the star. This means that some mechanism caused the matter of the disk to flow inward.

If angular momentum is transported from an inner region to an outer region of the disk, the azimuthal fluid speed decreases in the inner region and fluid flows inward to the star. The outer part of the disk will tend to move further out. Molecular viscosity alone turns out to be very ineffective at transporting angular momentum in a disk. We consider a plausible mechanism of efficient redistribution of angular momentum and energy across the disk via global nonaxisymmetric hydrodynamic instabilities driven by rotation. Analysis of astrophysical disks has been considered since the late nineteenth century, when Dyson (1893) investigated what he called “anchor rings.” Tohline (1980) investigated the collapse of rotating protostellar clouds resulting in the formation of rings. As with many systems in physics, the stability analyses began with simplified models, adding increasing complexity over time.

Serious attempts at stability analysis of non-self-gravitating disks began with Papaloizou & Pringle (1984, I and II) studying isentropic disks with power law differential rotation specified by $\Omega(\varpi) = \Omega_0 \left(\frac{\varpi}{R_0} \right)^{-q}$ with variables as defined in section 3.1. They found the disks to be dynamically unstable to nonaxisymmetric global modes. In their first paper, they treated disks of constant specific angular momentum, where $q = 2.0$, especially focusing on the special cases of a thin cylindrical shell and a thin isothermal ring. In their second paper, they included varying values of q and m . In spherical harmonics, the angular dependence of the Laplacian is proportional to $\Sigma Y_{l,m}(\theta, \varphi) P_l^m(\varphi) e^{im\varphi}$. In linearized systems, the azimuthal dependence of the perturbation takes a related form, proportional to $e^{im\varphi}$ (see Eqn. 3.2.1). A threshold of stability was found for low- m modes and slender tori such that disks were found to be unstable for a range of angular momentum profiles $\sqrt{3} < q < 2.0$. A Kelvin-Helmholtz-like instability was found to dominate disks for low q while sonic instability dominates systems near a constant specific angular momentum profile. These modes were later called P modes. These models included only the gravitational potential due to the central star, neglecting the self-gravity of the disk. In their third paper, Papaloizou & Pringle (1987) included work with higher order modes and looked at modes trapped at the inner and outer boundaries by an evanescent region around corotation, where the fluid speed equals the speed of the perturbation (Eqn. 3.2.12).

Kojima (1986, 1989) analyzed non-self-gravitating isentropic thick disks for $q = 2.0$ and $n = 0, 1.5, \text{ and } 3.0$ where n is defined as one-half the degrees of freedom of a particle, using a polytropic equation of state where $P = k \rho^{1+\frac{1}{n}}$ where P is pressure, ρ is mass density, and k is the polytropic constant. Kojima found the tori were unstable for almost all cases calculated and that the growth rate decreased for either sufficiently large or small radial widths, and also decreased with q . The growth rates showed little difference between his $n = 1.5$ and $n = 3.0$ calculations. The reported growth rates were higher for $n = 0, m = 2$ models. Kojima also introduced work integrals as valuable tools of analysis. We compare our non-self-gravitating models with his results in Section 5.1.2.

The important effect of self-gravity was first included in the analytic and numerical investigations of Goldreich, Goodman & Narayan (1986) of long wavelength modes found in slender, incompressible tori. Their simplified theory used a thin ribbon approximation to investigate the two-dimensional (2-D) incompressible limit of the narrow torus. They showed that two modes emerged, one with corotation at the density maximum, called the J mode (for the Jeans instability) and a second with corotation outside the ribbon, called the I mode (intermediate between P and J modes). We will discuss this further in the hydrodynamic instabilities section. Goodman & Narayan (1987) investigated the nonlinear evolution of the disk into planets. Goodman & Narayan (1988) further investigated I modes and J modes, adding self-gravity to their calculations for the cases of 3-D slender incompressible tori with $q = 2.0$ and 2-D slender incompressible tori with varying q . For their simplified models, they found that these disk instabilities were greatly influenced by self-gravity and were shown to be different in character from the P modes in that they were qualitatively independent of compressibility and vortensity, defined as vorticity normalized by surface density.

Lin & Papaloizou (1989) used a variational principle approach to study thin (flat) self-gravitating disks. They found modes which fell into three categories determined by the distribution of vortensity. One kind of mode is associated with extrema in vortensity, corresponding to a disk where corotation is located at the radius of the maximum density. A second mode depicts modes generated by the gradient of vortensity on the disk boundaries, corresponding to the existence of the corotation radius outside the disk. A third mode is associated with internal variations in the vortensity gradient. These modes show corotation inside the disk, but not necessarily at the density maximum.

An important development in the study of disks occurred in the late 1980's; it involved allowing the central star to move. For azimuthal mode numbers $m = 2$ and above, the m -fold symmetry of the disk allows it to be perturbed and evolve without the star moving off center. For the $m = 1$ case, typically the star is free to move in response to the disk, to hold the center of mass of the system fixed. Adams, Ruden & Shu (1989) included this effect in their calculation for infinitesimally thin disks. They found that $m = 1$ modes were unstable when $M_*/M_d < 1.0$, where M_*/M_d is the ratio of mass of the central star to the mass of the disk. Taga & Iye (1998) found 2-D disks with $n = 3.0$ to be

unstable to $m = 1$ modes for disks with masses lower than those of the central stars. Their emphasis was on modeling disks with no outer boundary. Noh, Vishniac & Cochran (1992) studied $m = 1$ modes in $q = 1.5$ disks for high and low disk masses with emphasis on sensitivity to the outer disk boundary conditions. They found that low mass disks, up to $M_*/M_d \approx 2.0$, were only unstable to $m = 1$ modes for a reflecting outer boundary, with growth rates increasing rapidly with an increase in disk mass.

Self-gravitating equilibrium disks were analyzed by Eriguchi & Hachisu (1983) and Hachisu & Eriguchi (1985). Tohline & Hachisu (1990) performed nonlinear calculations for $n = 1.5$, varying q , for extremely small mass stars, $10^{-9} < M_*/M_d < 10^{-6}$, making these disks fully self-gravitating. Their analysis included eight models but was extended in a second paper, Woodward, Tohline & Hachisu (1994) where a more extensive study was performed, this time including models where the star to disk ratio was much larger. We present a detailed comparison with this work in Section 5.1.4.

Nonlinear calculations on thin disks were done by Papaloizou & Savonije (1991), investigating I modes in disks which contain a small fraction of the total mass of the system. Papaloizou, Savonije & Heemskirk (1992) performed linear and nonlinear analysis on thin-self-gravitating disks for the $m = 1$ case with $n = 1.0$, finding that they were dynamically unstable for approximately $M_*/M_d \leq 1.0$.

Christodoulou & Narayan (1992) investigated I and J modes in linear and nonlinear 2-D slender, self-gravitating annuli. These were idealized models of thick disks, in that they were compressible and pressure-supported. Christodoulou (1993) continued to study annuli, relaxing the assumption of thinness, extending the annuli to include large radial thickness. This analysis showed that the I modes survived in-self-gravitating systems with no central mass, whereas they did not survive in the slender approximation. J modes were shown to survive only in slender annuli.

A review of angular momentum transport processes was compiled by Lin & Papaloizou (1995) summarizing mechanisms including magnetohydrodynamic instabilities as well as hydrodynamic processes including transport of angular momentum via propagating waves and the effects of self-gravity torque. A review concerning concepts underlying angular momentum transport in star formation by Bodenheimer (1995) includes discussion of transport mechanisms during evolutionary stages including

the creation of molecular cloud cores, protostars, and young stars with disks and binary companions.

Toman *et al.* (1995) investigated secular instabilities in polytropes driven by coupling of a perturbed star to a circumstellar disk. Andalib, Tohline & Christodoulou (1997) present a survey of P, I and J modes in a linear stability analysis of slender, incompressible tori with circular cross-sections for $q = 2.0$. We present a comparison with their findings in Section 5.1.1.

A review of fluid mechanics involved in young stellar objects by Shariff (2009) includes a summary of observed characteristics of various classes of objects, as well as discussions of various mechanisms involved, focusing on magnetic field effects, radiation transport and turbulence.

Hadley & Imamura (2010) performed linear stability analysis on-self-gravitating disks where $M_*/M_d = 0.0$. We include those models as the low-mass boundary of our parameter space survey and include them in our present analysis. We found that $m = 2$, I modes dominate for $0.16 < T/|W| < 0.25$. There is a small region where $m = 1$ modes dominate at slightly higher $T/|W|$, but higher $T/|W|$ models are dominated by $m = 3$ and 4 modes. There was good quantitative agreement of these results in that the linear and nonlinear eigenvalues agreed to within 5 - 10% and the eigenfunctions nearly overlaid each other on the scale of the plots. Our quasi-linear analysis indicated that self-gravity torque provided significant angular momentum transport, leading to mode saturation in the nonlinear regime. We did not see prompt fission in any toroids. This investigation raised questions. For example, we would like to know how adding a small mass to the system changes the evolution of the system, especially in the $m = 1$ case. What kinds of modes are excited as we increase M_*/M_d for slender and wide disks? What predictions do our linear calculations make for the nonlinear regime?

1.2. Present Work

The preceding section describes the work done on star-disk systems that are most relevant to our present study. Mathematically simple systems, such as infinitesimally thin

disks, self-gravitating annuli and tori with constant mass density and circular cross-sections, have been extensively studied. In our present study, we perform an extensive study of nonaxisymmetric global instabilities in thick, three-dimensional (3-D), self-gravitating, linear star-disk systems where the star is treated as a point mass. What we do here to further the progress of the field is to compile an extensive mapping of parameter space by calculating linear, self-gravitating, star-disk systems for $n = 1.5$, $q = 1.5, 1.75$ and 2.0 , for $0.0 \leq M_*/M_d \leq 100.0$ for slender and wide disks with a range $0.05 \leq r_-/r_+ \leq 0.70$ where r_-/r_+ is the ratio of the inner edge to the outer edge of a disk.

We discuss how the trends found in the non-self-gravitating disks of Kojima (1989) and thin disks systems carry over to self-gravitating thick disks, as well as how the extra degrees of freedom may excite new behaviors. We compare our findings with the slender incompressible tori studied by Andalib, Tohline and Christodoulou (1997) and with the infinitesimally thin, $m = 1$ models of Adams, Ruden & Shu (1989). We also make a detailed comparison with the nonlinear results of Woodward, Tohline, & Hachisu (1994).

We address many questions raised by our previous work on $M_*/M_d = 0.0$ disks. We perform quasi-linear analysis on a few linear models, representative of various mode types. We compare our quasi-linear modeling results with nonlinear results to gain insight about what will carry over from the linear to the nonlinear regime. We then use our linear results to develop a quasi-linear theory to model the development of disks unstable to nonaxisymmetric instabilities. Nonlinear models are computationally expensive to run. In future work, we will use our extensive linear database, coupled with the insight gained from our quasi-linear theory, to construct a sequence of nonlinear models to run which will provide a rich understanding of the behavioral trends over the nonlinear regime.

1.3. Organization of Dissertation

The remainder of the dissertation is organized as follows. In Chapter II, we present a short background of the physical problem and discussion of modes involved

with hydrodynamic gravitational disk instabilities. Chapter III introduces our mathematical methods and concepts. Chapter IV presents our results with Section 4.1 containing equilibrium model results, Section 4.2 presenting the results of the time-evolved models with subsections 4.2.1, 4.2.2, and 4.2.3 on $q = 1.5$, 1.75 and 2.0 results, respectively. Chapter V contains discussion with comparison of our results with those of previous studies and applications, a summary of our results and conclusions.

CHAPTER II

THE PHYSICAL PROBLEM

2.1. Disks and Disk Formation in Protostellar Systems

Star formation begins in Giant Molecular Clouds that extend for several tens of parsecs with masses between 10^5 and 3×10^6 solar masses (Shu, Adams & Lizano 1987), in small, internal clumps triggered toward contraction by external mechanisms such as shock waves or stellar winds. For the model of a spherically symmetric isothermal protostar, the free-fall time scale for the system to undergo gravitational collapse is on the order of 10^5 to 10^6 years (Tassoul 1978). If the angular velocity of the system is roughly equal to that of the galactic rotation, then a one solar mass cloud with a radius of 1000 AU would have a specific angular momentum $h \approx 1.4 \times 10^{17} \text{ m}^2/\text{s}$. Observations show that the specific angular momentum of a molecular cloud core is estimated to be $10^{18} \text{ m}^2/\text{s}$ (Bodenheimer 1995). The angular momentum of the protostellar cloud is far too high to allow it to collapse directly into a star (Larsen 1971), with only a few percent of the matter falling into the central object and the rest forming a surrounding disk (Tohline 2002). We can make a simple estimate of the radial extent of a disk formed from a uniformly spherical cloud core by assuming that gravitational collapse halts when the gravitational potential energy equals the rotational kinetic energy:

$$\frac{GM}{r} = \frac{J^2}{M^2 r^2} \quad \text{where } M \text{ is the mass of the system and } \frac{J}{M} \text{ is the specific angular}$$

momentum. If we estimate the mass of a cloud core to be one solar mass, we calculate the radius of the disk to be 2000 AU.

In our Solar System, over 99% of the matter of the system is contained in the central star, not in the planets. There must be a process or a collection of processes that provide angular momentum transfer through the disk allowing matter to accrete onto the star. Various mechanisms under investigation include turbulence, global hydrodynamic and magnetohydrodynamic instabilities (Balbus & Hawley 1998), and secular hydrodynamic instabilities.

2.2. Hydrodynamic Instabilities

Dynamical instabilities grow on a timescale on the order of the rotation of the disk, or equivalently the sound crossing time between the boundaries when the thermal energy and rotational energy are comparable, whereas secular instabilities grow on a dissipative timescale. In this work, we focus on modes of oscillation that generate dynamical instabilities. Several kinds of modes are possible in star/disk systems as a result of different driving mechanisms. Pressure, differential rotation and self-gravity all play roles as driving mechanisms in varying degrees for any given disk. The ratios of these quantities change as a result of the varying mass density configuration and angular momentum profile of the equilibrium structure. It may be that several modes are unstable in an evolving disk but that one with a much faster growth rate dominates the disk after a relatively short time.

What we have done here is an extensive mapping of parameter space to determine how modes are distributed, that is, how their driving mechanisms depend on the dynamic geometry of the disks. We find that sometimes boundaries between mode types are abrupt. In other regions of parameter space, thresholds between modal types are wider and exhibit characteristics such as beating as the waves of the different modes vie for global domination. In this section, we will provide a foundation for understanding different mode types.

The initial angular momentum profile of the disk sets the stage for the ultimate evolution of the disk because the angular momentum distribution probably plays a major role in the initial stability properties of the disk. Understanding what sort of mode will dominate this evolution is key to determining angular momentum transport. We currently have no *a priori* way of determining what velocity profile a disk should have. Turbulent viscosity in a disk is what causes it to deviate from Keplerian rotation, and we presently do not understand how to quantify it. Therefore, to model a differentially rotating disk, we impart a velocity profile and vary it as a parameter. We use a velocity profile

specified by a power law $\Omega(\varpi) = \Omega_0 \left(\frac{\varpi}{R_0} \right)^{-q}$ with variables as defined in Section 3.1. A

Keplerian rotation profile corresponds to the case where $q = 3/2$ and constant specific

angular momentum corresponds to $q = 2.0$. Pressure gradients in the disk cause the rotation to depart from Keplerian. Rayleigh (1916) showed that disks become locally axisymmetrically unstable if the pressure gradients are so large that $q > 2.0$, indicating the specific angular momentum decreases outward.

One of the mechanisms responsible for hydrodynamic instabilities in disks is a Kelvin-Helmholtz-like shear instability. It comes about when two fluid regions move with respect to each other, creating a velocity shear. Differential rotation in a disk provides the necessary velocity gradients for a Kelvin-Helmholtz instability to occur.

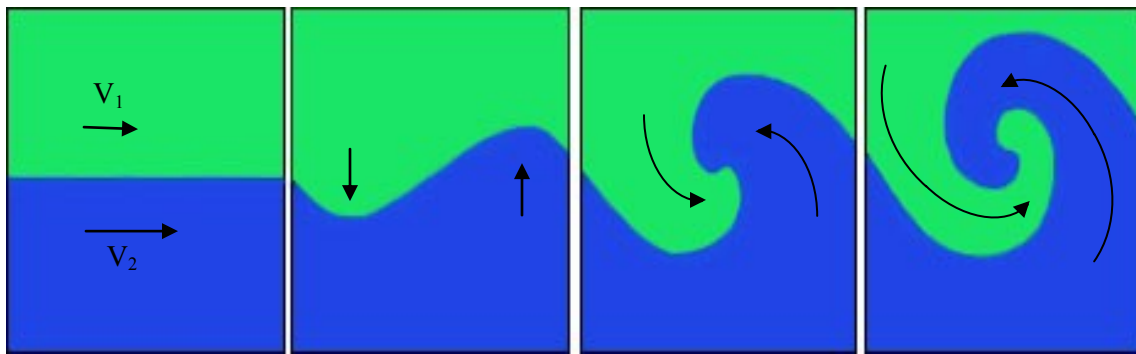


Fig. 2.1. Kelvin-Helmholtz instability diagram.

The Kelvin-Helmholtz instability produces rotations in a fluid, increasing localized vorticity, where vorticity is defined as the curl of the velocity. Vortensity is defined as mass column density divided by vorticity. Locations where the gradient of vortensity equals zero are likely sites for resonant instabilities to occur (Papaloizou & Savonije 1991).

The first type of mode identified in disks was the P mode, first reported by Papaloizou and Pringle (1984, I and II; 1986 III) in isentropic, non-self-gravitating disks with differential rotation. They found that disks are subject to Kelvin-Helmholtz-like shear instabilities for $q > \sqrt{3}$ and sonic instabilities near the upper limit of $q = 2.0$. Sonic instabilities involve the transport of energy and angular momentum via sound waves. The local speed of sound varies depending on the disk geometry because of pressure and density gradients in the disk. Goodman & Narayan (1988) and Christoudoulou & Narayan (1992) found the P modes exist in only a very narrow range of parameter space

in slender, self-gravitating tori. They claimed these modes were due to edge waves at the inner and outer edges which coupled across a forbidden zone surrounding the corotation radius. These edge waves are similar to surface waves in water but modified by shear and rotation. Christodoulou (1993) discussed the nature of “edge modes” that result from the interaction of two acoustic waves. It resembles a P mode in that they both exhibit trailing arms in the inner disk region but switch to leading after crossing the corotation radius. The edge modes have a more pronounced trailing spiral character in the outer region of the disk.

Goodman and Narayan (1986) included self-gravity in their study of hydrodynamic instability. The models they analyzed were slender 3-D incompressible annuli with constant specific angular momentum and 2-D incompressible slender annuli with arbitrary linear angular momentum profile (thin ribbon approximation). Their simplified mathematical models allowed them to look at the limits of low and high self-gravity. They found that self-gravity greatly influenced the behavior of the systems, inhibiting the P mode and establishing two other modes, called the J mode (for modes related to the Jeans instability) and the I mode (modes intermediate between P and J modes). The Jeans instability occurs when the radial free-fall time is shorter than the radial sound crossing time. When this is the case, pressure support cannot happen fast enough to counteract gravitational collapse. An identifying characteristic of these two modes for this simple case is the location of the corotation radius, where the angular speed of the perturbation wave equals that of the fluid in the disk. For P and J modes, the corotation radius falls exactly on the radius where the mass density of the disk is at a maximum. For I modes, the corotation radius is found outside the disk, either at a smaller radius than that of the inner edge, or outside the outer edge. Goodman and Narayan showed that I and J modes were qualitatively independent of compressibility and vortensity, so they could not be sonic or Kelvin-Helmholtz instabilities.

We tend to see J modes in disks that have small cross-section. The physics of our disks is more complicated than the thin ribbon approximation, and we do not strictly see corotation falling on the density maximum for J modes, or necessarily outside the disk for I modes. J modes are driven by the merger of two waves which use self-gravity as a restoring mechanism, and carry equal and opposite amounts of angular momentum. I

modes are also driven by the merger of two waves, but in this case the waves have different driving mechanisms. One wave is driven by self-gravity which causes azimuthal compressions and the other is driven by epicyclic motions of the fluid. These waves couple across corotation and may be damped by the Q -barrier (Eqn. 3.1.13).

Besides I and P modes, disks with $m = 1$ exhibit another kind of mode, called an A mode (Woodward, Tohline, & Hachisu 1994). This mode occurs in a narrow range of parameter space for small r/r_+ and $M_*/M_d \leq 1.0$. A modes are characterized by a single trailing arm with an angular extent of at least 2π radians. It has no phase shift in its $|\delta\rho/\rho_0$ eigenfunction near the radius of the maximum density or near corotation, nor does it show any sign of change as it crosses those radii. It is thought to be related to the motion of the central star. Adams, Ruden & Shu identified the mechanism responsible for the instability as SLING amplification (Stimulation by the Long-range Interaction of Newtonian Gravity). Sling amplification is characterized by a long, trailing, spiral density wave which reflects at the outer Lindblad resonance (Eqn. 3.2.13) and consequently becomes incident at the corotation radius. These findings were disputed by Woodward, Tohline & Hachisu who found similar long, trailing, spiral density waves in disks where $q = 2.0$, which by definition, have the Lindblad resonance at corotation. A more thorough discussion of the amplification mechanism will be given in Section 5.1.3.

CHAPTER III

METHODS

3.1. Equilibrium Methods

We analyze star/disk models by calculating equilibrium models and using the resulting mass density and angular momentum structures as initial conditions for the time-evolving models. We assume axisymmetry with rotation on cylinders and mirror symmetry across the equatorial plane for the equilibrium models. We use an isentropic energy conservation equation, which implies a polytropic equation of state, *i.e.*, the relationship between pressure and density is defined as $P = k\rho^{1+1/n}$ where P is pressure, ρ is mass density, $2n$ equals the degrees of freedom and k is the polytropic constant. We investigate models with $n = 3/2$. The velocity field is defined using a power law angular velocity distribution $\Omega(\varpi) = \Omega_0 \left(\frac{\varpi}{R_0} \right)^{-q}$ where R_0 is the radius of the density maximum, Ω_0 is the frequency of the fluid at R_0 , ϖ is the cylindrical radial coordinate and q is a parameter. “Keplerian” disks refer to the case where $q = 1.5$, and constant specific angular momentum is the limiting case of $q = 2$. We investigate models with $q = 1.5, 1.75$ and 2.0 .

Unless otherwise noted, all quantities presented are in polytropic units in which $G = k = M_* = 1$, where M_* is defined as the star mass. Conversion between polytropic units and physical units can be done using the transformations given in Williams & Tohline (1987).

Equilibrium calculations were done using inviscid hydrodynamic equations:

$$\partial_t \rho + \nabla \cdot (\rho \mathbf{v}) = 0 \quad (3.1.1)$$

$$\rho(\partial_t + \mathbf{v} \cdot \nabla) \mathbf{v} = -\nabla P - \rho \nabla \Phi_g \quad (3.1.2)$$

$$\nabla^2 \Phi_g = 4\pi G \rho \quad (3.1.3)$$

in steady state. Equilibrium solutions are found by setting time derivatives equal to zero in Equations (3.1.1-3.1.3), assuming axial symmetry, rotation about the z-axis, and rotation on cylinders, and following the self-consistent field approach of Hachisu (1986). This is an iterative approach, outlined below. In equilibrium, for a flow with axisymmetry which rotates on cylinders the mass continuity equation is identically zero. The momentum conservation equation becomes:

$$\nabla \left[H + \Phi_g - \int \Omega^2 \varpi d\varpi \right] = 0 \quad (3.1.4)$$

Where H is the enthalpy given by $H = \frac{\gamma}{\gamma-1} \frac{P}{\rho}$ where $\gamma \equiv 1 + \frac{1}{n}$. This implies:

$$H = -\Phi_g + \int \Omega^2 \varpi d\varpi + C \quad (3.1.5)$$

where C is an integration constant determined by the boundary conditions. Since we use polytropic units, two free parameters need to be defined in order to find C . It is convenient to define the inner and outer edges of the disk, r_- and r_+ , because mass density equals zero at these locations, simplifying our equation. Since all terms in the right-hand side of this equation depend only on mass density, we can make a guess for H using an arbitrary density distribution. We then solve the independent enthalpy equation for the mass density and then compare our results to the guessed density.

$$H = \frac{\gamma}{\gamma-1} \frac{P}{\rho} \quad \text{and} \quad \rho = \left(\frac{H}{k(1+n)} \right)^n \quad (3.1.6)$$

We outline the steps used in Eqns. 3.1.7 - 3.1.11.

$$\frac{\gamma}{\gamma-1} \frac{k\rho^{1+1/n}}{\rho} - \frac{GM_*}{\varpi} + \Phi_d - \int \Omega_0^2 R_0^{2q} \varpi^{-2q} \varpi d\varpi - C = 0 \quad (3.1.7)$$

Converting to dimensionless units:

$$\frac{\gamma}{\gamma-1} k(\rho_0 \eta)^{\frac{1}{n}} - \frac{GM_*}{R_0 \lambda} + \Phi_d - \Omega_0^2 R_0^{2q} R_0^{2-2q} \int \lambda^{1-2q} d\lambda - C = 0 \quad (3.1.8)$$

where $\eta \equiv \rho/\rho_0$. Using $\nabla^2 \Phi_d = 4\pi G\rho$, $\frac{1}{R_0^2} \Phi_0 = G\rho_0 \rightarrow \Phi_0 = G\rho_0 R_0^2$

$$\frac{\gamma}{\gamma-1} \eta^{\frac{1}{n}} - \frac{GM_*}{k\rho_0^{1/n} R_0} \frac{1}{\lambda} + \frac{\Phi_0}{k\rho_0^{1/n}} - \frac{\Omega_0^2 R_0^2}{k\rho_0^{1/n}} \Phi(\lambda) - \frac{C}{k\rho_0^{1/n}} = 0 \quad (3.1.9)$$

We define:

$$\frac{GM_*}{k\rho_0^{1/n} R_0} \equiv \frac{GM_*}{\Phi_0 R_0}, \frac{\Phi_0}{k\rho_0^{1/n}} \equiv 1, \frac{C}{k\rho_0^{1/n}} \equiv C', \frac{\Omega_0^2 R_0^2}{k\rho_0^{1/n}} \equiv h_0^2 \quad (3.1.10)$$

To get our final form:

$$\frac{\gamma}{\gamma-1} \eta^{\frac{1}{n}} - \frac{GM_*}{\Phi_0 R_0} \frac{1}{\lambda} + 1 - h_0^2 \Phi(\lambda) - C' = 0 \quad (3.1.11)$$

We make new guesses until a predetermined tolerance is met. We test for convergence by monitoring the change in the constants h_0^2 and C' , so the test is global in nature. We quantify the accuracy of our result using the virial theorem which states that the total kinetic energy, both rotational and thermal, plus one half the gravitational potential energy equals zero or $2T + W = 0$. In practice, this quantity does not equal zero, and we discard models which do not satisfy the virial equation better than about 10^{-4} times the total energy of the system.

The discretized equations are solved on a cylindrical grid of uniformly sized cells, as shown qualitatively in Fig 3.1.1. Scalar quantities are defined at cell centers while vector quantities are defined at cell vertices.

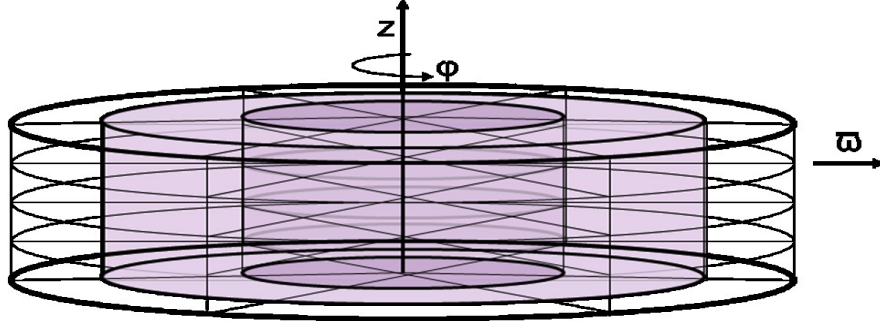


Fig. 3.1.1. Qualitative grid layout.

Equilibrium models of axisymmetric, differentially rotating, self-gravitating inviscid disks were calculated on a cylindrical coordinate system with uniformly spaced grids of 512x512.

The location of the mass density maximum in the equilibrium disk is important for understanding the character of the disk. Another radius that indicates the nature of the equilibrium disk is that of the vortensity extremum R_λ . We define vortensity λ as the mass column density divided by the local vorticity. Vorticity is the curl of the velocity field, so this quantity indicates the rotation of the fluid about the point in question. For our power-law velocities, vortensity is defined as:

$$\lambda = \frac{\Sigma}{(2-q)\Omega} \hat{z} \quad (3.1.12)$$

where Σ is the mass column density. Toomre (1964) calculated that thin disks suffer axisymmetric instability when the Q parameter falls below unity. Q is defined as:

$$Q = \frac{c_s \mathcal{K}}{\pi G \Sigma} \quad (3.1.13)$$

where c_s is the local sound speed and \mathcal{K} is the epicyclic frequency given by

$\kappa^2 = 2(2-q)\Omega^2$ for power-law rotation. For our thick disks, this restriction becomes

more complicated, and we may see an evanescent region surrounding the corotation radius through which waves may not propagate. We define the inner and outer boundaries as the Q_- and Q_+ respectively, at the radii where $Q = 1$. For some disks the inner or outer Q boundary may lie outside the disk. The width of the Q -barrier is a strong determining factor as to what type of mode dominates a disk. If it is wide, it can serve as a reflecting boundary for waves. If it is narrow the waves may penetrate the barrier. Plots depicting the Q -barrier results can be found in Fig. 4.1.6, with discussion included. Discussion involving the Q -barrier is also found in Section 5.1.3.

Figures 3.1.2 - 3.1.4 show equilibrium mass density contours in meridional slices of representative models to illustrate effects of varying M_*/M_d , q and r_-/r_+ where r_-/r_+ is the ratio of inner to outer edge of the disk. The contour levels show ten divisions between the maximum density for the model and an arbitrary small number, 10^{-30} . The horizontal and vertical axes depict the grid cells. We include approximate positions of Q_- and Q_+ . In Fig. 3.1.2 we fix $q = 1.5$ and $r_-/r_+ = 0.20$ while increasing star to disk mass ratio M_*/M_d . Here we show models with $M_*/M_d = 0.0, 1.0$ and 10.0 respectively for models (a), (b) and (c). Increasing M_*/M_d has an effect of generally flattening the disk, making some models considerably harder to resolve computationally.

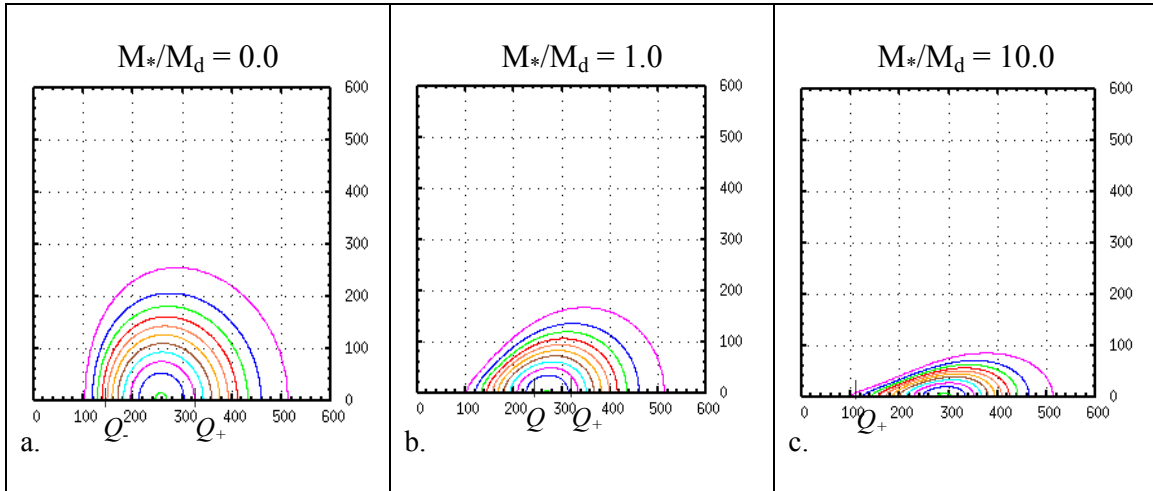


Fig. 3.1.2. Mass density contours for models of varying values of M_*/M_d . Models a, b and c have $M_*/M_d = 0.0, 1.0$ and 10.0 respectively.

Increasing the ratio of inner to outer disk radius r_-/r_+ , while keeping other parameters fixed, has an effect of generally giving a more circular cross section. We illustrate this in Fig. 3.1.3 where $r_-/r_+ = 0.10, 0.30$ and 0.50 for models (a), (b) and (c) respectively. Interestingly, increasing the mass of the star has qualitatively the same effect on the shape of the disk as decreasing r_-/r_+ . The models in Fig. 3.1.3 each have the parameters $q = 1.5$ and $M_*/M_d = 1.0$.

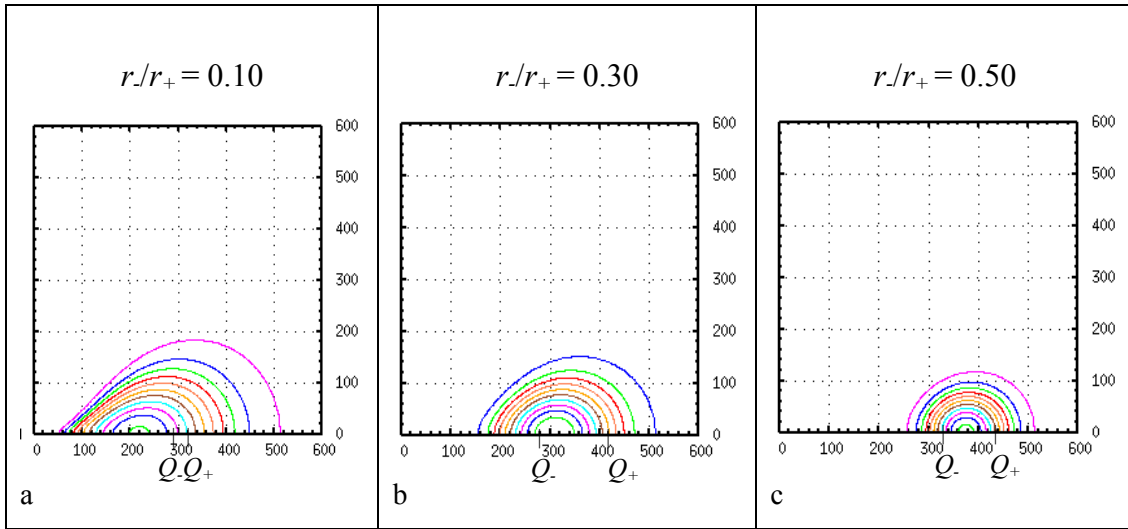


Fig.3.1.3. Mass density contours for models with $q = 1.5$ and $M_*/M_d = 1.0$, of varying r_-/r_+ . Models a, b and c have $r_-/r_+ = 0.10, 0.30$ and 0.50 , respectively.

Holding other parameters fixed and decreasing rotational power q has the effect of generally flattening the disk while moving the radius of the maximum density outward, as illustrated in the models of Fig. 3.1.4 using $r_-/r_+ = 0.40, M_*/M_d = 25.0$. Here, $q = 1.50, 1.75$ and 2.00 for models (a), (b) and (c) respectively. Increasing q makes the disks “puff up.” This can be illustrated using the virial theorem, $2(T_{\text{rot}} + T_{\text{thermal}}) + W = 0$. As q approaches 1.5, $T_{\text{rot}} / T_{\text{thermal}}$ increases, and the disk flattens.

Equilibrium mass density contours for selected models can be found in the appendices. Contour plots are shown at the beginning of Appendix A for $q = 1.5$ for the sequence $M_*/M_d = 0.0, 0.01, 0.1, 1.0, 5.0, 10.0, 25.0, 50.0$ and 100.0 ; with plots of $r_-/r_+ = 0.05, 0.10, 0.20, 0.30, 0.40,$ and 0.50 for each value of M_*/M_d . Appendix B and Appendix C begin with contour plots for $q = 1.75$ and 2.0 , respectively for

$M_*/M_d = 0.0, 0.01, 0.1, 1.0, 5.0, 10.0, 25.0, 50.0$ and the non-self-gravitating model, for the same sequence in $r./r_+$. Results and discussion of the equilibrium models can be found in Section 3.1. Equilibrium contour plots for characteristic mode types are shown in Fig. 3.2.5.

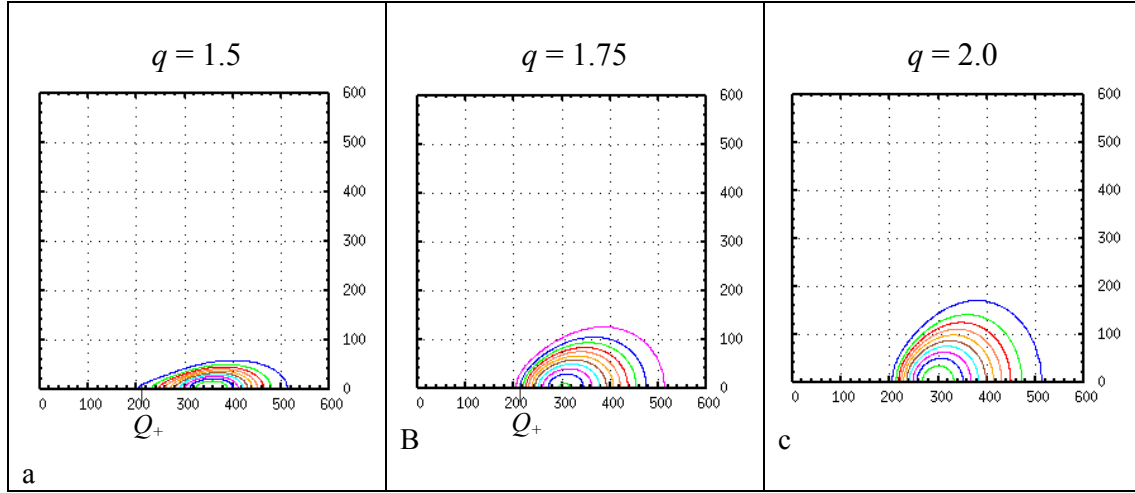


Fig. 3.1.4. Mass density contours for models with $r./r_+ = 0.20$, $M_*/M_d = 0.0$ for varying values of q . Models a, b and c have $q = 1.50, 1.75$ and 2.0 , respectively.

3.2. Methods for Time Dependent Calculations

We linearized the hydrodynamic equations to use in calculation of the time evolving models. Because time, t , and the azimuthal angle, φ , do not explicitly appear in the equations, we expect a solution where perturbed quantities, namely, mass density and velocities, take the form:

$$Q \equiv Q_0 + \delta Q(\boldsymbol{\omega}, z, t) \quad (3.2.1)$$

where $Q_0(\boldsymbol{\omega})$ is the equilibrium solution, $\delta Q(\boldsymbol{\omega}, z, t)$ is the perturbed amplitude in the meridional plane, with quantum number m . In cylindrical coordinates, the linearized hydrodynamic equations are:

$$\partial_t \delta \rho = -im\Omega \delta \rho - \frac{\rho_0}{\varpi} \delta v_\varpi - \delta v_\varpi \partial_\varpi \rho_0 - \delta v_z \partial_z \rho_0 - \rho_0 \left(\partial_\varpi \delta v_\varpi + \frac{im}{\varpi} \delta v_\phi + \partial_z \delta v_z \right) \quad (3.2.2)$$

$$\partial_t \delta v_\varpi = -im\Omega \delta v_\varpi + 2\Omega \delta v_\phi - \gamma \frac{P_0}{\rho_0^2} \partial_\varpi \delta \rho - (\gamma - 2) \frac{\delta \rho}{\rho_0^2} \partial_\varpi P_0 - \partial_\varpi \delta \Phi_g \quad (3.2.3)$$

$$\partial_t \delta v_\phi = -im\Omega \delta v_\phi - \frac{1}{\varpi} \delta v_\varpi \partial_\varpi (\Omega \varpi^2) - \frac{im}{\varpi} \frac{P_0}{\rho_0^2} \delta \rho - \frac{im}{\varpi} \delta \Phi_g \quad (3.2.4)$$

$$\partial_t \delta v_z = -im\Omega \delta v_z - \gamma \frac{P_0}{\rho_0^2} \partial_z \delta \rho - (\gamma - 2) \frac{\delta \rho}{\rho_0^2} \partial_z P_0 - \partial_z \delta \Phi_g \quad (3.2.5)$$

$$\nabla^2 \delta \Phi_g = 4\pi G \delta \rho \quad (3.2.6)$$

The perturbed quantities are complex, so each of the equations (3.2.1-3.2.6) represents a pair of equations.

Equilibrium values of mass density and angular momentum are used as the background for the temporally evolving, linearly perturbed equations. The initial values are the randomly perturbed linear values. Equations are solved using a finite difference scheme on the same grid as the equilibrium models and advanced in time using a fourth order Runge-Kutta method. The numerical code is described in detail in Toman *et al.* (1998) and Hadley & Imamura (2010). We used grid sizes of 512x512 for calculated models, and grid sizes of 256x256 and 1024x1024 for our convergence test. Boundary conditions consist of mirror symmetry about the equatorial plane. All perturbed velocities are set to zero on the surface of the disk while the mass density perturbation is unconstrained. Gravitational potential is set at the outermost grid boundaries, through the solution of:

$$\delta\Phi_g = -G \int \frac{\delta\rho}{|\mathbf{r}_x - \mathbf{r}|} d^3x \quad (3.2.7)$$

Care was taken to ensure that momentum was conserved in the case of $m = 1$ mode models; specifically, the point mass star was allowed to move, recalculating its position at each time step according to the force exerted on it from the perturbed disk. The gravitational potential due to the star's motion was added as a perturbation to the perturbed self-gravity of the disk to give the total perturbed gravity of the system.

We followed the growth of instability by monitoring $|\delta\rho|/\rho_0$ at three points in the equatorial plane of the disk. Typical plots of this behavior are shown in Fig. 3.2.1 for two unstable models (a) and (b) and a model (c) that was deemed stable. These models have parameters $m = 2$, $q = 1.5$, with $M_*/M_d = 0.0$, $r_-/r_+ = 0.40$ for (a), $M_*/M_d = 0.0$, $r_-/r_+ = 0.30$ for (b), and $M_*/M_d = 1.0$ with $r_-/r_+ = 0.10$ for model (c).

We monitor the growth of the perturbation at three radii to insure that the instability is global in nature. Mass density amplitudes are shown for radii near the inner edge of the disk, the center of the disk and near the outer edge of the disk. We determine a model to be stable if there is no discernable global growth after 30 - 40 MIRP's (rotations at the radius of the density maximum). For unstable models, the amplitudes fluctuate early in the evolution until the mode sets in and starts to dominate the disk and grow. We monitor the growth rate until it has remained constant to 3 significant figures for at least two of the three radii for 2500 iterations, then halt the model for analysis.

A comparison of the unstable plots shows that the model in (a) with $r_-/r_+ = 0.40$ is growing faster, reaching 3.27×10^{-9} in 4 MIRPs at the inner and outer edges of the disk while the model in (b) with $r_-/r_+ = 0.30$ in has reached 3.81×10^{-10} at the inner edge and a slightly lower amplitude at the outer edge. The growth rates are calculated to be and 0.356 and 0.305 for (a) and (b) respectively.

The phase plot shown in Fig. 3.2.2 is calculated using the real part of the density perturbation, depicting the phase angles as a function of time for the same three radial locations for the unstable model shown in Fig. 3.2.1 (a). The perturbation frequency in the model shown in (a) is calculated to be 1.73 while the frequency in (b) is calculated to be 1.04. We note that the inner and outer edges are approximately π radians out of phase,

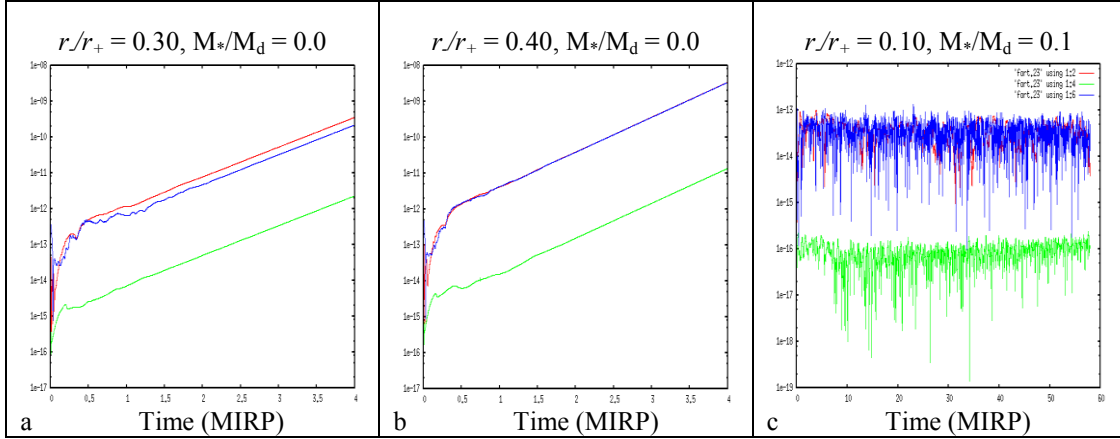


Fig. 3.2.1. Temporally evolving mass density perturbation amplitudes for unstable models a and b and a stable model c. Amplitudes are shown in red, green and blue for the inner edge, center, and outer edge of the disk, respectively.

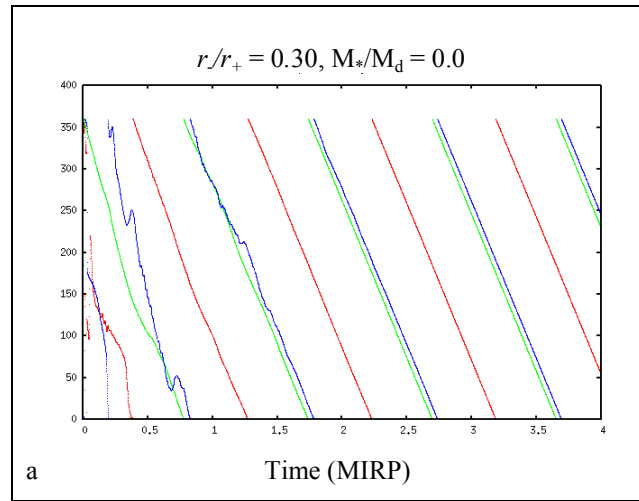


Fig. 3.2.2. Temporally evolving phase angle of the density perturbation for the unstable model shown in Fig. 3.2.2 a. Phase angles are shown in red, green and blue for the inner edge, center, and outer edge of the disk, respectively.

and that the middle of the disk in phase with the outer edge. This indicates that an abrupt phase shift happened between the inner edge and the center of the disk.

For further analysis, we examine the dispersion relation, obtained from Equations 3.2.2 - 3.2.6 via substitution. The form of the equation suggests that a combination of the

perturbed enthalpy and the perturbed gravitational potential $W \equiv \delta H + \delta \Phi_g$ is a more physical eigenfunction than $\delta \rho$,

$$\begin{aligned}
\frac{\delta \rho}{\rho_0} = & -\frac{1}{D\rho_0} \left(\frac{2m\Omega W}{\sigma\varpi} + \frac{\partial W}{\partial \varpi} \right) \frac{\partial \rho_0}{\partial \varpi} - \frac{1}{\rho_0 \sigma^2} \frac{\partial W}{\partial z} \frac{\partial \rho_0}{\partial z} \\
& - \frac{1}{\varpi D} \left(\frac{2m\Omega W}{\sigma\varpi} + \frac{\partial W}{\partial \varpi} \right) - \frac{1}{\sigma} \frac{\partial}{\partial \varpi} \left[\frac{\sigma}{D} \left(\frac{2m\Omega W}{\sigma\varpi} + \frac{\partial W}{\partial \varpi} \right) \right] \\
& + \frac{m}{\sigma^2 \varpi^2} \left\{ mW + \frac{\partial}{\partial \varpi} \left[\frac{\varpi^2 \Omega \sigma}{D} \left(\frac{2m\Omega W}{\sigma\varpi} + \frac{\partial W}{\partial \varpi} \right) \right] \right\} - \frac{1}{\sigma} \frac{\partial}{\partial z} \left(\frac{1}{\sigma} \frac{\partial W}{\partial z} \right)
\end{aligned} \tag{3.2.8}$$

where $D \equiv \sigma^2 - \kappa^2$, $\sigma \equiv \omega + m\Omega$, and κ is the epicyclic frequency, defined as:

$$\kappa^2 \equiv \frac{2\Omega}{\varpi} \frac{\partial(\Omega\varpi^2)}{\partial \varpi} = 2(2-q)\Omega^2. \tag{3.2.9}$$

In the case of constant specific angular momentum ($q = 2$), $\kappa^2 = 0$ so $D = \sigma^2$.

For our convention, the real part of ω refers to the frequency of the perturbation while the imaginary part refers to the growth rate. We define the normalized eigenvalues:

$$y_1(m) \equiv \frac{\omega_{re}}{\Omega_0} - m \tag{3.2.10}$$

$$y_2(m) \equiv \frac{|\omega_{im}|}{\Omega_0} \tag{3.2.11}$$

The corotation radius is defined as the radius where the real part of the perturbation frequency equals the frequency of the fluid. For power-law rotation, the corotation radius is calculated as:

$$\frac{R_{co}}{R_0} = \left(\frac{y_1(m)}{m} + 1 \right)^{\frac{1}{q}} \tag{3.2.12}$$

For higher frequency perturbations, the corotation moves toward a smaller radius. Qualitatively this can be understood because the fluid rotational speed decreases outward, thus a higher pattern frequency would match the fluid frequency at a smaller radius. If corotation lies inside R_θ , $y_1(m) < 0$ and if corotation lies outside R_θ , $y_1(m) > 0$. The inner and outer Lindblad resonances are located where the real part of the perturbation frequency equals $\pm \kappa$. For power law angular velocity, the locations of the inner and outer Lindblad resonances are related to the corotation radius by:

$$\frac{R_{LR}}{R_{co}} = \left(1 \pm \frac{\sqrt{4 - 2q}}{m} \right)^{\frac{1}{q}}. \quad (3.2.13)$$

The perturbation frequencies and corotation radii offer clues as to what kind of modes are present. For a J mode, corotation lies near R_θ and for I modes, corotation radii lie near the edge of the disk. Other distinctions in various parts of parameter space are not as clear, as we shall see. We wish to identify what driving mechanisms are responsible for the traits we see in the various modes. To gain insight, we examine plots showing the eigenfunctions and their phases. In Figs 3.2.3 - 3.2.5, we show representative plots of these functions for models representative of the different mode types.

Once the model has settled into a mode, the phase remains intact. We can plot an arbitrary phase to show the pattern that the perturbation forms as it sweeps around the disk. In Fig. 3.2.3 we show phase plots of $|\delta\rho|/\rho_0$ (blue) and W (red) amplitudes calculated along a radius in the equatorial plane for models representative of various modes. In the phase plots, the inner and outer edges of the disk are shown in blue, while the corotation radii are shown in turquoise and the radii of the equilibrium density maxima are plotted in pink. The equilibrium fluid flow is taken to be in the counterclockwise direction. Note that all radii shown in the figures are normalized by R_θ .

Model (a) illustrates a typical I^+ mode, with $m = 2$, $q = 1.5$, $r/r_+ = 0.30$ and $M_*/M_d = 0.0$. R_{co} is near the outer edge of the disk. In some models, it lies outside the disk entirely. There is a trailing π/m phase shift in $|\delta\rho|/\rho_0$ that lies close to R_θ ; in some cases the phase shift is seen to be leading. Outside the phase shift, $|\delta\rho|/\rho_0$ approaches the

outer edge in a barlike fashion. W is in phase with $|\delta\rho/\rho_0$ near the inner edge of the disk and with a leading arm that retains its sense as it crosses R_{co} , becoming out of phase for $\varpi > R_\theta$. In this model, W sweeps prograde, but in some models it is nearly barlike.

Model (b) in Fig. 3.2.3 depicts a typical Γ phase plot, with $m = 2$, $q = 1.5$, $r_-/r_+ = 0.60$ and $M_*/M_d = 0.1$. R_{co} lies near the inner edge of the disk, and in some cases falls at a smaller radius than that of r_- . Similarly to the Γ^+ modes, there is a trailing π/m phase shift in $|\delta\rho/\rho_0$ which in some cases is seen to be leading. The phase shift in Γ modes lies slightly outside R_θ . W is out of phase with $|\delta\rho/\rho_0$ at the inner edge, with a short leading arm that switches to trailing at R_{co} , coming into phase with $|\delta\rho/\rho_0$ at the outer edge.

Model (c) in Fig. 3.2.3 shows the phase plot of a typical J mode, with $m = 2$, $q = 1.5$, $r_-/r_+ = 0.40$ and $M_*/M_d = 0.0$. R_{co} is near R_θ and can be seen at radii that are slightly smaller or larger than R_θ . The $|\delta\rho/\rho_0$ phase exhibits a trailing arm that extends for π/m radians and tracks along R_θ but not as tightly as the phase shift seen in the I modes. W is in phase with $|\delta\rho/\rho_0$ at the inner edge, though this is somewhat relaxed in some models.

Model (d) in Fig. 3.2.3 is a typical P mode, with $m = 2$, $q = 2.0$, $r_-/r_+ = 0.50$ and $M_*/M_d = 100.0$; with R_{co} near R_θ . P modes are found in disks with high M_*/M_d ratios with weak self-gravity, as evidenced by the similarity of the $|\delta\rho/\rho_0$ and W phases. R_{co} is slightly outside R_θ in these disks. The phases exhibit a bar near the inner edge with a short leading phase shift along R_θ , switching to a short trailing arm outside R_θ .

Model (e) in Fig. 3.2.3 is an edge mode, with $m = 2$, $q = 2.0$, $r_-/r_+ = 0.20$ and $M_*/M_d = 100.0$. Like the P modes, edge modes occur in disks with high M_*/M_d but they persist to smaller M_*/M_d than the P modes. R_{co} lies slightly inside R_θ . In the inner part of the disk, edge modes are similar in structure to P modes but in the outer part of the disk they exhibit a trailing arm that extends very much farther, sometimes wrapping around the disk many times.

Model (f) in Fig. 3.2.3 illustrates behavior typical of an A mode, with $m = 1$, $q = 1.75$, $r_-/r_+ = 0.05$ and $M_*/M_d = 0.1$. R_{co} lies somewhat outside R_θ , and the $|\delta\rho/\rho_0$ phase is a long, trailing spiral arm with no apparent change as it crosses R_θ or R_{co} . W is in phase with $|\delta\rho/\rho_0$ at the inner edge but rapidly diverges into a leading arm that typically

changes to a trailing arm smoothly across the middle part of the disk, coming back into phase with $|\delta\rho|/\rho_0$ near the outer edge.

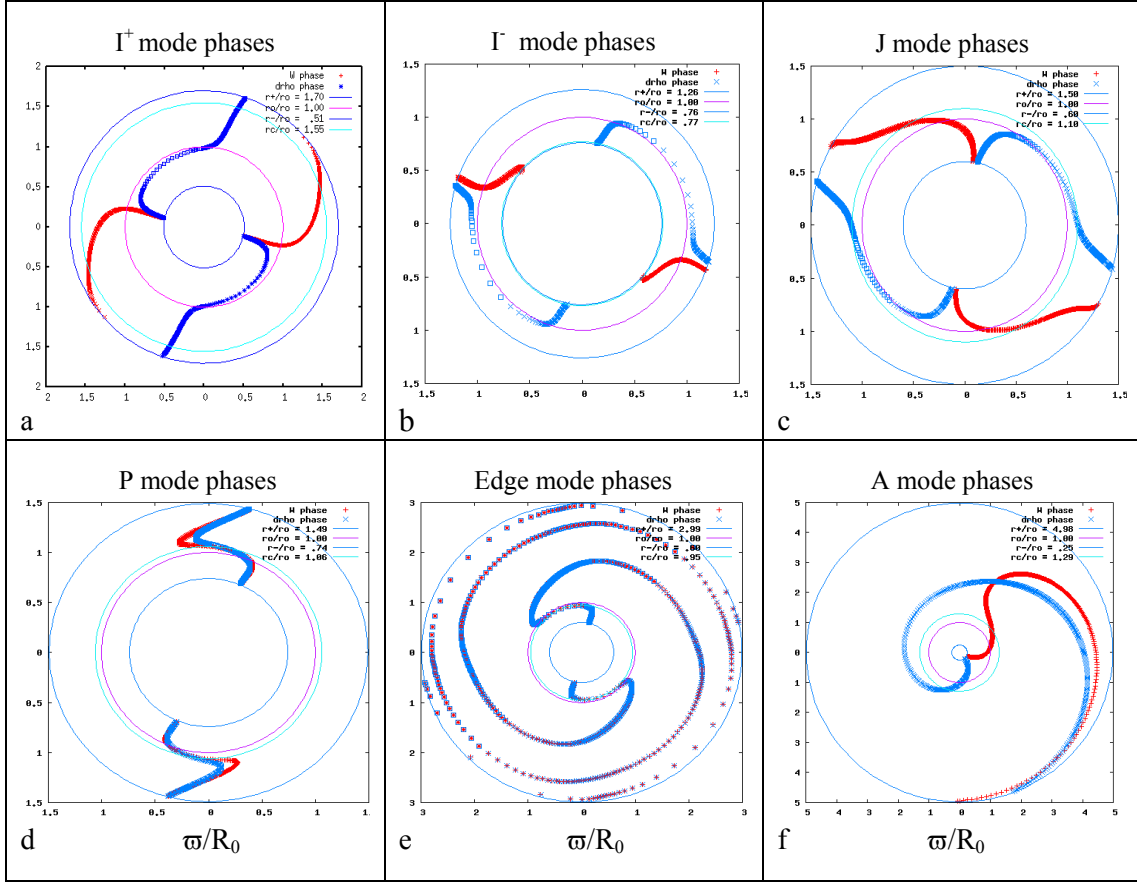


Fig. 3.2.3. W and $|\delta\rho|/\rho_0$ phases shown in red and blue, respectively, plotted in the equatorial plane for representative models of mode types I^+ , Γ , J , P , Edge and A .

In Fig. 3.2.4, we show W and $|\delta\rho|/\rho_0$ amplitudes of the eigenfunctions defined in Eq. 3.2.8, plotted radially across the equatorial plane of the disk for the same models highlighted as representative for mode types in Fig. 3.2.3. In the I^+ mode plot, we note a dip in the amplitude of $|\delta\rho|/\rho_0$ slightly inside R_0 , corresponding to the $|\delta\rho|/\rho_0$ phase shift in the I^+ phase plot. In a mathematical sense, this probably corresponds to the denominator of the dispersion relation approaching zero, forcing the numerator to approach zero faster than the denominator to avoid singularity. This typically indicates a resonance of some sort. The denominator may never strictly go to zero in parameter

space because the perturbations are complex quantities and the real and imaginary parts may not approach zero at the same time. The W amplitude has a shallow dip at a radius close to R_{co} .

The sharp dip in the $|\delta\rho|/\rho_0$ amplitude plot of the I mode lies somewhat outside R_θ , tracking the phase shift in $|\delta\rho|/\rho_0$. The W amplitude is nearly constant across the disk with a slight, shallow dip near the inner edge. The J mode amplitude plot has a dip in $|\delta\rho|/\rho_0$ near R_θ . The dip is not as sharp as that in the I mode plot, corresponding to the looser phase shift in the J mode. The dip in the W amplitude lies near R_{co} . The dips in $|\delta\rho|/\rho_0$ and W in the P mode plot are located near each other at slightly higher radii than R_θ , as would be expected, since $|\delta\rho|/\rho_0$ and W nearly coincide in the phase plot. The dip in W is slightly sharper than that of the I^+ mode, corresponding to the phase shift in W being slightly longer and more closely tied to R_{co} . The dip in $|\delta\rho|/\rho_0$ falls a little farther out than that of W , seemingly not corresponding to R_θ , but rather to the center of the leading arm. The amplitude plot for the edge mode shows several distinct dips, with the inner one corresponding to R_θ while the outer two roughly correspond to the trailing spiral.

The A mode amplitude has a dip near $\varpi/R_\theta = 2.0$, though there is no discerning feature of the phase plot to distinguish that radius. It may be, however, that it corresponds to a resonance in the dispersion relation. W has a dip close to the outer edge of the disk, but again, there is no discernable feature of the phase plot that correlates to that radius.

In Fig. 3.2.5 we present the equilibrium mass density contour plots for the models shown in Fig. 3.2.3, including the locations of the inner and outer edge of the Q -barrier, Q_- and Q_+ . The I modes and the J mode plots are all relatively symmetric compared to the other mode types, with density contours plotted as nearly concentric circles, harboring wide Q -barriers which span most of the inner parts of the disks. The I mode disk is very narrow compared to the rest of the mode types. The P mode and edge mode models do not have Q -barriers, since by definition, $Q = 0$ for $q = 2.0$ (see Eqns. 3.1.13 and 3.2.9). The P mode contour plot is asymmetric compared to the I and J modes, with the relatively large central star mass pulling the density maximum of the disk inward. The edge mode contour is even more skewed inward than the P mode. It also has a relatively massive central star, and the disk is wider, so that the inner edge of the disk is close to the star. The density maximum of this disk is displaced very far to the left of the geometric

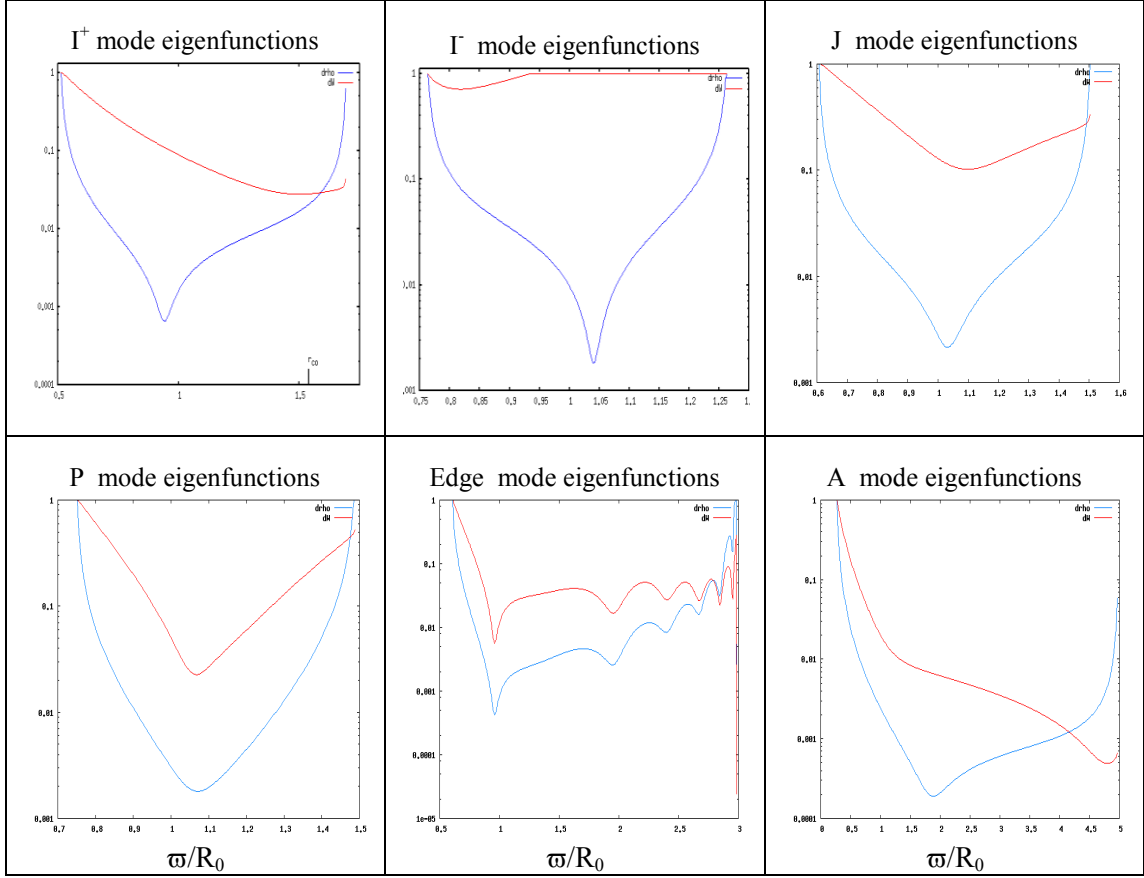


Fig. 3.2.4. W and $|\delta\rho|/\rho_0$ amplitudes in red and blue, respectively, plotted radially across the disk for the representative models introduced in Fig.3.2.3.

center of the disk. The A mode equilibrium disk is thick in vertical height and R_0 is very close to the inner edge of the disk. The inner edge of the disk is very close to the central star, but the star mass is relatively small. The mass of the opposite side of the disk pulls R_0 inward.

We continue analysis of these characteristic mode plots in later sections. The work integrals and stresses for these characteristic models are shown in Figs. 3.3.1 and 3.3.2, respectively. The self-gravity torques and perturbed angular momenta are shown in Fig. 3.4.1. In Section 5.2, we revisit these models in a discussion of the transport of angular momentum, and present plots showing the total angular momentum and the angular momentum transport time for the I and J modes in Fig. 5.2.1 and for the P, edge and A modes in Fig. 5.2.2. We estimate trends of the future evolution of the disks, and

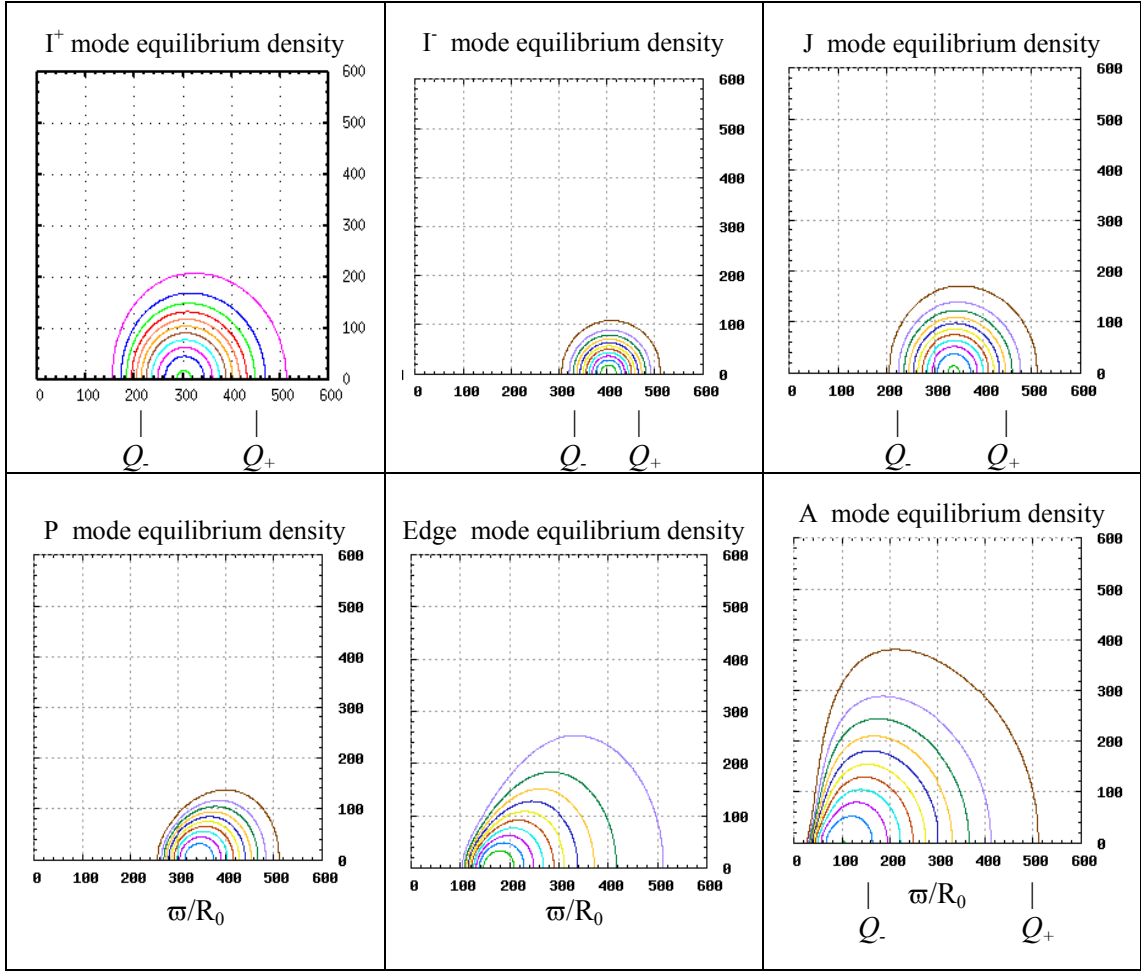


Fig. 3.2.5. Mass density contours along a meridional slice for the representative models introduced in Fig.3.2.3, with approximate locations of Q_- and Q_+ .

present plots of the angular momentum evolution and the angular velocity evolution in Figs. 5.2.3 and 5.2.4 respectively.

3.3. Work Integrals

For analysis purposes, we calculate the work done locally by the perturbed kinetic energy, and the perturbed enthalpy which accounts for the perturbation in the acoustic energy (see Kojima 1989). The perturbed kinetic energy and acoustic energy are designated as E_k and E_h respectively and, for a polytrope, are given by:

$$E_k \equiv \frac{1}{2} \rho_0 \langle \delta v_\varpi^2 + \delta v_\phi^2 + \delta v_z^2 \rangle \quad (3.3.1)$$

$$E_h \equiv \frac{1}{2} \gamma \frac{P_0}{\rho_0^2} \langle \delta \rho^2 \rangle \quad (3.3.2)$$

Here, the $\langle \delta Q \rangle$ brackets represent time-averaged perturbed quantities and are obviously second order. The total energy of the mode is the sum of the two.

$$\langle E \rangle \equiv \frac{1}{2} \rho_0 \langle \delta v_\varpi^2 + \delta v_\phi^2 + \delta v_z^2 \rangle + \frac{1}{2} \gamma \frac{P_0}{\rho_0^2} \langle \delta \rho^2 \rangle \quad (3.3.3)$$

The time derivative of the energy is the sum of the stresses involved:

$$\frac{d}{dt} \langle E \rangle = \sigma_R + \sigma_h + \sigma_G \quad (3.3.4)$$

where σ_R is the Reynolds stress, σ_h is the acoustic stress and σ_G is the work done by the perturbed gravitational forces. The Reynolds stress measures the energy arising from shear stress of the equilibrium structure which affects the perturbed model. Reynolds stress is defined as:

$$\sigma_R \equiv -\rho_0 \varpi \frac{\partial \Omega}{\partial \varpi} \langle \delta v_\varpi \delta v_\phi \rangle \quad (3.3.5)$$

The acoustic wave flux carried by the perturbation redistributes energy within the disk. It is defined as:

$$\sigma_h \equiv -\nabla \cdot \langle \delta P \delta \mathbf{v} \rangle \quad (3.3.6)$$

The work done by the perturbed gravity contains input from the self-gravity of the disk as well as motion of the central star in the $m = 1$ case and is defined as:

$$\sigma_G \equiv -\rho_0 \cdot \langle \delta \mathbf{v} \cdot \nabla (\delta \Phi_d + \delta \Phi_*) \rangle \quad (3.3.7)$$

where Φ_d is the gravitational potential of the disk and Φ_* is the gravitational potential of the star. The energy equation thus contains driving terms as well as damping terms. The growth time in terms of the work and stresses is given by:

$$\tau_w = 2 \frac{\int \langle E \rangle d^3x}{\int (\sigma_R + \sigma_G) d^3x} = 2 \times (\text{modal growth time}) \quad (3.3.8)$$

The acoustic wave stress integrates to zero over the disk so it is not included here.

Fig. 3.3.1 shows plots of the work integrals for the representative models introduced Fig. 3.3.1. The perturbed acoustic energy (E_h) is plotted in brown and the perturbed kinetic energy (E_k) is plotted in blue. E_h has two peaks in the I modes and the J mode plots, with the inner peaks considerably higher than the outer peaks, while E_k has one peak. The peak in E_k for the I^+ mode lies within the inner E_h peak, while for the I^- mode, it lies at the zero between the two E_h peaks. The minimum of the J mode E_h does not go to zero, lying between R_θ and R_{co} , similar to features in the eigenfunction plots as well as the δj and torque plots. This value agrees with the dip in the $|\delta \rho|/\rho_0$ eigenfunction since it is linear with $\delta \rho^2/\rho_0^2$. The perturbed kinetic energy shows a peak very close to the minimum in the torque.

The P mode work integral plot has two peaks in E_h lying close to the inner and outer edges with a broad valley between them. E_k has a peak which lies inside the inner E_h peak, with a shoulder across the central region, going to zero at the outer edge of the disk. The edge mode work integral plot also has a narrow E_h peak near the inner edge which contains the peak in E_k , but both functions have very low amplitudes except near the inner edge. The A mode work integrals have very low amplitude, negligible in the outer region. Every kind of mode pictured here shows work done by acoustic energy flux

dominant at the inner edge of the disk, with some inner region dominated by work done by kinetic energy. The P mode has the largest central region dominated by kinetic energy, compared to the other mode types.

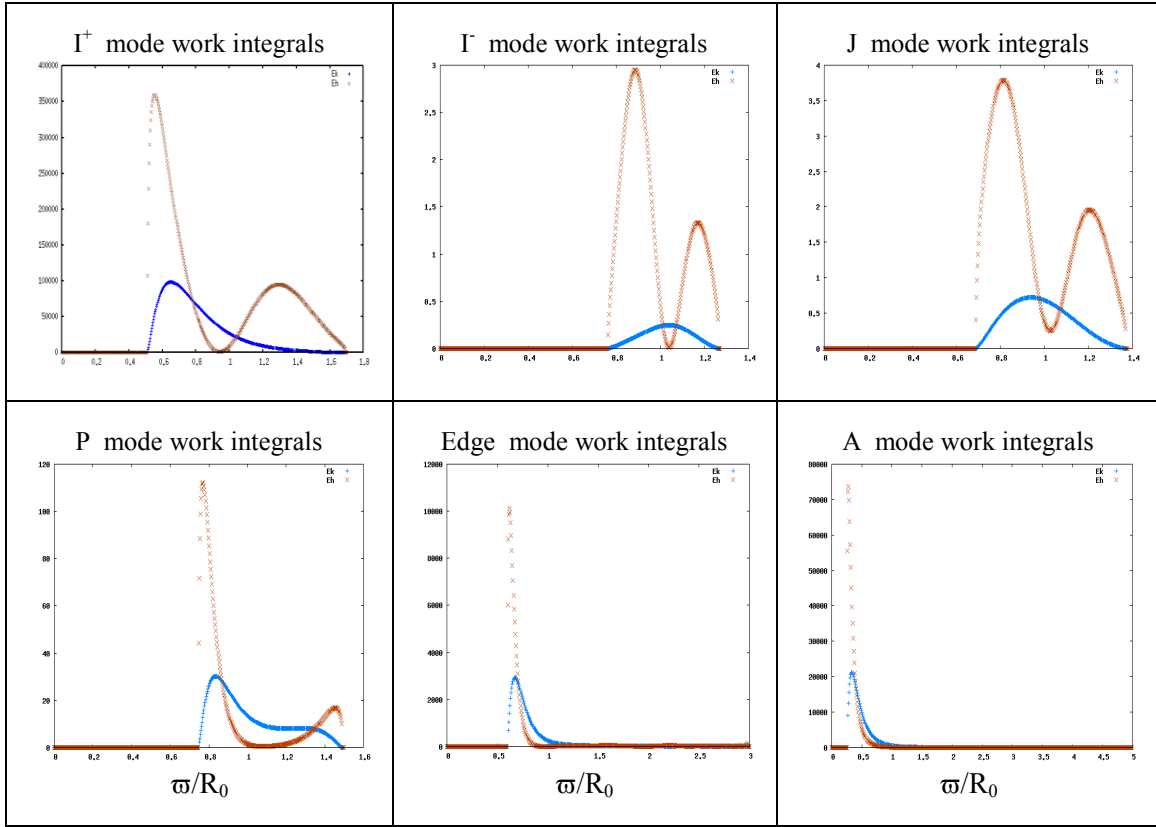


Fig. 3.3.1. Work integral plots are for representative models shown in Fig.3.2.3. Work done by kinetic energy is plotted in blue and work done by enthalpy is plotted in brown.

Fig. 3.3.2 shows stress plots for the models introduced in Fig. 3.2.1. The Reynolds stress (σ_R) arises from the fluid mass carrying the perturbed velocities. It is plotted in black, while the work done by the perturbed gravity (σ_G) is shown in red and the acoustic flux (σ_h) is plotted in blue. The stress plots of the I and J modes are similar to each other in that the inner and outer edges of the disk are dominated by σ_h while the middle of the disks have positive peaks in σ_G nearly coinciding with negative peaks in σ_h . The Γ^+ mode has a minimum in σ_h at a slightly smaller radius than that of σ_G , while the Γ mode shows the minimum in σ_h at a slightly larger radius than that of σ_G . The I and J mode plots also

have positive peaks in σ_R . The I^+ mode has a small region where σ_R dominates the other stresses, with the peak skewed toward the inner edge of the disk. There is no region of either the I^- or the J mode plot that is dominated by σ_R . The acoustic flux near the

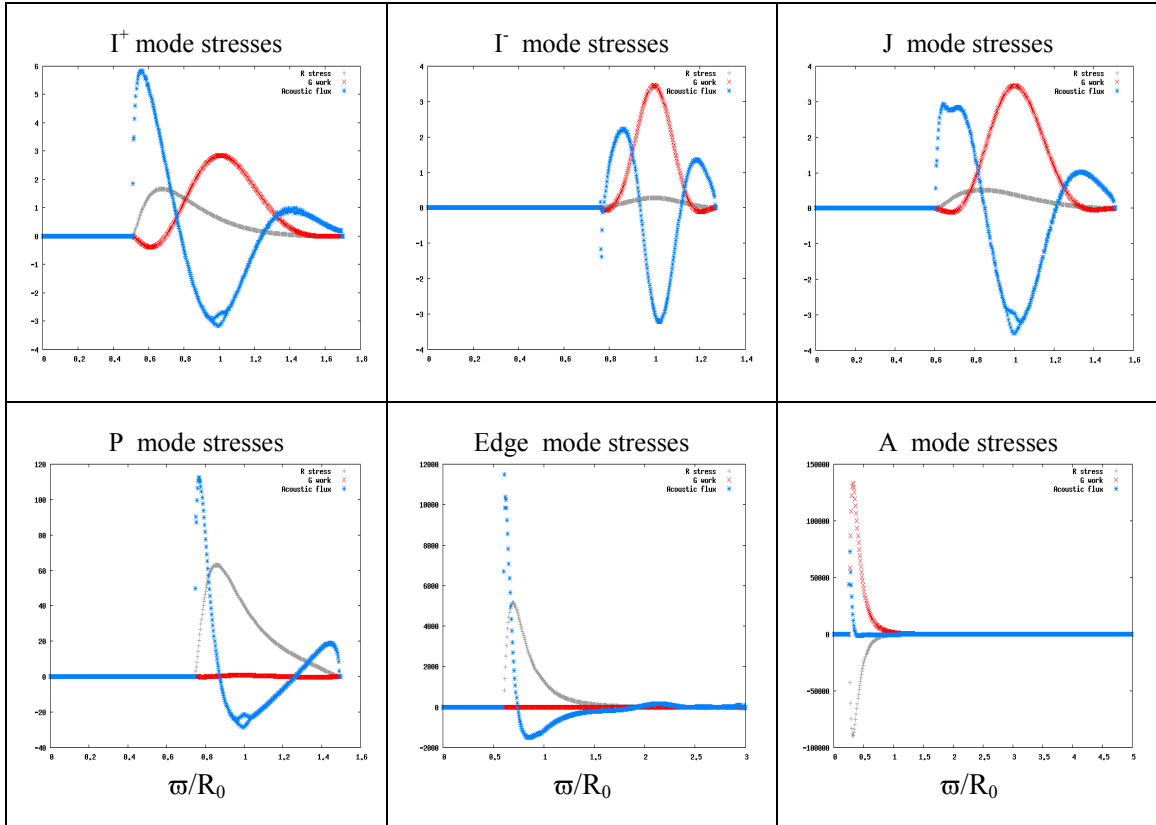


Fig. 3.3.2. Stress plots are given for the representative models shown in Fig.3.2.3. Reynold's stress, work done by gravity, and acoustic flux are plotted in black, red and blue respectively.

minimum of the I^+ mode shows difficulty in resolution. This is because it depends on spatial derivatives which may have small fluctuations.

The stress plots of the P and edge modes are similar in that they have very narrow spikes of σ_h dominating the inner edges with broad regions of positive σ_R which are offset by negative σ_h of lesser amplitude. The behaviors of σ_h in the P and edge modes diverge near the outer edge of the disk where the edge mode displays its typical wavy nature but the P mode has a positive peak. Both of these models have negligible σ_G ,

since their self-gravity is negligible. The A mode stress plot is qualitatively unlike the other modes in that it has negative σ_R and σ_h is dominated by σ_G . As seen in the torque and perturbed angular momentum plots, all major effects happen near the inner edge for the A mode.

3.4. Quasi-linear Theory

We next examine the self-gravity torque, τ , and the perturbed angular momentum, δj , plots of the models introduced in Fig. 3.2.3. We calculate the time-averaged quasi-linear torque involving the density perturbation amplitude and the perturbed gravitational potential. For $m = 1$ modes, the perturbed gravity includes the perturbation caused by the star motion as well as that of the self-gravity of the disk. We define the torque as:

$$\tau \equiv -m\pi \int |\delta\rho| |\delta\Phi| \sin(\phi_\rho - \phi_\Phi) dz \quad (3.4.1)$$

For details of the torque derivation, see Section 5.2.

The torque is normalized by the product of total angular momentum and the equilibrium rotational period at R_θ and the perturbed angular momentum is normalized by total angular momentum. We also normalize both quantities, and the following work integral and stress plots by the amplitude of the density perturbation summed over the disk.

In Fig. 3.4.1, we present torque plots for the representative models introduced in Fig. 3.2.3. For the I and J modes, the torque plots show character similar to each other, with negative τ for the inner part of the disk and positive τ for the outer part of the disk, crossing zero between R_θ and R_{co} . It should be noted that the phase plots for all three of these models also have inner bars with trailing arms in the inner disk region with a change in concavity outside R_θ . The value of τ for the P mode is positive in the inner region of the disk, switching to negative, then positive again near the outer edge. The corresponding P mode phase plot, shown in Fig. 3.2.3, has an inner bar, with a prograde shift switching to trailing in the outer disk region. The τ plot for the edge mode is similar

to that of the P mode in the inner disk region, but crosses zero more often in the outer region, corresponding to the wrapping of the spiral arms and the dips in the eigenfunctions amplitude plot shown in Fig. 3.2.4. The A mode τ plot is different in nature, with a steep negative spike in the inner disk region, probably corresponding to the motion of the central star. Fig. 3.4.1 also presents the perturbed angular momentum plots for the representative models of Fig. 3.2.3. The I and J mode plots are similar to each other in nature to their corresponding τ plots in that they are negative for the inner disk regions and positive for the outer regions.

There are some qualitative differences in the shapes of the plots. The I^+ mode, δj plot is narrower in the inner negative region, crossing zero at a smaller radius than the corresponding I^+ mode τ plot, such that δj and τ have different signs in the region around R_0 ; specifically, τ is negative while δj is positive. The outer region of the δj plot is broader and lower amplitude than the τ plot. The I mode, δj plot is more similar in overall shape to its corresponding τ plot, but there is also a region around R_0 where τ and δj have opposite sign. In this case, τ is positive and δj is negative. For the J mode, δj and τ cross zero near each other, at 1.036 and 1.047 respectively. The τ plot is more symmetric than the δj plot, in that the maximum and minimum values are about the same in absolute value, while the δj plot has a greater absolute value for its minimum than its maximum.

The P mode δj plot and τ plot are different in nature, exhibiting a sharp negative spike in the inner disk region for δj , opposite in sign from τ . The values of δj and τ agree in sign only for a small region near the outer edge of the disk. The edge mode δj also has a sharp, negative spike near the inner edge, opposite in sign from τ . It has a very low amplitude, positive region in the outer part of the disk. The A mode δj exhibits a negative spike near the inner edge and is negligible elsewhere.

Quasi-linear analysis may also prove to be important for investigating supercritical instability. In the nonlinear regime, another type of behavior has been noted, a class of disks whose growth saturates at a low amplitude (Woodward *et al.* 1994). It is plausible that Landau supercritical stability is the mechanism responsible for this behavior, hence the term “L modes.” The mechanism responsible for the low amplitude saturation of the instability involves interference of the dominant mode by harmonics

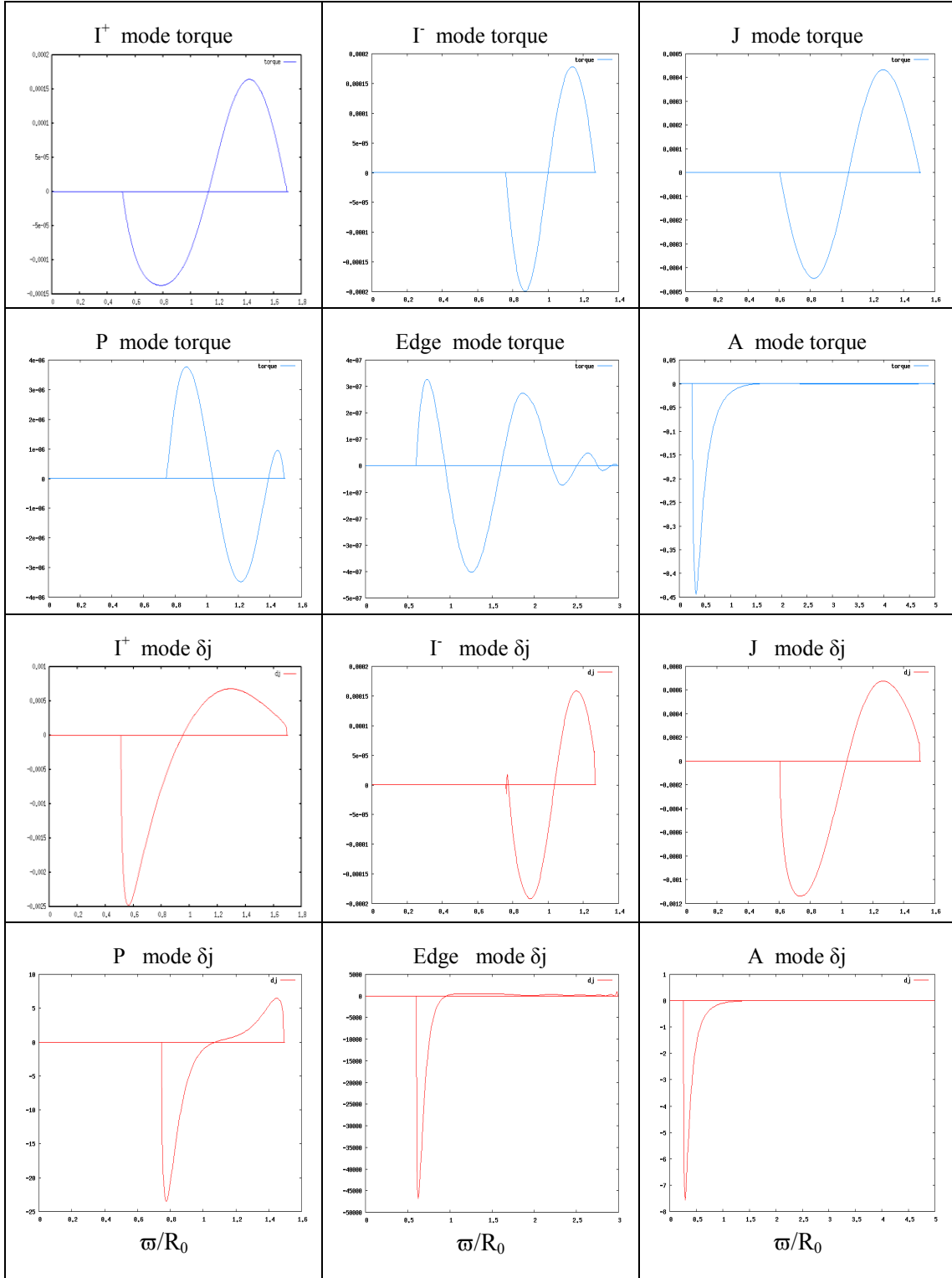


Fig. 3.4.1. Self-gravity torque plotted in blue and δ_j plotted in red for the representative models shown in Fig.3.2.3.

which are generated near a critical stability threshold, distorting the flow. Landau derived the following equation describing the instability:

$$\frac{d}{dt}|A|^2 = 2\sigma|A|^2 - l|A|^4 \quad (3.4.2)$$

where A is the amplitude of the dominant mode, σ is the perturbation frequency and l is a constant, known as Landau's constant (Drazin & Reid, 2004). This is a logistical function, which, when used in hydrodynamic stability calculations, indicates truncation. If $l = 0$, it reduces to the equation used to calculate linear growth. For $l > 0$, the second term on the right-hand side of the equation determines the amplitude at which the nonlinear growth of the mode will saturate. The L modes are not distinct modes *per se*, but rather a specific behavior seen within other mode types. We will discuss L modes more fully in section 5.1.4.

CHAPTER IV

RESULTS

4.1. Equilibrium Results

Our main goal is to understand how angular momentum transport affects evolution of disks over a large sampling of parameter space. Since any small random perturbation away from equilibrium will eventually result in the same temporally evolved model for a given equilibrium disk, the geometry and angular momentum structure must dictate what this result will be. Visual inspection of the mass density contour plots reveals little qualitative difference for small changes in the radial extent of the disk or in the star to disk mass ratio, yet as evidenced in the temporally evolved models, sometimes a very small change can result in a qualitatively different outcome. We calculated an extensive library of over 7700 equilibrium disk models in order to make detailed plots of quantities which may help to determine how an equilibrium disk will evolve. We monitor the virial error as an indication of the reliability of our results. Since angular momentum transport is of crucial importance, we plot the equilibrium total angular momentum. We are specifically studying global rotational and gravitational instabilities, so it is informative to know how $T/|W|$ varies over parameter space. We show plots of the maximum mass density and its radius as indications of the disk geometry. We map the Q -barrier to understand how this evanescent region plays a part in mode development. We present our equilibrium results here, and refer to them in later sections.

We present results for equilibrium models for $q = 1.50, 1.75$ and 2.00 for $0.070 < r_-/r_+ < 0.632$ and $0.007 < M_*/M_d < 128.5$. Since the M_*/M_d are given on a logarithmic axis, we will present the $M_*/M_d = 0.0$ separately. Two models for $q = 1.50$ with small r_-/r_+ and high M_*/M_d are missing because they did not converge to the required tolerance within 1000 iterations. We will refer to Figs A.1.0, B.1.0 and C.1.0 for tables of representative mass density contour plots, shown for meridional slices above the equatorial plane. The density contours represent 10% relative change in density. We show results of our equilibrium calculations in Figs. 4.1.1 - 4.1.8. In these semilog plots,

the domain of the horizontal axis is $3.0 \times 10^{-3} < M_*/M_d < 1.5 \times 10^2$ while the range of the vertical axis is $0.0 < r/r_+ < 0.70$.

We track the virial error of the models as shown in plots in the upper panels of Fig. 4.1.1. Virial error for $q = 1.5, 1.75$ and 2.0 increases for high r/r_+ and low M_*/M_d . It seems to track the Maximum Initial Rotation Period (MIRP) which is the equilibrium period at the radius of the maximum mass density ρ_0 as shown in the lower panels of Fig. 4.1.1. Qualitatively, we would expect that the MIRP should increase as r/r_+ increases since the disks become narrower and have subsequently higher $T/|W|$. We also see in Eqn. 3.1.10 that $\Omega_0^2 \propto R_0^{-2} \propto \rho_0^{2/3}$. This indicates that as the MIRP increases, the distance between the disk and the central star increases, and the mass density decreases. This would inherently tend to make the disk less stable, since the disk would be very far away from the star, rotating rapidly with low density, producing a higher virial error.

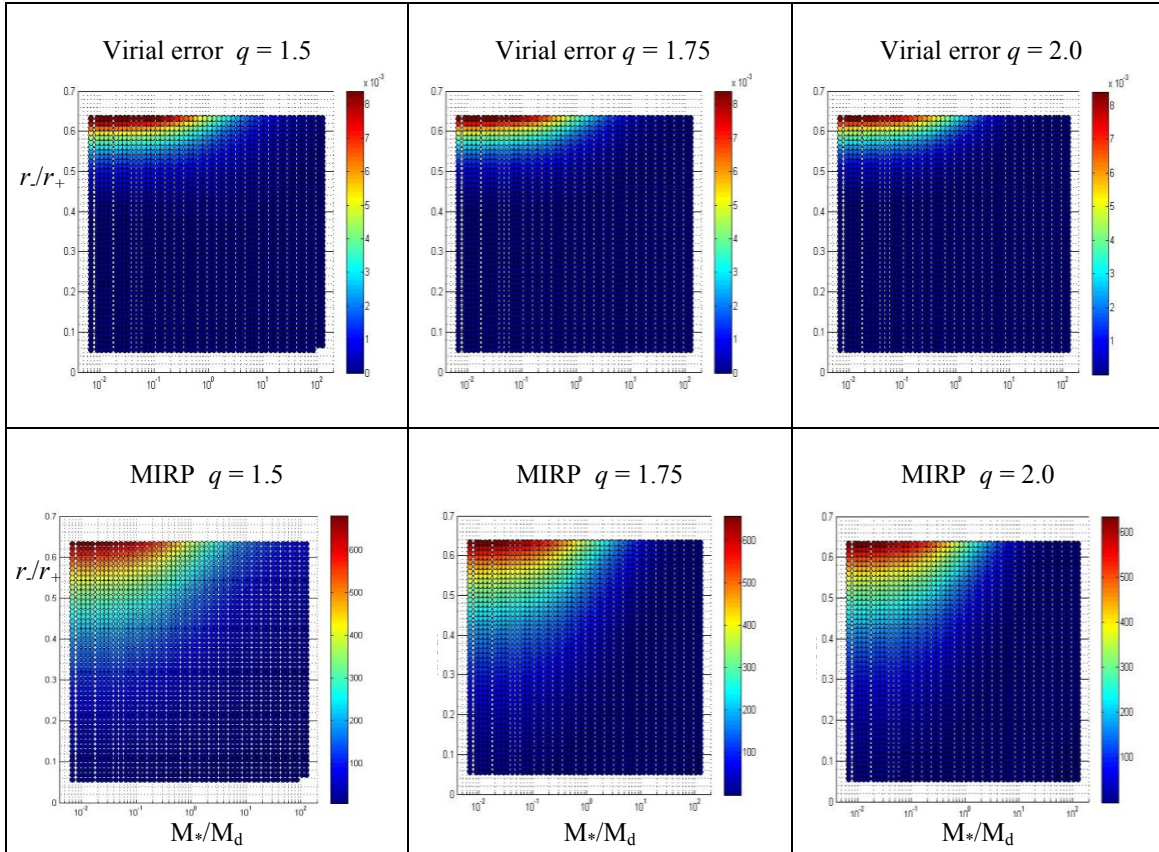


Fig. 4.1.1. Virial error (upper panels) and MIRP (lower panels) for $q = 1.50, 1.75$ and 2.0 .

Fig. 4.1.2 shows plots for total angular momentum J_{total} as q varies. We see that $q = 1.5$ disks exhibit larger total angular momentum for small r/r_+ and large M^*/M_d . The range of the color bars for the $q = 1.5$, 1.75 and 2.0 plots are 0 - 60, 0 - 18 and 0 - 12, respectively. From Figs A.1.0, B.1.0 and C1.0, it is obvious that the $q = 1.5$ disks are flatter than $q = 1.75$ and 2.0 disks, and R_0 is higher, increasing total angular momentum. Self-gravitating disks with $q = 1.5$ must have pressure gradients present to balance the self-gravity to support a Keplerian profile. For large M^*/M_d the frequency at R_0 approaches Keplerian frequency, since self-gravity is negligible in these disks. The pressure support is therefore also small, so the disks are flattened.

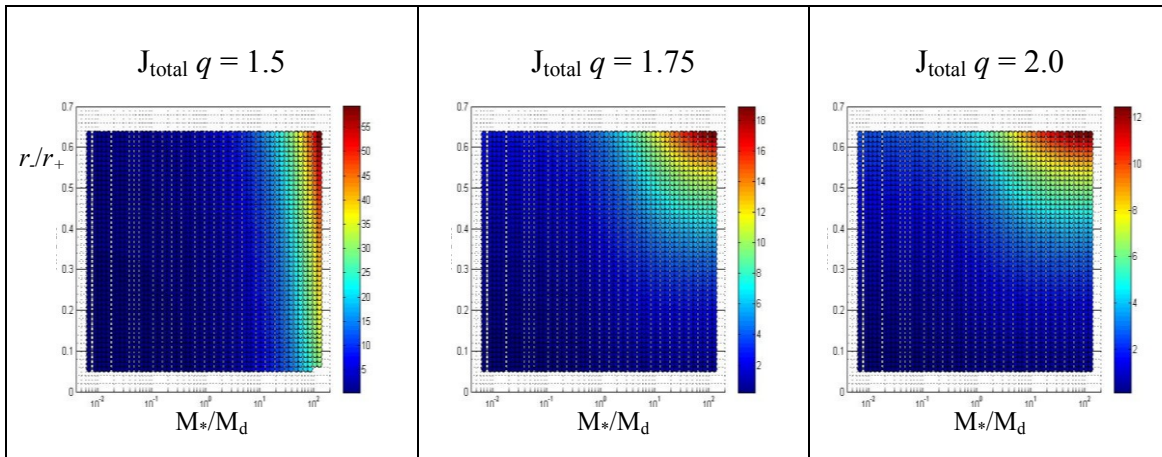


Fig. 4.1.2. Total angular momentum for $q = 1.50$, 1.75 and 2.0.

We normalize various radii in the disk using the radius of the maximum density R_0 , so it is useful to plot R_0 as well as the values of ρ_0 as shown in polytropic units in Figs. 4.1.3 and 4.1.4. In the upper panels we see that R_0 increases as r/r_+ since a narrower disk has the effect of the inner edge moving away from the central star. Examining mass density contour plots in Figs A.1.0, B.1.0 and C.1.0, it is obvious that for high r/r_+ and high M^*/M_d , smaller q lowers angular velocity toward the inner edge of the disk and increases it toward the outer edge which moves R_0 outward, giving qualitatively different results for $q = 1.5$ compared to those for $q = 1.75$ and 2.0. The color bars for $q = 1.75$ and 2.0 reach maximum values of 16, each. In Fig. 4.1.4, we again

see qualitatively different results for $q = 1.5$ as compared to $q = 1.75$ and 2.0 . The color bars next to the plots indicate that ρ_0 reaches maximum values 4 orders of magnitude higher for $q = 1.75$ and 2.0 than for $q = 1.5$.

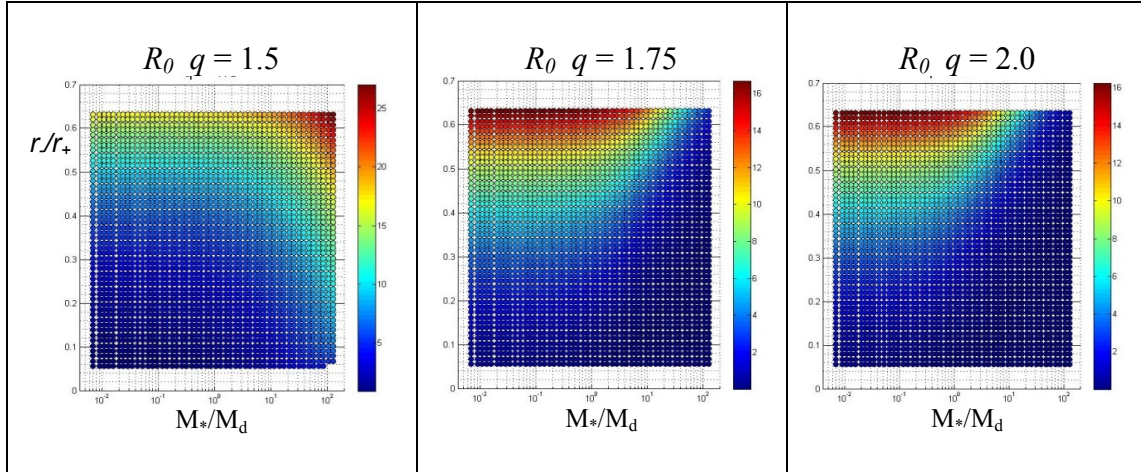


Fig.4.1.3. Location of R_0 for M^*/M_d vs. r/r_+ for $q = 1.50, 1.75$ and 2.0 .

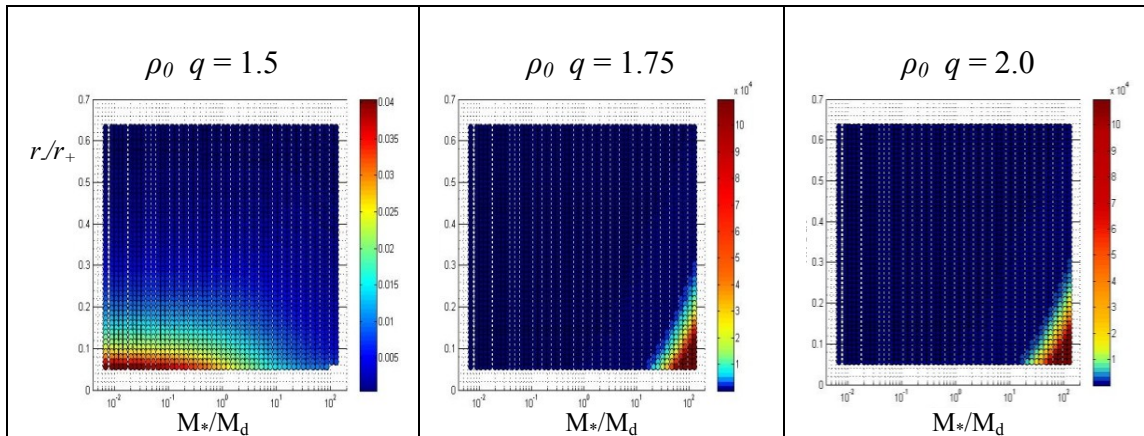


Fig.4.1.4. Maximum mass density ρ_0 for M^*/M_d vs. r/r_+ for $q = 1.50, 1.75$ and 2.0 .

Since our focus is on rotational and gravitational instabilities, one of the main parameters we use for analysis of equilibrium disks is the ratio of the rotational kinetic energy versus the gravitational potential energy, $T/|W|$. In Fig. 4.1.5 we show semilog plots of $T/|W|$ for M^*/M_d vs. r/r_+ for $q = 1.50, 1.75$ and 2.00 . The higher J_{total} of the

$q = 1.50$ disks is evident in the higher values of $T/|W|$ for large M^*/M_d . The color bar indicates rotational kinetic energy shows a maximum of ~ 0.5 as we would expect from the virial theorem for the largest M^*/M_d and r/r_+ . We see that varying q has little effect for large r/r_+ . $T/|W|$ decreases as r/r_+ decreases for high M^*/M_d models.

The lower panels in Fig. 4.1.5 shows $T/|W|$ vs. M^*/M_d for varying q . The color bars represent varying r/r_+ here. We see that is more variance in $T/|W|$ for low star mass models than high star mass models. As shown in Fig. 3.1.4, we see that the $q = 1.5$ models are considerably flatter than $q = 1.75$ and 2.0 models for large M^*/M_d . Their azimuthal velocities are higher toward the outer edge, displacing mass further out in the disk and increasing $T/|W|$.

The Q -barrier is defined as the region where the Toomre Q parameter is less than unity (eqn. 3.1.13). We see that $Q > 1.0$ in all of the models at r/R_0 and also at r_+/R_0 .

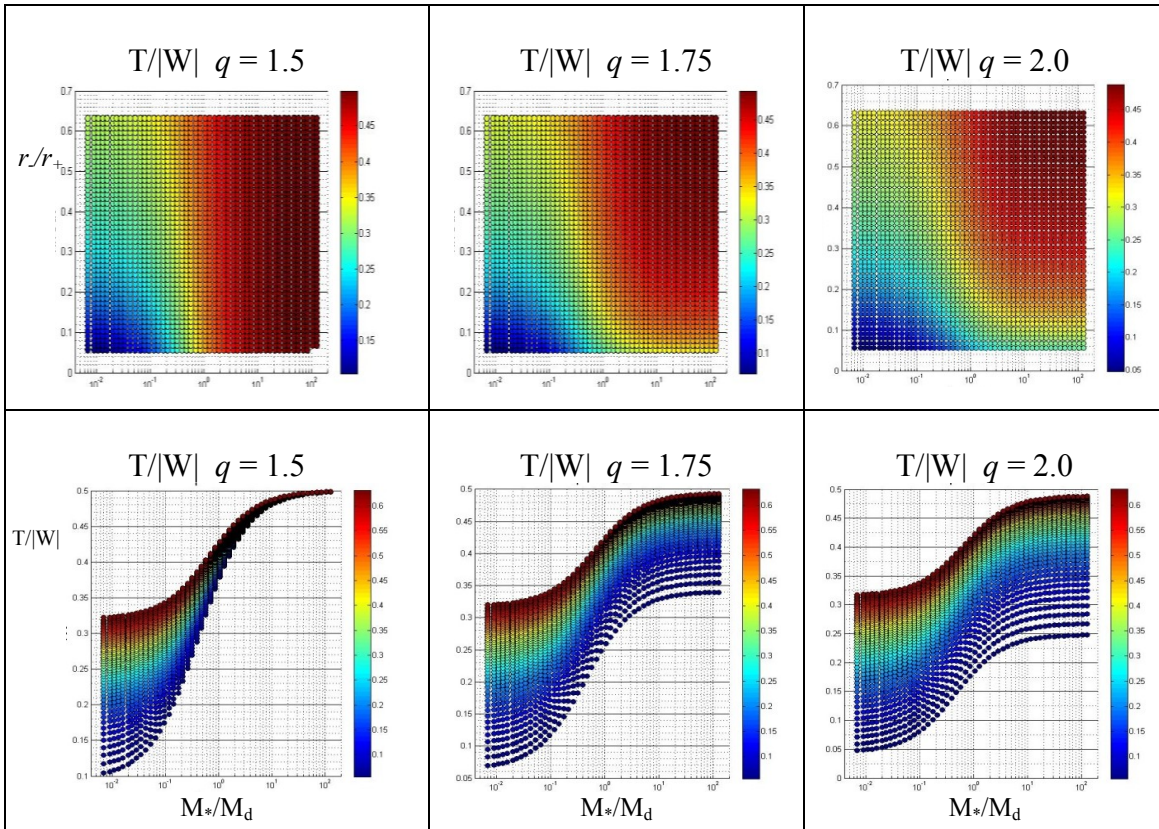


Fig. 4.1.5. $T/|W|$ for $q = 1.5, 1.75$ and 2.0 . In the upper panels, the color bar indicates $T/|W|$. In the lower panels, the color bar indicates the value of r/r_+ .

We define Q_- as the lowest value of ϖ/R_0 where $Q < 1.0$. Q_+ is defined as the right side of the region where $Q < 1.0$. If $Q > 1.0$ everywhere in the disk, $Q_- = 0.0$ and $Q_+ = r/R_0$. Fig. 4.1.6 displays Q_- and Q_+ for $q = 1.50$ and 1.75 . There are no plots included for $q = 2.0$ since $Q_- = Q_+ = 0$ for $q = 2.0$. We see qualitatively similar behavior for $q = 1.5$ and 1.75 but note the higher magnitudes shown on the color bars. The range of the Q_- plot for $q = 1.5$ is $0.0 < Q_- < 1.5$, whereas the range of the Q_- plot for $q = 1.75$ is $0.0 < Q_- < 3.5$. The dark blue areas on the right-hand side of the Q_- indicate the region of parameter space where there is no part of the disk in which $Q < 1.0$. In that region, Q_+ becomes the radius of the inner edge of the disk. The range of the Q_+ plot for $q = 1.5$ is $0.25 < Q_+ < 3.0$, whereas the range of the Q_+ plot for $q = 1.75$ is $0.5 < Q_+ < 5.5$.

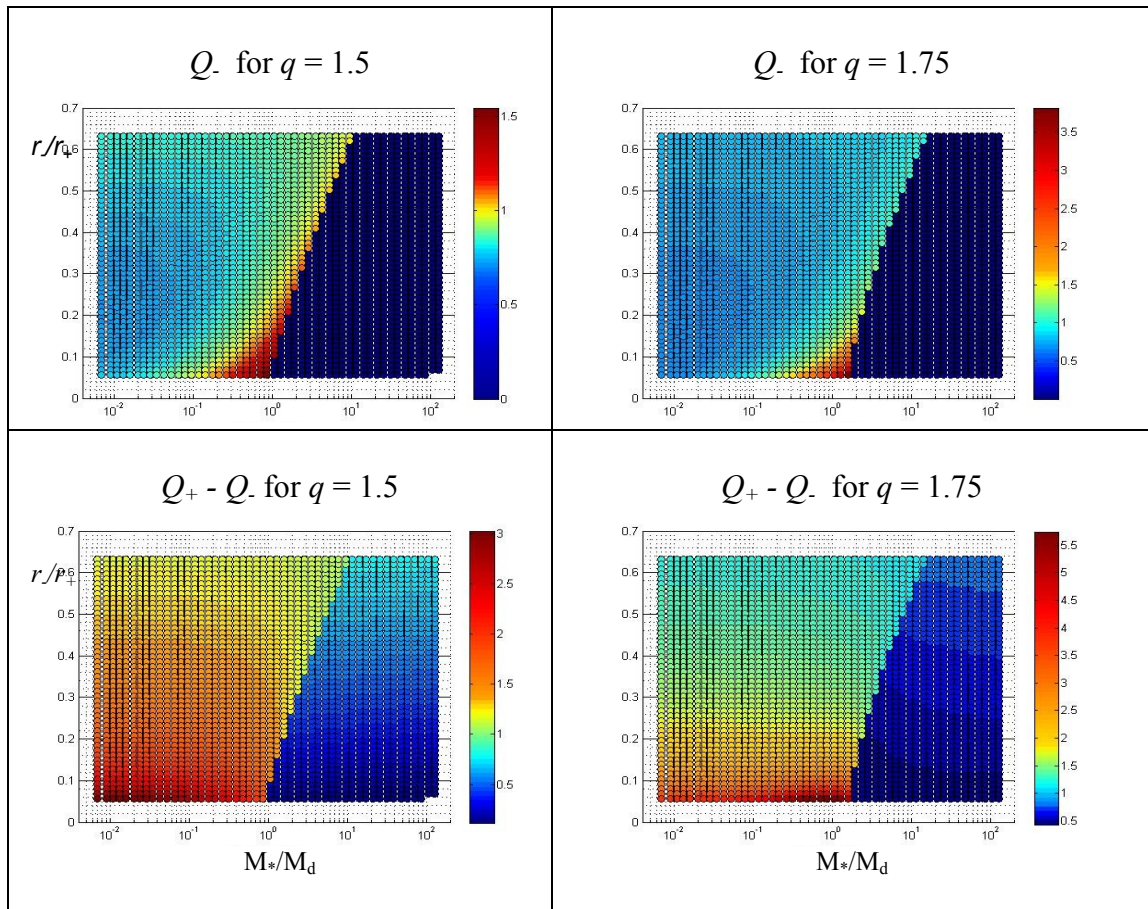


Fig. 4.1.6. Q_- , Q_+ and $Q_+ - Q_-$ for $q = 1.5$ and 1.75 .

The region where $Q < 1.0$ is wide, in general, for small M^*/M_d and decreases in width monotonically with M^*/M_d until it disappears. The minimum width of the $Q < 1.0$ region increases as r/r_+ decreases. Fig. 4.1.7 includes plots of the width of the Q -barrier, specifically, the difference of Q_+ and Q_- . We see that the width of the Q -barrier decreases as M^*/M_d increases, up to the division where the Q -barrier no longer exists in the disk.

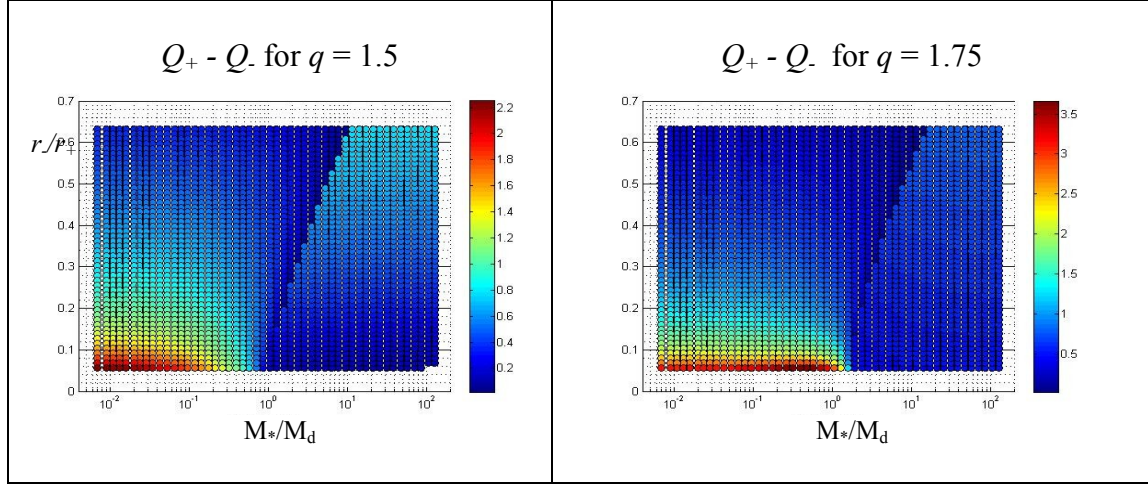


Fig. 4.1.7. $Q_+ - Q_-$ for $q = 1.5$ and 1.75 .

Next we examine how the effect of pressure compares with the effect of self-gravity in a disk. We follow the analysis of Christodoulou and Narayan (1992) who defined two self-gravity parameters for analysis of their self-gravitating slender annuli. To measure the strength of self-gravity compared to pressure, we define p , shown in Fig. 4.1.7:

$$p_n^2 \equiv \frac{4\pi G}{\Omega_0^2} \left(\frac{\Omega_0^2 R_0^2}{k(n+1)} \right)^n \quad (4.1.1)$$

To measure the strength of the self-gravity of the disk as compared to the gravity of the central star, we define η , shown in Fig. 4.1.8:

$$\eta \equiv \frac{\Omega_K^2}{\Omega_0^2} \text{ where } \Omega_K \equiv \frac{M_*}{R_0^3} \text{ in polytropic units.} \quad (4.1.2)$$

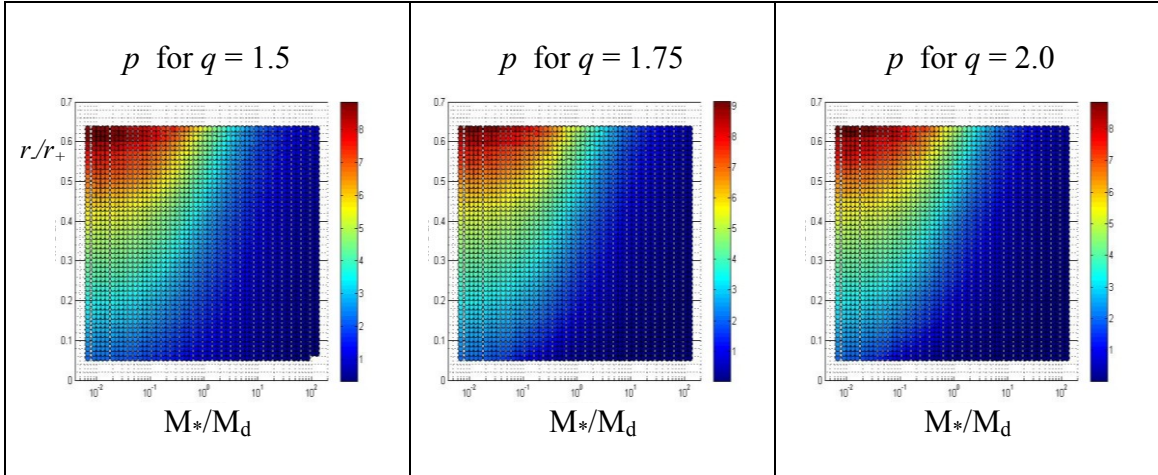


Fig. 4.1.8. Self-gravity parameter p for $q = 1.5, 1.75$ and 2.0 .

We will compare η and p plots with the general trends of behavior for the $q = 1.5, 1.75$ and 2.0 models in Sections 4.2.2, 4.2.3 and 4.2.4, respectively.

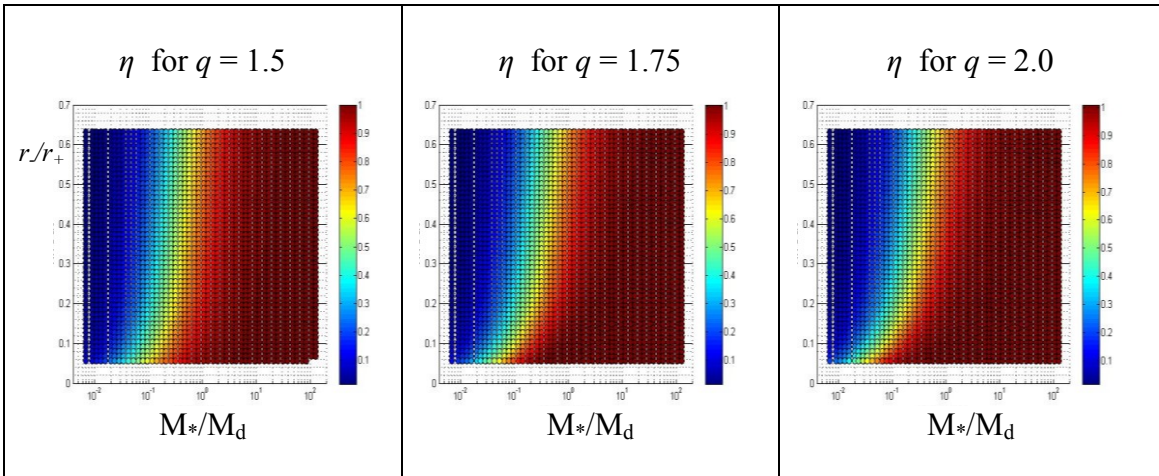


Fig. 4.1.9. Self-gravity parameter η for $q = 1.5, 1.75$ and 2.0 .

4.2. Linear Results

Here we present results for the time dependent models. We have calculated and analyzed over 2100 temporally evolved models in total. We begin by discussing similarities in trends for dominance of various m . In particular for small M_*/M_d low order modes dominate for small $r./r_+$ and higher order modes dominate as $r./r_+$ increases, regardless of q . As M_*/M_d increases, $m = 3$ and 4 become stable, or at least have very low growth rates and the lower m modes dominate to higher values of $r./r_+$. We will more closely examine the relationship between q and the regions of dominance for values of m in Figs. 4.2.1 and 4.2.2.

Three main realms of behavior become evident as we plot y_2 vs. $r./r_+$ for $M_* \ll M_d$, $M_* \approx M_d$ and $M_* \gg M_d$ and will examine characteristic plots for each realm in some detail, namely, the $M_*/M_d = 0.0$, 1.0 and 10.0 plots for $q = 1.5$. Fig.4.2.6 presents the y_2 values of M_*/M_d models in general, indicating the growth rates as functions of m . Fig. 4.2.7 presents the y_1 values of the same sequence of models. We have not included figures for $M_*/M_d > 10.0$ due to the sparse nature of the data, but do indicate modal dominance in Figs 4.2.1 and 4.2.2.

The perturbation frequencies that generate the y_1 values also allow us to calculate the corotation radii, R_{co} , for the given models. It is informative to map behavioral trends of regions of parameter space for given m and q . Figs 4.2.8 - 4.2.11 indicate general trends found as well as stability regions. We will give more detailed maps of the m , q slices of parameter spaces in the following subsections where $q = 1.5$, 1.75 and 2.0 are addressed separately. The main interest of this research is to understand how disks evolve, in particular, how torque causes angular momentum transport which modifies the structure of the disk. The behaviors of perturbed angular momentum and torque for different portions of parameter space are discussed. Trends in the stresses and work integrals for various parts of parameter space are also investigated.

We begin by charting which m modes dominate the disks for a given q , $r./r_+$ and M_*/M_d . Fig. 4.2.1 indicates which m values are unstable, in order of growth rates listed highest to lowest. For example, for $q = 1.5$, $M_*/M_d = 0.01$, $r./r_+ = 0.30$, the growth rate for $m = 2$ was the highest, followed by $m = 1$ and $m = 3$, while $m = 4$ was stable. The cells

of the table are colored by the dominant mode, with $m = 1, 2, 3$ and 4 shown in blue, green, yellow and red, respectively. Table 4.2.1 gives the modal dominance for $q = 1.5$ disks. The general trend is that higher m modes dominate as r/r_+ increases, with disks becoming stable as M_*/M_d increases. Smaller r/r_+ models become stable at lower ratios of M_*/M_d . As for modal dominance, there are a few outliers which can be understood by examining the y_2 plots in Fig. 4.2.6. For example, $m = 2$ dominates the models for $M_*/M_d = 1.0$ where $r/r_+ = 0.65$, where we would expect to see $m = 4$ dominance. Investigation of the y_2 values indicates that the $m = 2$ growth rate is slightly higher than that of the $m = 3$ mode, which can barely be discerned in the growth rate plots since the $m = 3$ data point lies near the $m = 2$ data point. The modal dominance tables are meant to be a quick reference of the overall trends of modal domination, with a clearer picture emerging as one investigates the data plots and tables. Note that some models have been omitted from the tables due to resolution issues. Similarly, the $q = 1.75$ table in Fig. 4.2.2 indicates that models for $M_*/M_d = 0.0$ and $r/r_+ < 0.20$ are stable while those models for

$q = 1.5$									
r/r_+	M_*/M_d								
	0.0	0.01	0.1	1.0	5.0	10.0	25.0	50.0	100.0
0.65	4 3 2 1	4 3 2 1	4 3 2 1	2 3 4 1	4 2 1	4 2	3 4 2	4	stable
0.60	4 3 2 1	4 3 2 1	4 3 1 2	4 3 2 1	3 4 2 1	3 2 4	3 4 2	3 4 2	stable
0.55	4 3 2 1	4 3 2 1	4 3 1 2	4 3 2 1	3 2 4	2 3 4	4 3 2	3 4	stable
0.50	4 3 1 2	4 3 1 2	4 3 1 2	3 4 2 1	2 3 4 1	2 3 4	3 4 1	3 4 2	stable
0.45	3 4 1 2	3 4 1 2	4 1 2 3	3 2 4 1	2 3 4 1	2 3 4	2 3 4	stable	stable
0.40	3 4 1 2	3 4 1 2	2 1 3 4	2 3 1 4	2 3 4 1	2 3 4 1	3 4 2	stable	stable
0.35	1 3 4 2	1 3 2 4	2 3 1 4	2 1 3 4	2 3 1 4	2 3 4	2 3	stable	stable
0.30	2 1	2 1 3	2 1 3	1 2 3 4	2 1 3 4	2 3 4	3 2	stable	stable
0.25	2 1	2 1	2 1 3	1 2 3	2 1	2 3	stable	stable	stable
0.20	2 1	2 1	1 2	1 2 3	2 1	2	stable	stable	stable
0.15	2 1	1 2	1 2	1 2	2 1 3	2	stable	stable	stable
0.10	1	1	1	1	1 2	2	stable	stable	stable
0.05	1	1	1 2 3	1	1	2	stable	stable	stable

Table 4.2.1. Approximate modal dominance regimes for $q = 1.5$ for $m = 1, 2, 3$, and 4 .

$q = 1.5$ are unstable to $m = 2$ modes, but it should also be noted that the growth rates for these $m = 2$ modes are very low. There are also unstable $m = 1$, $q = 1.75$ models reported for $M_*/M_d > 10.0$ but it should be noted that the growth rates are small, typically 0.01 - 0.04 MIRP's. Stability sets in for M_*/M_d as low as 5.0 for the lowest r/r_+ value tested.

The $q = 1.5$ table indicates a large region of $m = 2$ dominance for $M_*/M_d > 5.0$ that is not seen in the $q = 1.75$ or 2.0 models. There is further discussion of this in the characteristic region is for $M_* \gg M_d$, illustrated in Fig. 4.2.4. Perhaps one of the major points brought out in the modal dominance tables is that $q = 2.0$ models do not become stable at high M_*/M_d , but remain highly unstable to $m = 1$ modes. Growth rate plots are not pictured here for $q = 2.0$, $M_*/M_d > 10.0$ but are qualitatively similar to the plot shown for $M_*/M_d = 10.0$. In fact, with a few deviations, the modal dominance plots show strong similarity for $q = 1.5$, 1.75 and 2.0 for $M_*/M_d \leq 1.0$ and strongly diverge for higher M_*/M_d . Recalling the equilibrium results, it can be seen that for small M_*/M_d , $q = 1.5$, 1.75 and 2.0 have very similar total angular momentum as seen in Fig. 4.1.2, and $T/|W|$, as seen in Fig. 4.1.4, so it may not be so surprising that their evolution would be similar. $T/|W|$ diverges at about $M_*/M_d \geq 1.0$, for small r/r_+ , for $q = 1.5$ as opposed to $q = 1.75$ and 2.0, which are similar to each other. This is similar to the trend we note in the modal dominance tables. This would seem to indicate that higher $T/|W|$ in $M_*/M_d \geq 1.0$ tends to support $m = 2$ modes. However, there is nothing in the $T/|W|$ plots to suggest why $q = 1.75$ diverges from $q = 2.0$ for higher M_*/M_d . It should also be noted here that there is no Q -barrier as such in a $q = 2.0$ disk, since $Q = 0$ everywhere so $Q < 1$ everywhere. This is a trait that sets it apart from $q = 1.5$ and 1.75 and possibly contributes to the lack of a stable region for a $q = 2.0$.

Figs. 4.2.3 - 4.2.5 present $M_*/M_d = 0.0$, 1.0 and 10.0 plots for $q = 1.5$ as characteristic plots illustrating three main behavioral trends for y_2 vs. r/r_+ for $M_* \ll M_d$, $M_* \approx M_d$ and $M_* \gg M_d$. We first examine the plot of $M_*/M_d = 0.0$ shown in Fig. 4.2.3. We see that all m modes go toward stable at $r/r_+ = 0.05$ for $q = 1.5$ with $M_*/M_d = 0.0$. The phase plots in Fig. A.1.2.2 show that the $m = 2$ modes that dominate for $0.10 < r/r_+ < 0.30$ have R_{co} moving closer to r_+ as we expect from I modes. Models with $m = 1$ also exhibit R_{co} near r_+ for small r/r_+ but they change character to $R_{co} < r$ for $r/r_+ \geq 0.30$. We refer to these I modes as Γ^+ and Γ^- for convenience. The $m = 1$ growth

$q = 1.75$									
$r./r_+$	M_*/M_d								
	0.0	0.01	0.1	1.0	5.0	10.0	25.0	50.0	100.0
0.65	4 3 2 1	4 3 2 1	4 3 1 2	2 4 3 1	4 3 2	4 3 2	stable	stable	stable
0.60	4 3 2 1	4 3 2 1	4 3 1 2	4 3 2 1	3 4 2	3 2 4 1	3 1 2	1	stable
0.55	4 3 2 1	4 3 2 1	4 3 1 2	3 4 2 1	3 2 4 1	3 2 1	1 3	1	1
0.50	4 3 2 1	4 3 2 1	4 3 1 2	3 2 4 1	2 3 1 4	1 2 3 4	1	1	1
0.45	3 4 1 2	3 4 1 2	2 1 3 4	2 3 1 4	1 2	1	1	1	1
0.40	3 1 4 2	3 1 4 2	2 1 3 4	1 2 3	1 2	1	1	1	1
0.35	1 2	1 2 3	2 1 3	1 2	1 2 3	1	1	1	stable
0.30	2 1	2 1	2 1 3	1 2 3	1	1 3	1	1	stable
0.25	2 1	2 1	1	1	1	1	1	stable	stable
0.20	2	1 2	1 2	1	1	1	stable	stable	stable
0.15	stable	1	1 2	1	1	stable	stable	stable	stable
0.10	stable	1	1	1	1	stable	stable	stable	stable
0.05	stable	1	1	1	stable	stable	stable	stable	stable
$q = 2.0$									
0.65	4 3 2 1	4 3 2 1	4 3 2 1	4 2 3 1	4 3 2 1	3 4 1 2	1	1 3 2	2 3 1 4
0.60	4 3 2 1	4 3 2 1	4 3 1 2	3 4 2 1	3 2 4 1	1	1	1 2 4	2 1 4
0.55	4 3 2 1	4 3 2 1	4 3 1 2	3 4 2 1	1 2 3 4	1 4	1 2 3 4	1 2 3	2 1 3
0.50	3 4 2 1	3 4 1 2	4 1 2 3	3 2 1 4	1 3 2	1 4 3	1 3 2 4	1 2 3	1 2 3 4
0.45	3 4 1 2	3 4 1 2	2	1 2 3 4	1 3	1 3 4	1 4 3 2	1 4 2 3	1 2 3 4
0.40	3 1	1 2 3	2 1 3	1 2 3	1 4 2	1 3 2 4	1 2 4 3	1 2 4 3	1 2 3 4
0.35	2 1	2 1	2 1 3	1 2 4	1 2 4	1 2 4	1 2 3 4	1 2 3 4	1 2 3 4
0.30	2 4	2 1	1 2	1 2 3 4	1 3 2	1 2	1 2 3 4	1 2 3 4	1 2 3 4
0.25	2	1 2	1 2	1 2	1 3 4 2	1 2 3 4	1 2 3 4	1 2 3 4	1 2 3 4
0.20	stable	1	1 2	1 3	1 2 4	1 2 3 4	1 2 3 4	1 2 3 4	1 2 3 4
0.15	stable	1 2	1	1 2 3	1 2 3	1 2 3 4	1 2	1 2 3	1 2 3
0.10	stable	1 2	1 2	1 2 3	1 2 3	1 2 3 4	1 2 3	1 2 3	1 2 3
0.05	stable	1	1	1	1 2	1 2	1	1	1 2 3

Table 4.2.2. Approximate modal dominance regimes for $q = 1.75$ and 2.0 for $m = 1, 2, 3,$ and 4 .

rates are increasing where the $m = 2$ drop toward stable where they change from I to J modes, so the $m = 1$ modes dominate for a small region of parameter space. The $m = 3$ and 4 growth rates increase to overtake them for $r./r_+ > 0.35$ and exhibit J mode behavior for this region. The y_2 plot for $M_*/M_d = 0.01$ shows similar behavior except for the $m = 1$ modes at small $r./r_+$ which show increased growth rates due to the perturbation of the central star. These $m = 1$ modes have R_{co} near R_0 .

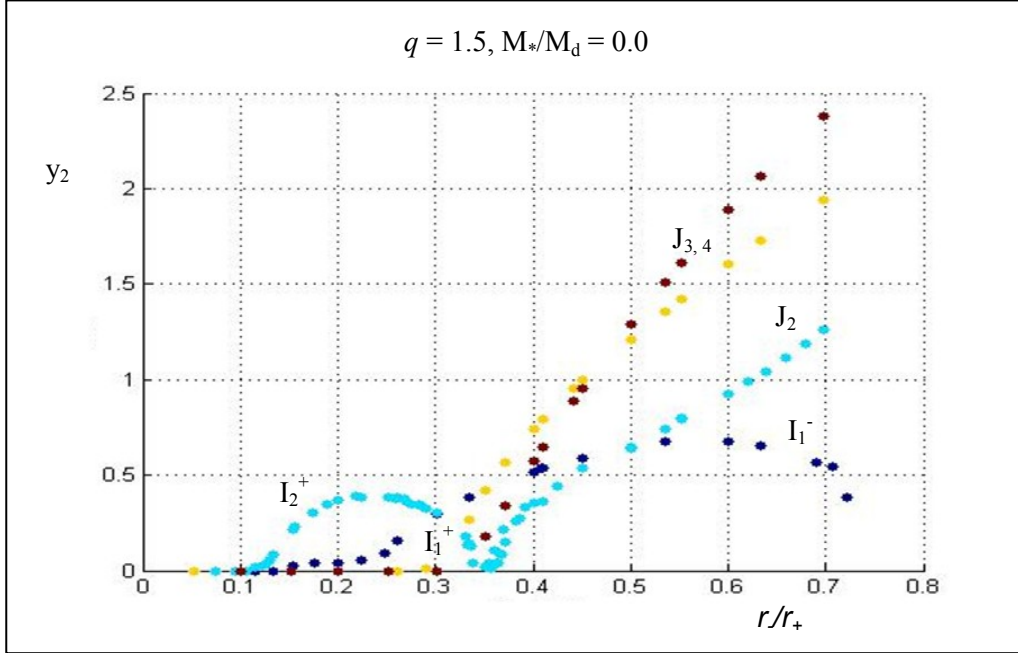


Fig. 4.2.3. First characteristic plot, for $M_* < M_d$, showing y_2 for $q = 1.5$, $M_*/M_d = 0.0$, with $m = 1, 2, 3$ and 4 plotted in dark blue, turquoise, yellow and red, respectively.

The second characteristic type of growth rate plot is for $M_* \approx M_d$, and we illustrate it using $q = 1.5$, $M_*/M_d = 1.0$ as shown in Fig. 4.2.4. The $m = 1$ modes now dominate for a much wider range of r/r_+ . As Fig. A.1.1 shows, the $m = 1$ modes exhibit R_{co} near R_0 for $0.05 \leq r/r_+ \leq 0.50$. For models with $m = 2$, I modes dominate a small region where the $m = 1$ modes decrease around $r/r_+ \approx 0.40$. For higher r/r_+ , the higher m modes dominate.

The third characteristic region is for $M_* \gg M_d$ illustrated in Fig. 4.2.4, with $q = 1.5$, $M_*/M_d = 10.0$. Models with $m = 1$ are stable over most of this region and the other modes all grow approximately monotonically with r/r_+ . I modes dominate almost the entire region with $m = 2$ growth rates the highest for all disks with $r/r_+ \leq 0.60$. Models with $q = 1.75$ and 2.0 exhibit trends in their growth rate plots for $M_*/M_d = 10.0$ that resemble those of lower $M_*/M_d = 1.0$ for $q = 1.5$. Growth rate plots for $M_*/M_d = 25.0$ and 50.0 qualitatively resemble this characteristic plot. For $q = 1.5$, disks become stable as M_*/M_d increases, with all disks stable at $M_*/M_d = 100.0$. Stability sets in for lower M_*/M_d for lower values of r/r_+ as is evidenced in Fig. 4.2.1. Most $m = 1$ models are stable for $M_*/M_d \geq 10.0$.

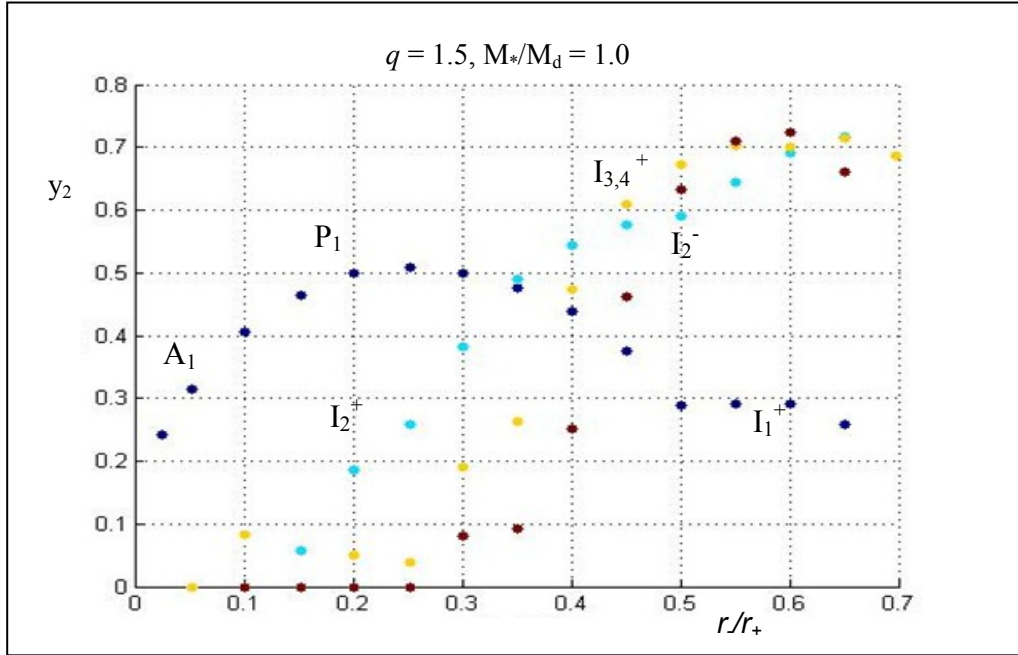


Fig. 4.2.4. Second characteristic plot, for $M_* \approx M_d$ with y_2 for $q = 1.5$, $M_*/M_d = 1.0$, with $m = 1, 2, 3$ and 4 plotted in dark blue, turquoise, yellow and red, respectively.

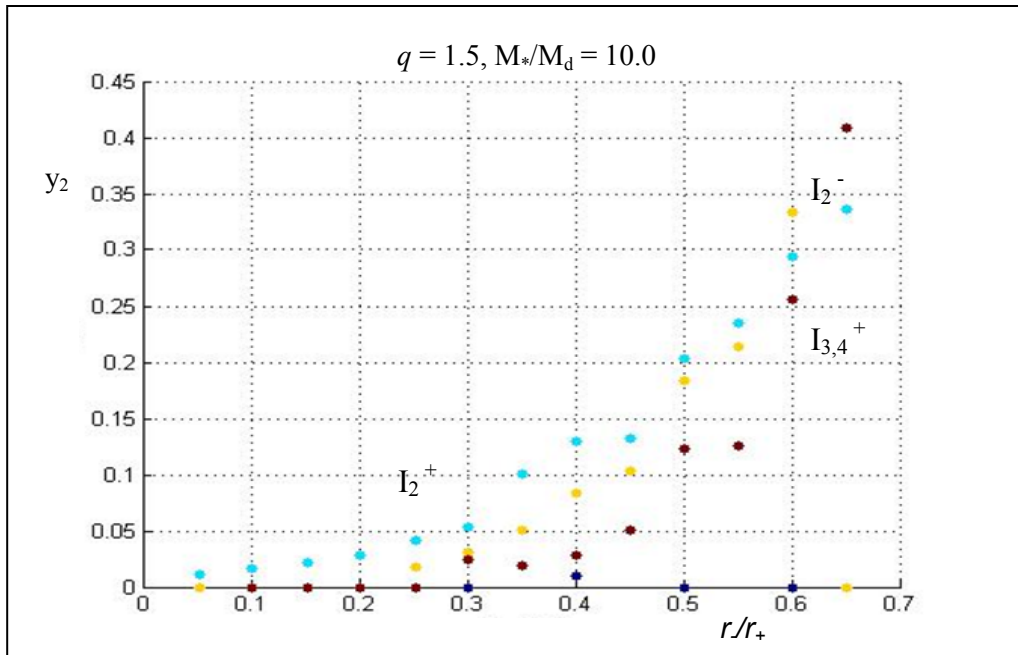


Fig. 4.2.5. Third characteristic plot, for $M_* > M_d$, with y_2 for $q = 1.5$, $M_*/M_d = 10.0$, with $m = 1, 2, 3$ and 4 plotted in dark blue, turquoise, yellow and red, respectively.

Fig. 4.2.6 presents y_2 eigenvalue plots for comparison of $q = 1.5, 1.75$ and 2.0 for selected values of M^*/M_d for $m = 1, 2, 3$ and 4 . This plot sequence illustrates the transitions between the regimes $M^*/M_d \ll 1.0$, $M^*/M_d \approx 1.0$, and $M^*/M_d \gg 1.0$. A more detailed description of these plots for the $q = 1.5$ case will be given in the $q = 1.5$ subsection, and references of the growth rates of individual models depicted in these plots can be found throughout this dissertation. Values of y_2 for selected models are found in Tables 4.2.2.1, 4.2.3.1 and 4.2.4.1 for $q = 1.5, 1.75$ and 2.0 , respectively.

Fig. 4.2.7 shows the y_1 eigenvalue plots for the same sequence of models. The y_1 values give insight about how the perturbation frequencies affect the mode dominance in the disks. For example, in the $q = 1.5, M^*/M_d = 0.0$ plot, there is a jump in the y_1 values around $r./r_+ \approx 0.35$ in the $m = 2$ eigenvalues which corresponds to a shift from the low frequency I modes to the higher frequency J modes. The jump from I to J mode frequencies is also seen in the $q = 1.75$ and $2.0, M^*/M_d = 0.0, m = 2$ plots at about the same $r./r_+$. A similar jump in y_1 for the $m = 1$ modes is obvious, occurring $r./r_+ \approx 0.24$ in the $q = 1.5$ plot. It is not seen in the $q = 1.75$ and 2.0 plots because $m = 1$ modes are stable for $r./r_+ < 0.25$. The $m = 3$ and 4 models are similar to each other in y_1 values, increasing monotonically with $r./r_+$. The $M^*/M_d = 0.01$ plots look similar to the $M^*/M_d = 0.0$ plots, with raised frequencies for low $r./r_+$ in the $m = 1$ mode as expected. The $M^*/M_d = 0.1$ plots indicate that the frequency shifts move toward higher $r./r_+$ for $m = 1$. Similarly to the trends noted for the growth rate plots, the y_1 plots seem to naturally group into behaviors associated with $M^* \ll M_d$, $M^* \approx M_d$ and $M^* \gg M_d$.

It can be seen from the absence of data points that there are regions of stability associated with the patterns of y_1 behavior. To visualize this further, Figs 4.2.8 - 4.2.11 show qualitative maps of parameter space defined by $r./r_+$ vs. M^*/M_d for $m = 1, 2, 3$ and 4 . These maps indicate approximate regions of stability as well as approximate regions defined by the corotation radius for unstable regions. Boundaries for $q = 1.5$ are given by blue, round-dotted lines, while boundaries for $q = 1.75$ and 2.0 are given by orange, dashed lines and black, square-dotted lines respectively. The $m = 2$ map indicates a region of J modes, where $R_{co} \approx R_0$, for roughly $0.0 \leq M^*/M_d < 0.10$ and $r./r_+ < 0.40$, where $q = 1.5, 1.75$ and 2.0 overlap that extends to $M^*/M_d < 1.0$ for $m = 3$ and 4 .

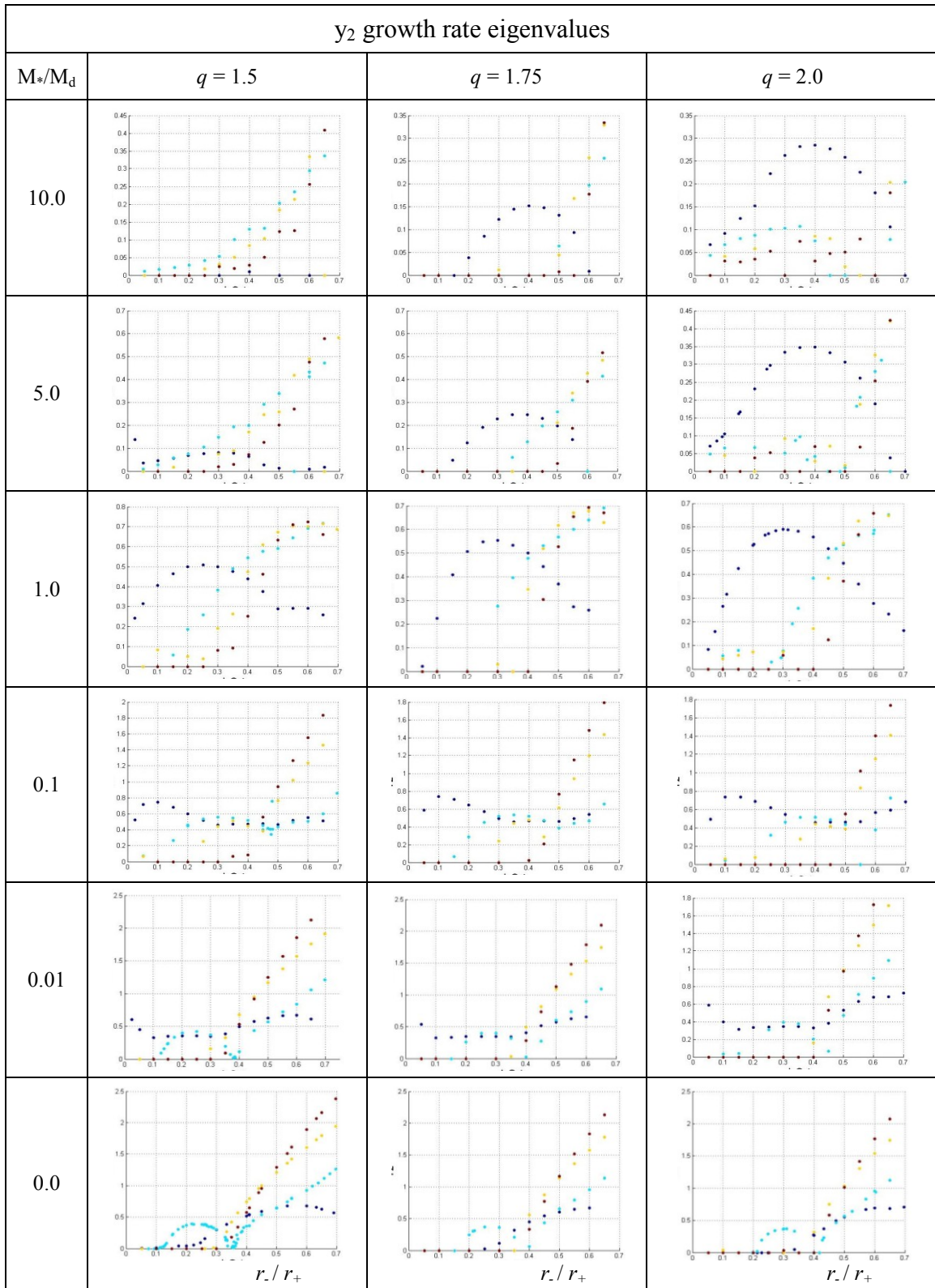


Fig. 4.2.6. y₂ eigenvalues for q = 1.5, 1.75 and 2.0. Values for m = 1, 2, 3 and 4 are shown in dark blue, turquoise, yellow and red, respectively.

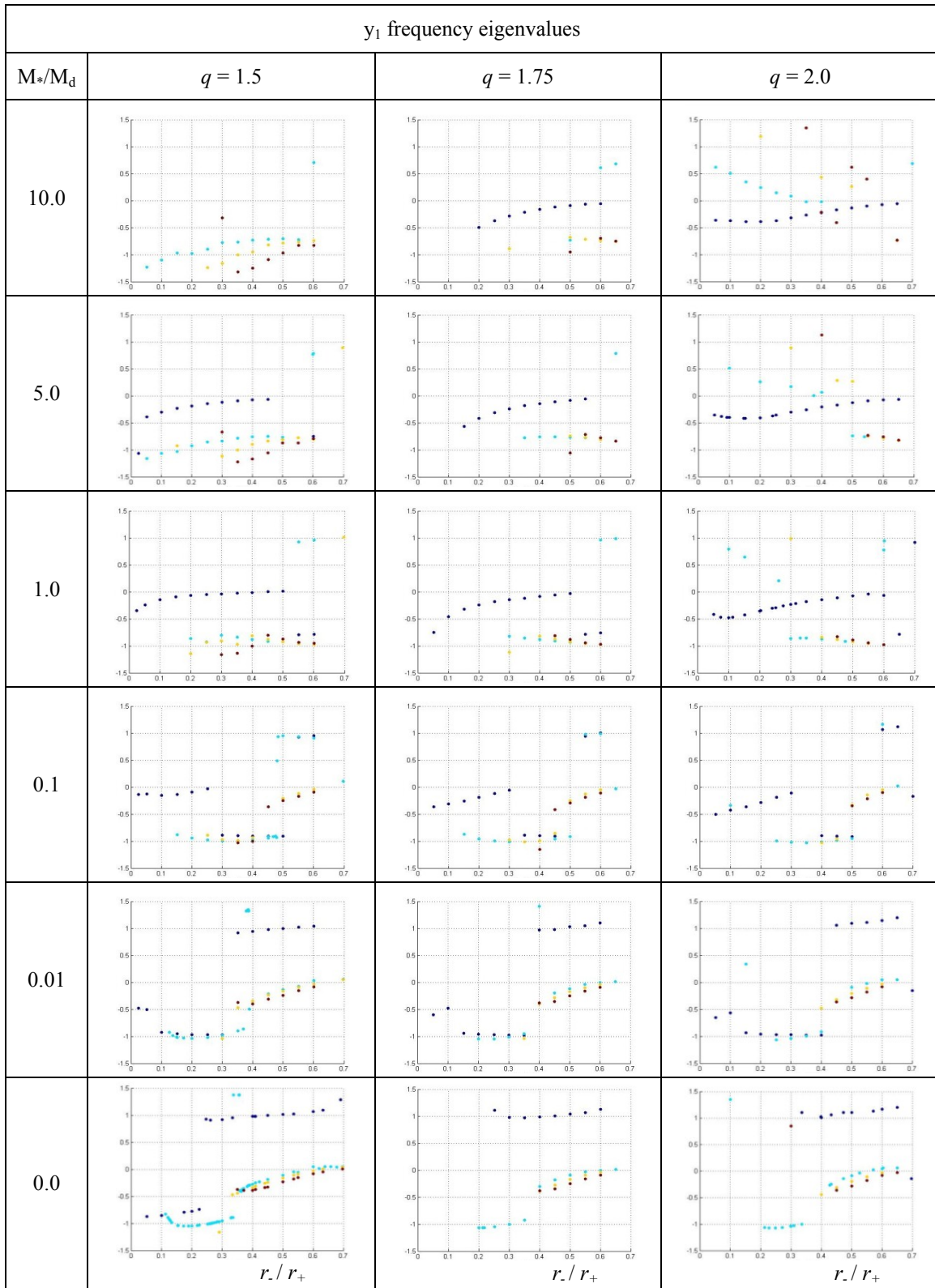


Fig. 4.2.7. y_1 eigenvalues for $q = 1.5, 1.75$ and 2.0 . Values for $m = 1, 2, 3$ and 4 are shown in dark blue, turquoise, yellow and red, respectively.

For $m = 1$, there is a smaller region where $R_0 < R_{co} < r_+$ and $r/r_+ > 0.60$, for $q = 2.0$, but no corresponding regions for $q = 1.5$ and 1.75 . The $m = 1$ map indicates that all values of q have an overlapping region where $R_{co} < r_-$ and $r/r_+ > 0.40$, with $M_*/M_d < 1.0$. The $m = 2$ map indicates a smaller region of overlapping q where $R_{co} \approx r_-$ for $r/r_+ > 0.50$ and $0.05 < M_*/M_d < 5.0$. The $m = 3$ and 4 modes do not support $R_{co} \approx r_-$ anywhere. All m maps indicate a region where $R_{co} \approx r_+$ for higher M_*/M_d than the $R_{co} \approx R_0$ and $R_{co} \approx r_-$ regions. The trend here is that for large r/r_+ , $R_{co} \approx r_+$, and R_{co} approaches R_0 as r/r_+ decreases. The $m = 1$ map indicates that $q = 1.75$ models are stable for $M_*/M_d < 0.01$ and $r/r_+ < 0.30$, while $q = 1.75$ models have a similar stable region reaching higher, to $r/r_+ < 0.40$. Both also have small stable regions for $M_*/M_d \approx 10.0$ and $r/r_+ > 0.60$. There is a stable region for $q = 1.5$ where $M_*/M_d \approx 7.0$ that is overlapped by $q = 1.75$ for $r/r_+ < 0.30$. Overlapping stable regions are found generally for all q , for low r/r_+ , for $m = 2, 3$ and 4 , extending to higher r/r_+ for $q = 1.5$ and 1.75 for large M_*/M_d . More detailed parameter space maps are presented in the $q = 1.5, 1.75$ and 2.0 Results sections. Figs. 4.2.12 - 4.2.14 indicate which models have been run for time-evolved systems for $q = 1.5, 1.75$ and 2.0 . Fig. 4.2.12 shows completed models with $M_*/M_d = 0.0$. Fig. 4.2.13 shows semilog plots for models with $M_*/M_d > 0.0$ for models with $m = 1, 2, 3$ and 4 for $q = 1.5$, while Fig. 4.2.14 shows similar plots, but for $q = 1.75$ and 2.0 .

For comparison, we calculated a sequence of models in which the self-gravity of the disk was not included in the calculation of the gravitational potential. We have included this sequence because it gives us insight into the behavior of P modes, allowing us to identify P mode traits in-self-gravitating disks. Unfortunately, we are not able to calculate non-self-gravitating models for $q = 1.5$ because of a singularity inherent in our method of calculating the gravitational potential. Plots for non-self-gravitating models for $q = 1.75$ and 2.0 can be found in Appendix B and Appendix C, displayed in the column that follows the column for $M_*/M_d = 50.0$. Discussion of non-self-gravitating models can be found in Section 5.1.2, comparing our results with those of Kojima (1986, 1989).

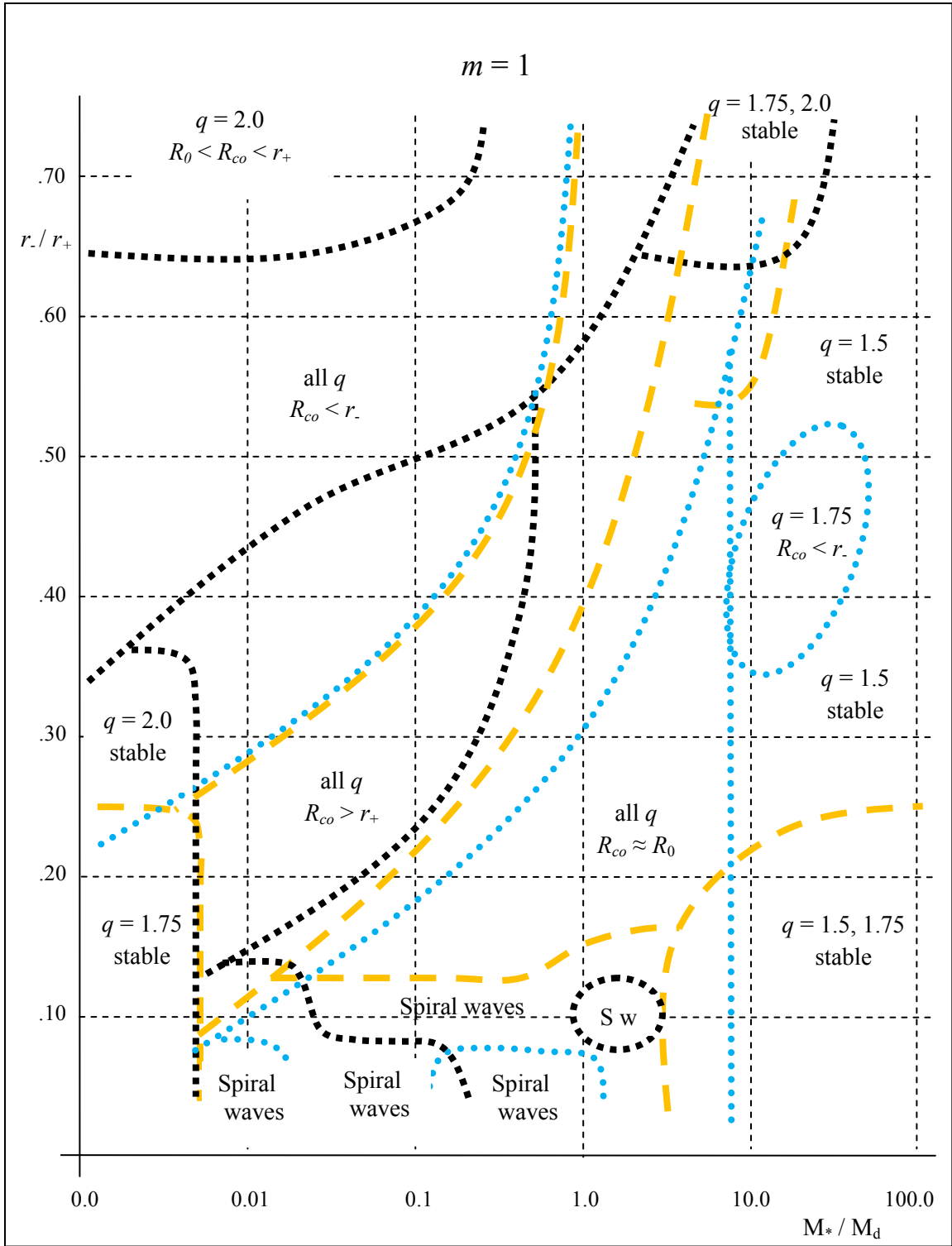


Fig. 4.2.8. Parameter space map for $m = 1$; $q = 1.5$ divisions in blue round-dotted lines, $q = 1.75$ in orange dashed lines and $q = 2.0$ in black square-dotted lines.

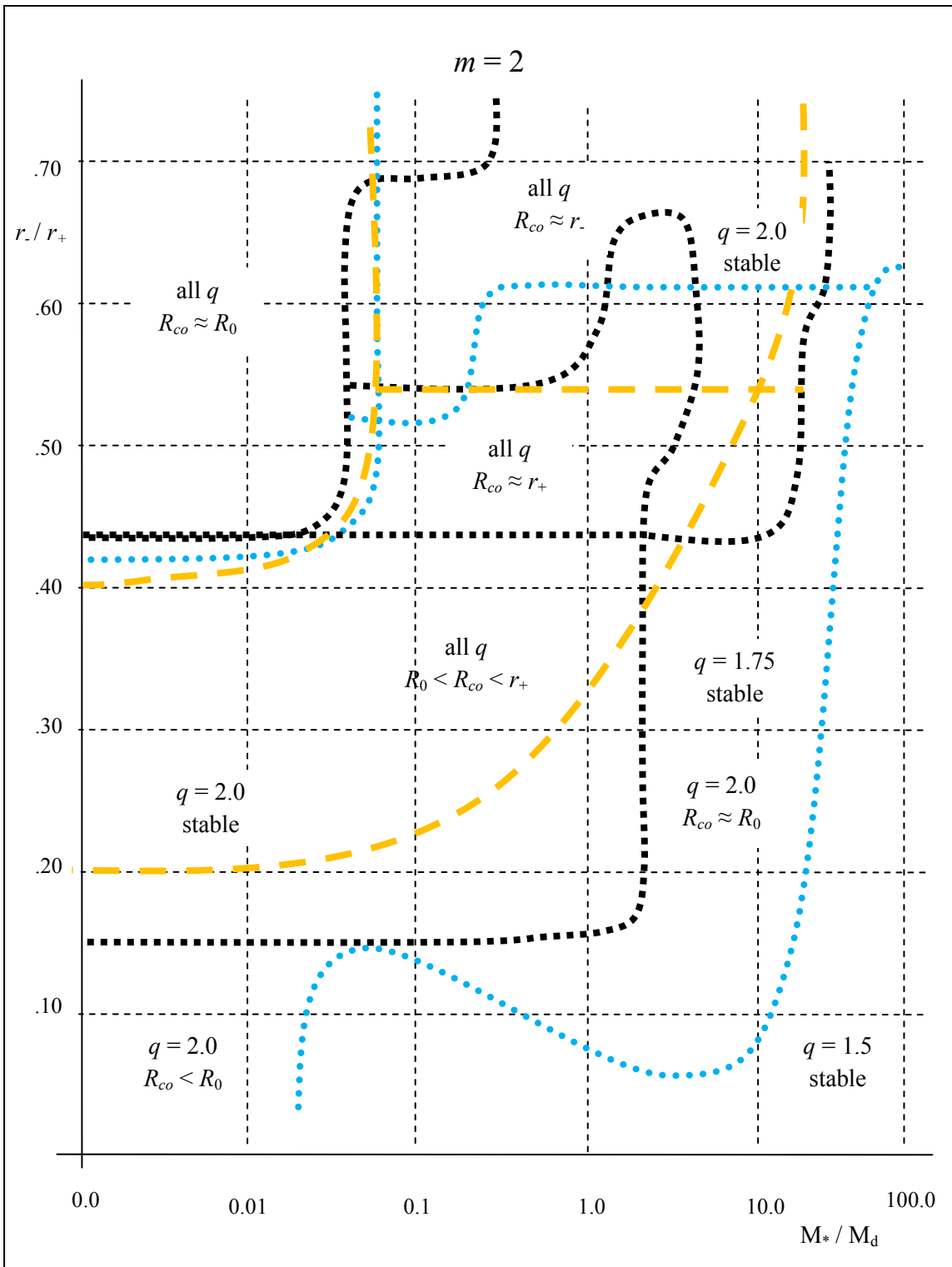


Fig. 4.2.9. Parameter space map for $m = 2$; $q = 1.5$ divisions in blue round-dotted lines, $q = 1.75$ in orange dashed lines and $q = 2.0$ in black square-dotted lines.

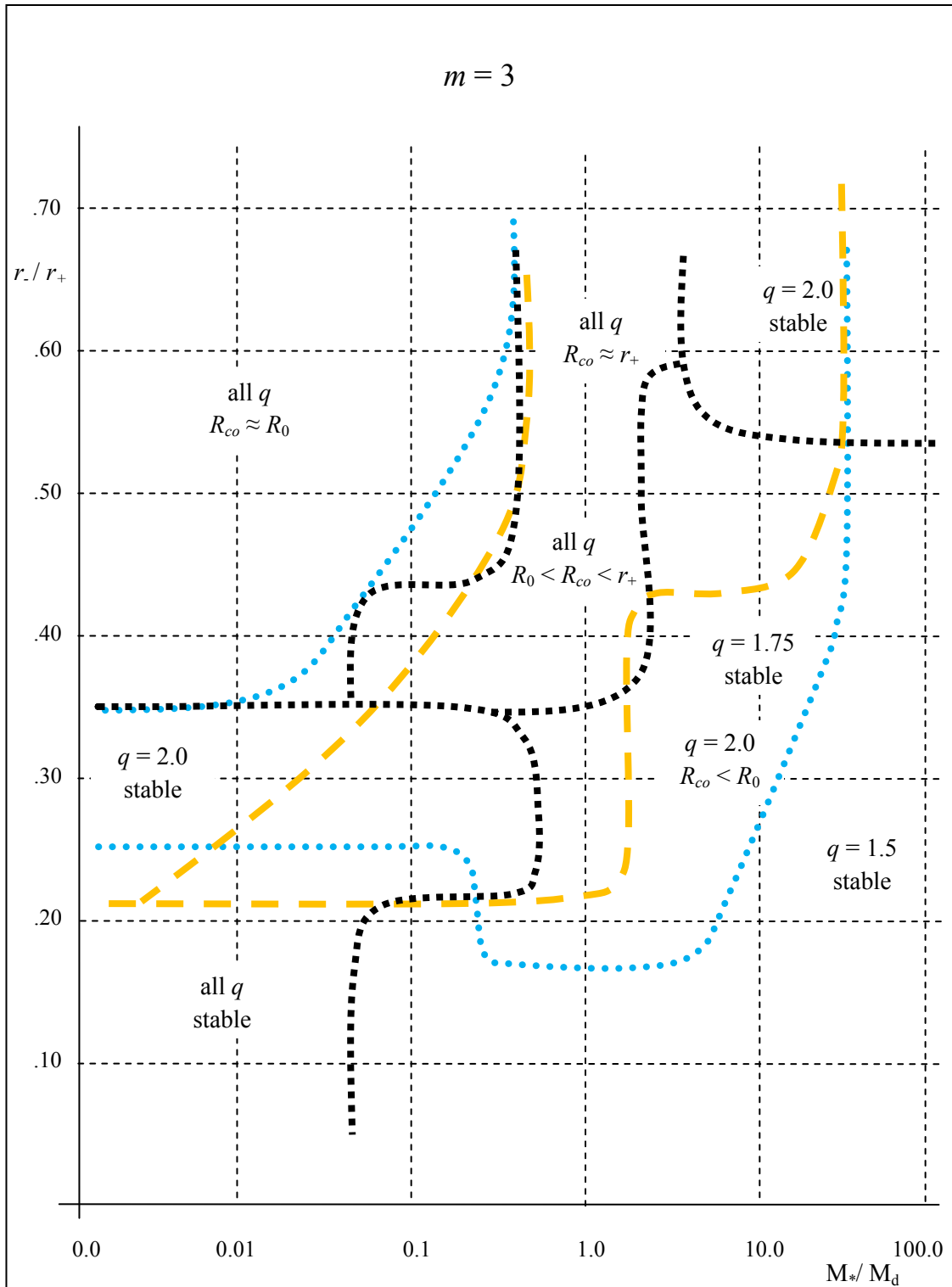


Fig. 4.2.10. Parameter space map for $m = 3$; $q = 1.5$ divisions in blue round-dotted lines, $q = 1.75$ in orange dashed lines and $q = 2.0$ in black square-dotted lines.

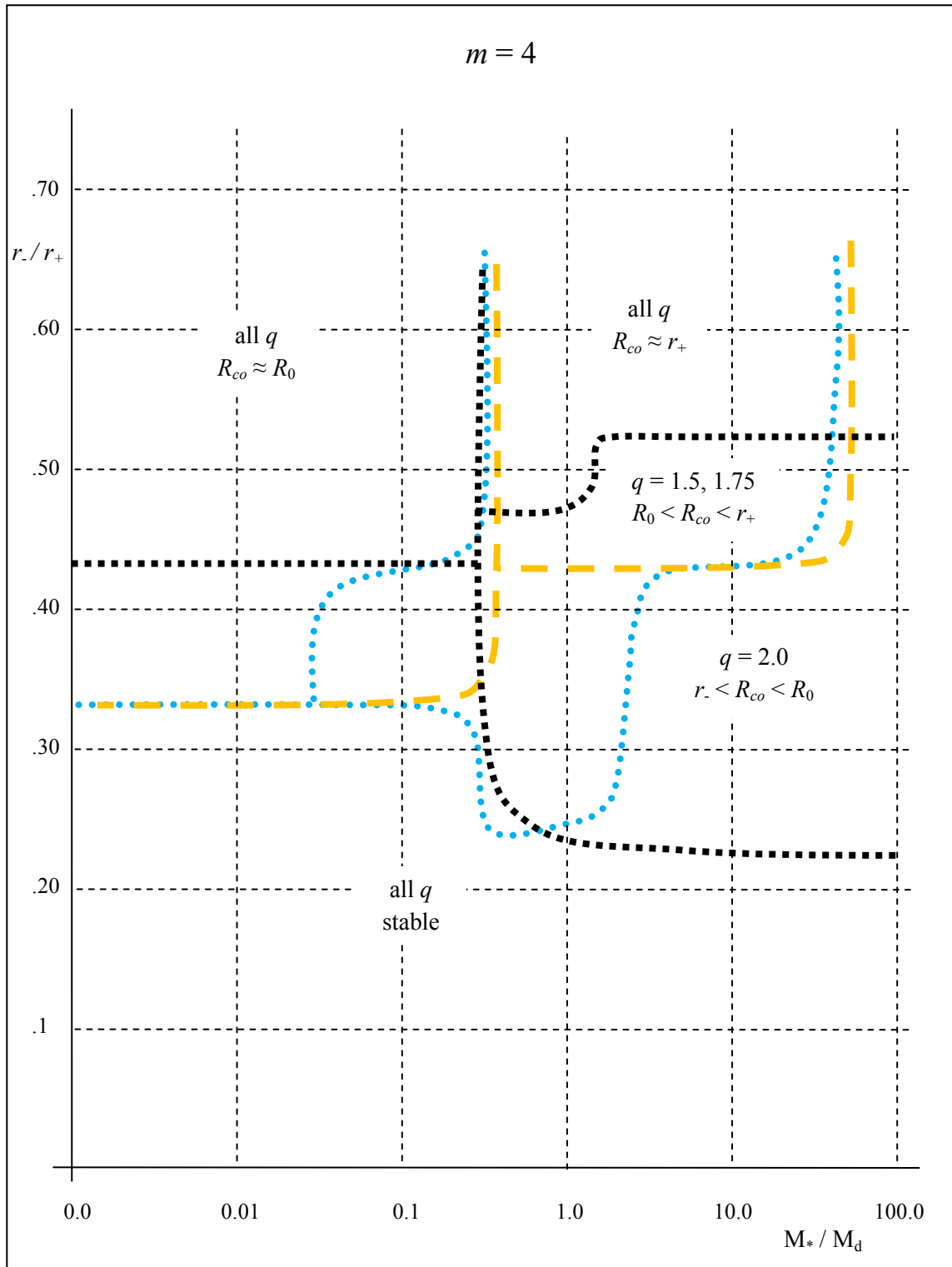


Fig. 4.2.11. Parameter space map for $m = 4$; $q = 1.5$ divisions in blue round-dotted lines, $q = 1.75$ in orange dashed lines and $q = 2.0$ in black square-dotted lines.

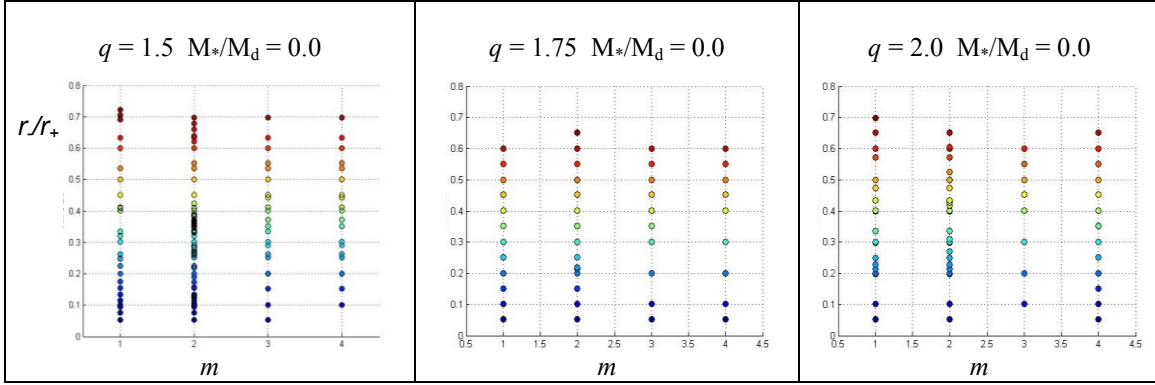


Fig. 4.2.12. $M_*/M_d = 0.0$ models run for $q = 1.5, 1.75$ and 2.0 .

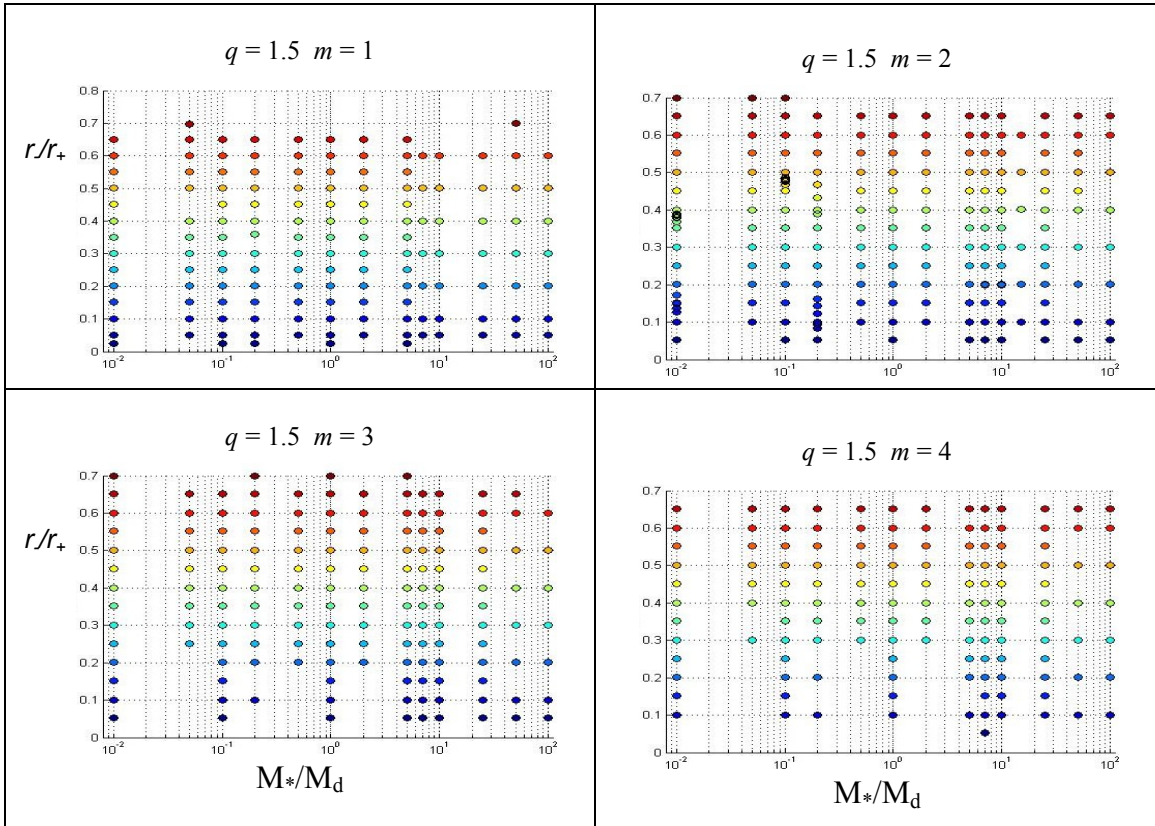


Fig. 4.2.13. $M_*/M_d > 0.0$ models run for $q = 1.5, m = 1, 2, 3$ and 4 .

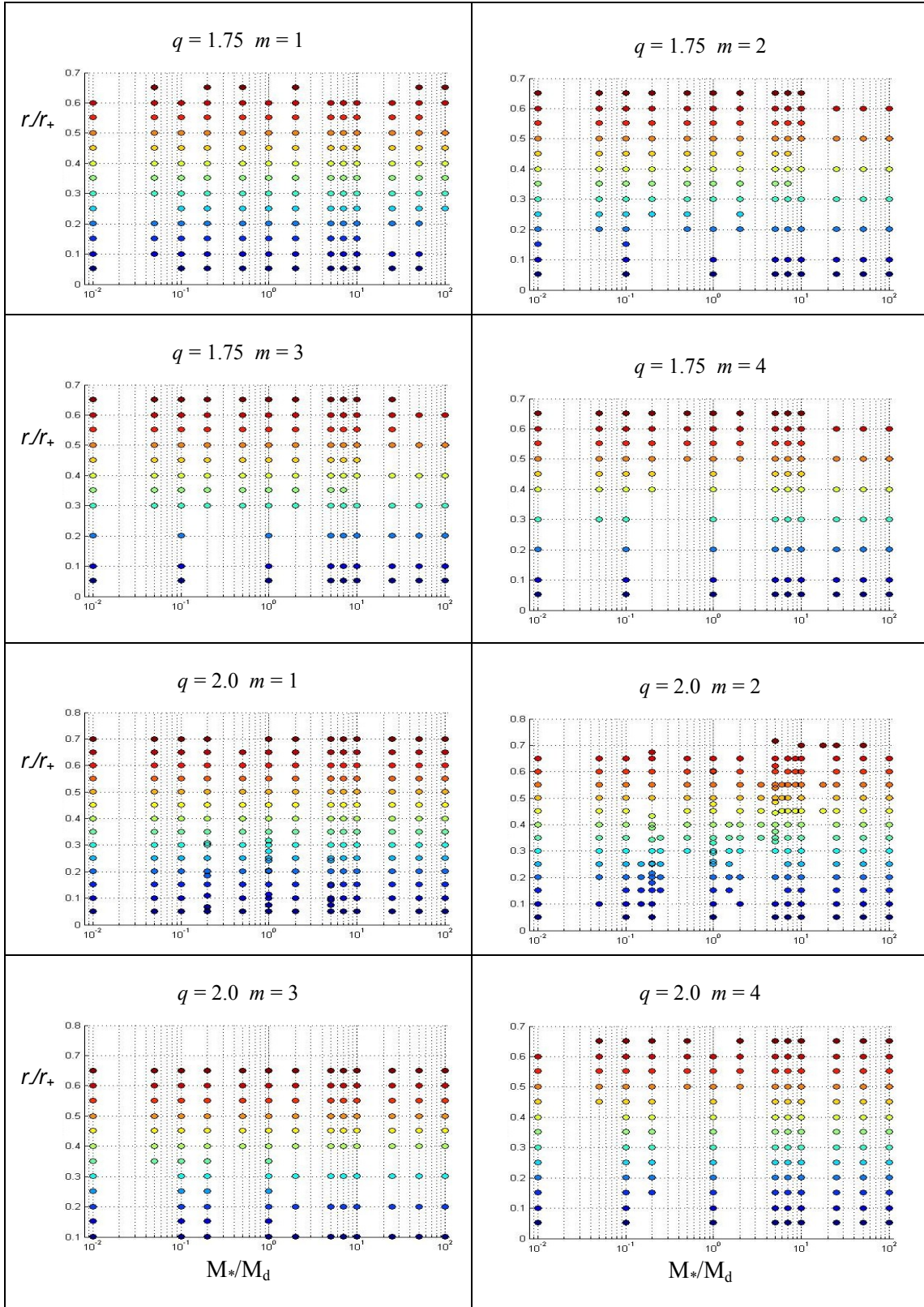


Fig. 4.2.14. Models with $M_*/M_d > 0.0$ for $q = 1.75$ and 2.0 , $m = 1, 2, 3$ and 4 .

4.2.1. Convergence Test

In this section, we address the effect of resolution on the results. For this study we have focused on models with 512 x 512 x 16 resolution for our temporally evolving models, since it gives us the highest resolution we can use for the number of models we wished to run. We made spot tests to aid in understanding how this choice of resolution would change the results when compared to 256 x 256 x 8 and 1024 x 1024 x 16. The resolution values are given by radial cells x height cells x azimuthal cells. We were able to use lower resolution in the azimuthal cells, since the perturbation goes as $e^{im\phi}$, allowing an analytical solution in this dimension. In the following discussion, we will drop the azimuthal cell numbers in the interest of space.

Fig. 4.2.1.1 illustrates the effects of varying resolution for disks with $q = 1.5$, $m = 2$, $M_*/M_d = 0.0$. The growth rates of the 256 x 256 models agree well with those of the 512 x 512 models for low $T/|W|$ and for high $T/|W|$, with less agreement near the I-J mode threshold. In general, models near thresholds are typically harder to resolve. What we see is that the 512 x 512 models vary more smoothly near threshold than do the 256 x 256 models, and that the threshold itself has moved to lower $T/|W|$ for the 512 x 512 models, from $T/|W| = 0.269$ for the 256 x 256 sequence to 0.260 for the 512 x 512 sequence. The growth rates of the data points at $T/|W| = 0.293$ for the 256 x 256 and the 512 x 512 models are 0.5441 and 0.6544 respectively, giving 17% difference. However, it may be more appropriate to compare the growth rate of the 256 x 256 data point with that of the 512 x 512 data point at $T/|W| = 0.282$, more closely matching the difference in $T/|W|$ above the transition from I modes to J modes. The 512 x 512 data point at $T/|W| = 0.282$ has a growth rate of 0.538, a difference of 0.5%. The 1024 x 1024 models seem to exhibit the same trend of shifting the I-J threshold even lower, but keeping a small percent difference when compared against models that are equidistant from the transition. The y_2 values for the 1024x1024 models agree well for $T/|W| < 0.21$, with less agreement with the lower resolution runs above the I-J mode threshold.

Convergence test using y_2 for $q = 1.5$, $m = 2$, $M_*/M_d = 0.0$

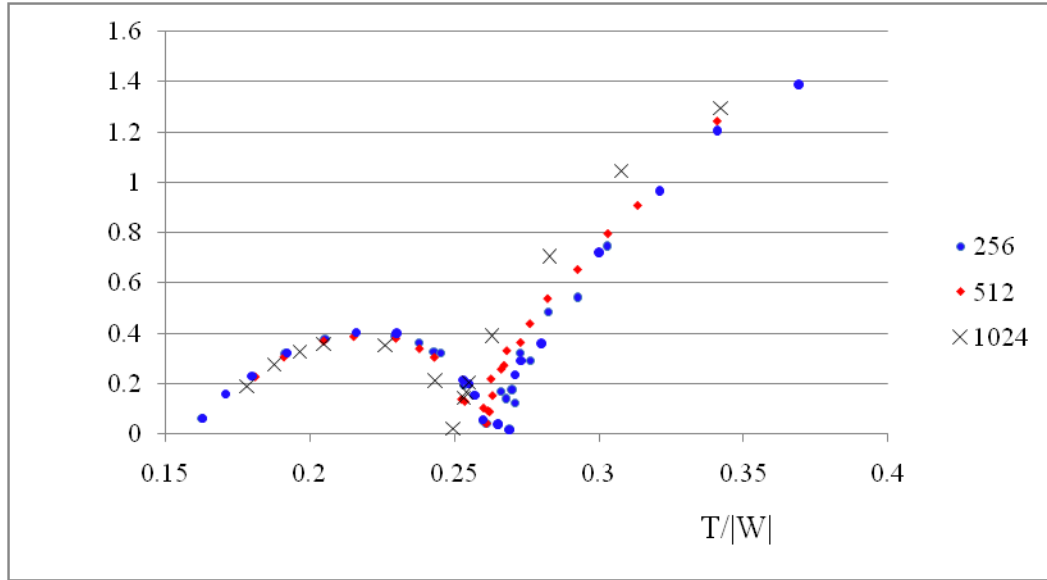


Fig. 4.2.1.1. Convergence test results for $q = 1.5$, $m = 2$, $M_*/M_d = 0.0$, with y_2 values for 256 x 256 x 8 resolution plotted with blue dots, 512 x 512 x 16 resolution plotted in red dots and 1024 x 1024 x 16 resolution plotted with black X's.

4.2.2. Results for $q = 1.5$ Models

The angular velocity distribution $q = 1.5$ is a Keplerian profile, and is an exact Keplerian model if $\Omega_0^2 = GM_*/R^3$. In the Keplerian limit, the central star contains the mass of the system, so self-gravity is negligible. Since there is no pressure support for a purely Keplerian disk, it would flatten into a two-dimensional object. It is possible to construct a disk with $q < 1.5$, for example, a Mestel disk is defined as a disk with $q = 1.0$ (Hunter, Ball & Gottesman 1984). These disks become unphysical for M_*/M_d a little greater than 0.0, since they are forced to be Keplerian at R_0 , but at smaller radii the frequency increases more slowly than that of a Keplerian disk, so there is no centrifugal support. This pushes R_0 to the inner edge, which creates an unphysical situation. Also, it has been analytically shown that for incompressible, non-self-gravitating disks, $q = \sqrt{3}$ is the lower stability threshold (Kojima 1989). In practice, $q = 1.5$ is typically used as the canonical lower limit for stability calculations, with $q = 2.0$ as the upper limit.

We begin detailed analysis of our results with $q = 1.5$, starting with analysis of eigenvalues for individual values of M_*/M_d , presented in Section 4.2 in Figs. 4.2.6 - 4.2.7, showing plots of y_1 and y_2 for M_*/M_d ratios of 0.0, 0.01, 0.1, 1.0, 5.0, 7.0, 10.0 and 25.0. We will closely examine the results for $M_*/M_d = 0.0$ and apply the trends we find to other M_*/M_d models. We find that $M_*/M_d = 0.0$ models are similar to $M_*/M_d = 0.01$ models, except for the $m = 1$ models, where motions of the central stars impact the behaviors of the $M_*/M_d = 0.01$ disks. There is no such impact for the $M_*/M_d = 0.0$ disks, since they do not possess central objects. For $M_*/M_d = 0.0$, the graph of y_2 , in Fig. 4.2.6, indicates that for models with $r./r_+ < 0.301$, the $m = 2$ mode dominates the disk; $m = 1$ modes dominate the disks for $0.301 < r./r_+ < 0.352$; $m = 3$ modes dominate for $0.352 < r./r_+ < 0.500$ and $m = 4$ modes dominate for $r./r_+ > 0.500$. The $T/|W|$ values for $r./r_+ = 0.301, 0.352$ and 0.500 are 0.243, 0.258 and 0.293, respectively.

Examining the behavior of the $m = 2$ modes, we see that growth rates are close to stable, with $y_2 < 0.1$ for $r./r_+ \approx 0.10$. As $r./r_+$ increases, the growth rates for the $m = 2$ modes increase to a peak at $r./r_+ = 0.224$ and then decrease toward stability around $0.338 < r./r_+ < 0.358$. Fig. 4.2.2.1 shows representative plots of this region. Recall that for each model, the $|\delta\rho|/\rho_0$ eigenfunction phase and amplitude are plotted in blue points, while the W eigenfunctions phase and amplitude are plotted in red points. The inner edge and outer edge are plotted in blue lines, while R_0 and R_{co} are plotted in pink and turquoise lines, respectively. The $r./r_+ = 0.115$ model shows qualitatively different behavior from the models with higher $r./r_+$. The $|\delta\rho|/\rho_0$ phase plot shows an inner bar with a roughly $\pi/4$ phase shift in the leading direction well inside R_0 , with a bar structure between the phase shift and the outer edge. The higher $r./r_+$ models have similar behavior except that the phase shift is trailing and covers $\approx \pi/2$. The $r./r_+ = 0.115$ model exhibits a trailing $3\pi/4$ phase shift in the W eigenfunction inside R_{co} with an outer bar, while the higher $r./r_+$ models exhibit leading arms for W , which cross R_{co} . All of the $|\delta\rho|/\rho_0$ eigenfunction plots have sharp dips that increase in radius toward R_0 as $r./r_+$ increases. The W eigenfunction for the $r./r_+ = 0.115$ model has a sharp dip where the W phase plot has its phase shift but the W plots for the higher $r./r_+$ models curve smoothly through their minima, and correspondingly, there is no abrupt phase shift in the W phase plots.

The stress plots show qualitatively different behavior as well. Recall that σ_R is the Reynold's stress, plotted in black, while σ_h is the acoustic flux, plotted in blue, and σ_G is the stress due to gravitational work, plotted in red. The inner region of the $r./r_+ = 0.115$ model has negative σ_R and σ_h , while σ_G is positive. The extrema of σ_R , σ_h , and σ_G lie at approximately the same radius, and the zeroes of these functions are close to R_θ . The higher $r./r_+$ Models have positive peaks for σ_R and σ_h near the inner disk edge with a peak for σ_G that lies close to R_θ . There is an increase of σ_G with $r./r_+$ which overtakes σ_R and σ_h as the growth rate passes its maximum value, indicating that self-gravity is becoming a stronger influence, as we would expect, as the disk narrows. Fig. A.1.6 shows more stress plots near this sequence in parameter space. Note the poor resolution of the stress plot for $M_*/M_d = 0.01$, $r./r_+ = 0.10$. The stress calculation involves spatial derivatives on second order quantities and consequently suffers resolution problems, as we will also see in models with other q and m .

We notice that the work integral plots indicate that acoustic flux, E_h , plotted in brown, is becoming more important in the outer region of the disk as $r./r_+$ increases. It dominates the work due to kinetic energy, E_k , plotted in blue, near the inner edge, both showing peaks near the same radius. E_h goes to zero at a radius that approaches R_θ as $r./r_+$ increases.

Comparing the self-gravity torque, τ , with the perturbed angular momentum, δj , we see that the $r./r_+ = 0.115$ model shows a small region near the inner disk edge where the τ is positive but δj has a steep negative spike. As the radius increases, τ becomes negative, and then positive. The τ plots of the higher $r./r_+$ models are positive in the inner disk region and negative in the outer region, without the small, positive τ near the inner edge. They do have a steep negative spike in δj , which become broader as $r./r_+$ increases.

Inspection of the $m = 2$ phase plots in Fig. A.2.1 shows that across the region of stability $0.338 < r./r_+ < 0.358$, R_{co} switches from near the outer edge of the disk (indicative of an I mode) to close to R_θ , which is a characteristic of a J mode. The phase plots remain similar in appearance otherwise, with the $|\delta\rho|/\rho_0$ phase exhibiting a trailing arm with a phase shift of $\pi/2$, and the W phase exhibiting a leading arm roughly centered on R_{co} . We see evidence of the $m = 2$ threshold between I and J modes in the $M_*/M_d = 0.0$ plot for y_I vs. $r./r_+$, which exhibits an abrupt shift from the lower frequencies of the I

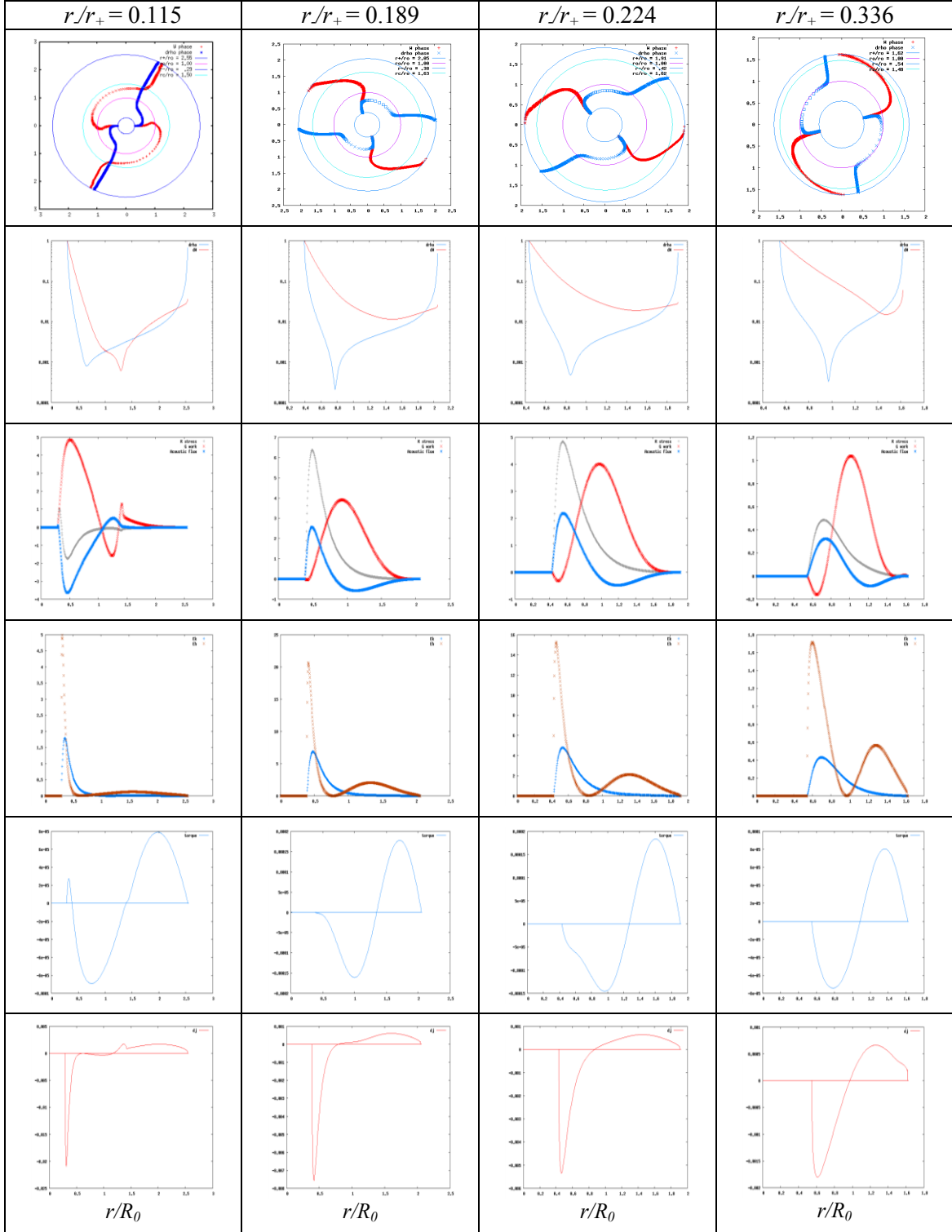


Fig. 4.2.2.1. Analysis plots for $M_*/M_d = 0.0$, $q = 1.5$ and $m = 2$. The top row is $|\delta\rho|/\rho_0$ phases, the second row is $|\delta\rho|/\rho_0$ amplitudes, the third row is stresses, the fourth row is work integrals, the fifth row is τ , and the sixth row is δj .

modes to the higher J mode frequencies. The stress plots show qualitative differences across the I-J threshold, as can be seen in Fig. A.2.6. The amplitude σ_G is much higher for J modes than it is for I modes. Also, there is a small region in the J mode plots where σ_R dominates in the J mode plots, and no such region in the I mode plots.

We now examine the general behavior of $m = 1$ modes for $M_*/M_d = 0.0$. Representative plots showing eigenfunction phases, eigenfunction amplitudes, self-gravity torques, perturbed angular momenta, work integrals and stresses can be found in Figs. A.1.1. - A.1.6. The growth rates, as shown in Fig. 4.2.6, increase up to $r./r_+ \approx 0.55$ and then decline. R_{co} lies outside the disk (at a larger radius) for $0.05 < r./r_+ < 0.20$ and changes to lying inside the disk near its inner edge for $0.20 < r./r_+ < 0.40$. For the models where $r./r_+ > 0.40$, R_{co} falls between the star and disk, moving inward as $r./r_+$ decreases. The $|\delta\rho|/\rho_0$ eigenfunction plots show sharper dips than their $m = 2$ counterparts. The $|\delta\rho|/\rho_0$ phase plots for $0.05 < r./r_+ < 0.20$ show a pronounced barlike structure in the inner disk region, with a rapid π phase shift at R_θ , returning to a bar that continues to the outer edge of the disk. W phase plots show an intact bar through the disk except for near the outer edge. As $r./r_+$ increases, the bar becomes less pronounced and W phase plots show a leading arm that changes inflection at R_{co} . Torque plots are negative in the inner disk region and positive in the outer region for $0.05 < r./r_+ < 0.20$ models, but develop second zeroes for higher $r./r_+$ models. Work integral plots are also similar for low $r./r_+$, but for $r./r_+ > 0.30$, the peak in E_k coincides with the zero in E_h , whereas this does not happen for $m = 2$ models until $r./r_+ = 0.60$. Stress plots for $0.05 < r./r_+ < 0.20$ models are poorly resolved due to a high frequency oscillation in the perturbation. The stress plots for $r./r_+ > 0.20$ indicate that σ_R is dominated by σ_G and σ_h everywhere. σ_G plots have a peak near the center of the disk while σ_h plots have a negative peak near the disk center, with positive peaks near the inner and outer edges.

Models with $m = 3$ and $m = 4$ are stable below $r./r_+ = 0.30$ and 0.40 respectively. The unstable models have R_{co} approaching R_θ as $r./r_+$ increases, consistent with J mode character. The stress plots for $m = 3$ and $m = 4$ are similar in character to those of $m = 1$ models. Representative plots of $m = 3$ and $m = 4$ functions can be found in Figs. A.3.1 through A.4.6.

As we move to the systems with $M_*/M_d = 0.01$ we see a qualitative difference in the growth rates of the $m = 1$ models, though the pattern of the $m = 2, 3$ and 4 growth rates is similar to that of the $M_*/M_d = 0.0$ systems, as indicated in Fig. 4.2.6. For $m = 1$, $M_*/M_d = 0.01$ models exhibit higher growth rates than $M_*/M_d = 0.0$ models, for models with $r./r_+ < 0.20$. The $m = 1$ modes dominate the disks, with higher growth rates than the $m = 2, 3$ and 4 models, in the $M_*/M_d = 0.01$ disks. This is probably due to the motion of the star for the $m = 1$ models. In an $m = 1$ model, the central object may move to conserve the center of mass of the system, while higher m models do not exhibit star motion.

The $|\delta\rho|/\rho_0$ phase plots of the $m = 1$ models, shown in Fig. A.1.1, show behavior unlike that seen for the $M_*/M_d = 0.0$ disks. They exhibit an inner bar that crosses R_{co} and R_θ at roughly a perpendicular angle, changing to a trailing arm that smoothly approaches the outer edge of the disk. The W phase plots exhibit a leading arm that curls around the disk for π radians, and connects to the outer edge nearly perpendicularly. The models with increasing $r./r_+$ have a leading arm with a rapid π shift in $|\delta\rho|/\rho_0$, and barlike structures inside and outside the phase shift. The W phase plots are barlike throughout the disks. These phase plots resemble those of the $M_*/M_d = 0.0$ systems, but with a trailing $|\delta\rho|/\rho_0$ arm. The eigenfunction plot of the $r./r_+ = 0.05$, $M_*/M_d = 0.01$ disk is qualitatively different, with a blunt dip far to the outer part of the disk, as shown in Fig. A.1.2.

Perturbed angular momentum plots for $m = 1$, $M_*/M_d = 0.01$, $r./r_+ = 0.10$ disks, shown in A.1.4, are different in character than the $M_*/M_d = 0.0$ models. They show positive δj for the inner disk area, whereas $M_*/M_d = 0.0$ models have negative δj in that region. The $r./r_+ = 0.05$ models have negative values of δj for the inner disk areas for $M_*/M_d = 0.1$ and 0.01 models, but the $M_*/M_d = 0.01$ disk does not have an extensive region of positive δj in the outer disk area. Comparison of the torque plots also shows qualitatively different behavior. The $M_*/M_d = 0.01$, $r./r_+ = 0.10$ disk shows opposite sign, compared to the $M_*/M_d = 0.0$, $r./r_+ = 0.10$ model. The τ plot for the $M_*/M_d = 0.01$, $r./r_+ = 0.05$ model, shown in Fig. A.1.3, strongly resembles the corresponding δj plot, but the $M_*/M_d = 0.0$, $r./r_+ = 0.05$ τ function crosses zero much further out in the disk than its δj function does. The stress plots, shown in Fig. A.1.6 for the $M_*/M_d = 0.0$ disks, are so poorly resolved that a comparison cannot be made and the work integral plots show little qualitative difference, as seen in Fig. A.1.5.

The character of the phase plot of the $M_*/M_d = 0.01$, $r_-/r_+ = 0.20$ model, shown in Fig. A.1.1, resembles that of the corresponding $M_*/M_d = 0.0$ model except that the phase shift is leading for the former and trailing for the latter. The $r_-/r_+ = 0.40$, $M_*/M_d = 0.0$ phase resembles that of the $r_-/r_+ = 0.30$, $M_*/M_d = 0.0$ disk. The higher r_-/r_+ models become more similar to each other as the influence of the central star becomes less effective, as the inner edge of the disk moves away from the star. The growth rates for the $M_*/M_d = 0.01$ models, shown in Fig. 4.2.6, exhibit character similar to the $M_*/M_d = 0.0$ disks, for the higher r_-/r_+ models. The I-J threshold for $m = 2$, $M_*/M_d = 0.01$ models is narrower and lies at higher r_-/r_+ than that for $M_*/M_d = 0.0$ models.

As we increase M_*/M_d to 0.1, we begin to see a change in the $m = 3$ and 4 modes as r_-/r_+ increases. As Fig. 4.2.6 indicates, they are stable below $r_-/r_+ = 0.20$ and 0.30, respectively, but as r_-/r_+ increases, they exhibit unstable models with R_{co} well beyond R_0 . R_{co} falls very near R_0 for the $r_-/r_+ = 0.50$ model. The growth rates for $m = 3$ models dip across the I-J threshold. We do not see such a dip in the $m = 4$ growth rates. The I-J threshold for $m = 2$ models continues to move toward increasing r_-/r_+ and we see a dip in growth rates around $r_-/r_+ = 0.48$. The $m = 1$ models continue to dominate for $r_-/r_+ < 0.20$, and show a decrease in growth rates for the lowest r_-/r_+ values. The phase plot for the $m = 1$, $r_-/r_+ = 0.28$ model, shown in Fig. A.1.1, has characteristics unlike other models discussed, in that R_{co} lies near R_0 , and there is a leading π phase shift in $|\delta\rho|/\rho_0$ that occurs well outside R_0 , followed by an abrupt change to a trailing arm.

The growth rates, in general, for the $M_*/M_d = 1.0$ models show some qualitative differences, as seen in Fig. 4.2.6. Models with $m = 1$ continue to dominate for $r_-/r_+ < 0.30$, but now the growth rate drops to a threshold between I and J modes between $r_-/r_+ = 0.50$ and 0.60. There is a small region around $r_-/r_+ = 0.40$ where $m = 2$ modes dominate, followed by domination by $m = 3$ and then $m = 4$ modes, and all of the modes exhibit a drop in growth rates as r_-/r_+ increases beyond 0.60. For $M_*/M_d = 5.0$, the $m = 1$ modes show similar behavior, in that they reach a peak around $r_-/r_+ = 0.30$, but the peak growth rate has diminished, allowing the $m = 2$ modes to dominate over a wider region, for $r_-/r_+ > 0.20$. The $m = 2$ growth rates are slightly higher than those for $m = 3$ for the region $r_-/r_+ < 0.60$, and $m = 4$ does not dominate the disk for any r_-/r_+ . This trend

continues as the star to disk mass ratio increases, with $m = 1$ approaching stable everywhere and $m = 2$ dominating the disks for $r./r_+ < 0.60$ for $M*/M_d = 7.0$ and 10.0 .

Fig. 4.2.2.2, shows trends over parameter space for $m = 1$. The red dashed lines show approximate boundaries determined by the location of R_{co} , and blue dashed lines show approximate boundaries for regions of stability. The region in the upper left area of the parameter space map harbors Γ modes, those with R_{co} near $r_.$ Disks with $r./r_+ > 0.45$ in this region have $R_{co} < r_.$ while those with $r./r_+ \leq 0.45$ have $R_{co} > r_.$ Torque plots also change behavior here, with τ in the region $r./r_+ > 0.45$ exhibiting a second negative area near the outer edge of the disk, while for models with $r./r_+ \leq 0.50$, τ has appositive minimum near the outer disk edge, and no negative τ . δj is negative for the inner disk region and positive for the outer part of the disk everywhere in the Γ region.

The left boundary of this region marks an abrupt transition between Γ^- modes and Γ^+ modes, where R_{co} switches from near the inner disk edge to outside the outer disk edge. There is also a change in behavior of τ across this boundary. Γ^- modes have τ negative for the inner disk region and positive for the outer region, while Γ^+ modes positive in the inner disk and negative outside R_θ . This is possibly due to the effect of the motion of the central star, since τ in the $M*/M_d = 0.0$ disks retains the character of the Γ modes. The character of δj is different from τ , opposite in sign in many plots. The transition between Γ and J modes is abrupt. As $M*/M_d$ increases to 5.0 , for $r./r_+ < 0.10$, R_{co} moves away from R_θ such that $R_{co} > R_\theta$. Phase plots change character over this region. For models near the I mode boundary, the $|\delta\rho|/\rho_0$ phase has I mode character, while the character of the W phase is different, with a leading arm. As $M*/M_d$ increases, the W phase becomes almost barlike for small $r./r_+$ models. For models where $r./r_+ \geq 0.40$, $|\delta\rho|/\rho_0$ and W phases both exhibit leading arms. A modes, characterized by a smooth spiral arm and no phase shift, occupy the region with $r./r_+ < 0.10$ and $M*/M_d \leq 1.0$.

There are a few models with $R_{co} < r_.$ for $M*/M_d \geq 7.0$ for $r./r_+ \approx 0.40$, but these models take 30 - 50 MIRPs to settle into mode in the outer disk regions and may be numerically unstable. In general, the disks appear to be stable for $M*/M_d \geq 7.0$ except for these and other possibly numerically unstable models.

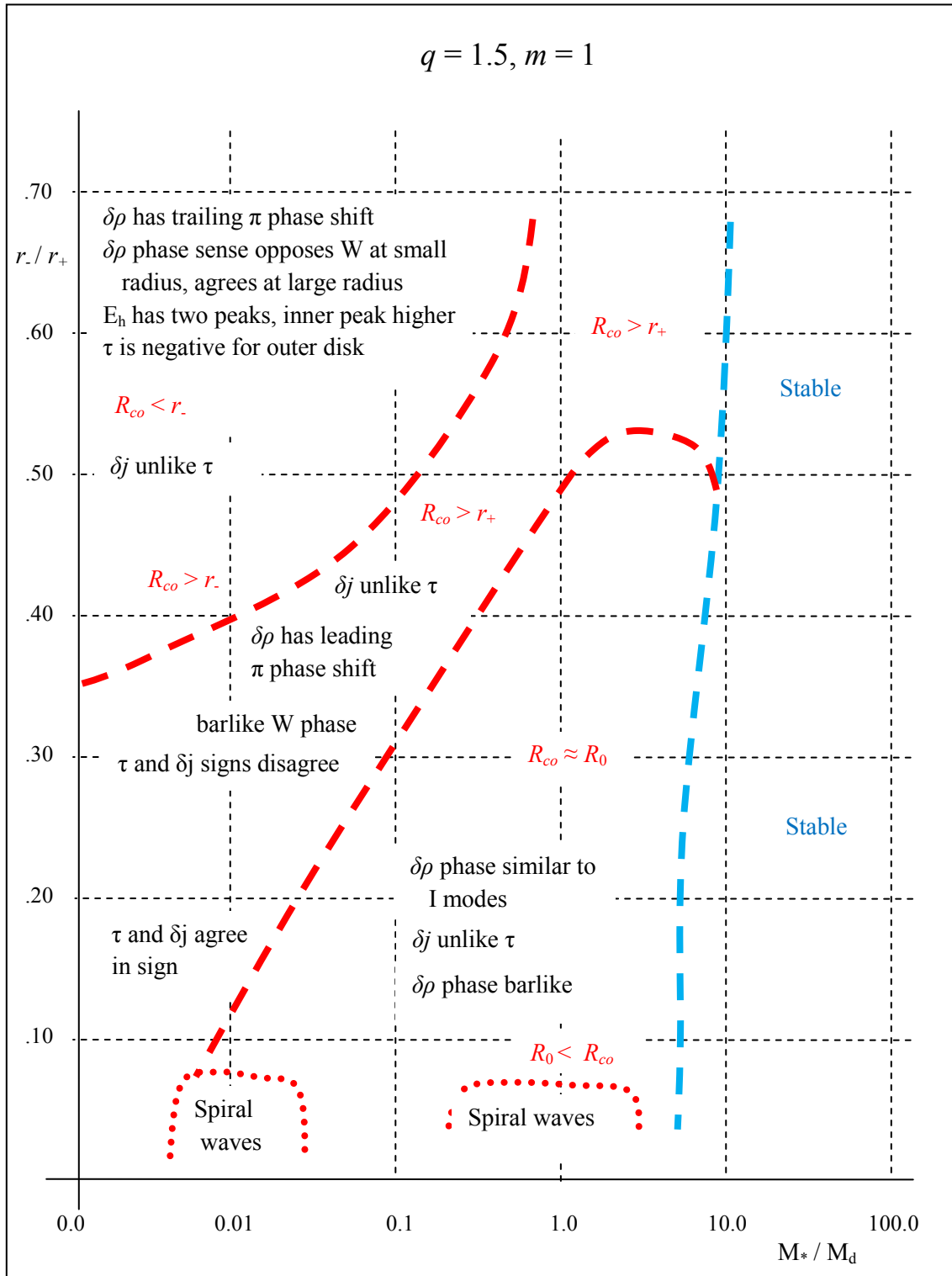


Fig. 4.2.2.2. Parameter space map for $q = 1.5, m = 1$, with modal divisions shown with red dashed lines and stability thresholds shown in blue dashed lines.

We will next evaluate trends across parameter space for $q = 1.5$, $m = 2$ modes, shown in Fig. 4.2.2.3. For the region $0.40 < r./r_+ < 0.60$ and $0.0 < M_*/M_d < 0.01$, $|\delta\rho|/\rho_0$ and W eigenfunctions have minima at roughly the same radii. This region is presumed to harbor J modes, since the disks are narrow, with R_{co} near R_θ . The phases of $|\delta\rho|/\rho_0$ and W lie in different senses and are not in phase anywhere for $r./r_+ > 0.50$, but they come into phase right at the inner disk edge for $r./r_+ = 0.40$ models. Self-gravity is obviously important in these models, since M_*/M_d is zero or small.

Self-gravity torque is negative for the inner disk region and positive for the outer disk region with the sign change near R_θ . The δj plots are similar in character to the τ plots in that they are negative and positive over the same regions, with the zeroes roughly at the same radii. The E_h plots include two strong peaks with the maximum of the inner peak roughly twice the magnitude of the maximum of the outer peak. The E_h minimum does not reach zero for $r./r_+ > 0.50$ models. E_k plots have a maximum near the center of the disk for $r./r_+ = 0.60$ models, where E_h plots have a minimum. E_k plots become skewed toward the inner edge as $r./r_+$ decreases. For small $r./r_+$ models, the E_k maximum lie at the same radius as the maximum of E_h .

The stresses show similar behavior between $M_*/M_d = 0.0$ and 0.01 models in this region. σ_G dominates over most of the disk while σ_h dominates near the inner and outer edge. The location of the maxima of σ_G and σ_R roughly coincide with the minimum of σ_h for $r./r_+ = 0.60$, as the disk cross-section approaches circular. Amplitudes of the σ_G and σ_R are equal at roughly $0.83 R_\theta$. As $r./r_+$ decreases, the σ_R maximum moves closer to $r_.$, but σ_h grows in amplitude and continues to dominate the region. The stresses are not well resolved for the $r./r_+ = 0.05$ and 0.10 models.

Models in the region where $0.20 < r./r_+ < 0.30$ and $0.0 < M_*/M_d < 0.01$ have R_{co} near the outer disk edge, characteristic of I modes. We find I mode character for $M_*/M_d = 0.1$ where $0.20 < r./r_+ < 0.40$, for $M_*/M_d = 1.0$ where $0.30 < r./r_+ < 0.50$, and for the range $5.0 < M_*/M_d < 15.0$ where $0.40 < r./r_+ < 0.60$. In general, as the star to disk mass ratio increases, I modes appear for narrower disks. The I mode phase plots show character somewhat similar to the J mode phase plots, with a barlike region in the inner part of the disk before diverging in character in the outer disk regions. As M_*/M_d

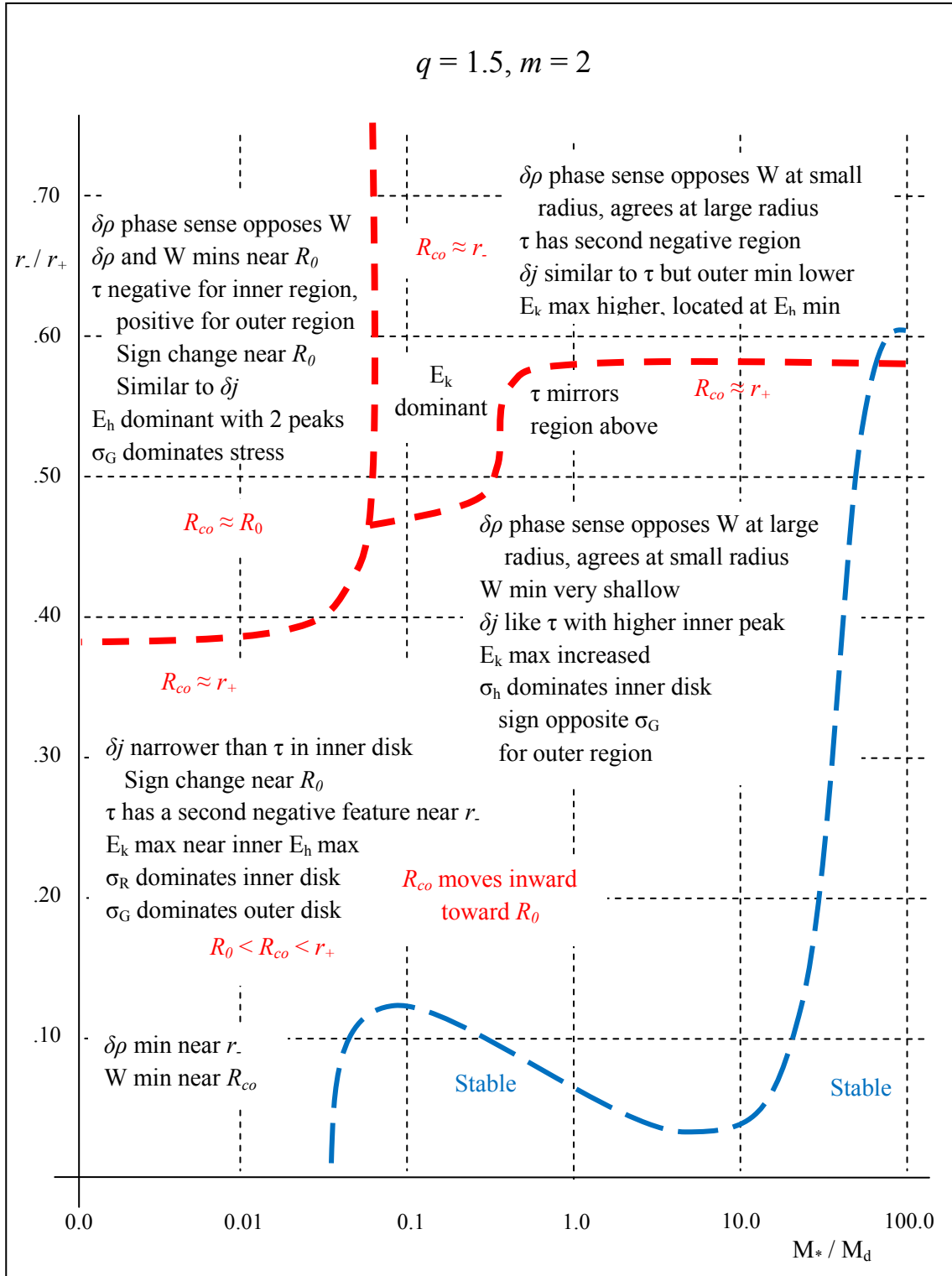


Fig. 4.2.2.3. Parameter space map for $q = 1.5, m = 2$, with modal divisions shown with red dashed lines and stability thresholds shown in blue dashed lines.

increases, the bar changes to a smoothly trailing, spiral arm, with $|\delta\rho|/\rho_0$ and W in phase. The dip in the $|\delta\rho|/\rho_0$ eigenfunction plot continues to reside near R_0 but the W eigenfunction typically shows a very shallow dip in this region.

The τ plots and δj plots show considerably different character from each other. Torque plots for $M^*/M_d = 0.0$ and 0.01 resemble those for higher $r./r_+$ models but the δj plots are much narrower in the inner disk regions, opposite in sign to τ . Moving to higher M^*/M_d models, some τ plots develop a small region near the inner disk edge where they are positive. For higher M^*/M_d , the δj plots have a sharp positive spike near the inner edge, and negligible amplitude otherwise.

The stress plots show no qualitative change across the I-J boundary in that the σ_G maximum remains centered in the disk with an amplitude that decreases with M^*/M_d , as the maxima of σ_R and σ_h grow, dominating the inner disk regions. The σ_h minimum remains near the σ_G maximum. The work integrals are similar to those of the higher $r./r_+$ region for $M^*/M_d = 0.0$ and 0.01 with the outer peak in E_h decreasing with $r./r_+$. As M^*/M_d increases, the outer peak increases in strength, and then decreases.

The region with $r./r_+ \geq 0.50$ and $M^*/M_d > 0.1$ has R_{co} near the inner edge of the disk. At small radii, the $|\delta\rho|/\rho_0$ and W are no longer in phase, with a $\pi/2$ difference that decreases with M^*/M_d . The dip in the $|\delta\rho|/\rho_0$ eigenfunction plots moves toward the outer edge as M^*/M_d increases and the W eigenfunctions develop double dips. The τ plots are mirror images of those directly below, with the same M^*/M_d but smaller $r./r_+$, and show a second negative region in the outer part of the disk. The δj plots resemble the τ plots in nature, but the minimum in the outer disk area extends to a much lower magnitude. The stress plots resemble those of the J mode region for the lower M^*/M_d models. The peak in E_k grows substantially as M^*/M_d increases toward stable models.

Comparing the $q = 1.5$, $m = 2$ modes with the $q = 2.0$, $m = 2$ modes, a major difference is that $q = 1.5$ models become stable for large M^*/M_d , while $q = 2.0$ models do not. For $r./r_+ = 0.60$, $q = 1.5$ disks become stable for $M^*/M_d \geq 100.0$. As M^*/M_d decreases, the disks become stable for lower and lower $r./r_+$, as shown in Fig. 4.2.2.3. We see no disks with extensively wrapped spiral arms, but see stable disks instead. Models for $0.0 \leq M^*/M_d \leq 0.01$, for large $r./r_+$, are J modes, similar to the $q = 2.0$ models. The main trends of the I mode regions are also similar to $q = 2.0$ models, with $R_{co} \approx r.$ existing

for higher M^*/M_d models and $R_{co} \approx r_+$ for lower M^*/M_d models, but in the $q = 1.5$ case, this region extends to higher M^*/M_d models until the disks reach stability. Phase plots around $M^*/M_d = 0.1$ and $r./r_+ = 0.40$ are very similar in character for $q = 1.5$ and 2.0 models. As M^*/M_d increases, the outer bar in the $|\delta\rho|/\rho_0$ phase plots stretches more into a trailing arm. This appears to be an edge mode characteristic but we are unable to do a direct comparison with non-self-gravitating models because of our inability to calculate them for $q = 1.5$, as mentioned in Section 3.2.

We see multiple minima in the eigenfunctions amplitude plots for small $r./r_+$ with $R_{co} \approx R_\theta$, similar to the $q = 2.0$ models, but for $q = 1.5$ the minima occur with more frequency toward the inner edge of the disk. Traits of δj and τ are similar to the $q = 2.0$ models for $M^*/M_d \leq 0.10$ but diverge for higher M^*/M_d , especially for low $r./r_+$ disks where they fluctuate rapidly, possibly due to numerical instability. Work integrals are similar for the regions as divided by the position of R_{co} . For $q = 1.5$ disks, the Γ region extends to higher M^*/M_d , and traits arise there that are not evident in the $q = 2.0$ disks. In that region, the $q = 1.5$ disks show an increase in the peak in E_k . Stresses for the $q = 1.5$ disks with $M^*/M_d = 0.0$ do not peak in σ_h in the inner and outer disk, but are similar to those in the $q = 2.0$ models for $M^*/M_d = 0.01$, for $r./r_+ > 0.40$. The trends of the stresses are different for $r./r_+ < 0.40$ in that the $q = 1.5$ disks are dominant in σ_R near the inner edge of the disks, where the $q = 2.0$ disks are dominant in σ_h near the inner edge.

The maps for the $m = 3$ and 4 regions of parameter space are relatively simpler than those for $m = 1$ and 2. The region where $R_{co} \approx R_\theta$ extends to larger M^*/M_d than that for $m = 2$. The $|\delta\rho|/\rho_0$ and W phase plots show character similar to those for $m = 2$, but with higher m -fold symmetry. The $|\delta\rho|/\rho_0$ eigenfunction has a very shallow minimum. Work integrals have two peaks, but the minimum separating them is considerably higher than zero in magnitude. τ and δj resemble each other in nature, with a negative inner region and a positive outer region. The boundary between the $R_{co} \approx R_\theta$ region and the $R_{co} \approx r_+$ region is abrupt. The $|\delta\rho|/\rho_0$ and W phase plots in the $R_{co} \approx r_+$ have inner bars in phase with each other for $r < R_\theta$. The $|\delta\rho|/\rho_0$ have a trailing $m\pi$ phase shift on R_θ . Outside R_θ , the W phase has a short leading arm, while the $|\delta\rho|/\rho_0$ phase has a trailing arm that extends farther as M^*/M_d increases. The stable regions extend to $M^*/M_d = 0.0$ and all

disks are stable for $r/r_+ < 0.30$ for $m = 3$ models and $r/r_+ < 0.40$ for $m = 4$ models, again, discounting a few models that settle into mode after tens of MIRPs.

In Fig. 4.2.2.6, we merge the general trends of the parameter maps for $m = 1, 2, 3$ and 4, in black, blue, orange and red, respectively. We show the parameter space trends plotted against self-gravity parameters p and η in Figs. 4.2.2.7 and 4.2.2.8, respectively, with some of the parameter map colors lightened to aid in discerning them against the plots of the parameters p and η . Since p and η only depend on equilibrium quantities, there is no inclusion of the effect of the motion of the star in the $m = 1$ case.

The parameter p provides a measure of the relative importance of self-gravity to pressure, as defined in Equation 4.1.1. We can see that the highest values for p are in the upper right, as we would expect, since self-gravity is dominant where M_*/M_d is small and r/r_+ is large, where the disk is narrow. The contours of constant p tend to track along the boundaries of the I and J modes in this region. The stability thresholds, shown in solid lines, do not seem to follow the contours of p .

The parameter η provides a measure of the relative importance of self-gravity to the gravitational potential of the central star, respectively, as defined in Equation 4.1.2. There is not an obvious relationship between the contours of constant η and the boundaries of the I and J modes, but the stability thresholds of the $m = 1$ and 2 modes follow a horizontal path in this parameter space, similar to the contours of constant η .

The parameter space maps are meant to be only general qualitative representations. Table 4.2.2.1 provides $q = 1.5$ values for $T/|W|$, r/r_+ , r/R_0 , r_+/R_0 , $y_2(m)$ and $y_1(m)$ for $m = 1, 2, 3$ and 4, for $M_*/M_d = 0.0, 0.01, 0.1, 1.0, 5.0$, and 10.0. Note that where $y_2(m) = 0.0$, no value of $y_1(m)$ exists. $M_*/M_d = 10.0$ data was truncated in the interest of space.

Plots of corotation radii and y_1 eigenfunction values are provided in Fig. 4.2.2.9 for $m = 1, 2, 3$ and 4; and y_2 eigenfunction values are provided in Fig. 4.2.2.10. The R_{co} magnitudes have been truncated to 5.0 for graphing purposes.

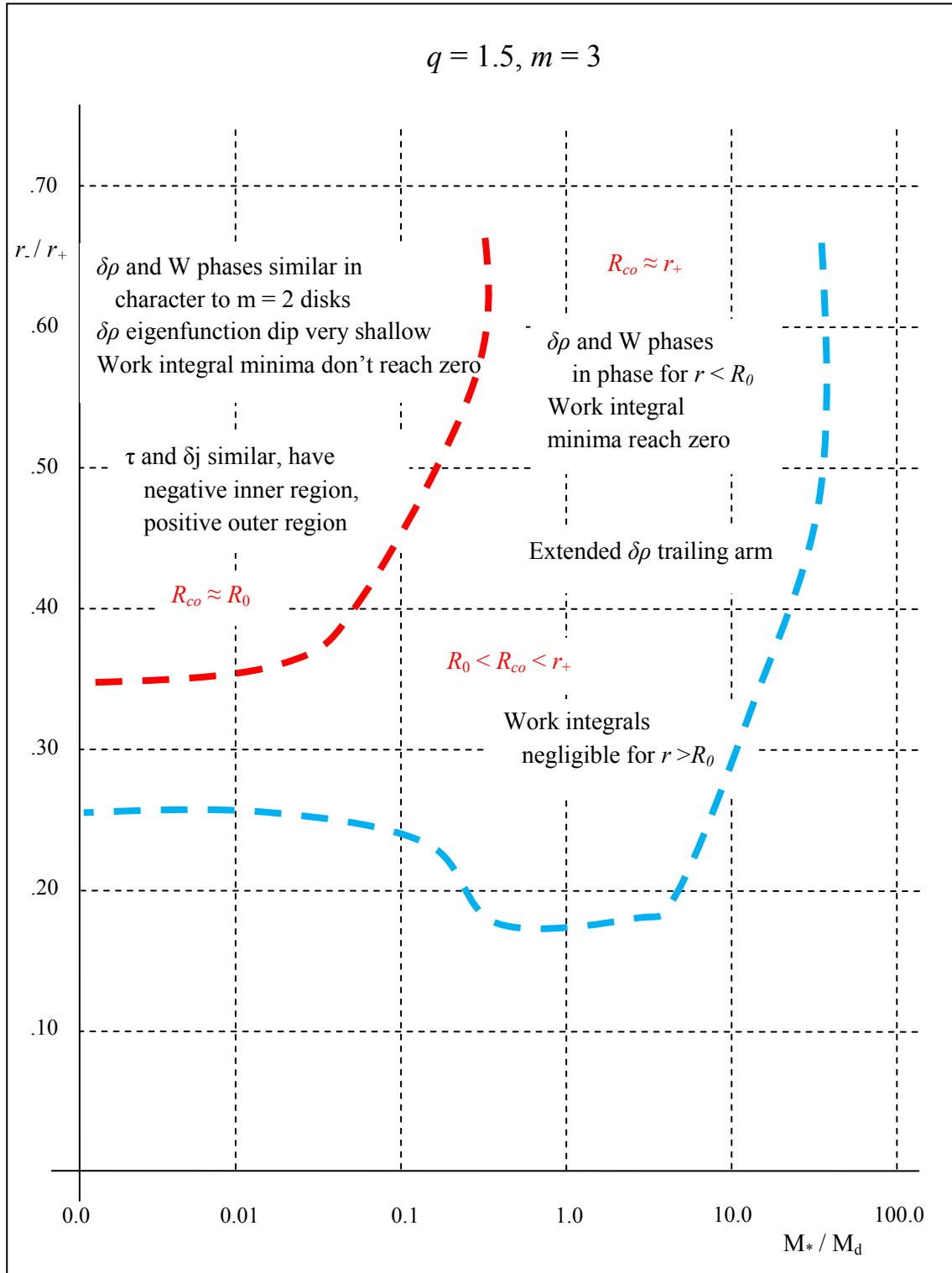


Fig. 4.2.2.4. Parameter space map for $q = 1.5, m = 3$, with modal divisions shown with red dashed lines and stability thresholds shown in blue dashed lines.

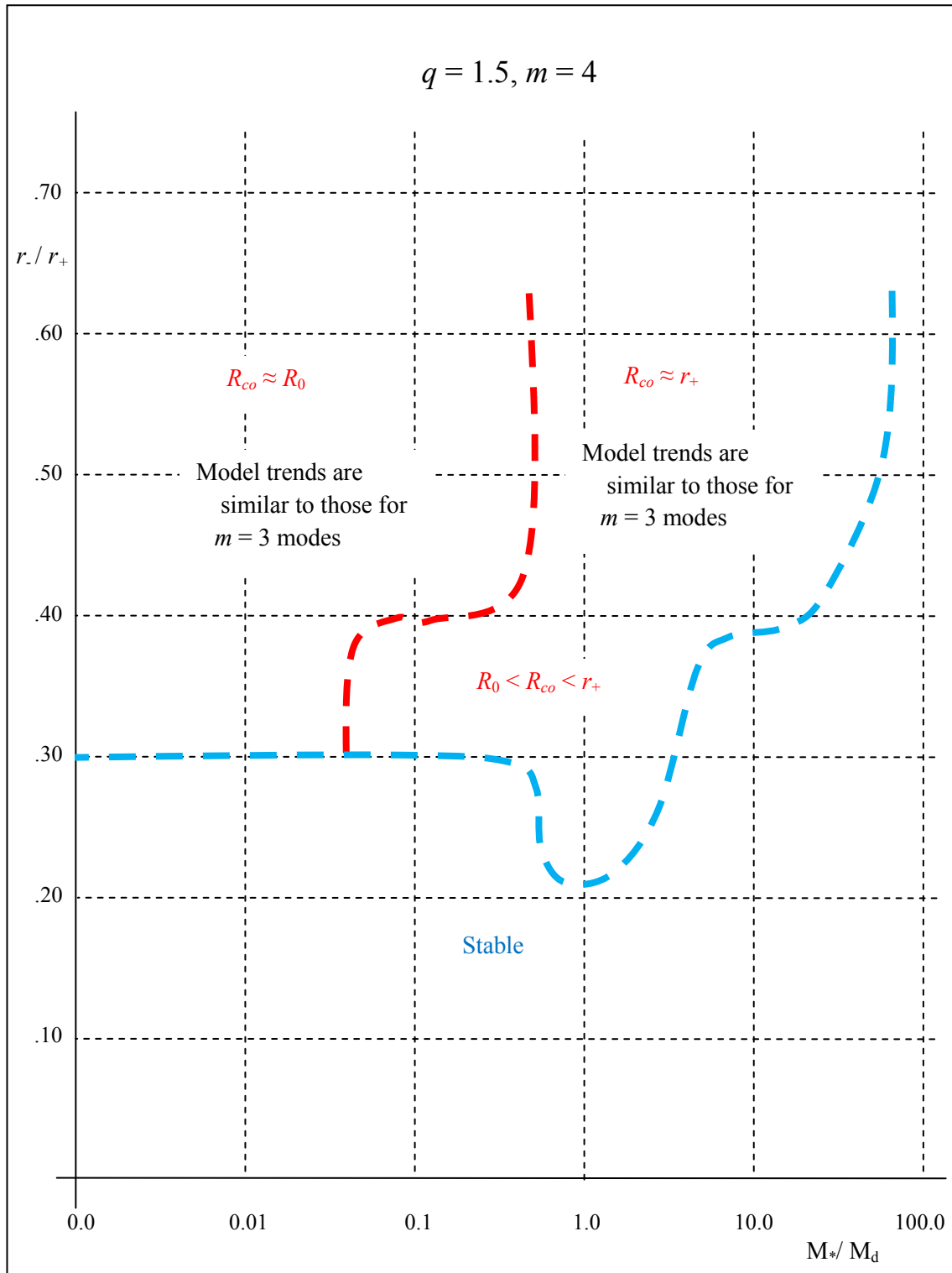


Fig. 4.2.2.5. Parameter space map for $q = 1.5, m = 4$, with modal divisions shown with red dashed lines and stability thresholds shown in blue dashed lines.

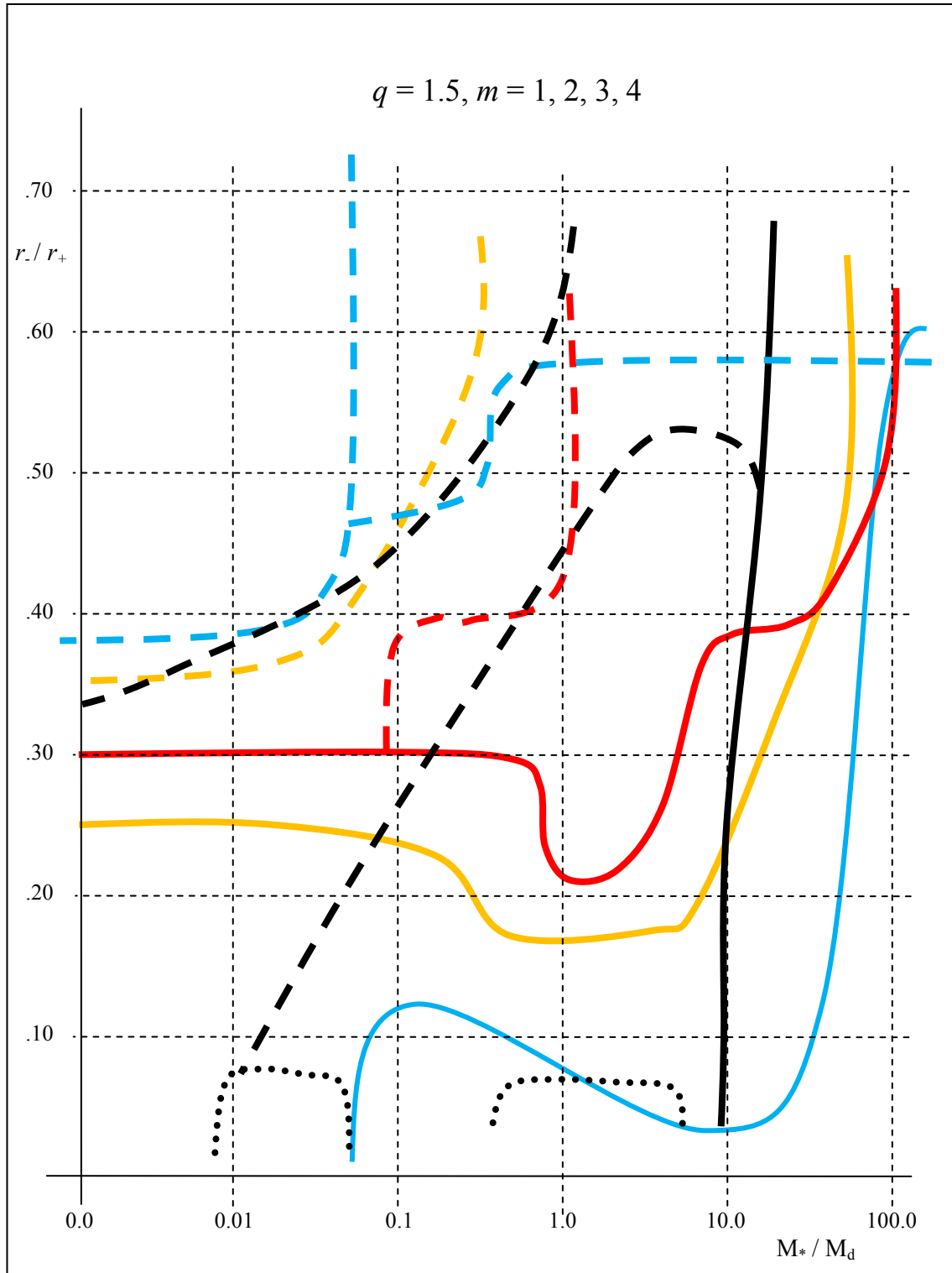


Fig. 4.2.2.6. Parameter space map for $q = 1.5$, $m = 1, 2, 3$ and 4 , shown in black, blue, orange and red dashed lines, respectively. Solid lines are boundaries of stable models.

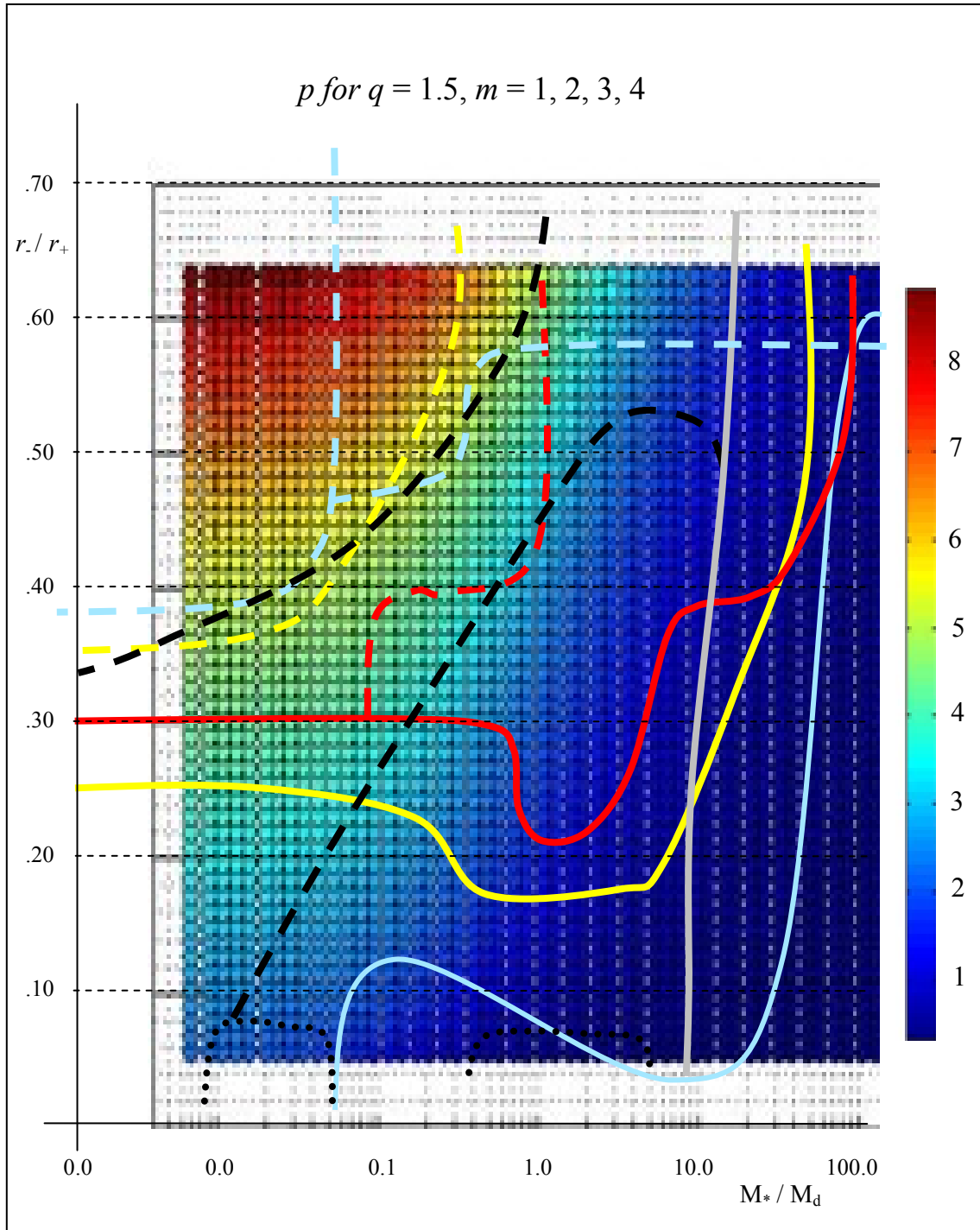


Fig. 4.2.2.7. Parameter space map overlaid on self-gravity parameter p for $q = 1.5, m = 1, 2, 3$ and 4 , shown in black, blue, orange and red dashed lines, respectively. Solid lines are boundaries of stable models. Some colors were lightened.

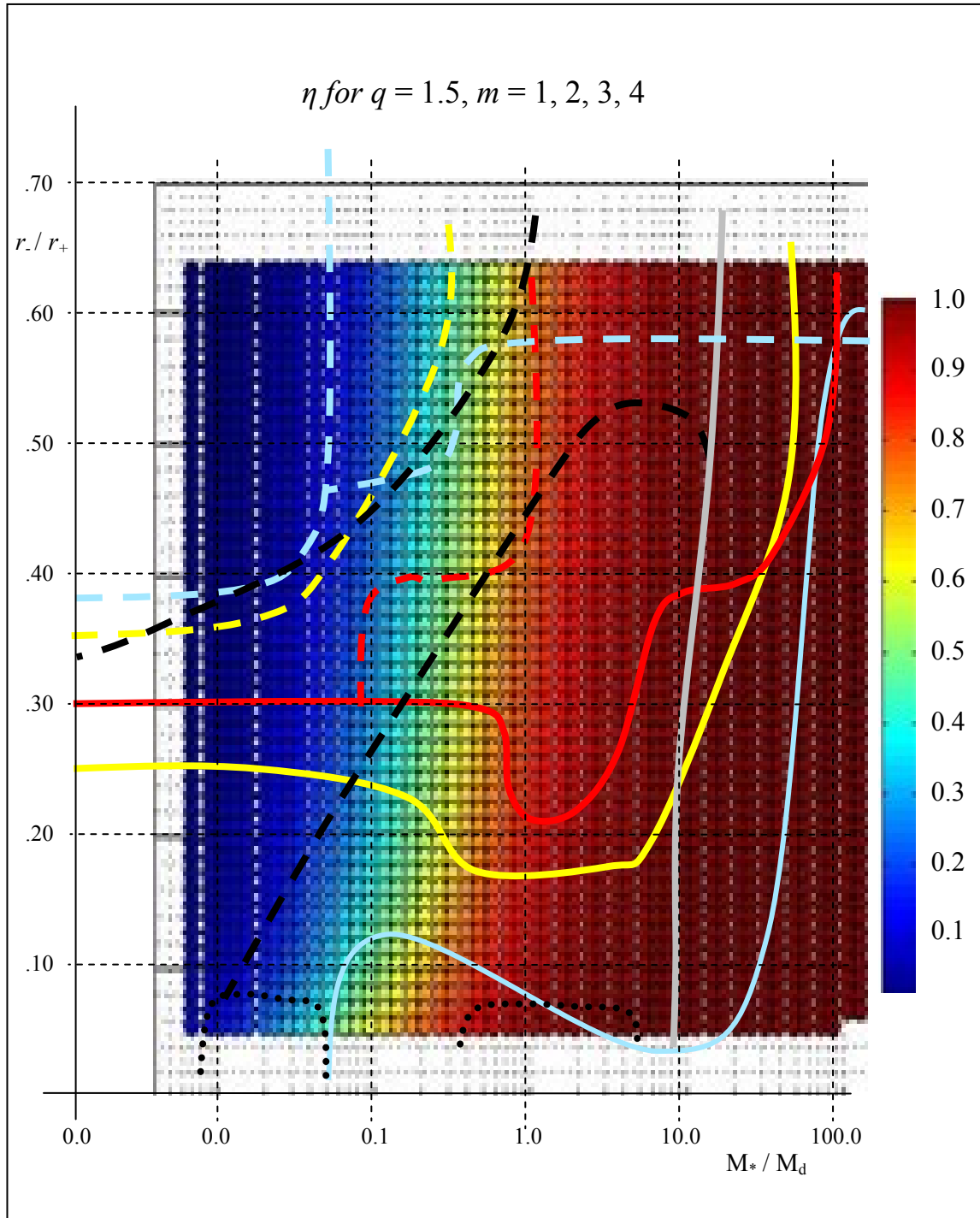


Fig. 4.2.2.8. Parameter space map overlaid on self-gravity parameter η for $q = 1.5, m = 1, 2, 3$ and 4 , shown in black, blue, orange and red dashed lines, respectively. Solid lines are boundaries of stable models. Some colors were lightened.

Eigenvalues for $q = 1.5$ models											
T/ W	r/r_+	r_+/R_o	r/R_o	$y_2(1)$	$y_2(2)$	$y_2(3)$	$y_2(4)$	$y_1(1)$	$y_1(2)$	$y_1(3)$	$y_1(4)$
$M_*/M_d = 0.0$											
0.092	0.052	3.583	0.186	0.005	0.000	0.000	0.000	-0.874			
0.143	0.101	2.680	0.270	0.011	0.000	0.000	0.000	-0.859			
0.205	0.201	2.006	0.403	0.038	0.369	0.000	0.000	-0.772	-1.045		
0.243	0.301	1.699	0.511	0.298	0.305	0.000	0.000	0.918	-0.955		
0.271	0.401	1.508	0.604	0.519	0.356	0.741	0.576	0.974	-0.273	-0.335	-0.394
0.293	0.500	1.374	0.688	0.647	0.646	1.211	1.287	1.010	-0.113	-0.158	-0.235
0.313	0.600	1.268	0.761	0.680	0.910	1.608	1.890	1.068	0.026	-0.028	-0.084
$M_*/M_d = 0.01$											
0.103	0.052	3.558	0.185	0.451	0.000	0.000	0.000	-0.504			
0.151	0.101	2.680	0.270	0.325	0.000	0.000	0.000	-0.926			
0.211	0.201	2.006	0.403	0.356	0.396	0.000	0.000	-0.966	-1.037		
0.248	0.301	1.699	0.511	0.349	0.369	0.158	0.000	-0.970	-0.975	-1.037	
0.274	0.401	1.508	0.604	0.490	0.110	0.678	0.532	0.947	-0.344	-0.346	-0.395
0.296	0.500	1.374	0.688	0.628	0.565	1.166	1.249	0.995	-0.139	-0.162	-0.238
0.316	0.600	1.268	0.761	0.669	0.840	1.567	1.852	1.043	0.030	-0.027	-0.084
$M_*/M_d = 0.1$											
0.174	0.052	3.348	0.174	0.717	0.000	0.000	0.000	-0.123			
0.207	0.101	2.598	0.262	0.745	0.000	0.000	0.000	-0.157			
0.252	0.201	1.990	0.400	0.600	0.457	0.000	0.000	-0.092	-0.947		
0.282	0.301	1.693	0.509	0.457	0.558	0.441	0.000	-0.891	-0.999	-0.968	
0.304	0.401	1.504	0.602	0.473	0.515	0.448	0.087	-0.907	-0.981	-0.935	-1.005
0.321	0.500	1.371	0.686	0.465	0.437	0.765	0.940	-0.905	0.955	-0.205	-0.254
0.338	0.600	1.268	0.761	0.553	0.504	1.239	1.553	0.953	0.905	-0.037	-0.094
$M_*/M_d = 1.0$											
0.373	0.052	2.797	0.145	0.315	0.000	0.000	0.000	-0.245			
0.381	0.101	2.347	0.237	0.406	0.000	0.000	0.000	-0.141			
0.394	0.201	1.908	0.383	0.499	0.187	0.050	0.000	-0.065	-0.863	-1.142	
0.404	0.301	1.660	0.499	0.499	0.383	0.191	0.081	-0.041	-0.800	-0.911	-1.163
0.412	0.401	1.495	0.599	0.438	0.544	0.475	0.252	-0.013	-0.879	-0.809	-1.006
0.418	0.500	1.367	0.684	0.289	0.591	0.673	0.634	0.013	-0.929	-0.923	-0.876
0.424	0.600	1.265	0.760	0.292	0.691	0.700	0.723	-0.781	0.965	-0.977	-0.955
$M_*/M_d = 5.0$											
0.463	0.052	2.402	0.125	0.035	0.008	0.000	0.000	-0.391	-1.159		
0.465	0.101	2.123	0.214	0.046	0.029	0.000	0.000	-0.302	-1.066		
0.468	0.201	1.814	0.364	0.068	0.075	0.000	0.000	-0.186	-0.929		
0.470	0.301	1.618	0.487	0.081	0.149	0.076	0.019	-0.114	-0.836	-1.119	-0.670
0.472	0.401	1.473	0.590	0.065	0.199	0.170	0.072	-0.073	-0.758	-0.895	-1.172
0.474	0.500	1.360	0.680	0.013	0.339	0.259	0.202	-0.763	-0.768	-0.811	-0.871
0.476	0.600	1.262	0.758	0.010	0.432	0.490	0.476	-0.747	0.784	-0.812	-0.790
$M_*/M_d = 10.0$											
0.480	0.052	2.284	0.119	0.000	0.011	0.000	0.000		-1.233		
0.481	0.101	2.030	0.205	0.000	0.016	0.000	0.000		-1.102		
0.482	0.201	1.763	0.354	0.000	0.028	0.000	0.000		-0.981		
0.483	0.301	1.593	0.479	0.000	0.053	0.031	0.025		-0.780	-1.162	-0.317
0.484	0.401	1.461	0.585	0.000	0.130	0.084	0.028		-0.734	-0.955	-1.249

Table 4.2.2.1. Characteristic radii, $y_1(m)$ and $y_2(m)$ values for selected $q = 1.5$ models.

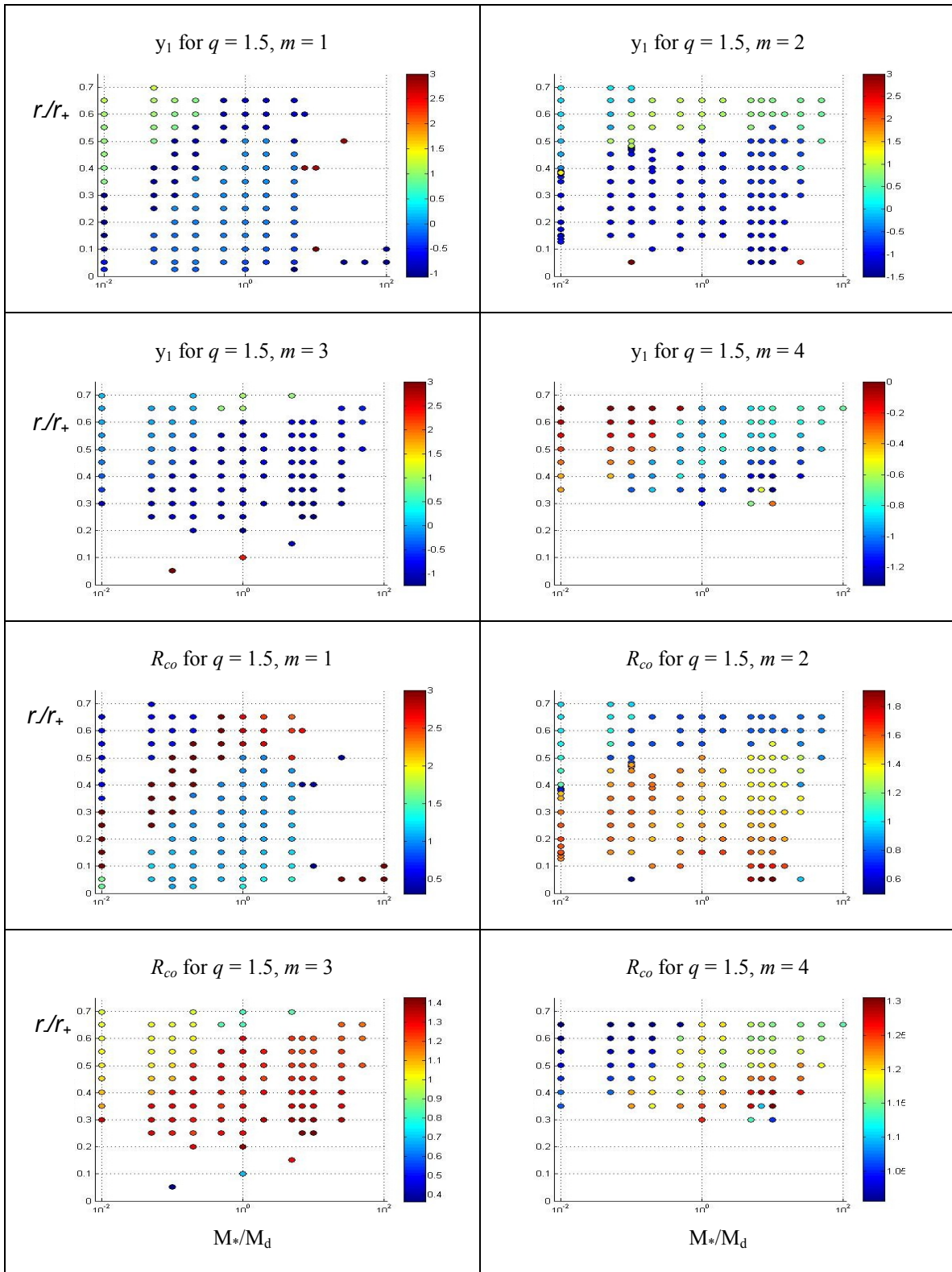


Fig. 4.2.2.9. y_1 frequency eigenvalues and corotation radii for $q = 1.5$, $m = 1, 2, 3$ and 4.

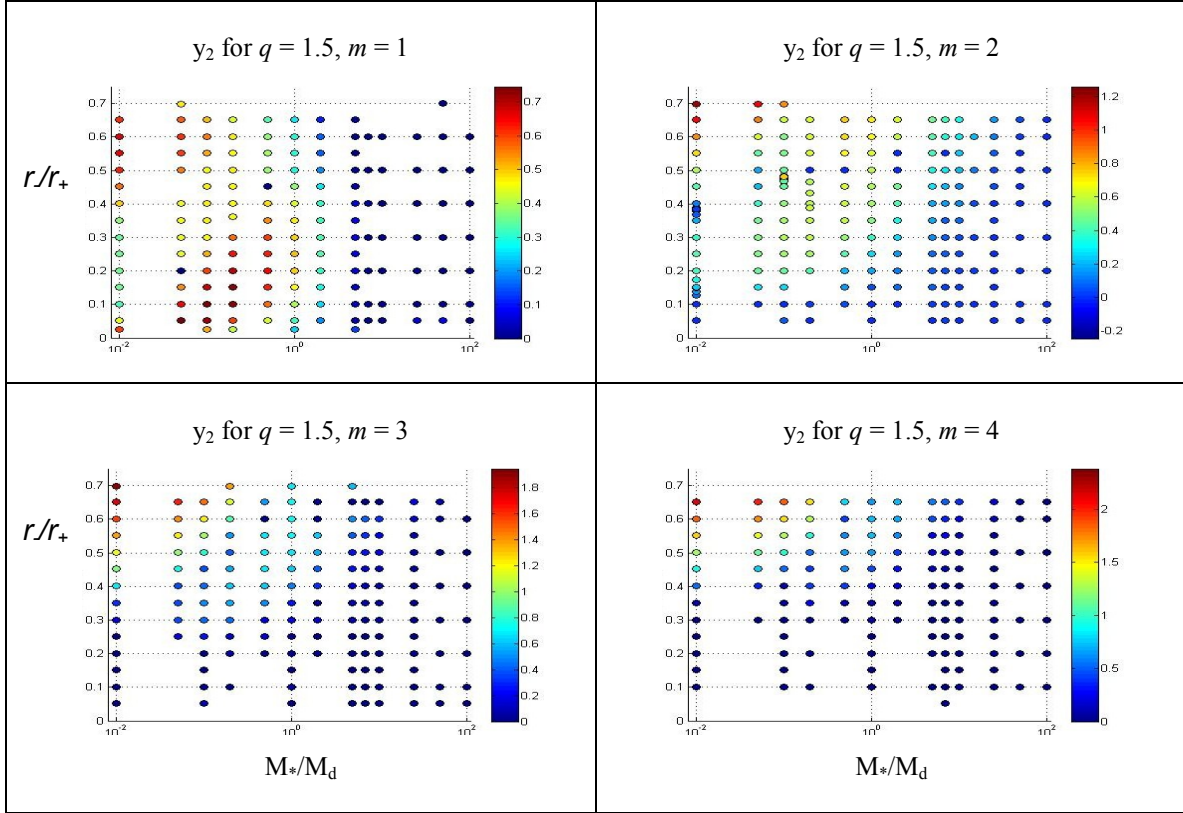


Fig. 4.2.2.10. y_2 growth rate eigenvalues for $q = 1.5$, $m = 1, 2, 3$ and 4 .

4.2.3. Results for $q = 1.75$ Models

The $q = 1.75$ models represent the parameter space between the Keplerian angular velocity profile of $q = 1.5$ and the limiting case of $q = 2.0$, and share traits of both. In the equilibrium results, we see that in plots where the results diverge for the differing q , $q = 1.75$ results resemble $q = 2.0$ more closely than $q = 1.5$ results, as evidenced in the plots of total angular momentum, location of the maximum mass density, $T/|W|$, etc. Fig. 4.2.3, depicting modal dominance, also indicates agreement between $q = 1.75$ and $q = 2.0$ with a notable exception in the region of stability. Models with $q = 1.75$ are more stable, especially for high M_*/M_d , where $q = 2.0$ models are seldom stable. Where the traits of the $q = 1.75$ models resemble those of the $q = 1.5$ and 2.0 models, the reader is

referred to those sections for detailed descriptions of the models. In this section, we will discuss where behaviors of the models diverge from those of the $q = 1.5$ and 2.0 disks. General traits of the $q = 1.75$ models are shown for $m = 1, 2, 3,$ and 4 in Figs. 4.2.3.1 - 4.2.3.4. Plots of y_1, R_{co} and y_2 are shown in Figs. 4.2.3.8 and 4.2.3.9.

Fig. 4.2.3.1 indicates that the $m = 1$ models, in the region where $R_{co} < r_-$ and $R_{co} > r_+$, behave qualitatively like $q = 1.5$ and models in that the parameter space is roughly divided up similarly, though the extent of the regions is somewhat different, as indicated in the parameter space maps. They differ from the $q = 2.0$ behavior in the region where $R_{co} \approx R_\theta$ in that there is a strong resemblance to P modes only for $r./r_+ \geq 0.60$ for $M^*/M_d \geq 25.0$. Non-self-gravitating models are stable $0.30 < r./r_+ < 0.60$ and bear no resemblance to self-gravitating models for $r./r_+ < 0.30$. The self-gravitating $q = 1.75$ models do not exhibit extensive wrapping and are stable in the region of parameter space where $q = 2.0$ models exhibit extensively wrapping spiral arms, characteristic of edge modes. Disks with small M^*/M_d , close to the I mode region, exhibit traits similar to those for the $q = 2.0$ models. A modes, with spiral waves, occupy a larger region than is found for either $q = 1.5$ or 2.0 , as indicated in Fig. 4.2.3.1. The $q = 1.75$ A mode region is bounded by stable regions at the low M^*/M_d end as well as at the high M^*/M_d end, and more models are found for higher $r./r_+$ than are found for $q = 1.5$ or 2.0 . Discussions of the A mode models can be found in Section 5.1.3, involving the $m = 1$ case, and Section 5.1.4, concerning a comparison with our results and those of Woodward, Tohline & Hachisu (1994).

Models for $m = 2$ exhibit traits similar to those for $q = 2.0$ in the J mode region where $M^*/M_d < 0.1$ and $r./r_+ < 0.40$, as well as in the region where $R_{co} \approx r_-$. The extents of these regions are roughly similar, with the main difference being that the $R_{co} \approx r_-$ region extends to higher $M^*/M_d = 25.0$ for $q = 1.75$ models, whereas the $q = 2.0$ models are stable for $10.0 \leq M^*/M_d < 50.0$. The main difference seen in $q = 1.75$ models, as compared to $q = 2.0$ models, is that there is no P mode region where $R_{co} \approx R_\theta$, as $q = 1.75$ models are stable for the region of parameter space where $q = 2.0$ models exhibit this behavior.

The $m = 3$ and 4 models have increasingly smaller unstable regions of parameter space for $q = 1.75$ models, even more than is seen with the $q = 1.5$ models. The main trends inherent to the J mode regions of the $q = 1.75$ models are similar to those of the $q = 2.0$ models. The I^+ regions are similar in that they have R_{co} near the outer edge or outside the disk for $r/r_+ = 0.40$, smoothly moving inward toward R_0 as r/r_+ decreases. There are no regions where $R_{co} < R_0$, as is seen in the $q = 2.0$ models, and no models resembling P modes.

In Fig. 4.2.3.5, we merge the general trends of the parameter maps for $m = 1, 2, 3$ and 4 , in black, blue, orange and red dashed lines, respectively. Solid lines indicate stability thresholds, using the same color coding for $m = 1, 2, 3$ and 4 . We show the parameter space trends plotted against self-gravity parameters p and η in Figs. 4.2.3.6 and 4.2.3.7, respectively, with some of the parameter map colors lightened to aid in discerning them against the parameters p and η plots. Similarly to the $q = 1.5$ models, we see that the boundaries for the I and J modes tend to follow the contours of constant p , but for $q = 1.75$, the stability thresholds for $m = 2, 3$ and 4 also track along contours of p . This is because we do not see P and edge modes for these models, so the I boundaries are also stability thresholds. The $m = 1$ stability threshold has been lightened to grey, to make it more visible against the dark blue of the low p values. It bears little resemblance to the qualitative shape of the p contours. We see there is little resemblance between these modal boundaries and the contours of constant η .

The parameter space maps are meant to be only general qualitative representations. Table 4.2.3.1 provides $q = 1.75$ values for $T/|W|$, r/r_+ , r/R_0 , r_+/R_0 , $y_2(m)$ and $y_1(m)$ for $m = 1, 2, 3$ and 4 , for $M^*/M_d = 0.0, 0.01, 0.1, 1.0, 5.0$, and 10.0 . Note that where $y_2(m) = 0.0$, no value of $y_1(m)$ exists. Plots of corotation radii and y_1 eigenfunction values are provided in Fig. 4.2.3.8 for $m = 1, 2, 3$ and 4 ; and y_2 eigenfunction values are provided in Fig. 4.2.3.9. The R_{co} magnitudes have been truncated to 5.0 for graphing purposes.

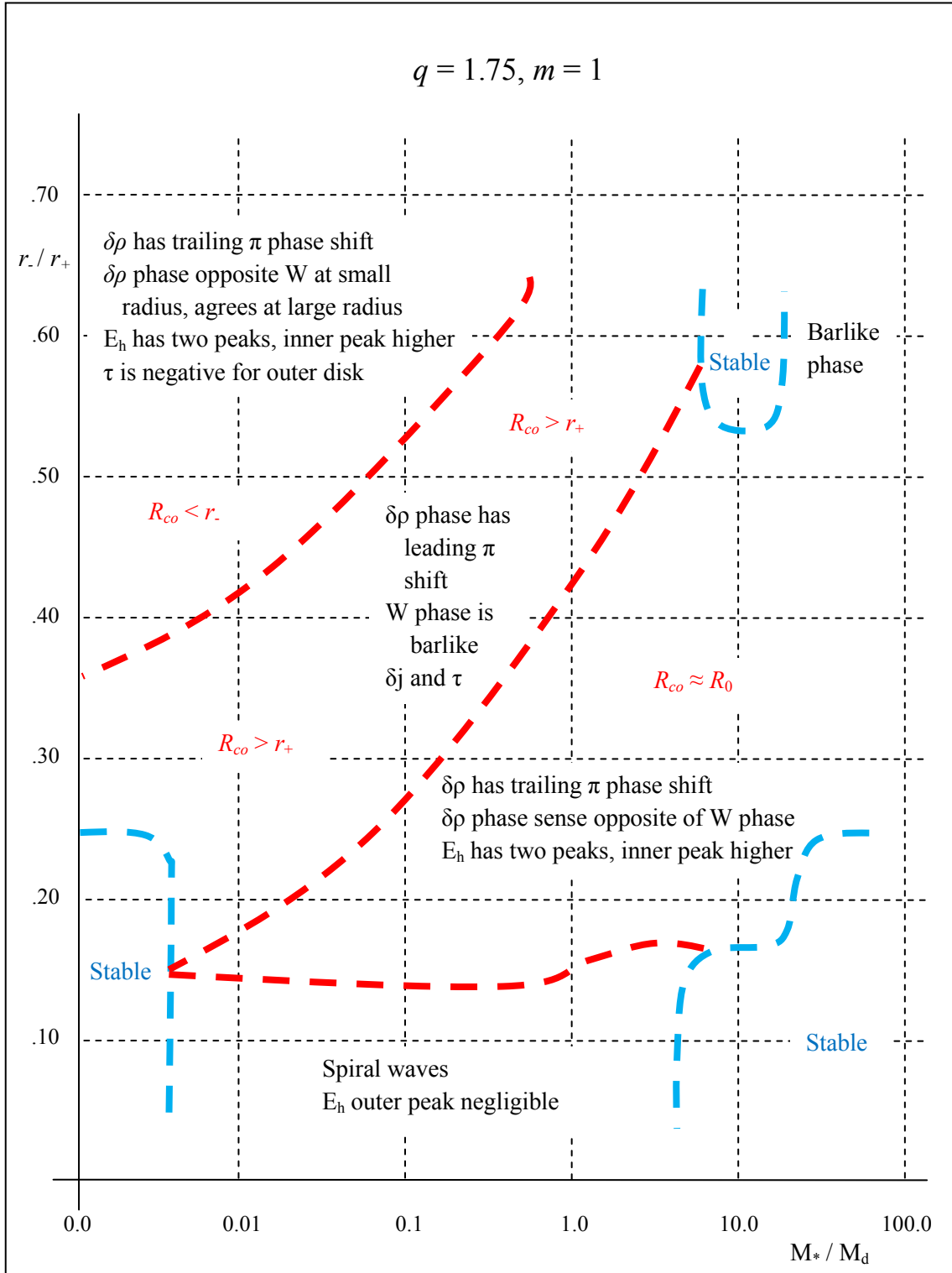


Fig. 4.2.3.1. Parameter space map for $q = 1.75, m = 1$, with modal divisions shown with red dashed lines and stability thresholds shown in blue dashed lines.

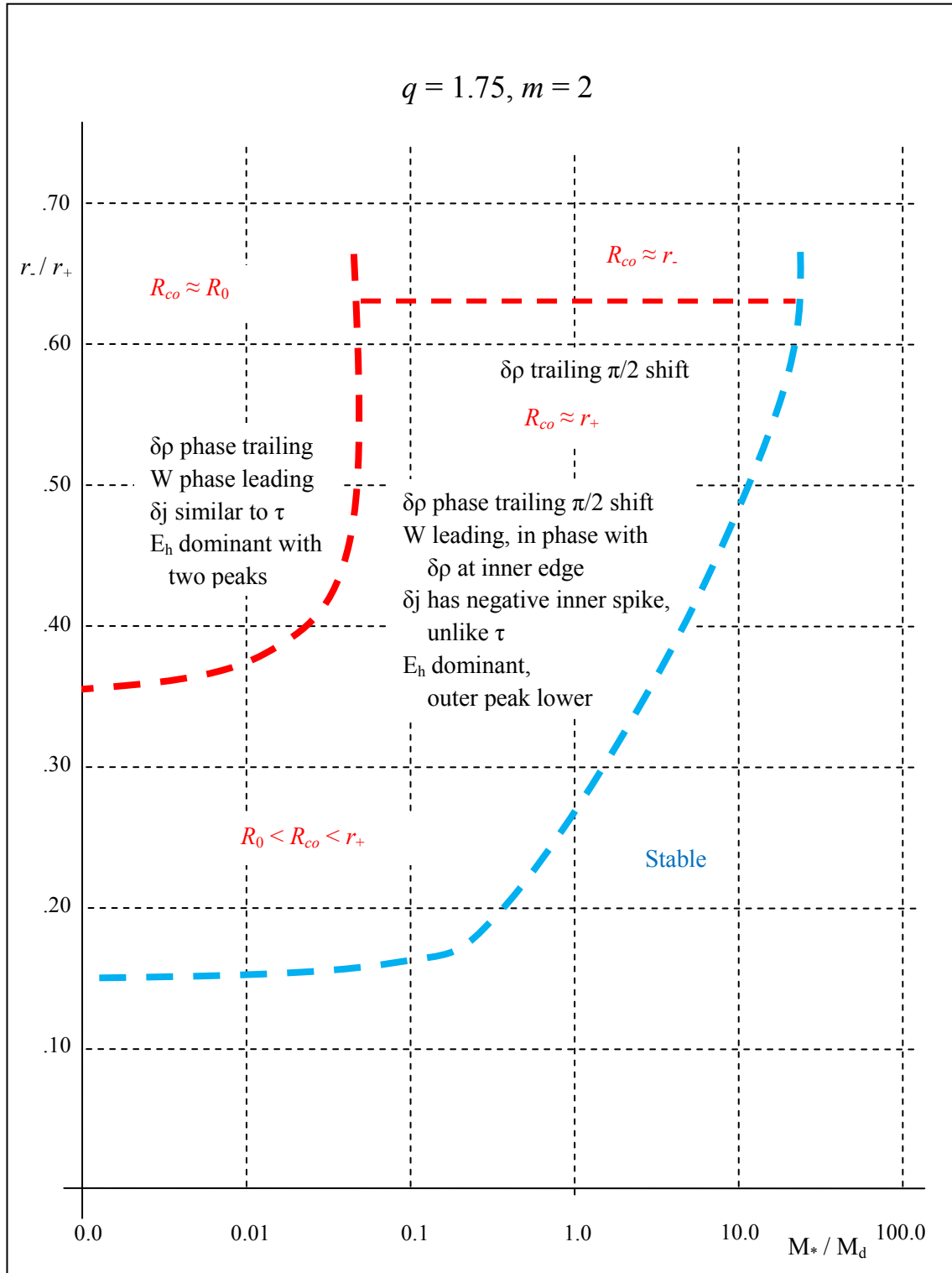


Fig. 4.2.3.2. Parameter space map for $q = 1.75, m = 2$, with modal divisions shown with red dashed lines and stability thresholds shown in blue dashed lines.

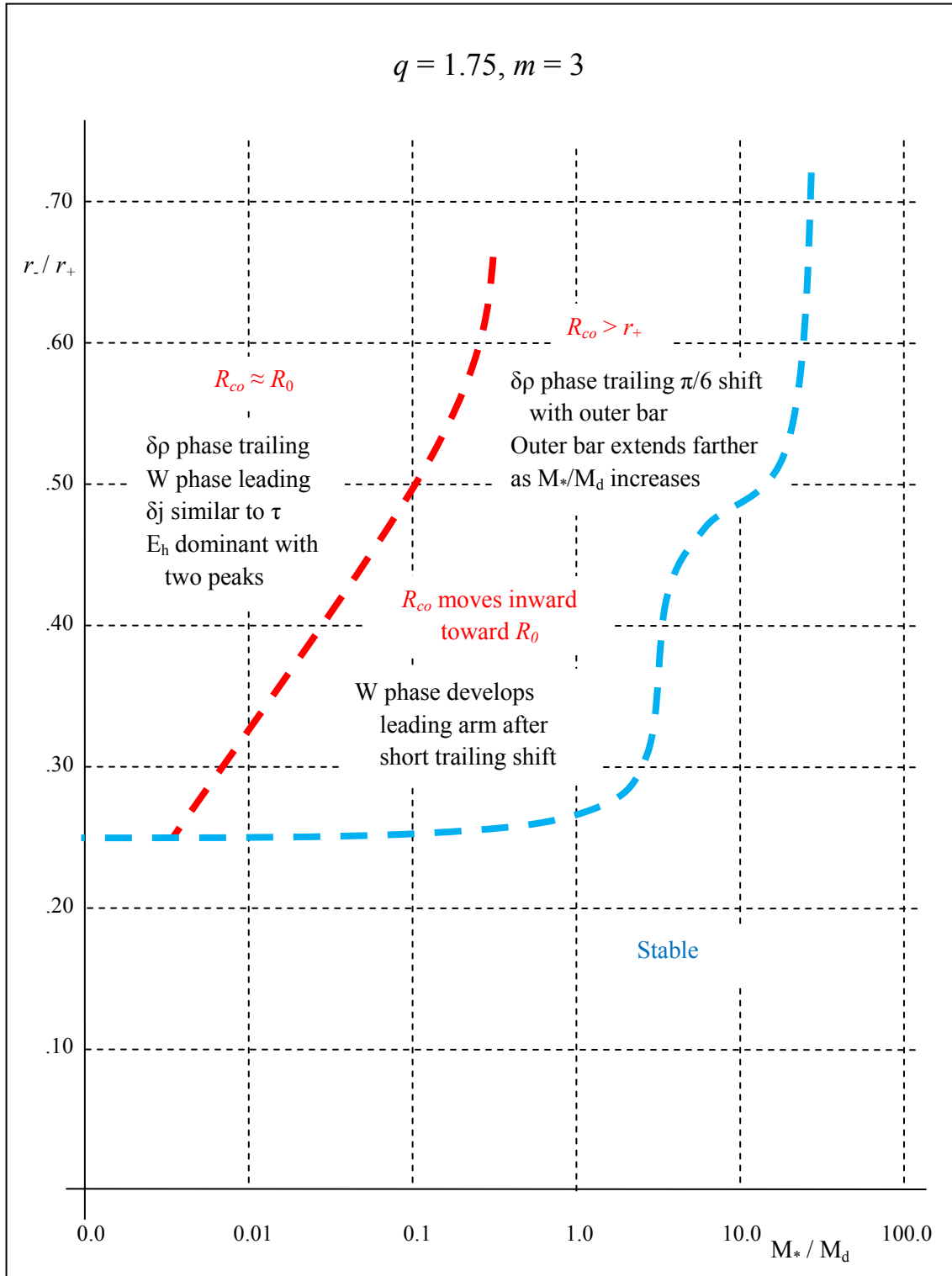


Fig. 4.2.3.3. Parameter space map for $q = 1.75, m = 3$, with modal divisions shown with red dashed lines and stability thresholds shown in blue dashed lines.

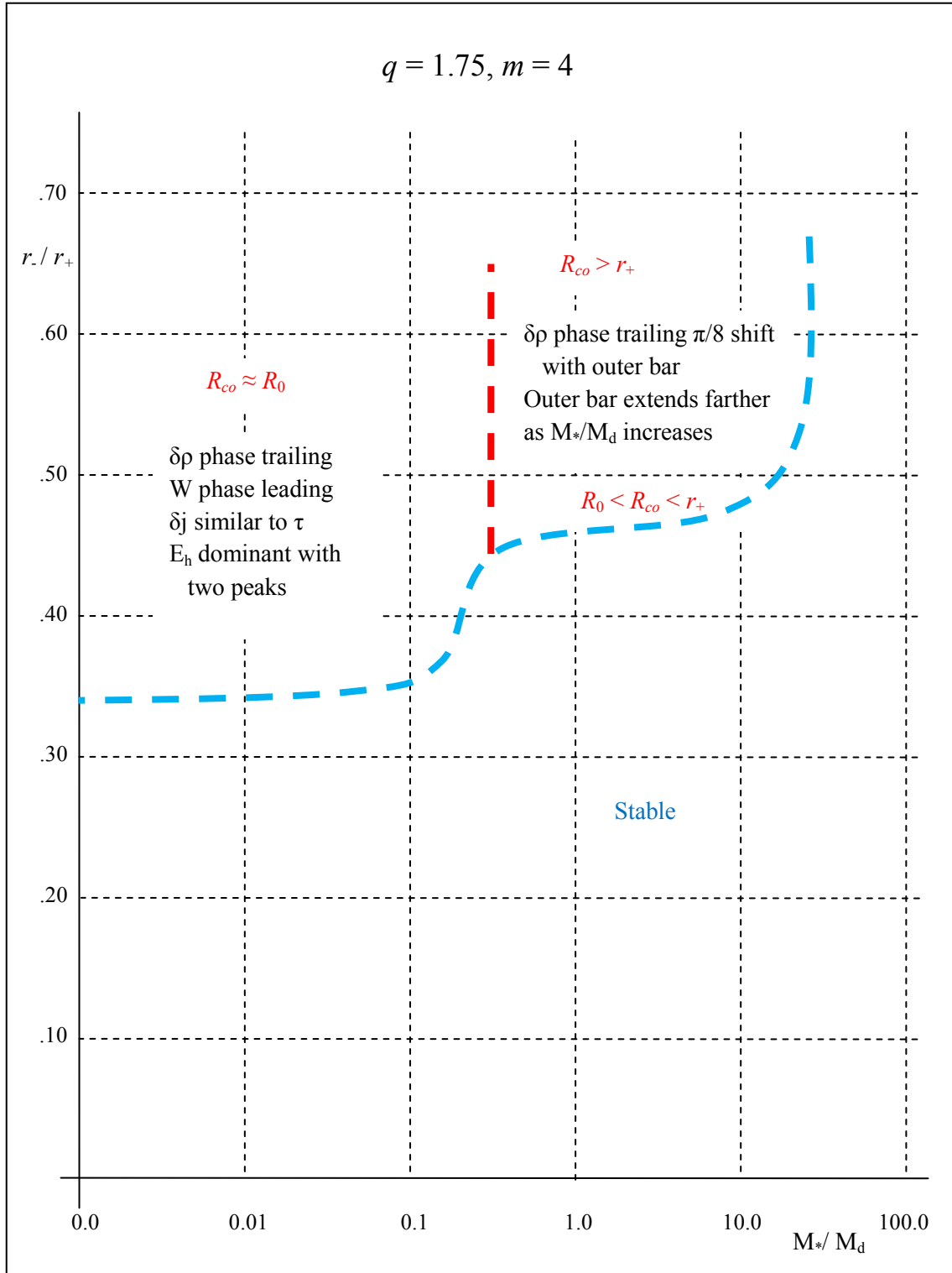


Fig. 4.2.3.4. Parameter space map for $q = 1.75, m = 4$, with modal divisions shown with red dashed lines and stability thresholds shown in blue dashed lines.

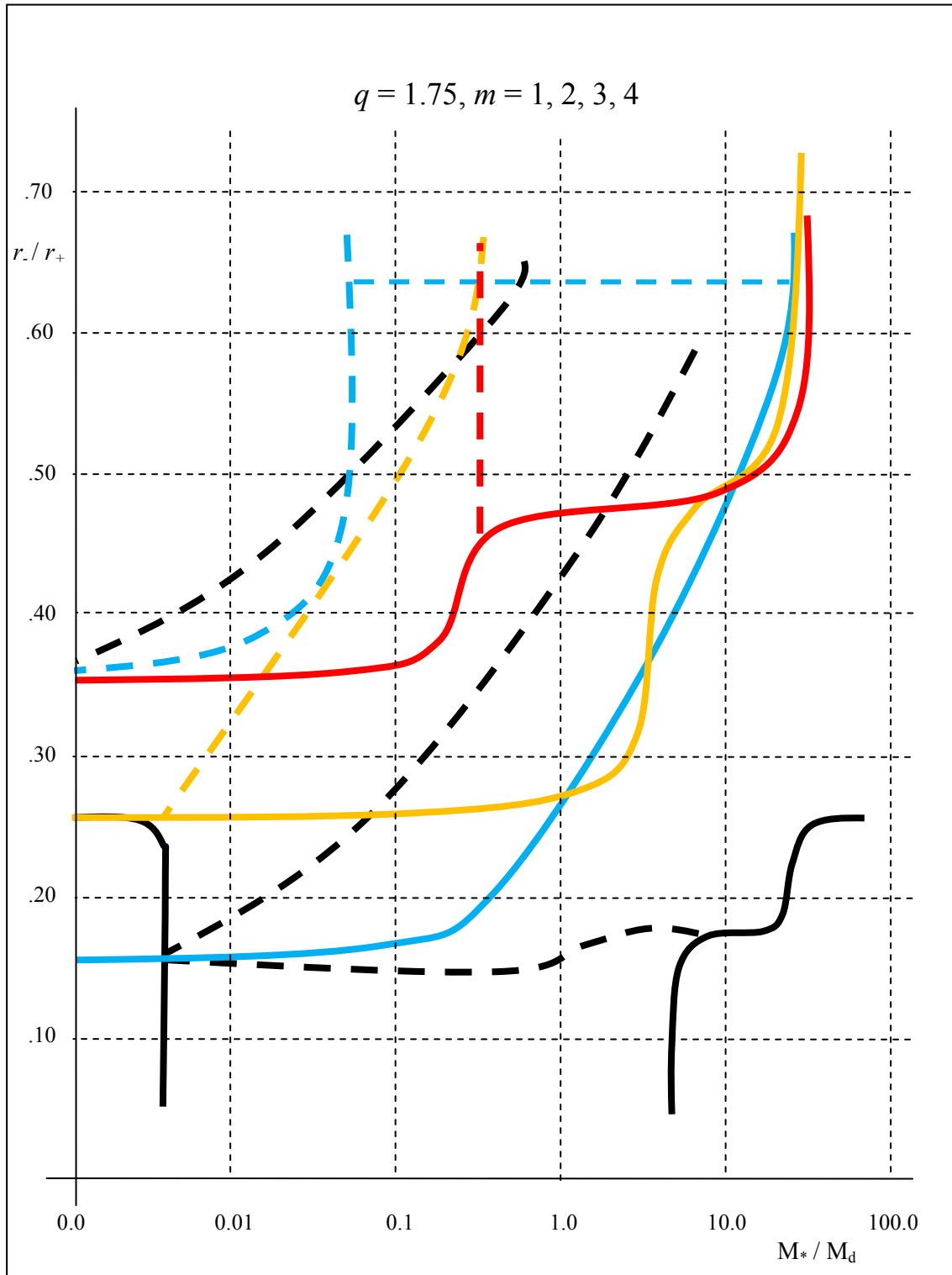


Fig. 4.2.3.5. Parameter space map for $q = 1.75$, $m = 1, 2, 3$ and 4 , shown in black, blue, orange and red dashed lines, respectively. Solid lines are boundaries of stable models.

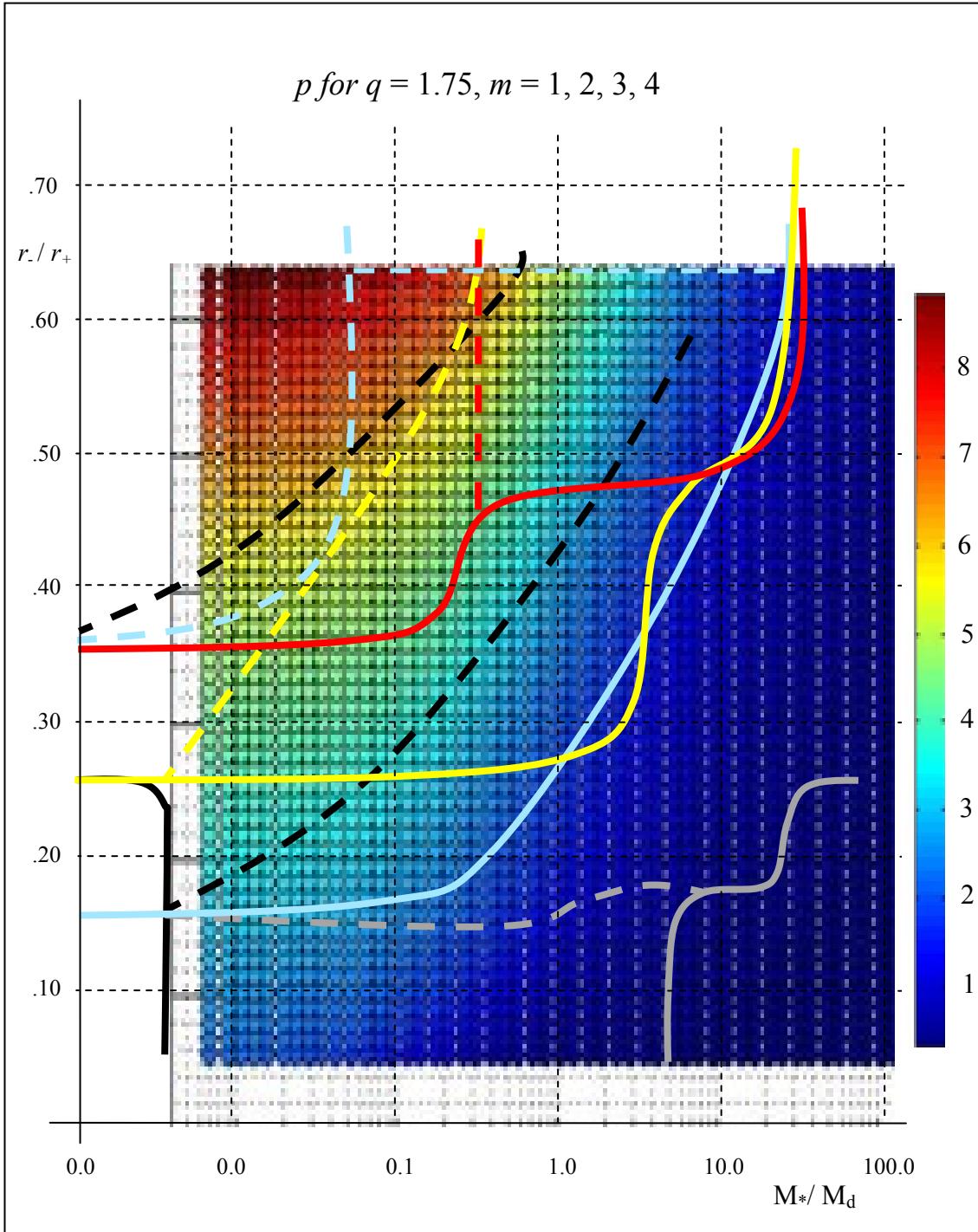


Fig. 4.2.3.6. Parameter space map overlaid on self-gravity parameter p for $q = 1.75$, $m = 1, 2, 3$ and 4 , shown in black, blue, orange and red, respectively dashed lines. Solid lines are boundaries of stable models. Some colors were lightened.

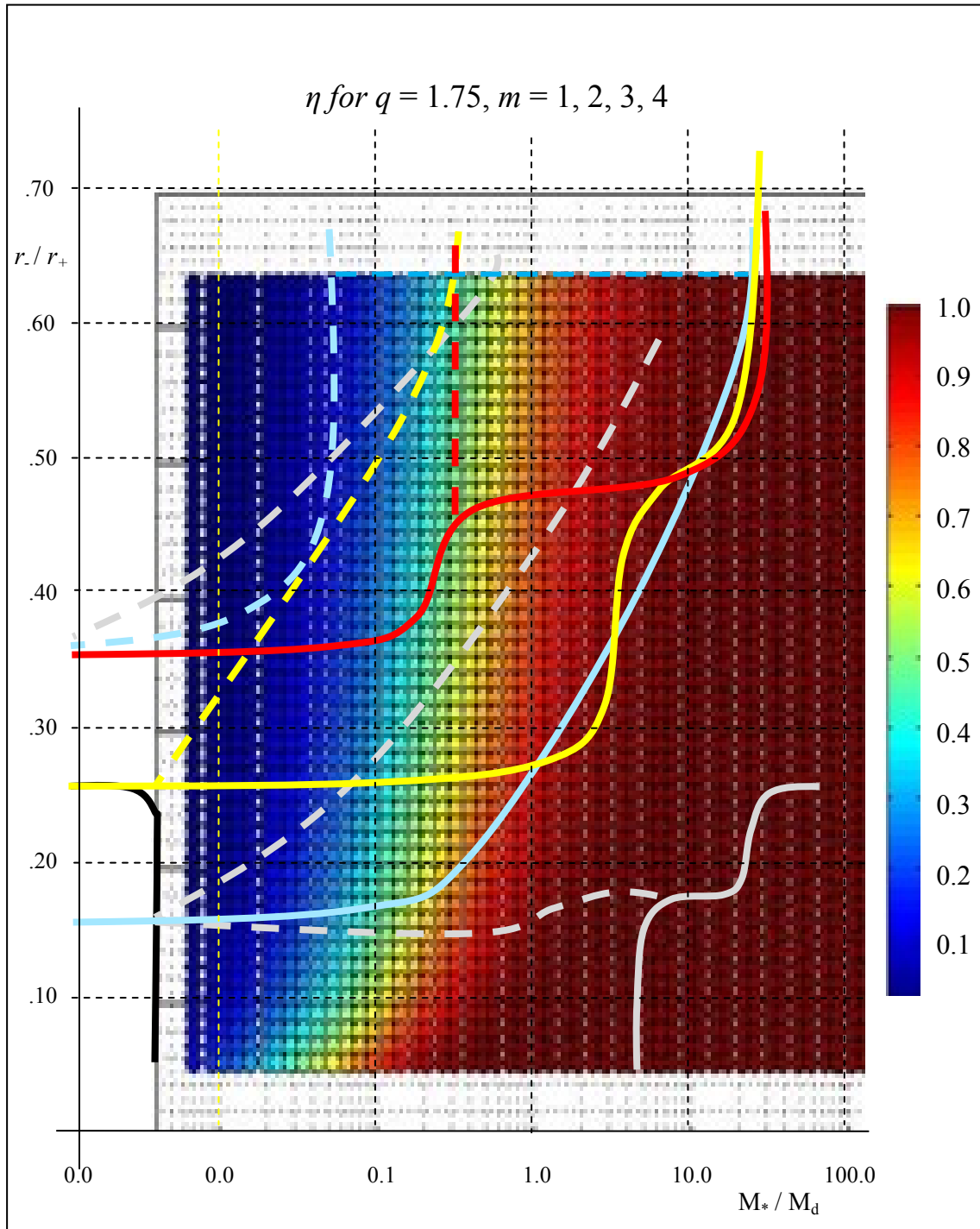


Fig. 4.2.3.7. Parameter space map overlaid on self-gravity parameter η for $q = 1.75$, $m = 1, 2, 3$ and 4 , shown in black, blue, orange and red dashed lines, respectively. Solid lines are boundaries of stable models. Some colors were lightened.

Eigenvalues for $q = 1.75$											
T/ W	r/r_+	r_+/R_o	r/R_o	$y_2(1)$	$y_2(2)$	$y_2(3)$	$y_2(4)$	$y_1(1)$	$y_1(2)$	$y_1(3)$	$y_1(4)$
$M_*/M_d = 0.0$											
0.183	0.201	2.097	0.421	0.000	0.247	0.000	0.000		-1.064		
0.230	0.301	1.733	0.521	0.116	0.360	0.000	0.000	0.981	-1.005		
0.262	0.401	1.522	0.610	0.449	0.064	0.559	0.332	0.983	-0.306	-0.387	-0.381
0.288	0.500	1.378	0.690	0.602	0.654	1.137	1.163	1.038	-0.093	-0.169	-0.248
0.311	0.600	1.272	0.763	0.667	0.958	1.577	1.830	1.123	-0.008	-0.040	-0.095
$M_*/M_d = 0.01$											
0.067	0.052	4.237	0.220	0.534	0.000	0.000	0.000	-0.599			
0.118	0.101	2.977	0.300	0.327	0.000	0.000	0.000	-0.476			
0.189	0.201	2.097	0.421	0.345	0.261	0.000	0.000	-0.963	-1.052		
0.234	0.301	1.733	0.521	0.348	0.402	0.000	0.000	-0.974	-1.015		
0.266	0.401	1.522	0.610	0.406	0.026	0.492	0.279	0.966	1.411	-0.400	-0.379
0.291	0.500	1.378	0.690	0.575	0.604	1.096	1.126	1.035	-0.115	-0.175	-0.252
0.313	0.600	1.272	0.763	0.652	0.896	1.535	1.790	1.099	-0.005	-0.039	-0.096
$M_*/M_d = 0.1$											
0.114	0.052	4.981	0.259	0.587	0.000	0.000	0.000	-0.362			
0.162	0.101	3.103	0.313	0.738	0.000	0.000	0.000	-0.315			
0.226	0.201	2.114	0.424	0.647	0.289	0.000	0.000	-0.189	-0.956		
0.267	0.301	1.739	0.523	0.492	0.521	0.240	0.000	-0.057	-1.011	-0.975	
0.295	0.401	1.526	0.611	0.464	0.520	0.475	0.024	-0.902	-0.997	-0.997	-1.158
0.316	0.500	1.378	0.690	0.459	0.389	0.614	0.765	-0.914	-0.920	-0.247	-0.294
0.335	0.600	1.272	0.763	0.537	0.464	1.197	1.480	1.003	0.990	-0.052	-0.109
$M_*/M_d = 1.0$											
0.251	0.052	8.168	0.424	0.023	0.000	0.000	0.000	-0.752			
0.300	0.101	4.100	0.414	0.225	0.000	0.000	0.000	-0.463			
0.352	0.201	2.315	0.465	0.507	0.000	0.000	0.000	-0.240			
0.381	0.301	1.801	0.541	0.553	0.275	0.029	0.000	-0.146	-0.823	-1.117	
0.399	0.401	1.545	0.619	0.500	0.478	0.348	0.000	-0.081	-0.878	-0.818	
0.411	0.500	1.385	0.693	0.370	0.567	0.617	0.527	-0.028	-0.931	-0.923	-0.880
0.421	0.600	1.272	0.763	0.259	0.639	0.679	0.693	-0.762	0.960	-0.977	-0.968
$M_*/M_d = 5.0$											
0.414	0.201	2.652	0.532	0.125	0.000	0.000	0.000	-0.415			
0.440	0.301	1.945	0.585	0.228	0.000	0.000	0.000	-0.239			
0.455	0.401	1.608	0.644	0.247	0.129	0.000	0.000	-0.140	-0.761		
0.465	0.500	1.412	0.707	0.197	0.259	0.211	0.035	-0.083	-0.769	-0.739	-1.056
0.471	0.600	1.281	0.769	0.000	0.364	0.426	0.392		0.810	-0.807	-0.780
$M_*/M_d = 10.0$											
0.426	0.201	2.752	0.553	0.039	0.000	0.000	0.000	-0.496			
0.451	0.301	2.006	0.603	0.123	0.000	0.000	0.000	-0.284			
0.466	0.401	1.644	0.659	0.152	0.000	0.000	0.000	-0.165			
0.475	0.500	1.428	0.715	0.131	0.064	0.044	0.007	-0.088	-0.730	-0.680	-0.953
0.481	0.600	1.291	0.775	0.009	0.197	0.258	0.178	-0.055	0.606	-0.737	-0.699

Table 4.2.3.1. Characteristic radii, $y_1(m)$ and $y_2(m)$ values for selected $q = 1.75$ models.

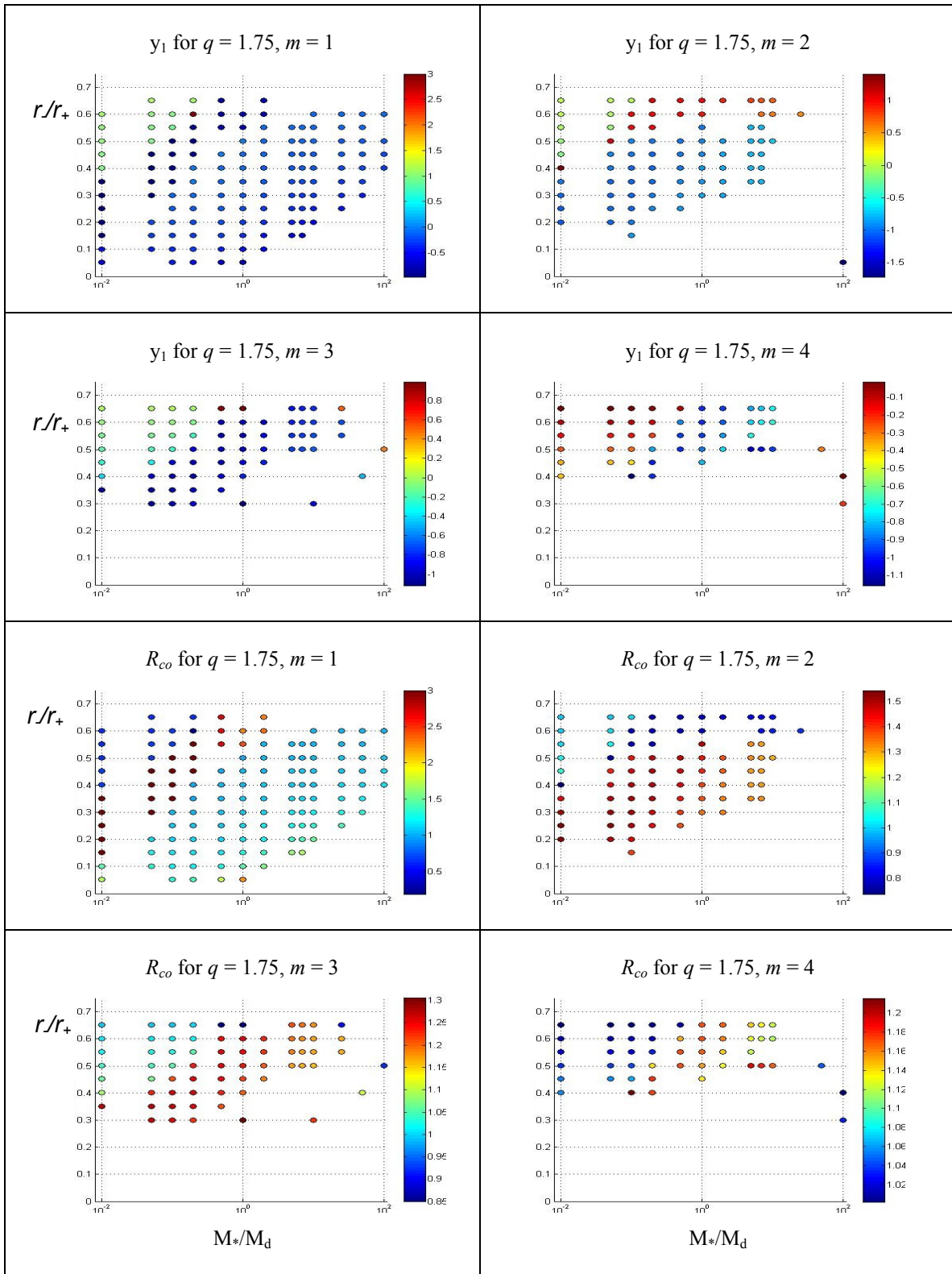


Fig. 4.2.3.8. y_1 frequency eigenvalues and corotation radii for $q = 1.75, m = 1, 2, 3$ and 4.

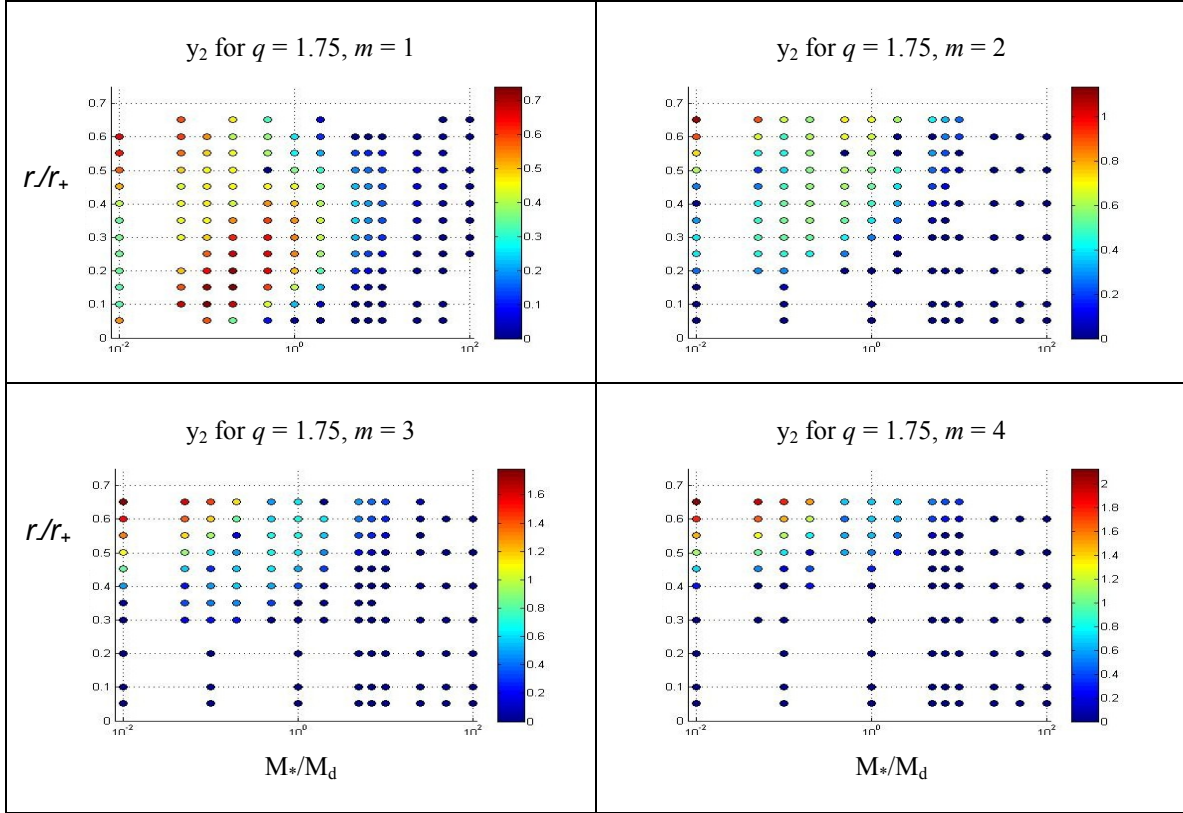


Fig. 4.2.3.9. y_2 growth rate eigenvalues for $q = 1.75$, $m = 1, 2, 3$ and 4 .

4.2.4. Results for $q = 2.0$ Models

Thin disks have been shown to be unstable to axisymmetric instabilities when specific angular momentum decreases radially outward (Rayleigh 1916). For a power law angular velocity profile, $q = 2.0$ is the bounding case, with constant specific angular momentum. We have mapped trends for $m = 1, 2, 3$ and 4 and will present analysis of these maps, supported by tables of representative plots in Figs. A.3.0 - A.3.6.

The character of the $|\delta\rho|/\rho_0$ and W phase plots varies across the regions shown in the parameter space map for $q = 2.0$, $m = 1$ shown in Fig. 4.2.4.3. In the region of very high r/r_+ and small M^*/M_d , the $|\delta\rho|/\rho_0$ phase plots exhibit a trailing arm of roughly π extent while the W phase plots exhibit a shorter leading arm and are out of phase everywhere with $|\delta\rho|/\rho_0$. Corotation is about halfway between R_0 and r_+ here. Phase plots of $|\delta\rho|/\rho_0$ in the I mode regions show an inner bar with a leading π shift and a small outer

bar, with the phase shift switching to trailing for $r./r_+ < 0.50$ for Γ modes. W phases show a short leading shift, switching to a short trailing arm in the region where $R_{co} < r_.$, but are more barlike where $R_{co} > r_.$. As M_*/M_d increases into the region where R_{co} is near R_0 , a few models near that threshold exhibit trailing $|\delta\rho|/\rho_0$ with a π phase shift and leading W phases. With a further increase of M_*/M_d , the $|\delta\rho|/\rho_0$ phase begins leading as well, and smoothly transitions across the region, to closely resemble the P modes of the non-self-gravitating models. Large M_*/M_d and $r./r_+$ $|\delta\rho|/\rho_0$ phase plots exhibit a leading arm of approximately $\pi/2$, smoothly changing to a shorter leading arm, switching to a trailing arm that lengthens and wraps more as $r./r_+$ decreases. These models also begin to exhibit a second, then multiple minima in the eigenfunction amplitude plots. This was mentioned by Christodoulou (1993) as a hallmark of edge modes, as well as the pronounced spiral nature with extensive wrapping.

Perturbed angular momentum plots display character similar to that of the self-gravity torque plots in the region where M_*/M_d is small and $r./r_+$ is large; δj and τ are negative in the inner part of the disk and positive in the outer part, changing sign near R_0 with approximately the same magnitudes at the maxima and minima. In the I mode regions, the character is similar except that the has opposite sign. For the models with larger M_*/M_d than the I mode regions, δj and τ are similar in sign but here the amplitudes of the maxima and minima are different, with the negative values of the minima much larger than the positive values of the maxima. As $r./r_+$ decreases, the negative regions become increasingly narrow spikes.

In the work integral plots, E_h exhibits two peaks with a minimum separating them that goes to zero near R_0 in the area M_*/M_d is small and $r./r_+$ is large. As M_*/M_d increases and $r./r_+$ decreases, the second peak shrinks in magnitude and becomes negligible. In the region where M_*/M_d increases and $r./r_+ > 0.40$, the second peak remains and the minimum ceases to go to zero. The stresses for small $M_*/M_d = 0.0$, large $r./r_+$ have two maxima for σ_h , which dominate the inner and outer regions of the disk. The minimum between the peaks is negative and lies at approximately the same radius as the maximum of σ_G . The maximum of σ_R is much smaller than that of σ_G . A few other threshold models display this behavior, but for most of parameter space, the inner and outer peaks of σ_h are not present. The green lines in the map indicate the boundaries of the stress behavior. The

region with smaller M_*/M_d is dominated by σ_G , while σ_h dominates the region with higher M_*/M_d , as we would expect. Stresses in the region $M_*/M_d > 25.0$ take on behavior similar to that of the non-self-gravitating models. Acoustic flux dominates for $r \approx r_+$ and becomes negative for most of the rest of the disk. There are two regions of stable models, one for disks with $M_*/M_d = 0.0$ and $r/r_+ \leq 0.30$ and a second region for $r/r_+ = 0.70$ with $5.0 \leq M_*/M_d \leq 10.0$. A modes, with spiral arms, are found in the regions indicated for small r/r_+ . For more detail about A modes, see Section 5.1.3.

We next discuss the trends shown in Fig. 4.2.4.4 for models with $q = 2.0$ and $m = 2$. Some of the trends we noticed for $q = 2.0$ and $m = 1$ are present for $m = 2$ models. In particular, we see a stable region for $M_*/M_d = 10.0$ and large r/r_+ . There is also an I mode region where $R_{co} \approx r_+$, but it extends to $M_*/M_d = 0.0$ for $0.30 \leq r/r_+ \leq 0.40$ and continues diagonally to $r/r_+ = 0.60$ for a small region around $M_*/M_d = 5.0$. There is a region where $R_{co} \approx r_+$ with a much smaller extent, only existing for models with $M_*/M_d \geq 0.60$.

There are two regions where $R_{co} \approx R_0$, but other than the location of corotation, the behavior depicted in the plots is very different. Plots for disks with small $M_*/M_d = 0.0$ and large r/r_+ exhibit characteristics similar to those in the same region for $q = 2.0$ and $m = 1$, but with R_{co} closer to R_0 . Disks to the right of the I mode region in our map strongly approximate characteristics found in the non-self-gravitating models. Extensive wrapping occurs in $r/r_+ = 0.10$ models for $M_*/M_d \geq 1.0$, indicative of edge modes. Work integrals, stresses, and perturbed angular momenta all exhibit tendencies similar to those of the non-self-gravitating models. We see multiple minima in the eigenfunction amplitudes in the region with $R_{co} \approx R_0$ where r/r_+ is small. The minima occur with more frequency toward the outer edge of the disk. Models with $M_*/M_d \geq 25.0$ and $r/r_+ \geq 0.50$ exhibit short trailing arms and one minimum in the eigenfunction amplitude plot, traits indicative of P modes.

δj behavior resembles that of $q = 2.0$ and $m = 1$ but τ has different character. It does not resemble δj , except for small $M_*/M_d = 0.0$ with large r/r_+ . For other regions, δj has a steep negative narrow spike near the inner edge of the disk, similar to $m = 1$ models but τ , generally crosses zero more often as M_*/M_d increases. The character of the work integral plots is extremely similar to that of the $m = 1$ models.

We note some models in the region of parameter space between P modes and edge modes that seem to exhibit characteristics of both. For example, the phase plot for the model with $q = 2.0$, $m = 2$, $M_*/M_d = 50.0$ and $r_-/r_+ = 0.40$ exhibits an inner bar with a short leading arm, rapidly switching to a short trailing arm near R_0 , which is a hallmark of a P mode, but then the phase switches again to leading, and back to trailing, as shown in Fig. 4.2.4.1. The W phase tracks the $|\delta\rho|/\rho_0$ phase closely. The multiple minima in the eigenfunction amplitude plot are indicative of an edge mode, but typically edge modes exhibit a long, trailing spiral arm.

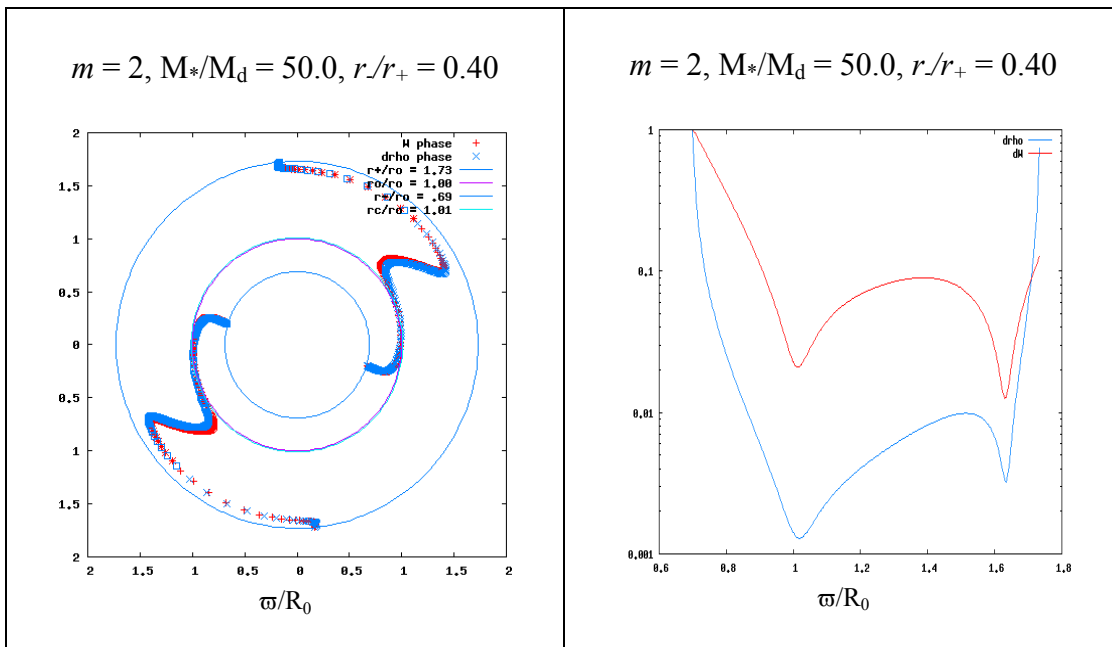


Fig. 4.2.4.1. Eigenfunction phase and amplitude plots for the model with parameters of $q = 2.0$, $m = 2$, $M_*/M_d = 50.0$ and $r_-/r_+ = 0.40$.

Another model that exhibits character not seen elsewhere is the model with parameters $q = 2.0$, $m = 2$, $M_*/M_d = 5.0$ and $r_-/r_+ = 0.40$. We show the eigenfunction phase and amplitude plots for this model in Fig. 4.2.4.2. It is interesting to note that the plots of this model bear a strong resemblance to those of the non-self-gravitating models for $m = 2$, $q = 1.75$. This model exhibits an inner bar with a short leading arm that switches to trailing less sharply than that of the $M_*/M_d = 50.0$ model, and no second leading shift is present. The W phase does not track the $|\delta\rho|/\rho_0$ phase closely, as would be

expected for a model with a lower M_*/M_d ratio. However, the character of the W phase has a characteristic trait present in the W phase of the $M_*/M_d = 50.0$ model, a second forward shift. Note the double minima of the W amplitude. The $M_*/M_d = 5.0$ model has a sharper first minimum, whereas the second minimum is sharper in the $M_*/M_d = 50.0$ model. Perhaps the most important distinction between these two models is that $R_{co} = 1.01$ for the $M_*/M_d = 50.0$ model but $R_{co} = 0.98$ for the $M_*/M_d = 5.0$ model. It seems likely that R_{co} passing through 1.00 marks the threshold between P modes and edge modes. It is also interesting to note that Woodward, Tohline & Hachisu mention that a characteristic of L modes is that corotation lies near R_θ . This will be discussed further in Section 5.1.4. Character traits of both of these models remained intact when run at a higher resolution of $1024 \times 1024 \times 16$.

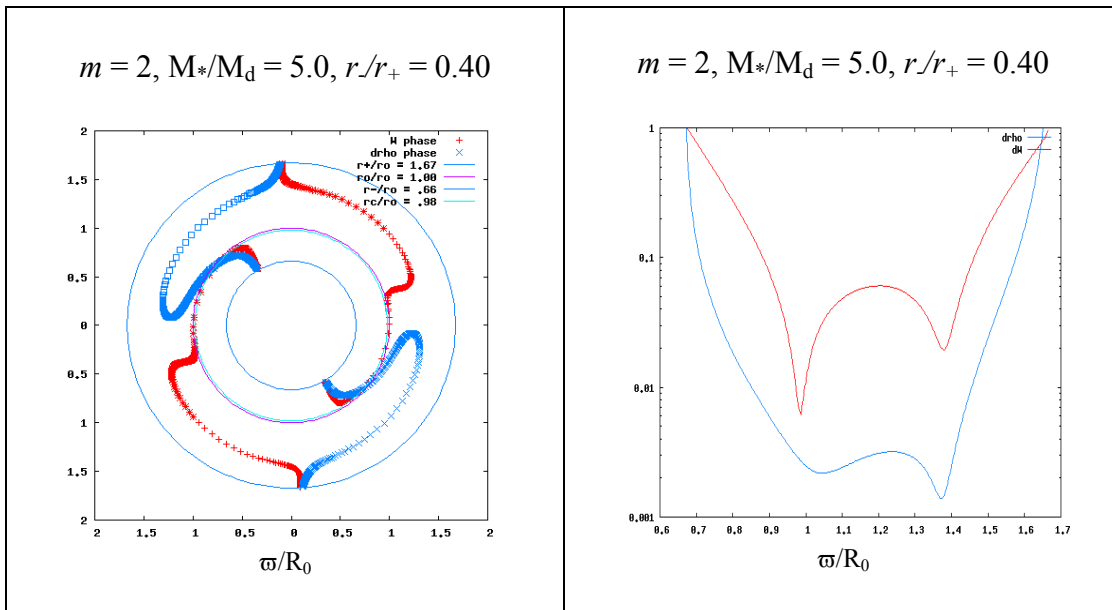


Fig. 4.2.4.2. Eigenfunction phase and amplitude plots for the model with parameters of $q = 2.0$, $m = 2$, $M_*/M_d = 5.0$ and $r/r_+ = 0.40$.

Fig. 4.2.4.5 indicates trends of $q = 2.0$, $m = 3$ models. One noticeable difference with $q = 1.5$, $m = 2$ models and $q = 2.0$, $m = 1$ and $m = 2$ models is that there is no region where $R_{co} \approx r$ anywhere in this part of parameter space. There is a region where $R_{co} \approx R_0$ for small M_*/M_d and high r/r_+ as in the previously examined parts of parameter space. The region with larger M_*/M_d exhibits $R_{co} \approx r_+$ for high r/r_+ with R_{co} moving inward,

changing to $R_{co} < R_0$ as shown. Phases of disks with $M^*/M_d \geq 1.0$ and $r./r_+ \leq 0.10$ show extensive wrapping, as seen with the $q = 2.0$, $m = 2$ disks. Some disks in this region exhibit complicated behavior, switching back and forth from leading to trailing arms. These models take 10 - 20 MIRPs to settle into mode and may be numerically unstable. The transition between J modes and I modes for $r./r_+ = 0.60$ is abrupt. For $r./r_+ = 0.40$, the transition is smoother. There seem to be two kinds of behavior present in the non-self-gravitating models, with a transition between them happening near $r./r_+ < 0.40$. The behavior of the lower $r./r_+$ P modes extends into the self-gravitating models while that of the higher $r./r_+$ is not evident in the self-gravitating models. This was not observed in the $m = 1$ and 2 models. Trends for $q = 2.0$, $m = 4$ models, shown in Fig. 4.2.3.6, are very similar to the trends we see in the $q = 2.0$, $m = 3$ models, with slightly shifted boundaries to the regions of parameter space.

In Fig. 4.2.4.7, we merge the general trends of the parameter maps for $m = 1, 2, 3$ and 4, in black, blue, orange and red, respectively. We show the parameter space trends plotted against self-gravity parameters p and η in Figs. 4.2.4.8 and 4.2.4.9, respectively, with some of the parameter map colors lightened to aid in discerning them against the parameters p and η plots. The modal boundaries I and J for $q = 2.0$ do not follow the contours of constant p as clearly as what was seen in the $q = 1.5$ and 1.75 cases. We do see that for $q = 2.0$, the shape of the p contours in the upper right corner is more horizontally flattened against the top of the plot. The I and J boundaries tend to be flatter in this sense as well. There are obviously features of the parameter space boundaries that do not correspond to the contours of p though it could be argued that the regions of stability in $m = 2$, shown in solid light blue lines, somewhat follow the contour of constant p . It is difficult to see any relationship between the modal boundaries and stability thresholds with the contours of constant η .

Table 4.2.4.1 provides $q = 2.0$ values for $T/|W|$, $r./r_+$, $r./R_0$, r_+/R_0 , $y_2(m)$ and $y_1(m)$ for $m = 1, 2, 3$ and 4, for $M^*/M_d = 0.0, 0.01, 0.1, 1.0, 5.0$, and 10.0. Note that where $y_2(m) = 0.0$, no value of $y_1(m)$ exists. Figs. 4.2.4.7 - 4.2.4.8 plot the eigenvalues and corotation radii for $m = 1, 2, 3$ and 4.

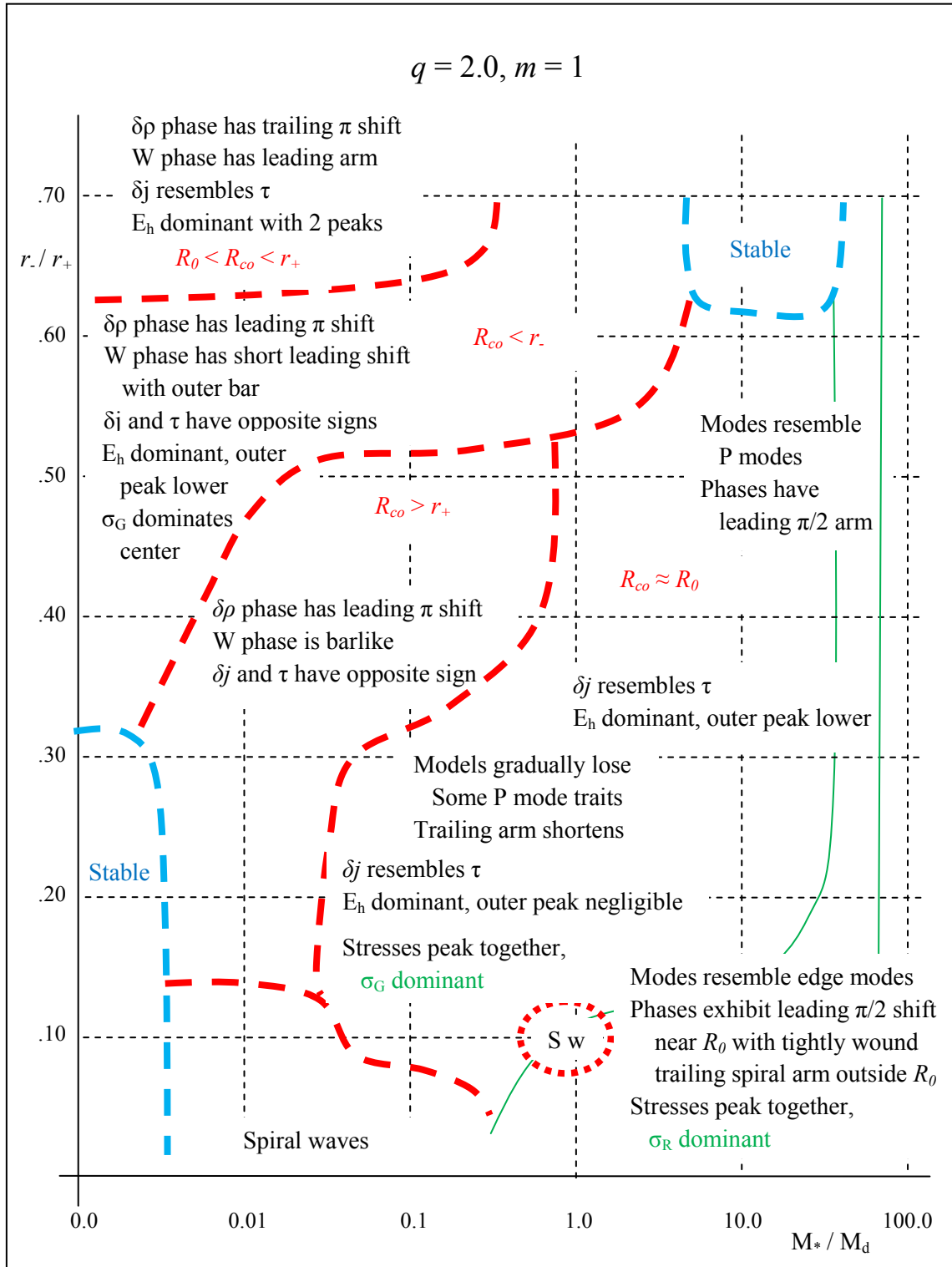


Fig. 4.2.4.3. Parameter space map for $q = 2.0, m = 1$, with modal divisions shown with red dashed lines and stability thresholds shown in blue dashed lines.

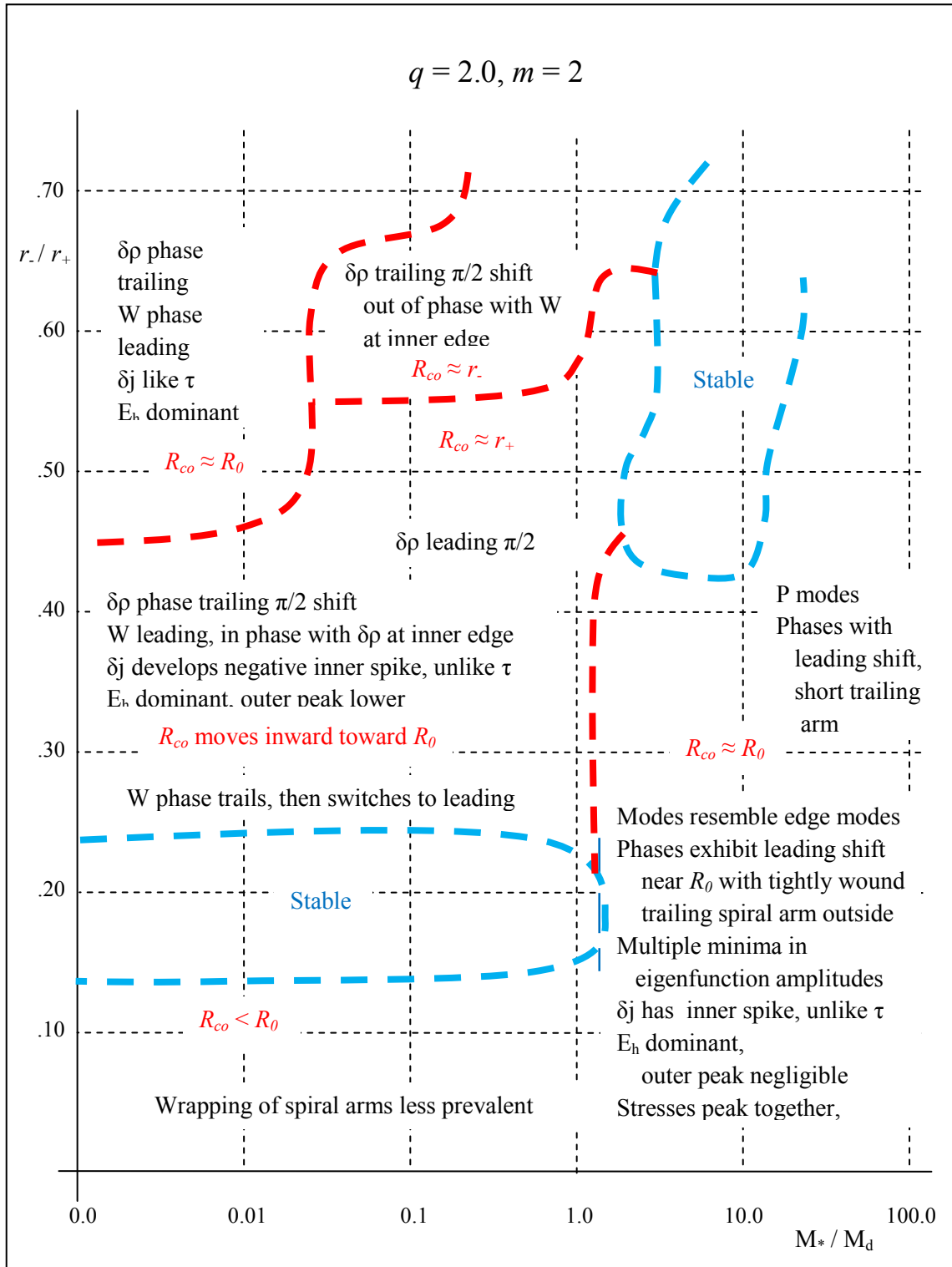


Fig. 4.2.4.4. Parameter space map for $q = 2.0, m = 2$, with modal divisions shown with red dashed lines and stability thresholds shown in blue dashed lines.

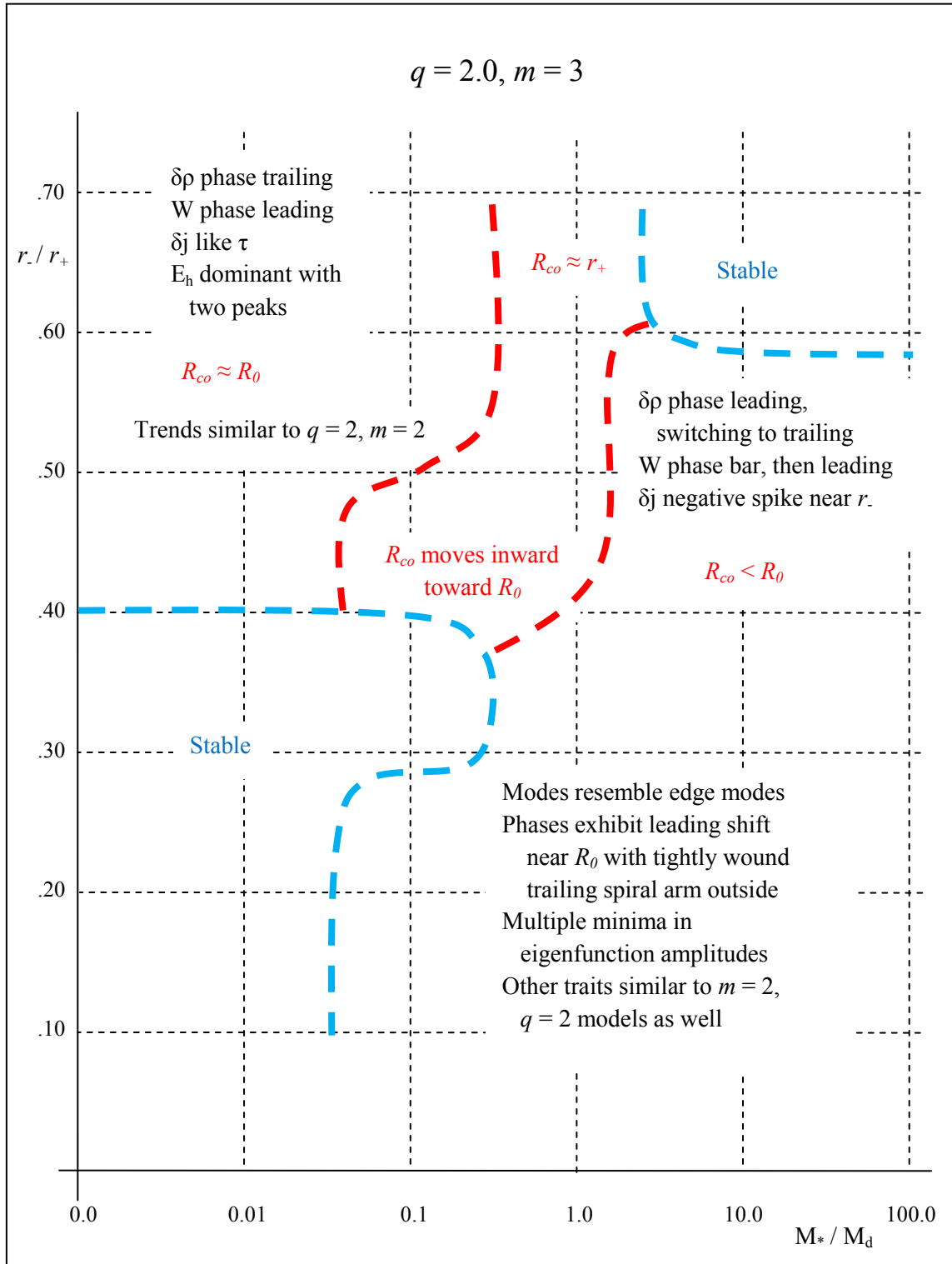


Fig. 4.2.4.5. Parameter space map for $q = 2.0, m = 3$, with modal divisions shown with red dashed lines and stability thresholds shown in blue dashed lines.

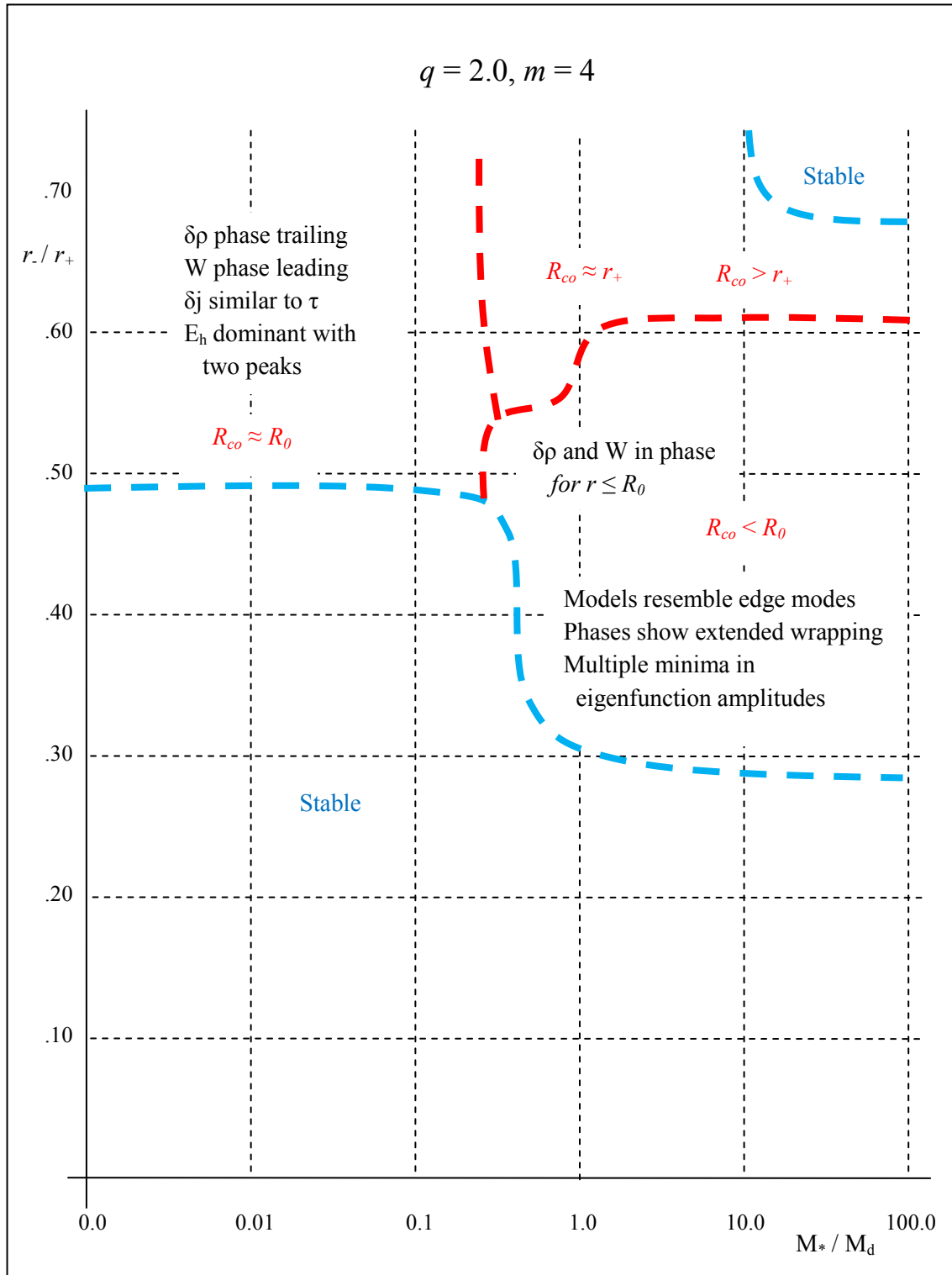


Fig. 4.2.4.6. Parameter space map for $q = 2.0, m = 4$, with modal divisions shown with red dashed lines and stability thresholds shown in blue dashed lines.

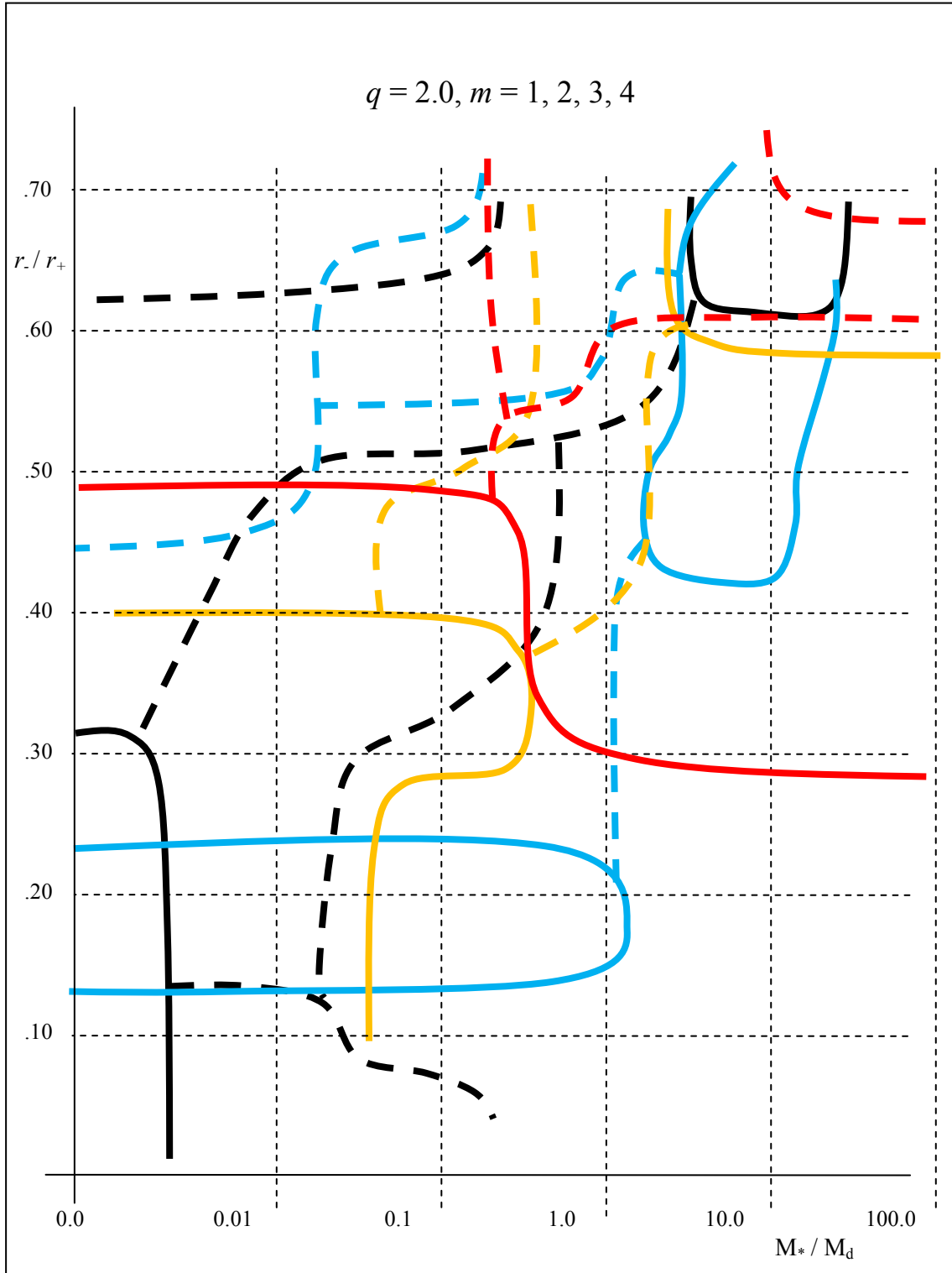


Fig. 4.2.4.7. Parameter space map for $q = 2.0, m = 1, 2, 3$ and 4, shown in black, blue, orange and red dashed lines, respectively. Solid lines are boundaries of stable models.

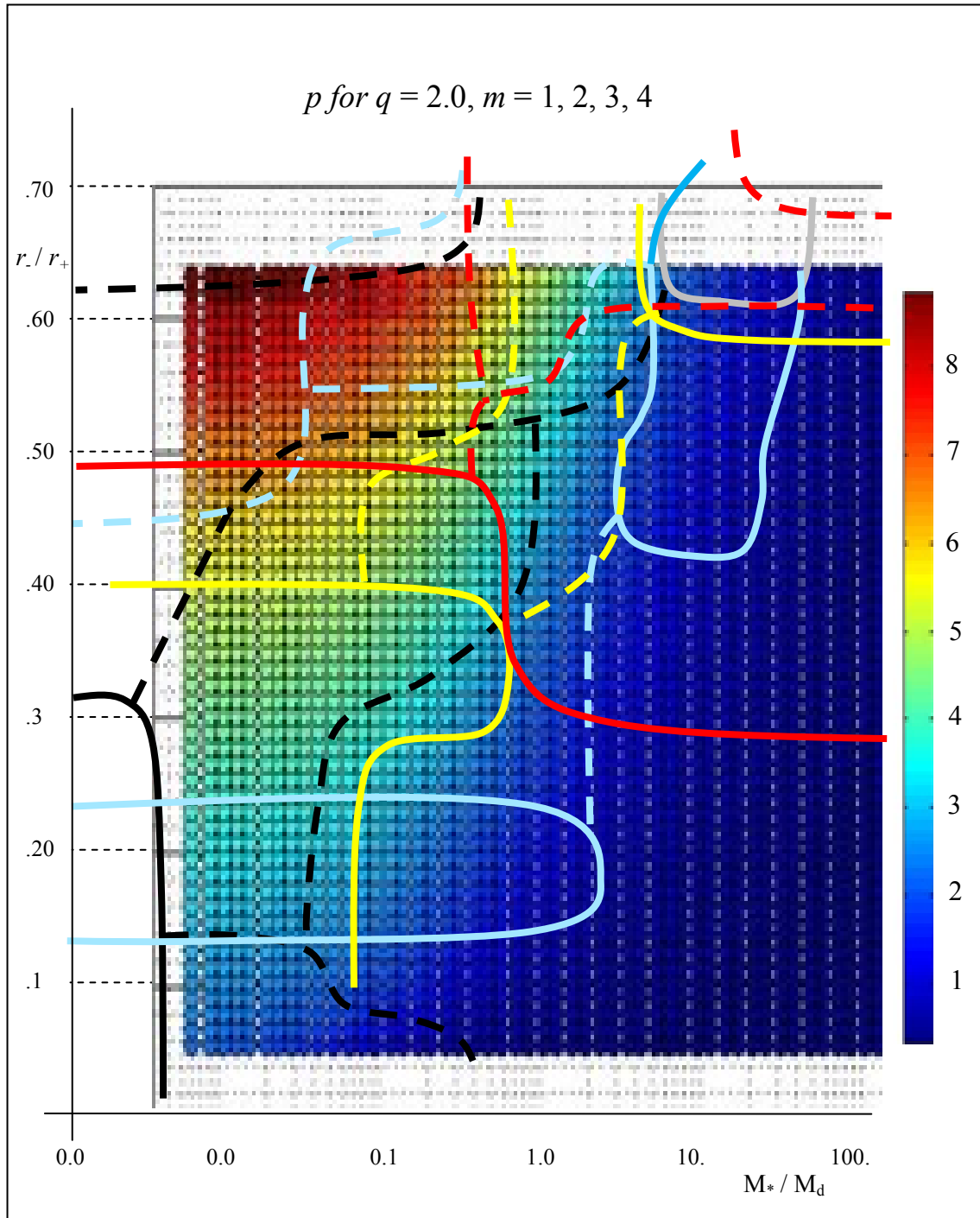


Fig. 4.2.4.8. Parameter space map overlaid on the self-gravity parameter p for $q = 2.0$, $m = 1, 2, 3$ and 4 , shown in black, blue, orange and red dashed lines, respectively. Solid lines are boundaries of stable models. Some colors were lightened.

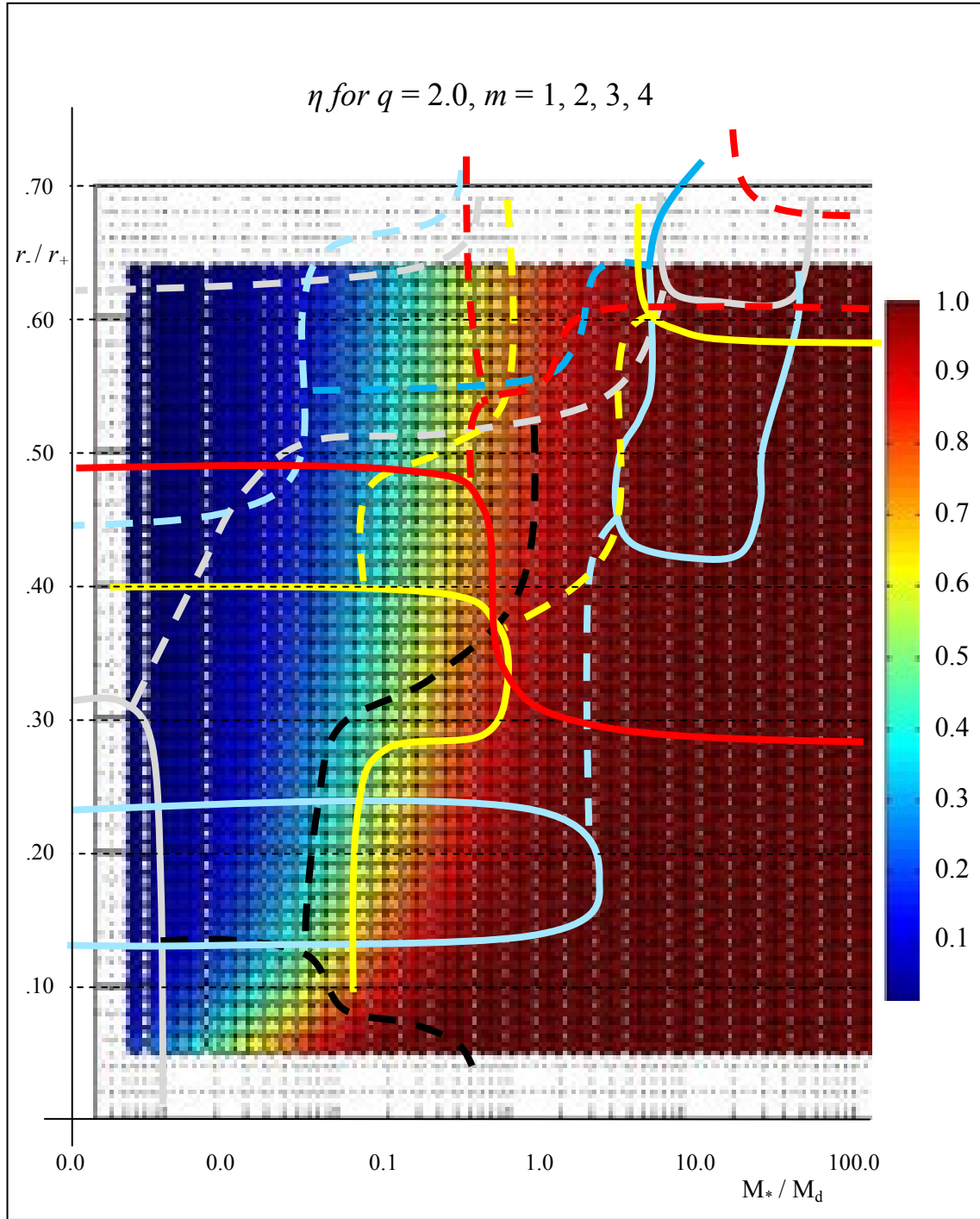


Fig. 4.2.4.9. Parameter space map overlaid on the self-gravity parameter η for $q = 2.0$, $m = 1, 2, 3$ and 4 , shown in black, blue, orange and red dashed lines, respectively. Solid lines are boundaries of stable models. Some colors were lightened.

Eigenvalues for $q = 2.0$ models											
T/ W	r_+/r_+	r_+/R_o	r_+/R_o	$y_2(1)$	$y_2(2)$	$y_2(3)$	$y_2(4)$	$y_1(1)$	$y_1(2)$	$y_1(3)$	$y_1(4)$
$M_*/M_d = 0.0$											
0.217	0.301	1.770	0.532	0.000	0.366	0.000	0.000		-1.042		
0.254	0.401	1.535	0.615	0.265	0.000	0.321	0.000	1.001		-0.441	
0.283	0.500	1.385	0.693	0.555	0.570	1.036	1.013	1.104	-0.088	-0.201	-0.285
0.308	0.600	1.272	0.763	0.690	0.956	1.537	1.763	1.164	0.039	-0.029	-0.086
$M_*/M_d = 0.01$											
0.093	0.101	3.262	0.329	0.398	0.000	0.000	0.000	-0.569			
0.169	0.201	2.196	0.441	0.335	0.000	0.000	0.000	-0.958			
0.221	0.301	1.770	0.532	0.344	0.392	0.000	0.000	-0.973	-1.043		
0.258	0.401	1.540	0.617	0.327	0.201	0.162	0.000	-0.977	-0.916	-0.480	
0.286	0.500	1.385	0.693	0.531	0.469	0.986	0.969	1.091	-0.096	-0.207	-0.289
0.310	0.600	1.272	0.763	0.674	0.890	1.493	1.722	1.141	0.045	-0.029	-0.088
$M_*/M_d = 0.1$											
0.077	0.052	6.673	0.346	0.493	0.000	0.000	0.000	-0.505			
0.128	0.101	3.583	0.361	0.733	0.000	0.000	0.000	-0.429			
0.202	0.201	2.244	0.451	0.685	0.000	0.000	0.000	-0.282			
0.251	0.301	1.788	0.538	0.543	0.459	0.000	0.000	-0.110	-1.022		
0.286	0.401	1.545	0.619	0.453	0.514	0.440	0.000	-0.898	-1.012	-1.035	
0.311	0.500	1.385	0.693	0.462	0.436	0.389	0.548	-0.918	-0.948	-0.328	-0.346
0.332	0.600	1.272	0.763	0.565	0.374	1.149	1.401	1.069	1.160	-0.046	-0.105
$M_*/M_d = 1.0$											
0.177	0.052	9.542	0.495	0.084	0.000	0.000	0.000	-0.419			
0.239	0.101	4.885	0.493	0.265	0.000	0.044	0.000	-0.478		2.592	
0.314	0.201	2.585	0.519	0.522	0.000	0.072	0.000	-0.352		1.856	
0.358	0.301	1.908	0.574	0.591	0.076	0.072	0.000	-0.235	-0.868	0.986	
0.386	0.401	1.588	0.636	0.557	0.383	0.172	0.000	-0.141	-0.873	-0.841	
0.404	0.500	1.404	0.703	0.446	0.525	0.532	0.371	-0.074	-0.929	-0.928	-0.892
0.417	0.600	1.278	0.767	0.278	0.573	0.658	0.657	-0.063	0.772	-0.981	-0.978
$M_*/M_d = 5.0$											
0.224	0.052	10.11	0.525	0.070	0.049	0.000	0.000	-0.356	0.712		
0.291	0.101	5.346	0.539	0.104	0.066	0.044	0.000	-0.399	0.517	-2.080	
0.368	0.201	2.876	0.577	0.230	0.067	0.028	0.038	-0.405	0.261	-0.201	2.598
0.411	0.301	2.063	0.620	0.334	0.051	0.091	0.045	-0.305	0.168	0.889	1.862
0.438	0.401	1.671	0.669	0.348	0.042	0.028	0.069	-0.208	0.064	0.499	1.130
0.455	0.500	1.444	0.723	0.305	0.010	0.017	0.039	-0.131	-0.742	0.265	0.480
0.466	0.600	1.294	0.777	0.189	0.280	0.326	0.254	-0.078	-0.784	-0.789	-0.760
$M_*/M_d = 10.0$											
0.232	0.052	10.31	0.535	0.067	0.043	0.000	0.000	-0.367	0.621		
0.301	0.101	5.402	0.545	0.092	0.067	0.041	0.031	-0.376	0.502	-2.144	-0.609
0.378	0.201	2.942	0.591	0.152	0.087	0.058	0.035	-0.389	0.239	1.186	2.373
0.421	0.301	2.114	0.636	0.262	0.103	0.000	0.000	-0.320	0.082		
0.448	0.401	1.705	0.683	0.285	0.075	0.086	0.032	-0.220	-0.024	0.433	-0.215
0.465	0.500	1.465	0.733	0.258	0.000	0.019	0.051	-0.138		0.263	0.614
0.476	0.600	1.307	0.785	0.181	0.000	0.000	0.000	-0.078			

Table 4.2.4.1. Characteristic radii, $y_1(m)$ and $y_2(m)$ values for selected $q = 2.0$ models.

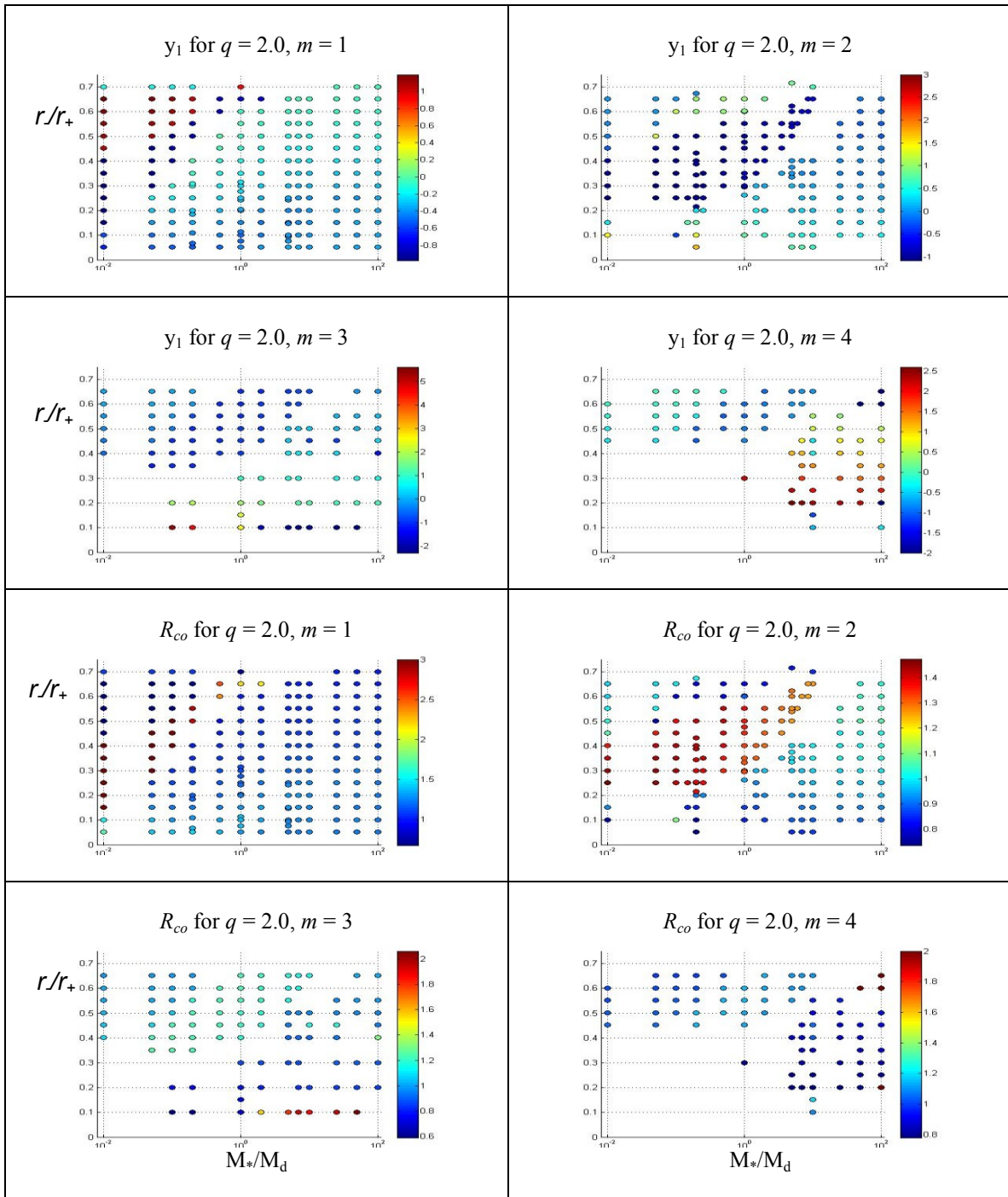


Fig. 4.2.4.10. y_1 frequency eigenvalues and corotation radii for $q = 2.0, m = 1, 2, 3$ and 4 .

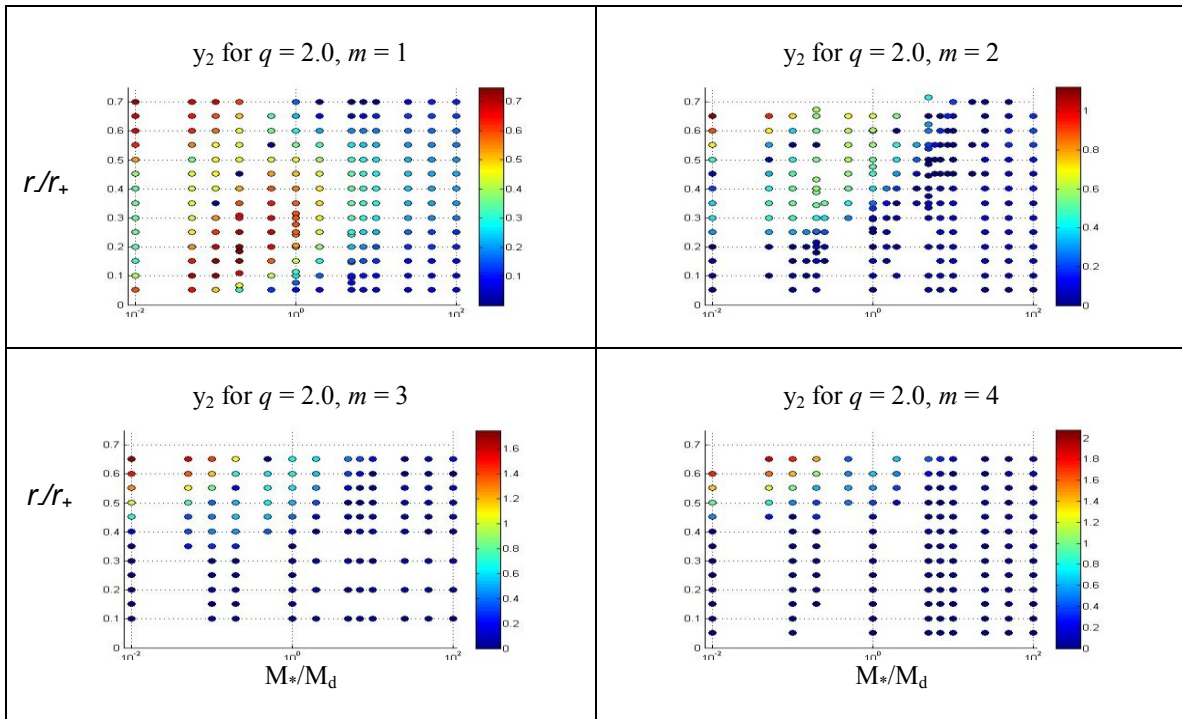


Fig. 4.2.4.11. y_2 growth rate eigenvalues for $q = 2.0, m = 1, 2, 3$ and 4 .

CHAPTER V

DISCUSSION AND CONCLUSION

5.1. Comparison with Earlier Work

In this section, we compare our results with earlier studies. In Section 5.1.1, we compare results with those found by Andalib, Tohline and Christodoulou (1997). They studied simplified tori, with constant density and circular cross-sections. Section 5.1.2 addresses the non-self-gravitating models of Kojima (1986, 1989). We calculated models where the self-gravity of the disk has not been added to the gravitational potential calculation. We directly compare our results with Kojima's where possible, and extend our calculations to include models with lower $r./R_0$, for comparison with our general models. In Section 5.1.3, we qualitatively compare results with several groups who address the eccentric instabilities found in the $m = 1$ case, where the motion of the central star is instrumental in determining the behavior of the model. In Section 5.1.4, we make a direct comparison with the nonlinear models calculated by Woodward, Tohline, & Hachisu (1994).

5.1.1. Comparison with Andalib, Tohline and Christodoulou

In this section we compare our results with work done by Andalib, Tohline and Christodoulou (1997), hereafter ATC. This group performed linear stability analysis on slender incompressible tori with constant specific angular momentum (ICT). The constraints produce tori of constant density and circular cross-sections. Equilibrium models were constructed on 256×256 grids. They solved a system of equations in the narrow torus approximation by directly expanding the gravitational potential and a velocity potential in a series of modified Bessel functions. They found that P modes for these models were found only in nearly Keplerian disks, with $0.999976 \leq \eta \leq 1.00003$, where $\eta \equiv \Omega_K^2 / \Omega_0^2$. We could not make a direct comparison with their results, since the character exhibited in non-self-gravitating models, which do support P modes, smoothly

changes as we decrease M_*/M_d . However, the appearance of our phase plots for $q = 2.0$ suggests that our models exhibit P mode characteristics for $0.980 \leq \eta \leq 1.002$, a wider range than that reported by ATC. In general, trend seemed to agree in that $\eta \approx 1$ was necessary for P modes. ATC found their ICT models supported P modes for $M_*/M_d < 8.70 \times 10^3$ and $a/R_0 < 0.02733$ where a is the radius of the circular cross-section. We find P mode characteristics in disks with much smaller M_*/M_d ratios, around $M_*/M_d = 5.0$ and $r/R_0 \approx 0.60$.

Figs. 5.1.1.1 - 5.1.1.2 compare the instability thresholds of our I and J modes with those reported by ATC. The dot-dashed line in Fig 5.1.1.1 indicates the threshold for I modes found by ATC. The data points represent our lowest $T/|W|$, I mode models. We have adopted their horizontal axis here; note that the horizontal axis is scaled by M_d/M_* for values less than 1.0 while the right side is scaled by $2 - M_*/M_d$.

The general nature of their I mode threshold agrees well with our data points, given the constraints inherent in the ATC models. Our data is color-coded as indicated. The details presented by ATC indicate that the $m = 1$ models lie just above the curve with higher modes entering for higher $T/|W|$ for $M_d/M_* \geq 0.5$ and the models are tightly clustered for small M_d/M_* . Our models are also tightly clustered for small M_d/M_* , but we show no I modes for $m = 1$ models where $M_*/M_d > 7.0$. Our analysis also indicates that the $m = 2$ threshold is lower than that for $m = 1$ models. It should be noted that while ATC did include self-gravity in their simulations, no mention was made of a gravitational perturbation due to the motion of the central star. Also, their equations were simplified by the narrow-torus approximation. Many of our threshold models, especially for the I modes, fall well outside the regime where this approximation is appropriate. For example, our $m = 1$ threshold for $M_*/M_d = 0.01$ occurs in a relatively wide disk at $r./r_+ = 0.152$. Our $M_*/M_d = 0.01$ disks visibly deviate from around $r./r_+ = 0.40$. The solid green line indicates where the highest growth rate of the I mode is matched by that of a J mode model for the same M_*/M_d , indicating the threshold above which J modes dominate I modes.

Fig. 5.1.1.2 shows our $q = 2$, J mode threshold data points plotted against the curve given by ATC. Our threshold lies at higher $T/|W|$ than is indicated by their survey,

ATC Comparison of I Mode Thresholds

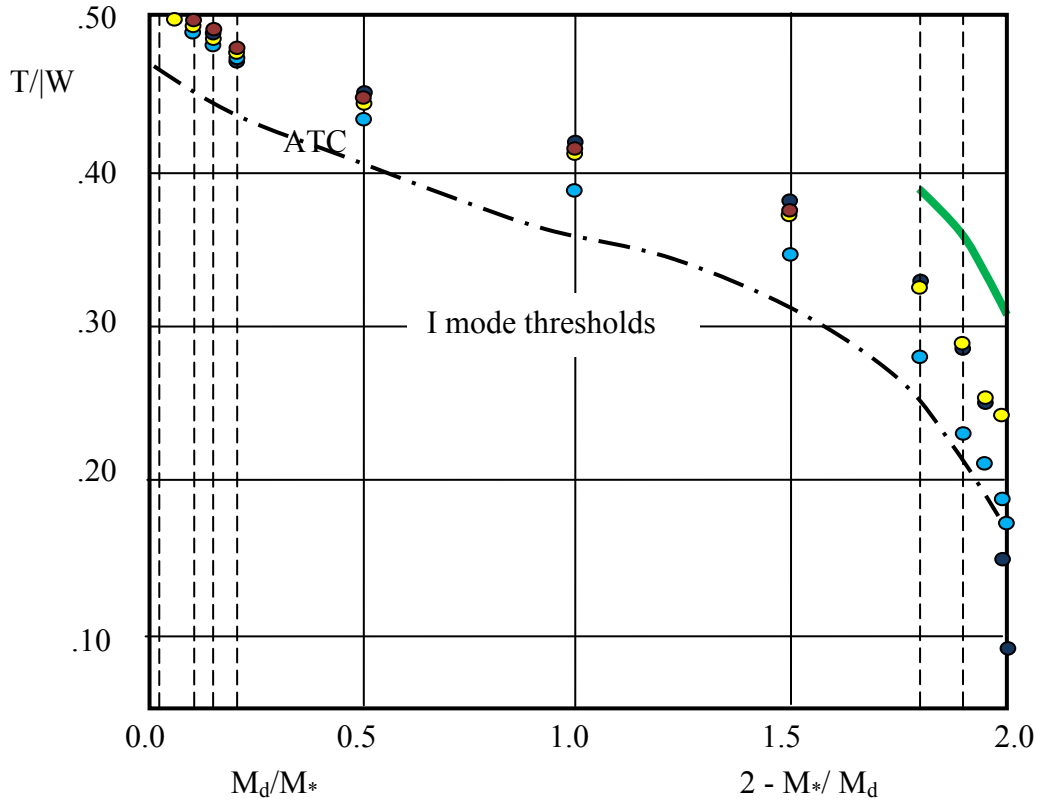


Fig. 5.1.1.1. I mode threshold comparison with ATC is illustrated with the dot-dashed line showing the ATC curve. Our data points are colored with $m = 1, 2, 3$ and 4 in dark blue, blue, yellow and red, respectively. The green line shows where the J modes begin to dominate the I modes.

but it appears to follow the same kind of curve, although not very far. Their analysis included very much higher m modes than we calculated, and most of the unstable models for $M_d/M_* < 1.0$, were for higher m . They show only one unstable $m = 2$ model on their plot, and no $m = 1$ models. We show no $m = 1$ models unstable to J modes as well.

It should be noted that ATC results showed J modes for higher M_d/M_* than our results indicate. This could be due to the fact that we only see the dominant modes of each model run. They have also indicated that their fastest growing J modes have higher m values than what we have included in our study. For example, their models with $0.0 < M_d/M_* < 0.188$ report that J modes with $m = 5$ have growth rates equal to I modes with $m = 2$. At $M_d/M_* = 1.177$, ATC reports that the growth rates of $m = 3$, I modes equal

the growth rates of J modes with $m = 8$; and they report equal growth rates for $m = 7$, I modes and $m = 23$, J modes at $M_d/M_* = 12.516$. ATC results show that J modes dominate the region of high $T/|W|$ for every value of M_d/M_* across parameter space. We do not see that result in our models.

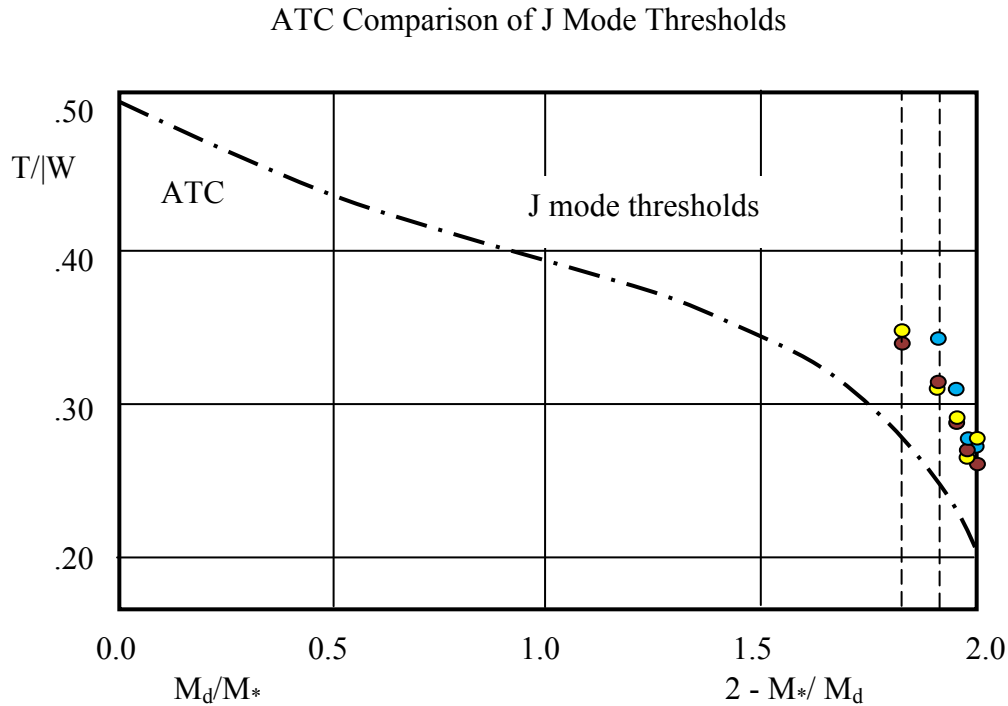


Fig. 5.1.1.2. J mode threshold comparison with ATC is illustrated with the dot-dashed line showing the ATC curve. Our data points are colored $m = 2, 3$ and 4 in blue, yellow and red, respectively.

5.1.2. Comparison with Kojima

Calculating models with no self-gravity aids in identifying the mechanisms responsible for the structure of the various modes encountered. We have included discussion of non-self-gravitating models in the results of the $q = 1.75$ and 2.0 models in sections 4.2.2 - 4.2.4. We have included plots of the non-self-gravitating models in the Appendix B and Appendix C.

We compare our results for $q = 2.0$ non-self-gravitating simulations with work done by Kojima (1986, 1989). Kojima's models were calculated using a finite-element

method with 289 nodes. The dot-dashed, dashed and long-dashed lines in Fig.5.1.2.1 represent results presented by Kojima for $q = 2.0$, $m = 1, 2$ and 4 modes, respectively. The data points indicate our corresponding results with $m = 1, 2$ and 4 , depicted in dark blue, blue and red dots, respectively. Since self-gravity of the disk was not included in these calculations, we also did not include gravitational perturbations due to star motion in the $m = 1$ case.

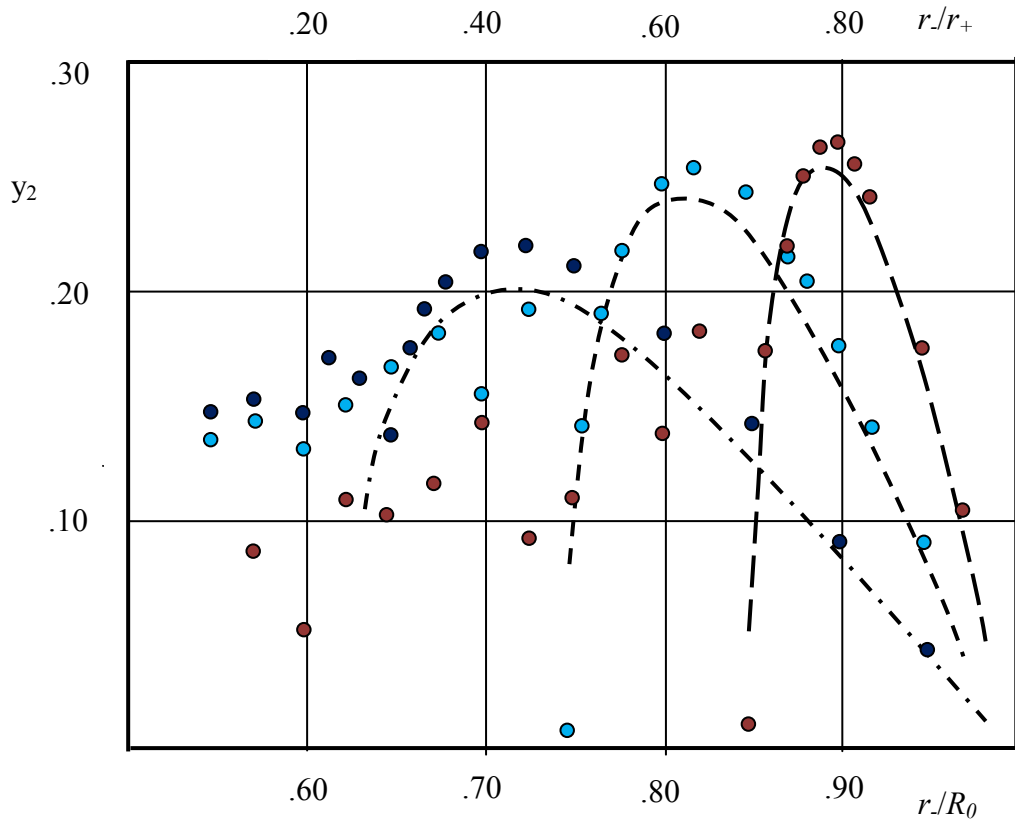


Fig. 5.1.2.1. Comparison of y_2 eigenfunction values with Kojima. The dot-dashed, dashed, and long-dashed lines indicate Kojima's data for $m = 1, 2$, and 4 . Our data points are colored with $m = 1, 2$, and 4 in dark blue, blue, and red, respectively.

There is generally good agreement in the trends of the growth rates shown, in the regions of parameter space that overlap between the two studies. Our peak growth rates tend to be $\sim 0.10\%$ higher than those reported by Kojima, but the sequences of models for each value of m tend to follow similar curves for varying $r./r_+$. However, many of our models fall outside this region into lower $r./r_+$ and the trends in the growth rates qualitatively change there. Typically, the lower $r./r_+$ models exhibit edge modes, which

can have spiral arms that can wrap several times, making resolution a problem, as can be seen in Fig. 5.1.2.2. We typically also see P modes and edge modes in the self-gravitating models for the corresponding regions of parameter space, where high M_*/M_d makes the effects of the disk self-gravity negligible when compared to the gravitational potential of the central star.

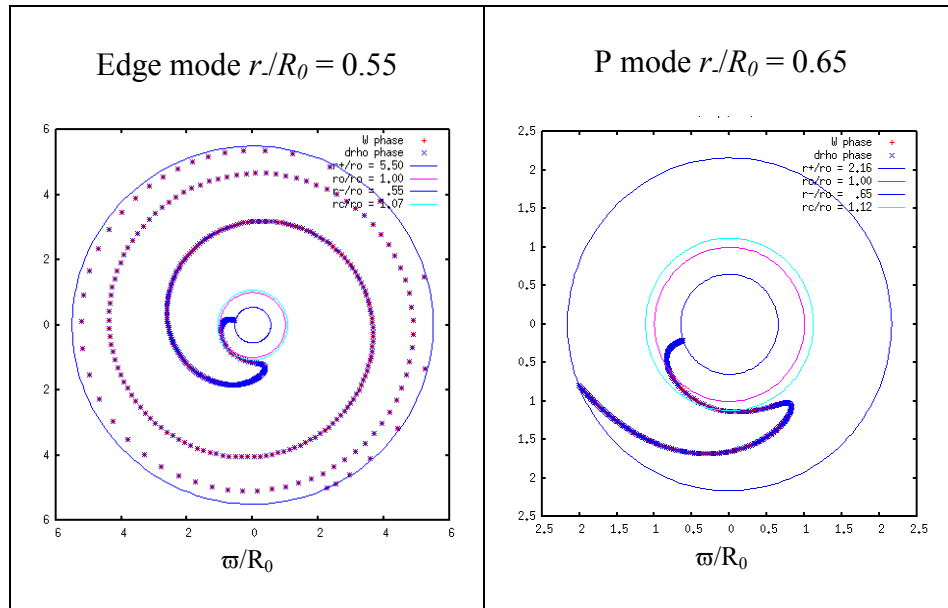


Fig. 5.1.2.2. Models illustrating an edge mode vs. a P mode for non-self-gravitating disks.

5.1.3. Star Motion for $m = 1$ Modes

In the $m = 1$ case, the star may move to conserve the center of mass of the system, in response to forcing from the perturbed mass of the disk, exciting what is known as an “eccentric instability.” In a system where the star mass is much less than the mass of the disk, the star is rapidly driven toward the disk. When the star mass is comparable to the disk mass, the offset mass of the disk tends to pull the star back toward its equilibrium position. The angular motion of the star is slower than that of the matter in the disk, so the star induces negative angular momentum in the disk, while gaining positive angular momentum itself. At R_{co} , the pattern speed of the density perturbation equals the fluid speed. Inside corotation, the perturbation pattern frequency is less than the fluid

frequency, with the opposite true at radii larger than R_{co} . The perturbed energy of the mode per unit area and angular momentum per unit area are negative inside R_{co} and positive outside R_{co} .

Spiral instabilities develop when disturbances are amplified by feedback mechanisms as density waves propagate or tunnel across the corotation resonance (Tsang & Lai 2008). A density wave incident on the corotation resonance will be partially transmitted and partially reflected. We illustrate this situation in Fig. 5.1.3.1, using the approximate locations of the pertinent radii for the A mode model introduced in Fig. 3.2.3, with the angular momentum inside and outside R_{co} identified as J^- and J^+ , respectively, in the interest of space. The incident, reflected and transmitted waves are identified by subscripts of i, r and t, respectively. The inner and outer radii of the disk are denoted by solid black lines. R_0 and R_{co} are denoted by solid purple and blue lines, respectively. The inner and outer Lindblad resonances are marked in red dotted lines, and labeled as R_{Lin} and R_{Lout} , respectively. The inner and outer Q -barrier boundaries are marked by green dashed lines. Unless otherwise noted, all radii are labeled with the notation used elsewhere in this document.

The transmitted wave carries the opposite sign of energy and angular momentum into the region. Because of a change of sign of a conserved action, the reflected wave increases in amplitude (Narayan, Goldreich & Goodman 1987). The perturbed energy and angular momentum grows larger (more positive) in the region outside R_{co} and smaller (more negative) in the region inside R_{co} . This is commonly known as the “corotation amplifier.” For spiral modes to grow in amplitude, there must be a feedback mechanism. One such mechanism may be that reflected waves are incident upon another reflecting surface, which causes them to again encounter the corotation resonance and increase upon re-reflection. The Lindblad resonance would provide a reflecting surface to redirect waves back toward R_{co} (Adams, Ruden & Shu 1989). Reflection at the outer edge of the disk would also serve to redirect the waves (Heemskerck, Papaloizou & Savonije 1992).

Adams, Ruden & Shu (1989), hereafter ARS, were the first group to include the effects of the motion of the star in their star/disk calculations. They modeled thin (2-D) disks with $M^*/M_d \approx 1$, with a “nearly Keplerian” rotation curve, meaning that the gravitational potential of the star dominated the self-gravity of the disk everywhere

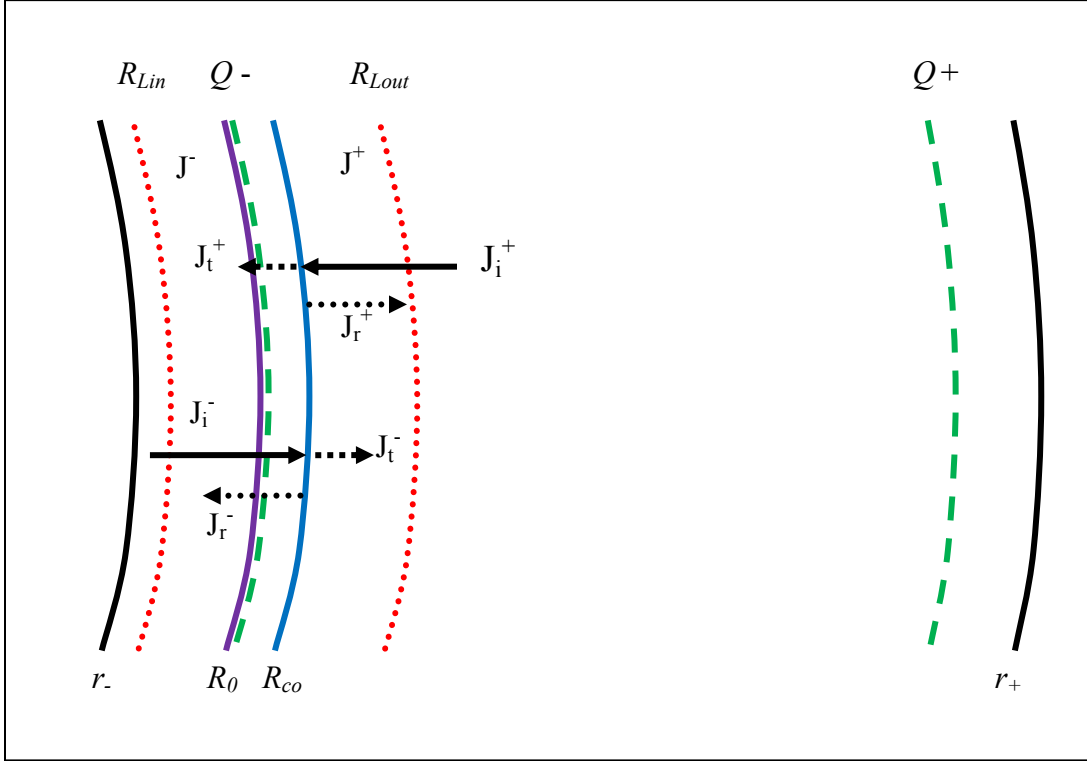


Fig. 5.1.3.1. Schematic illustration of transmission and reflection of waves across the corotation resonance, with pertinent radii identified as noted above.

except near the outer edge. They imposed a constant “confining pressure” outside the disk and used power law distributions for mass density and temperature. Their results indicate that growth rates of spiral $m = 1$ modes decrease with increasing M_*/M_d over a range of $0.91 < M_*/M_d \leq 3.0$. We confirmed that we only saw spiral wave modes when the central star was allowed to move. Our results show growth rates decreasing with increasing M_*/M_d for A mode models with $q = 1.5$, $r_-/r_+ = 0.05$ over the range $0.2 < M_*/M_d \leq 1.0$.

Fig. 5.1.3.2 shows our phase plots for the sequence of models for $m = 1$, $q = 1.5$, $r_-/r_+ = 0.05$, for $0.0 \leq M_*/M_d \leq 5.0$; the models with $M_*/M_d > 5.0$ were stable. The first model, with $M_*/M_d = 0.0$ shows a split bar structure. With no central star present, the disk must conserve angular momentum itself, and can do so with this configuration. The addition of a small amount of mass changes the nature of the instability, as seen in the $M_*/M_d = 0.01$ model. The star’s small relative mass allows it to rapidly fall toward the

maximum of the gravitational potential in the disk (Heemskirk, Papaloizou & Savonije 1992), resulting in the short spiral arm seen in the $M_*/M_d = 0.01$ phase plot. As the relative star to disk mass increases, the spiraling motion of the star becomes slower, as witnessed in the phase plots for $0.2 \leq M_*/M_d \leq 1.0$. There are models in the sequence that show a different character, perhaps a blending of the two strategies. The models with $M_*/M_d = 0.05$ and 0.1 , as well as the model at $M_*/M_d = 2.0$ exhibit a configuration that is like a split bar structure, except that the “bars” are like segments of spiral arcs offset by the motion of the star, connected by a phase shift. The $M_*/M_d = 5.0$ model exhibits characteristics of a P mode, which may be expected for the relatively high M_*/M_d .

We also report A mode behavior for $q = 1.75$ disks, which will also be discussed in Section 5.1.4. The A mode regime is shifted to higher M_*/M_d for a given $r./r_+$. We find A modes in the region $0.1 \leq M_*/M_d \leq 1.0$ for $r./r_+ = 0.05$; for $r./r_+ = 0.10$, A modes are found in the region $0.5 \leq M_*/M_d \leq 2.0$, and for $r./r_+ = 0.15$, the region $1.0 \leq M_*/M_d \leq 5.0$ contains A modes. Our $q = 2.0$ models have A modes for the ranges $r./r_+ = 0.05$ in the region $0.0 \leq M_*/M_d \leq 0.2$, and for $r./r_+ = 0.10$ for $0.5 \leq M_*/M_d \leq 1.0$. We find that growth rates decrease with increasing mass for the $q = 1.75$ and 2.0 model sequences. We also note that growth rates increase for increasing $r./r_+$ for constant M_*/M_d , in agreement with ARS.

Another result of ARS concerned sensitivity of $m = 1$ mode to the Q -barrier. Propagation of waves is inhibited inside the Q -barrier, reducing amplification of reflected waves. ARS found that the absence of a Q -barrier induced amplification of the perturbation at “catastrophic rates.” Our simulations do not support this finding. Increasing M_*/M_d , keeping $r./r_+$ constant at a small value, as shown in Fig. 4.1.6, we see that the Q -barrier disappears for $M_*/M_d > 1.0$, for $q = 1.5$ and 1.75 . For $q = 1.5$, when the Q -barrier disappears, the dominant modes in the disks are P modes, with stable models for $M_*/M_d > 7.0$; while $q = 1.75$ models become stable for $M_*/M_d > 1.0$. Our $q = 2.0$ models have $Q = 0$ everywhere in the disk, so $Q < 1$ across the disk. Our calculations show growth rates increasing, in general, as q increases.

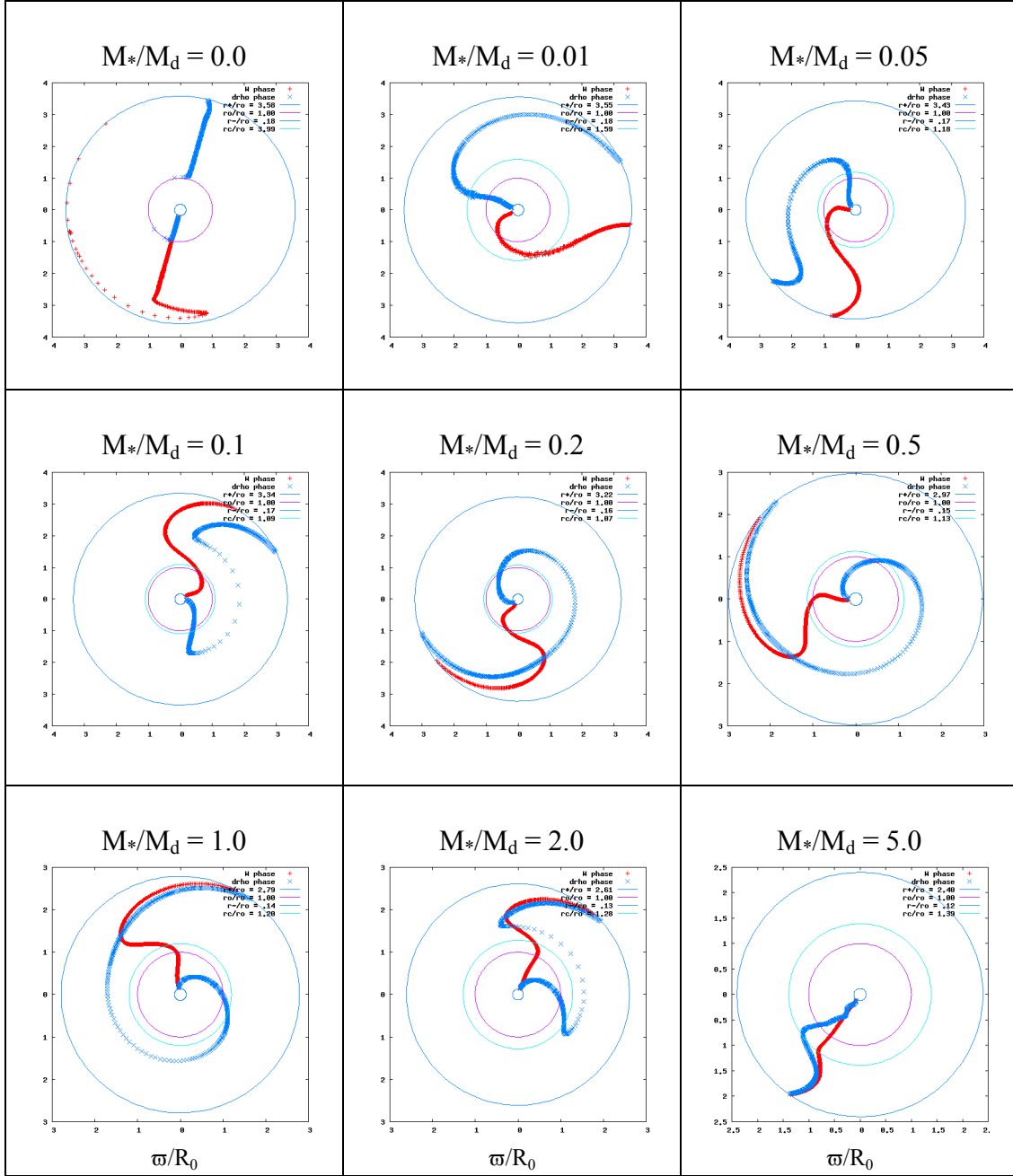


Fig. 5.1.3.2. Phase plots for the $m = 1$ sequence of models with $q = 1.5$, $r_-/r_+ = 0.05$, for varying M_*/M_d as shown.

Heemskirk, Papaloizou & Savonije (1992), hereafter HPS, performed linear and nonlinear analysis on thin (2-D), self-gravitating, $m = 1$ disks. They used a polytropic equation of state with $\gamma = 2$. They imposed an equilibrium velocity determined by:

$$\Omega^2 r = \frac{c^2}{\Sigma} \frac{d\Sigma}{dr} + \frac{GM_*}{r^2} + \frac{d\Phi}{dr} \quad (5.1.3.1)$$

where c is the sound speed and Σ is the surface density. Their analysis agreed with ARS, in that they also found that stars moved in outward spirals in response to forcing by the disk, but they found that stars with systems with $M_*/M_d > 1.0$ became stable, and argued that the reason was that R_{co} moved outside the disk. We see stable disks for $q = 1.75$ when $M_*/M_d > 1.0$, but for $q = 1.5$ we see P modes dominate before stability sets in, as noted above. For $q = 2.0$, we see edge modes for $M_*/M_d \geq 1.0$. P modes and edge modes do not have corotation outside the disk; R_{co} lies near R_θ . HPS did not find outer Lindblad resonances within their disks that exhibited spiral mode behavior, and attributed the reflecting edge to the outer edge of the disk, in disagreement with ARS. We find outer Lindblad resonances within our disks that exhibit spiral modes. HPS found that growth rates decreased with increasing M_*/M_d , in agreement with ARS as well as our study.

Noh, Vishniac, & Cochran (1991) performed linear analysis on $m = 1$ modes in a thin (2-D), isentropic disks for a two fluid system, including dust and gas. They imposed power law rotation with $q = 1.5$ and set the width of the disks at $r./r_+ = 10^{-5}$. They showed that an $m = 1$ instability persists in disks with no Lindblad resonance as long as a reflecting boundary is present at the outer edge of the disk. Our results agree with this. They also modeled disks with higher m , and showed that low mass disks, specifically $M_*/M_d = 0.05$, are stable for all m except for $m = 1$, a result that disagreed with ARS. Our results qualitatively agree with Noh, Vishniac, & Cochran. In a second paper, Noh, Vishniac, & Cochran (1992), they confirmed their previous results, using the same rotation profile as ARS.

Taga & Iye (1998) performed linear analysis on 2-D, polytropic, $m = 1$, fluid disks which had no inner or outer edge. They did include a “softening parameter” near the central massive object. They report finding eccentric instabilities, even though there was no outer reflecting edge to supply a feedback mechanism for corotation amplification. They also found that instability set in at $M_*/M_d = 0.01$, lower than that reported by ARS. They found the growth rate decreased with M_*/M_d , in agreement with ARS. We also show an unstable model at $M_*/M_d = 0.01$ for $r./r_+ = 0.05$, exhibiting a

trailing spiral that persists over approximately π radians. Our models for $M_*/M_d = 0.05$ and 0.1, however, appear to be P modes, not A modes. Phase plots for our $m = 1, q = 1.5$ models can be seen in Fig. A.1.1.2. Fig. 5.1.3.3 shows our y_2 values for $m = 1, q = 1.5$ models with $r./r_+ = 0.05$ for varying M_*/M_d .

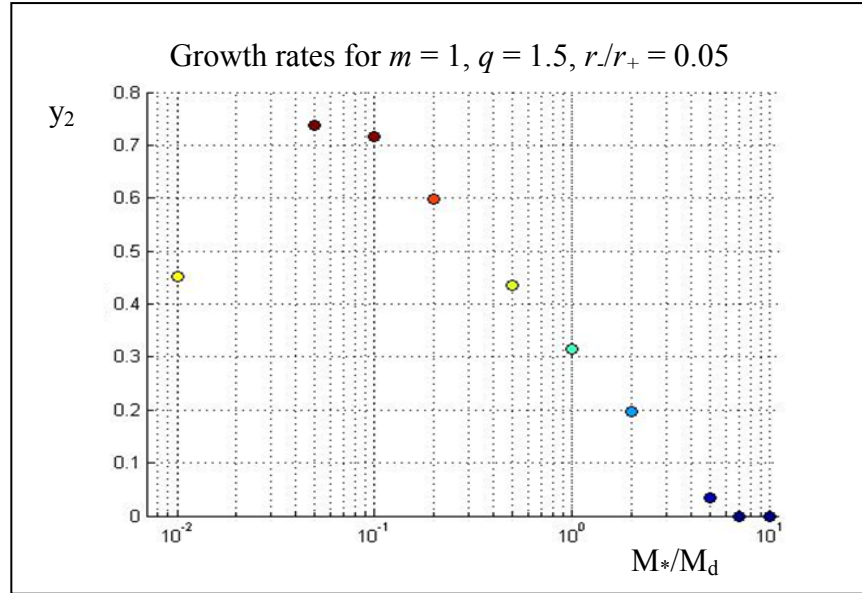


Fig. 5.1.3.3. Growth rates vs. M_*/M_d for $m = 1, q = 1.5, r./r_+ = 0.05$.

5.1.4. Comparison with Woodward, Tohline and Hachisu

The third body of work and the most direct comparison for our work is that by Woodward, Tohline, & Hachisu (1994), hereafter WTH. This paper presents nonlinear simulations of $q = 2.0$ disks, containing fifteen $m = 1$ and nineteen $m = 2$ models with $M_*/M_d = 0.2, 1.0$ and 5.0 ; as well as 7 simulations of $M_*/M_d = 0.0$ with $q = 1.5, 1.75$ and 2.0 . The radial x vertical x azimuthal resolution of their models was typically $64 \times 32 \times 64$ zones while narrower disks were calculated at $128 \times 32 \times 64$. Our models were calculated at a resolution of $512 \times 512 \times 16$, and we calculated the models specifically for this comparison at $256 \times 256 \times 8$ as well. We chose inner radii to match the $T/|W|$ values quoted in their paper as closely as possible, but we were not able to agree exactly to the

three significant figures quoted. Figs. 5.1.4.1 and 5.1.4.3 present y_1 and y_2 values for comparison.

We begin by examining the $m = 1$, $M_*/M_d = 0.2$ comparison. WTH indicated high uncertainty in the growth rate of their $T/|W| = 0.10$, $r./r_+ = 0.051$ model. Our lower and higher resolution values agreed within 3% difference with each other, but showed relatively poor agreement with WTH. Plots of the eigenfunction amplitudes, phases and temporal evolution of the WTH models were available in Woodward's dissertation (1986). The phase plot of this model showed similar character to that of our model, with trends associated with A modes seen in the study by ARS, a trailing spiral arm extending from the inner edge to the outer edge, spanning approximately 2π degrees. Agreement was closer for the $T/|W| = 0.12$ models with divergence between our models and those of WTH as $T/|W|$ increased. The character of the phase plots also diverged, with WTH models continuing to exhibit A mode character through the $T/|W| = 0.166$ model while our phases took on P mode character, with an inner bar crossing R_0 and R_{co} , then exhibiting a leading π phase shift, switching to a trailing arm extending for $\pi/2$ radians. As $T/|W|$ increased, the WTH models also changed to character better associated with P modes as well.

Comparing the $m = 1$, $M_*/M_d = 1.0$ models, we see that the WTH models indicate the two lower $T/|W|$ models to be A modes, changing to P modes for the higher $T/|W|$ models. Our lowest $T/|W|$ model has the nature of an edge mode, similar in the inner disk to a P mode but with a more extended trailing arm in the outer disk, trailing for 3π radians. Our model at $T/|W| = 0.25$ has the character of an A mode, with the higher $T/|W|$ models exhibiting P mode traits, similar to those of WT. The $m = 1$, $M_*/M_d = 5.0$ WT models indicate A modes extending to higher $T/|W|$, changing to a P mode for the $T/|W| = 0.39$ model. The phase plots for our corresponding models show edge modes switching to a P mode for the highest $T/|W|$ model. In general, the nonlinear WTH models show A modes for a larger span of both $T/|W|$ and M_*/M_d than do our linear calculations for the $m = 1$ models, considering the models that we calculated to agree with the WTH models.

We did find models with phase plots resembling those of the A modes for $r./r_+ = 0.05$ in the region $0.0 \leq M_*/M_d \leq 0.2$ and for $r./r_+ = 0.10$ in the region $0.5 \leq M_*/M_d \leq 1.0$. We also report A mode behavior for $q = 1.75$ disks that were not

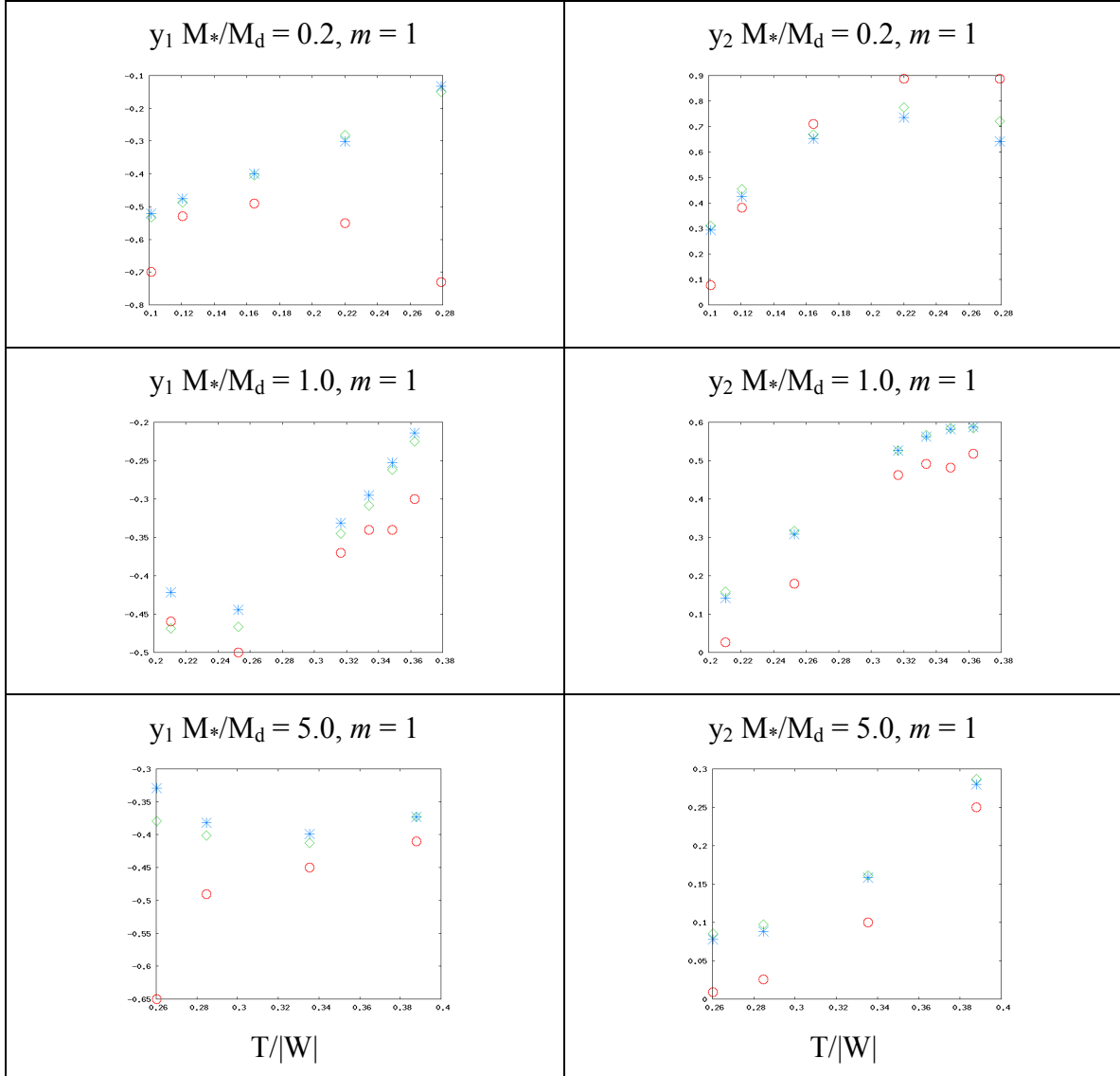


Fig. 5.1.4.1 Comparison of y_1 and y_2 values with WTH y_1 and y_2 values for $m = 1$ models. The red circles represent WTH data, the green diamonds represent our 512 x 512 data and the blue stars represent our 256 x 256 data points.

covered in the WTH study, over the ranges noted in Section 5.1.3. We noticed a qualitative trend in the $|\delta\rho|/\rho_0$ eigenfunctions amplitude plots in that a second minimum was beginning to emerge in these models very near the outer edge of the disk. Fig. 5.1.4.2 compares A modes and edge modes using two $q = 2.0$, $m = 1$, $r/r_+ = 0.05$ models, with eigenfunction amplitude plots in the top row and phase plots in the bottom row.

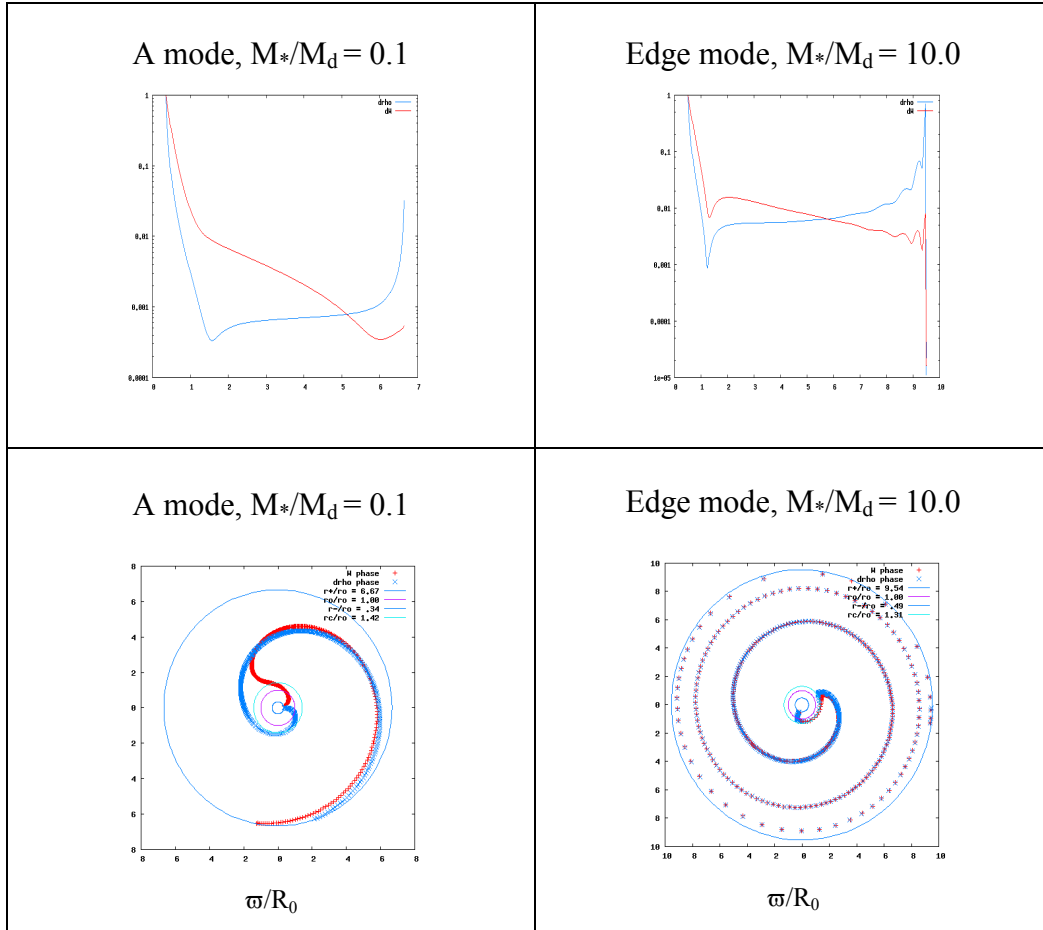


Fig. 5.1.4.2 Comparison of A mode plots and edge mode plots.

Neither the nonlinear or linear calculations show any A modes for $m = 2$ disks for $q = 2.0$. There is good general agreement between our calculations and those of WTH for the $m = 2$, $M^*/M_d = 0.0$ disks, as seen in Fig. 5.1.4.3. These disks are of varying q , with $q = 2.0$ for the lowest $T/|W|$ model, $q = 1.75$ for the $T/|W| = 0.19$ model and $q = 1.5$ for the rest. Our calculations yielded lower y_1 values and higher y_2 values than those of WT for the $q = 2.0$ model. Both studies indicated this model to be an I mode but ours had a leading $\pi/2$ phase shift while that of the WTH model was trailing. Our models switched to trailing as $T/|W|$ increased and more closely matched the eigenvalues and nature of the WTH results. The models exhibited I modes except for the highest $T/|W|$ model, which was a J mode. The growth rates diverged for the $T/|W| = 0.25$ model, probably because of its proximity to the threshold between I and J modes.

The $m = 2$, $M_*/M_d = 0.2$ disks also agree well between our calculations and those of WTH and the behaviors seen in the phase plots is similar. Both studies indicate a stable model at $T/|W| = 0.22$ with leading phase shift I modes at $T/|W| = 0.26$ changing to trailing I modes at $T/|W| = 0.29$. Our eigenvalues diverge at the $T/|W| = 0.36$ model, with WT indicating high uncertainty, while our calculation indicates a J mode for that model.

The plot of the comparison of y_1 values for the $m = 2$, $M_*/M_d = 1.0$ disks spans a much smaller range than that of most of the other y_1 plots. The trend is similar with our values approximately 10% higher in magnitude. The y_2 trend is also similar for these models. The WTH phase plot for the $T/|W| = 0.422$ is not well resolved and is difficult to use for comparison. Our model took 10 MIRPs to settle into mode and the nonlinear calculation had saturated before then. The rest of the models in this sequence were similar in eigenvalues and behavior, I modes with leading phase shifts and corotation increasingly near the outer disk edge as $T/|W|$ increased, with the $T/|W|$ model indicating a trailing arm with corotation near the inner edge of the disk.

There were discrepancies between the studies for the last sequence of models, with $m = 2$ and $M_*/M_d = 5.0$. Eigenvalues for the $T/|W| = 0.42$ and 0.43 models have been indicated to be very uncertain by WTH, with the modes possibly identified as L modes. The phase plots of these models are hard to discern for comparison with ours, but we do agree that corotation lies very nearly exactly at R_0 . Our eigenfunctions plots indicate a second dip just beginning to emerge. The next two models as $T/|W|$ increases are labeled as L modes by WTH, with no uncertainty indicated in their growth rates. Our calculations for these two models disagree, depicting models that are solidly stable, showing no hint of growth by 40 MIRPs. The last three models qualitatively agree between the studies as far as the I mode nature of the plots and the values of the growth rates. There is agreement in the y_1 values for the $T/|W| = 0.46$ model while the other y_1 values were not reported by WTH. We also calculated $m = 1, 3$ and 4 models for this sequence, and found that the lowest four $T/|W|$ models were dominated by $m = 1$ modes and the highest $T/|W|$ model was dominated by the $m = 3$ mode. These results were not included in the study by WTH, since the odd modes were not calculated for these models. Table 5.1.4.1 includes the eigenvalues plotted in Figs. 5.4.1.1 and 5.4.1.3.

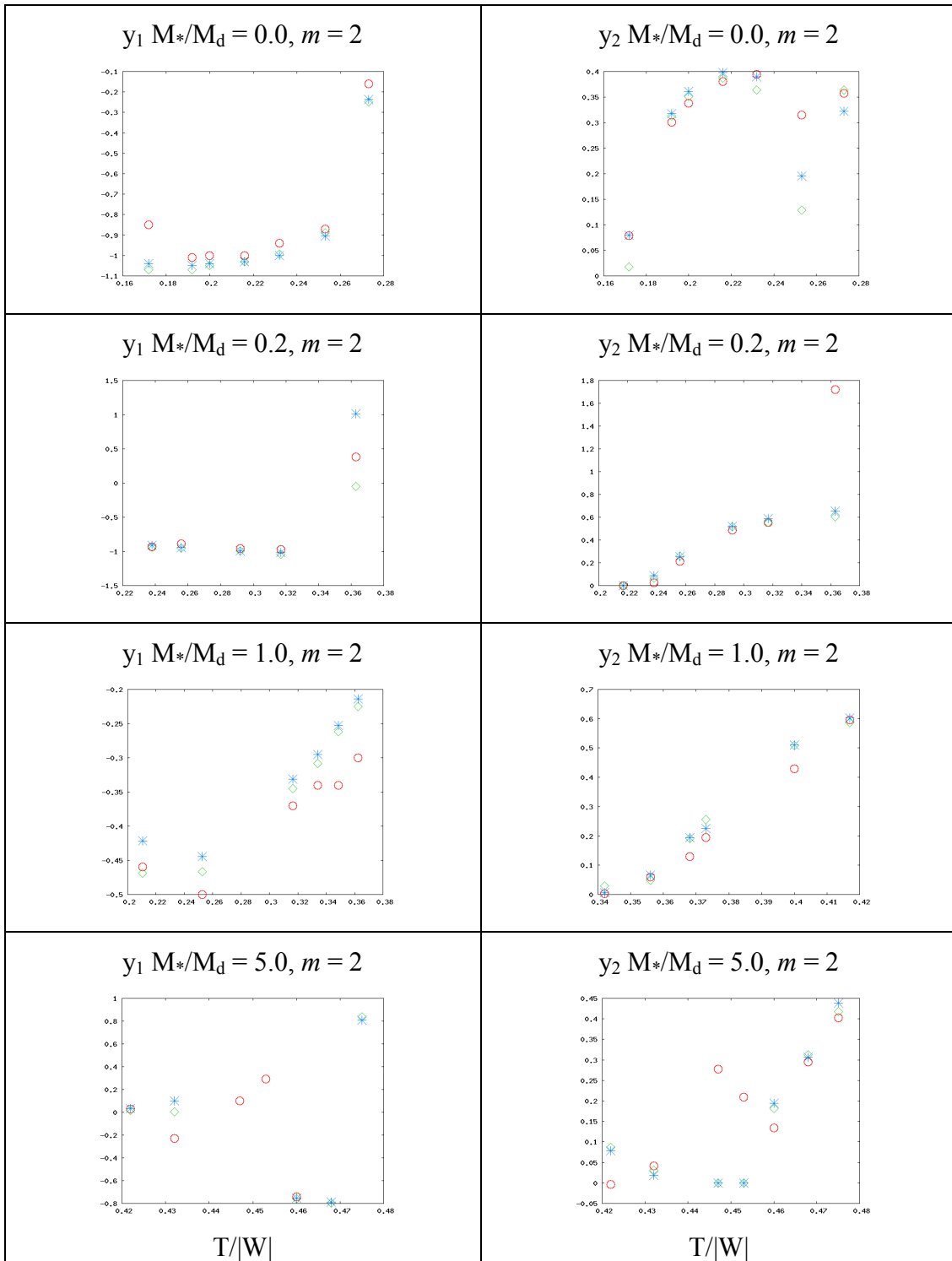


Fig. 5.1.4.3 Comparison of our y_1 and y_2 values with WTH y_1 and y_2 values for $m = 2$ models. The red circles represent WTH data, the green diamonds represent our 512 x 512 data and the blue stars represent our 256 x 256 data points.

Eigenvalues for WTH comparison models							
T/ W	r_-/r_+	$y_1(m)$ WTH	$y_1(m)$ 512	$y_1(m)$ 256	$y_2(m)$ WTH	$y_2(m)$ 512	$y_2(m)$ 256
$M_s/M_d = 0.2$		$m = 1$					
0.101	0.051	-0.700	-0.533	-0.521	0.077	0.311	0.293
0.121	0.067	-0.530	-0.488	-0.476	0.382	0.455	0.426
0.165	0.110	-0.490	-0.405	-0.400	0.710	0.669	0.651
0.220	0.185	-0.550	-0.281	-0.302	0.887	0.776	0.735
0.279	0.307	-0.730	-0.150	-0.133	0.888	0.721	0.642
$M_s/M_d = 1.0$							
0.211	0.075	-0.460	-0.469	-0.422	0.027	0.159	0.141
0.253	0.114	-0.500	-0.467	-0.444	0.179	0.316	0.308
0.316	0.205	-0.370	-0.345	-0.331	0.462	0.526	0.527
0.334	0.240	-0.340	-0.308	-0.295	0.492	0.567	0.562
0.349	0.276	-0.340	-0.262	-0.253	0.482	0.585	0.582
0.363	0.315	-0.300	-0.225	-0.214	0.518	0.585	0.587
$M_s/M_d = 5.0$							
0.260	0.074	-0.650	-0.379	-0.329	0.009	0.085	0.078
0.285	0.092	-0.490	-0.401	-0.382	0.026	0.097	0.088
0.335	0.148	-0.450	-0.413	-0.399	0.100	0.161	0.158
0.388	0.241	-0.410	-0.373	-0.373	0.250	0.287	0.280
$M_s/M_d = 0.2$		$m = 2$					
0.238	0.216	-0.930	-0.939	-0.913	0.027	0.066	0.086
0.256	0.252	-0.890	-0.951	-0.943	0.211	0.257	0.256
0.292	0.344	-0.960	-0.996	-0.993	0.486	0.516	0.519
0.317	0.432	-0.970	-1.040	-1.014	0.554	0.553	0.586
0.363	0.672	0.380	-0.051	1.016	1.721	0.603	0.653
$M_s/M_d = 1.0$							
0.342	0.260	-0.850	0.210	0.204	0.004	0.029	0.006
0.356	0.295	-0.770	-0.868	-0.865	0.060	0.049	0.067
0.368	0.331	-0.810	-0.855	-0.839	0.129	0.192	0.195
0.373	0.350	-0.820	-0.854	-0.851	0.195	0.256	0.226
0.400	0.476	-0.900	-0.915	-0.912	0.430	0.508	0.510
0.417	0.602	...	0.940	0.944	0.597	0.587	0.603
$M_s/M_d = 5.0$							
0.422	0.335	0.030	0.019	0.032	-0.004	0.086	0.079
0.432	0.374	-0.230	0.006	0.100	0.041	0.031	0.018
0.447	0.445	0.100			0.278	0.000	0.000
0.453	0.484	0.290			0.209	0.000	0.000
0.460	0.539	-0.740	-0.758	-0.753	0.134	0.182	0.194
0.468	0.622		-0.795	-0.789	0.295	0.312	0.307
0.475	0.715		0.836	0.810	0.402	0.418	0.438

Table 5.1.4.1 WTH comparison models, $y_1(m)$ and $y_2(m)$ eigenvalues.

5.2. Applications of Quasi-linear Torque Calculations

Our main interest in calculating disk models is to understand the process of angular momentum transport. An important reason for performing a thorough mapping of parameter space of the linear regime is to gain an understanding of which models to calculate using the more computationally expensive nonlinear code to sparsely sample the parameter space in a meaningful way. Self-gravity torque is one mechanism that can be responsible for transport of angular momentum, and we present here applications of torque calculations that can provide qualitative insight into the predicted behavior of nonlinear disks.

Torque density is simply the cross product of the radial component with the force density.

$$\boldsymbol{\tau} = \mathbf{r} \times \mathbf{f} \quad (5.2.1)$$

To find an expression for the force density, we recast the momentum conservation equation. From Section 3.1, we have:

$$\rho(\partial_t + \mathbf{v} \cdot \nabla) \mathbf{v} = -\nabla P - \rho \nabla \Phi_g \quad (5.2.2)$$

Using the continuity equation, 3.1.1, we can write:

$$\partial_t(\rho \mathbf{v}) = \rho \partial_t \mathbf{v} + \mathbf{v} \partial_t \rho = \rho \partial_t \mathbf{v} + \mathbf{v} [-\nabla \cdot (\rho \mathbf{v})] \quad (5.2.3)$$

Using substitution, after cancellations, we rewrite Equation 5.2.2 using dyadic notation:

$$\partial_t(\rho \mathbf{v}) + \nabla \cdot (\rho \mathbf{v} \mathbf{v} - \bar{\mathbf{I}} P) = -\rho \nabla \Phi_g \quad (5.2.4)$$

where $\bar{\mathbf{I}}$ is the identity dyadic matrix. Crossing $\boldsymbol{\omega}$ into Equation 5.2.4, we get:

$$\partial_t(\rho v_\phi \varpi) = -\left\{ \boldsymbol{\omega} \times \left[\nabla \cdot (\rho \mathbf{v} \mathbf{v} - \bar{\mathbf{I}} P) \right] \right\} \cdot \hat{\mathbf{z}} - \left[\boldsymbol{\omega} \times \rho \nabla \Phi_g \right] \cdot \hat{\mathbf{z}} \quad (5.2.5)$$

When linearized, only the z-component survives, since $\boldsymbol{\omega}$ crossed into the radial component is zero, and the cosine terms integrate to zero around the disk.

The left-hand term is the total torque. The first term on the right-hand side is the torque caused by the energy carried in the waves, while the second term will give the torque due to self-gravity. The linearized self-gravity torque becomes:

$$\tau \equiv -\varpi \frac{1}{\varpi} \partial_\varpi \left[(\rho_0 + \delta\rho e^{im\phi}) (\Phi_0 + \delta\Phi e^{im\phi}) \right] \quad (5.2.6)$$

The zeroth order terms are identically zero from the equilibrium condition, and the first order terms integrate to zero around the disk. We are left with second order terms:

$$\tau \equiv -m\pi \int |\delta\rho| |\delta\Phi| \sin(\phi_p - \phi_\phi) dz \quad (5.2.7)$$

We integrate the torque over the height of the disk. Note we have only kept cross terms here, and have dropped $\delta\rho^2$ and $\delta\Phi^2$ terms, as we are interested in the interaction of self-gravity with the perturbed mass density of the disk. We can use the torque calculation to get an idea of how the disk would evolve in a nonlinear simulation. In the sequence of plots in Figs. 5.2.1 and 5.2.2, we recall the mass density contours and torque plots of the representative models introduced in Fig. 3.2.3, and now include plots showing the angular momentum and transport time. Torque is normalized by $\delta\rho^2$, which implies that nonlinear saturation by the mode should happen when the density perturbation amplitude equals unity. This is a standardized normalization and may not be appropriate for all models. The transport time is calculated as J/τ normalized by MIRP. Note that the transport time is shown in semilog plots.

In the linear approximation, we assume that there is no mass flux across the annuli affecting a change in angular momentum, the self-gravity torque acting on a mass ring is the only effect we are investigating here. The first column of Fig. 5.2.1 introduces

the transport time calculated for the representative Γ^+ mode model. The sharp peak of the transport time indicates approximately where τ goes to zero. Since this is a discrete calculation, typically the exact zero has been stepped over. Near the inner edge of the disk, the transport time is very low, around 0.01 MIRP. This means that the angular momentum of that mass ring will completely dissipate within a very short time. Since the torque is negative there, the mass of the ring would tend to move inward toward the star in a nonlinear simulation. At the mass density maximum, R_0 , the transport time is about 5.0 MIRPs, also moving inward. Somewhat outside density maximum, at about $1.13 R_0$, the torque changes sign. The matter of the disk outside this radius will gain angular momentum due to the self-gravity torque and tend to move outward in a nonlinear simulation. This also happens on a MIRPish time scale, becoming more rapid toward the outer edge of the disk where the mass density is low. The linear prediction of the evolution of this disk is that it will significantly evolve in a few MIRPs, spreading out. The inner region will move toward the star, the region near the zero of the torque will remain fixed, and the outer part of the disk will move farther out.

The Γ^- mode plots tell a somewhat different story. The general shapes of the plots are similar, and the disk will also spread on a similar timescale, but here the zero of the torque lies at $1.015 R_0$, so the densest part of the disk will remain more stationary, with the timescale at R_0 calculated to be 147 MIRPs. The outer edges will still spread on a MIRPish timescale but not as much of the mass of the disk is involved in the spread. Note that the shoulders of the transport time plot are not as broad as those of the Γ^+ mode, indicating that more of the dense part of the disk will evolve slowly. The J mode model exhibits a narrower peak in the transport time, indicating that only the matter in the disk that is rather close to the zero in τ will remain relatively stationary as compared to the Γ^- mode. At R_0 , the transport time is 3.56 MIRPs, so the J mode disk will spread apart faster, like the Γ^+ mode.

The evolution of the P mode is expected to be qualitatively different. The torque in the inner region of the disk is positive, increasing angular momentum and driving the inner disk outward. This region includes the densest part of the disk as well; the zero of

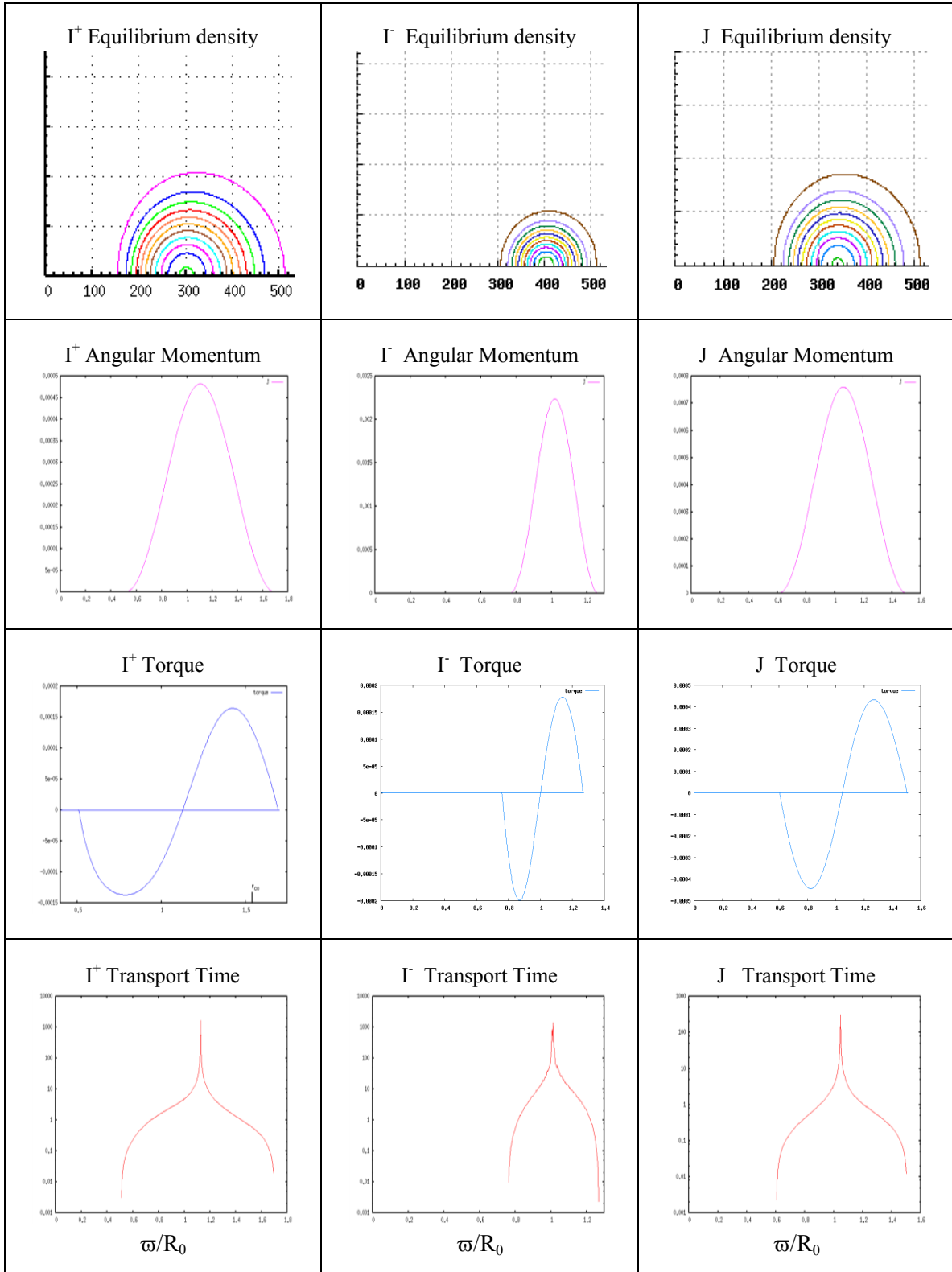


Fig. 5.2.1. Mass density contours, angular momentum, self-gravity torque and angular momentum transport time for the representative I and J modes, shown in Fig.3.2.3.

the torque lies at about $1.04 R_0$. Most of the outer region of the disk will be driven inward, with only the outermost region, where the mass density is small, spreading outward. The transport time plot thus predicts that the disk will slowly contract into a narrower configuration, fissioning off the outer edge of the disk. It should also be noted that the timescale for this is very large, much higher than those of the I and J modes. The transport time at R_0 is 423 MIRPs and remains at tens of MIRPs throughout most of the inner disk region. This indicates that the self-gravity torque is not efficient enough to limit the growth to saturate into a mode. The torque from the wave propagation must be more important than the self-gravity mechanism for determining the evolution of the disk. This makes sense, since the P modes lie in the high M_*/M_d part of parameter space where self-gravity is not important. The Edge mode disk also shows evolution on a long timescale, somewhat similar to that of the P mode; with this particular model fissioning into three separate rings. Again, this would take so long to occur that the wave propagation would dominate the evolution of the disk.

The transport time of the A mode model is extremely short; at R_0 , the timescale is 0.043 MIRPs. This suggests that our normalization using $|\delta\rho|^2 = 1$ is not appropriate for this model. What it means in this case is that the evolution prompted by the self-gravity torque would significantly change the structure of the disk before the mode could set in. The torque is negative in the inner disk region, with torque changing sign well outside the density maximum at $1.52 R_0$. The inner edge of this disk is close to the star, compared to the other representative modes discussed. The timescale and torque plots suggest that the matter of the disk will most likely flow onto the star in a very short time. The outer matter of the disk mostly flows inward as well, with a narrow region moving outward. The density of the outer part of the disk is very low. Most of the matter of the disk is contained in the region where the matter will flow inward, onto the star.

Fig. 5.2.3 displays plots of the projected evolution of the angular momentum due to the self-gravity torque of the representative I^+ and I^- mode models, while Fig. 5.2.4 shows angular momentum evolution for the representative J and A mode models. For the I and J modes, we show successive timesteps of 0.1 MIRP and for the A mode we have taken timesteps of 0.01MIRP. The I and J modes show angular momentum increasing in the outer part of the disk and decreasing in the inner disk region. The A mode shows a

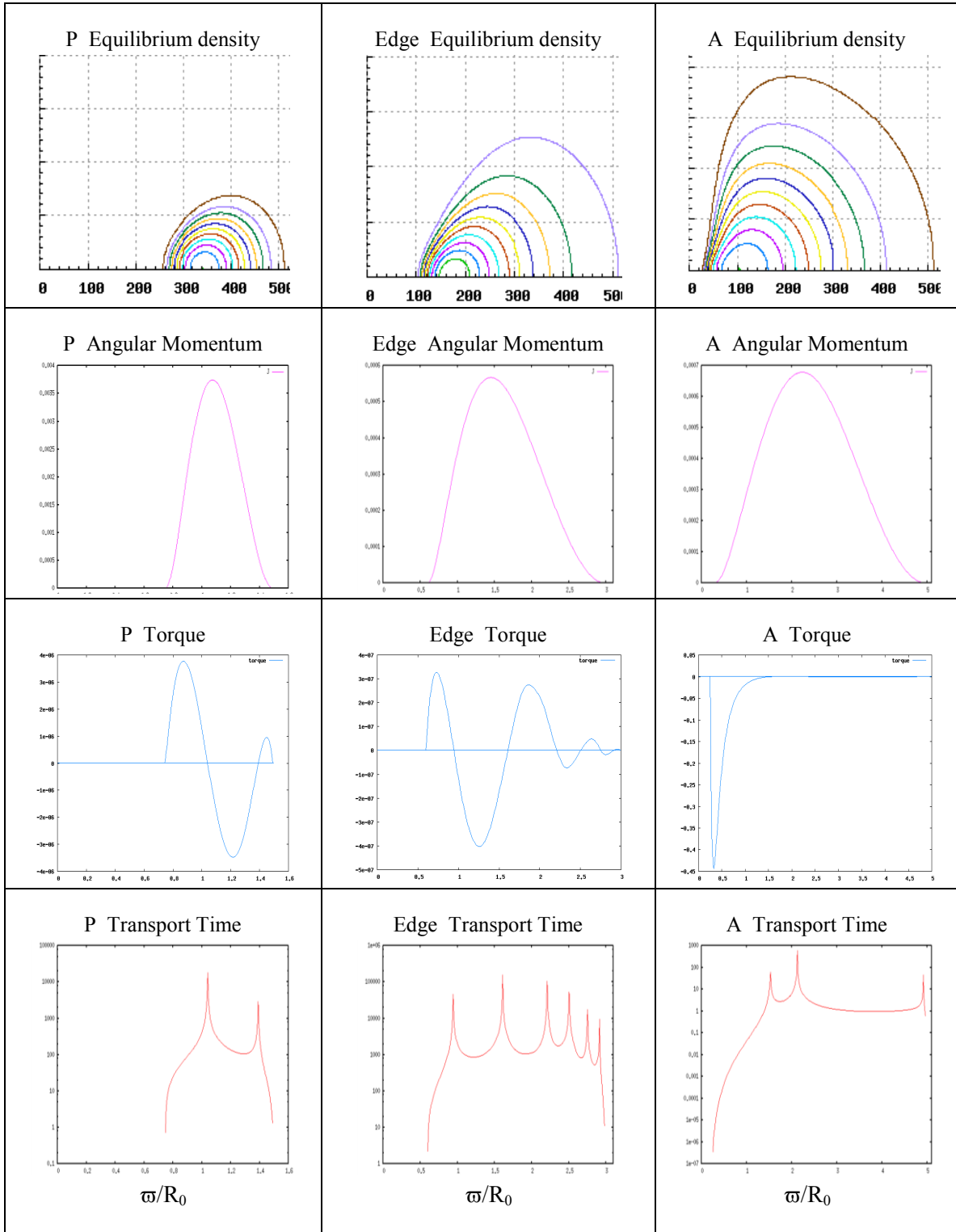


Fig. 5.2.2. Mass density contours, angular momentum, self-gravity torque and angular momentum transport time for the representative P, edge, and A modes, shown in Fig. 3.2.3.

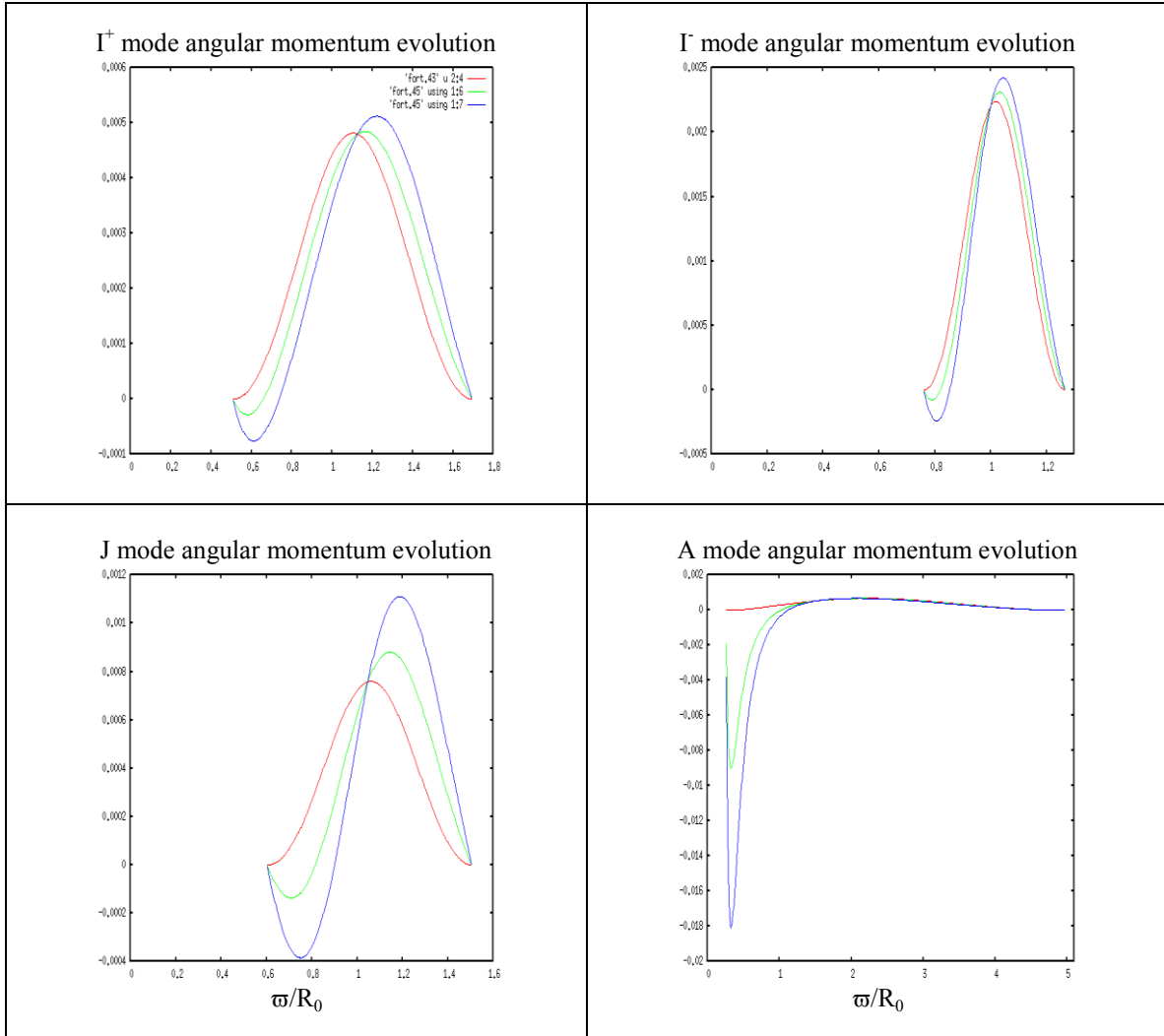


Fig. 5.2.3. Evolution of angular momentum for the representative I^+ , I , J and A mode models introduced in Fig.3.2.3. The original angular momentum is plotted in red, while green and blue are angular momenta at time intervals of 0.5 and 1.0 MIRPs, respectively, for the I and J modes and 0.05 and 0.1 MIRPs, respectively, for the A mode.

very different evolution, with the angular momentum rapidly becoming negative near the inner edge of the disk.

Figs. 5.2.5 and 5.2.6 show the angular velocity profiles predicted by the evolution driven by self-gravity torque, with the original velocity shown in red, while green and blue plots show advanced velocity profiles as noted. These plots indicate that the disks will evolve rapidly near the inner and outer edges. Near the inner edges, the velocity decreases as the fluid of the disk falls toward the central star. The velocity raises toward

the outer edge as the disk spreads. Note that the timesteps are smaller for the A mode model, with a dramatic decrease in velocity near the inner edge but little change near the outer edge of the disk.

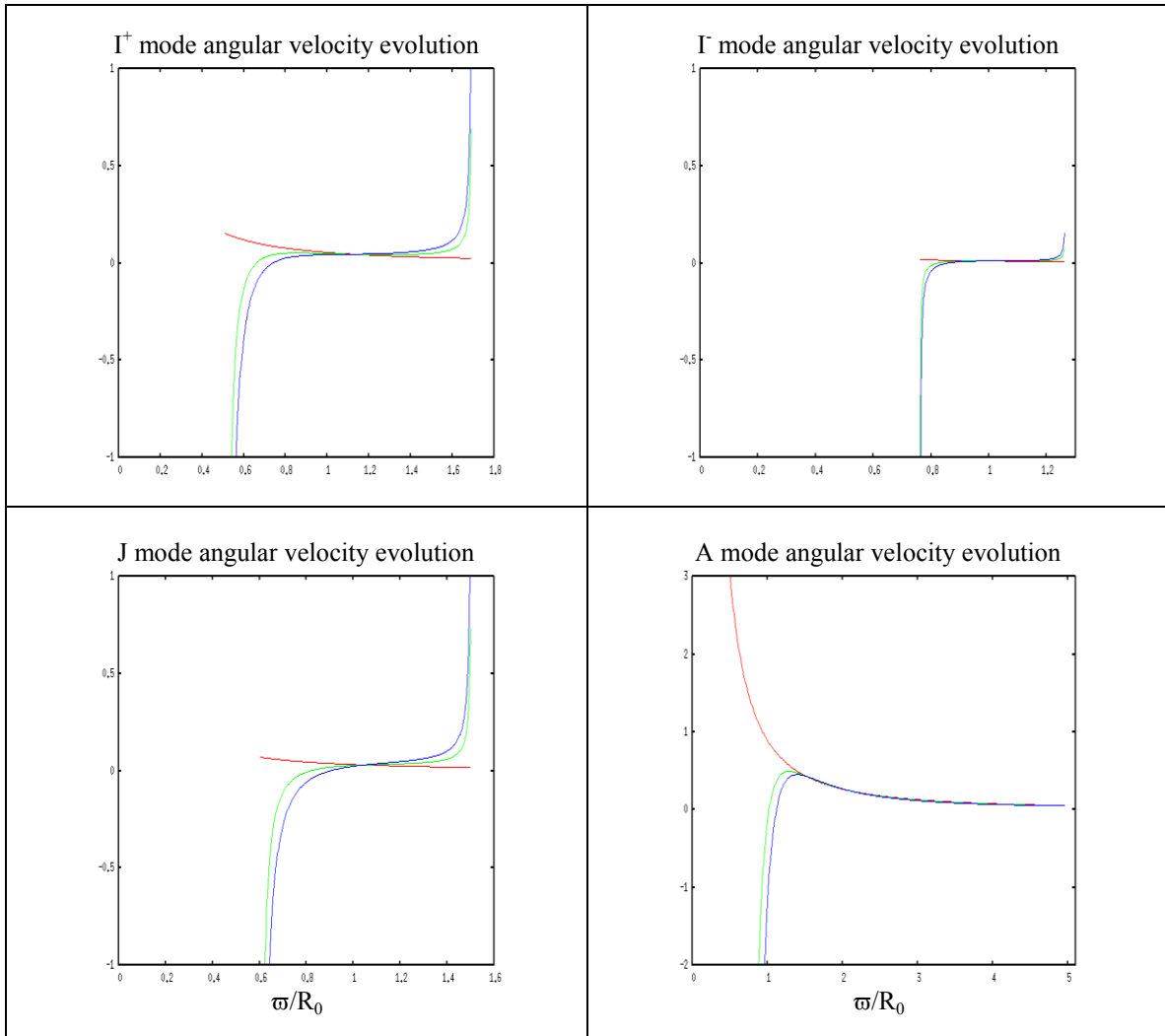


Fig. 5.2.4. Evolution of angular velocity for the representative I^+ , I , J and A mode models introduced in Fig.3.2.3. The original angular momentum is plotted in red, while green and blue are angular momenta at time intervals of 0.5 and 1.0 MIRPs, respectively, for the I and J modes and 0.05 and 0.1 MIRPs, respectively, for the A mode.

5.3. Conclusions

We have presented an extensive study of thick, polytropic, self-gravitating linear star/disk systems. We have compared our results with earlier studies done on slender, incompressible tori by ATC, non-self-gravitating models calculated by Kojima, several 2-D studies focused on the $m = 1$ eccentric instability, and the 3-D nonlinear study done by WTH. Our results generally agree well with previous studies with a few exceptions. Our results agree with the ICT study of ATC as far as the general shape of the I mode threshold, except for the fact that we show the $m = 2$ threshold to be lower than that of the $m = 1$ case. One major difference is that our calculations account for the motion of the star in the $m = 1$ case, where they did not. Also, we show J modes in a much smaller region of parameter space than was evident in the ATC results. We agreed qualitatively with the studies involving star motion in the $m = 1$ case; our models exhibited eccentric spiral instabilities similar to those seen by the earlier 2-D studies, in models with and without outer Lindblad resonances. Our results for non-self-gravitating models agreed well with those of Kojima, in the region of parameter space where our models overlapped with his, where the disks support P modes. We also calculated models for lower $T/|W|$ than did Kojima, into the realm where disks suffer edge mode instabilities with long trailing arms which require greater resolution. Our models mostly agreed with the nonlinear calculations by WTH, with the main differences being that our growth rates diverged for models where we saw edge modes but WTH reported P modes; and the fact that we saw stable models where WTH reported L modes.

Our general results consisted of analysis of ~ 7700 equilibrium models and ~ 2200 temporally evolving models. Our analysis of equilibrium models included mapping trends of quantities that would prove to be helpful in understanding the evolving models, such as $T/|W|$ and the Q -barrier.

The rich spectrum of temporally evolving models has provided general information about where I+, I-, J, A, P and edge modes lie in parameter space, as evidenced by the parameter space plots in the general results section, which show trends for individual values of m , combining information about $q = 1.5, 1.75$ and 2.0 . We also provide modal dominance tables, which indicate the order of the growth rates for $m = 1,$

2, 3 and 4 as a function of M_*/M_d and r_-/r_+ . We also plot y_1 and y_2 vs. r_-/r_+ for a representative sampling of values of M_*/M_d , and discuss characteristic plots illustrating three main behavioral trends for y_2 vs. r_-/r_+ for $M_* \ll M_d$, $M_* \approx M_d$ and $M_* \gg M_d$. We present individual subsections for $q = 1.5, 1.75$ and 2.0 , with detailed analysis of the behaviors inherent to sections of parameter space for each value of m . We see A modes present for $m = 1$ models for $M_*/M_d < 1.0$ for small r_-/r_+ , changing to stable for $q = 1.5$ and 1.75 as M_*/M_d increases, changing to edge modes for $q = 2.0$ as M_*/M_d increases. We see J modes present in $m > 1$ models, for large r_-/r_+ and small M_*/M_d . P modes and edge modes reside in the regions where M_*/M_d is large, with P modes at higher r_-/r_+ than edge modes. Between the P/edge mode and A mode regions and the region of J modes, we find I modes. We note that models become stable for high M_*/M_d , especially for low r_-/r_+ for models with $q = 1.5$ and 1.75 but not for $q = 2.0$. We offer detailed analysis of the various unstable regions with respect to information gleaned from the eigenfunction amplitude and phase plots, work integrals, stresses, perturbed angular momentum and self-gravity torque plots.

We analyze characteristic Γ^+ , Γ , J, P, edge and A mode models using quasi-linear analysis involving the self-gravity torque, inferring behavior that might be expected in nonlinear models. We see that for I and J modes, the angular momentum transport in the disks will tend to spread the disks out; the inner edge will move inward toward the star and the outer edge will move outward. The P and edge modes will not be greatly affected by the self-gravity torque, and the A mode will rapidly spread most of the disk mass inward toward the central star. While we cannot specifically address the question regarding the relative amount of the mass of the Solar System contained in the Sun, we can say that our quasi-linear analysis indicates that there are types of disks in which the angular momentum transport will cause matter to flow inward onto the star.

Perhaps one of the most important conclusions of this work is the finding that essentially all disk systems for $q = 1.5$ and 1.75 are unstable for $M_*/M_d > 25$ or 50 . This reduces the parameter space where young stellar object disks can exist for a reasonable length of time. Since we do observe disks, it must mean that there is a mechanism causing stability in these disks that is outside our study. Perhaps our assumption of

constant entropy is too restrictive. Maybe the addition of heating and cooling mechanisms in the equation of state will provide different trends in the stability regimes.

In future research, we will use the wealth of data produced by this study to determine which computationally expensive, nonlinear models to run to gain a fruitful picture of the complicated parameter space that our linear study suggests. We will rely on the knowledge gained by this linear study to aid in guiding studies of planet migration. We will also use it as a basis for comparison with models without the adiabatic restriction, utilizing a full conservation of energy equation with heating and cooling terms. In the future, we hope to include magnetic fields in our disk calculations as well. This broad study of the linear realm of polytropic disks will serve as a basis of many future studies.

APPENDIX A

PLOTS FOR SELECTED $q = 1.5$ MODELS

Appendix A contains a sequence of model plots for $q = 1.5$ models, including $M_*/M_d = 0.0, 0.01, 0.1, 1.0, 5.0, 10.0, 25.0, 50.0$ and 100.0 . In general, figures labeled "a" contain plots for $M_*/M_d = 0.0, 0.01$ and 0.1 ; figures labeled "b" contain plots for $M_*/M_d = 1.0, 5.0$ and 10.0 ; and figures labeled "c" contain plots for $M_*/M_d = 25.0, 50.0$ and 100.0 . For each of these values of M_*/M_d , we include plots for models for $r./r_+ = 0.05, 0.10, 0.20, 0.30, 0.40$ and 0.50 . All radii depicted in the plots are normalized by R_0 . Stable and unresolved models are labeled as such. All of the functions plotted in the appendices are defined identically to similar plots found in the body of the dissertation.

Figs. A.1.0 a, b and c contain equilibrium mass density contour plots. The contours are defined with ten equally spaced levels between 10^{-30} maximum mass density for the individual model. The horizontal and vertical axes measure the grid spacing of 512×512 , with tick marks in increments of 50.

The first number after the "A" in the plot number indicates the value of m . Plots for $m = 1$ models are given in Figs. A.1.1 - A.1.6, plots for $m = 2$ models are given in Figs. A.2.1 - A.2.6, plots for $m = 3$ models are given in Figs. A.3.1 - A.3.6, and plots for $m = 4$ models are given in Figs. A.4.1 - A.4.6. In the descriptions below, we will refer to the sequences as A. m .1, A. m .2, etc, for the plot sequences in m . The second number after the "A" in the plot number indicates the type of function plotted. With the exception of the eigenfunction phase plots, all of the function plots for $m = 1, 2, 3$ and 4 plots have r/R_0 on the horizontal axes while the vertical axes depict the function values.

The A. m .1 c contain eigenfunction phase plots, shown in cylindrical coordinates where the horizontal and vertical axes depict the radial coordinate, normalized by R_0 . The W phase is plotted with red points while the $|\delta\rho/\rho_0$ phase is plotted with blue points. The inner and outer edges of the disks are shown in blue lines, while R_0 and R_{co} are shown in pink and turquoise, respectively.

The A. m .2 figures contain eigenfunction amplitude plots. W phase is plotted with red points while the $|\delta\rho/\rho_0$ phase is plotted with blue points. The amplitudes are

normalized to the maximum value found in the disk, so they scale to 1.0 at the top of the vertical axis. The *A.m.3* plots show the torque due to self-gravity, plotted in blue, while the *A.m.4* plots show the perturbed angular momentum, plotted in red. The *A.m.5* plots show the work integrals. The work done by perturbed enthalpy is plotted in brown and the work done by kinetic energy is plotted in blue. The *A.m.6* plots show the stresses. Reynold's stress is plotted in black, while the stress due to the work done by gravity is plotted in red and the stress due to acoustic flux is plotted in blue.

In cases where there are no plots shown, no model was calculated for that M_*/M_d and r_-/r_+ . Typically this occurs when the model is in a section of parameter space that is obviously stable, as indicated by surrounding models.

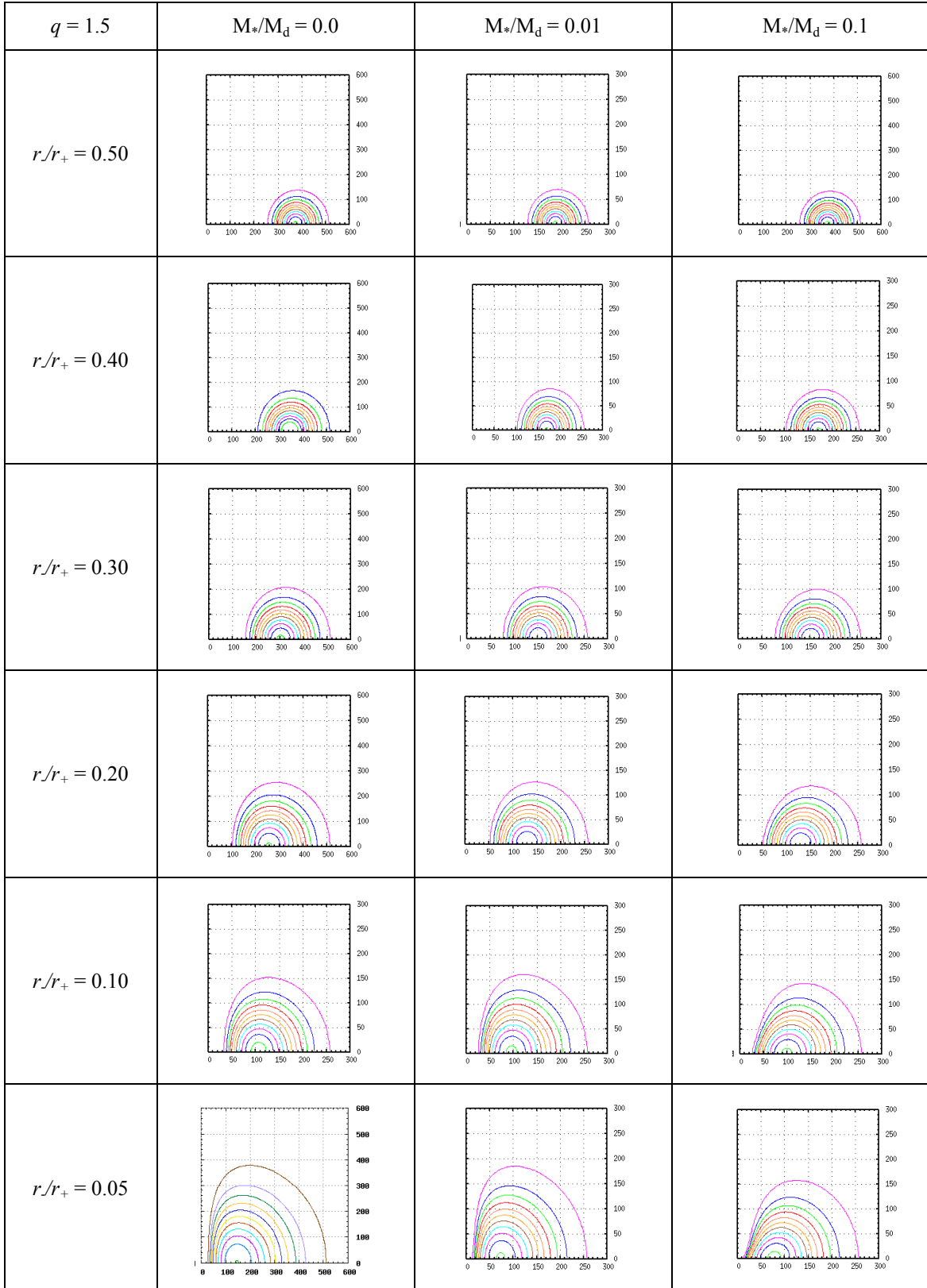


Fig. A.1.0.a. Equilibrium mass density contour plots of meridional slices for $q = 1.5$.

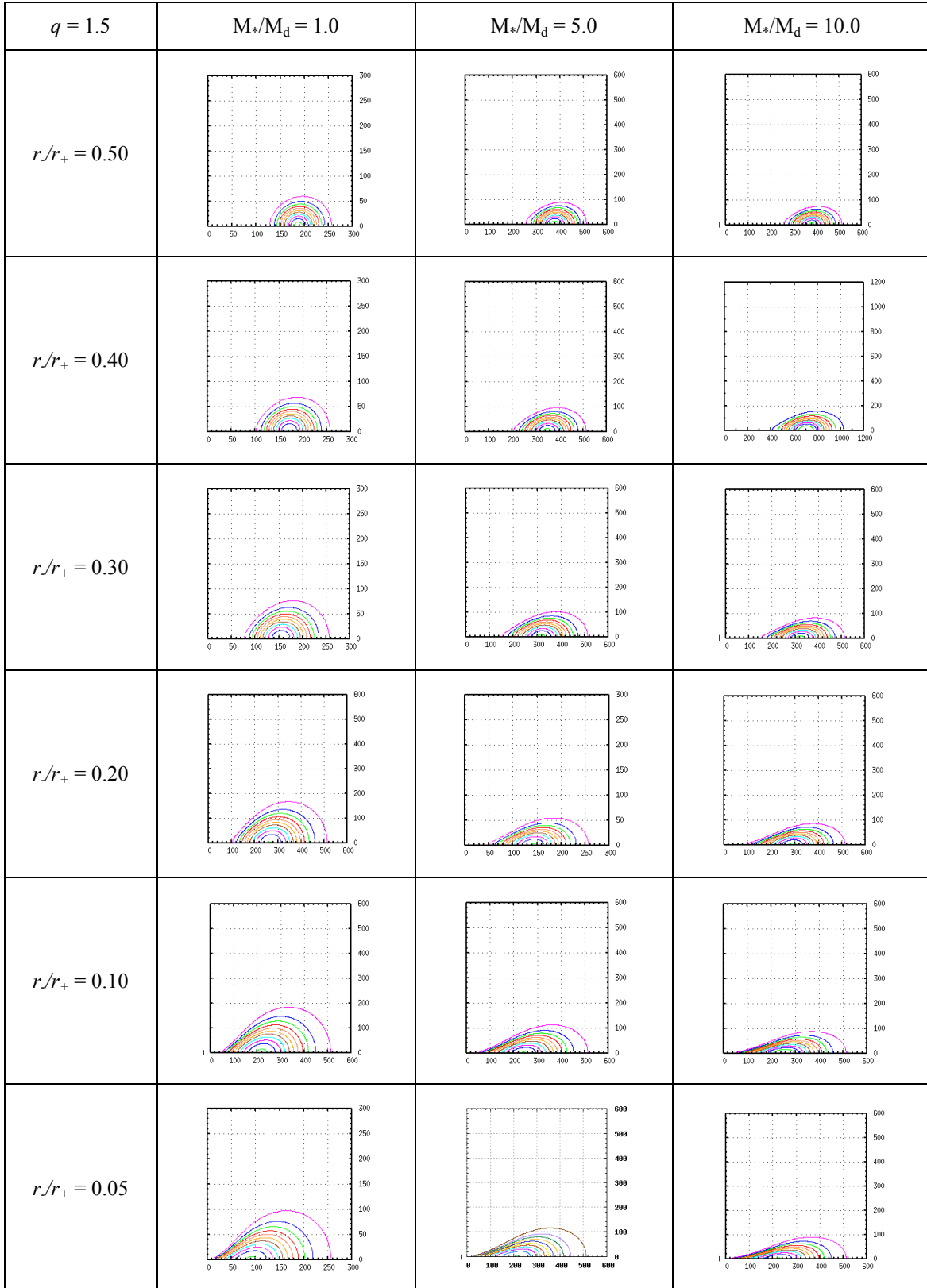


Fig. A.1.0.b. Equilibrium mass density contours of meridional slices for $q = 1.5$.

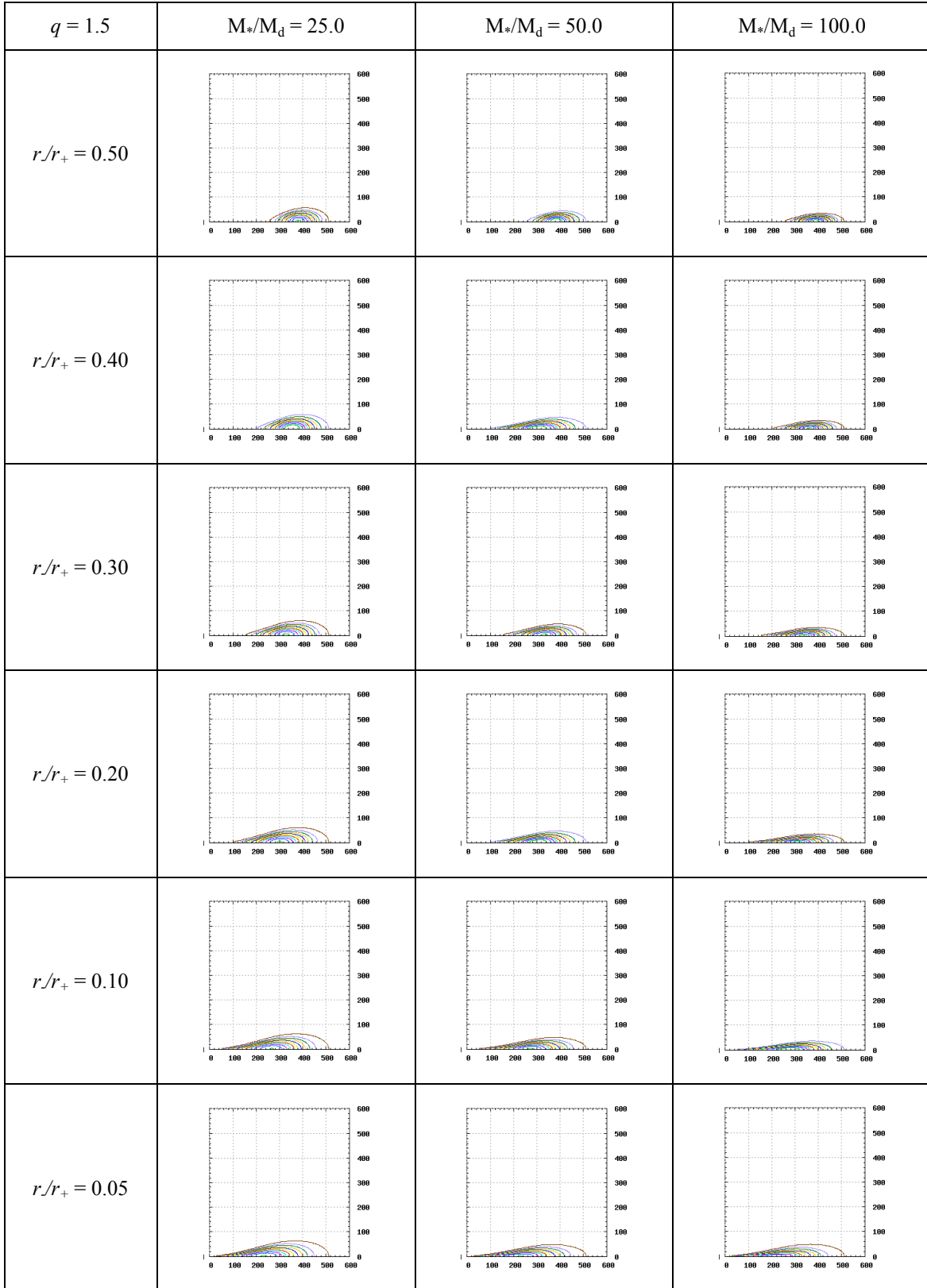


Fig. A.1.0.c. Equilibrium mass density contours of meridional slices for $q = 1.5$.

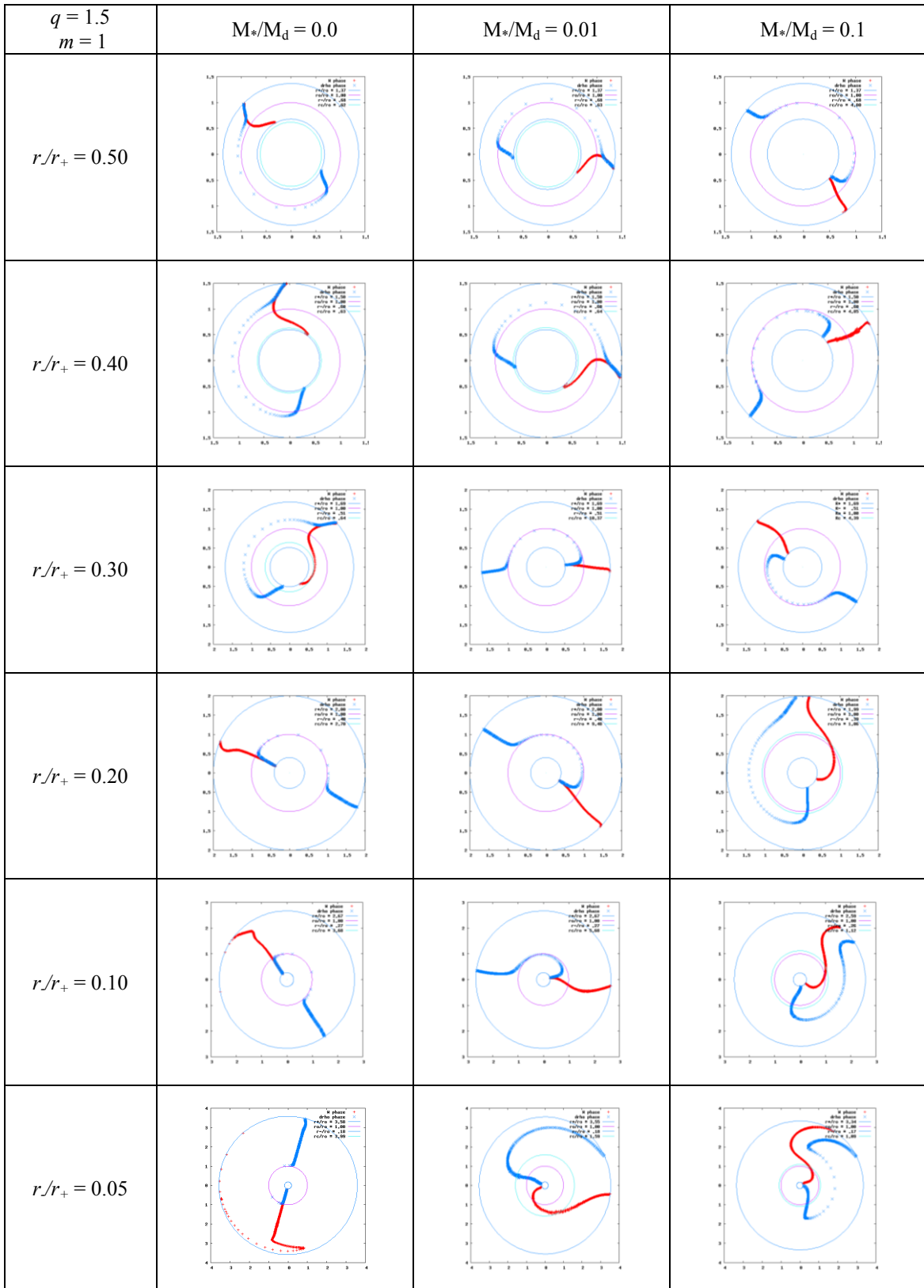


Fig. A.1.1.a. Eigenfunction phases for $q = 1.5$, $m = 1$.

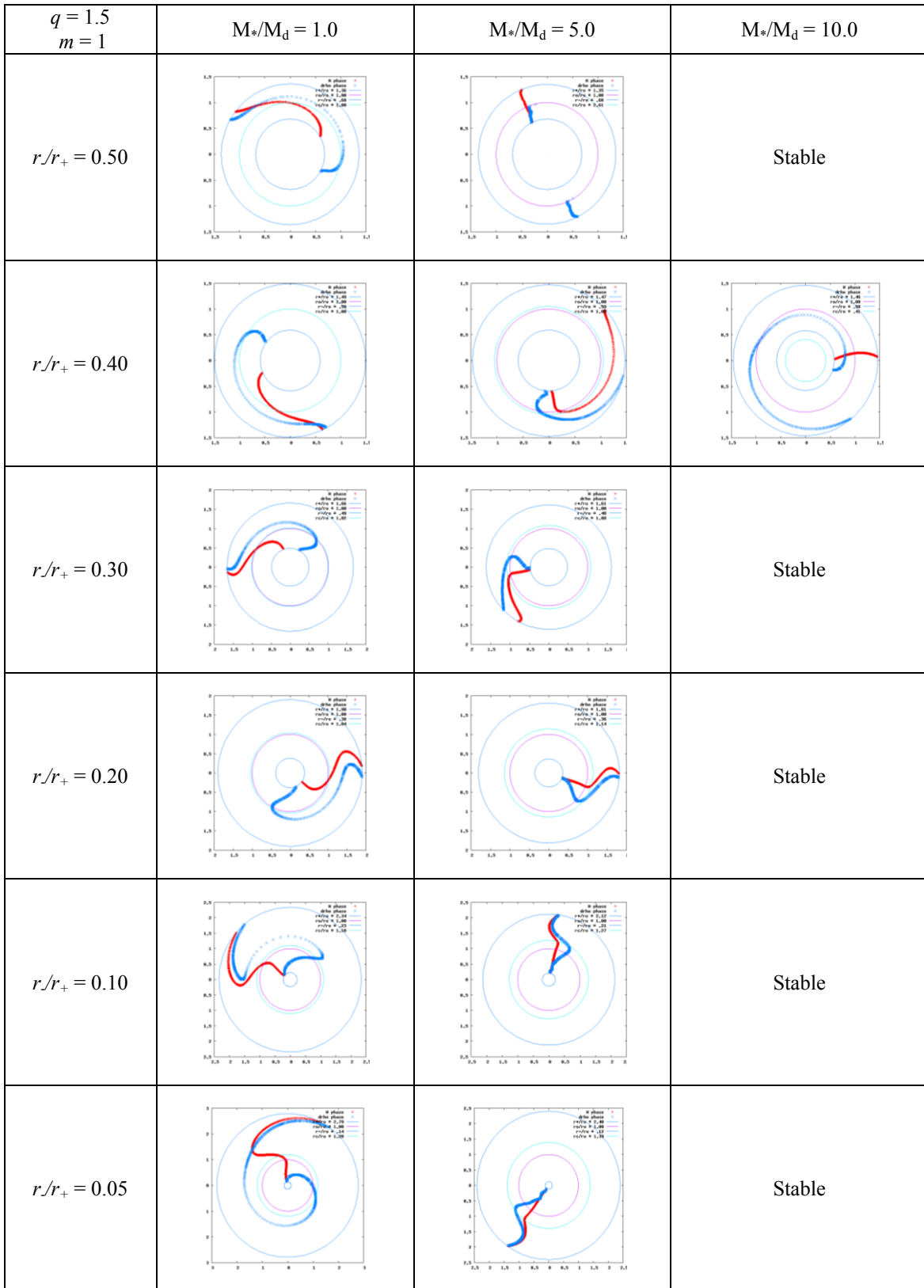


Fig. A.1.1.b. Eigenfunction phases for $q = 1.5$, $m = 1$.

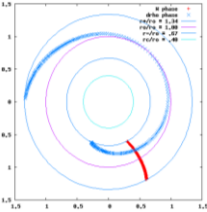
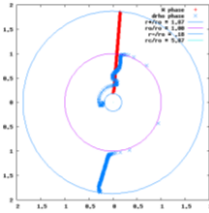
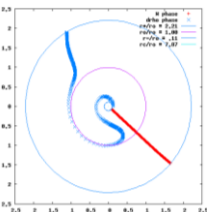
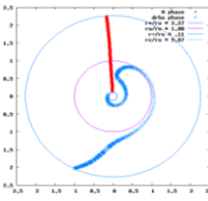
$q = 1.5$ $m = 1$	$M^*/M_d = 25.0$	$M^*/M_d = 50.0$	$M^*/M_d = 100.0$
$r/r_+ = 0.50$		Stable	Stable
$r/r_+ = 0.40$	Stable	Stable	Stable
$r/r_+ = 0.30$	Stable	Stable	Stable
$r/r_+ = 0.20$	Stable	Stable	
$r/r_+ = 0.10$	Stable	Stable	Stable
$r/r_+ = 0.05$			Stable

Fig. A.1.1.c. Eigenfunction phases for $q = 1.5$, $m = 1$.

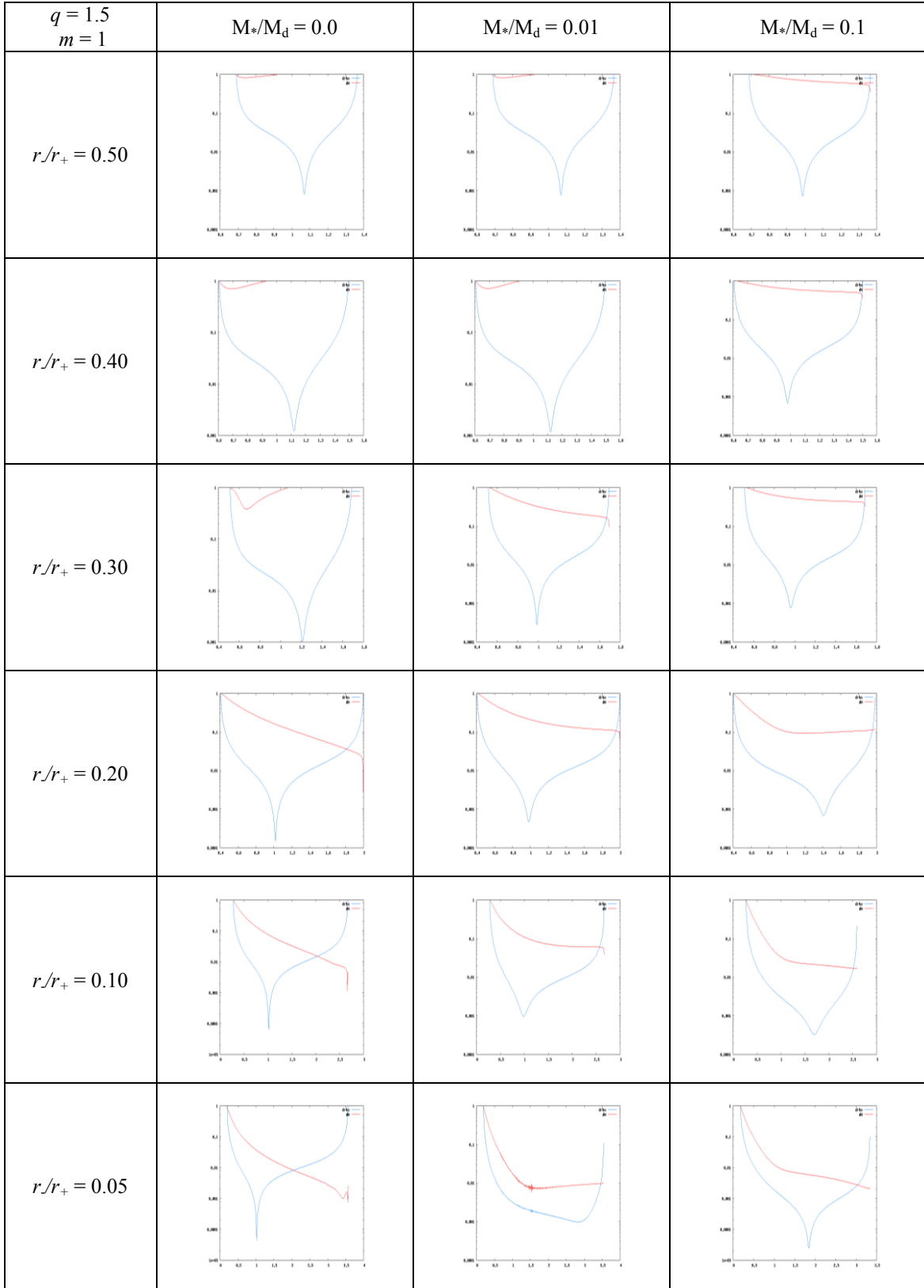


Fig. A.1.2.a. Eigenfunction amplitudes $|\delta\rho|/\rho$ and W for $q = 1.5$, $m = 1$.

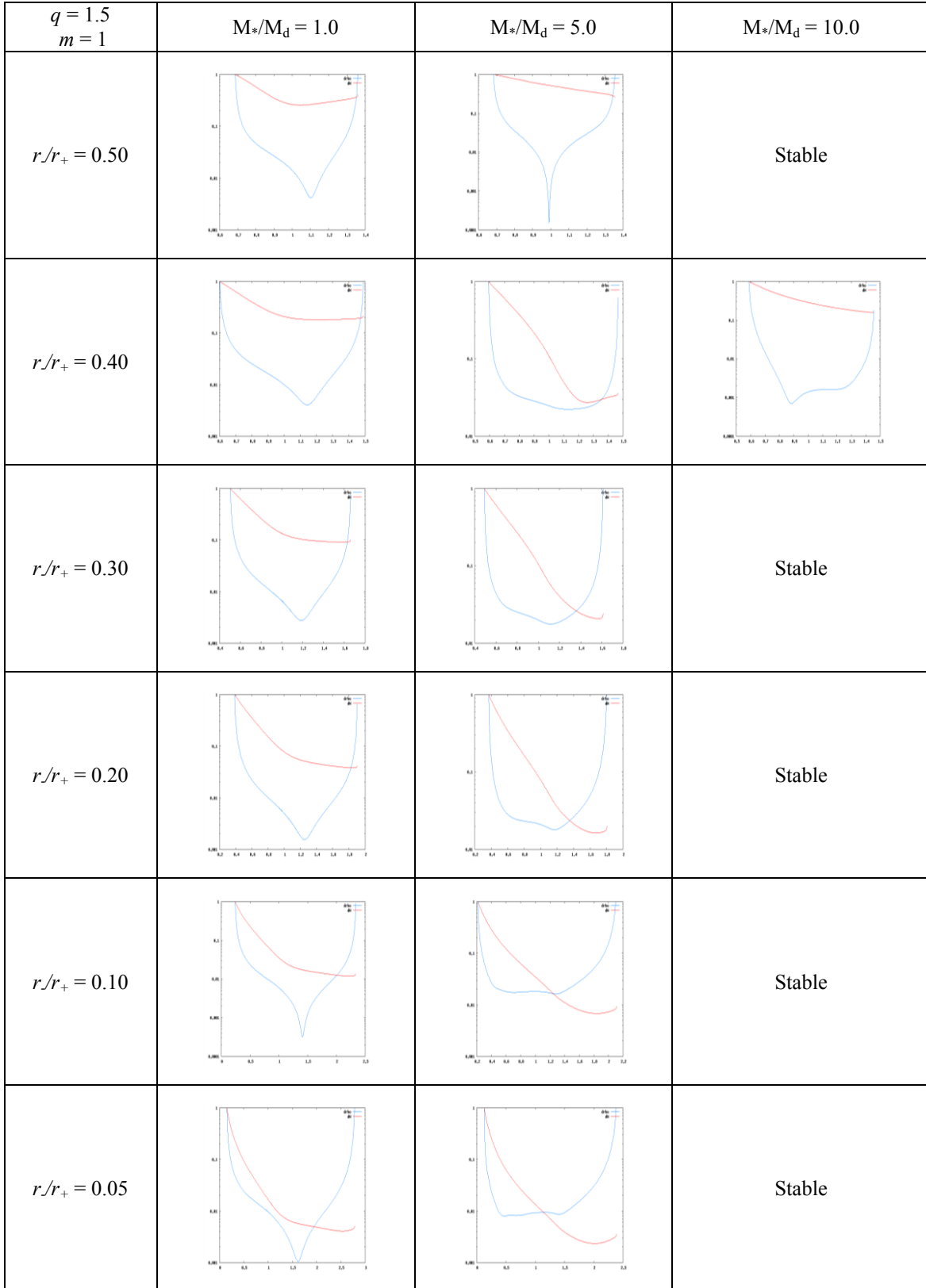


Fig. A.1.2.b. Eigenfunction amplitudes $|\delta\rho|/\rho$ and W for $q = 1.5$, $m = 1$.

$q = 1.5$ $m = 1$	$M_*/M_d = 25.0$	$M_*/M_d = 50.0$	$M_*/M_d = 100.0$
$r/r_+ = 0.50$		Stable	Stable
$r/r_+ = 0.40$	Stable	Stable	Stable
$r/r_+ = 0.30$	Stable	Stable	Stable
$r/r_+ = 0.20$	Stable	Stable	Stable
$r/r_+ = 0.10$	Stable	Stable	
$r/r_+ = 0.05$			Stable

Fig. A.1.2.c. Eigenfunction amplitudes $|\delta\rho|/\rho$ and W for $q = 1.5$, $m = 1$.

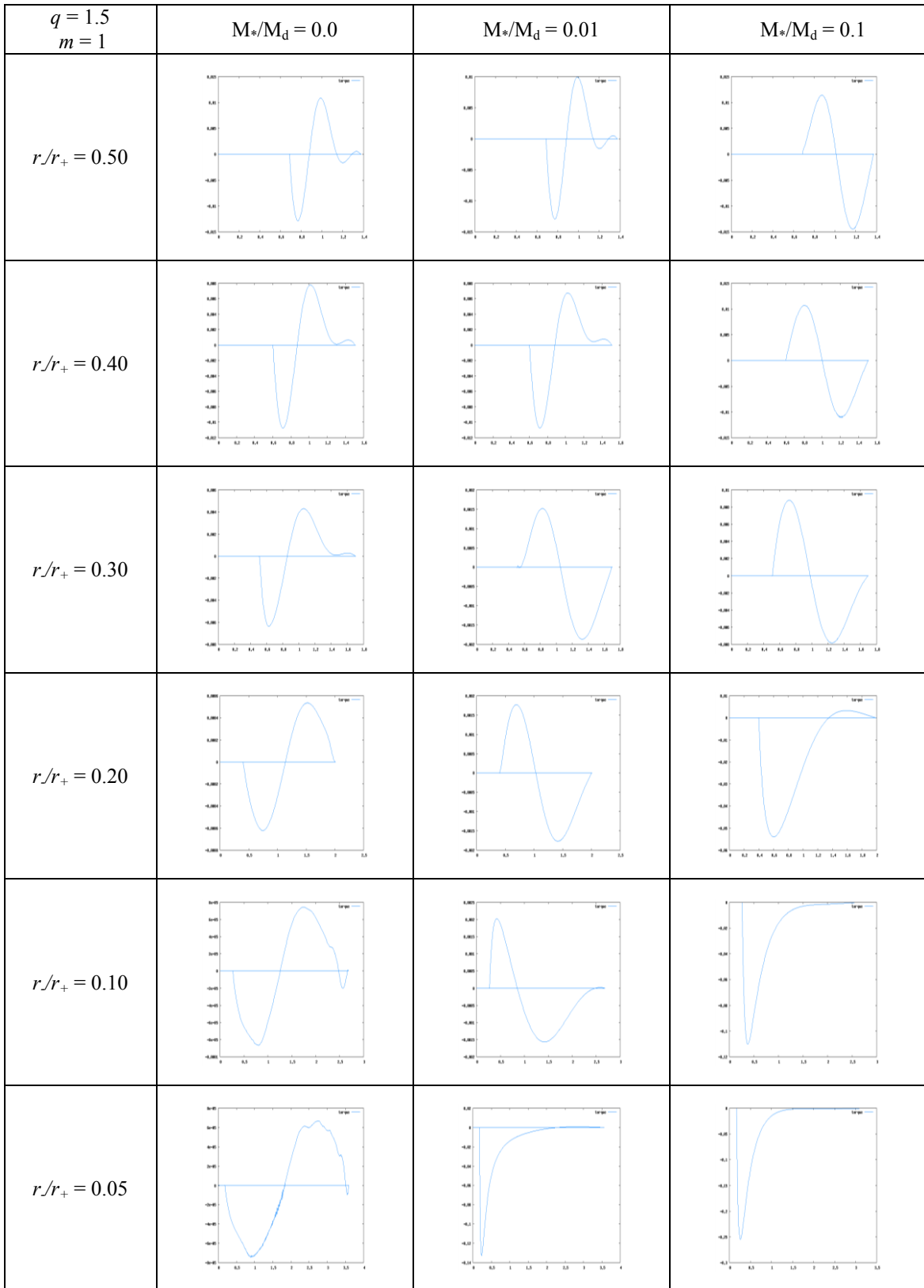


Fig. A.1.3.a. Self-gravitational torque for $q = 1.5$, $m = 1$.

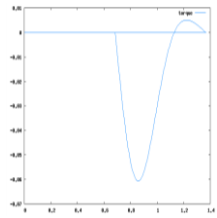
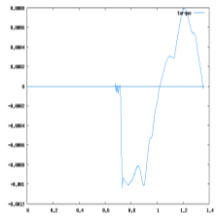
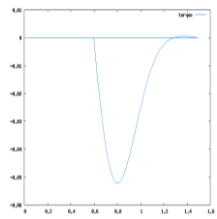
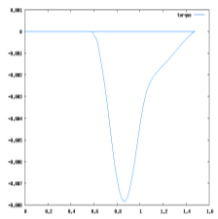
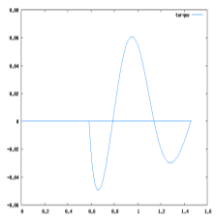
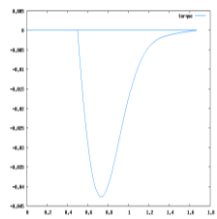
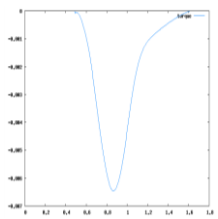
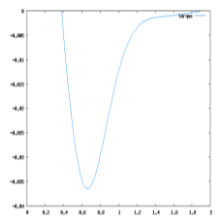
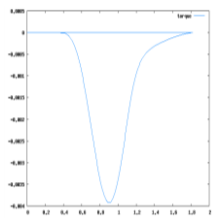
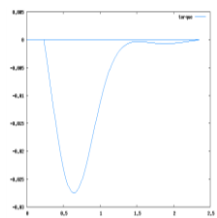
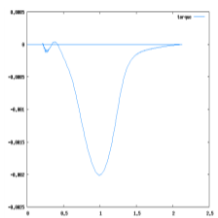
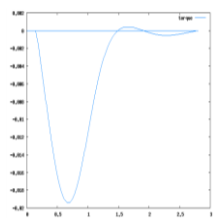
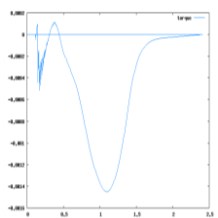
$q = 1.5$ $m = 1$	$M_*/M_d = 1.0$	$M_*/M_d = 5.0$	$M_*/M_d = 10.0$
$r/r_+ = 0.50$			Stable
$r/r_+ = 0.40$			
$r/r_+ = 0.30$			Stable
$r/r_+ = 0.20$			Stable
$r/r_+ = 0.10$			Stable
$r/r_+ = 0.05$			Stable

Fig. A.1.3.b. Self-gravitational torque for $q = 1.5$, $m = 1$.

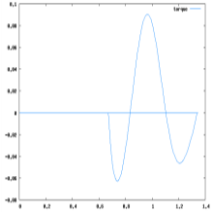
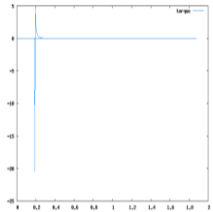
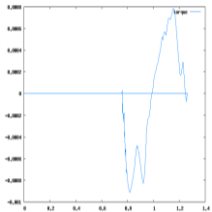
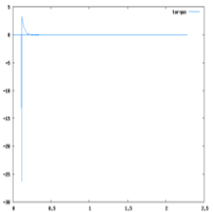
$q = 1.5$ $m = 1$	$M_*/M_d = 25.0$	$M_*/M_d = 50.0$	$M_*/M_d = 100.0$
$r/r_+ = 0.50$		Stable	Stable
$r/r_+ = 0.40$	Stable	Stable	Stable
$r/r_+ = 0.30$	Stable	Stable	Stable
$r/r_+ = 0.20$	Stable	Stable	Stable
$r/r_+ = 0.10$	Stable	Stable	
$r/r_+ = 0.05$			Stable

Fig. A.1.3.c. Self-gravitational torque for $q = 1.5$, $m = 1$.

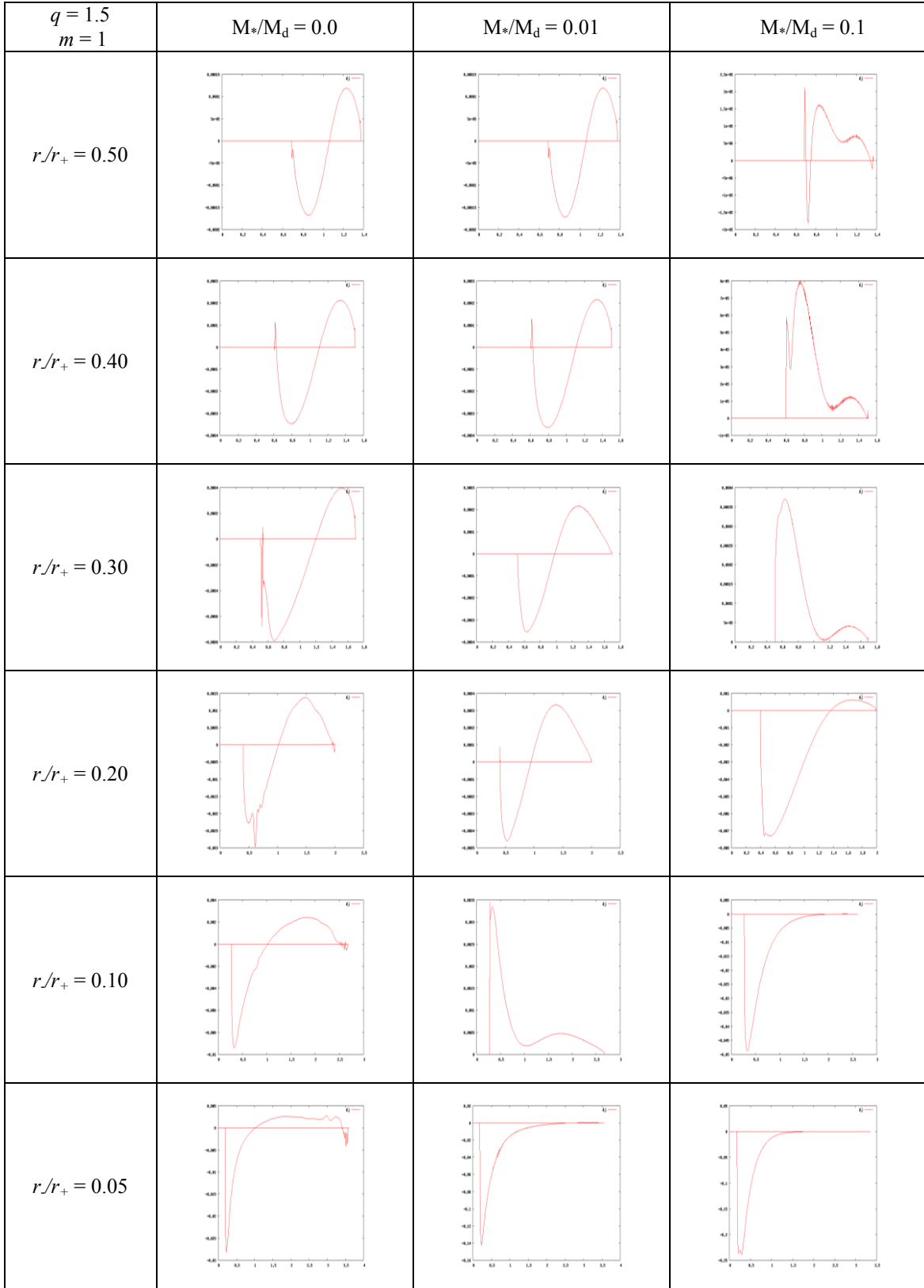


Fig. A.1.4.a. Perturbed angular momentum for $q = 1.5$, $m = 1$.

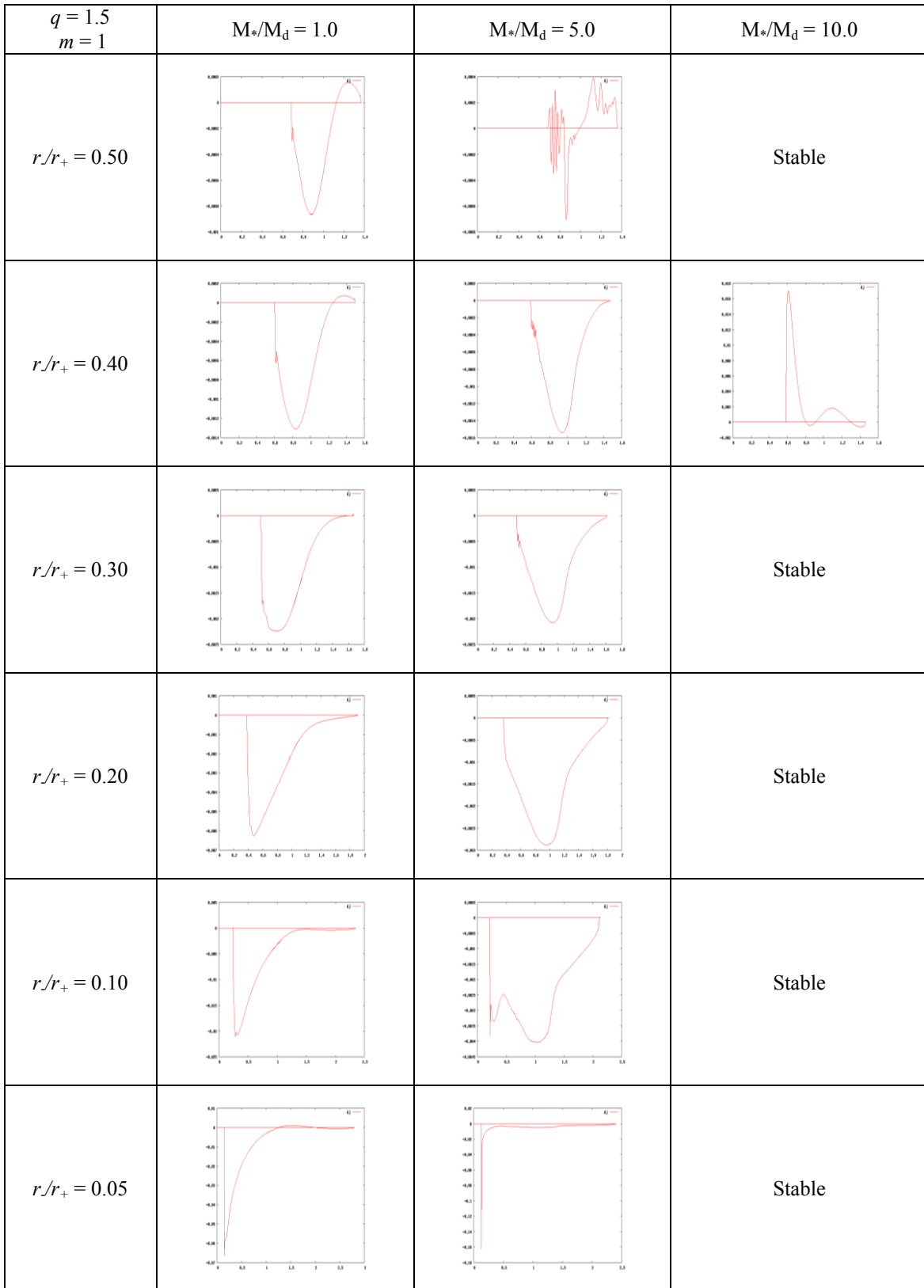


Fig. A.1.4.b. Perturbed angular momentum for $q = 1.5$, $m = 1$.

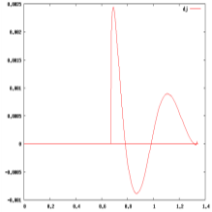
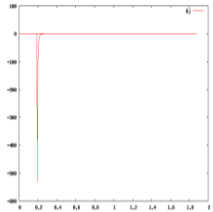
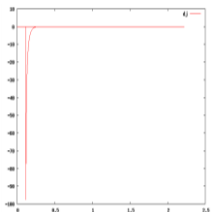
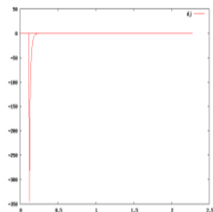
$q = 1.5$ $m = 1$	$M_*/M_d = 25.0$	$M_*/M_d = 50.0$	$M_*/M_d = 100.0$
$r/r_+ = 0.50$		Stable	Stable
$r/r_+ = 0.40$	Stable	Stable	Stable
$r/r_+ = 0.30$	Stable	Stable	Stable
$r/r_+ = 0.20$	Stable	Stable	Stable
$r/r_+ = 0.10$	Stable	Stable	
$r/r_+ = 0.05$			Stable

Fig. A.1.4.c. Perturbed angular momentum for $q = 1.5$, $m = 1$.

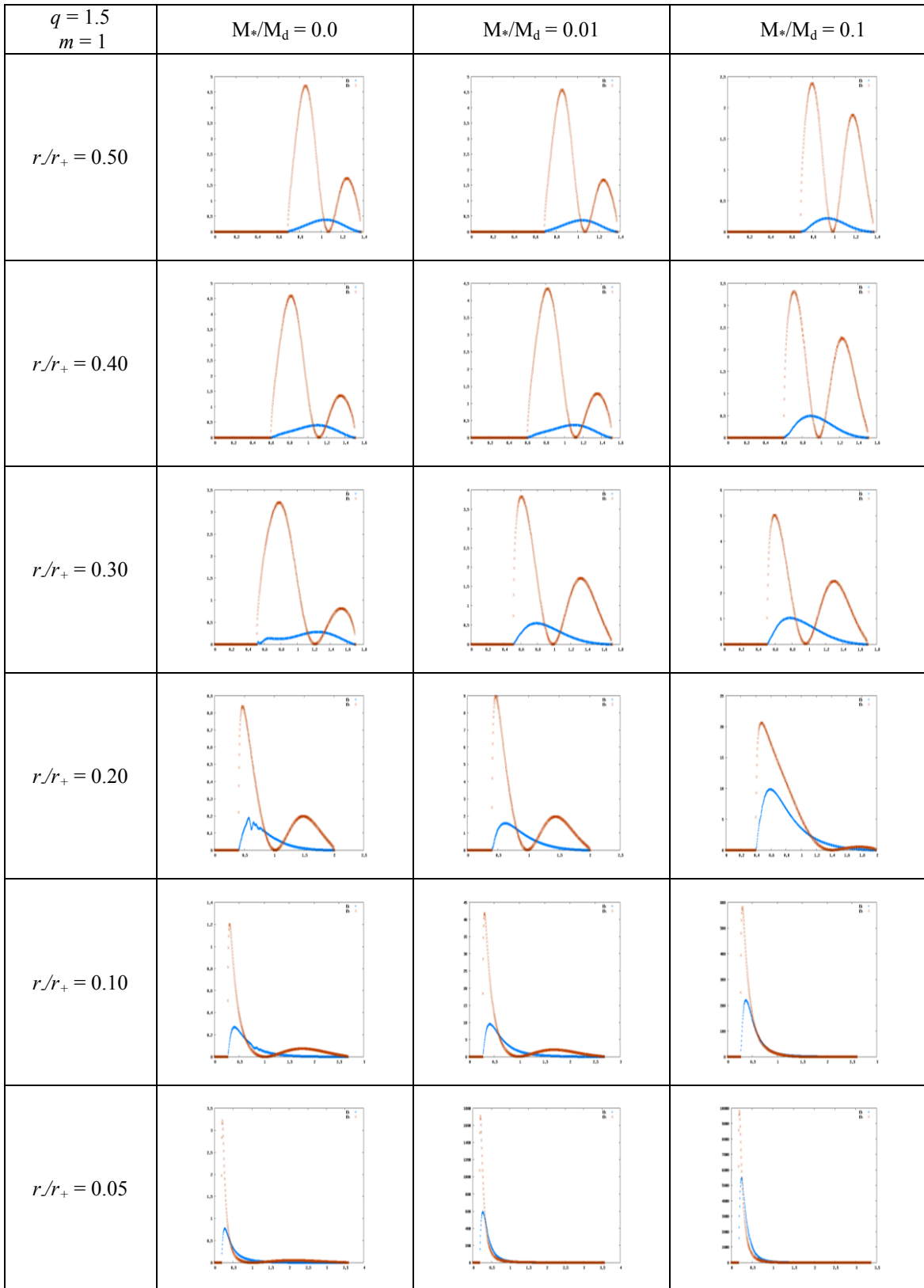


Fig. A.1.5.a. Work integrals for $q = 1.5$, $m = 1$.

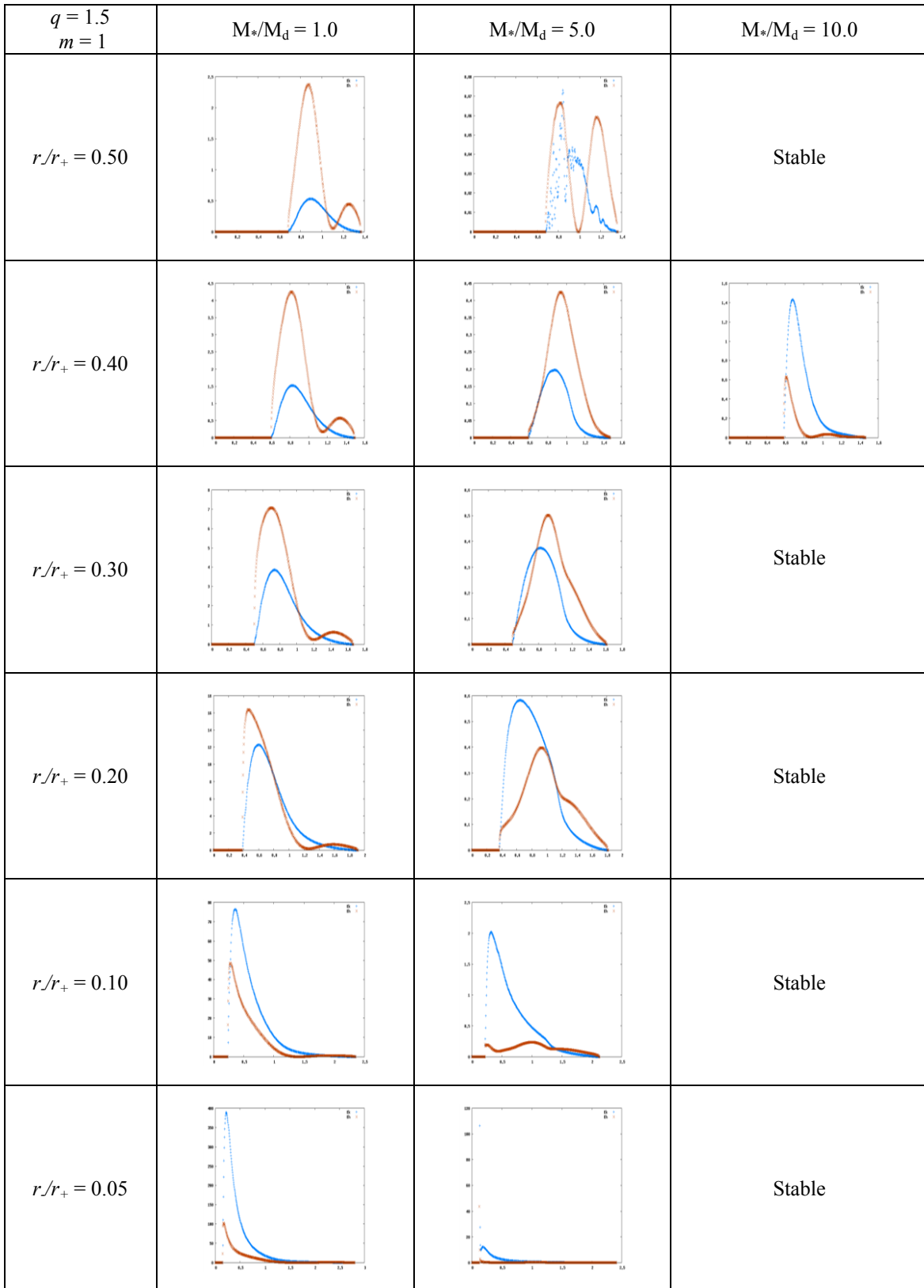


Fig. A.1.5.b. Work integrals for $q = 1.5$, $m = 1$.

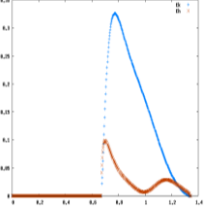
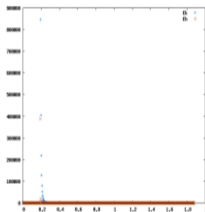
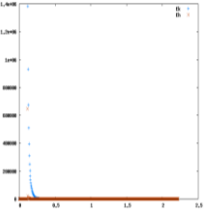
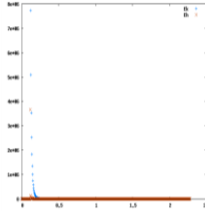
$q = 1.5$ $m = 1$	$M_*/M_d = 25.0$	$M_*/M_d = 50.0$	$M_*/M_d = 100.0$
$r/r_+ = 0.50$		Stable	Stable
$r/r_+ = 0.40$	Stable	Stable	Stable
$r/r_+ = 0.30$	Stable	Stable	Stable
$r/r_+ = 0.20$	Stable	Stable	Stable
$r/r_+ = 0.10$	Stable	Stable	
$r/r_+ = 0.05$			Stable

Fig. A.1.5.c. Work integrals for $q = 1.5$, $m = 1$.

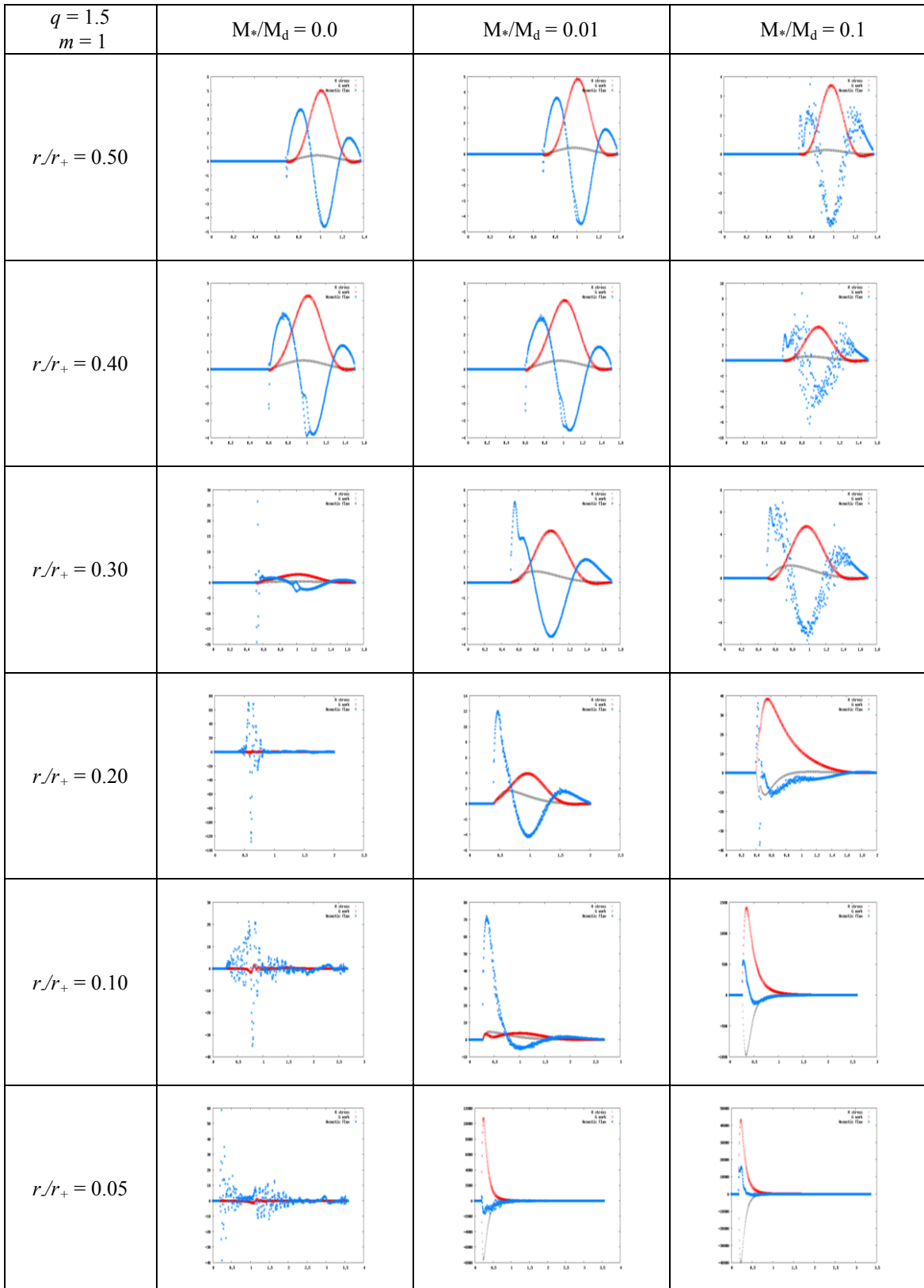


Fig. A.1.6.a. Stresses for $q = 1.5$, $m = 1$.

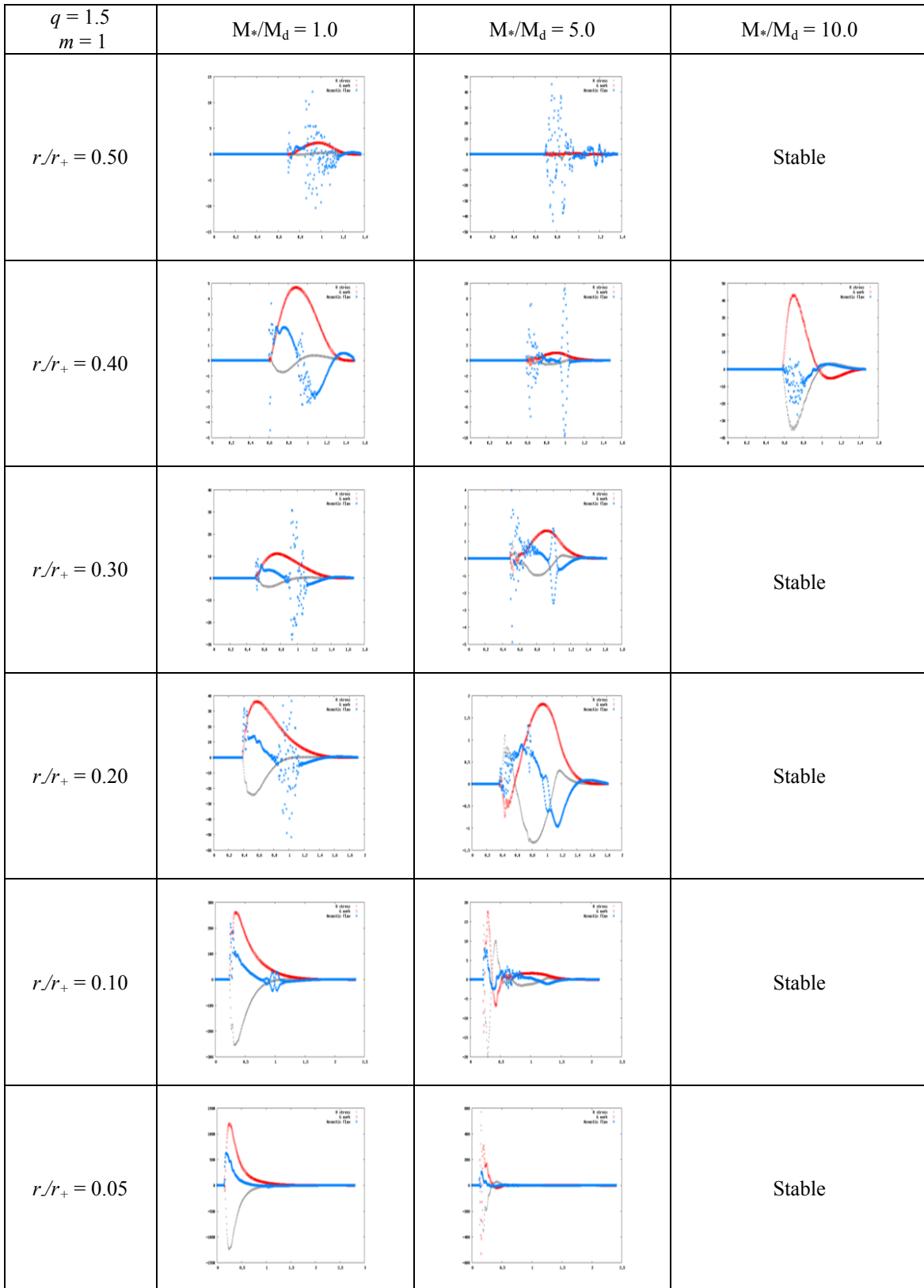


Fig. A.1.6.b. Stresses for $q = 1.5$, $m = 1$.

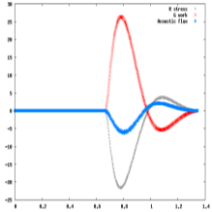
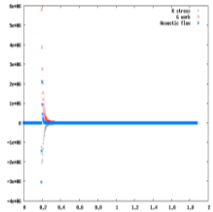
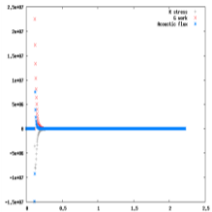
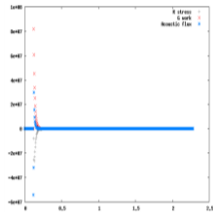
$q = 1.5$ $m = 1$	$M^*/M_d = 25.0$	$M^*/M_d = 50.0$	$M^*/M_d = 100.0$
$r/r_+ = 0.50$		Stable	Stable
$r/r_+ = 0.40$	Stable	Stable	Stable
$r/r_+ = 0.30$	Stable	Stable	Stable
$r/r_+ = 0.20$	Stable	Stable	Stable
$r/r_+ = 0.10$	Stable	Stable	
$r/r_+ = 0.05$			Stable

Fig. A.1.6.c. Stresses for $q = 1.5$, $m = 1$.

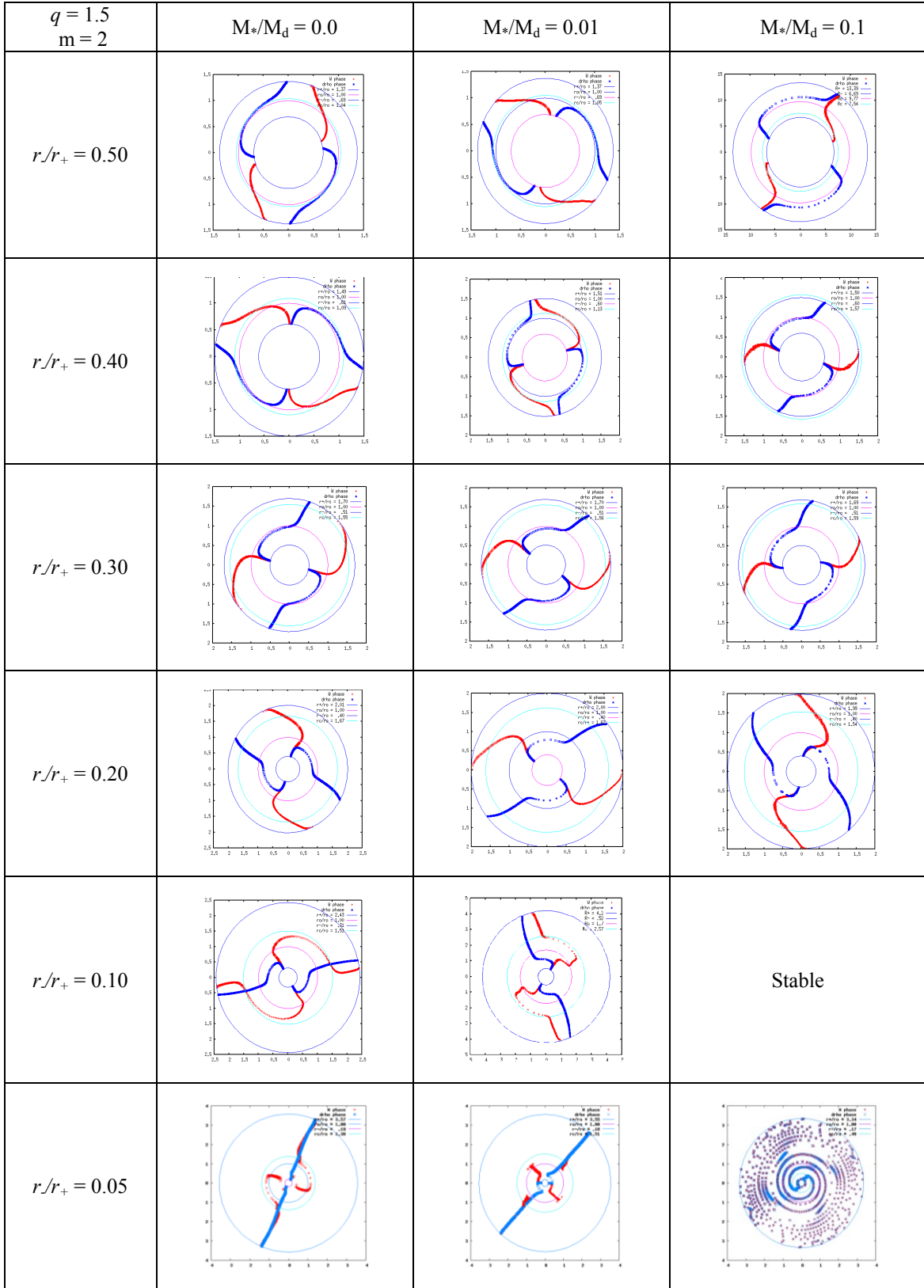


Fig. A.2.1.a. Eigenfunction phases for $q = 1.5$, $m = 2$.

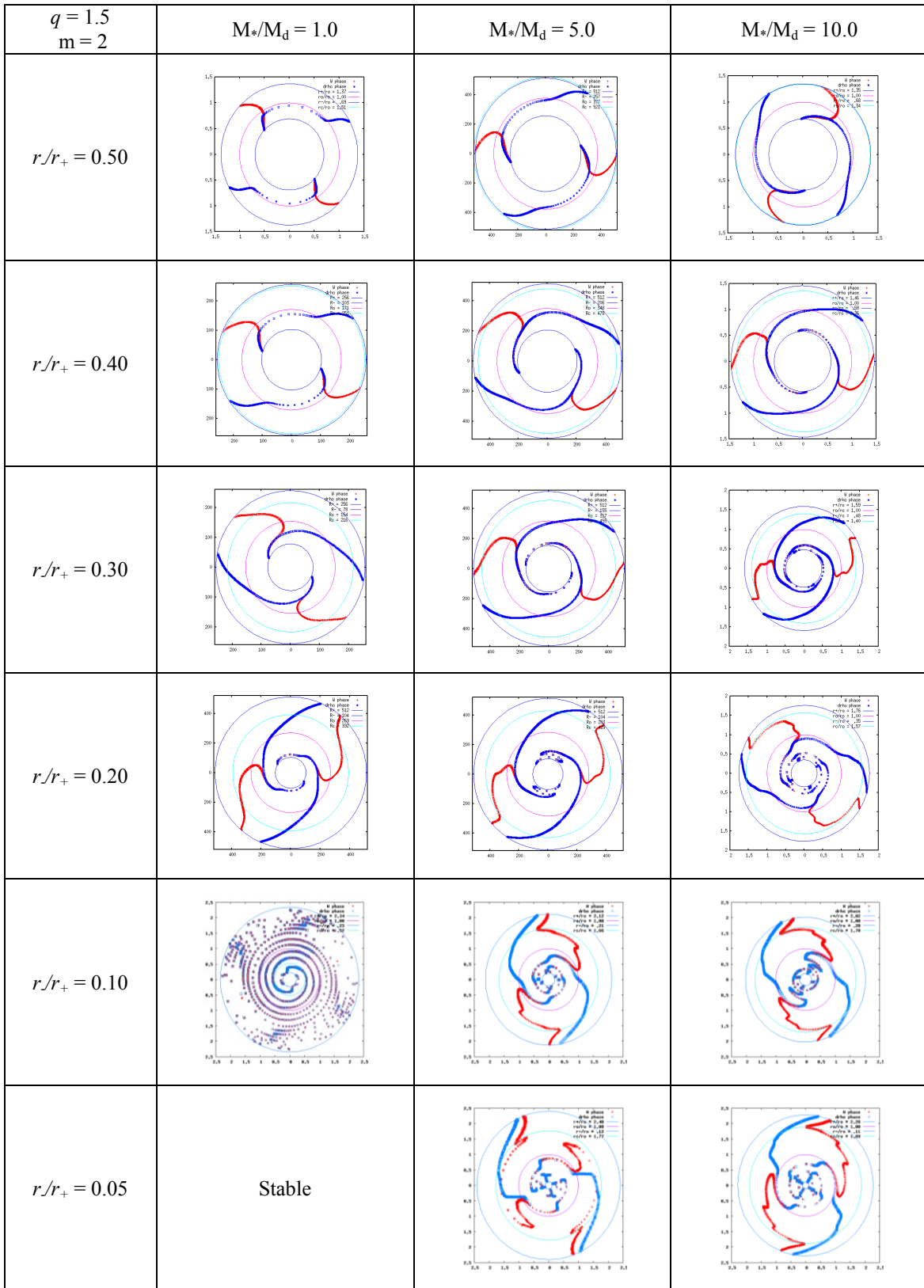


Fig. A.2.1.b. Eigenfunction phases for $q = 1.5$, $m = 2$.

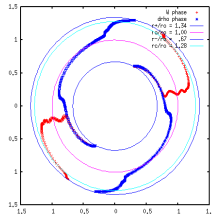
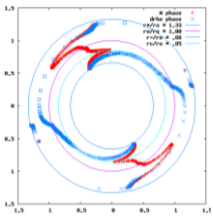
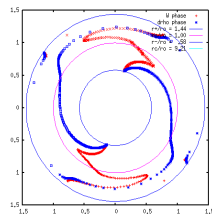
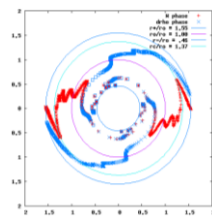
$q = 1.5$ $m = 2$	$M_*/M_d = 25.0$	$M_*/M_d = 50.0$	$M_*/M_d = 100.0$
$r/r_+ = 0.50$			Stable
$r/r_+ = 0.40$		Stable	Stable
$r/r_+ = 0.30$		Stable	Stable
$r/r_+ = 0.20$	Stable	Stable	Stable
$r/r_+ = 0.10$	Stable	Stable	Stable
$r/r_+ = 0.05$	Stable	Stable	Equilibrium model did not converge

Fig. A.2.1.c. Eigenfunction phases for $q = 1.5$, $m = 2$.

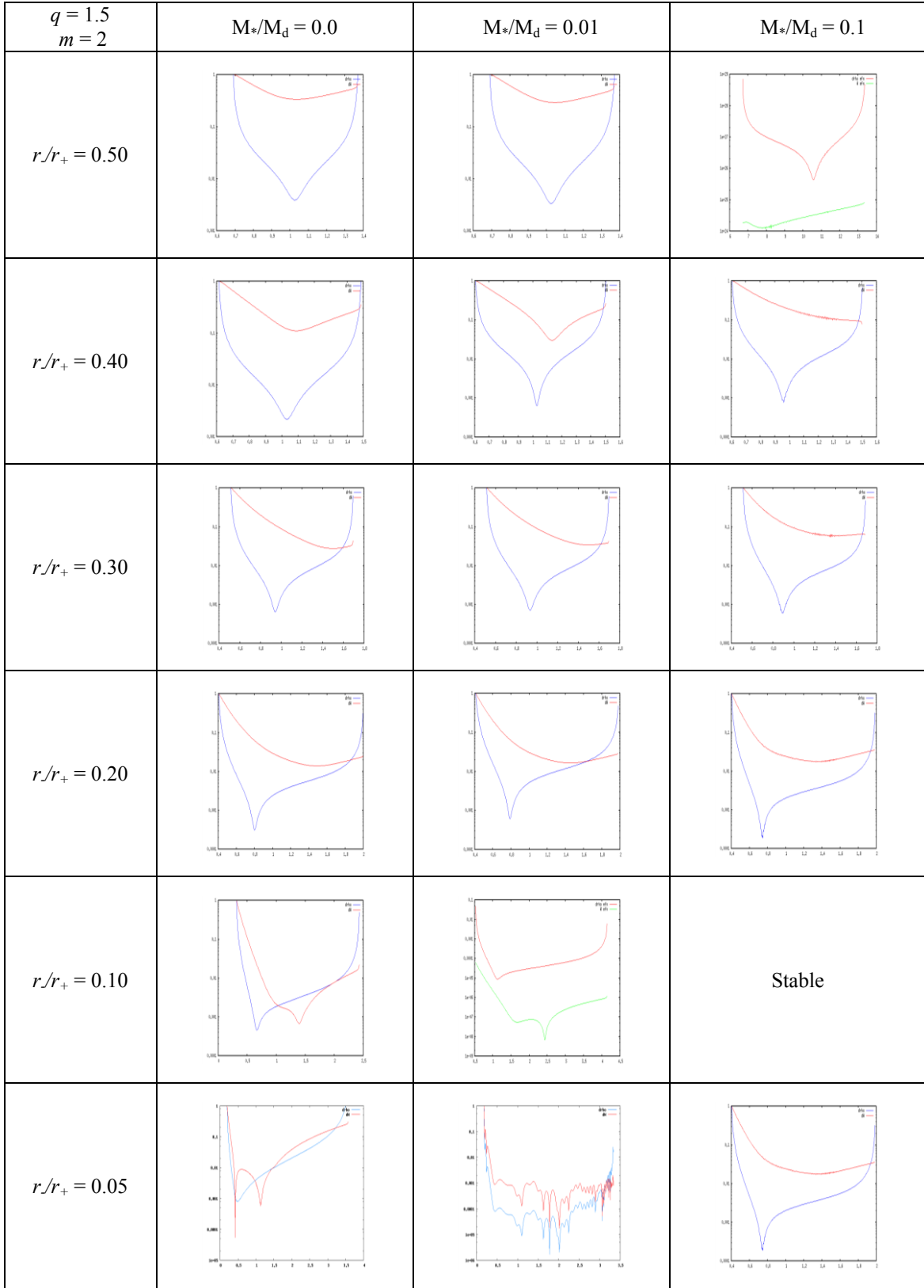


Fig. A.2.2.a. Eigenfunction amplitudes $|\delta\rho|/\rho$ and W for $q = 1.5$, $m = 2$.

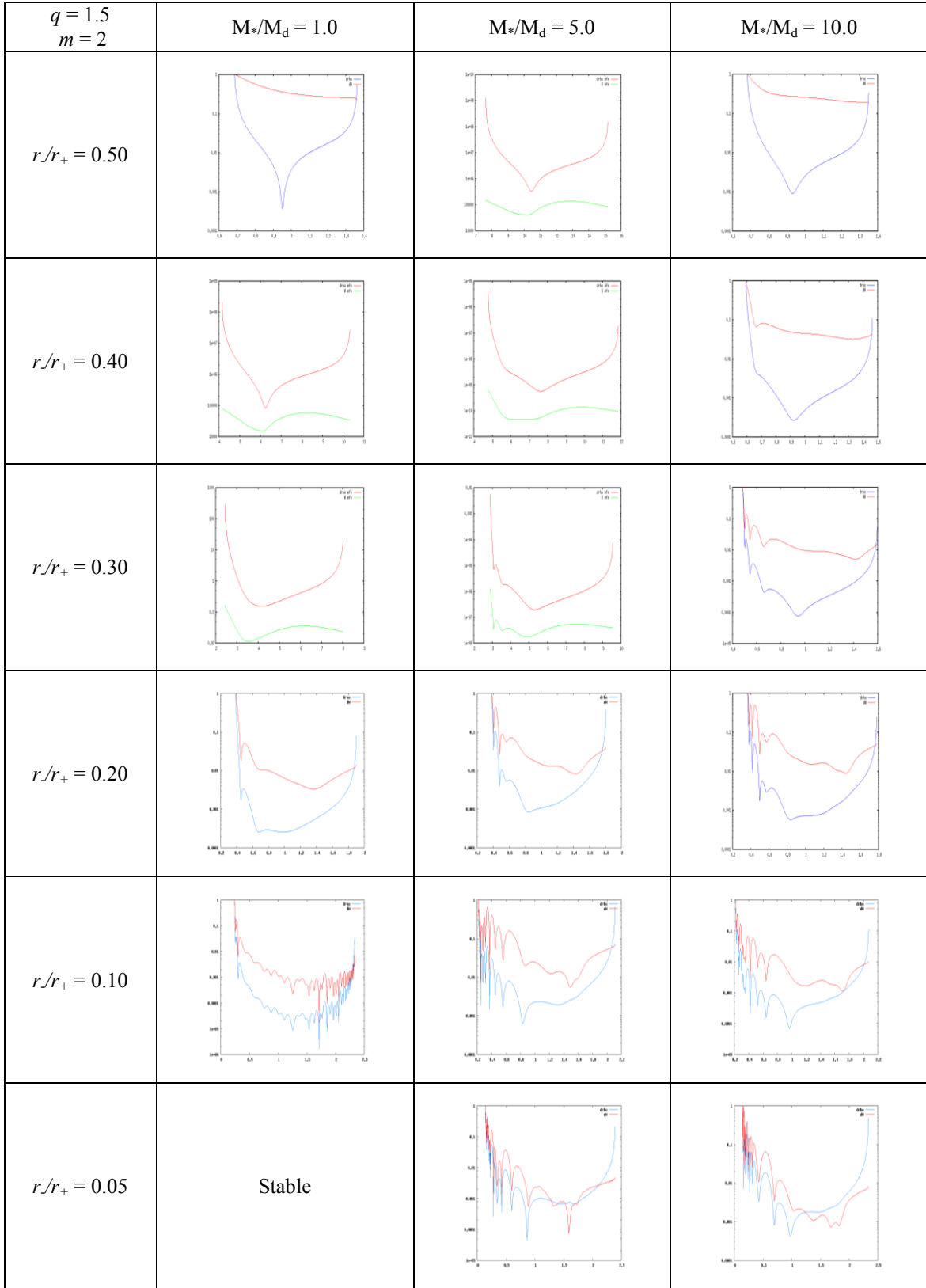


Fig. A.2.2.b. Eigenfunction amplitudes $|\delta\rho|/\rho$ and W for $q = 1.5$, $m = 2$.

$q = 1.5$ $m = 2$	$M_*/M_d = 25.0$	$M_*/M_d = 50.0$	$M_*/M_d = 100.0$
$r/r_+ = 0.50$			Stable
$r/r_+ = 0.40$		Stable	Stable
$r/r_+ = 0.30$		Stable	Stable
$r/r_+ = 0.20$	Stable	Stable	Stable
$r/r_+ = 0.10$	Stable	Stable	Stable
$r/r_+ = 0.05$	Stable	Stable	Equilibrium model did not converge

Fig. A.2.2.c. Eigenfunction amplitudes $|\delta\rho|/\rho$ and W for $q = 1.5$, $m = 2$.

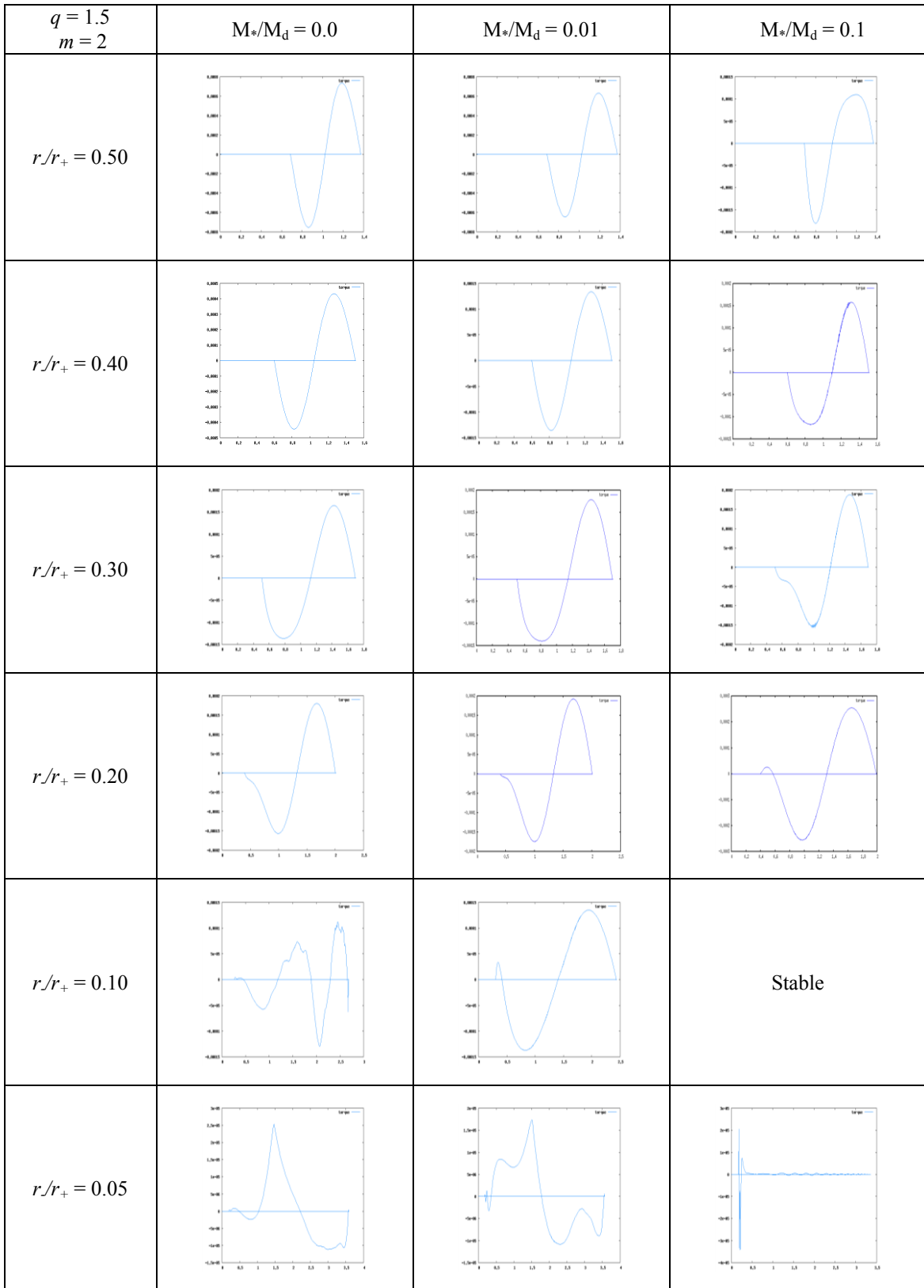


Fig. A.2.3.a. Self-gravitational torque for $q = 1.5$, $m = 2$.

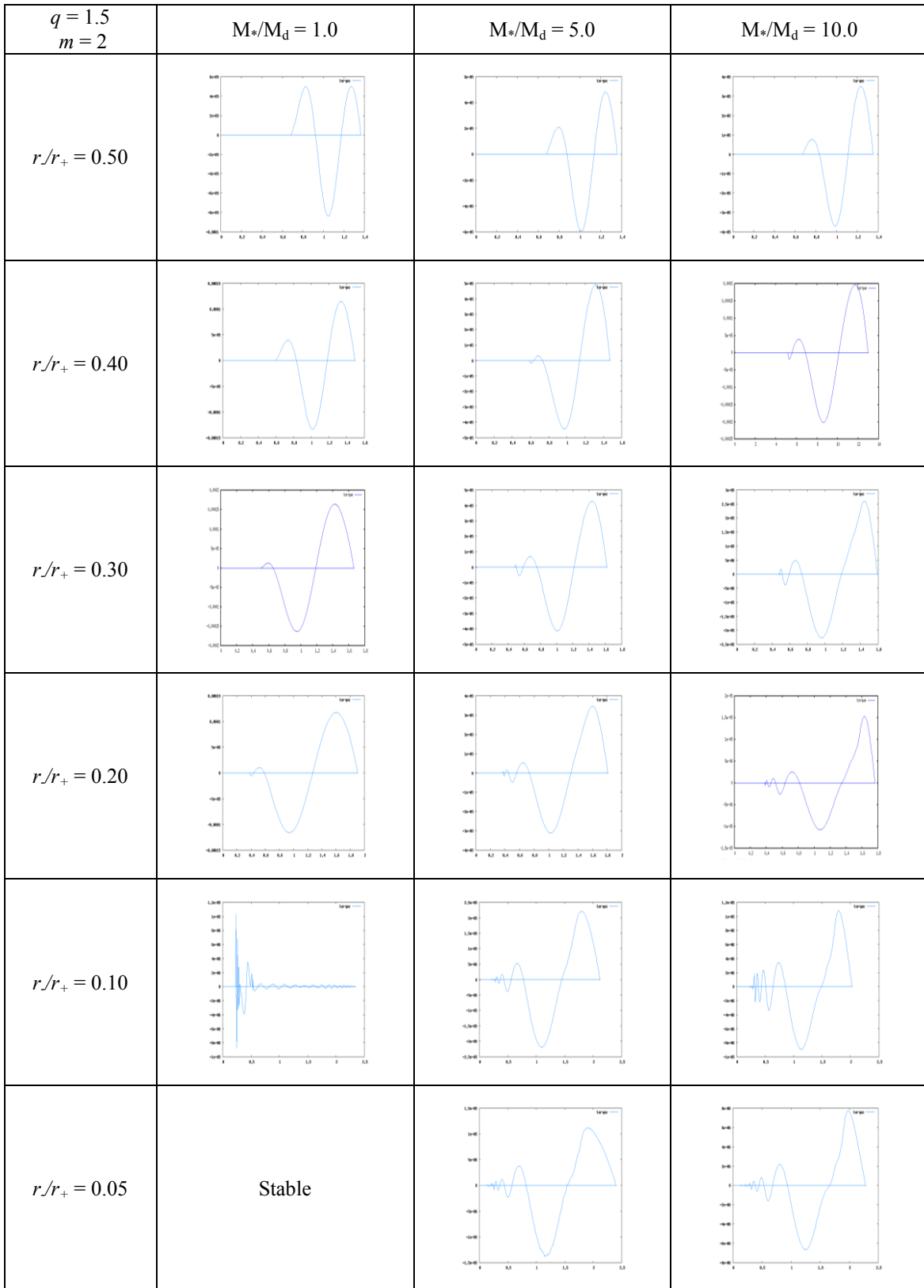


Fig. A.2.3.b. Self-gravitational torque for $q = 1.5$, $m = 2$.

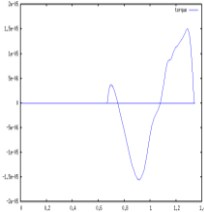
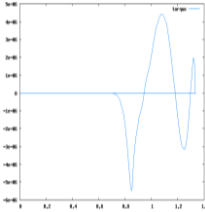
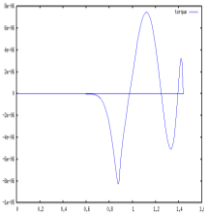
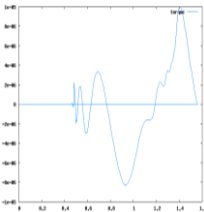
$q = 1.5$ $m = 2$	$M_*/M_d = 25.0$	$M_*/M_d = 50.0$	$M_*/M_d = 100.0$
$r/r_+ = 0.50$			Stable
$r/r_+ = 0.40$		Stable	Stable
$r/r_+ = 0.30$		Stable	Stable
$r/r_+ = 0.20$	Stable	Stable	Stable
$r/r_+ = 0.10$	Stable	Stable	Stable
$r/r_+ = 0.05$	Stable	Stable	Equilibrium model did not converge

Fig. A.2.3.c. Self-gravitational torque for $q = 1.5$, $m = 2$.

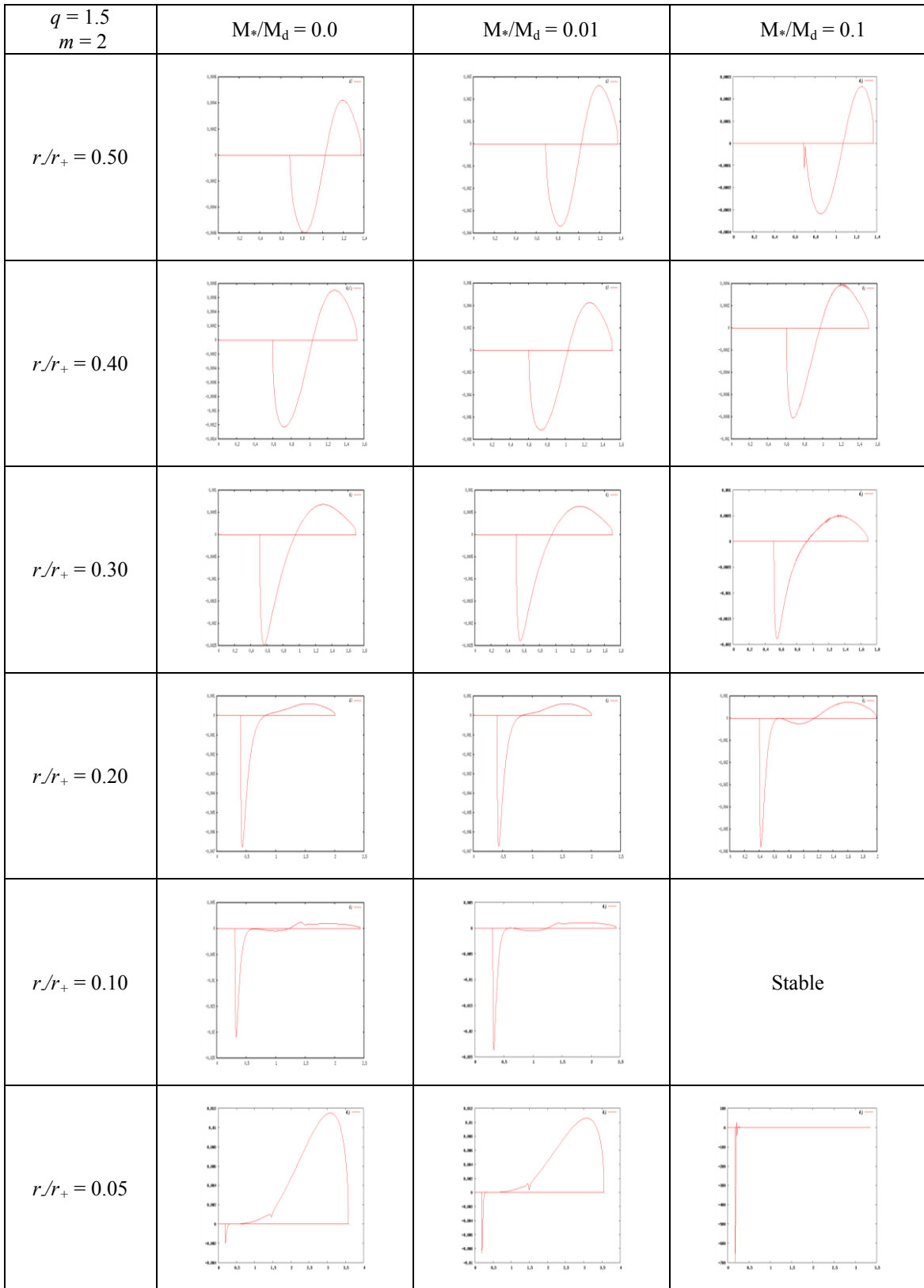


Fig. A.2.4.a. Perturbed angular momentum for $q = 1.5$, $m = 2$.

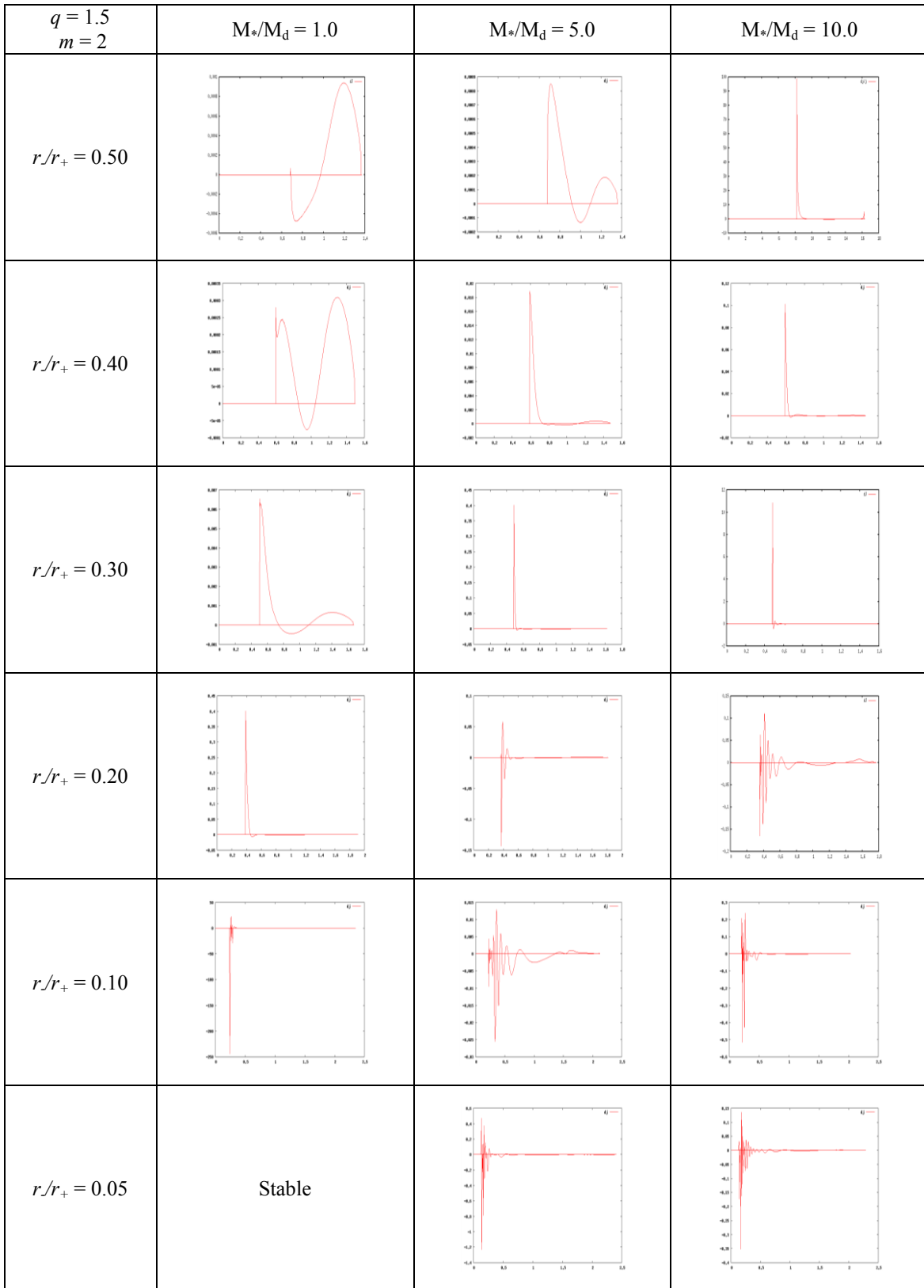


Fig. A.2.4.b. Perturbed angular momentum for $q = 1.5$, $m = 2$

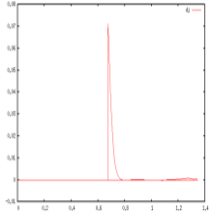
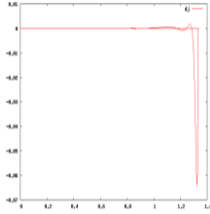
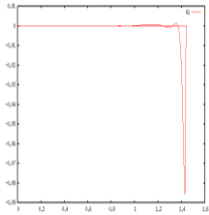
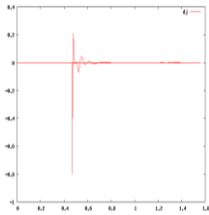
$q = 1.5$ $m = 2$	$M^*/M_d = 25.0$	$M^*/M_d = 50.0$	$M^*/M_d = 100.0$
$r/r_+ = 0.50$			Stable
$r/r_+ = 0.40$		Stable	Stable
$r/r_+ = 0.30$		Stable	Stable
$r/r_+ = 0.20$	Stable	Stable	Stable
$r/r_+ = 0.10$	Stable	Stable	Stable
$r/r_+ = 0.05$	Stable	Stable	Equilibrium model did not converge

Fig. A.2.4.c. Perturbed angular momentum for $q = 1.5$, $m = 2$.

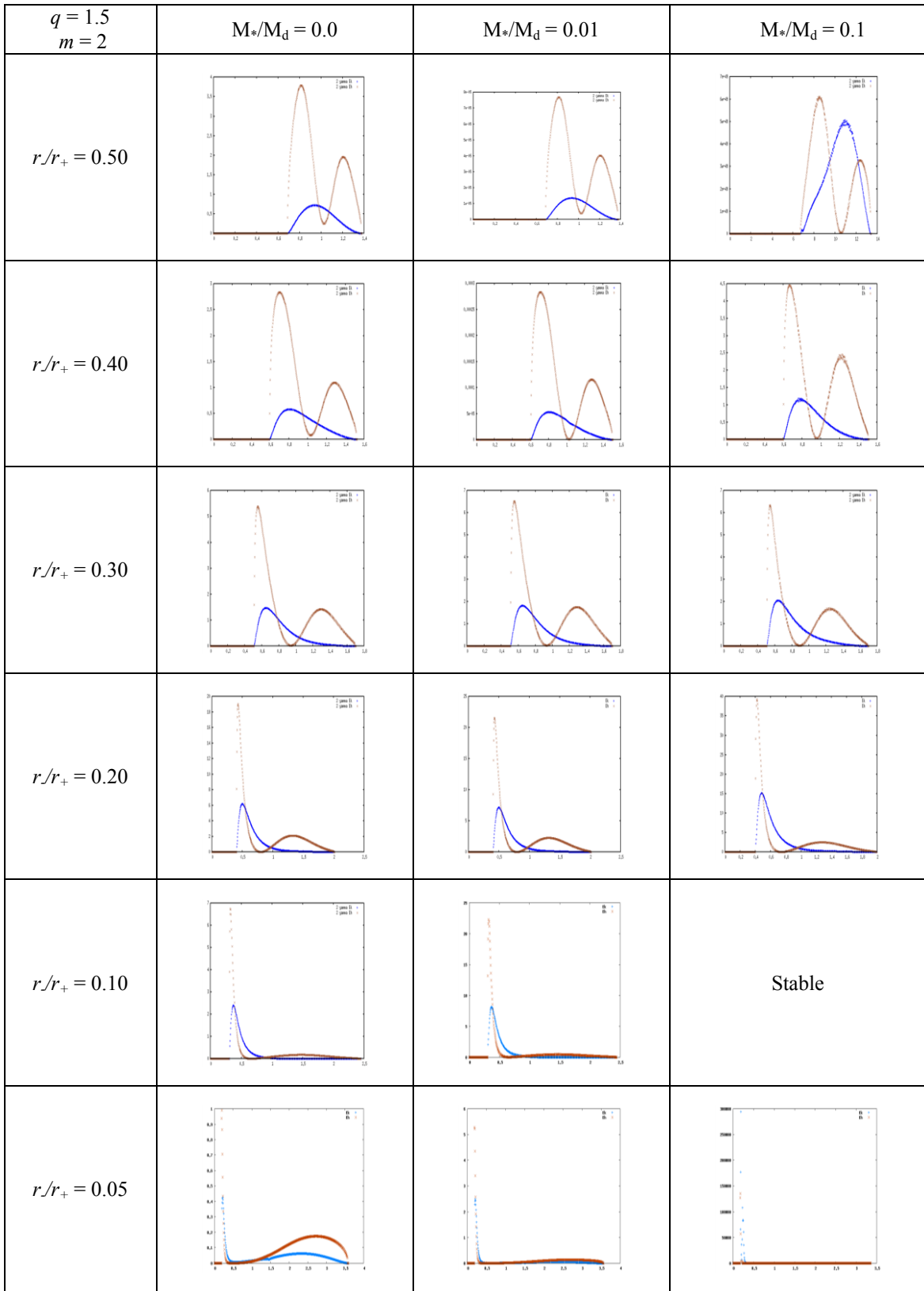


Fig. A.2.5.a. Work integrals for $q = 1.5$, $m = 2$.

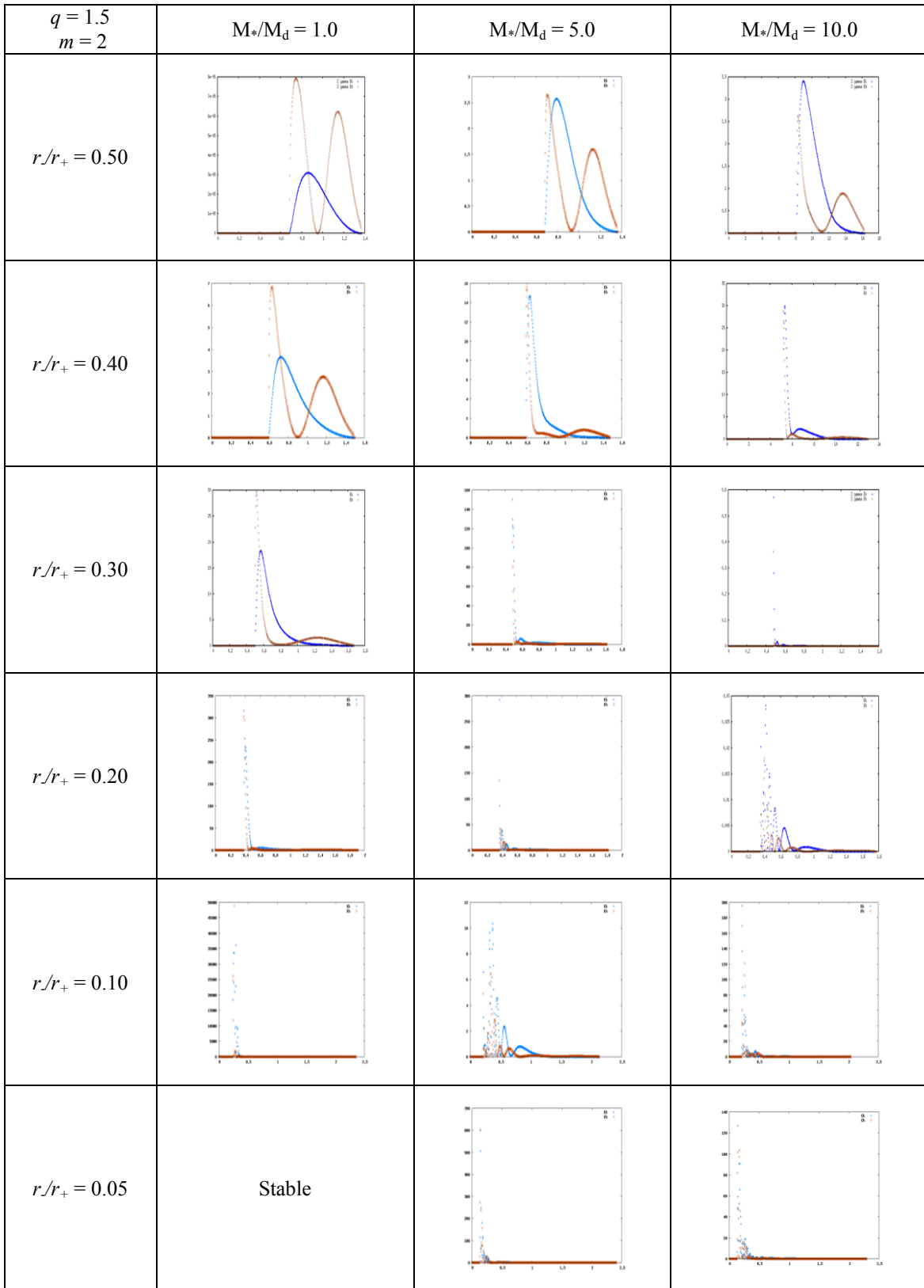


Fig. A.2.5.b. Work integrals for $q = 1.5$, $m = 2$.

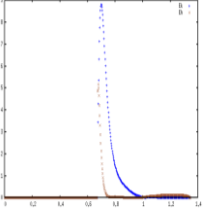
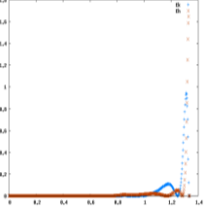
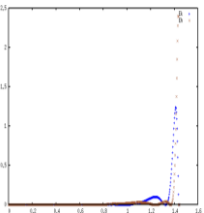
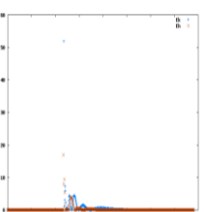
$q = 1.5$ $m = 2$	$M_*/M_d = 25.0$	$M_*/M_d = 50.0$	$M_*/M_d = 100.0$
$r/r_+ = 0.50$			Stable
$r/r_+ = 0.40$		Stable	Stable
$r/r_+ = 0.30$		Stable	Stable
$r/r_+ = 0.20$	Stable	Stable	Stable
$r/r_+ = 0.10$	Stable	Stable	Stable
$r/r_+ = 0.05$	Stable	Stable	Equilibrium model did not converge

Fig. A.2.5.c. Work integrals for $q = 1.5$, $m = 2$.

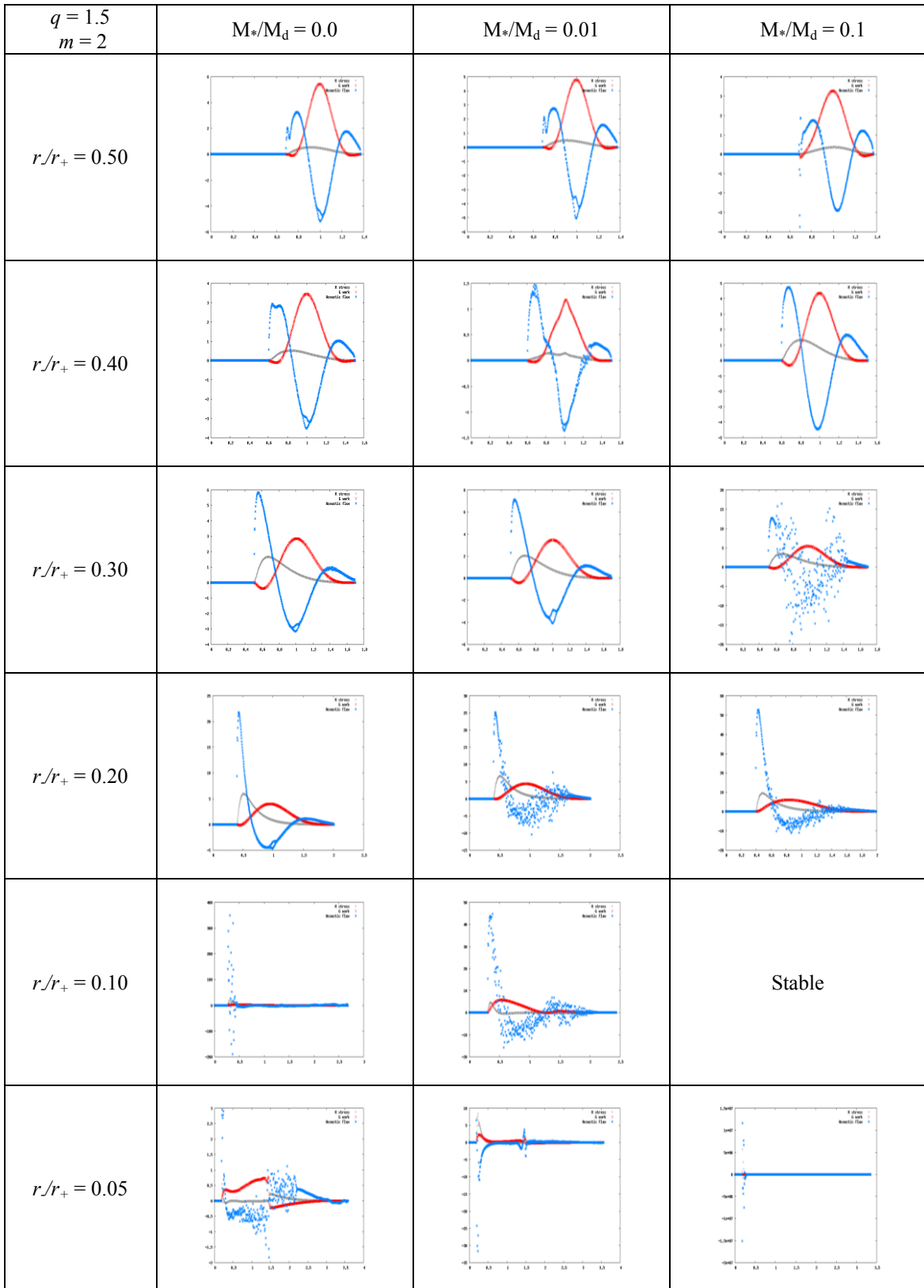


Fig. A.2.6.a. Stresses for $q = 1.5$, $m = 2$.

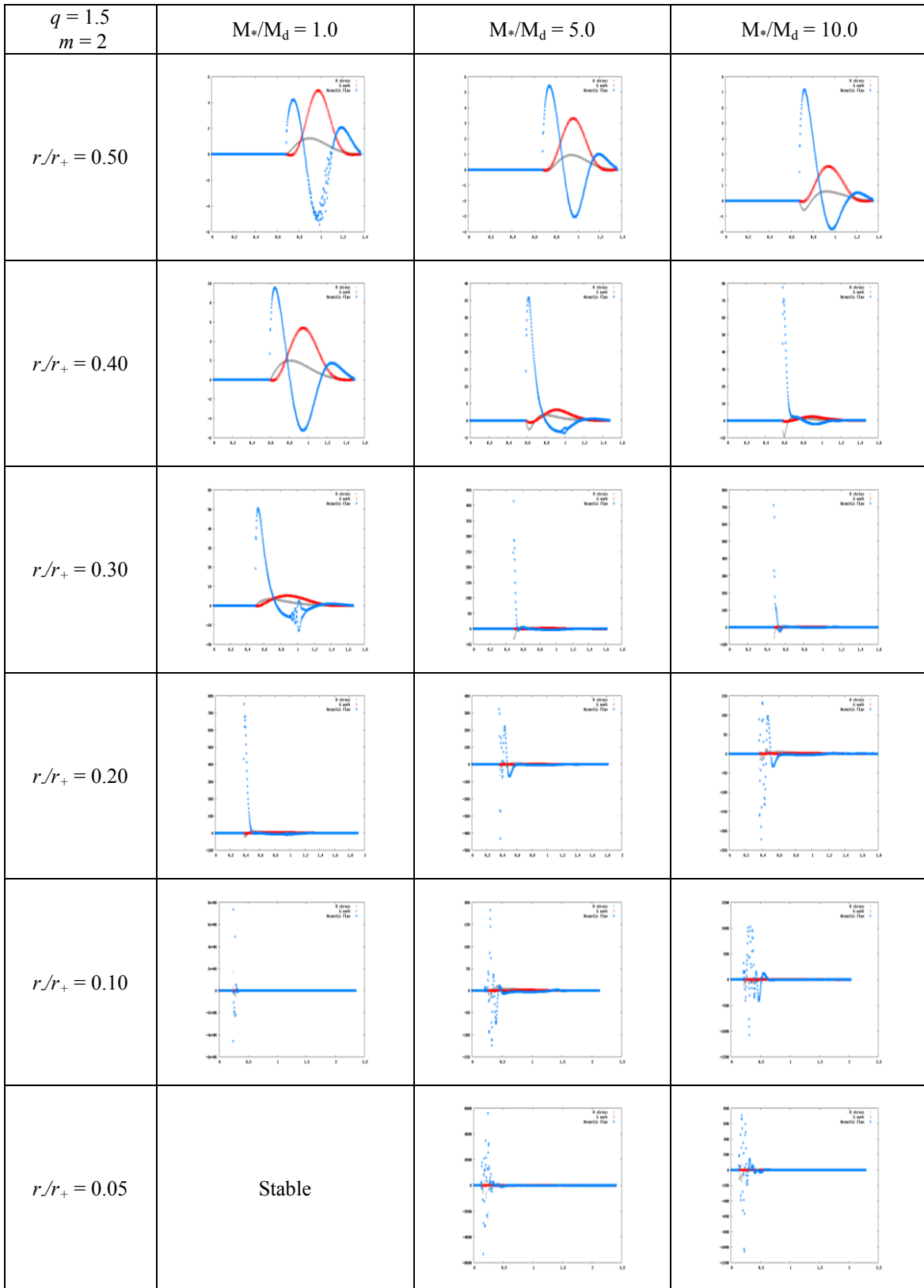


Fig. A.2.6.b. Stresses for $q = 1.5$, $m = 2$.

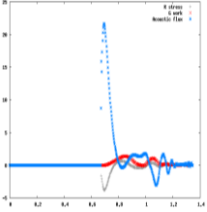
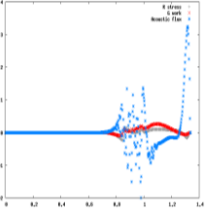
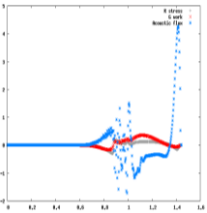
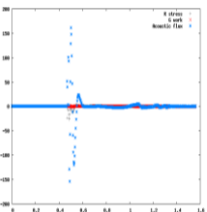
$q = 1.5$ $m = 2$	$M^*/M_d = 25.0$	$M^*/M_d = 50.0$	$M^*/M_d = 100.0$
$r/r_+ = 0.50$			Stable
$r/r_+ = 0.40$		Stable	Stable
$r/r_+ = 0.30$		Stable	Stable
$r/r_+ = 0.20$	Stable	Stable	Stable
$r/r_+ = 0.10$	Stable	Stable	Stable
$r/r_+ = 0.05$	Stable	Stable	Equilibrium model did not converge

Fig. A.2.6.c. Stresses for $q = 1.5$, $m = 2$.

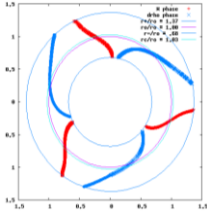
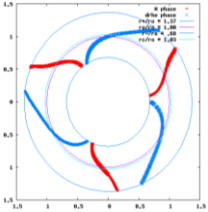
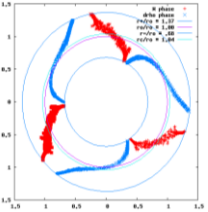
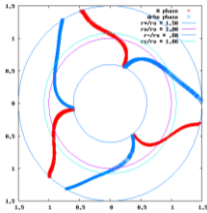
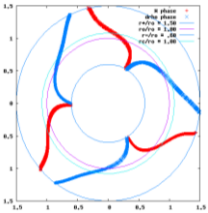
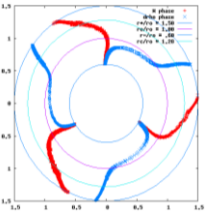
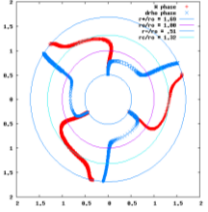
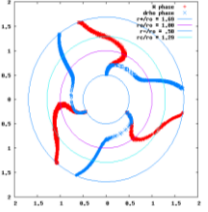
$q = 1.5$ $m = 3$	$M_*/M_d = 0.0$	$M_*/M_d = 0.01$	$M_*/M_d = 0.1$
$r/r_+ = 0.50$			
$r/r_+ = 0.40$			
$r/r_+ = 0.30$	Stable		
$r/r_+ = 0.20$	Stable	Stable	Stable
$r/r_+ = 0.10$	Stable	Stable	Stable
$r/r_+ = 0.05$	Stable	Stable	Stable

Fig. A.3.1.a. Eigenfunction phases for $q = 1.5$, $m = 3$.

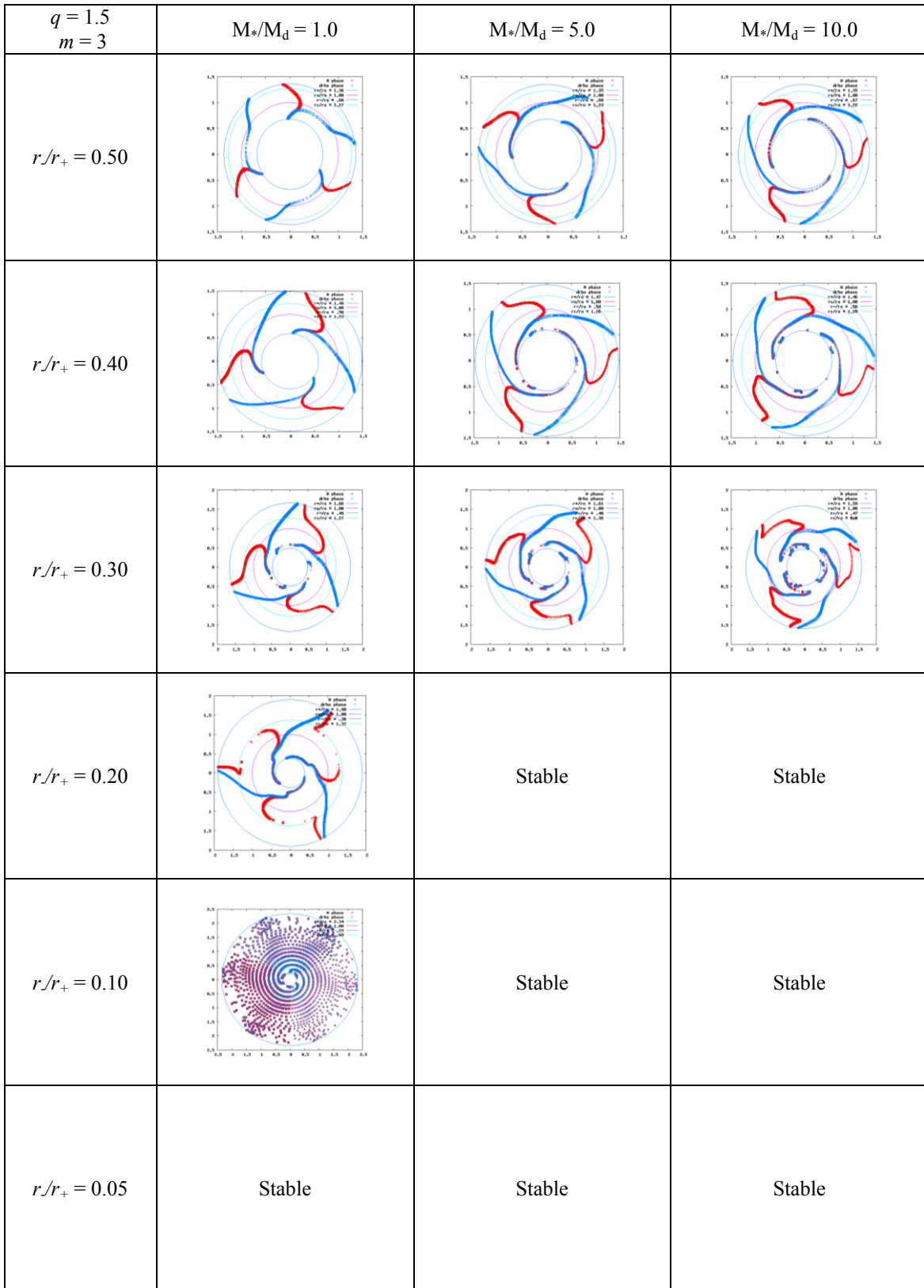


Fig. A.3.1.b. Eigenfunction phases for $q = 1.5$, $m = 3$.

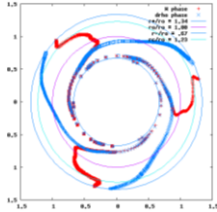
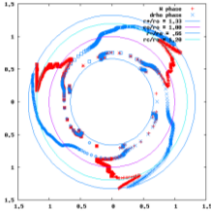
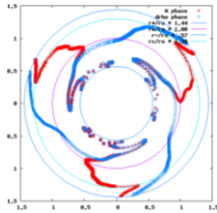
$q = 1.5$ $m = 3$	$M_*/M_d = 25.0$	$M_*/M_d = 50.0$	$M_*/M_d = 100.0$
$r/r_+ = 0.50$			Stable
$r/r_+ = 0.40$		Stable	Stable
$r/r_+ = 0.30$	Stable	Stable	Stable
$r/r_+ = 0.20$	Stable	Stable	Stable
$r/r_+ = 0.10$	Stable	Stable	Stable
$r/r_+ = 0.05$	Stable	Stable	Stable

Fig. A.3.1.c. Eigenfunction phases for $q = 1.5$, $m = 3$.

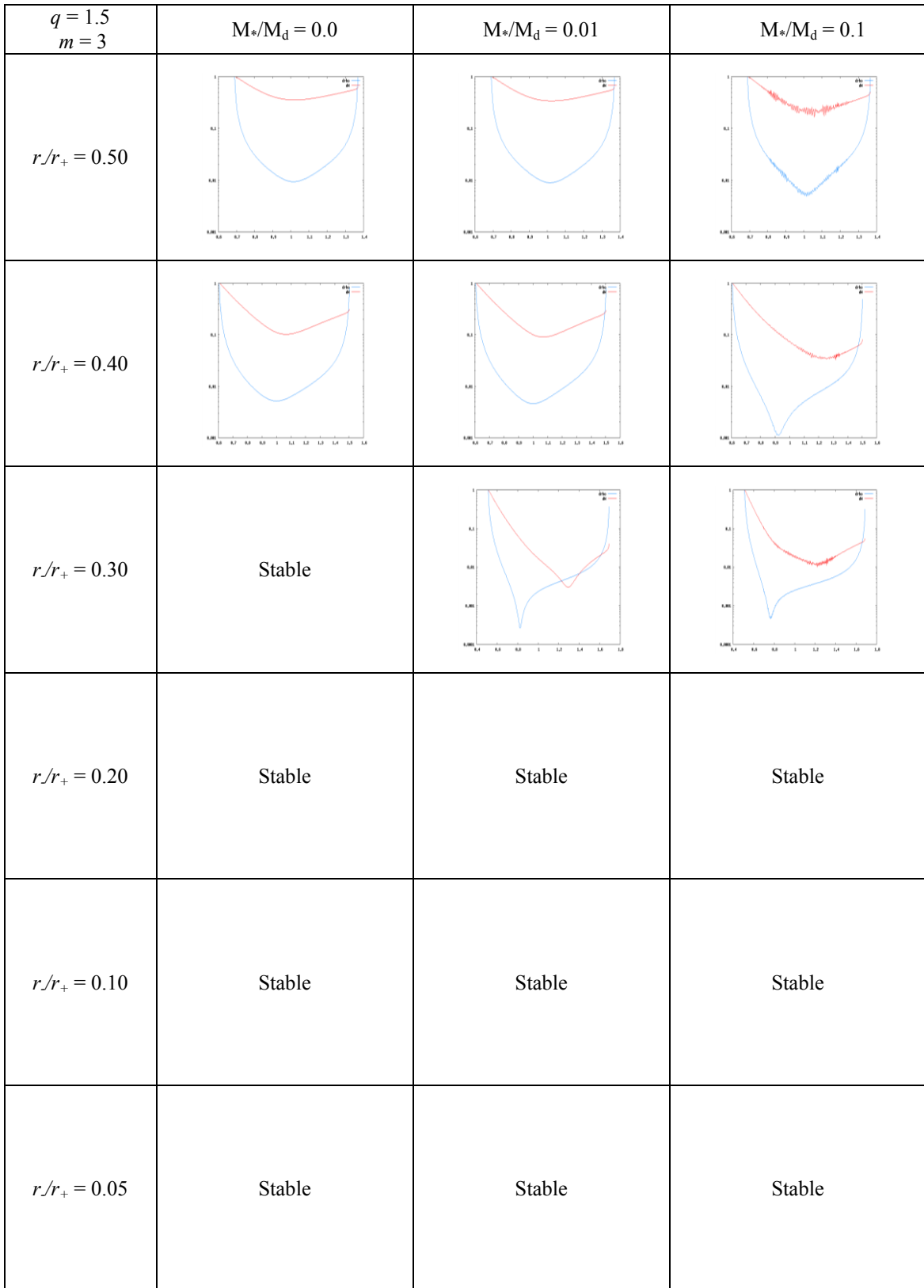


Fig. A.3.2.a. Eigenfunction amplitudes $|\delta\rho|/\rho$ and W for $q = 1.5$, $m = 3$.

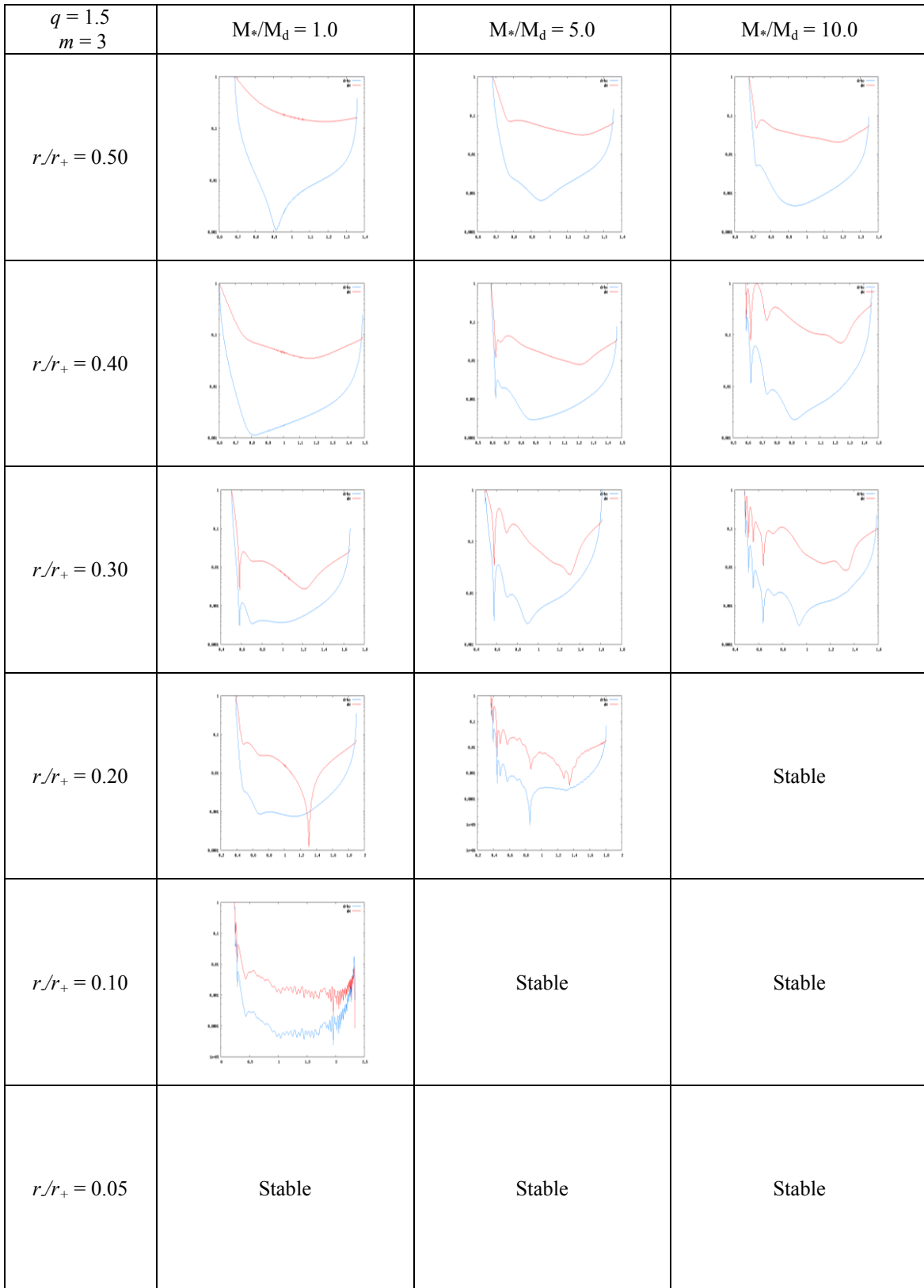


Fig. A.3.2.b. Eigenfunction amplitudes $|\delta\rho|/\rho$ and W for $q = 1.5$, $m = 3$.

$q = 1.5$ $m = 3$	$M_*/M_d = 25.0$	$M_*/M_d = 50.0$	$M_*/M_d = 100.0$
$r/r_+ = 0.50$			Stable
$r/r_+ = 0.40$		Stable	Stable
$r/r_+ = 0.30$	Stable	Stable	Stable
$r/r_+ = 0.20$	Stable	Stable	Stable
$r/r_+ = 0.10$	Stable	Stable	Stable
$r/r_+ = 0.05$	Stable	Stable	Stable

Fig. A.3.2.c. Eigenfunction amplitudes $|\delta\rho|/\rho$ and W for $q = 1.5$, $m = 3$.

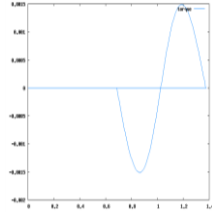
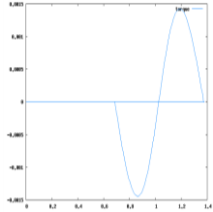
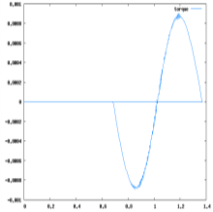
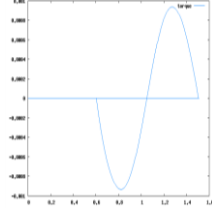
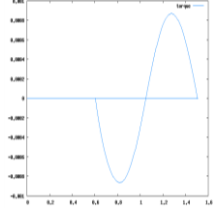
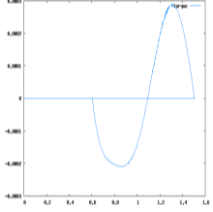
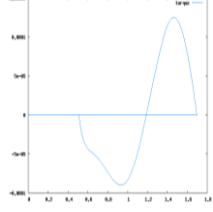
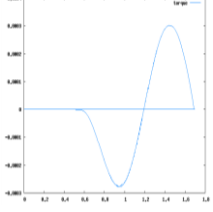
$q = 1.5$ $m = 3$	$M_*/M_d = 0.0$	$M_*/M_d = 0.01$	$M_*/M_d = 0.1$
$r/r_+ = 0.50$			
$r/r_+ = 0.40$			
$r/r_+ = 0.30$	Stable		
$r/r_+ = 0.20$	Stable	Stable	Stable
$r/r_+ = 0.10$	Stable	Stable	Stable
$r/r_+ = 0.05$	Stable	Stable	Stable

Fig. A.3.3.a. Self-gravitational torque for $q = 1.5$, $m = 3$.

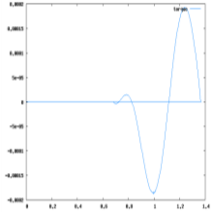
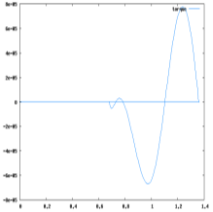
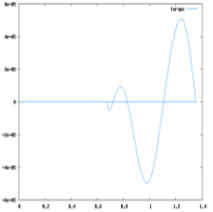
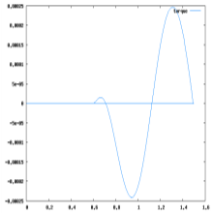
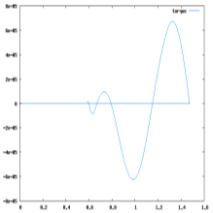
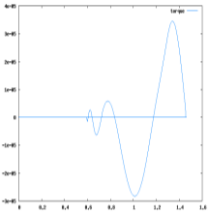
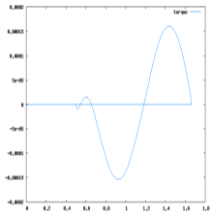
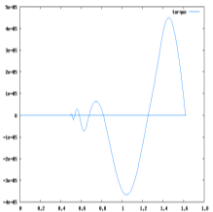
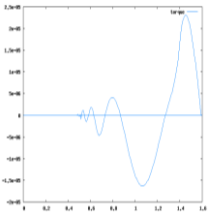
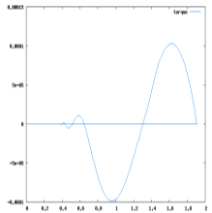
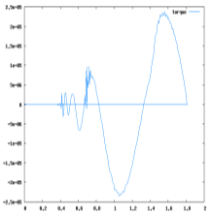
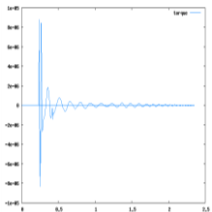
$q = 1.5$ $m = 3$	$M_*/M_d = 1.0$	$M_*/M_d = 5.0$	$M_*/M_d = 10.0$
$r/r_+ = 0.50$			
$r/r_+ = 0.40$			
$r/r_+ = 0.30$			
$r/r_+ = 0.20$			Stable
$r/r_+ = 0.10$		Stable	Stable
$r/r_+ = 0.05$	Stable	Stable	Stable

Fig. A.3.3.b. Self-gravitational torque for $q = 1.5$, $m = 3$.

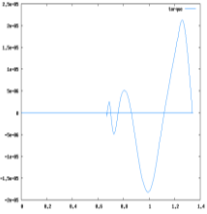
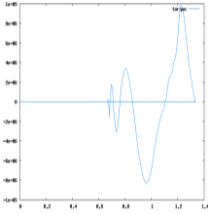
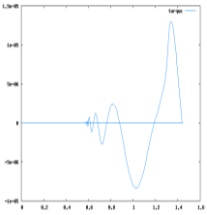
$q = 1.5$ $m = 3$	$M_*/M_d = 25.0$	$M_*/M_d = 50.0$	$M_*/M_d = 100.0$
$r/r_+ = 0.50$			Stable
$r/r_+ = 0.40$		Stable	Stable
$r/r_+ = 0.30$	Stable	Stable	Stable
$r/r_+ = 0.20$	Stable	Stable	Stable
$r/r_+ = 0.10$	Stable	Stable	Stable
$r/r_+ = 0.05$	Stable	Stable	Stable

Fig. A.3.3.c. Self-gravitational torque for $q = 1.5$, $m = 3$.

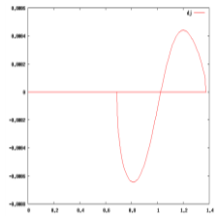
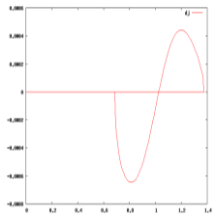
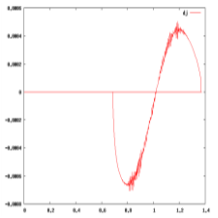
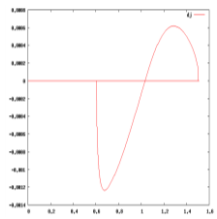
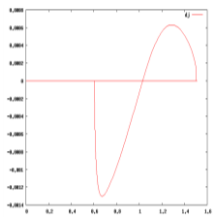
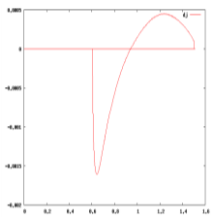
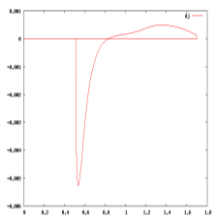
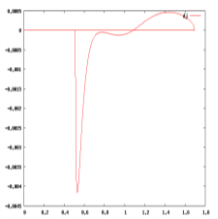
$q = 1.5$ $m = 3$	$M^*/M_d = 0.0$	$M^*/M_d = 0.01$	$M^*/M_d = 0.1$
$r/r_+ = 0.50$			
$r/r_+ = 0.40$			
$r/r_+ = 0.30$	Stable		
$r/r_+ = 0.20$	Stable	Stable	Stable
$r/r_+ = 0.10$	Stable	Stable	Stable
$r/r_+ = 0.05$	Stable	Stable	Stable

Fig. A.3.4.a. Perturbed angular momentum for $q = 1.5$, $m = 3$.

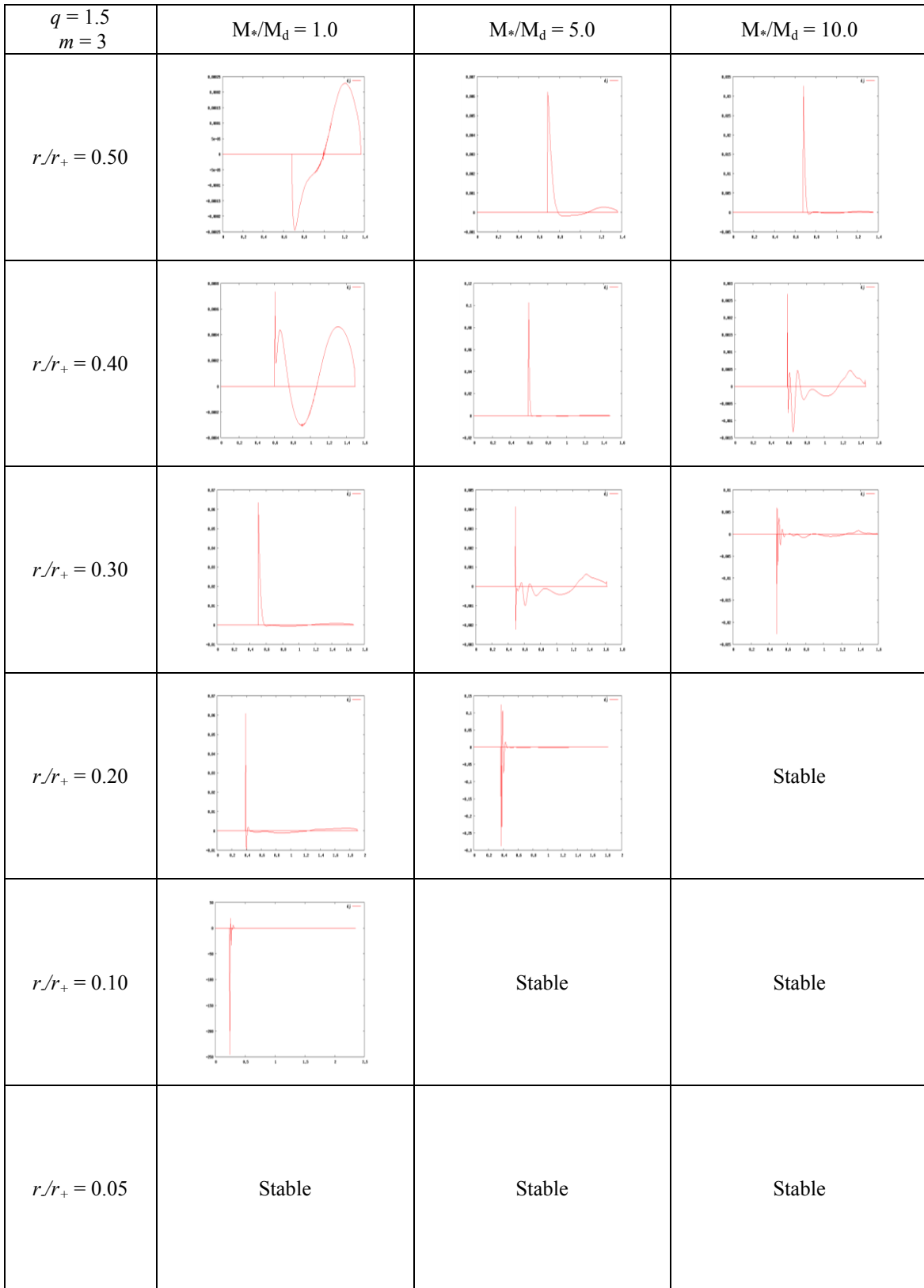


Fig. A.3.4.b. Perturbed angular momentum for $q = 1.5$, $m = 3$.

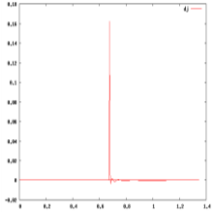
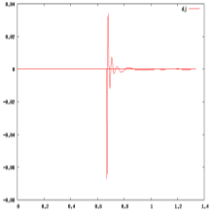
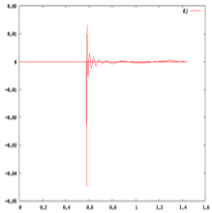
$q = 1.5$ $m = 3$	$M_*/M_d = 25.0$	$M_*/M_d = 50.0$	$M_*/M_d = 100.0$
$r/r_+ = 0.50$			Stable
$r/r_+ = 0.40$		Stable	Stable
$r/r_+ = 0.30$	Stable	Stable	Stable
$r/r_+ = 0.20$	Stable	Stable	Stable
$r/r_+ = 0.10$	Stable	Stable	Stable
$r/r_+ = 0.05$	Stable	Stable	Stable

Fig. A.3.4.c. Perturbed angular momentum for $q = 1.5$, $m = 3$.

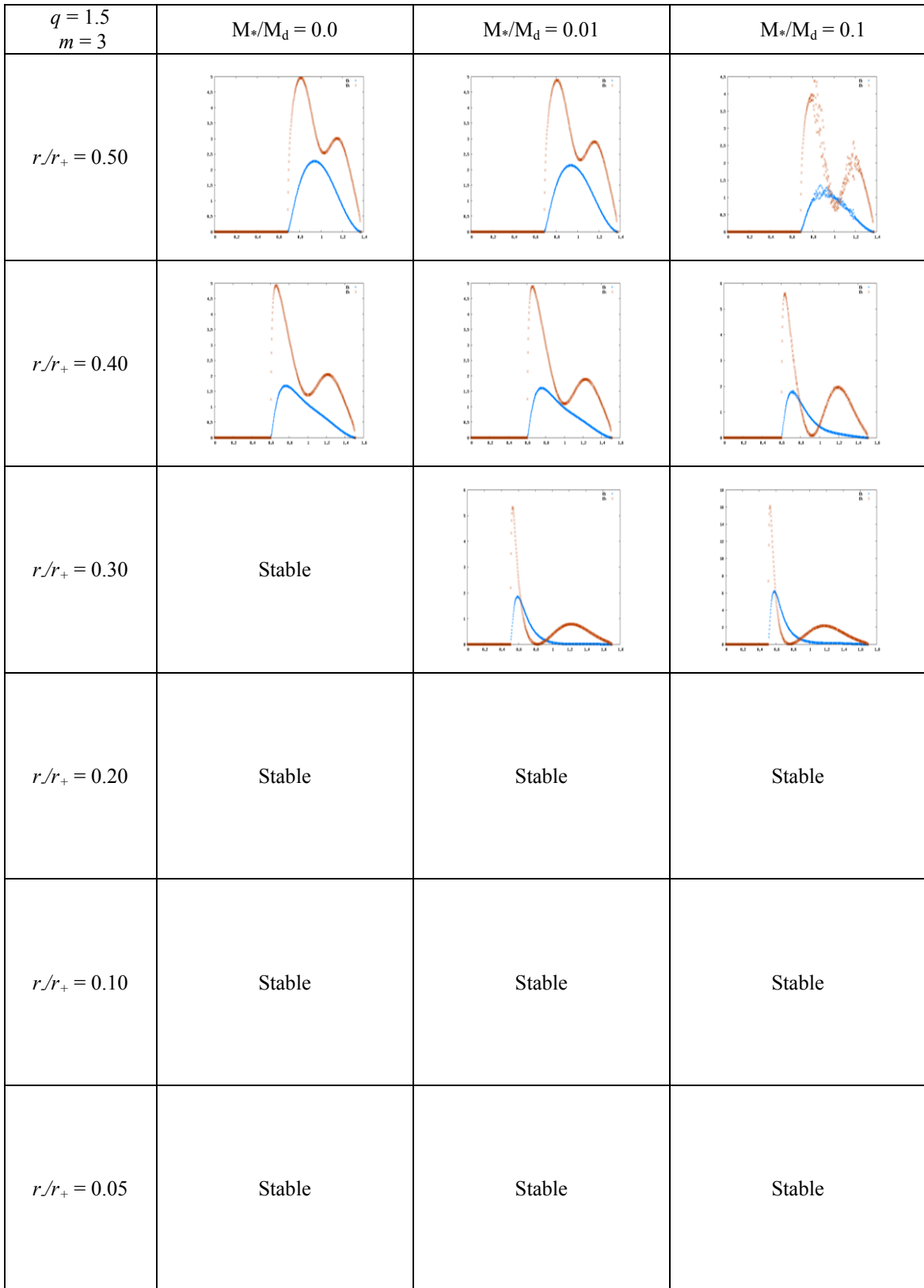


Fig. A.3.5.a. Work integrals for $q = 1.5$, $m = 3$.

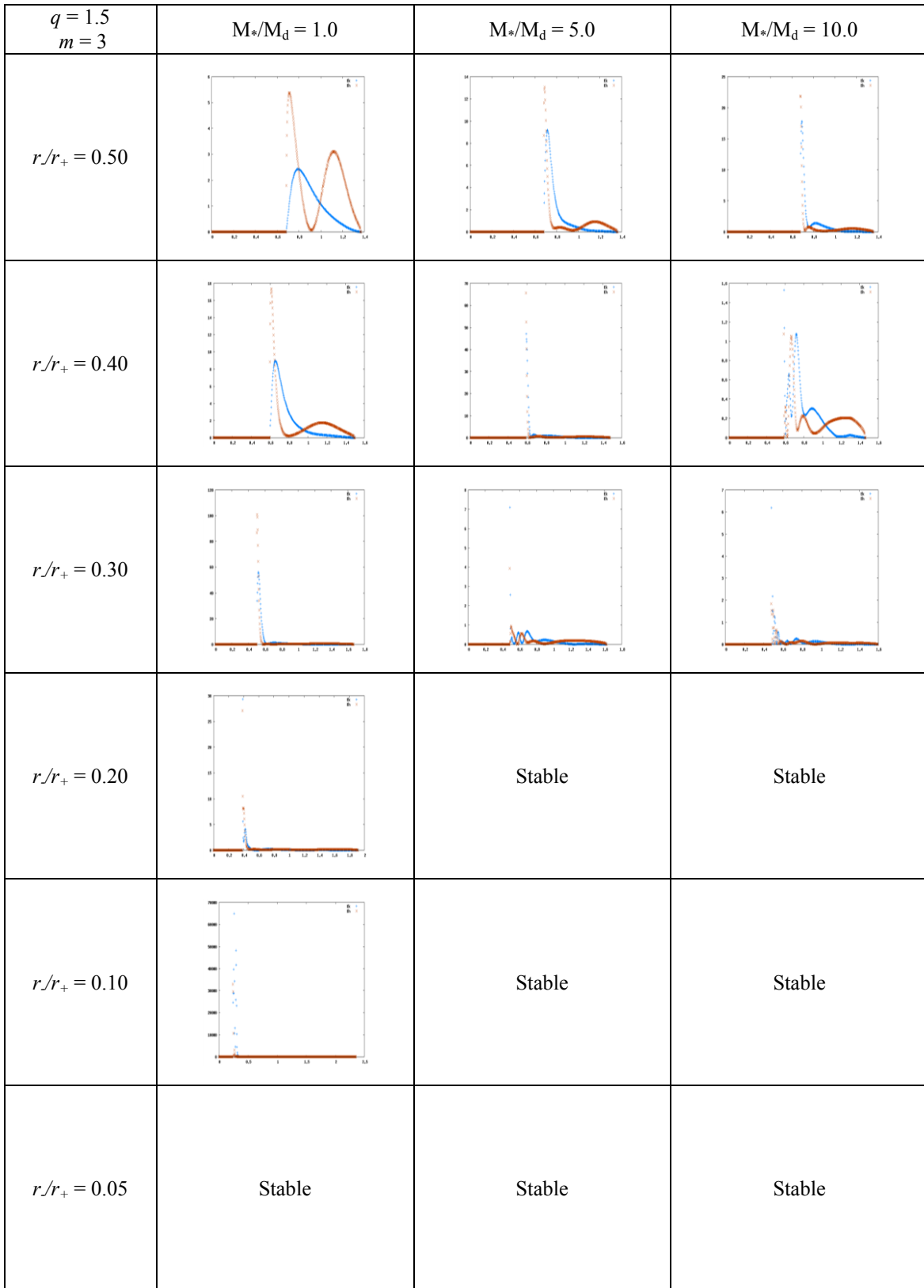


Fig. A.3.5.b. Work integrals for $q = 1.5$, $m = 3$.

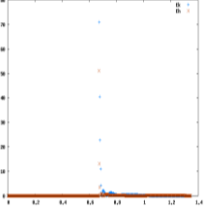
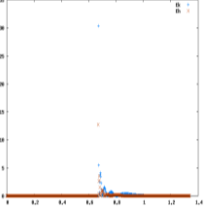
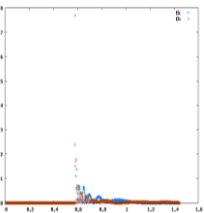
$q = 1.5$ $m = 3$	$M_*/M_d = 25.0$	$M_*/M_d = 50.0$	$M_*/M_d = 100.0$
$r/r_+ = 0.50$			Stable
$r/r_+ = 0.40$		Stable	Stable
$r/r_+ = 0.30$	Stable	Stable	Stable
$r/r_+ = 0.20$	Stable	Stable	Stable
$r/r_+ = 0.10$	Stable	Stable	Stable
$r/r_+ = 0.05$	Stable	Stable	Stable

Fig. A.3.5.c. Work integrals for $q = 1.5$, $m = 3$.

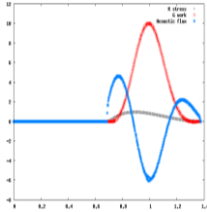
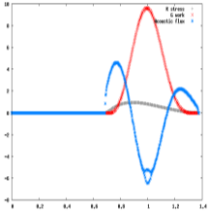
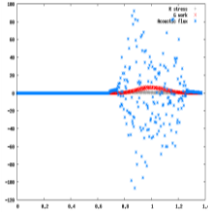
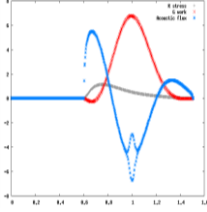
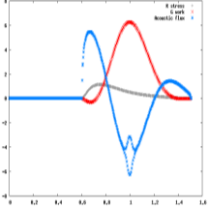
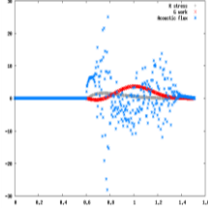
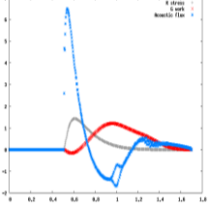
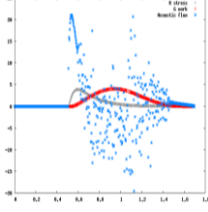
$q = 1.5$ $m = 3$	$M_*/M_d = 0.0$	$M_*/M_d = 0.01$	$M_*/M_d = 0.1$
$r/r_+ = 0.50$			
$r/r_+ = 0.40$			
$r/r_+ = 0.30$	Stable		
$r/r_+ = 0.20$	Stable	Stable	Stable
$r/r_+ = 0.10$	Stable	Stable	Stable
$r/r_+ = 0.05$	Stable	Stable	Stable

Fig. A.3.6.a. Stresses for $q = 1.5$, $m = 3$.

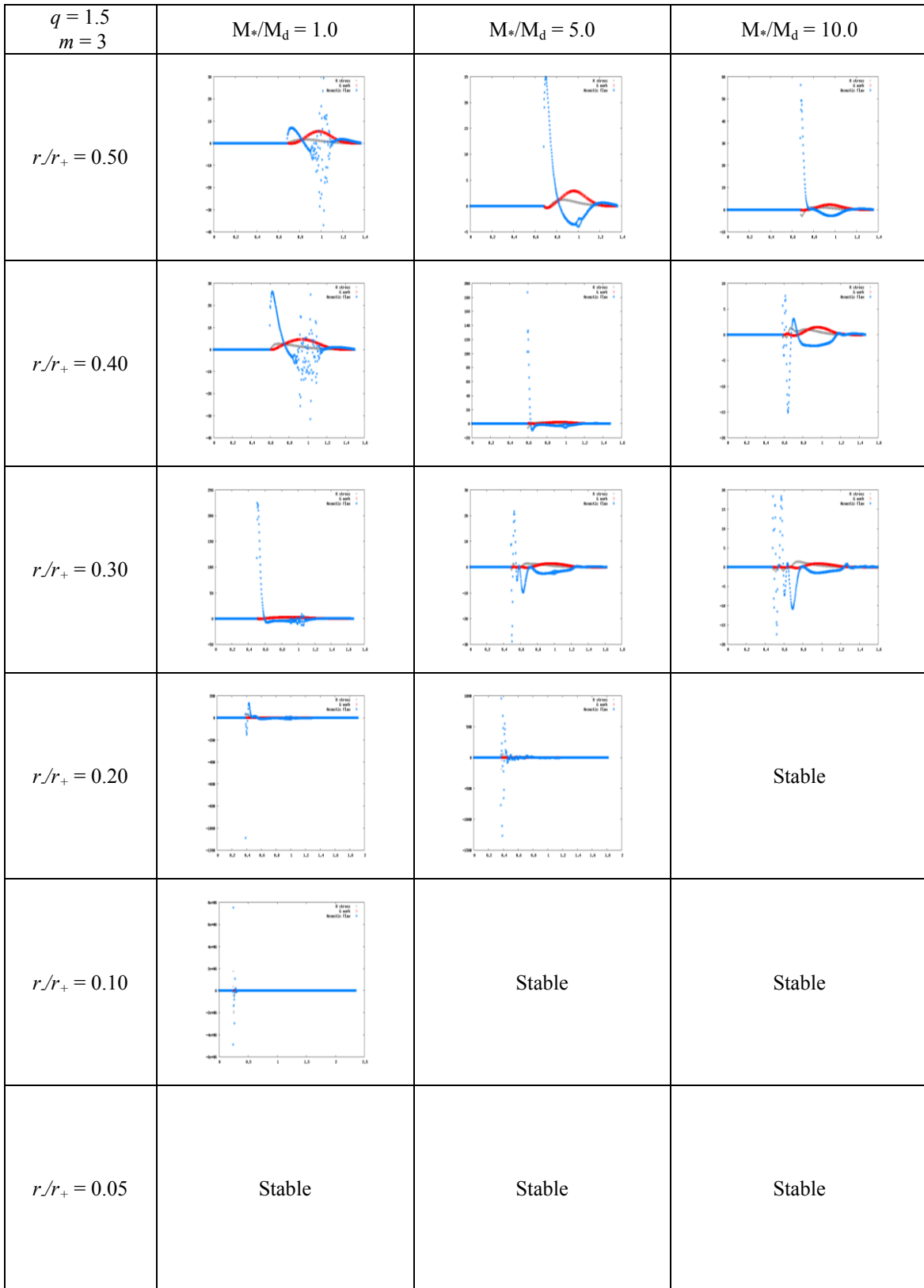


Fig. A.3.6.b. Stresses for $q = 1.5$, $m = 3$.

$q = 1.5$ $m = 3$	$M_*/M_d = 25.0$	$M_*/M_d = 50.0$	$M_*/M_d = 100.0$
$r/r_+ = 0.50$			Stable
$r/r_+ = 0.40$		Stable	Stable
$r/r_+ = 0.30$	Stable	Stable	Stable
$r/r_+ = 0.20$	Stable	Stable	Stable
$r/r_+ = 0.10$	Stable	Stable	Stable
$r/r_+ = 0.05$	Stable	Stable	Stable

Fig. A.3.6.c. Stresses for $q = 1.5$, $m = 3$.

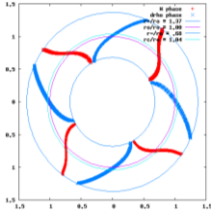
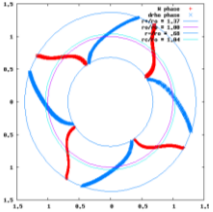
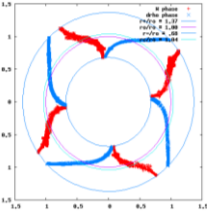
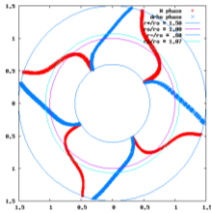
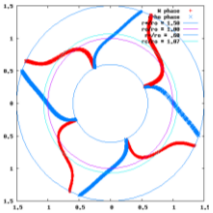
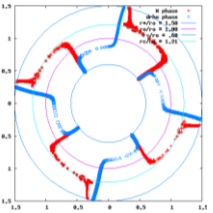
$q = 1.5$ $m = 4$	$M_*/M_d = 0.0$	$M_*/M_d = 0.01$	$M_*/M_d = 0.1$
$r/r_+ = 0.50$			
$r/r_+ = 0.40$			
$r/r_+ = 0.30$	Stable	Stable	Stable
$r/r_+ = 0.20$	Stable	Stable	Stable
$r/r_+ = 0.10$	Stable	Stable	Stable
$r/r_+ = 0.05$			

Fig. A.4.1.a. Eigenfunction phases for $q = 1.5$, $m = 4$.

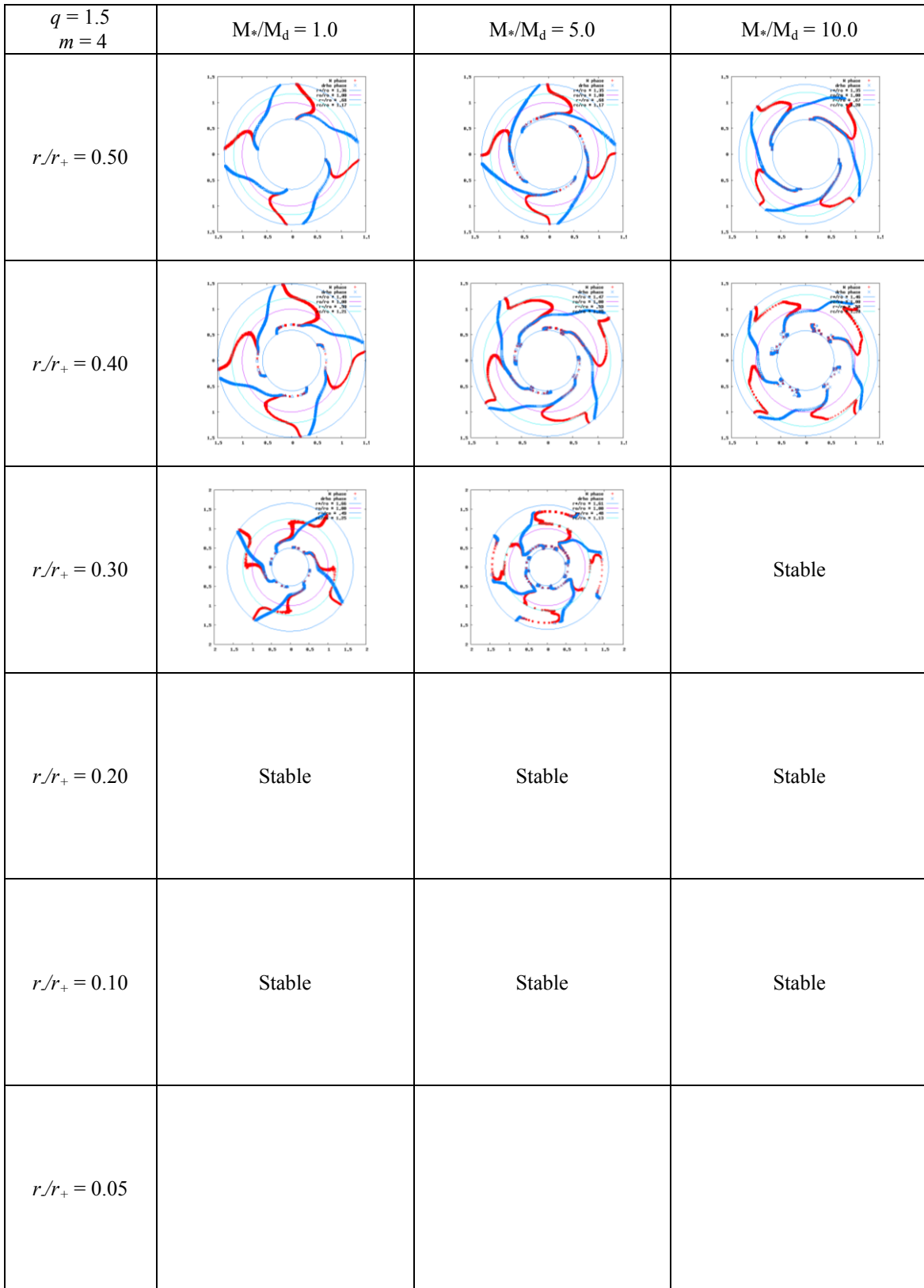


Fig. A.4.1.b. Eigenfunction phases for $q = 1.5$, $m = 4$.

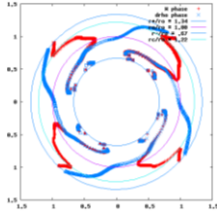
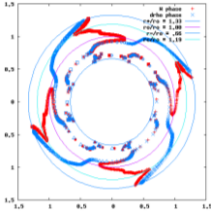
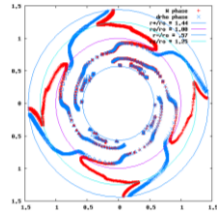
$q = 1.5$ $m = 4$	$M_*/M_d = 25.0$	$M_*/M_d = 50.0$	$M_*/M_d = 100.0$
$r/r_+ = 0.50$			Stable
$r/r_+ = 0.40$		Stable	Stable
$r/r_+ = 0.30$	Stable	Stable	Stable
$r/r_+ = 0.20$	Stable	Stable	Stable
$r/r_+ = 0.10$	Stable	Stable	Stable
$r/r_+ = 0.05$			

Fig. A.4.1.c. Eigenfunction phases for $q = 1.5$, $m = 4$.

$q = 1.5$ $m = 4$	$M_*/M_d = 0.0$	$M_*/M_d = 0.01$	$M_*/M_d = 0.1$
$r/r_+ = 0.50$			
$r/r_+ = 0.40$			
$r/r_+ = 0.30$	Stable	Stable	Stable
$r/r_+ = 0.20$	Stable	Stable	Stable
$r/r_+ = 0.10$	Stable	Stable	Stable
$r/r_+ = 0.05$			

Fig. A.4.2.a. Eigenfunction amplitudes $|\delta\rho|/\rho$ and W for $q = 1.5$, $m = 4$.

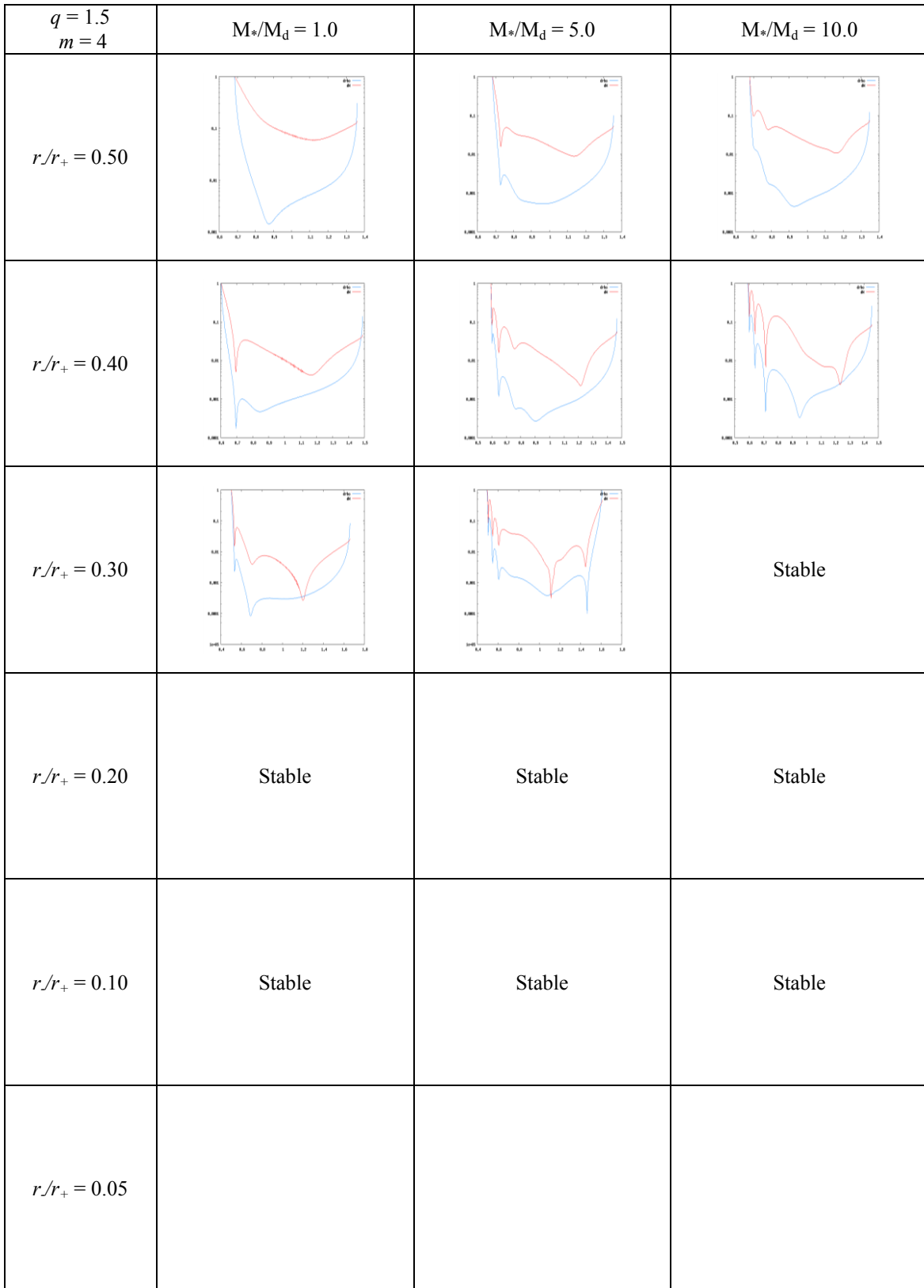


Fig. A.4.2.b. Eigenfunction amplitudes $|\delta\rho|/\rho$ and W for $q = 1.5$, $m = 4$.

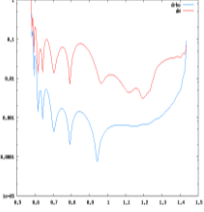
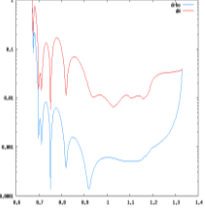
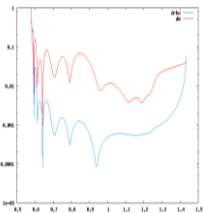
$q = 1.5$ $m = 4$	$M_*/M_d = 25.0$	$M_*/M_d = 50.0$	$M_*/M_d = 100.0$
$r/r_+ = 0.50$			Stable
$r/r_+ = 0.40$		Stable	Stable
$r/r_+ = 0.30$	Stable	Stable	Stable
$r/r_+ = 0.20$	Stable	Stable	Stable
$r/r_+ = 0.10$	Stable	Stable	Stable
$r/r_+ = 0.05$			

Fig. A.4.2.c. Eigenfunction amplitudes $|\delta\rho|/\rho$ and W for $q = 1.5$, $m = 4$.

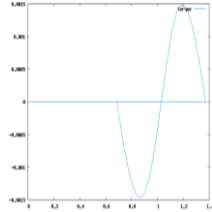
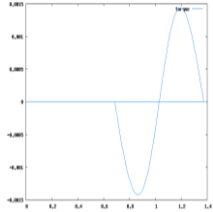
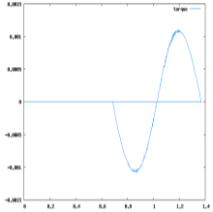
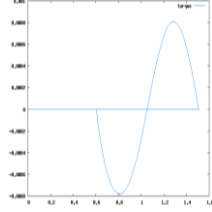
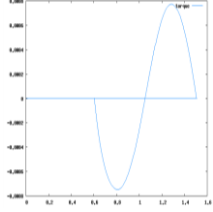
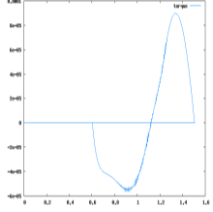
$q = 1.5$ $m = 4$	$M_*/M_d = 0.0$	$M_*/M_d = 0.01$	$M_*/M_d = 0.1$
$r/r_+ = 0.50$			
$r/r_+ = 0.40$			
$r/r_+ = 0.30$	Stable	Stable	Stable
$r/r_+ = 0.20$	Stable	Stable	Stable
$r/r_+ = 0.10$	Stable	Stable	Stable
$r/r_+ = 0.05$			

Fig. A.4.3.a. Self-gravitational torque for $q = 1.5$, $m = 4$.

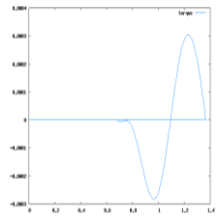
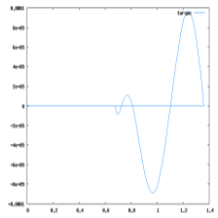
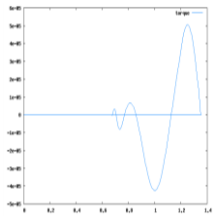
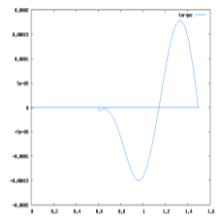
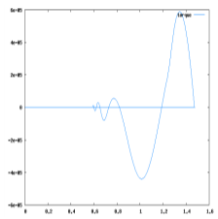
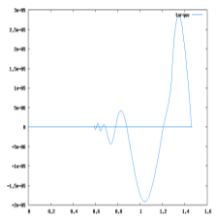
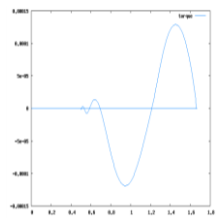
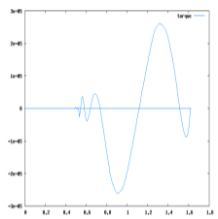
$q = 1.5$ $m = 4$	$M_*/M_d = 1.0$	$M_*/M_d = 5.0$	$M_*/M_d = 10.0$
$r/r_+ = 0.50$			
$r/r_+ = 0.40$			
$r/r_+ = 0.30$			Stable
$r/r_+ = 0.20$	Stable	Stable	Stable
$r/r_+ = 0.10$	Stable	Stable	Stable
$r/r_+ = 0.05$			

Fig. A.4.3.b. Self-gravitational torque for $q = 1.5$, $m = 4$.

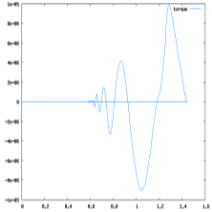
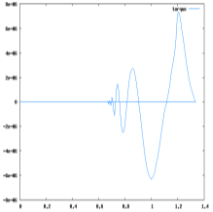
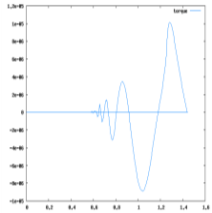
$q = 1.5$ $m = 4$	$M_*/M_d = 25.0$	$M_*/M_d = 50.0$	$M_*/M_d = 100.0$
$r/r_+ = 0.50$			Stable
$r/r_+ = 0.40$		Stable	Stable
$r/r_+ = 0.30$	Stable	Stable	Stable
$r/r_+ = 0.20$	Stable	Stable	Stable
$r/r_+ = 0.10$	Stable	Stable	Stable
$r/r_+ = 0.05$			

Fig. A.4.3.c. Self-gravitational torque for $q = 1.5$, $m = 4$.

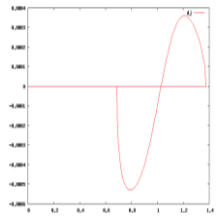
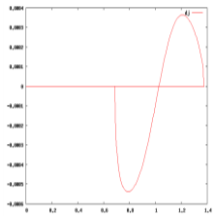
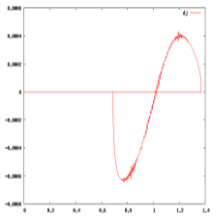
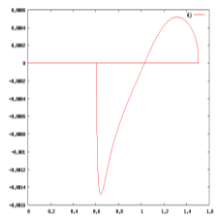
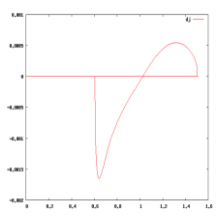
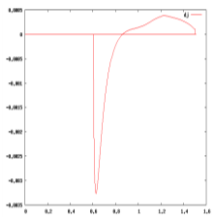
$q = 1.5$ $m = 4$	$M_*/M_d = 0.0$	$M_*/M_d = 0.01$	$M_*/M_d = 0.1$
$r/r_+ = 0.50$			
$r/r_+ = 0.40$			
$r/r_+ = 0.30$	Stable	Stable	Stable
$r/r_+ = 0.20$	Stable	Stable	Stable
$r/r_+ = 0.10$	Stable	Stable	Stable
$r/r_+ = 0.05$			

Fig. A.4.4.a. Perturbed angular momentum for $q = 1.5$, $m = 4$.

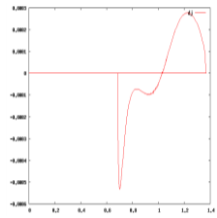
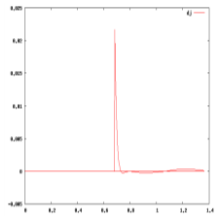
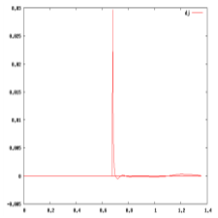
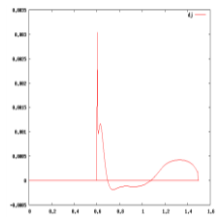
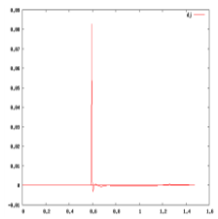
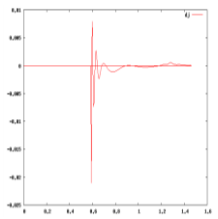
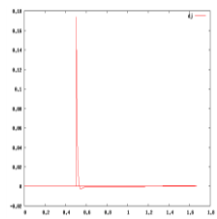
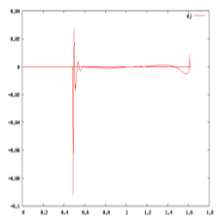
$q = 1.5$ $m = 4$	$M_*/M_d = 1.0$	$M_*/M_d = 5.0$	$M_*/M_d = 10.0$
$r/r_+ = 0.50$			
$r/r_+ = 0.40$			
$r/r_+ = 0.30$			Stable
$r/r_+ = 0.20$	Stable	Stable	Stable
$r/r_+ = 0.10$	Stable	Stable	Stable
$r/r_+ = 0.05$			

Fig. A.4.4.b. Perturbed angular momentum for $q = 1.5$, $m = 4$.

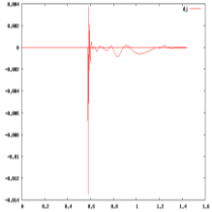
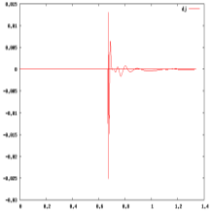
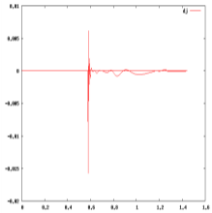
$q = 1.5$ $m = 4$	$M^*/M_d = 25.0$	$M^*/M_d = 50.0$	$M^*/M_d = 100.0$
$r/r_+ = 0.50$			Stable
$r/r_+ = 0.40$		Stable	Stable
$r/r_+ = 0.30$	Stable	Stable	Stable
$r/r_+ = 0.20$	Stable	Stable	Stable
$r/r_+ = 0.10$	Stable	Stable	Stable
$r/r_+ = 0.05$			

Fig. A.4.4.c. Perturbed angular momentum for $q = 1.5$, $m = 4$.

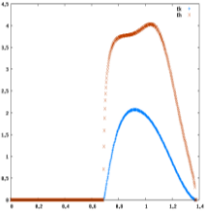
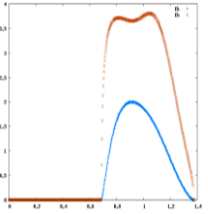
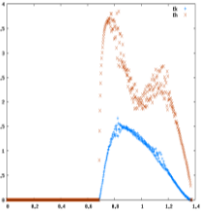
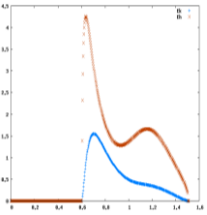
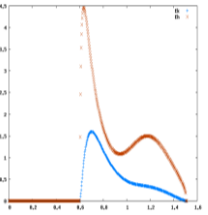
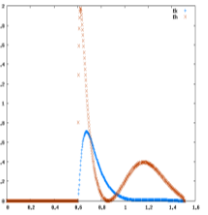
$q = 1.5$ $m = 4$	$M_*/M_d = 0.0$	$M_*/M_d = 0.01$	$M_*/M_d = 0.1$
$r/r_+ = 0.50$			
$r/r_+ = 0.40$			
$r/r_+ = 0.30$	Stable	Stable	Stable
$r/r_+ = 0.20$	Stable	Stable	Stable
$r/r_+ = 0.10$	Stable	Stable	Stable
$r/r_+ = 0.05$			

Fig. A.4.5.a. Work integrals for $q = 1.5$, $m = 4$.

$q = 1.5$ $m = 4$	$M_*/M_d = 1.0$	$M_*/M_d = 5.0$	$M_*/M_d = 10.0$
$r/r_+ = 0.50$			
$r/r_+ = 0.40$			
$r/r_+ = 0.30$			Stable
$r/r_+ = 0.20$	Stable	Stable	Stable
$r/r_+ = 0.10$	Stable	Stable	Stable
$r/r_+ = 0.05$			

Fig. A.4.5.b. Work integrals for $q = 1.5$, $m = 4$.

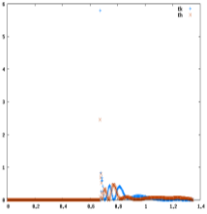
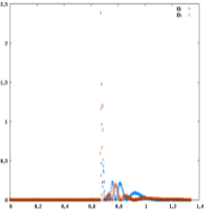
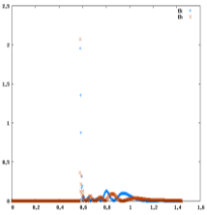
$q = 1.5$ $m = 4$	$M_*/M_d = 25.0$	$M_*/M_d = 50.0$	$M_*/M_d = 100.0$
$r/r_+ = 0.50$			Stable
$r/r_+ = 0.40$		Stable	Stable
$r/r_+ = 0.30$	Stable	Stable	Stable
$r/r_+ = 0.20$	Stable	Stable	Stable
$r/r_+ = 0.10$	Stable	Stable	Stable
$r/r_+ = 0.05$			

Fig. A.4.5.c. Work integrals for $q = 1.5$, $m = 4$.

$q = 1.5$ $m = 4$	$M_*/M_d = 0.0$	$M_*/M_d = 0.01$	$M_*/M_d = 0.1$
$r/r_+ = 0.50$			
$r/r_+ = 0.40$			
$r/r_+ = 0.30$	Stable	Stable	Stable
$r/r_+ = 0.20$	Stable	Stable	Stable
$r/r_+ = 0.10$	Stable	Stable	Stable
$r/r_+ = 0.05$			

Fig. A.4.6.a. Stresses for $q = 1.5$, $m = 4$.

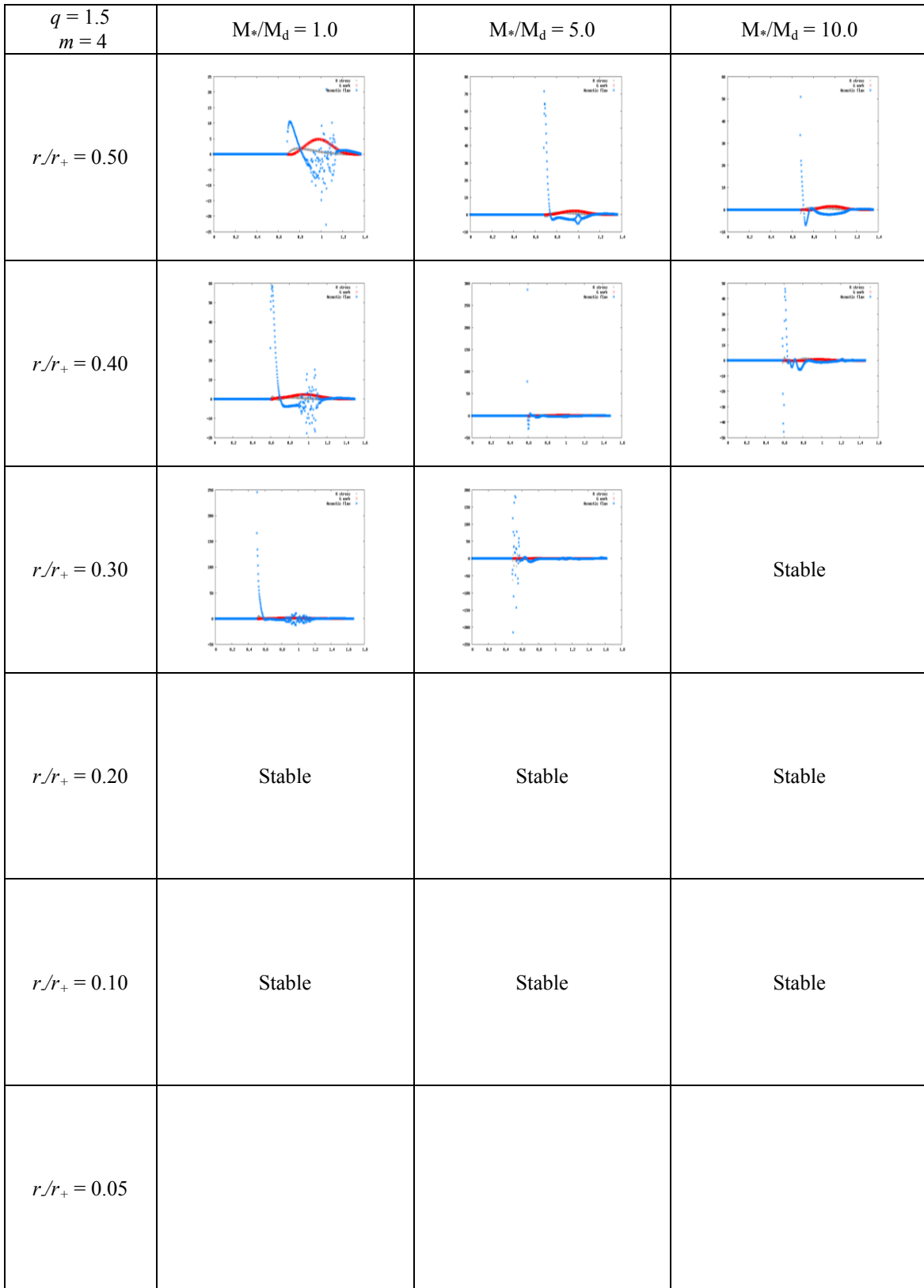


Fig. A.4.6.b. Stresses for $q = 1.5$, $m = 4$.

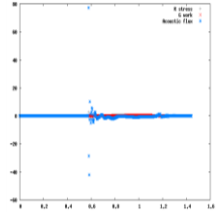
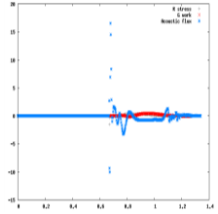
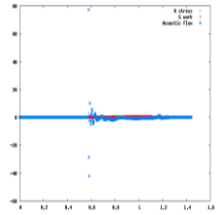
$q = 1.5$ $m = 4$	$M^*/M_d = 25.0$	$M^*/M_d = 50.0$	$M^*/M_d = 100.0$
$r/r_+ = 0.50$			Stable
$r/r_+ = 0.40$		Stable	Stable
$r/r_+ = 0.30$	Stable	Stable	Stable
$r/r_+ = 0.20$	Stable	Stable	Stable
$r/r_+ = 0.10$	Stable	Stable	Stable
$r/r_+ = 0.05$			

Fig. A.4.6.c. Stresses for $q = 1.5$, $m = 4$.

APPENDIX B

PLOTS FOR SELECTED $q = 1.75$ MODELS

Appendix B contains a sequence of model plots for $q = 1.75$ models, including $M_*/M_d = 0.0, 0.01, 0.1, 1.0, 5.0, 10.0, 25.0$ and 50.0 . The column to the right of the $M_*/M_d = 50.0$ column contains non-self-gravitating models. In general, figures labeled "a" contain plots for $M_*/M_d = 0.0, 0.01$ and 0.1 ; figures labeled "b" contain plots for $M_*/M_d = 1.0, 5.0$ and 10.0 ; and figures labeled "c" contain plots for $M_*/M_d = 25.0, 50.0$ and non-self-gravitating models. For each of these values of M_*/M_d , we include plots for models for $r./r_+ = 0.05, 0.10, 0.20, 0.30, 0.40$ and 0.50 . All radii depicted in the plots are normalized by R_0 . Stable and unresolved models are labeled as such. All of the functions plotted in the appendices are defined identically to similar plots found in the body of the dissertation.

Please refer to the beginning of Appendix A for a description of the figure numbering system as well as descriptions of the individual functions plotted. Note there are no plots shown for self-gravity torque in the non-self-gravity column, since it is zero by definition for those models. Also, there are typically no non-self-gravitating models calculated for $r./r_+ = 0.05$ due to resolution issues.

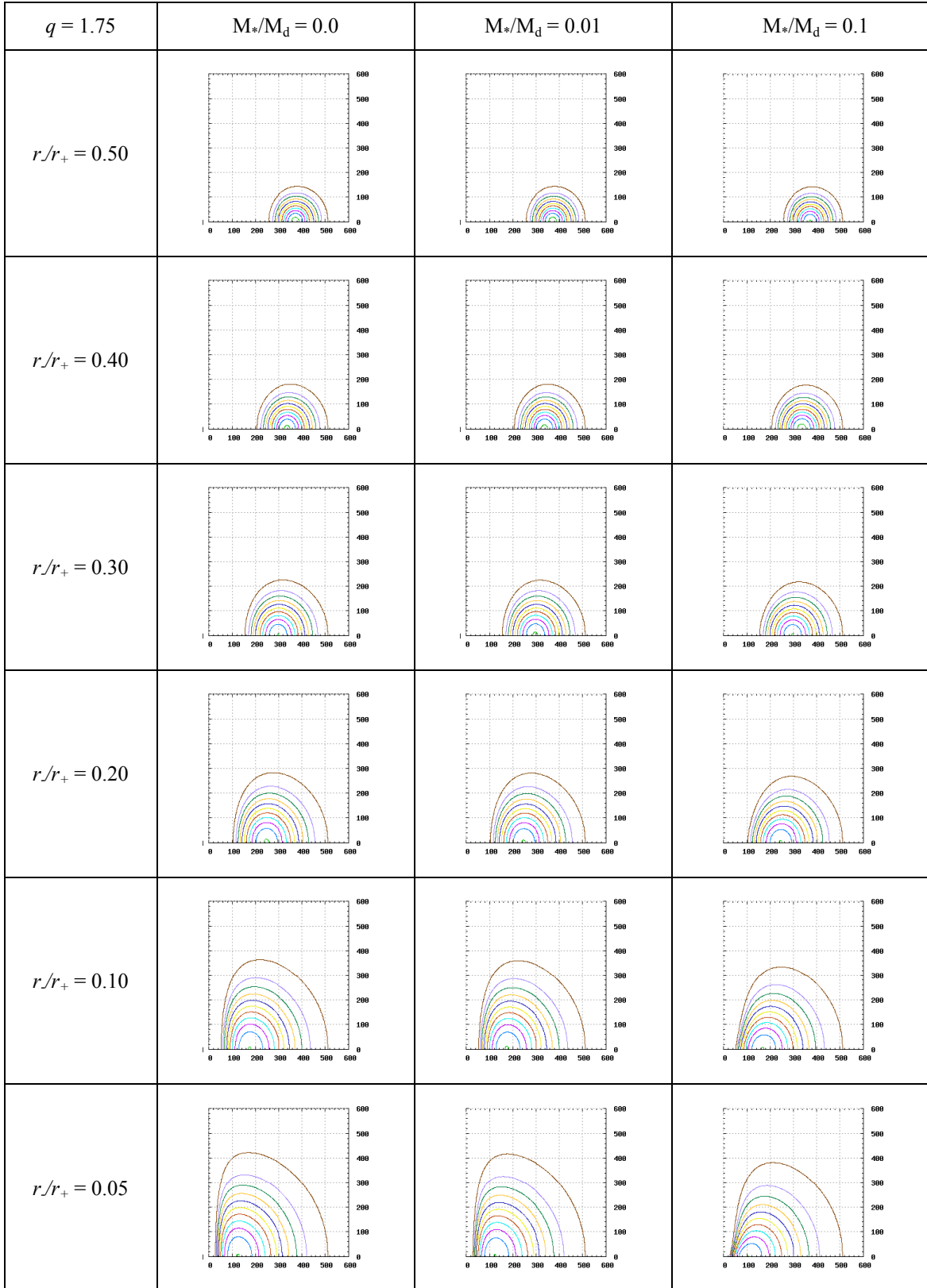


Fig. B.1.0.a. Equilibrium mass density contour plots of meridional slices for $q = 1.75$.

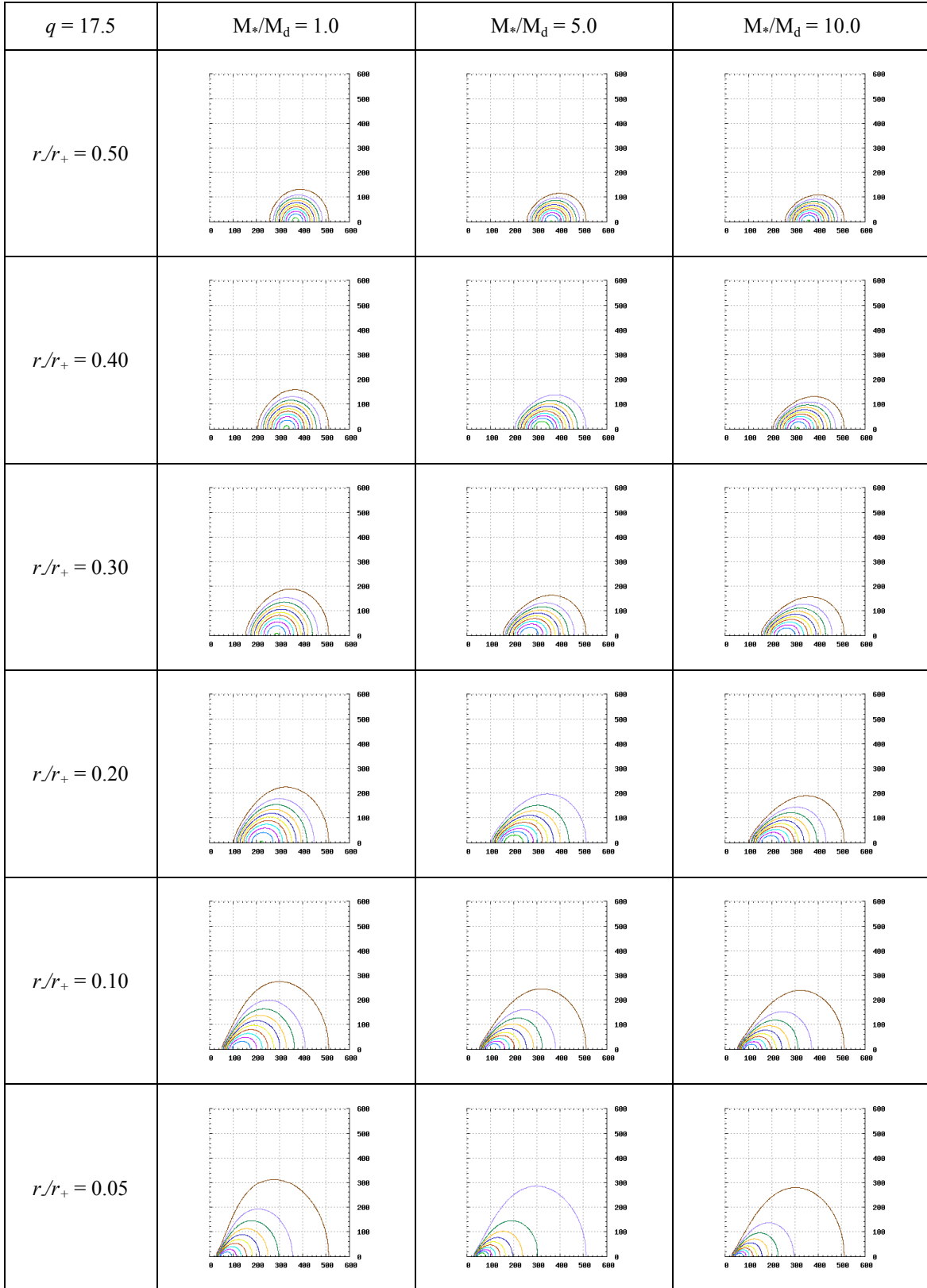


Fig. B.1.0.b. Equilibrium mass density contours of meridional slices for $q = 1.75$.

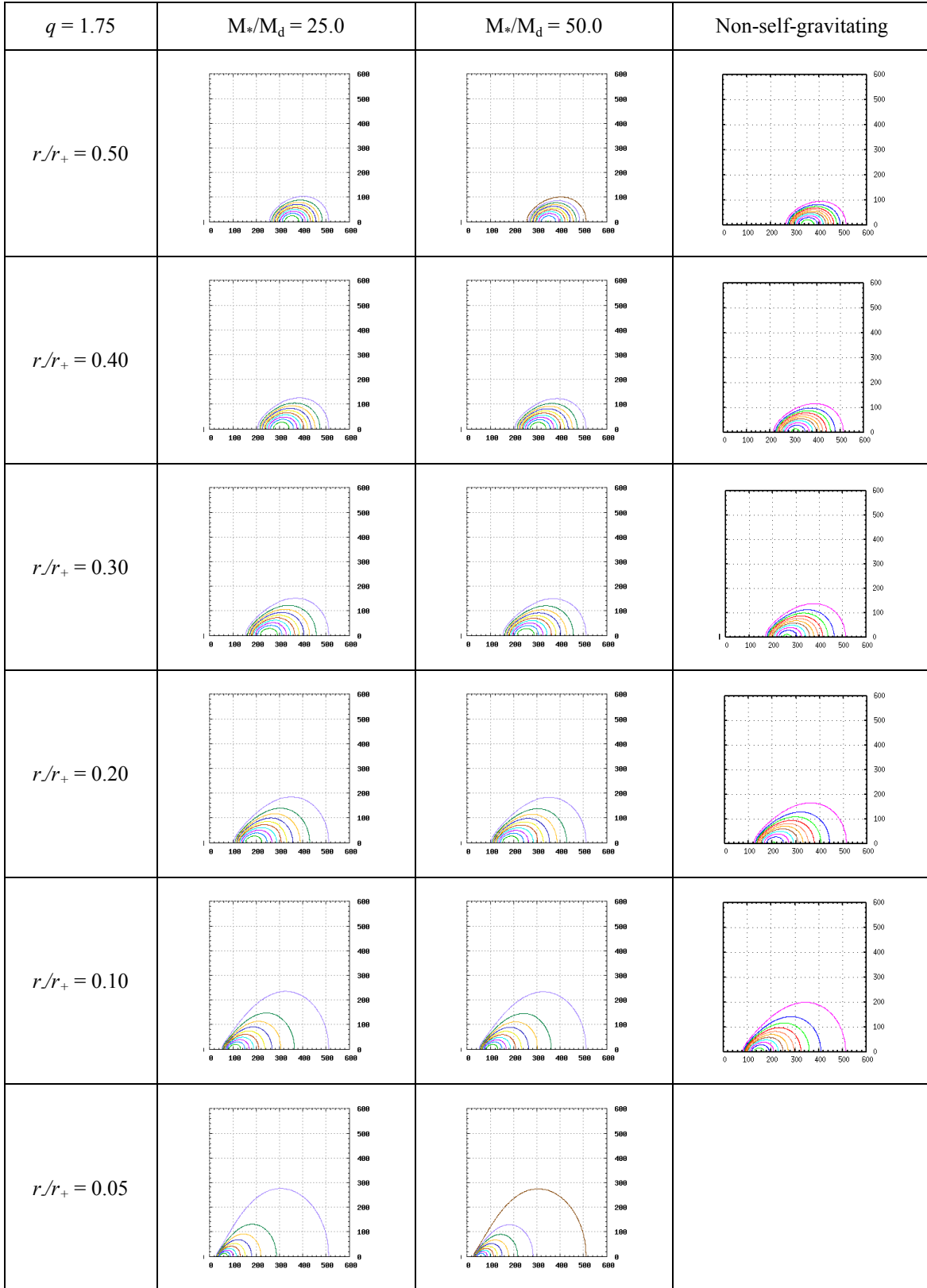


Fig. B.1.0.c. Equilibrium mass density contours of meridional slices for $q = 1.75$.

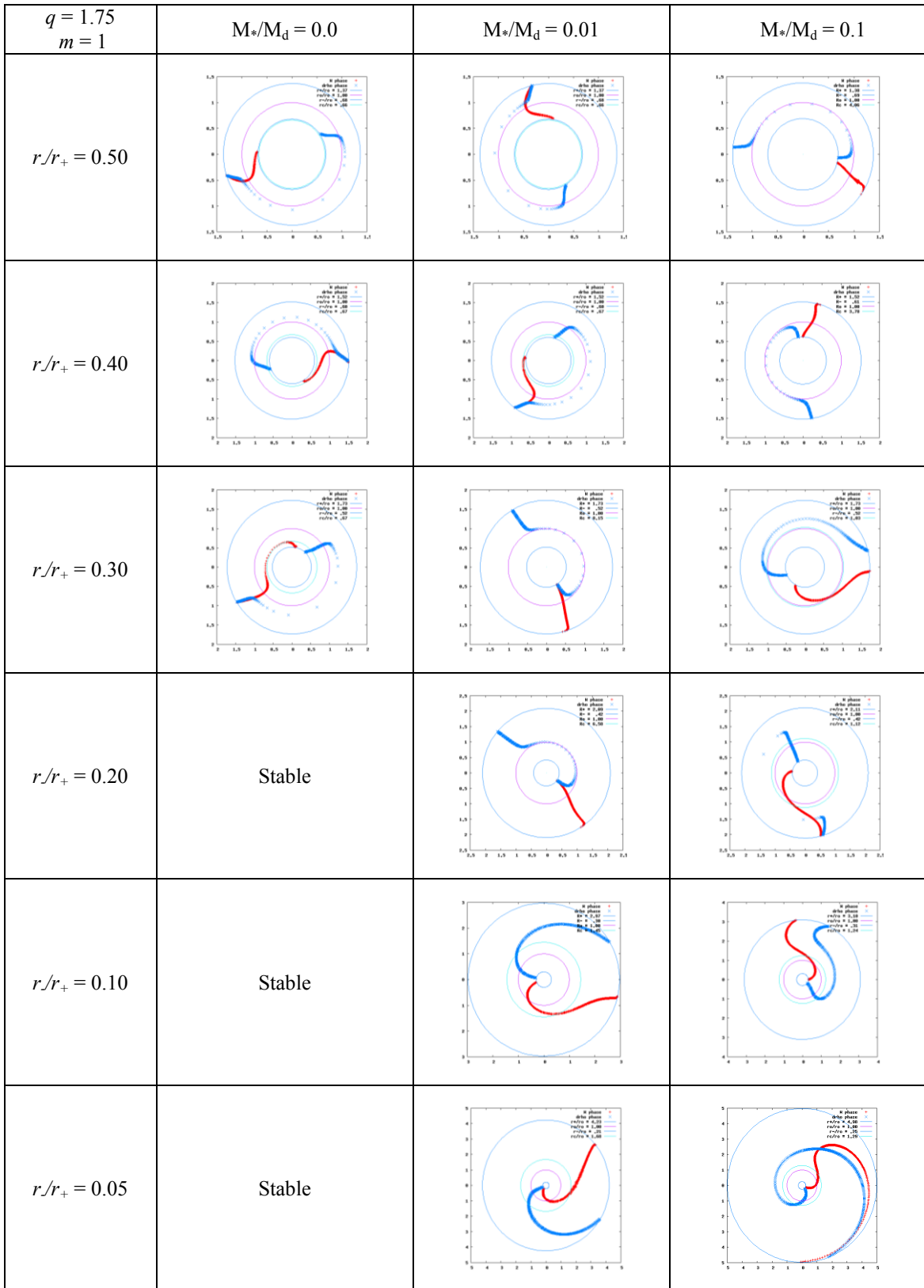


Fig. B.1.1 a Eigenfunction phases for $q = 1.75$, $m = 1$

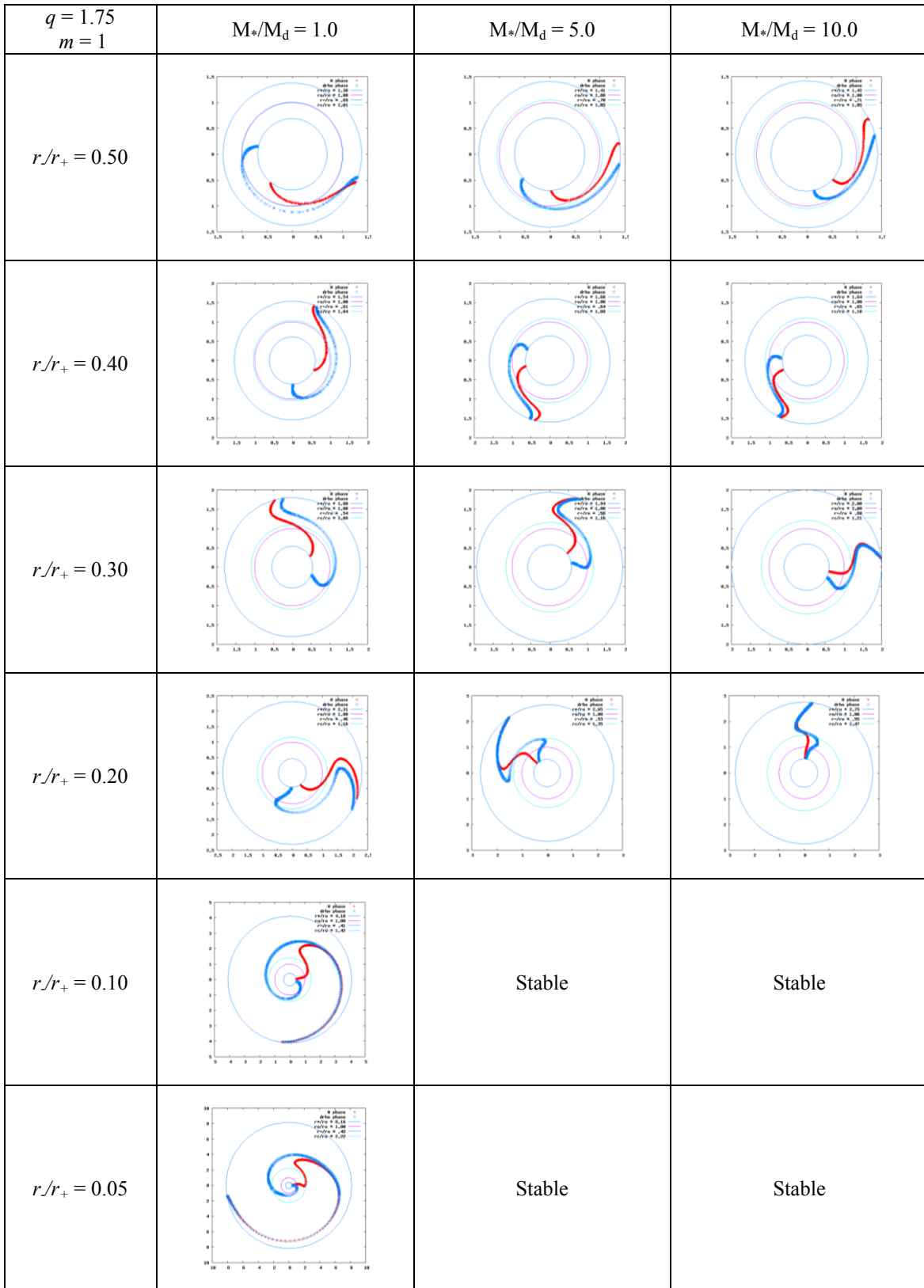


Fig. B.1.1.b. Eigenfunction phases for $q = 1.75$, $m = 1$

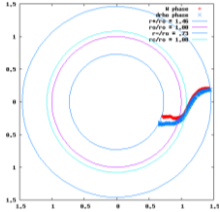
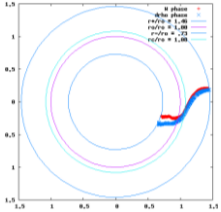
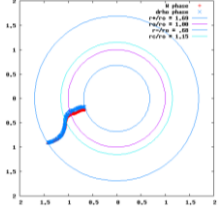
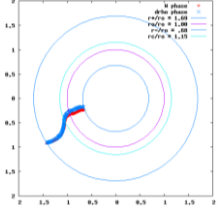
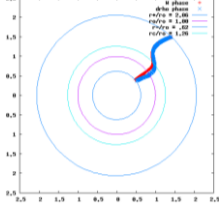
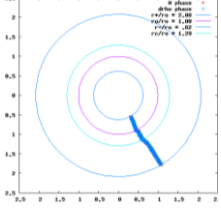
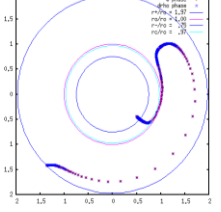
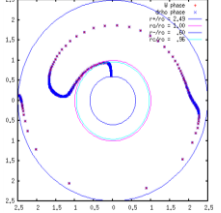
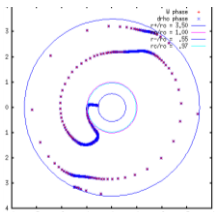
$q = 1.75$ $m = 1$	$M_*/M_d = 25.0$	$M_*/M_d = 50.0$	Non-self-gravitating
$r/r_+ = 0.50$			Stable
$r/r_+ = 0.40$			Stable
$r/r_+ = 0.30$			
$r/r_+ = 0.20$	Stable	Stable	
$r/r_+ = 0.10$	Stable	Stable	
$r/r_+ = 0.05$	Stable	Stable	

Fig. B.1.1.c. Eigenfunction phases for $q = 1.75$, $m = 1$

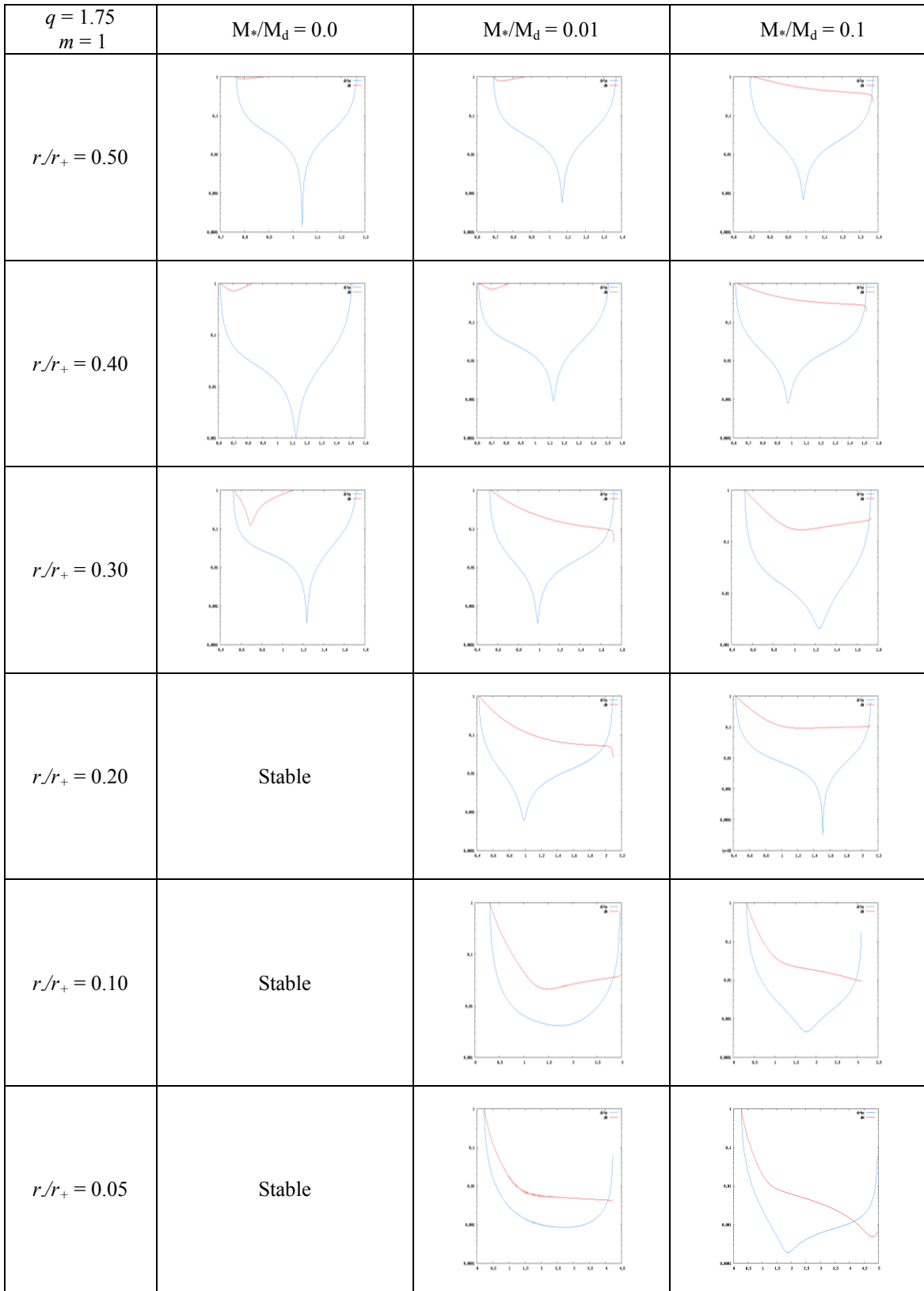


Fig. B.1.2.a. Eigenfunction amplitudes $|\delta\rho|/\rho$ and W for $q = 1.75$, $m = 1$

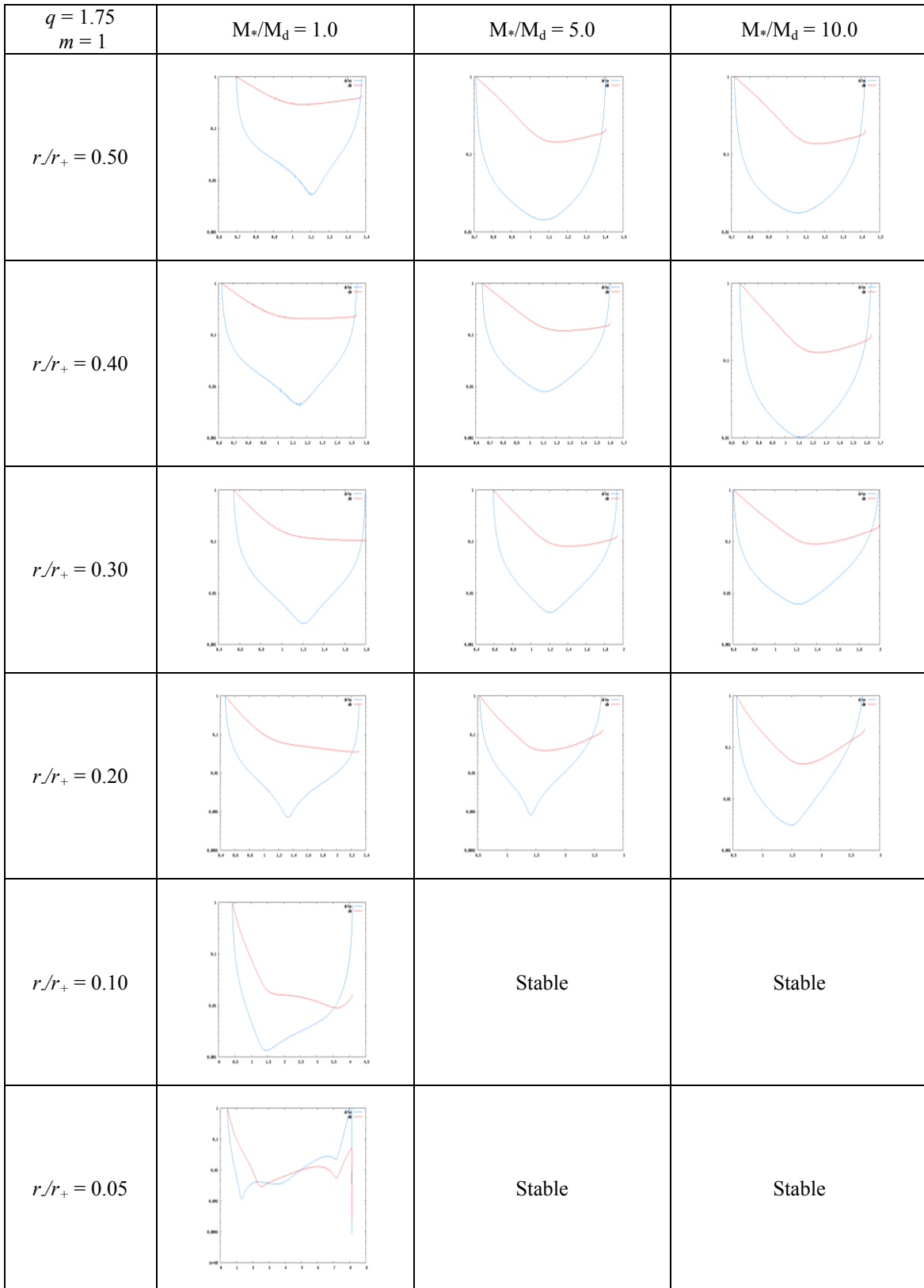


Fig. B.1.2.b. Eigenfunction amplitudes $|\delta\rho|/\rho$ and W for $q = 1.75$, $m = 1$

$q = 1.75$ $m = 1$	$M_*/M_d = 25.0$	$M_*/M_d = 50.0$	Non-self-gravitating
$r/r_+ = 0.50$			Stable
$r/r_+ = 0.40$			Stable
$r/r_+ = 0.30$			
$r/r_+ = 0.20$	Stable	Stable	
$r/r_+ = 0.10$	Stable	Stable	
$r/r_+ = 0.05$	Stable	Stable	

Fig. B.1.2.c. Eigenfunction amplitudes $|\delta\rho|/\rho$ and W for $q = 1.75$, $m = 1$

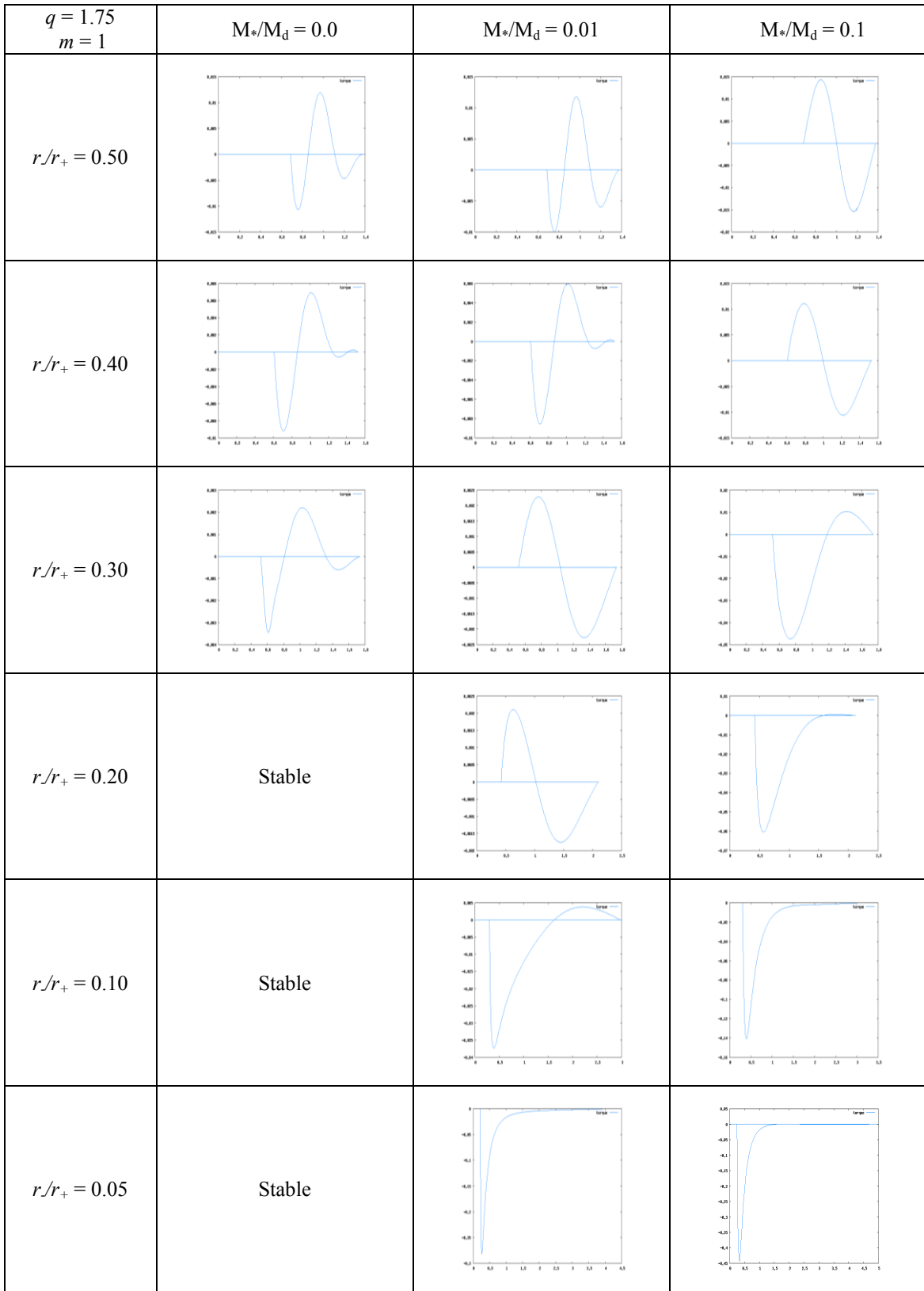


Fig. B.1.3.a. Self-gravitational torque for $q = 1.75$, $m = 1$

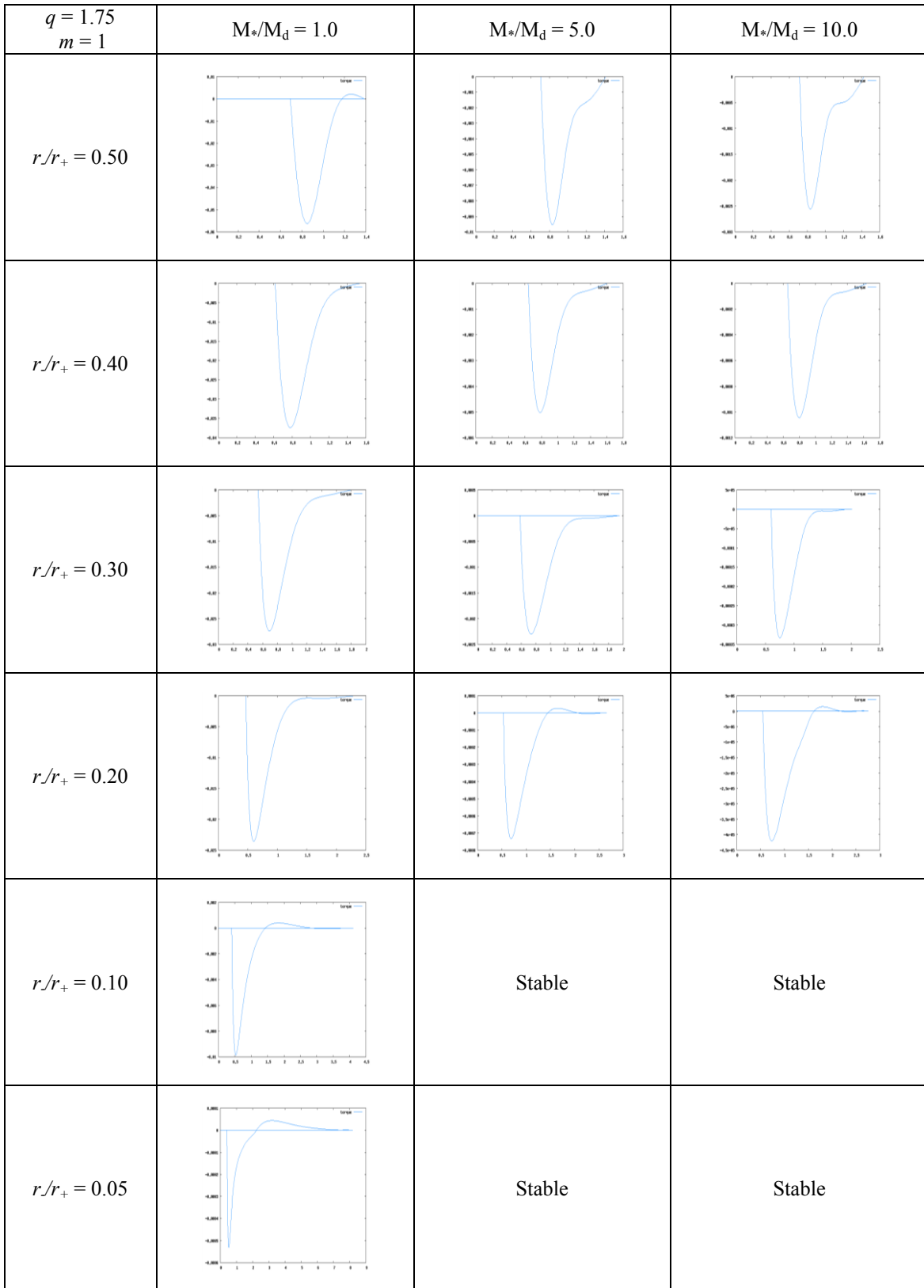


Fig. B.1.3.b. Self-gravitational torque for $q = 1.75$, $m = 1$

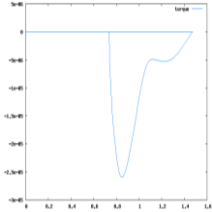
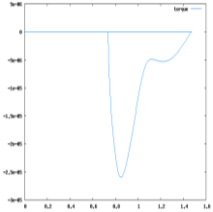
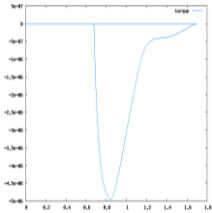
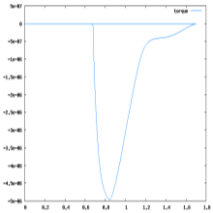
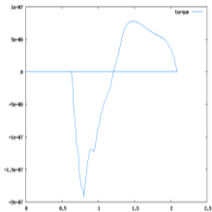
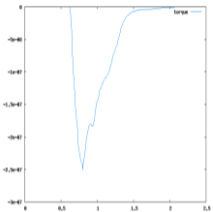
$q = 1.75$ $m = 1$	$M_*/M_d = 25.0$	$M_*/M_d = 50.0$	Non-self-gravitating
$r/r_+ = 0.50$			
$r/r_+ = 0.40$			
$r/r_+ = 0.30$			
$r/r_+ = 0.20$	Stable	Stable	
$r/r_+ = 0.10$	Stable	Stable	
$r/r_+ = 0.05$	Stable	Stable	

Fig. B.1.3.c. Self-gravitational torque for $q = 1.75$, $m = 1$

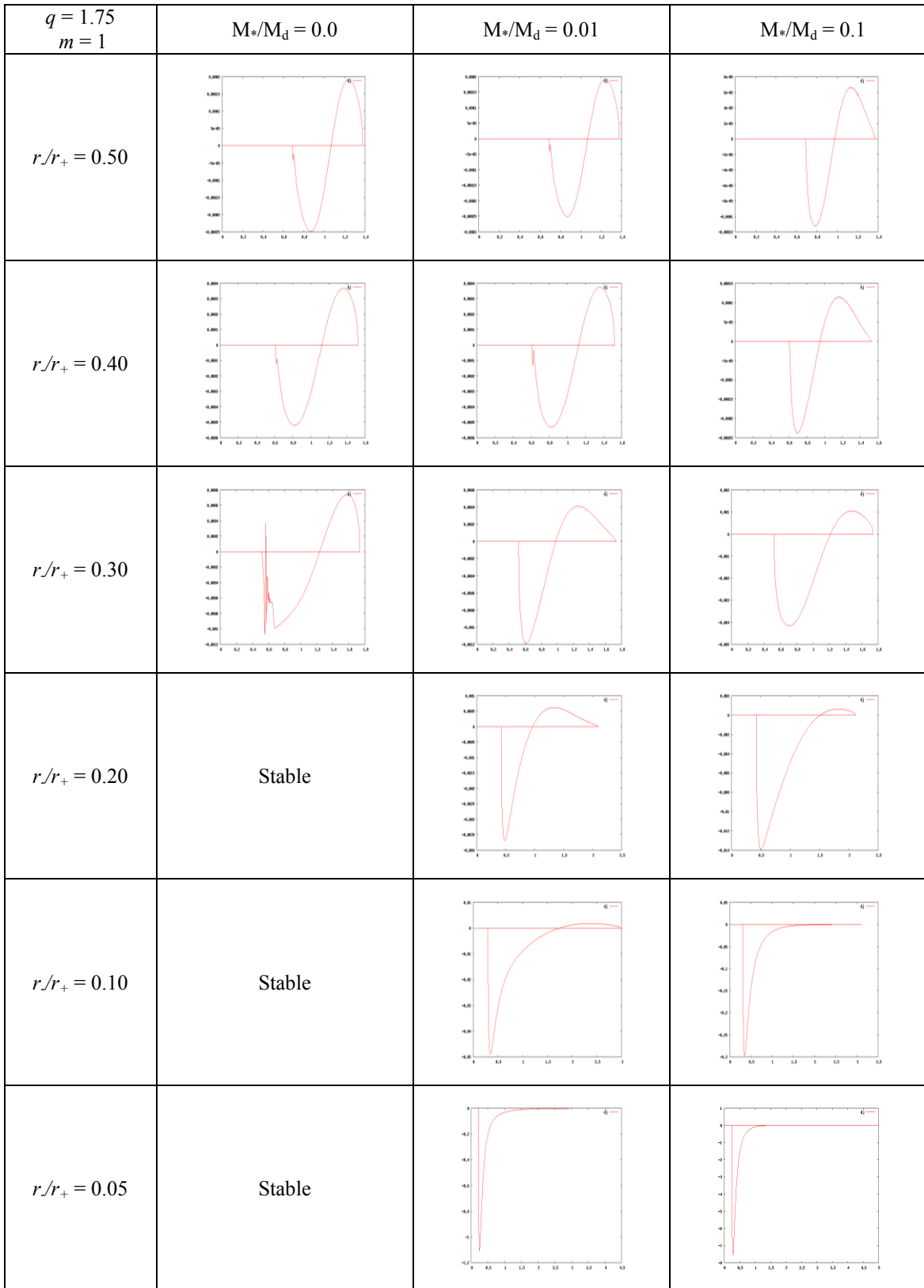


Fig. B.1.4.a. Perturbed angular momentum for $q = 1.75$, $m = 1$

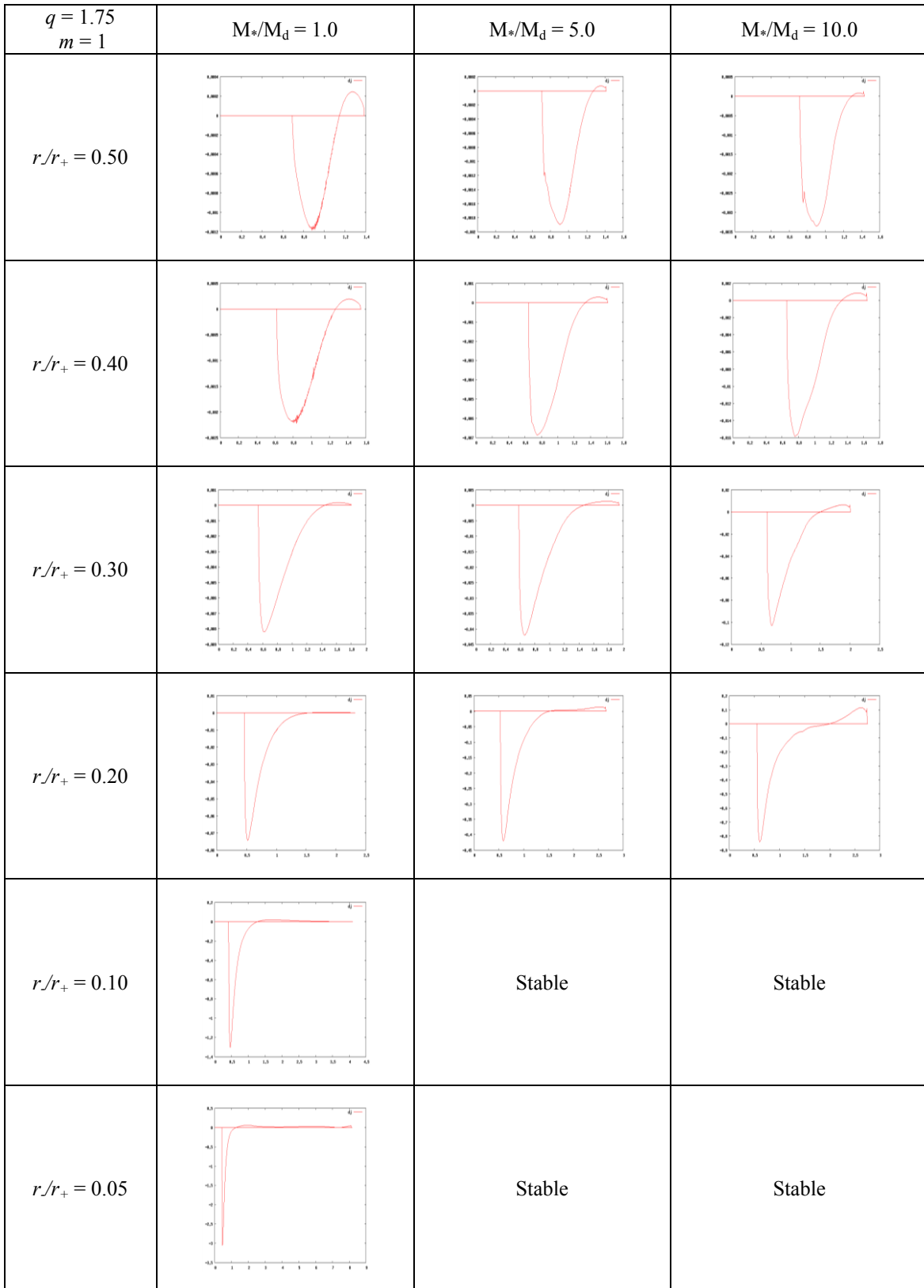


Fig. B.1.4.b. Perturbed angular momentum for $q = 1.75$, $m = 1$

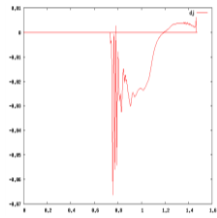
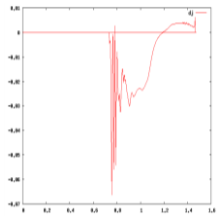
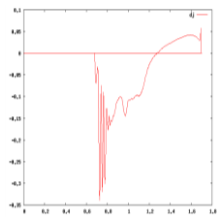
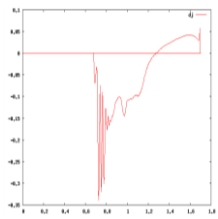
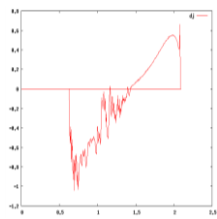
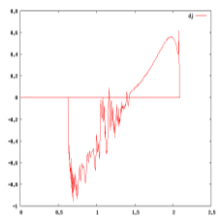
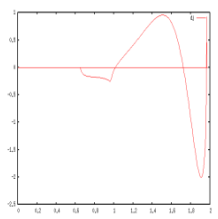
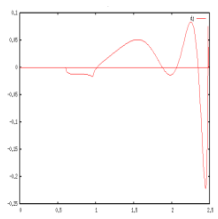
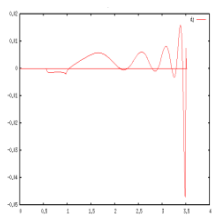
$q = 1.75$ $m = 1$	$M_*/M_d = 25.0$	$M_*/M_d = 50.0$	Non-self-gravitating
$r/r_+ = 0.50$			Stable
$r/r_+ = 0.40$			Stable
$r/r_+ = 0.30$			
$r/r_+ = 0.20$	Stable	Stable	
$r/r_+ = 0.10$	Stable	Stable	
$r/r_+ = 0.05$	Stable	Stable	

Fig. B.1.4.c. Perturbed angular momentum for $q = 1.75$, $m = 1$

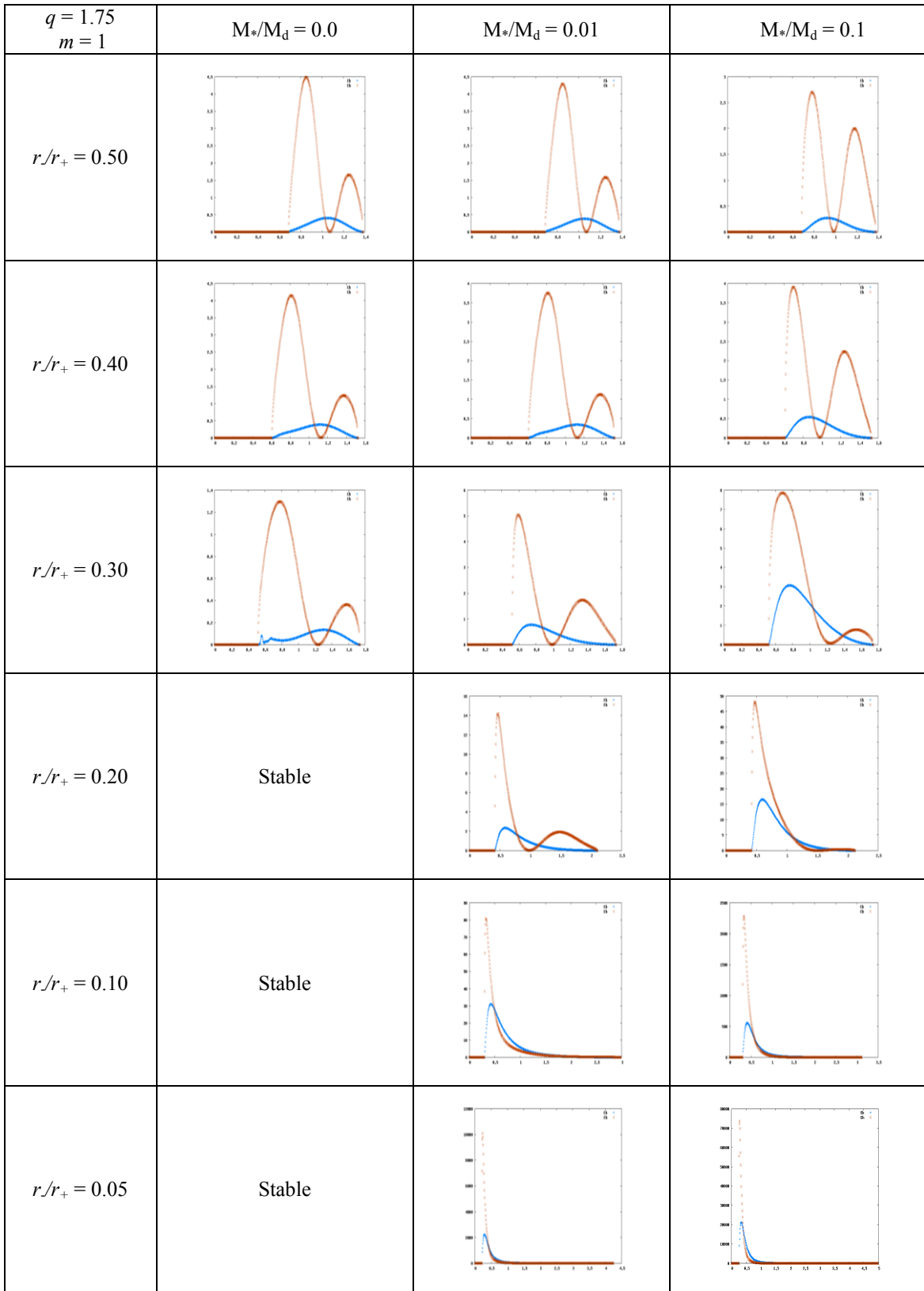


Fig. B.1.5.a. Work integrals for $q = 1.75$, $m = 1$

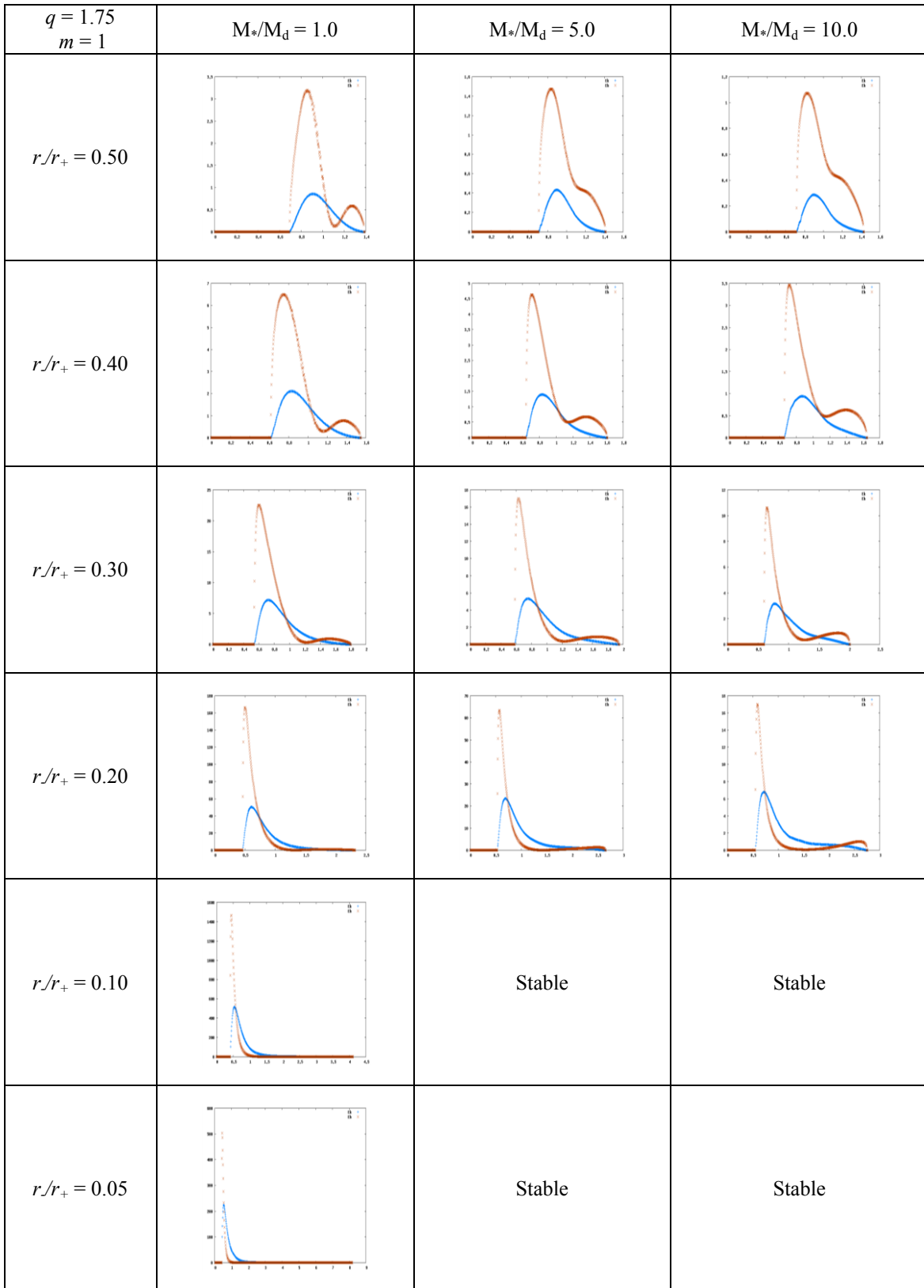


Fig. B.1.5.b. Work integrals for $q = 1.75$, $m = 1$

$q = 1.75$ $m = 1$	$M_*/M_d = 25.0$	$M_*/M_d = 50.0$	Non-self-gravitating
$r/r_+ = 0.50$			Stable
$r/r_+ = 0.40$			Stable
$r/r_+ = 0.30$			
$r/r_+ = 0.20$	Stable	Stable	
$r/r_+ = 0.10$	Stable	Stable	
$r/r_+ = 0.05$	Stable	Stable	

Fig. B.1.5.c. Work integrals for $q = 1.75$, $m = 1$

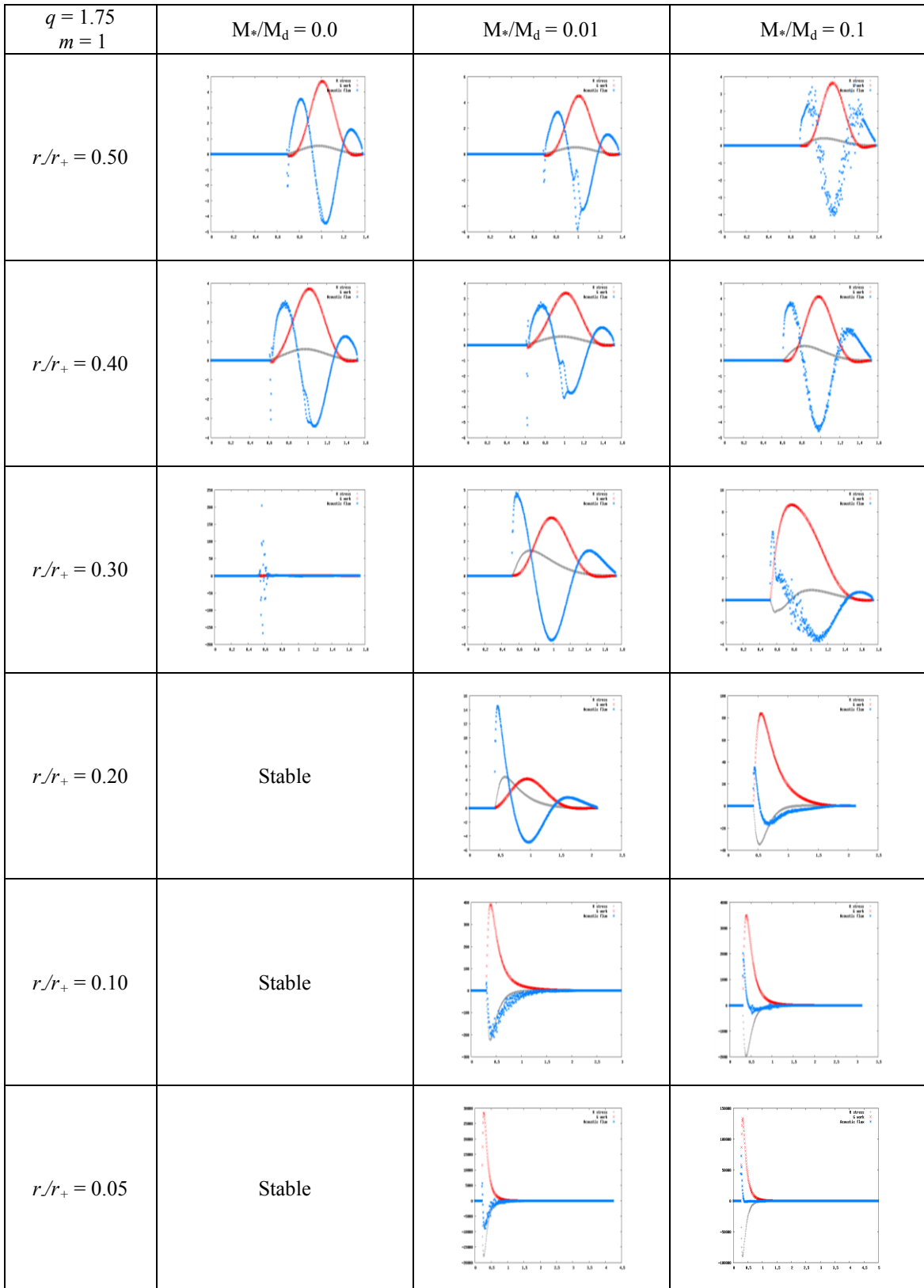


Fig. B.1.6.a. Stresses for $q = 1.75$, $m = 1$

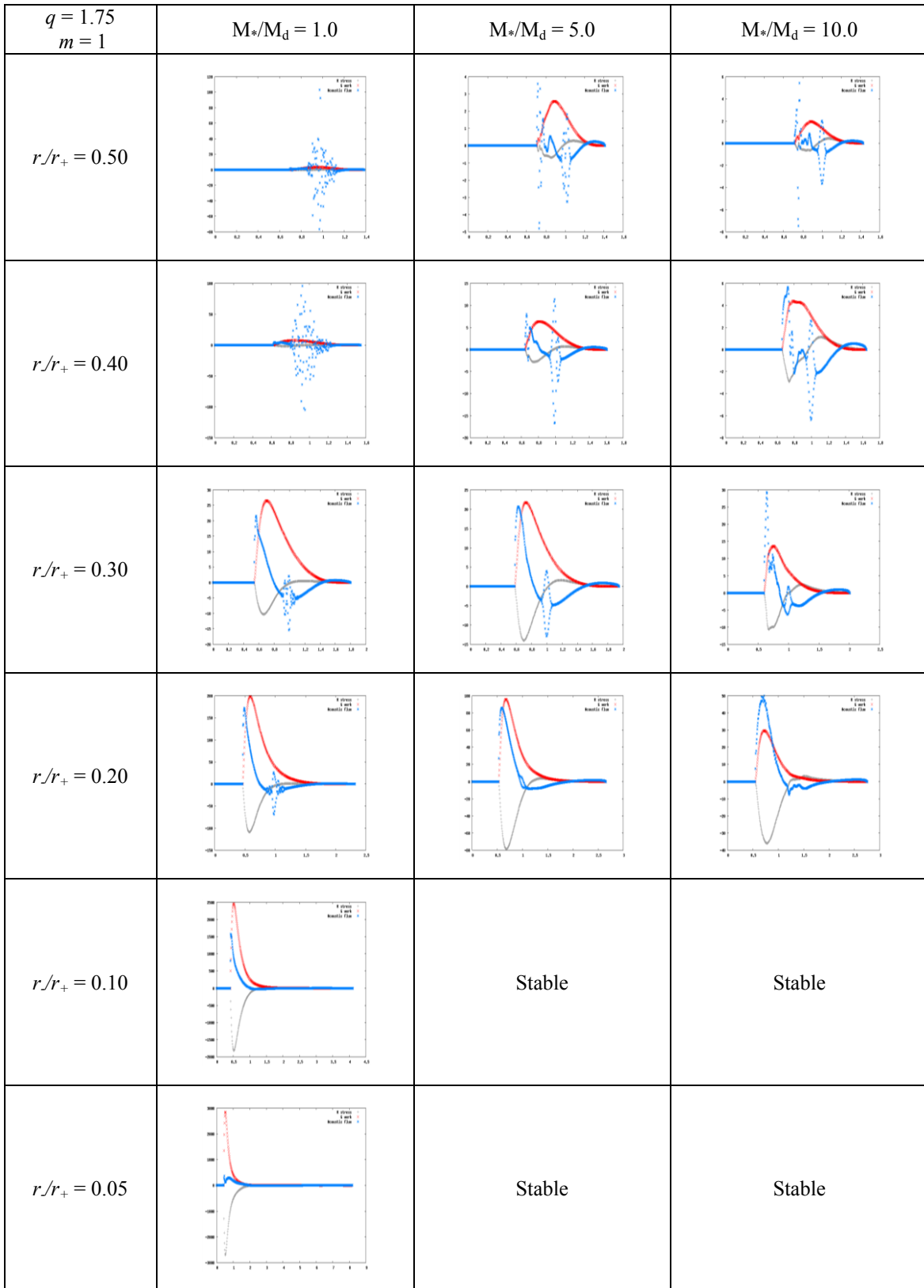


Fig. B.1.6.b. Stresses for $q = 1.75$, $m = 1$

$q = 1.75$ $m = 1$	$M_*/M_d = 25.0$	$M_*/M_d = 50.0$	Non-self-gravitating
$r/r_+ = 0.50$			Stable
$r/r_+ = 0.40$			Stable
$r/r_+ = 0.30$			
$r/r_+ = 0.20$	Stable	Stable	
$r/r_+ = 0.10$	Stable	Stable	
$r/r_+ = 0.05$	Stable	Stable	

Fig. B.1.6.c. Stresses for $q = 1.75$, $m = 1$

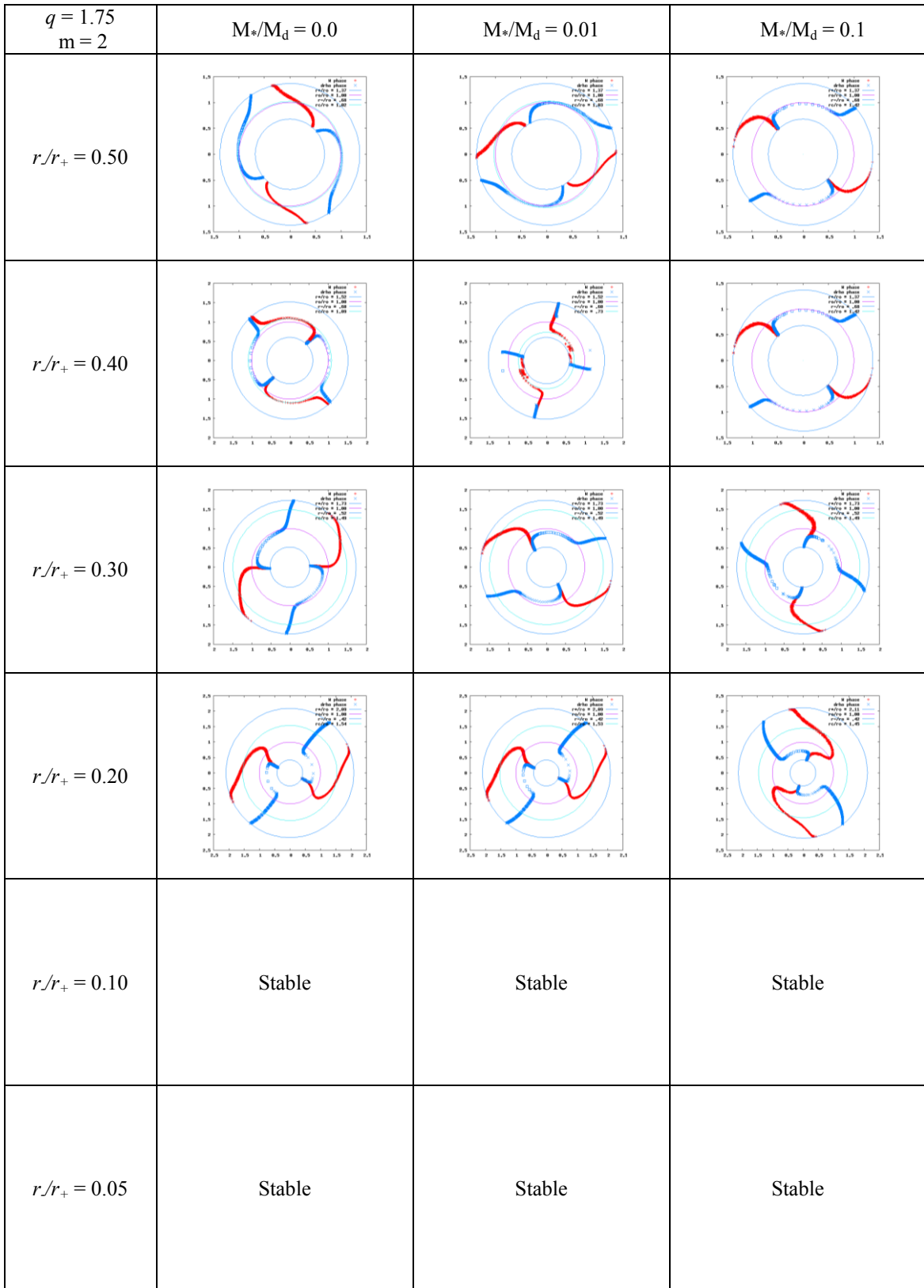


Fig. B.2.1 a Eigenfunction phases for $q = 1.75$, $m = 2$

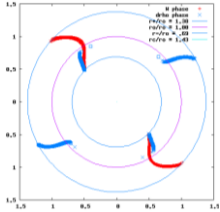
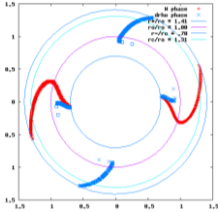
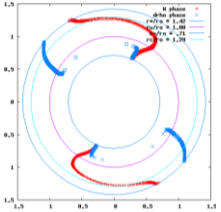
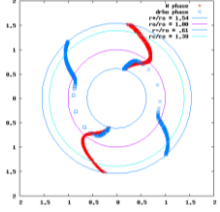
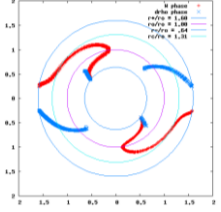
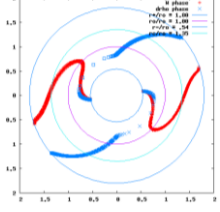
$q = 1.75$ $m = 2$	$M_*/M_d = 1.0$	$M_*/M_d = 5.0$	$M_*/M_d = 10.0$
$r/r_+ = 0.50$			
$r/r_+ = 0.40$			Stable
$r/r_+ = 0.30$		Stable	Stable
$r/r_+ = 0.20$	Stable	Stable	Stable
$r/r_+ = 0.10$	Stable	Stable	Stable
$r/r_+ = 0.05$	Stable	Stable	Stable

Fig. B.2.1.b. Eigenfunction phases for $q = 1.75, m = 2$

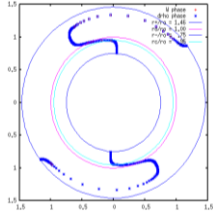
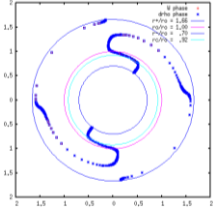
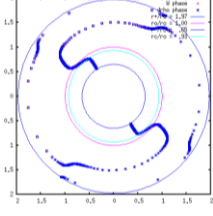
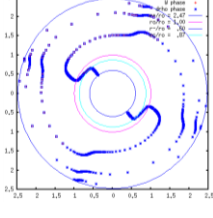
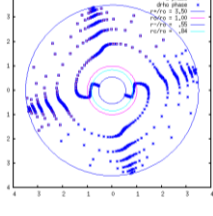
$q = 1.75$ $m = 2$	$M_*/M_d = 25.0$	$M_*/M_d = 50.0$	Non-self-gravitating
$r/r_+ = 0.50$	Stable	Stable	
$r/r_+ = 0.40$	Stable	Stable	
$r/r_+ = 0.30$	Stable	Stable	
$r/r_+ = 0.20$	Stable	Stable	
$r/r_+ = 0.10$	Stable	Stable	
$r/r_+ = 0.05$	Stable	Stable	

Fig. B.2.1.c. Eigenfunction phases for $q = 1.75$, $m = 2$

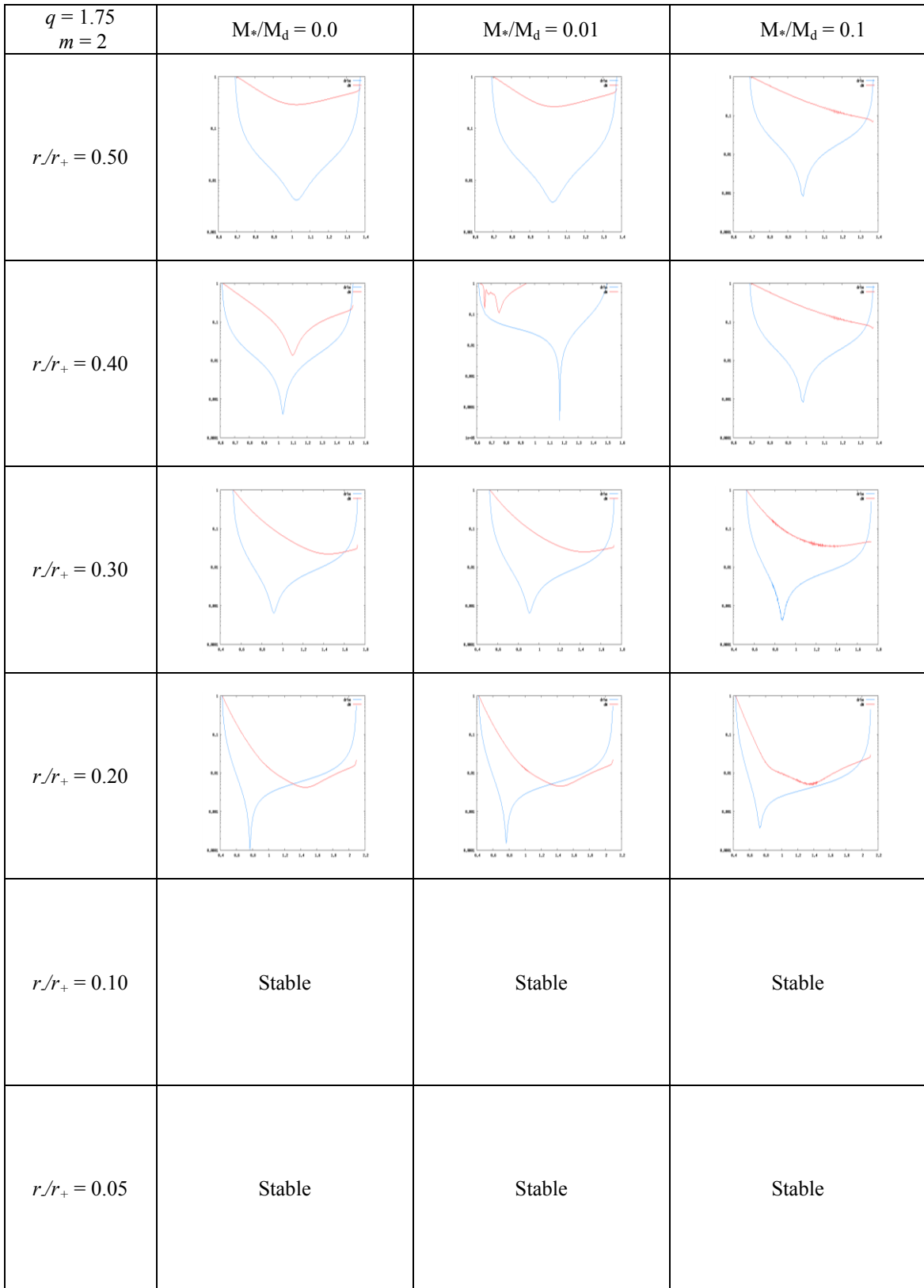


Fig. B.2.2.a. Eigenfunction amplitudes $|\delta\rho|/\rho$ and W for $q = 1.75$, $m = 2$

$q = 1.75$ $m = 2$	$M_*/M_d = 1.0$	$M_*/M_d = 5.0$	$M_*/M_d = 10.0$
$r/r_+ = 0.50$			
$r/r_+ = 0.40$			Stable
$r/r_+ = 0.30$		Stable	Stable
$r/r_+ = 0.20$	Stable	Stable	Stable
$r/r_+ = 0.10$	Stable	Stable	Stable
$r/r_+ = 0.05$	Stable	Stable	Stable

Fig. B.2.2.b. Eigenfunction amplitudes $|\delta\rho|/\rho$ and W for $q = 1.75$, $m = 2$

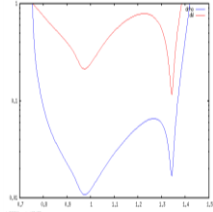
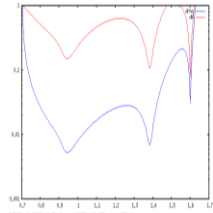
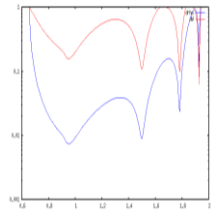
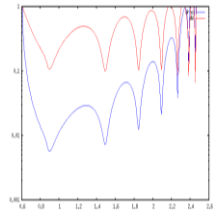
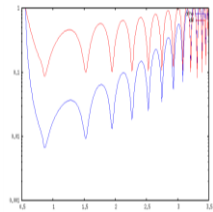
$q = 1.75$ $m = 2$	$M_*/M_d = 25.0$	$M_*/M_d = 50.0$	Non-self-gravitating
$r/r_+ = 0.50$	Stable	Stable	
$r/r_+ = 0.40$	Stable	Stable	
$r/r_+ = 0.30$	Stable	Stable	
$r/r_+ = 0.20$	Stable	Stable	
$r/r_+ = 0.10$	Stable	Stable	
$r/r_+ = 0.05$	Stable	Stable	

Fig. B.2.2.c. Eigenfunction amplitudes $|\delta\rho|/\rho$ and W for $q = 1.75$, $m = 2$

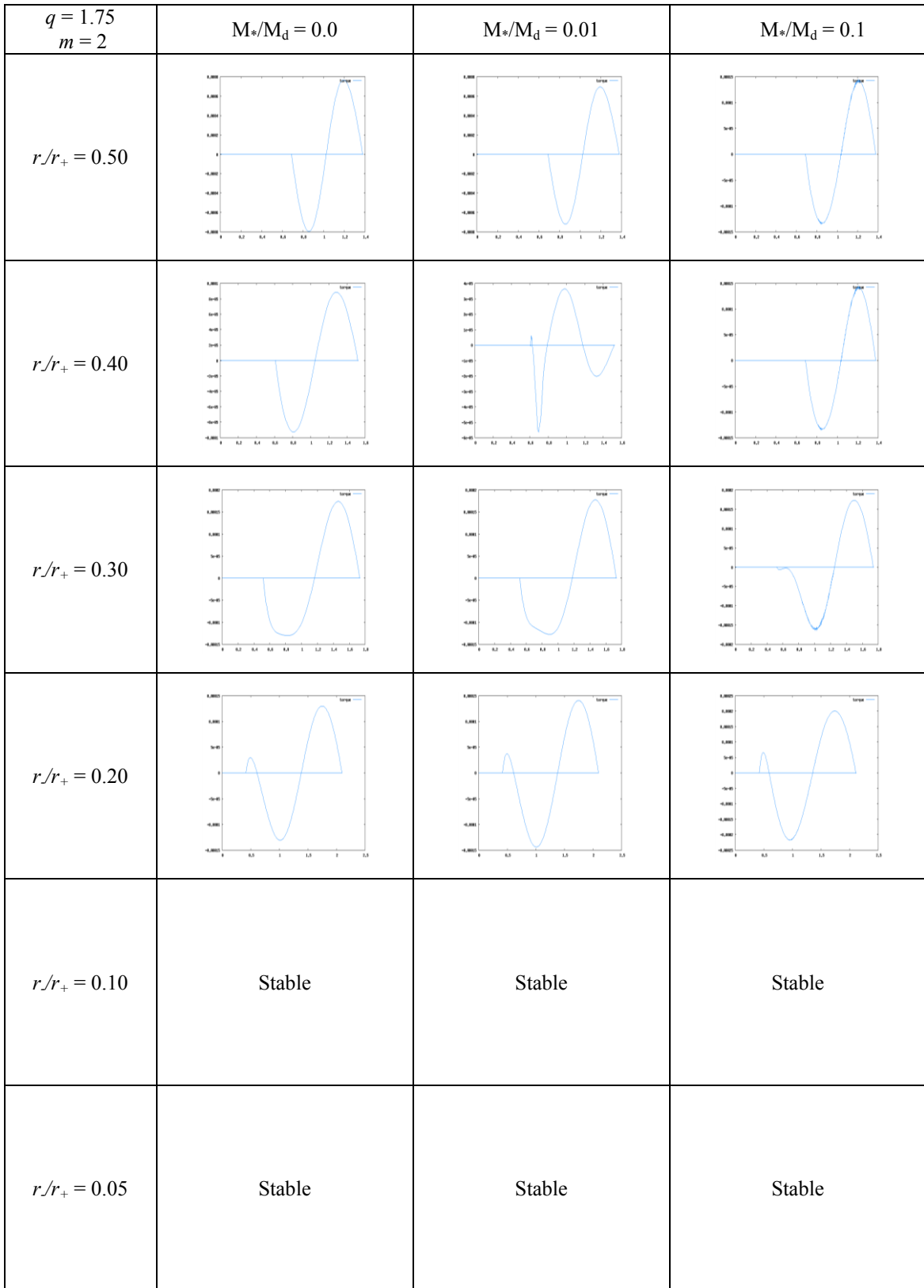


Fig. B.2.3.a. Self-gravitational torque for $q = 1.75$, $m = 2$

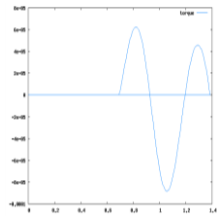
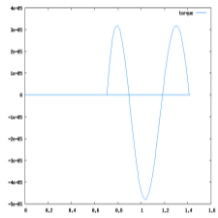
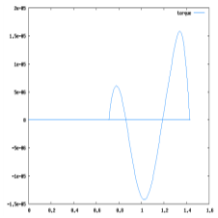
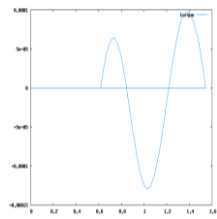
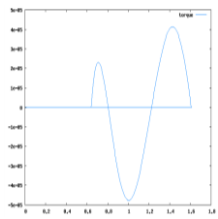
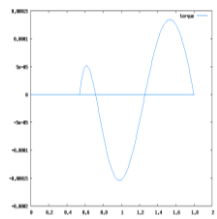
$q = 1.75$ $m = 2$	$M_*/M_d = 1.0$	$M_*/M_d = 5.0$	$M_*/M_d = 10.0$
$r/r_+ = 0.50$			
$r/r_+ = 0.40$			Stable
$r/r_+ = 0.30$		Stable	Stable
$r/r_+ = 0.20$	Stable	Stable	Stable
$r/r_+ = 0.10$	Stable	Stable	Stable
$r/r_+ = 0.05$	Stable	Stable	Stable

Fig. B.2.3.b. Self-gravitational torque for $q = 1.75$, $m = 2$

$q = 1.75$ $m = 2$	$M_*/M_d = 25.0$	$M_*/M_d = 50.0$	Non-self-gravitating
$r/r_+ = 0.50$	Stable	Stable	
$r/r_+ = 0.40$	Stable	Stable	
$r/r_+ = 0.30$	Stable	Stable	
$r/r_+ = 0.20$	Stable	Stable	
$r/r_+ = 0.10$	Stable	Stable	
$r/r_+ = 0.05$	Stable	Stable	

Fig. B.2.3.c. Self-gravitational torque for $q = 1.75$, $m = 2$

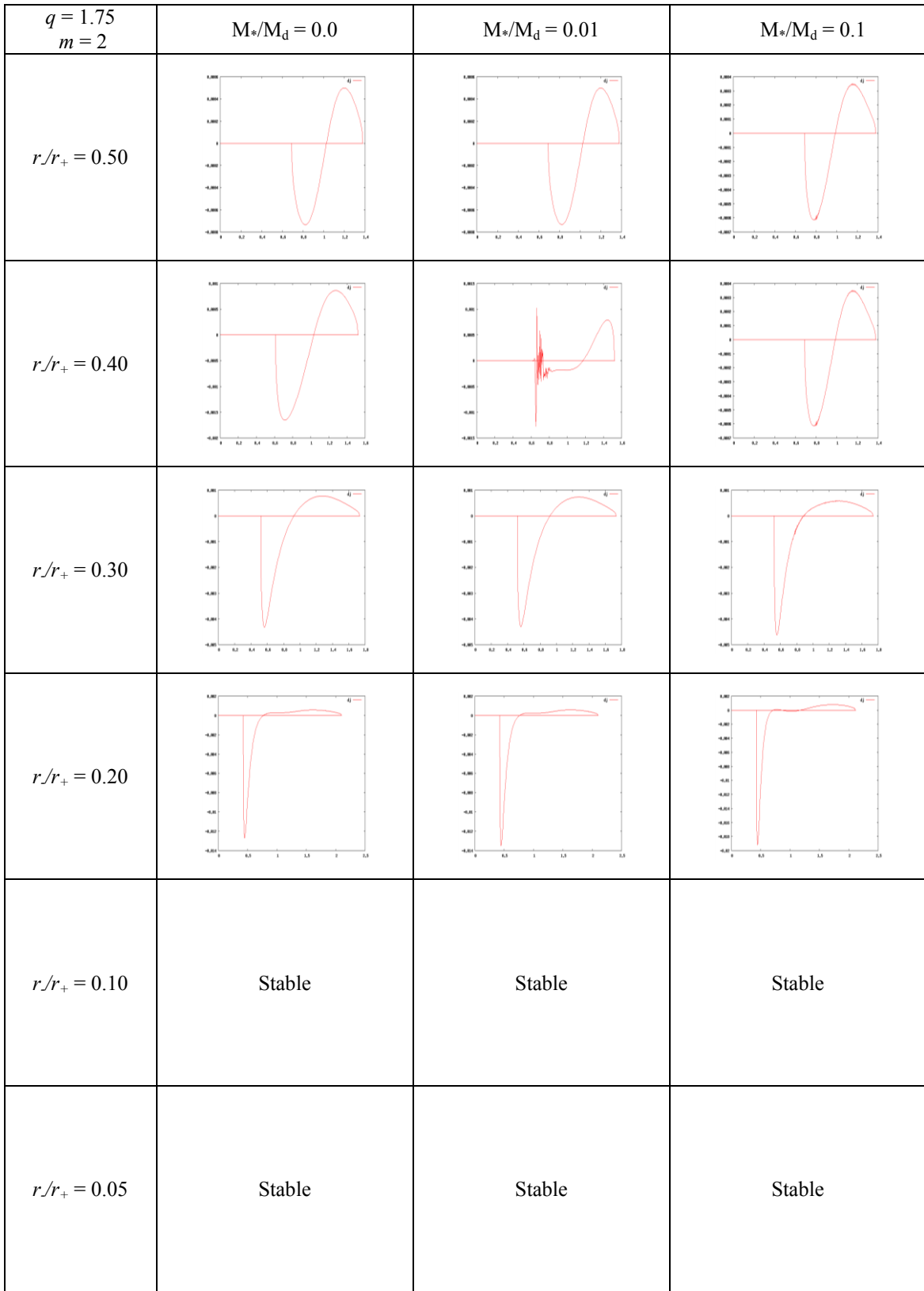


Fig. B.2.4.a. Perturbed angular momentum for $q = 1.75$, $m = 2$

$q = 1.75$ $m = 2$	$M_*/M_d = 1.0$	$M_*/M_d = 5.0$	$M_*/M_d = 10.0$
$r/r_+ = 0.50$			
$r/r_+ = 0.40$			
$r/r_+ = 0.30$		Stable	Stable
$r/r_+ = 0.20$	Stable	Stable	Stable
$r/r_+ = 0.10$	Stable	Stable	Stable
$r/r_+ = 0.05$	Stable	Stable	Stable

Fig. B.2.4.b. Perturbed angular momentum for $q = 1.75$, $m = 2$

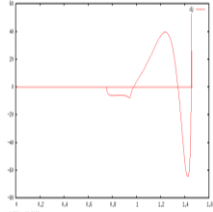
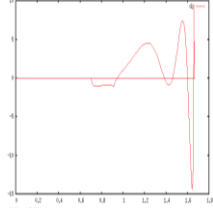
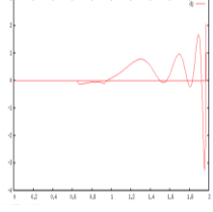
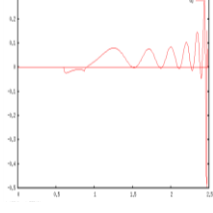
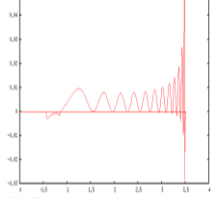
$q = 1.75$ $m = 2$	$M_*/M_d = 25.0$	$M_*/M_d = 50.0$	Non-self-gravitating
$r/r_+ = 0.50$	Stable	Stable	
$r/r_+ = 0.40$	Stable	Stable	
$r/r_+ = 0.30$	Stable	Stable	
$r/r_+ = 0.20$	Stable	Stable	
$r/r_+ = 0.10$	Stable	Stable	
$r/r_+ = 0.05$	Stable	Stable	

Fig. B.2.4.c. Perturbed angular momentum for $q = 1.75$, $m = 2$

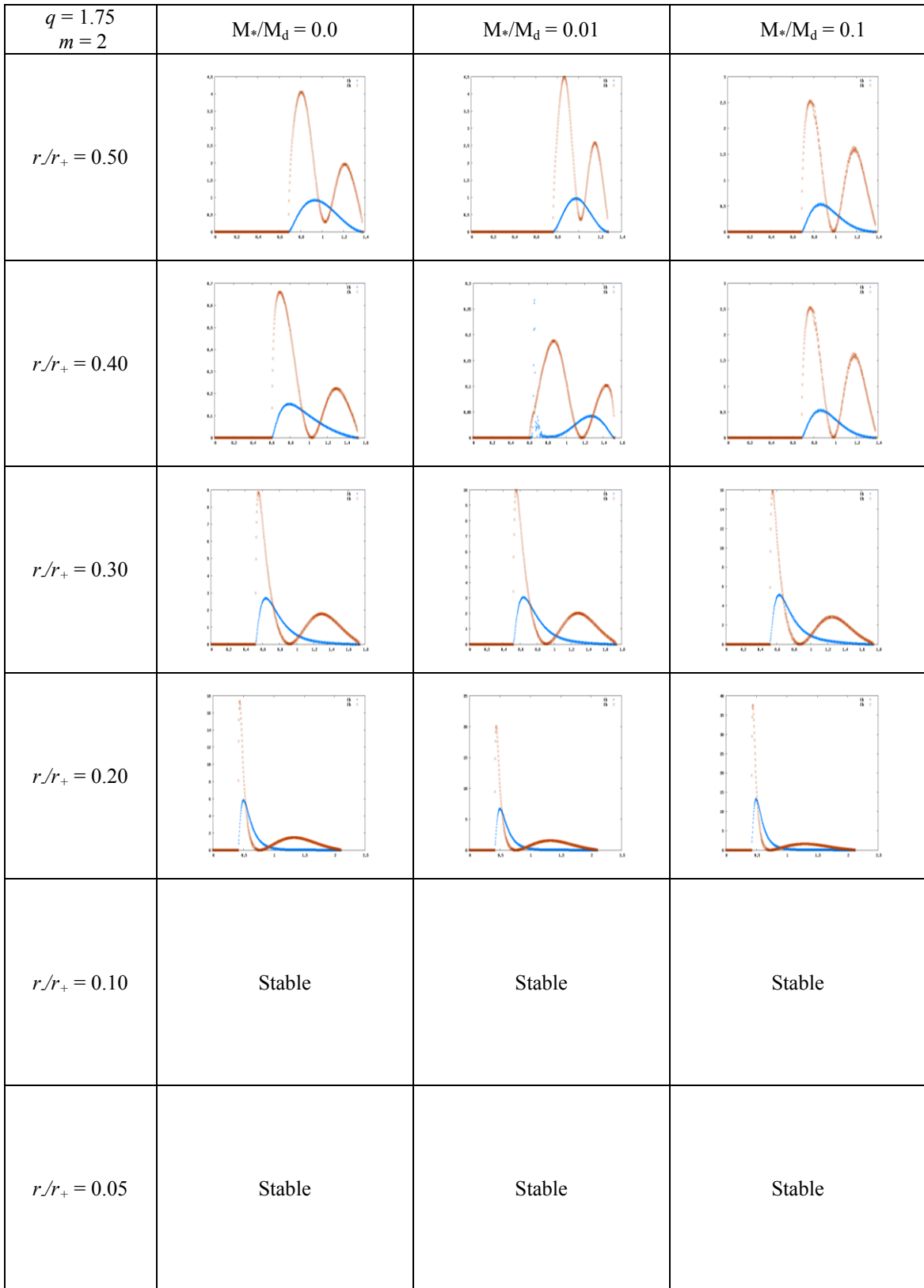


Fig. B.2.5.a. Work integrals for $q = 1.75$, $m = 2$

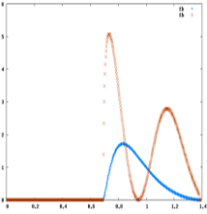
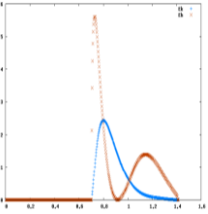
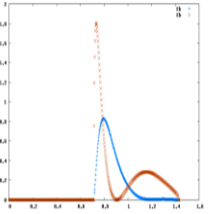
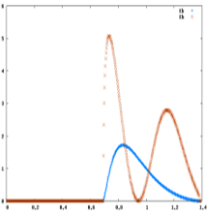
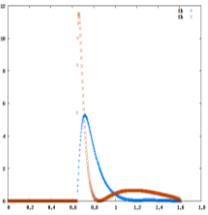
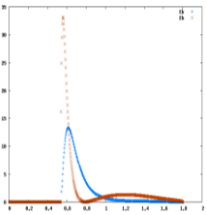
$q = 1.75$ $m = 2$	$M_*/M_d = 1.0$	$M_*/M_d = 5.0$	$M_*/M_d = 10.0$
$r/r_+ = 0.50$			
$r/r_+ = 0.40$			Stable
$r/r_+ = 0.30$		Stable	Stable
$r/r_+ = 0.20$	Stable	Stable	Stable
$r/r_+ = 0.10$	Stable	Stable	Stable
$r/r_+ = 0.05$	Stable	Stable	Stable

Fig. B.2.5.b. Work integrals for $q = 1.75$, $m = 2$

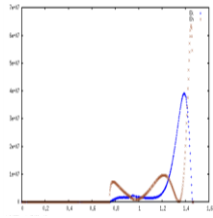
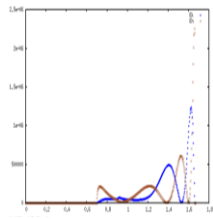
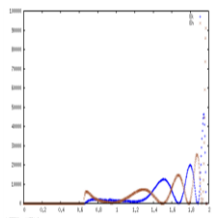
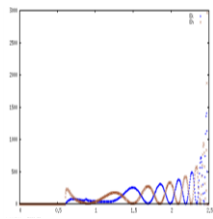
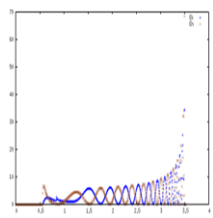
$q = 1.75$ $m = 2$	$M_*/M_d = 25.0$	$M_*/M_d = 50.0$	Non-self-gravitating
$r/r_+ = 0.50$	Stable	Stable	
$r/r_+ = 0.40$	Stable	Stable	
$r/r_+ = 0.30$	Stable	Stable	
$r/r_+ = 0.20$	Stable	Stable	
$r/r_+ = 0.10$	Stable	Stable	
$r/r_+ = 0.05$	Stable	Stable	

Fig. B.2.5.c. Work integrals for $q = 1.75$, $m = 2$
254

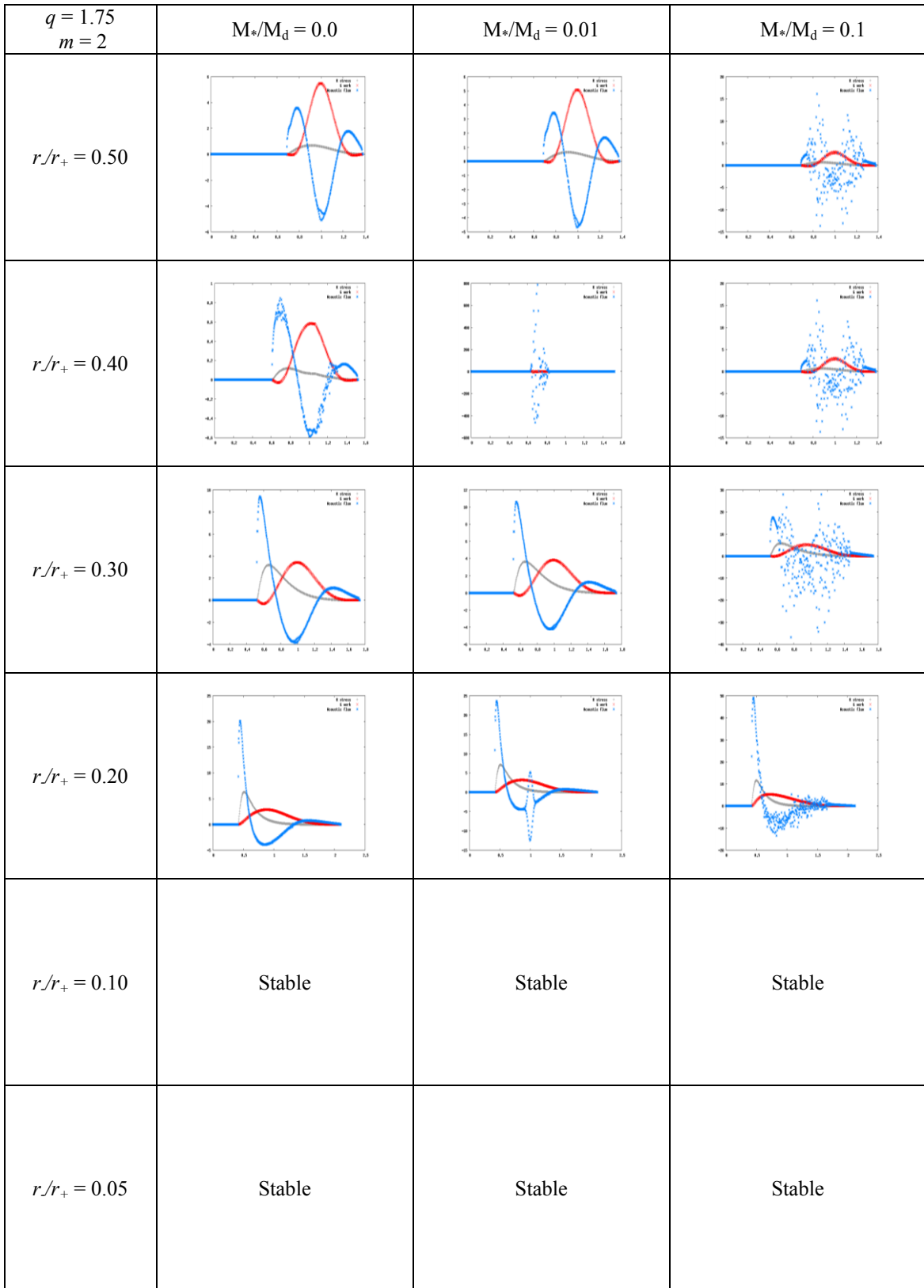


Fig. B.2.6.a. Stresses for $q = 1.75$, $m = 2$

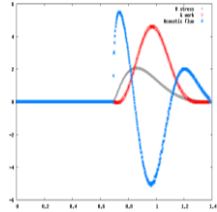
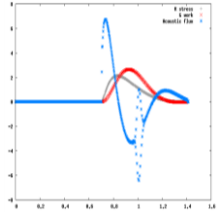
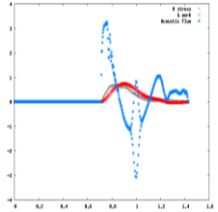
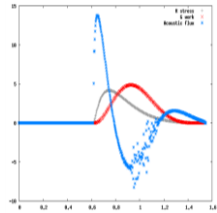
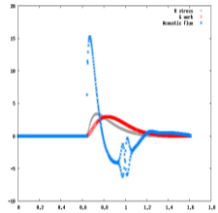
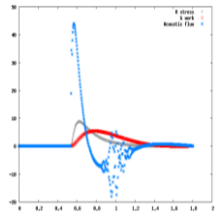
$q = 1.75$ $m = 2$	$M_*/M_d = 1.0$	$M_*/M_d = 5.0$	$M_*/M_d = 10.0$
$r/r_+ = 0.50$			
$r/r_+ = 0.40$			Stable
$r/r_+ = 0.30$		Stable	Stable
$r/r_+ = 0.20$	Stable	Stable	Stable
$r/r_+ = 0.10$	Stable	Stable	Stable
$r/r_+ = 0.05$	Stable	Stable	Stable

Fig. B.2.6.b. Stresses for $q = 1.75$, $m = 2$

$q = 1.75$ $m = 2$	$M_*/M_d = 25.0$	$M_*/M_d = 50.0$	Non-self-gravitating
$r/r_+ = 0.50$	Stable	Stable	
$r/r_+ = 0.40$	Stable	Stable	
$r/r_+ = 0.30$	Stable	Stable	
$r/r_+ = 0.20$	Stable	Stable	
$r/r_+ = 0.10$	Stable	Stable	
$r/r_+ = 0.05$	Stable	Stable	

Fig. B.2.6.c. Stresses for $q = 1.75$, $m = 2$

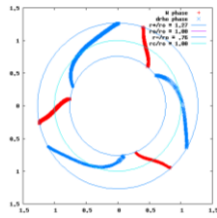
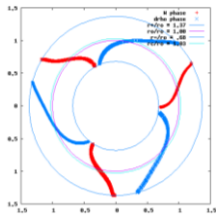
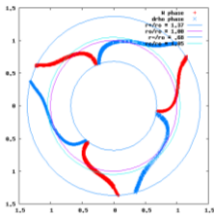
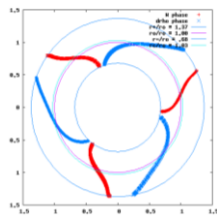
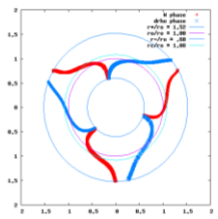
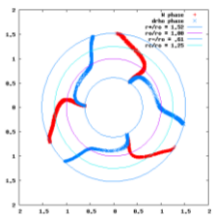
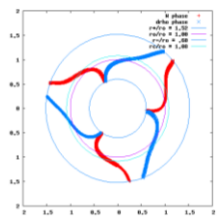
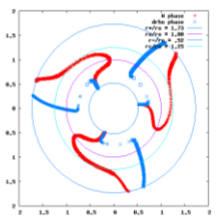
$q = 1.75$ $m = 3$	$M_*/M_d = 0.0$	$M_*/M_d = 0.01$	$M_*/M_d = 0.1$
$r/r_+ = 0.50$			
$r/r_+ = 0.40$			
$r/r_+ = 0.30$		Stable	
$r/r_+ = 0.20$	Stable	Stable	Stable
$r/r_+ = 0.10$	Stable	Stable	Stable
$r/r_+ = 0.05$	Stable	Stable	Stable

Fig. B.3.1 a Eigenfunction phases for $q = 1.75$, $m = 3$.

$q = 1.75$ $m = 3$	$M_*/M_d = 1.0$	$M_*/M_d = 5.0$	$M_*/M_d = 10.0$
$r/r_+ = 0.50$			
$r/r_+ = 0.40$		Stable	Stable
$r/r_+ = 0.30$	Stable	Stable	Stable
$r/r_+ = 0.20$	Stable	Stable	Stable
$r/r_+ = 0.10$	Stable	Stable	Stable
$r/r_+ = 0.05$	Stable	Stable	Stable

Fig. B.3.1.b. Eigenfunction phases for $q = 1.75$, $m = 3$.

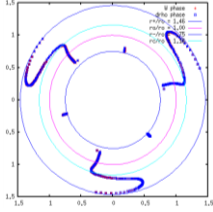
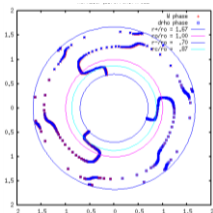
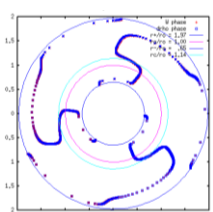
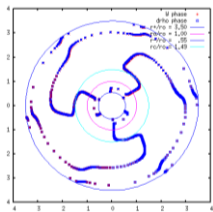
$q = 1.75$ $m = 3$	$M_*/M_d = 25.0$	$M_*/M_d = 50.0$	Non-self-gravitating
$r/r_+ = 0.50$	Stable	Stable	
$r/r_+ = 0.40$	Stable	Stable	
$r/r_+ = 0.30$	Stable	Stable	
$r/r_+ = 0.20$	Stable	Stable	Stable
$r/r_+ = 0.10$	Stable	Stable	
$r/r_+ = 0.05$	Stable	Stable	

Fig. B.3.1.c. Eigenfunction phases for $q = 1.75$, $m = 3$.

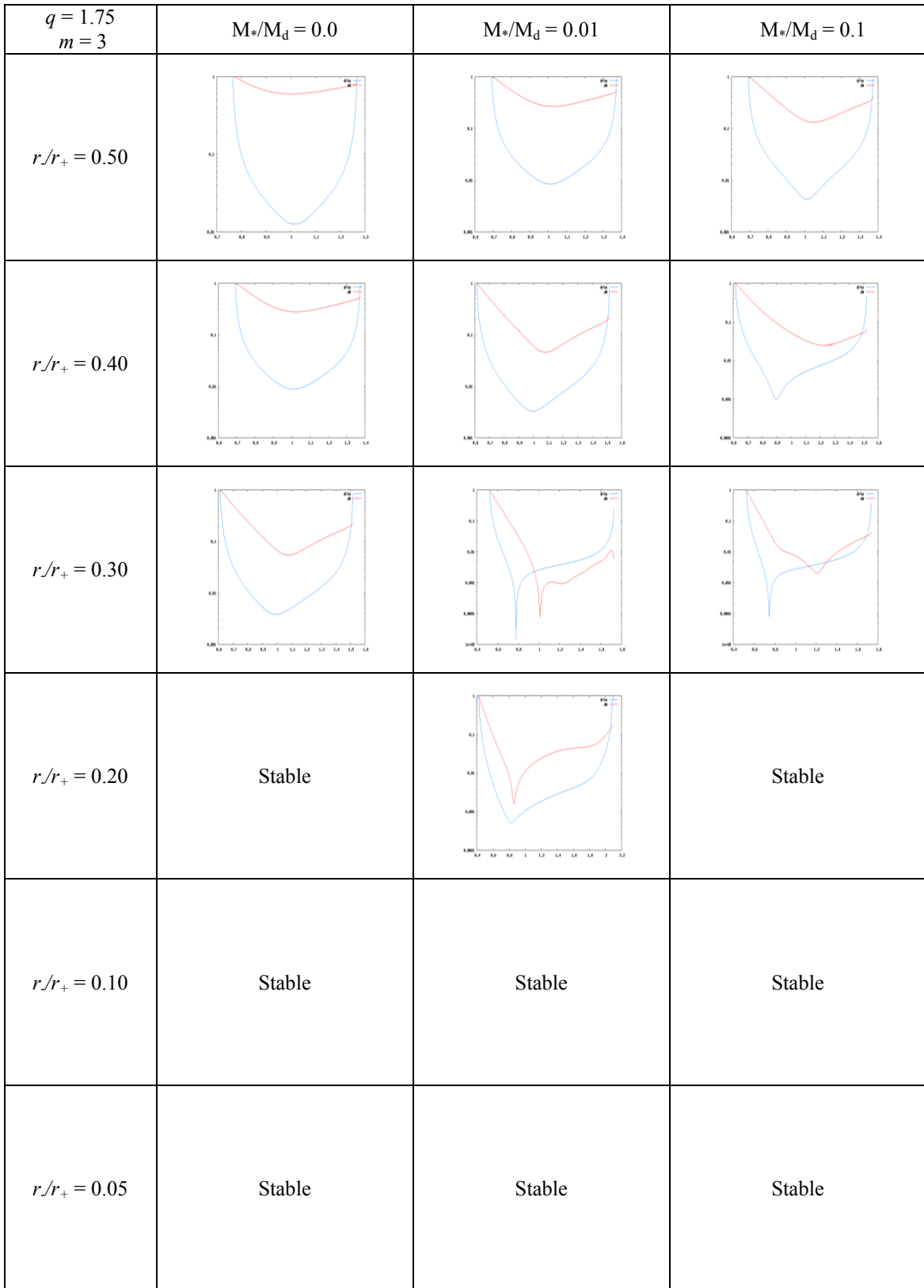


Fig. B.3.2.a. Eigenfunction amplitudes $|\delta\rho|/\rho$ and W for $q = 1.75$, $m = 3$.

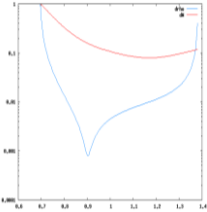
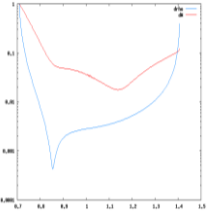
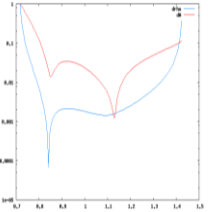
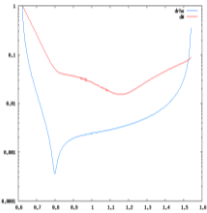
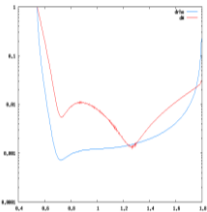
$q = 1.75$ $m = 3$	$M_*/M_d = 1.0$	$M_*/M_d = 5.0$	$M_*/M_d = 10.0$
$r/r_+ = 0.50$			
$r/r_+ = 0.40$		Stable	Stable
$r/r_+ = 0.30$		Stable	Stable
$r/r_+ = 0.20$	Stable	Stable	Stable
$r/r_+ = 0.10$	Stable	Stable	Stable
$r/r_+ = 0.05$	Stable	Stable	Stable

Fig. B.3.2.b. Eigenfunction amplitudes $|\delta\rho|/\rho$ and W for $q = 1.75$, $m = 3$.

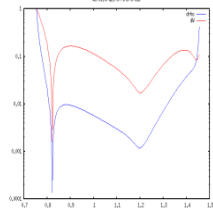
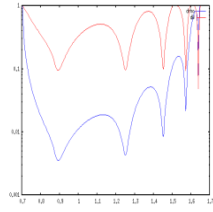
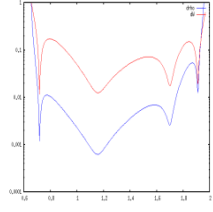
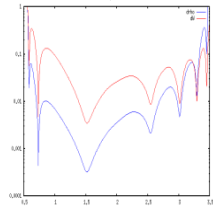
$q = 1.75$ $m = 3$	$M_*/M_d = 25.0$	$M_*/M_d = 50.0$	Non-self-gravitating
$r/r_+ = 0.50$	Stable	Stable	
$r/r_+ = 0.40$	Stable	Stable	
$r/r_+ = 0.30$	Stable	Stable	
$r/r_+ = 0.20$	Stable	Stable	Stable
$r/r_+ = 0.10$	Stable	Stable	
$r/r_+ = 0.05$	Stable	Stable	

Fig. B.3.2.c. Eigenfunction amplitudes $|\delta\rho|/\rho$ and W for $q = 1.75$, $m = 3$.

$q = 1.75$ $m = 3$	$M^*/M_d = 0.0$	$M^*/M_d = 0.01$	$M^*/M_d = 0.1$
$r/r_+ = 0.50$			
$r/r_+ = 0.40$			
$r/r_+ = 0.30$			
$r/r_+ = 0.20$	Stable		Stable
$r/r_+ = 0.10$	Stable	Stable	Stable
$r/r_+ = 0.05$	Stable	Stable	Stable

Fig. B.3.3.a. Self-gravitational torque for $q = 1.75$, $m = 3$.

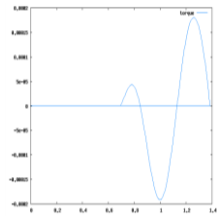
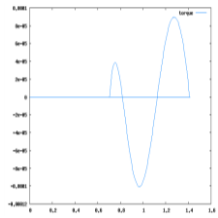
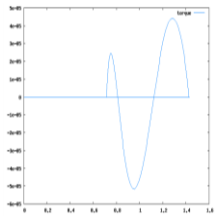
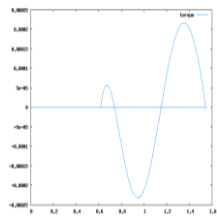
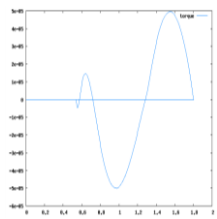
$q = 1.75$ $m = 3$	$M_*/M_d = 1.0$	$M_*/M_d = 5.0$	$M_*/M_d = 10.0$
$r/r_+ = 0.50$			
$r/r_+ = 0.40$		Stable	Stable
$r/r_+ = 0.30$		Stable	Stable
$r/r_+ = 0.20$	Stable	Stable	Stable
$r/r_+ = 0.10$	Stable	Stable	Stable
$r/r_+ = 0.05$	Stable	Stable	Stable

Fig. B.3.3.b. Self-gravitational torque for $q = 1.75$, $m = 3$.

$q = 1.75$ $m = 3$	$M_*/M_d = 25.0$	$M_*/M_d = 50.0$	Non-self-gravitating
$r/r_+ = 0.50$	Stable	Stable	
$r/r_+ = 0.40$	Stable	Stable	
$r/r_+ = 0.30$	Stable	Stable	
$r/r_+ = 0.20$	Stable	Stable	
$r/r_+ = 0.10$	Stable	Stable	
$r/r_+ = 0.05$	Stable	Stable	

Fig. B.3.3.c. Self-gravitational torque for $q = 1.75$, $m = 3$.

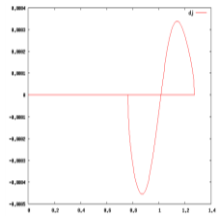
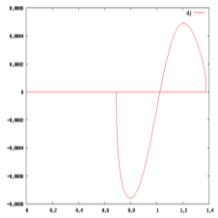
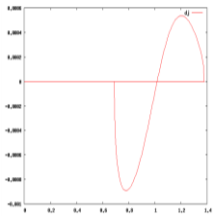
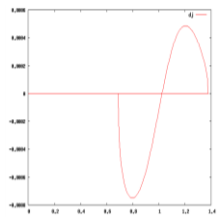
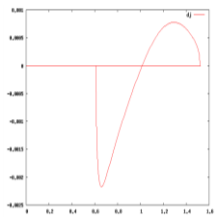
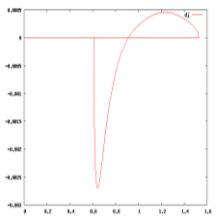
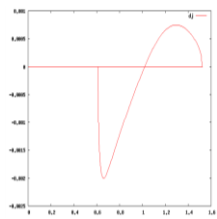
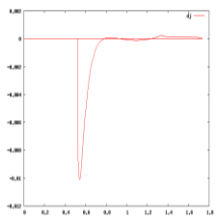
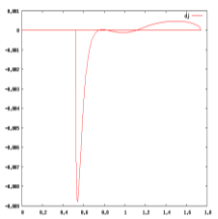
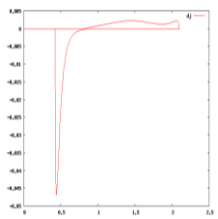
$q = 1.75$ $m = 3$	$M^*/M_d = 0.0$	$M^*/M_d = 0.01$	$M^*/M_d = 0.1$
$r/r_+ = 0.50$			
$r/r_+ = 0.40$			
$r/r_+ = 0.30$			
$r/r_+ = 0.20$	Stable		Stable
$r/r_+ = 0.10$	Stable	Stable	Stable
$r/r_+ = 0.05$	Stable	Stable	Stable

Fig. B.3.4 a Perturbed angular momentum for $q = 1.75$, $m = 3$.

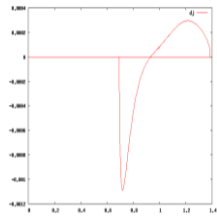
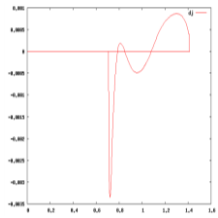
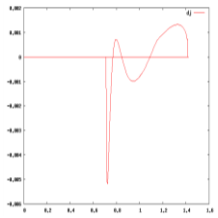
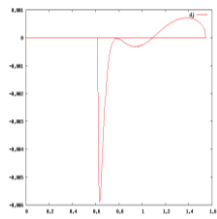
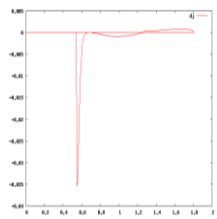
$q = 1.75$ $m = 3$	$M_*/M_d = 1.0$	$M_*/M_d = 5.0$	$M_*/M_d = 10.0$
$r/r_+ = 0.50$			
$r/r_+ = 0.40$		Stable	Stable
$r/r_+ = 0.30$		Stable	Stable
$r/r_+ = 0.20$	Stable	Stable	Stable
$r/r_+ = 0.10$	Stable	Stable	Stable
$r/r_+ = 0.05$	Stable	Stable	Stable

Fig. B.3.4.b. Perturbed angular momentum for $q = 1.75$, $m = 3$.

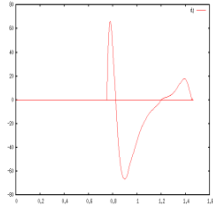
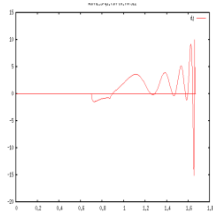
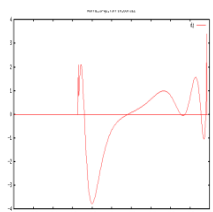
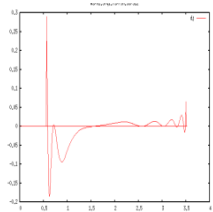
$q = 1.75$ $m = 3$	$M_*/M_d = 25.0$	$M_*/M_d = 50.0$	Non-self-gravitating
$r/r_+ = 0.50$	Stable	Stable	
$r/r_+ = 0.40$	Stable	Stable	
$r/r_+ = 0.30$	Stable	Stable	
$r/r_+ = 0.20$	Stable	Stable	Stable
$r/r_+ = 0.10$	Stable	Stable	
$r/r_+ = 0.05$	Stable	Stable	

Fig. B.3.4.c. Perturbed angular momentum for $q = 1.75$, $m = 3$.

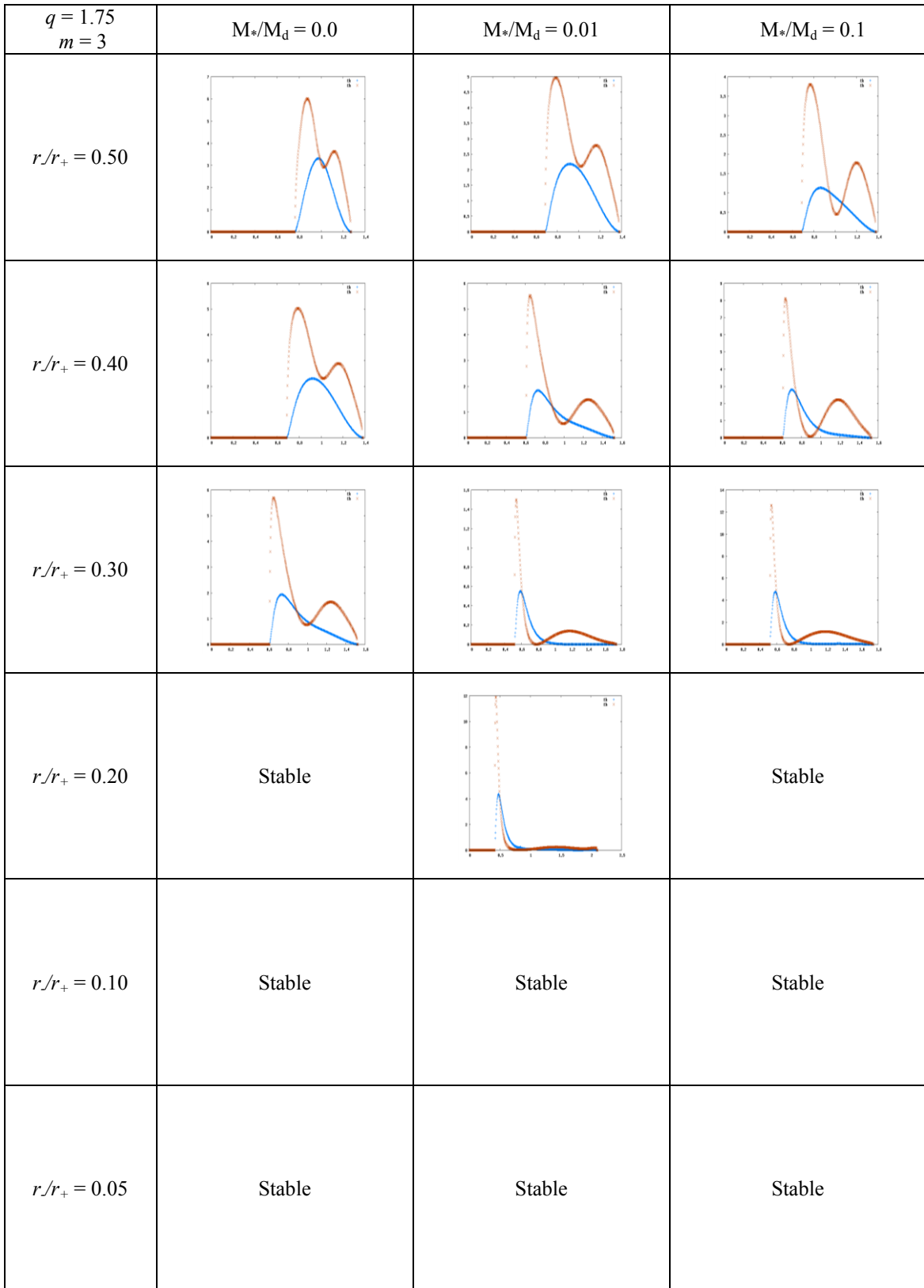


Fig. B.3.5.a. Work integrals for $q = 1.75$, $m = 3$.

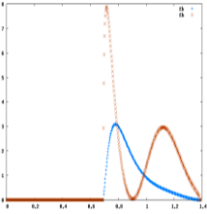
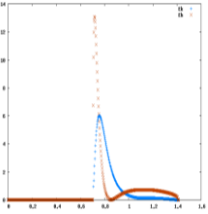
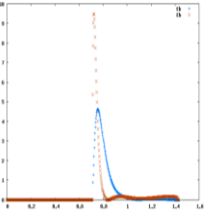
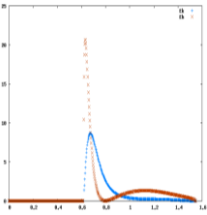
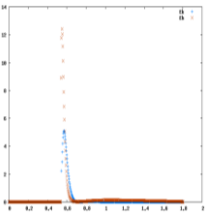
$q = 1.75$ $m = 3$	$M_*/M_d = 1.0$	$M_*/M_d = 5.0$	$M_*/M_d = 10.0$
$r/r_+ = 0.50$			
$r/r_+ = 0.40$		Stable	Stable
$r/r_+ = 0.30$		Stable	Stable
$r/r_+ = 0.20$	Stable	Stable	Stable
$r/r_+ = 0.10$	Stable	Stable	Stable
$r/r_+ = 0.05$	Stable	Stable	Stable

Fig. B.3.5.b. Work integrals for $q = 1.75$, $m = 3$.

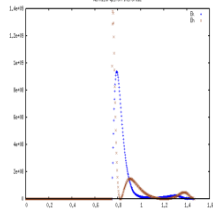
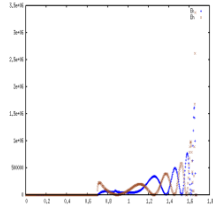
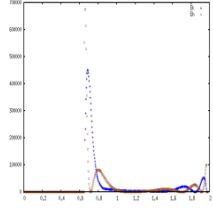
$q = 1.75$ $m = 3$	$M_*/M_d = 25.0$	$M_*/M_d = 50.0$	Non-self-gravitating
$r/r_+ = 0.50$	Stable	Stable	
$r/r_+ = 0.40$	Stable	Stable	
$r/r_+ = 0.30$	Stable	Stable	
$r/r_+ = 0.20$	Stable	Stable	Stable
$r/r_+ = 0.10$	Stable	Stable	Stable
$r/r_+ = 0.05$	Stable	Stable	

Fig. B.3.5.c. Work integrals for $q = 1.75$, $m = 3$.

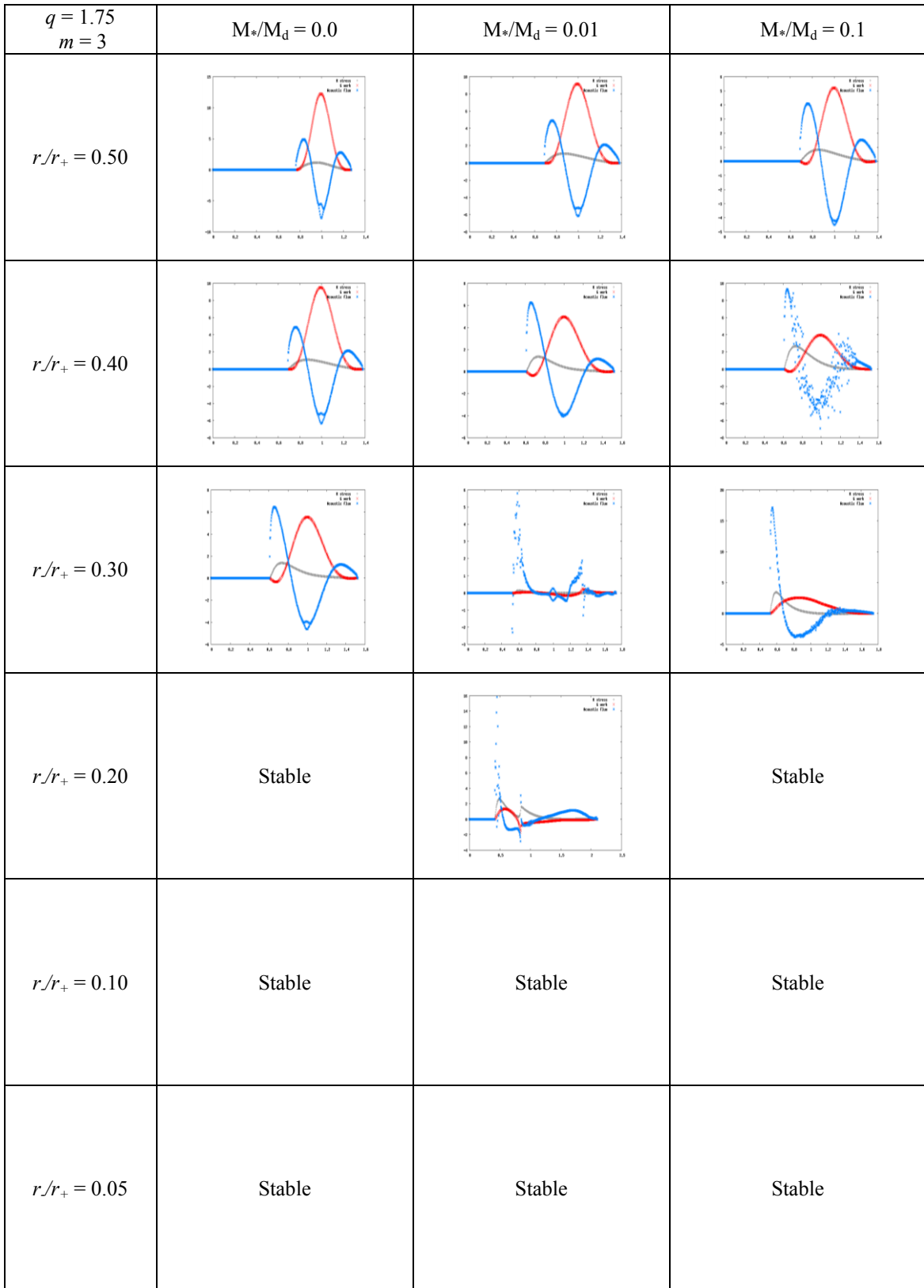


Fig. B.3.6.a. Stresses for $q = 1.75$, $m = 3$.

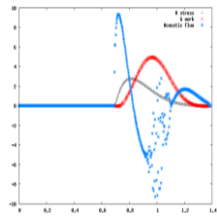
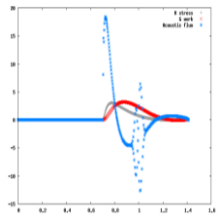
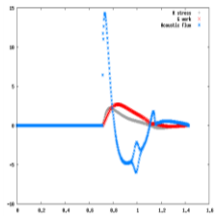
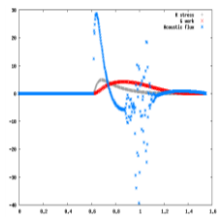
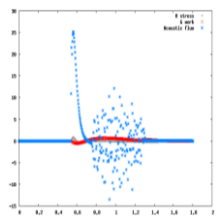
$q = 1.75$ $m = 3$	$M_*/M_d = 1.0$	$M_*/M_d = 5.0$	$M_*/M_d = 10.0$
$r/r_+ = 0.50$			
$r/r_+ = 0.40$		Stable	Stable
$r/r_+ = 0.30$		Stable	Stable
$r/r_+ = 0.20$	Stable	Stable	Stable
$r/r_+ = 0.10$	Stable	Stable	Stable
$r/r_+ = 0.05$	Stable	Stable	Stable

Fig. B.3.6.b. Stresses for $q = 1.75$, $m = 3$.

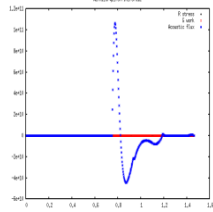
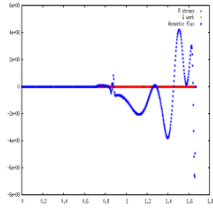
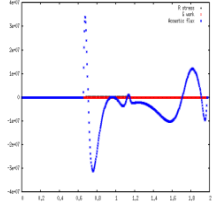
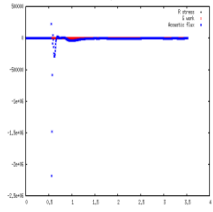
$q = 1.75$ $m = 3$	$M_*/M_d = 25.0$	$M_*/M_d = 50.0$	Non-self-gravitating
$r/r_+ = 0.50$	Stable	Stable	
$r/r_+ = 0.40$	Stable	Stable	
$r/r_+ = 0.30$	Stable	Stable	
$r/r_+ = 0.20$	Stable	Stable	Stable
$r/r_+ = 0.10$	Stable	Stable	
$r/r_+ = 0.05$	Stable	Stable	

Fig. B.3.6.c. Stresses for $q = 1.75$, $m = 3$.

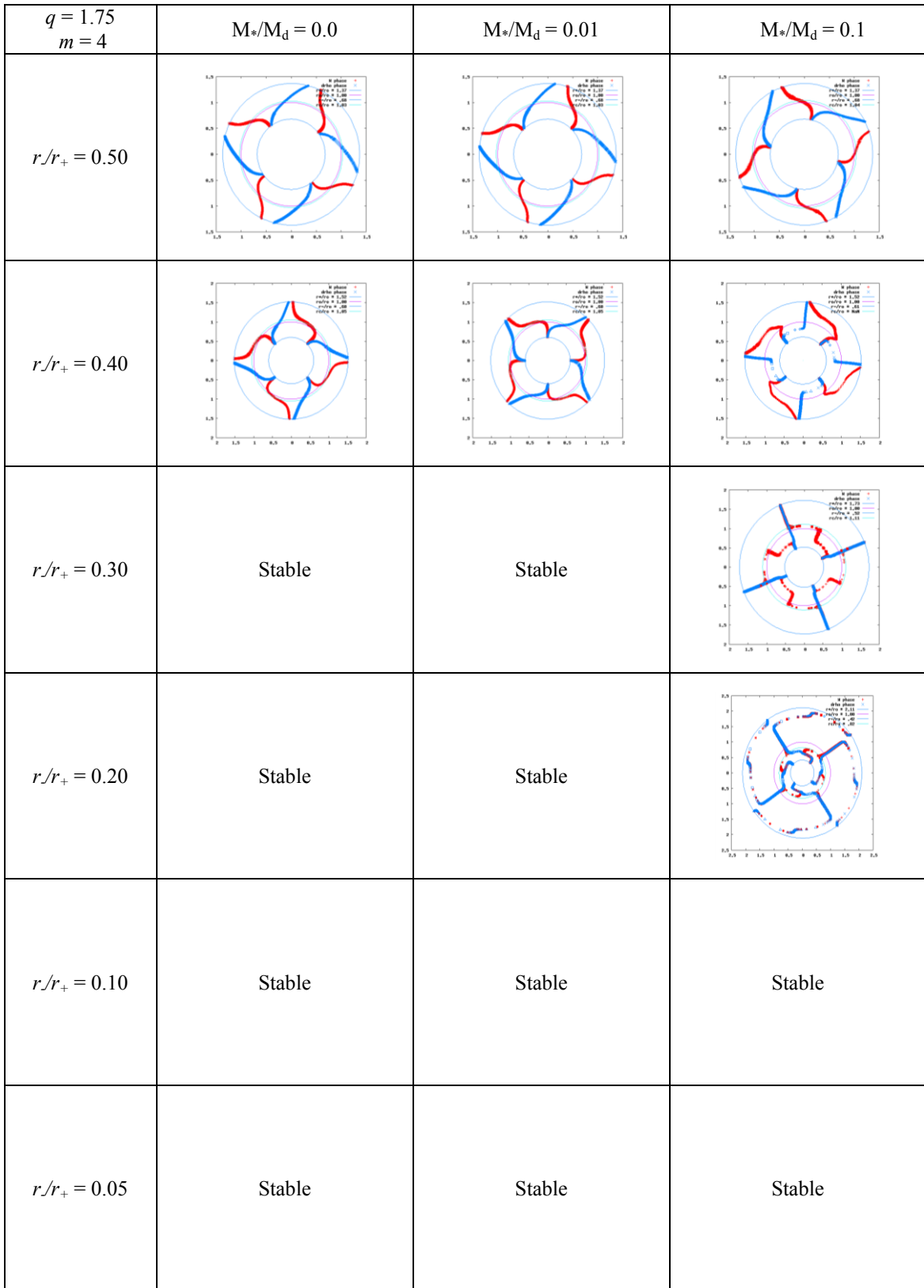


Fig. B.4.1 a Eigenfunction phases for $q = 1.75$, $m = 4$.

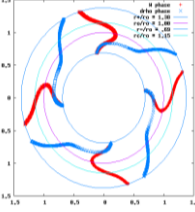
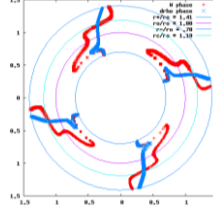
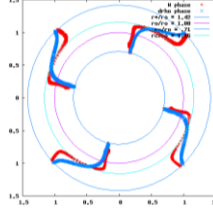
$q = 1.75$ $m = 4$	$M_*/M_d = 1.0$	$M_*/M_d = 5.0$	$M_*/M_d = 10.0$
$r/r_+ = 0.50$			
$r/r_+ = 0.40$	Stable	Stable	Stable
$r/r_+ = 0.30$	Stable	Stable	Stable
$r/r_+ = 0.20$	Stable	Stable	Stable
$r/r_+ = 0.10$	Stable	Stable	Stable
$r/r_+ = 0.05$	Stable	Stable	Stable

Fig. B.4.1.b. Eigenfunction phases for $q = 1.75$, $m = 4$.

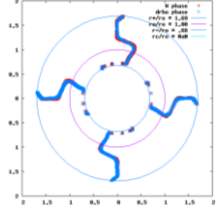
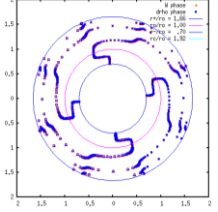
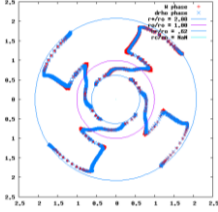
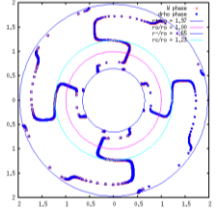
$q = 1.75$ $m = 4$	$M_*/M_d = 25.0$	$M_*/M_d = 50.0$	Non-self-gravitating
$r/r_+ = 0.50$	Stable	Stable	Unresolved
$r/r_+ = 0.40$	Stable		
$r/r_+ = 0.30$	Stable		
$r/r_+ = 0.20$	Stable	Stable	Stable
$r/r_+ = 0.10$	Stable	Stable	Stable
$r/r_+ = 0.05$	Stable	Stable	Stable

Fig. B.4.1.c. Eigenfunction phases for $q = 1.75$, $m = 4$.

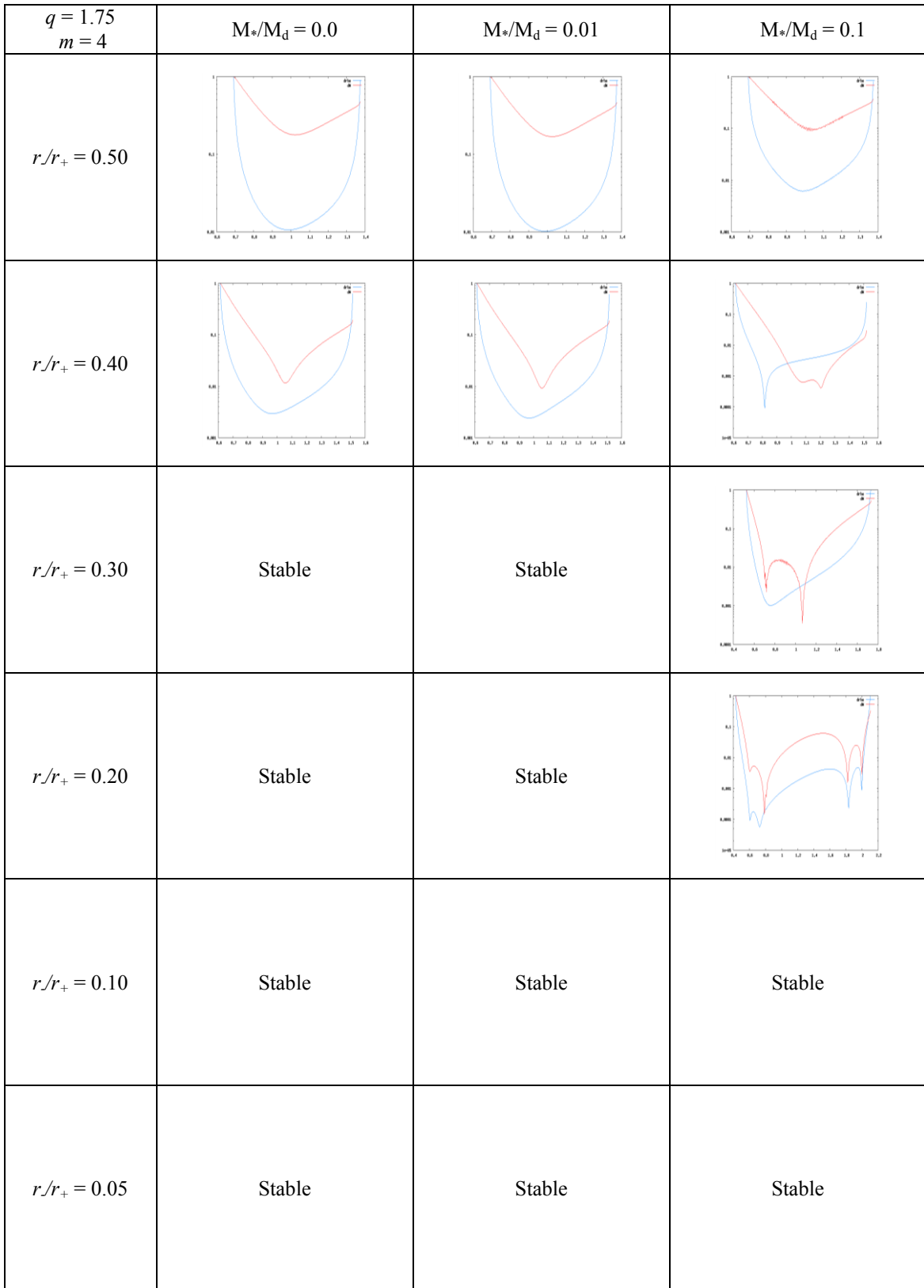


Fig. B.4.2.a. Eigenfunction amplitudes $|\delta\rho|/\rho$ and W for $q = 1.75$, $m = 4$.

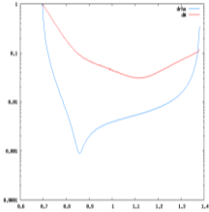
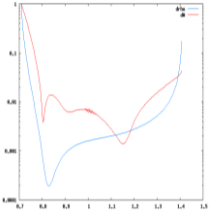
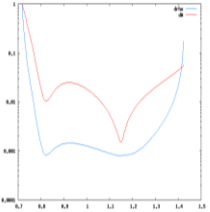
$q = 1.75$ $m = 4$	$M_*/M_d = 1.0$	$M_*/M_d = 5.0$	$M_*/M_d = 10.0$
$r/r_+ = 0.50$			
$r/r_+ = 0.40$	Stable	Stable	Stable
$r/r_+ = 0.30$	Stable	Stable	Stable
$r/r_+ = 0.20$	Stable	Stable	Stable
$r/r_+ = 0.10$	Stable	Stable	Stable
$r/r_+ = 0.05$	Stable	Stable	Stable

Fig. B.4.2.b. Eigenfunction amplitudes $|\delta\rho|/\rho$ and W for $q = 1.75$, $m = 4$.

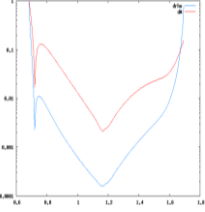
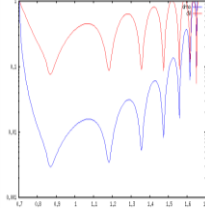
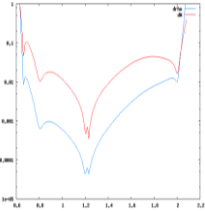
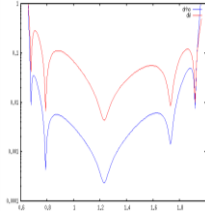
$q = 1.75$ $m = 4$	$M_*/M_d = 25.0$	$M_*/M_d = 50.0$	Non-self-gravitating
$r/r_+ = 0.50$	Stable	Stable	Unresolved
$r/r_+ = 0.40$	Stable		
$r/r_+ = 0.30$	Stable		
$r/r_+ = 0.20$	Stable	Stable	Stable
$r/r_+ = 0.10$	Stable	Stable	Stable
$r/r_+ = 0.05$	Stable	Stable	

Fig. B.4.2.c. Eigenfunction amplitudes $|\delta\rho|/\rho$ and W for $q = 1.75$, $m = 4$.

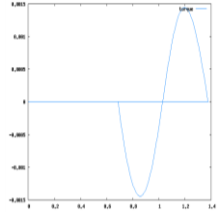
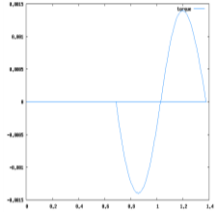
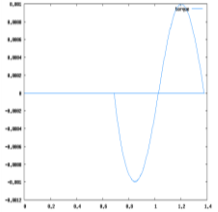
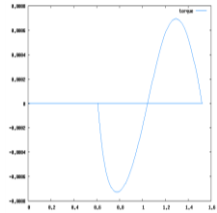
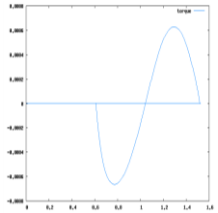
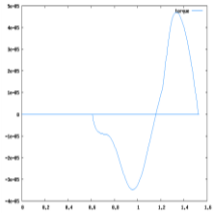
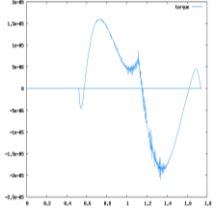
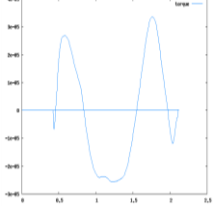
$q = 1.75$ $m = 4$	$M_*/M_d = 0.0$	$M_*/M_d = 0.01$	$M_*/M_d = 0.1$
$r/r_+ = 0.50$			
$r/r_+ = 0.40$			
$r/r_+ = 0.30$	Stable	Stable	
$r/r_+ = 0.20$	Stable	Stable	
$r/r_+ = 0.10$	Stable	Stable	Stable
$r/r_+ = 0.05$	Stable	Stable	Stable

Fig. B.4.3.a. Self-gravitational torque for $q = 1.75$, $m = 4$.

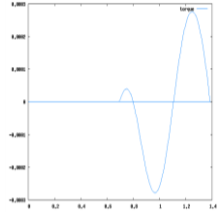
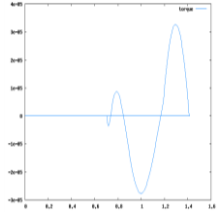
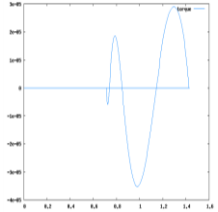
$q = 1.75$ $m = 4$	$M_*/M_d = 1.0$	$M_*/M_d = 5.0$	$M_*/M_d = 10.0$
$r/r_+ = 0.50$			
$r/r_+ = 0.40$	Stable	Stable	Stable
$r/r_+ = 0.30$	Stable	Stable	Stable
$r/r_+ = 0.20$	Stable	Stable	Stable
$r/r_+ = 0.10$	Stable	Stable	Stable
$r/r_+ = 0.05$	Stable	Stable	Stable

Fig. B.4.3.b. Self-gravitational torque for $q = 1.75$, $m = 4$.

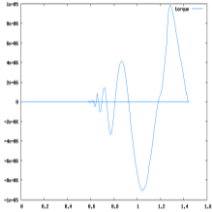
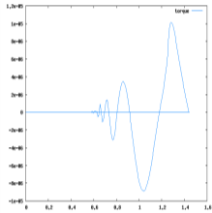
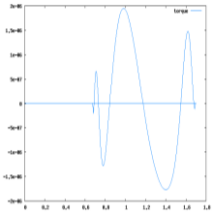
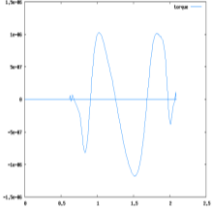
$q = 1.75$ $m = 4$	$M_*/M_d = 25.0$	$M_*/M_d = 50.0$	Non-self-gravitating
$r/r_+ = 0.50$		Stable	
$r/r_+ = 0.40$			
$r/r_+ = 0.30$	Stable		
$r/r_+ = 0.20$	Stable	Stable	
$r/r_+ = 0.10$	Stable	Stable	
$r/r_+ = 0.05$	Stable	Stable	

Fig. B.4.3.c. Self-gravitational torque for $q = 1.75$, $m = 4$.

$q = 1.75$ $m = 4$	$M^*/M_d = 0.0$	$M^*/M_d = 0.01$	$M^*/M_d = 0.1$
$r/r_+ = 0.50$			
$r/r_+ = 0.40$			
$r/r_+ = 0.30$	Stable	Stable	
$r/r_+ = 0.20$	Stable	Stable	
$r/r_+ = 0.10$	Stable	Stable	Stable
$r/r_+ = 0.05$	Stable	Stable	Stable

Fig. B.4.4 a Perturbed angular momentum for $q = 1.75$, $m = 4$.

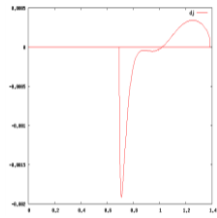
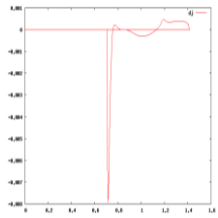
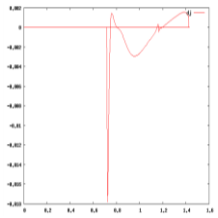
$q = 1.75$ $m = 4$	$M_*/M_d = 1.0$	$M_*/M_d = 5.0$	$M_*/M_d = 10.0$
$r/r_+ = 0.50$			
$r/r_+ = 0.40$	Stable	Stable	Stable
$r/r_+ = 0.30$	Stable	Stable	Stable
$r/r_+ = 0.20$	Stable	Stable	Stable
$r/r_+ = 0.10$	Stable	Stable	Stable
$r/r_+ = 0.05$	Stable	Stable	Stable

Fig. B.4.4.b. Perturbed angular momentum for $q = 1.75$, $m = 4$.

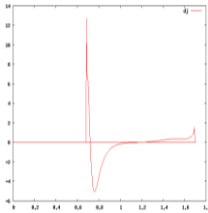
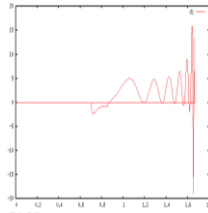
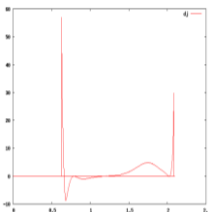
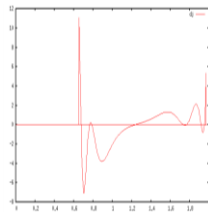
$q = 1.75$ $m = 4$	$M_*/M_d = 25.0$	$M_*/M_d = 50.0$	Non-self-gravitating
$r/r_+ = 0.50$	Stable	Stable	Unresolved
$r/r_+ = 0.40$	Stable		
$r/r_+ = 0.30$	Stable		
$r/r_+ = 0.20$	Stable	Stable	Stable
$r/r_+ = 0.10$	Stable	Stable	Stable
$r/r_+ = 0.05$	Stable	Stable	

Fig. B.4.4.c. Perturbed angular momentum for $q = 1.75$, $m = 4$.

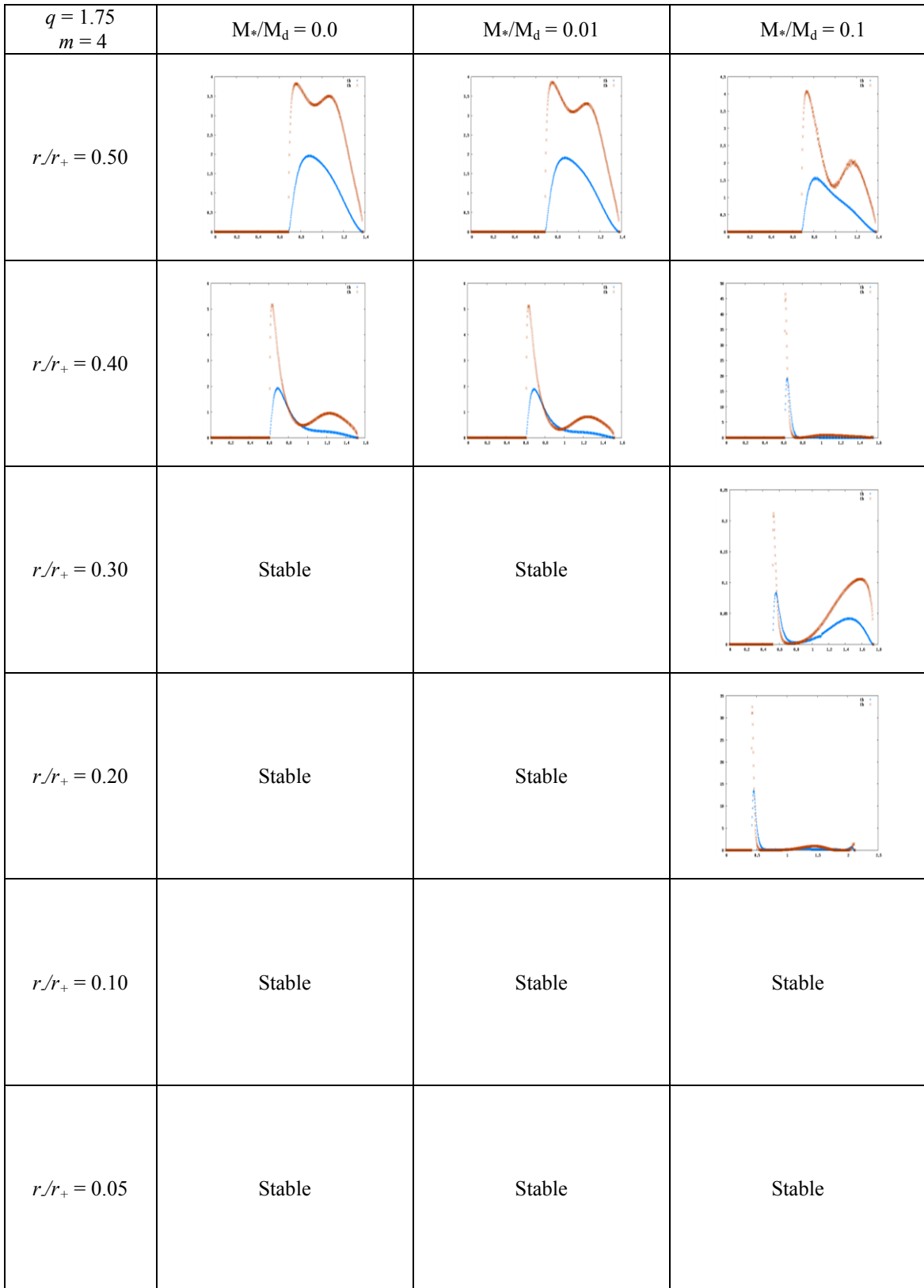


Fig. B.4.5.a. Work integrals for $q = 1.75$, $m = 4$.

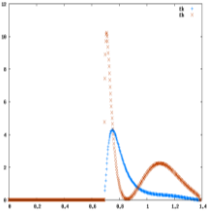
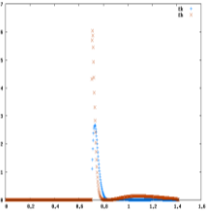
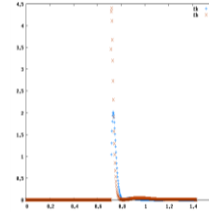
$q = 1.75$ $m = 4$	$M_*/M_d = 1.0$	$M_*/M_d = 5.0$	$M_*/M_d = 10.0$
$r/r_+ = 0.50$			
$r/r_+ = 0.40$	Stable	Stable	Stable
$r/r_+ = 0.30$	Stable	Stable	Stable
$r/r_+ = 0.20$	Stable	Stable	Stable
$r/r_+ = 0.10$	Stable	Stable	Stable
$r/r_+ = 0.05$	Stable	Stable	Stable

Fig. B.4.5.b. Work integrals for $q = 1.75$, $m = 4$.

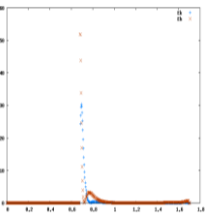
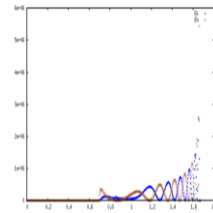
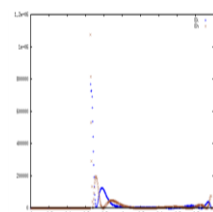
$q = 1.75$ $m = 4$	$M_*/M_d = 25.0$	$M_*/M_d = 50.0$	Non-self-gravitating
$r/r_+ = 0.50$	Stable	Stable	Unresolved
$r/r_+ = 0.40$	Stable		
$r/r_+ = 0.30$	Stable	Stable	
$r/r_+ = 0.20$	Stable	Stable	Stable
$r/r_+ = 0.10$	Stable	Stable	Stable
$r/r_+ = 0.05$	Stable	Stable	

Fig. B.4.5 c Work integrals for $q = 1.75$, $m = 4$.

$q = 1.75$ $m = 4$	$M_*/M_d = 0.0$	$M_*/M_d = 0.01$	$M_*/M_d = 0.1$
$r/r_+ = 0.50$			
$r/r_+ = 0.40$			
$r/r_+ = 0.30$	Stable	Stable	
$r/r_+ = 0.20$	Stable	Stable	
$r/r_+ = 0.10$	Stable	Stable	Stable
$r/r_+ = 0.05$	Stable	Stable	Stable

Fig. B.4.6.a. Stresses for $q = 1.75$, $m = 4$.

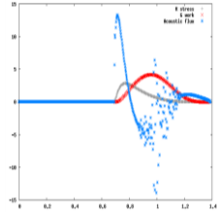
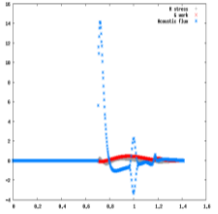
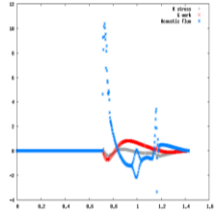
$q = 1.75$ $m = 4$	$M_*/M_d = 1.0$	$M_*/M_d = 5.0$	$M_*/M_d = 10.0$
$r/r_+ = 0.50$			
$r/r_+ = 0.40$	Stable	Stable	Stable
$r/r_+ = 0.30$	Stable	Stable	Stable
$r/r_+ = 0.20$	Stable	Stable	Stable
$r/r_+ = 0.10$	Stable	Stable	Stable
$r/r_+ = 0.05$	Stable	Stable	Stable

Fig. B.4.6.b. Stresses for $q = 1.75$, $m = 4$.

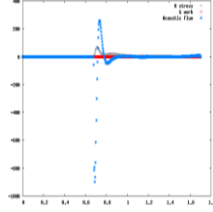
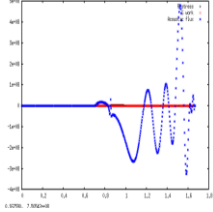
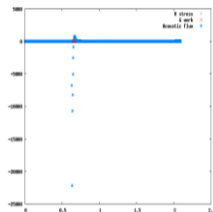
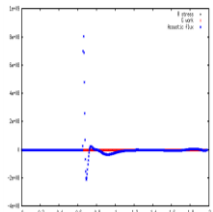
$q = 1.75$ $m = 4$	$M_*/M_d = 25.0$	$M_*/M_d = 50.0$	Non-self-gravitating
$r/r_+ = 0.50$	Stable	Stable	Unresolved
$r/r_+ = 0.40$	Stable		
$r/r_+ = 0.30$	Stable		
$r/r_+ = 0.20$	Stable	Stable	Stable
$r/r_+ = 0.10$	Stable	Stable	Stable
$r/r_+ = 0.05$	Stable	Stable	

Fig. B.4.6.c. Stresses for $q = 1.75$, $m = 4$.

APPENDIX C

PLOTS FOR SELECTED $q = 2.0$ MODELS

Appendix B contains a sequence of model plots for $q = 2.0$ models, including $M_*/M_d = 0.0, 0.01, 0.1, 1.0, 5.0, 10.0, 25.0$ and 50.0 . The column to the right of the $M_*/M_d = 50.0$ column contains non-self-gravitating models. In general, figures labeled "a" contain plots for $M_*/M_d = 0.0, 0.01$ and 0.1 ; figures labeled "b" contain plots for $M_*/M_d = 1.0, 5.0$ and 10.0 ; and figures labeled "c" contain plots for $M_*/M_d = 25.0, 50.0$ and non-self-gravitating models. For each of these values of M_*/M_d , we include plots for models for $r./r_+ = 0.05, 0.10, 0.20, 0.30, 0.40$ and 0.50 . All radii depicted in the plots are normalized by R_0 . Stable and unresolved models are labeled as such. All of the functions plotted in the appendices are defined identically to similar plots found in the body of the dissertation.

Please refer to the beginning of Appendix A for a description of the figure numbering system as well as descriptions of the individual functions plotted. Note there are no plots shown for self-gravity torque in the non-self-gravity column, since it is zero by definition for those models. Also, there are typically no non-self-gravitating models calculated for $r./r_+ = 0.05$ due to resolution issues.

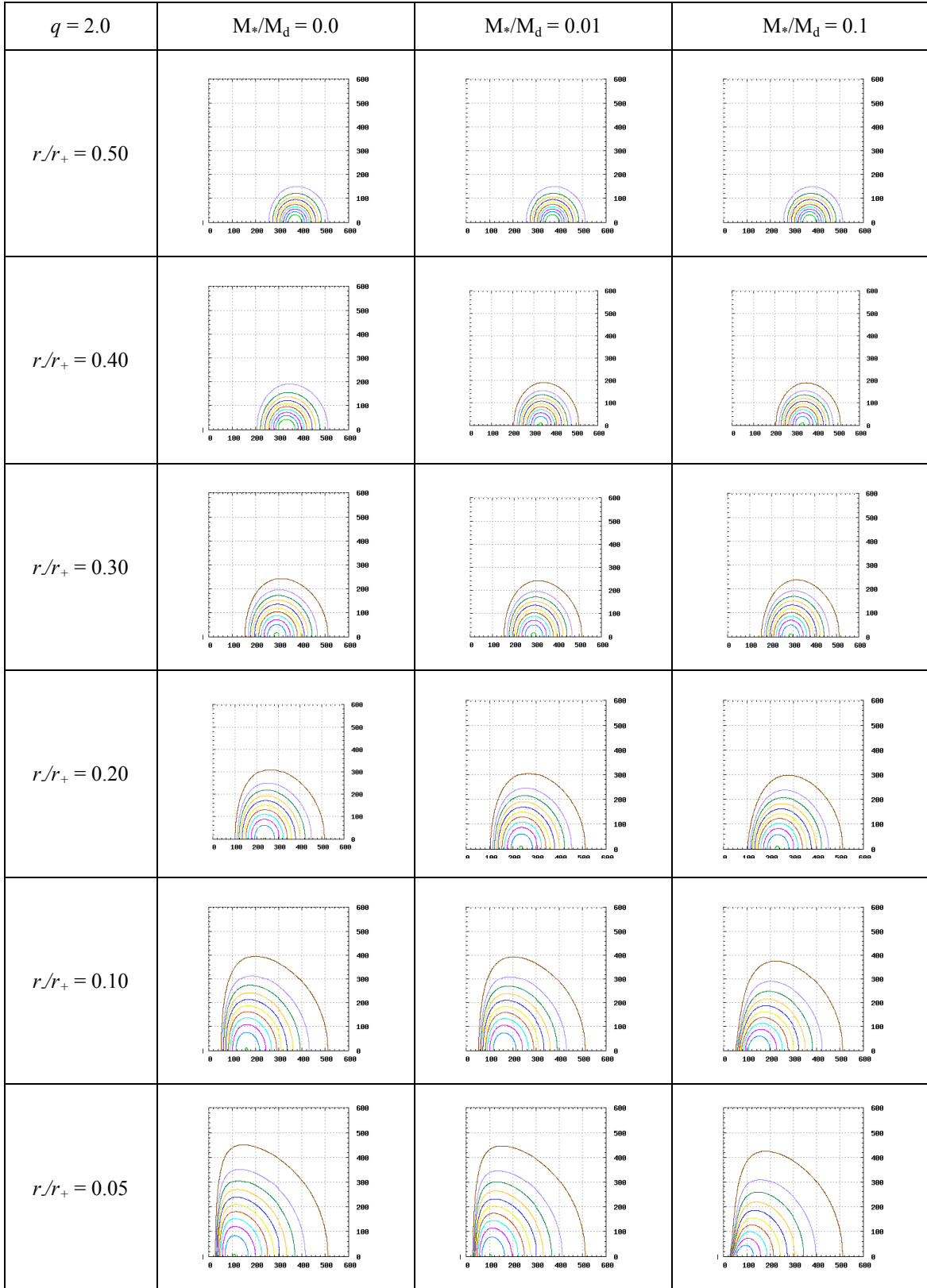


Fig. C.1.0.a. Equilibrium mass density contour plots of meridional slices for $q = 2.0$.

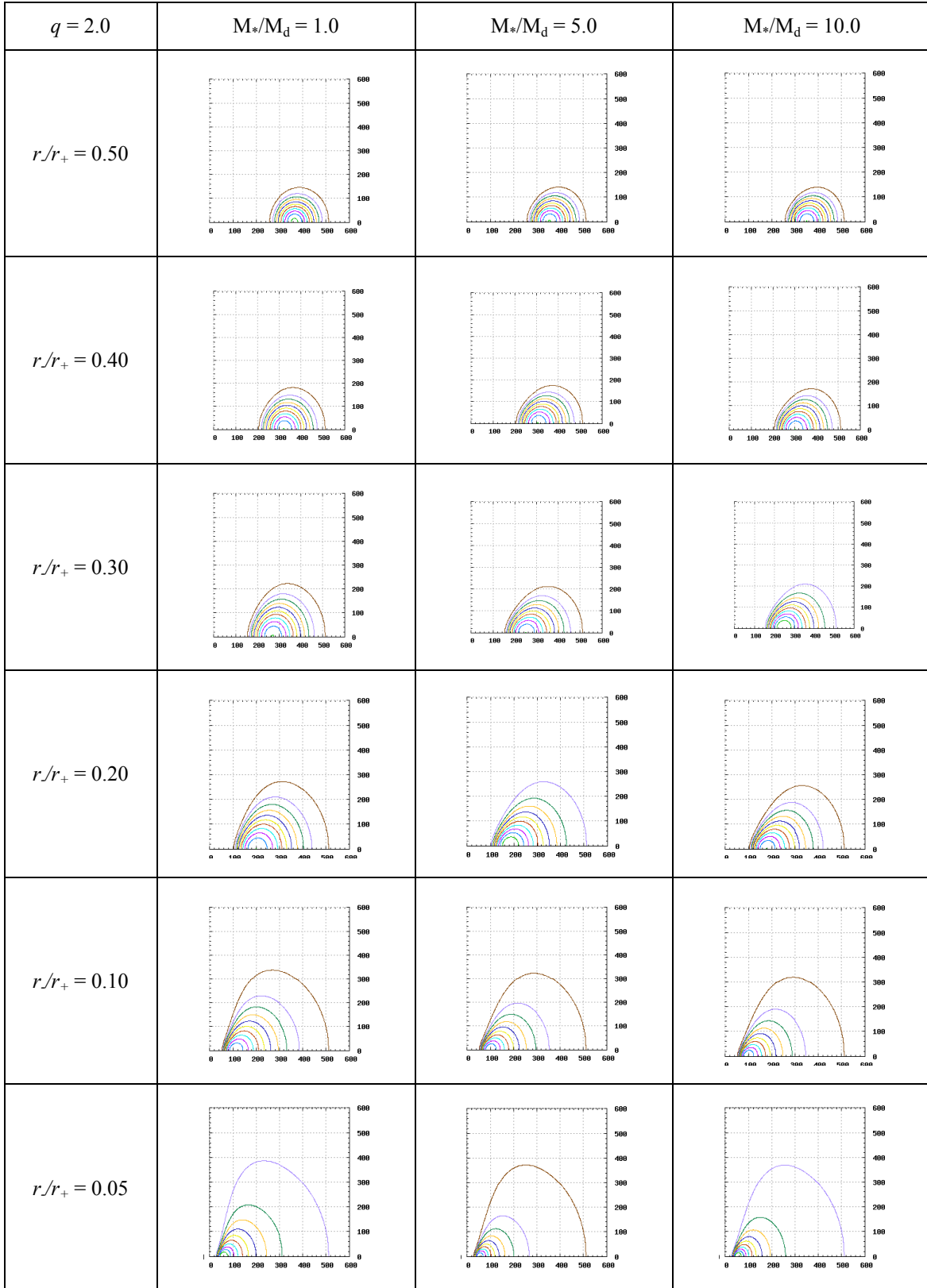


Fig. C.1.0.b. Equilibrium mass density contours of meridional slices for $q = 2.0$.

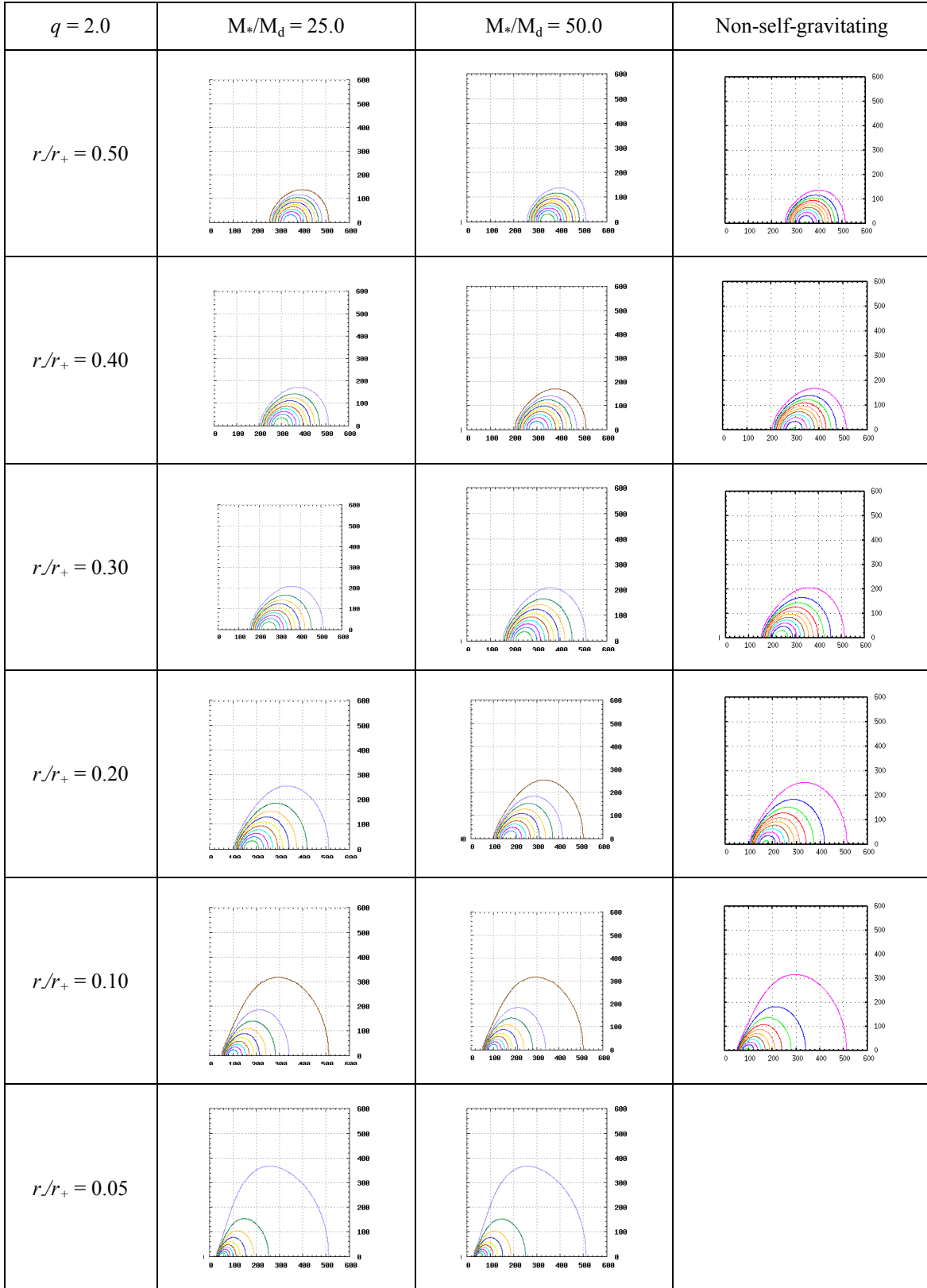


Fig. C.1.0.c. Equilibrium mass density contours of meridional slices for $q = 2.0$.

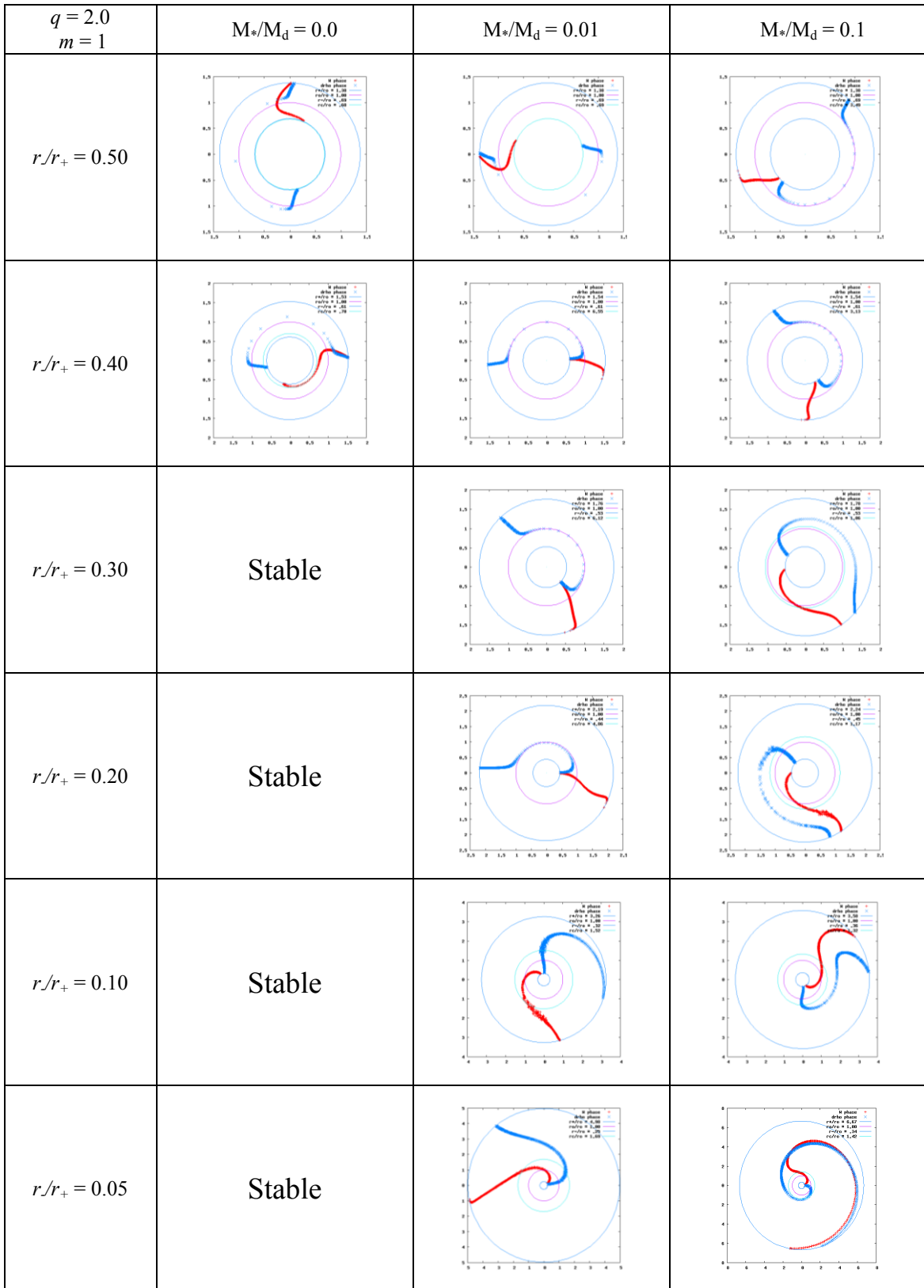


Fig. C.1.1 a Eigenfunction phases for $q = 2.0$, $m = 1$

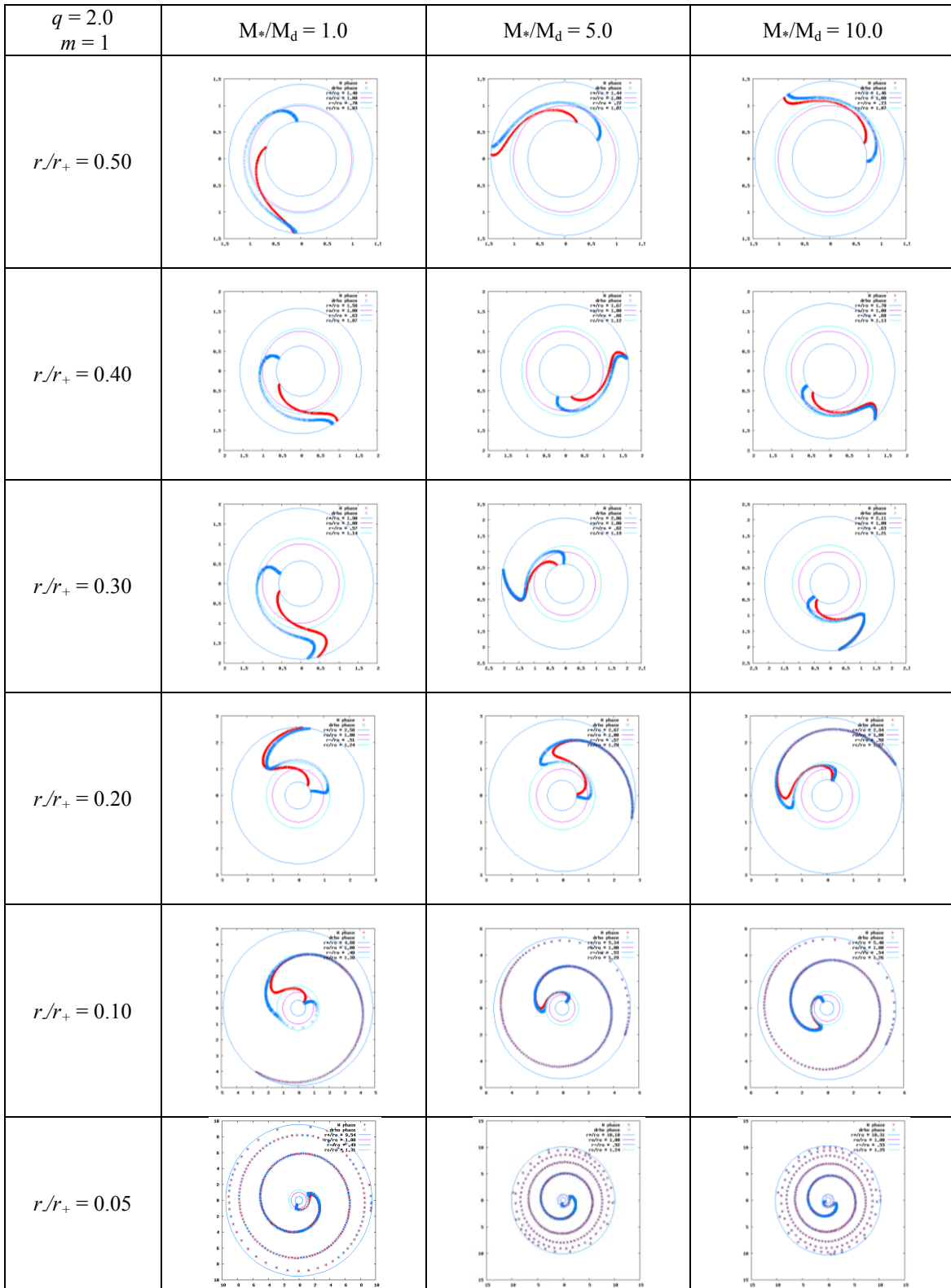


Fig. C.1.1.b. Eigenfunction phases for $q = 2.0$, $m = 1$

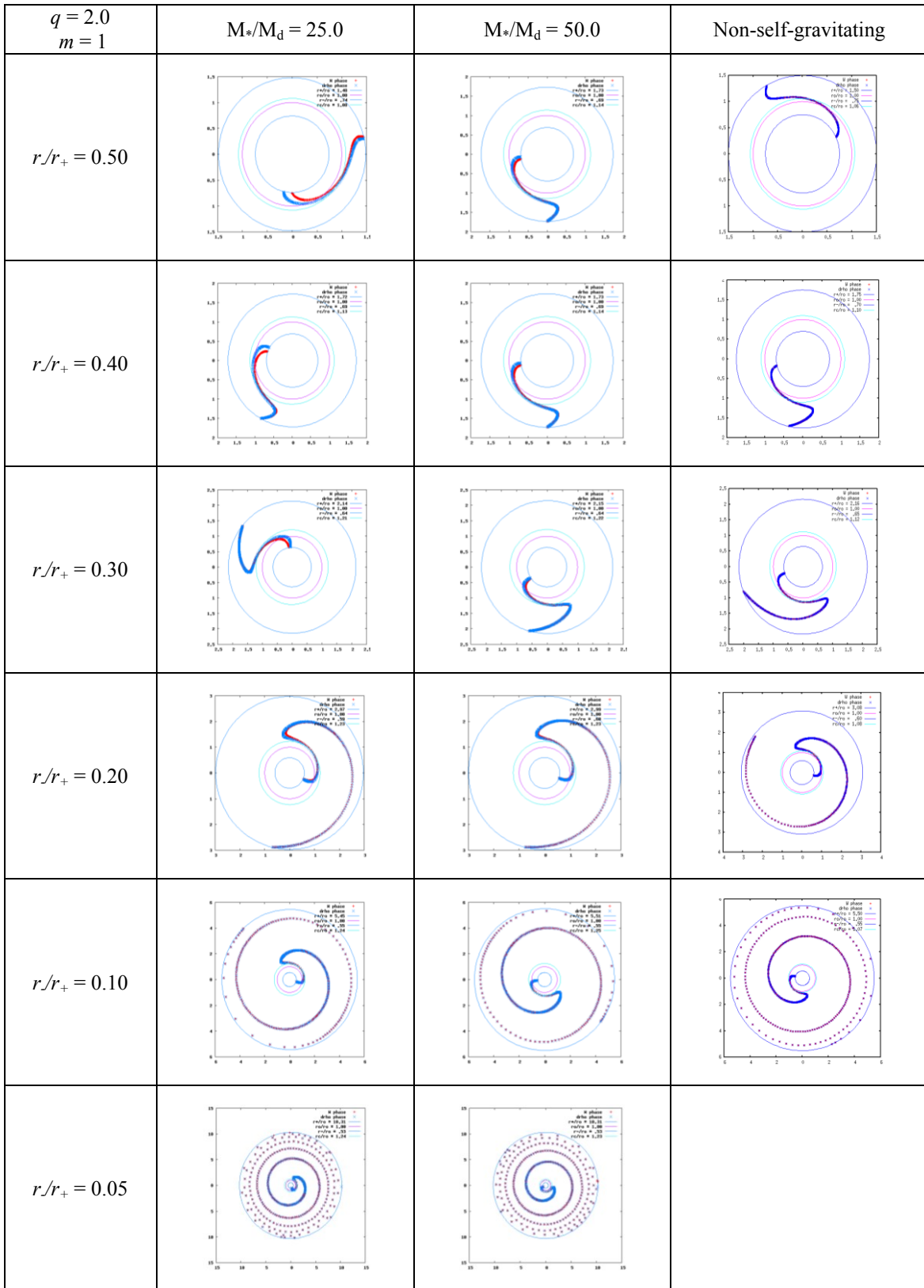


Fig. C.1.1.c. Eigenfunction phases for $q = 2.0$, $m = 1$
300

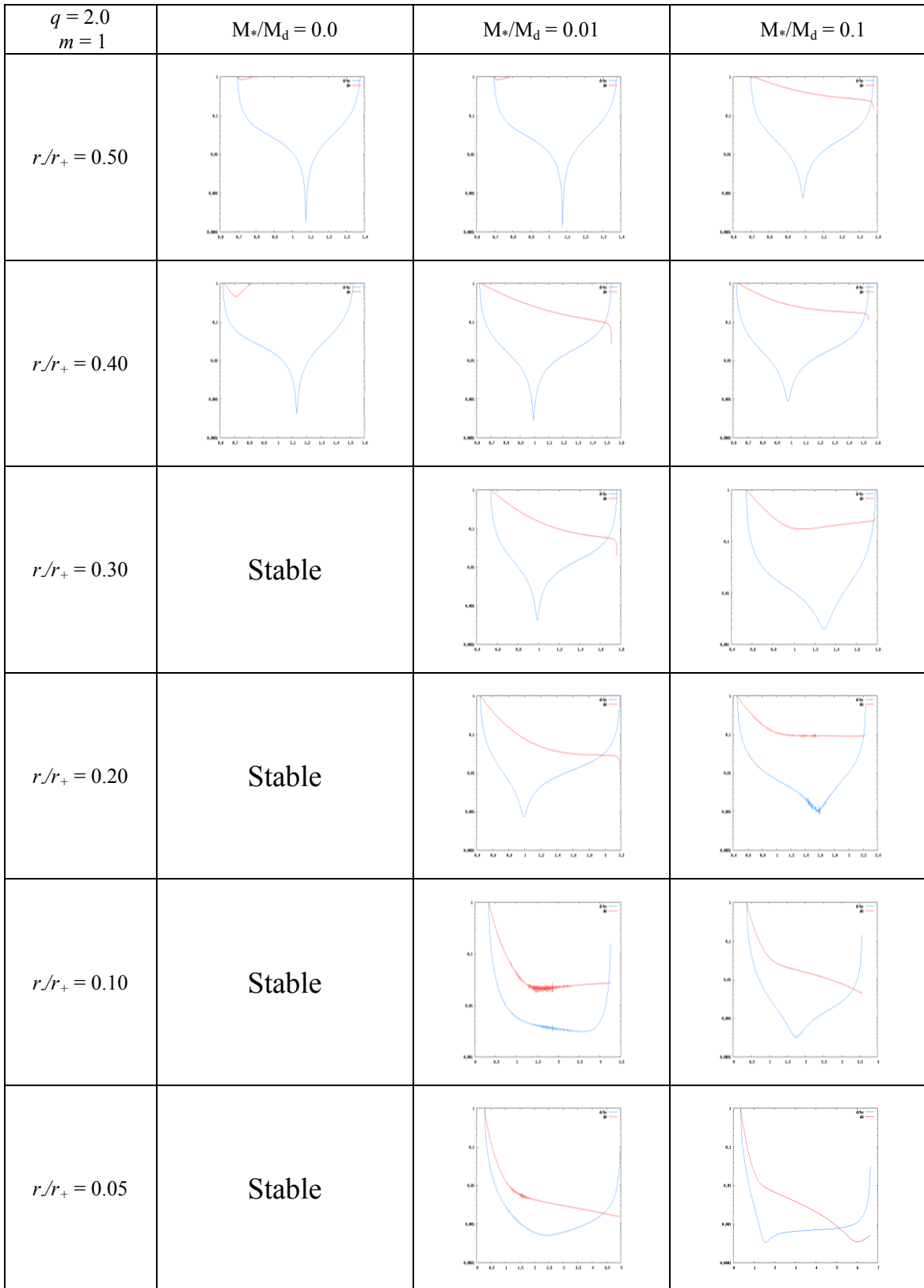


Fig. C.1.2.a. Eigenfunction amplitudes $|\delta\rho|/\rho$ and W for $q = 2.0$, $m = 1$

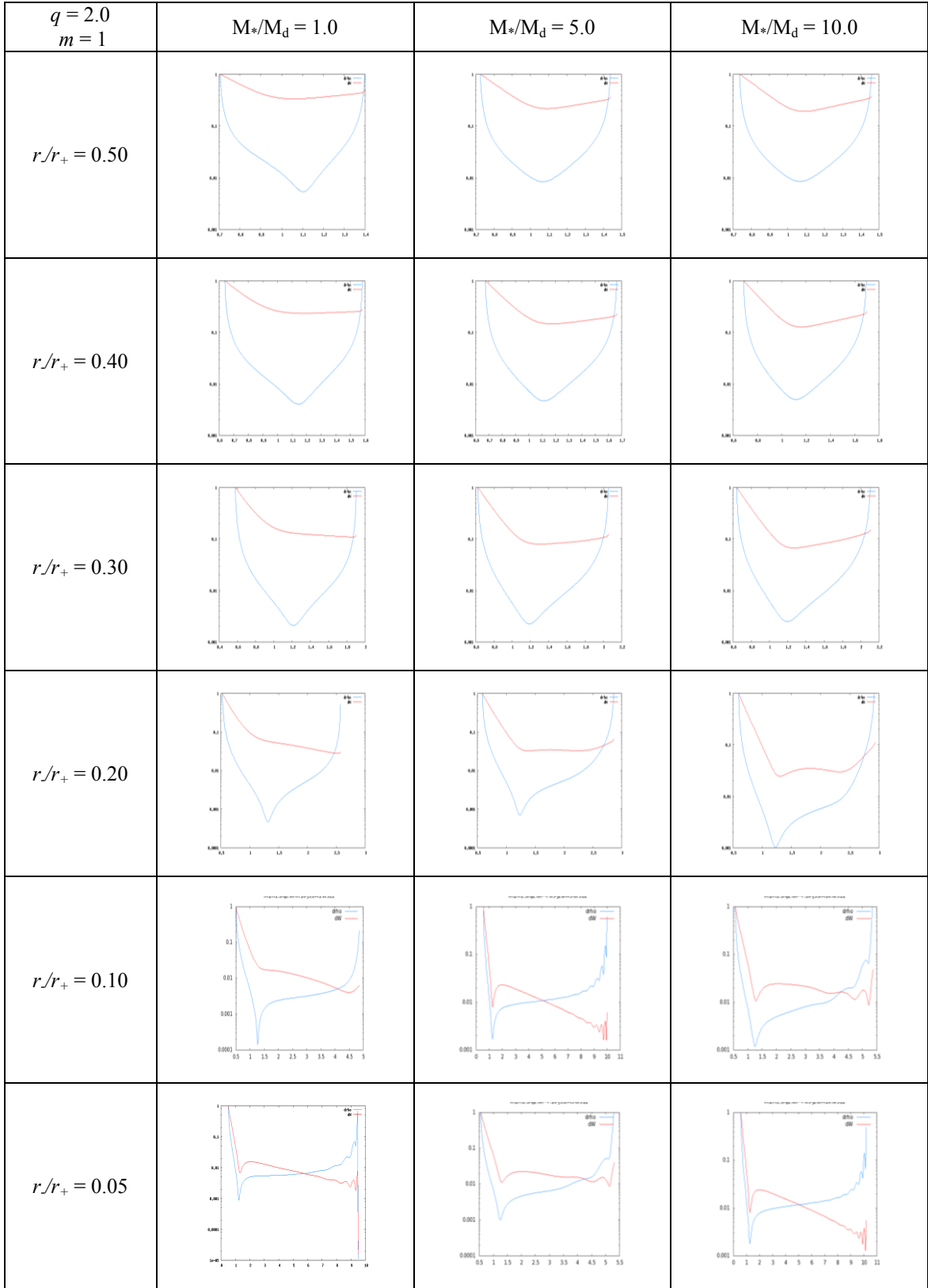


Fig. C.1.2.b. Eigenfunction amplitudes $|\delta\rho|/\rho$ and W for $q = 2.0$, $m = 1$

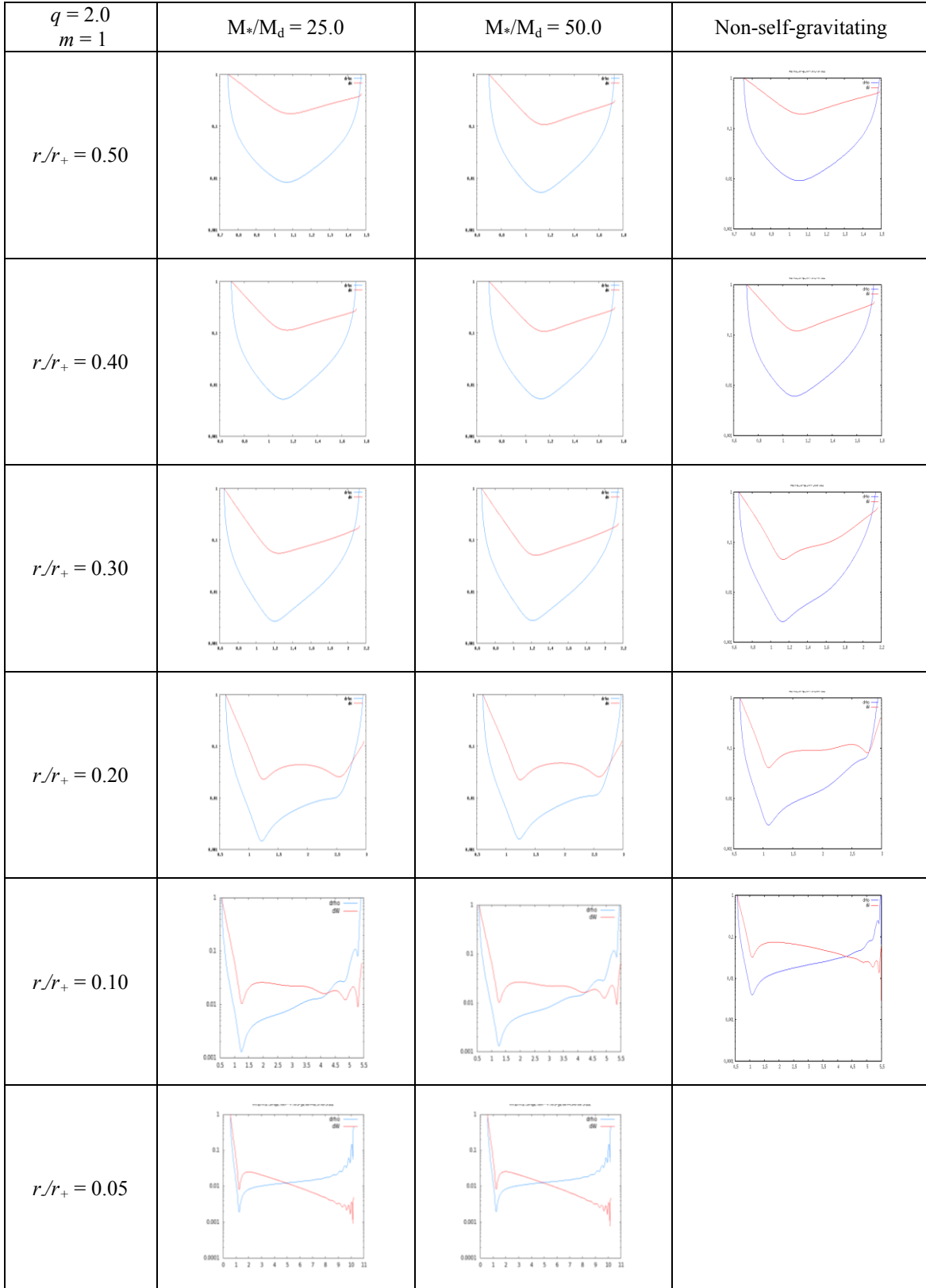


Fig. C.1.2.c. Eigenfunction amplitudes $|\delta\rho|/\rho$ and W for $q = 2.0$, $m = 1$

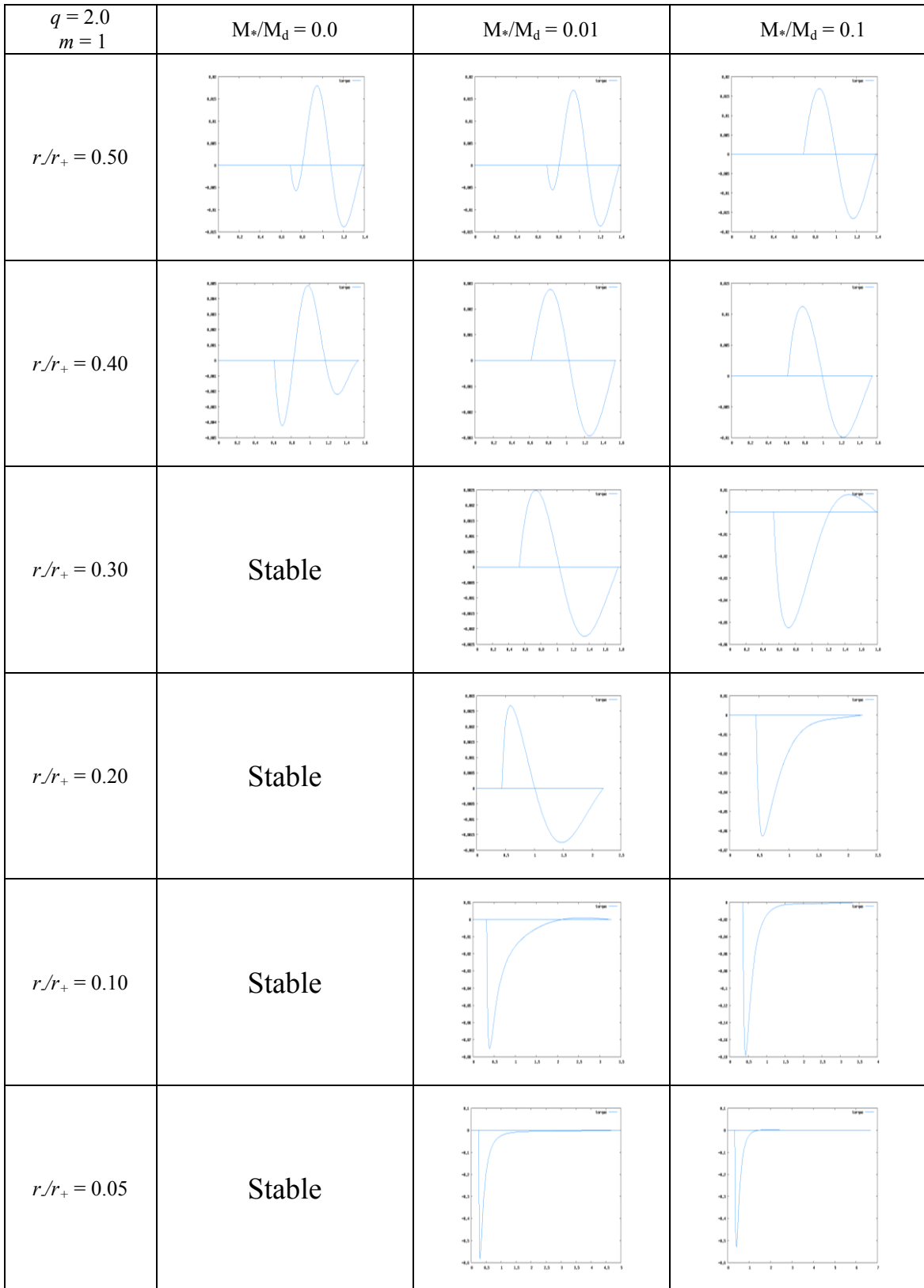


Fig. C.1.3.a. Self-gravitational torque for $q = 2.0$, $m = 1$

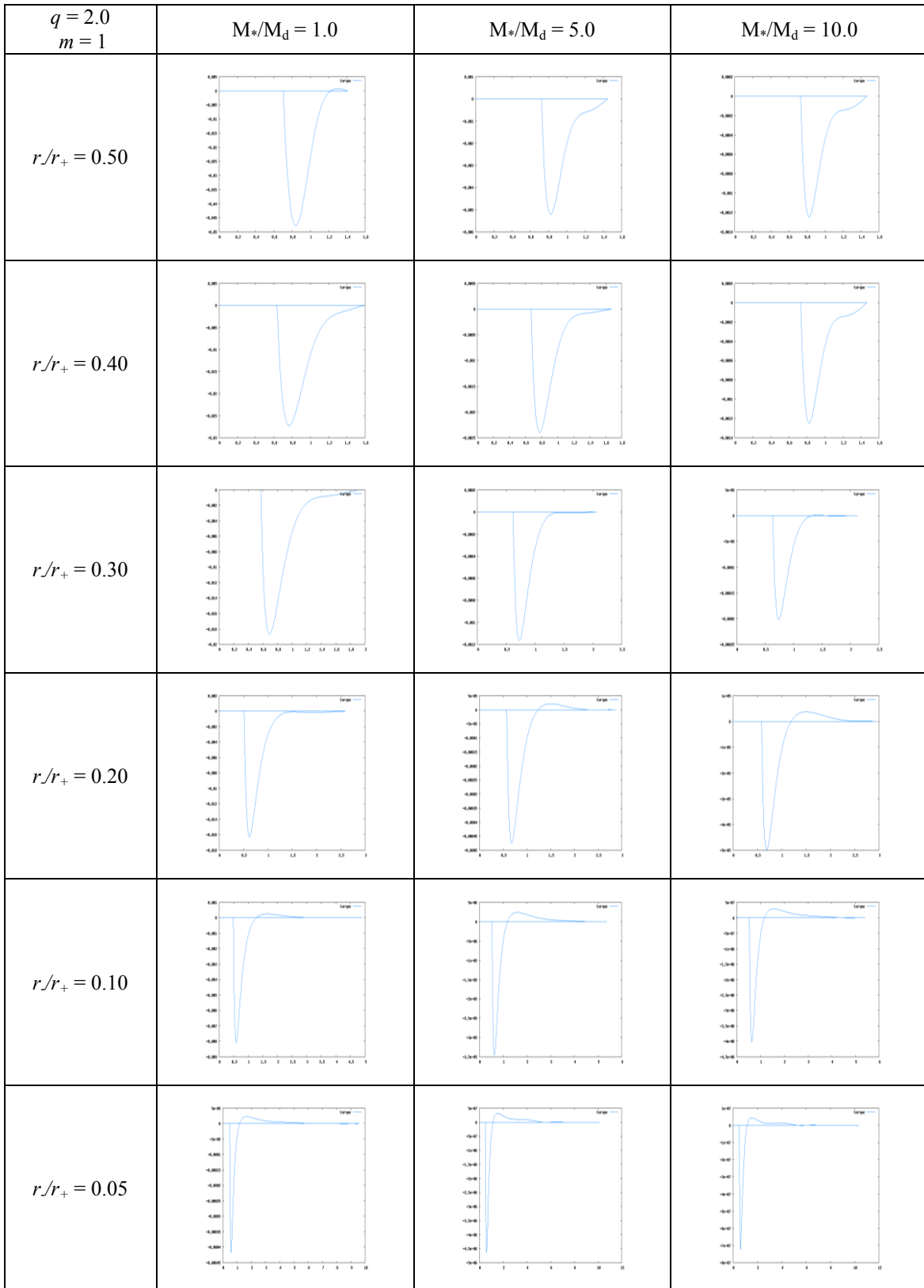


Fig. C.1.3.b. Self-gravitational torque for $q = 2.0$, $m = 1$

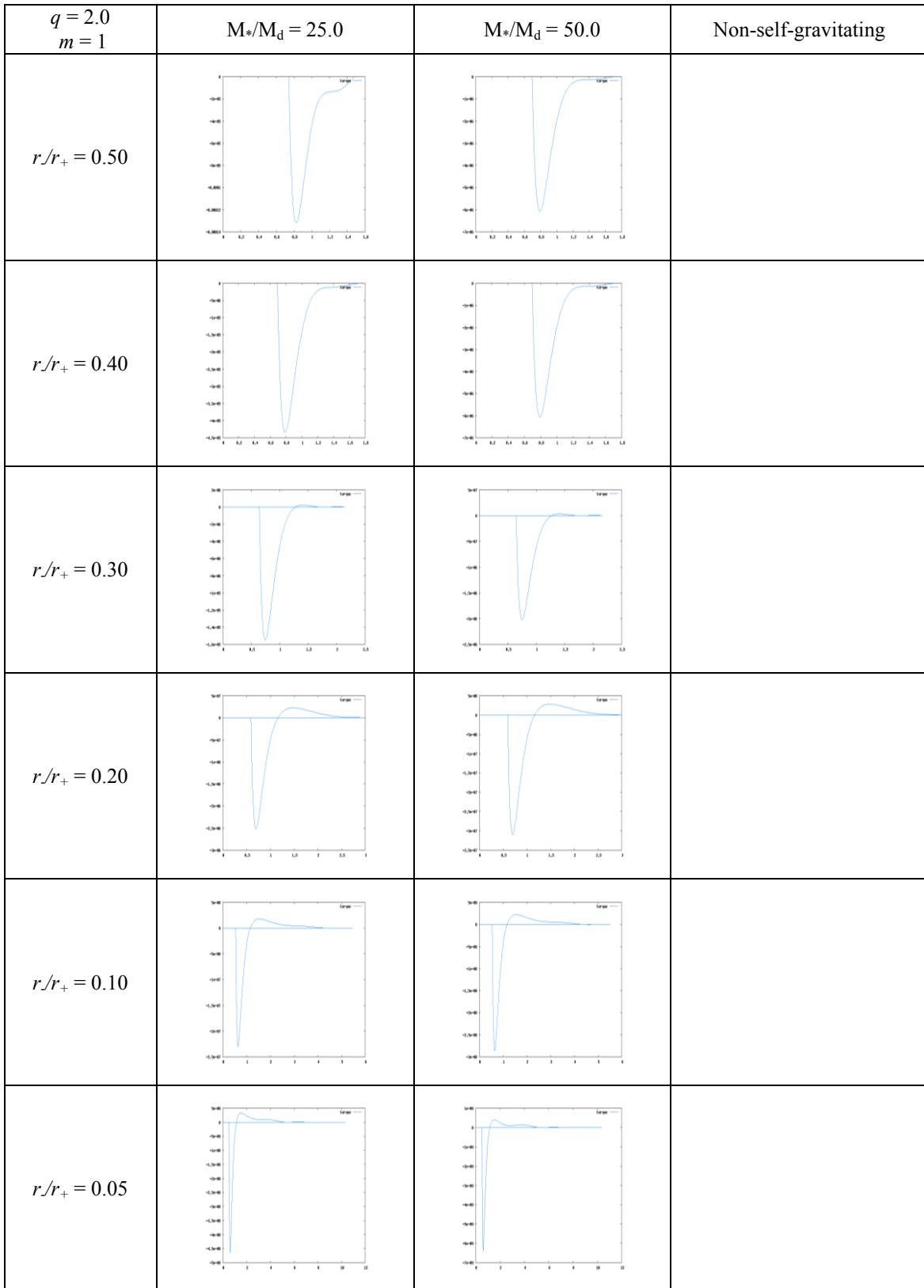


Fig. C.1.3.c. Self-gravitational torque for $q = 2.0$, $m = 1$

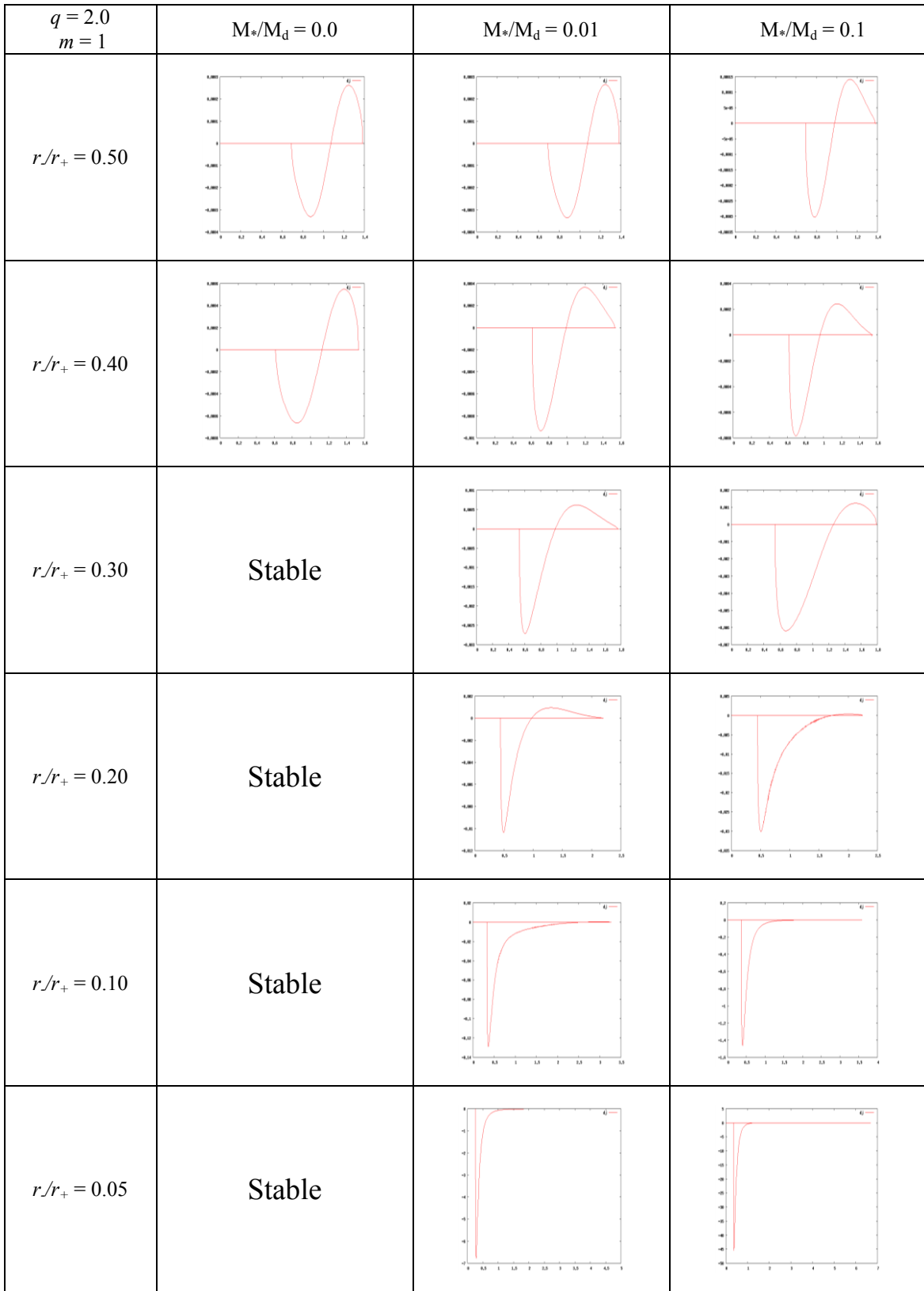


Fig. C.1.4 a Perturbed angular momentum for $q = 2.0$, $m = 1$

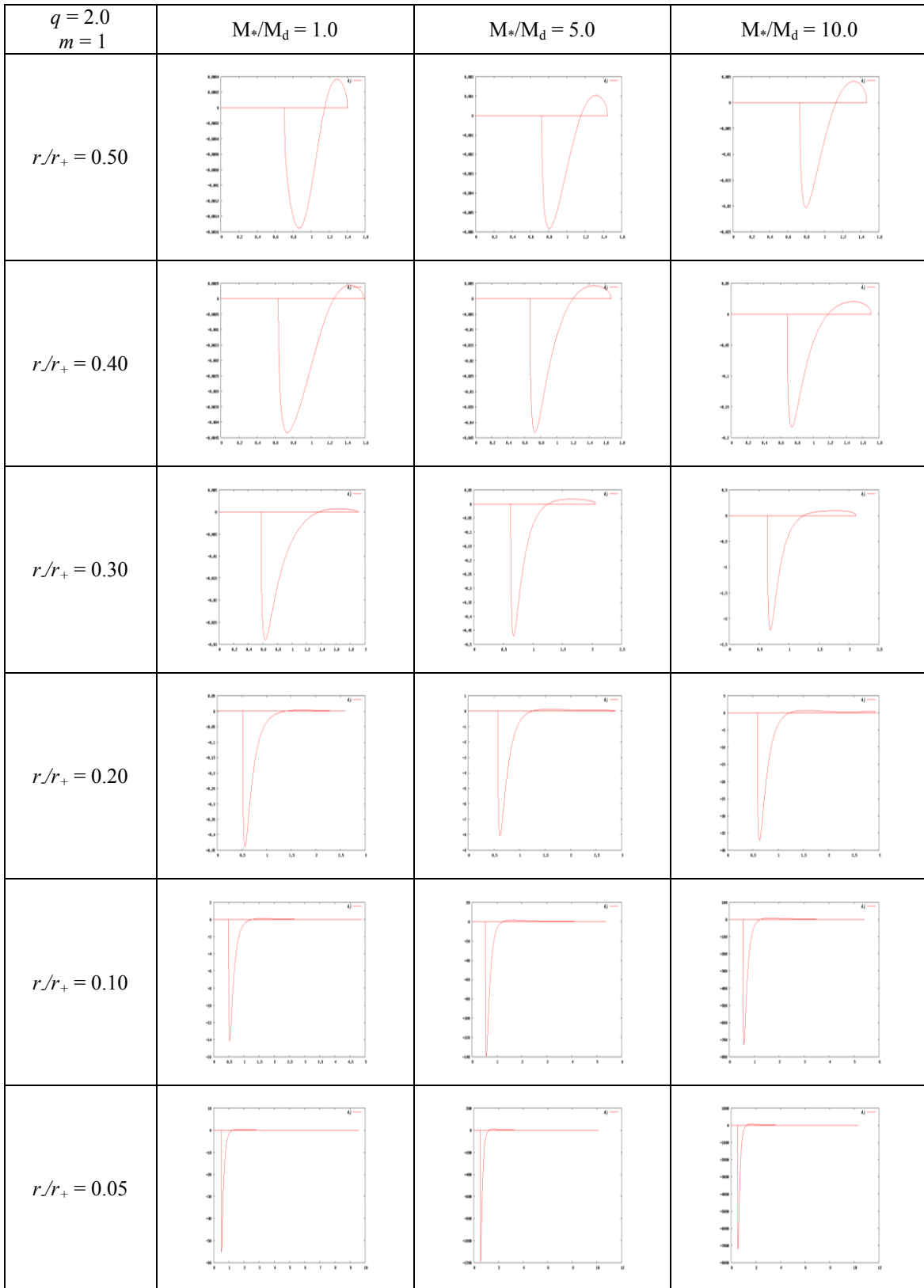


Fig. C.1.4.b. Perturbed angular momentum for $q = 2.0$, $m = 1$

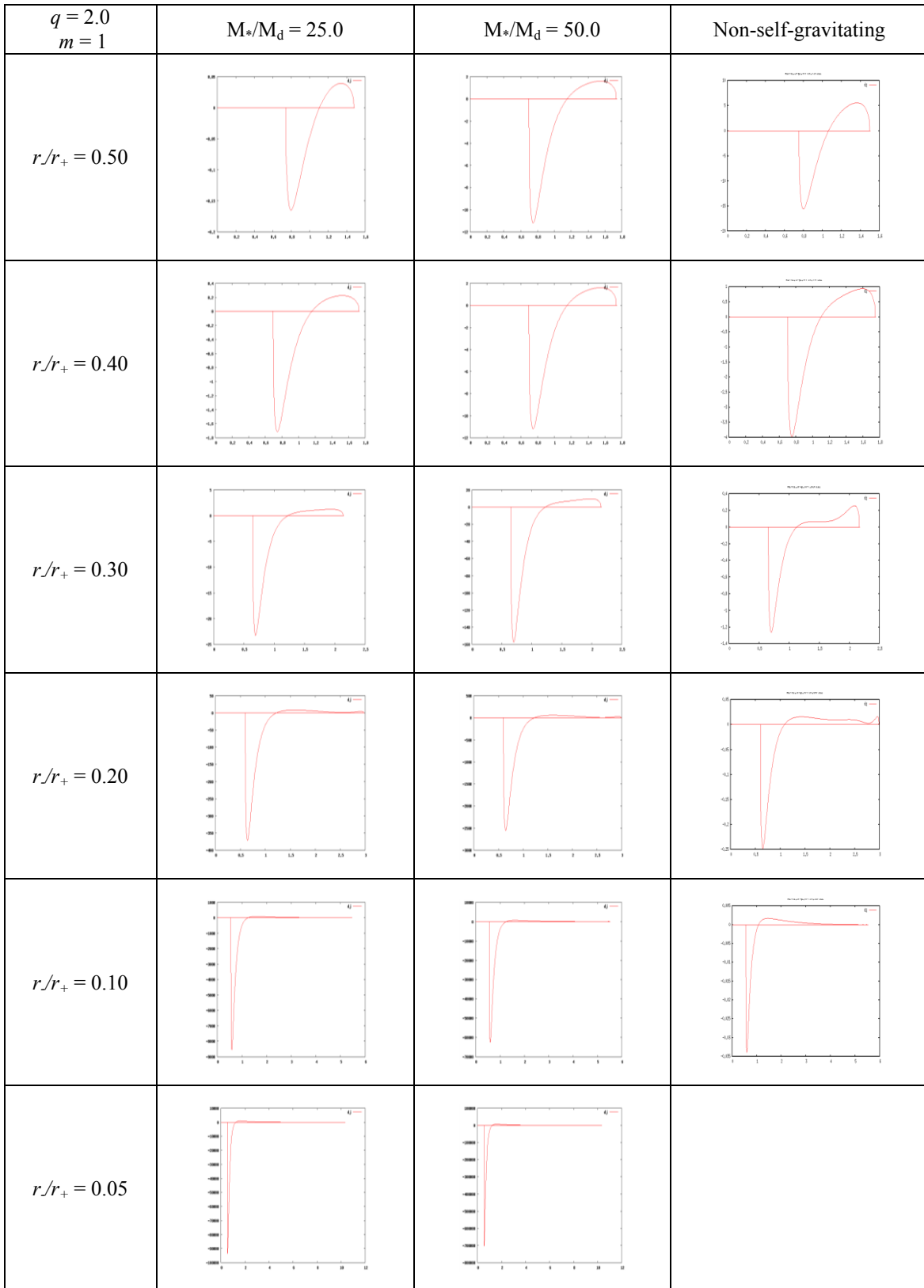


Fig. C.1.4.c. Perturbed angular momentum for $q = 2.0$, $m = 1$

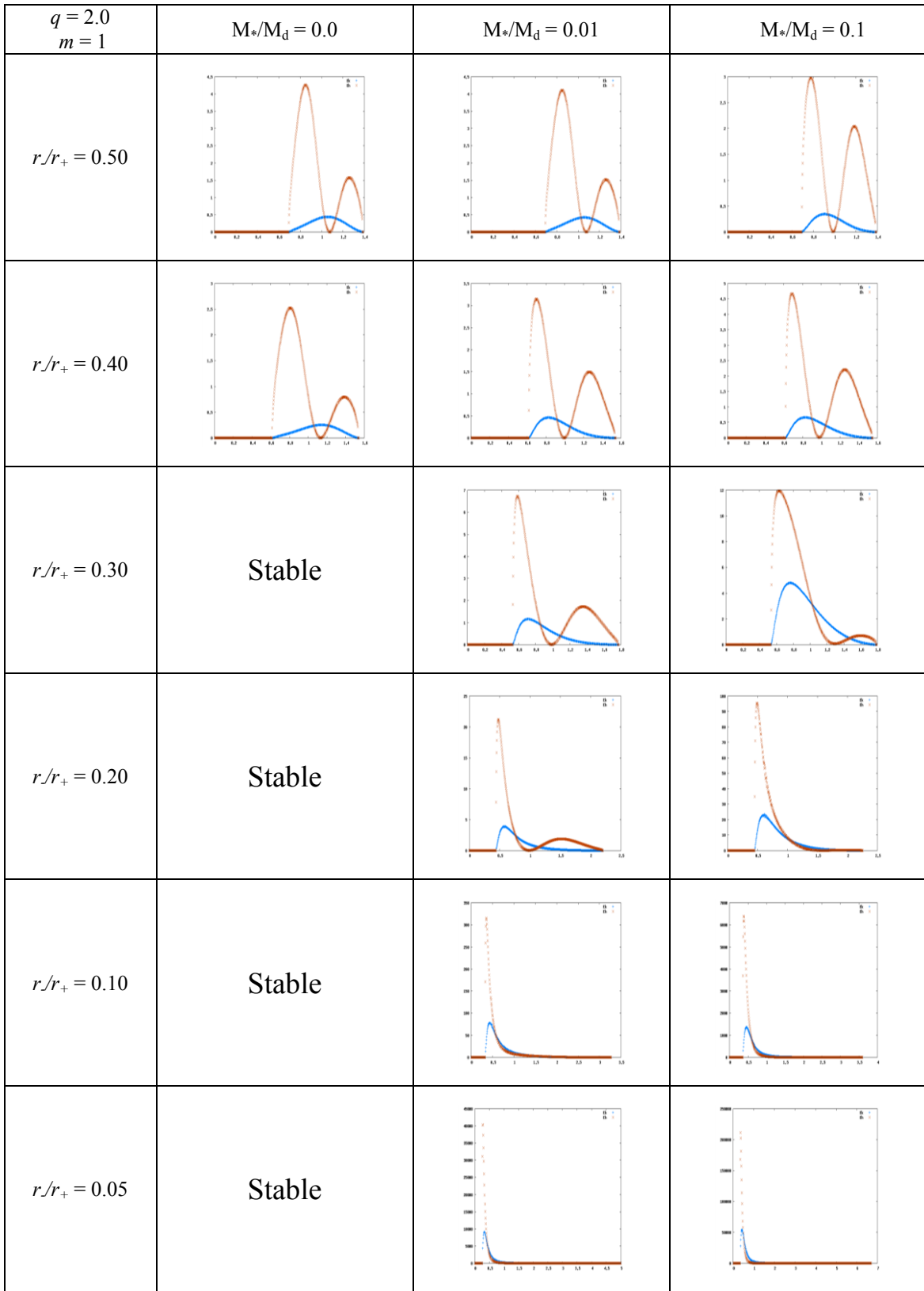


Fig. C.1.5.a. Work integrals for $q = 2.0$, $m = 1$

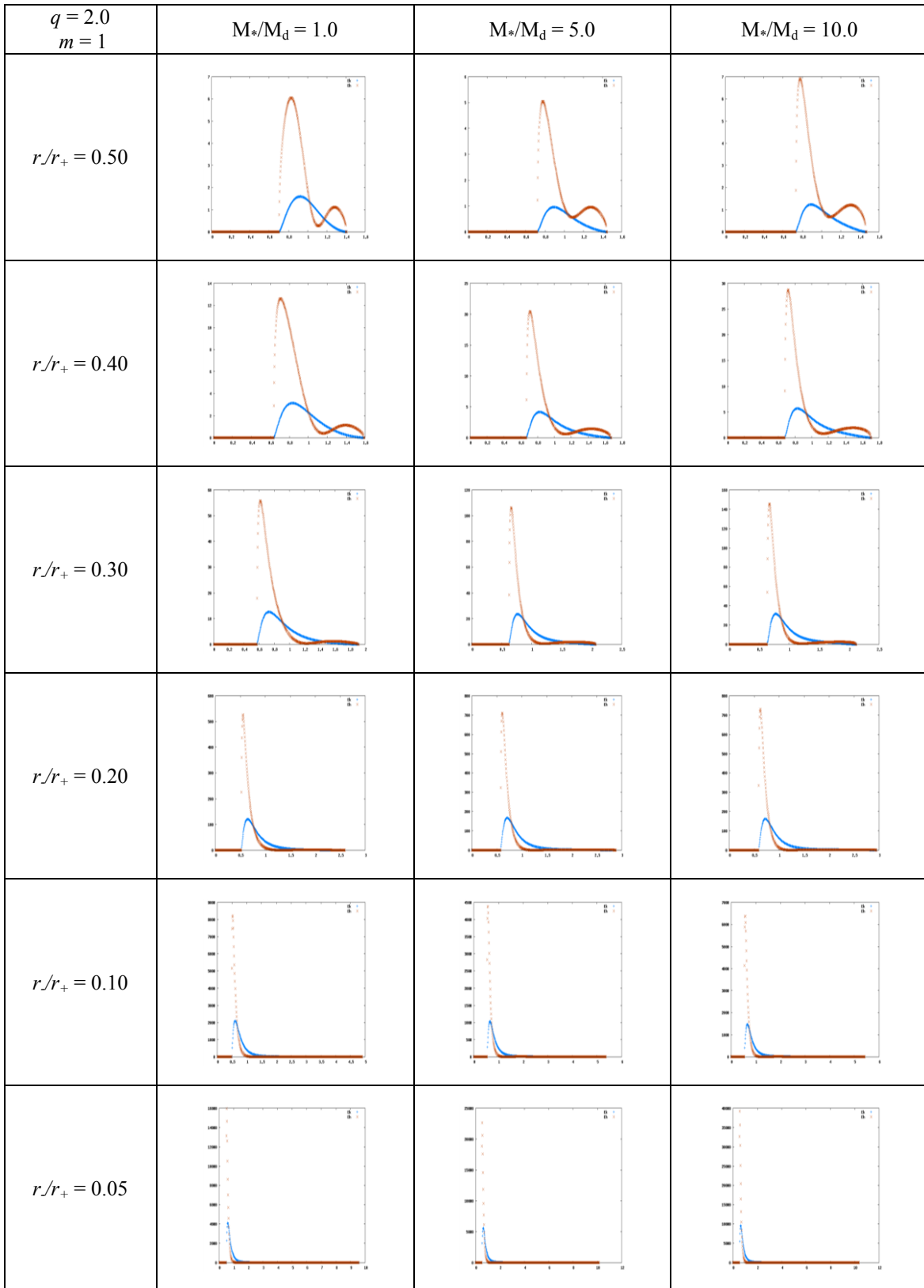


Fig. C.1.5.b. Work integrals for $q = 2.0$, $m = 1$

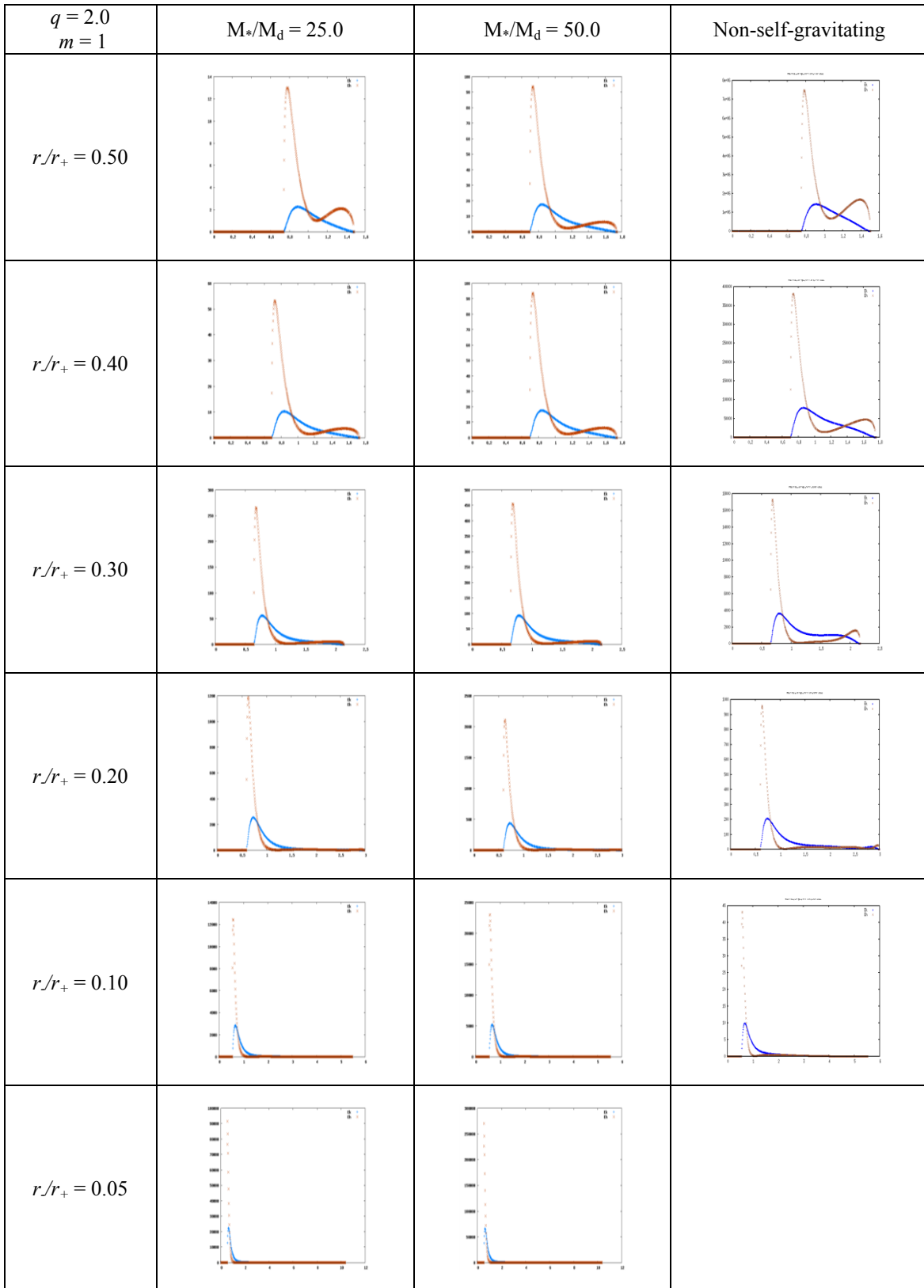


Fig. C.1.5.c. Work integrals for $q = 2.0$, $m = 1$
312

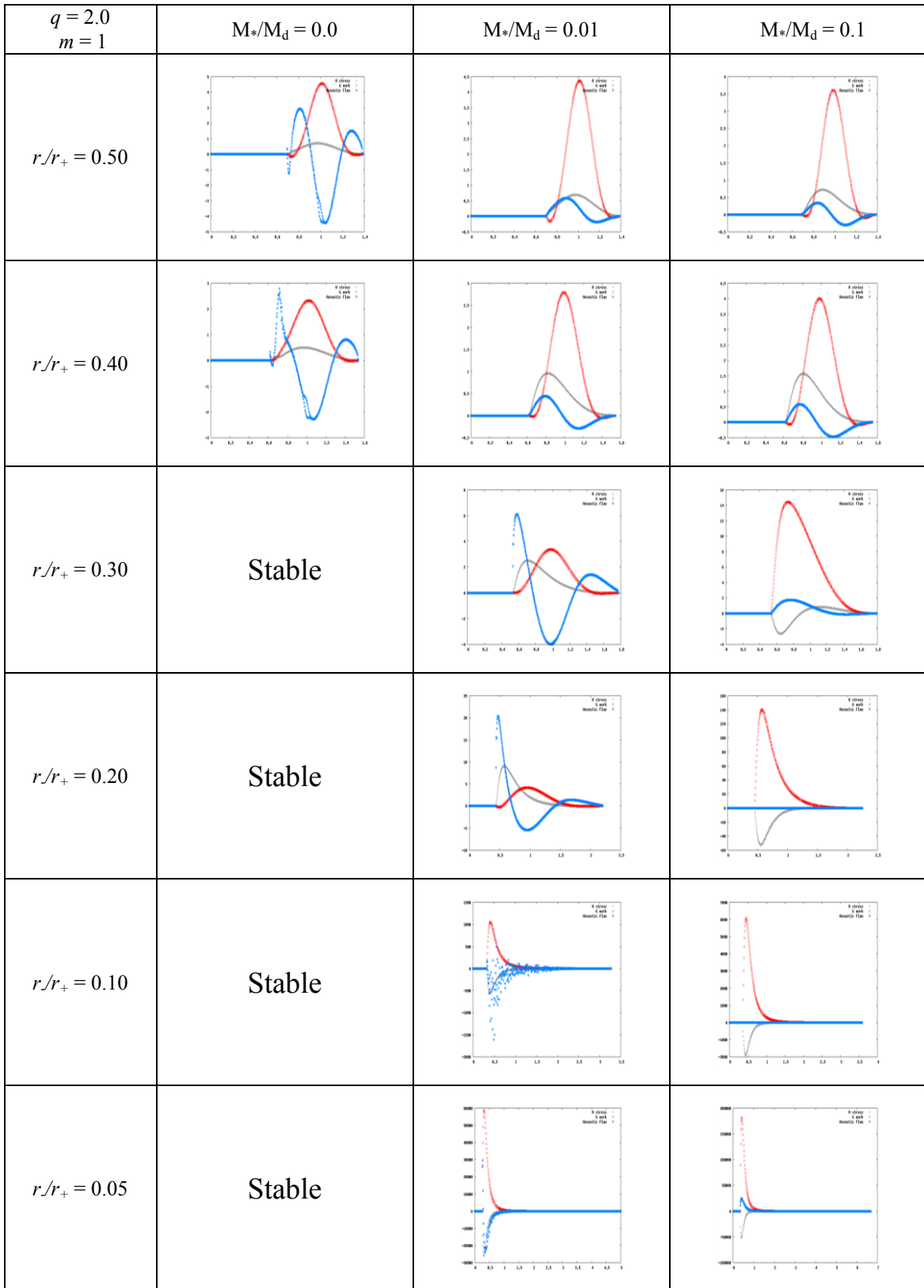


Fig. C.1.6.a. Stresses for $q = 2.0$, $m = 1$

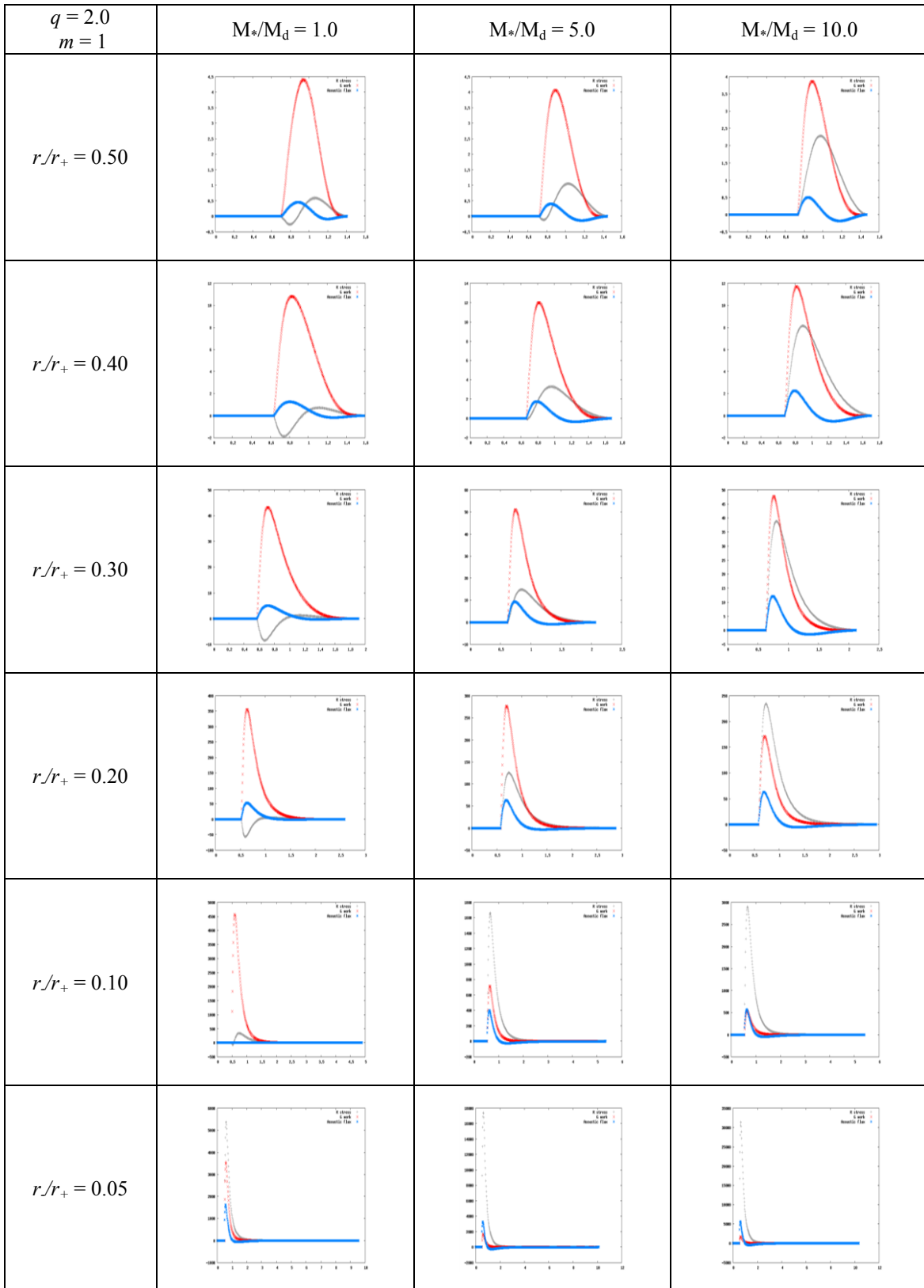


Fig. C.1.6.b. Stresses for $q = 2.0$, $m = 1$

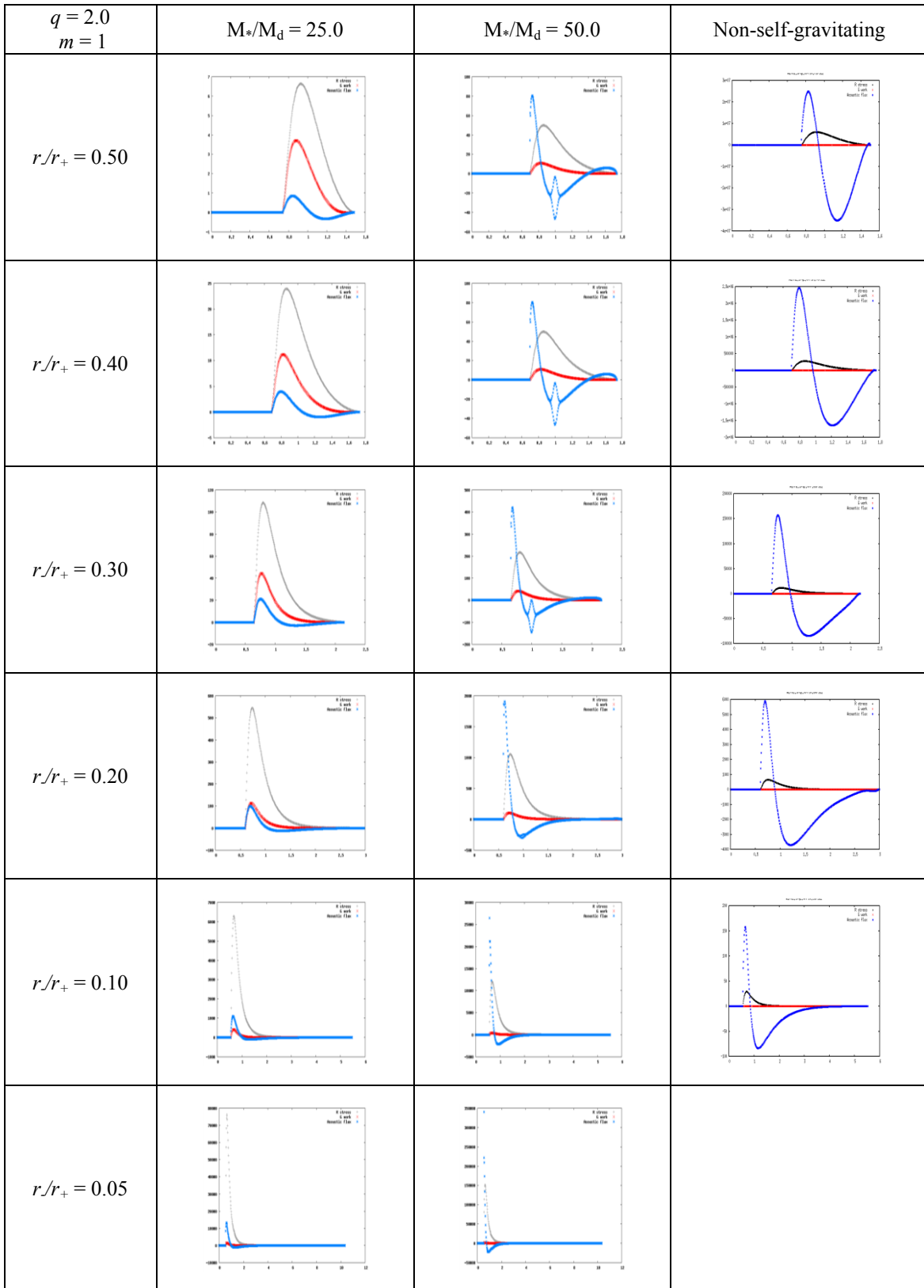


Fig. C.1.6.c. Stresses for $q = 2.0$, $m = 1$

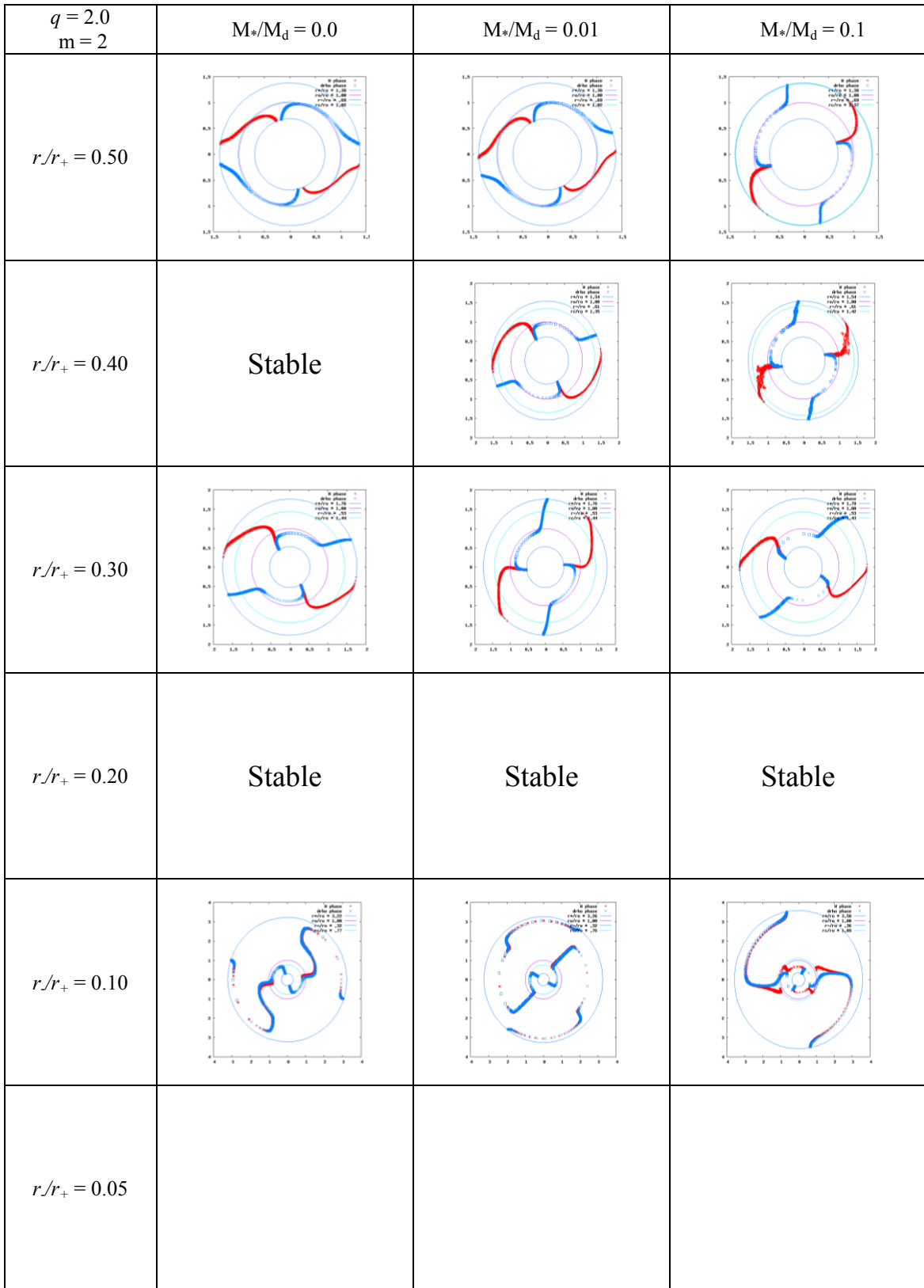


Fig. C.2.1 a Eigenfunction phases for $q = 2.0, m = 2$

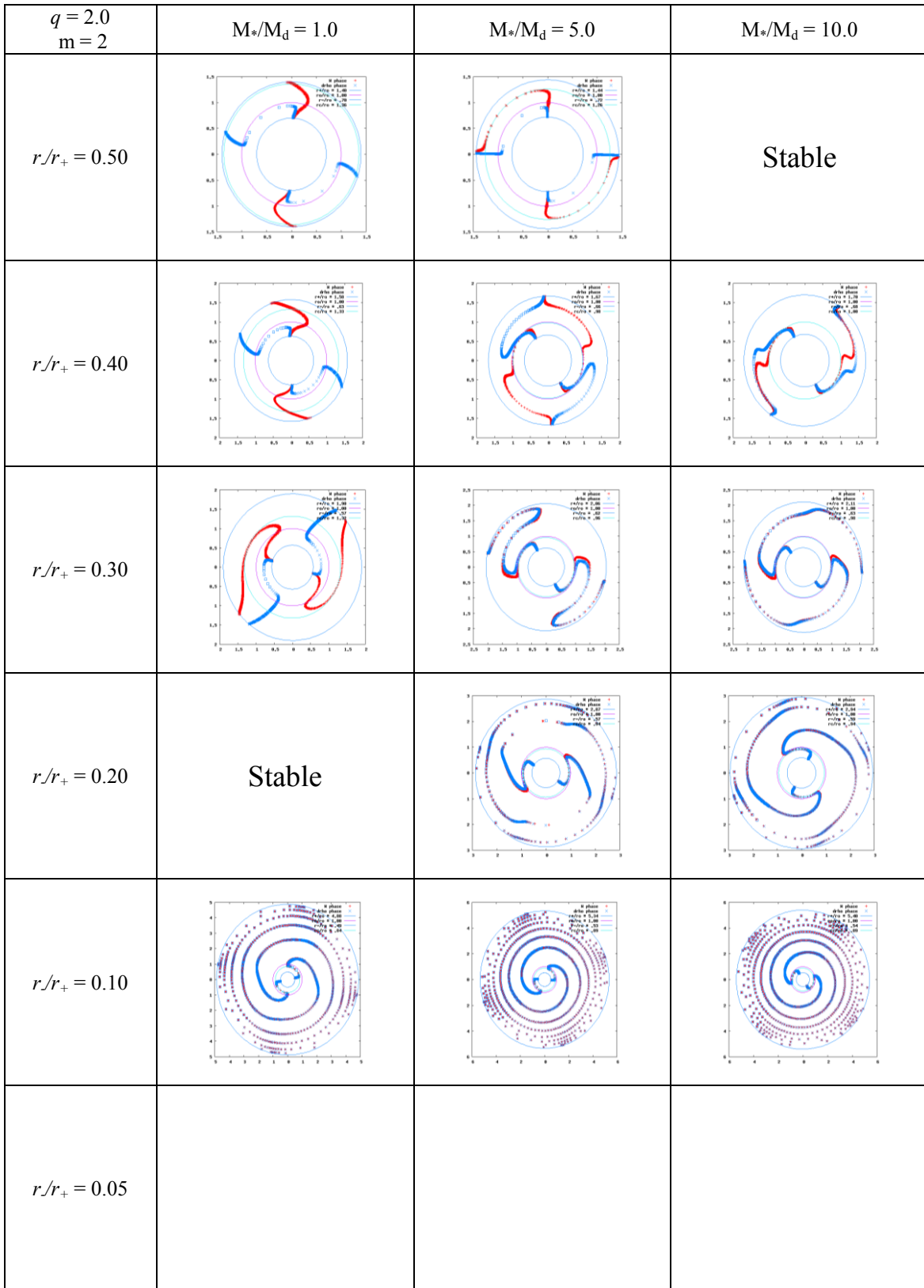


Fig. C.2.1.b. Eigenfunction phases for $q = 2.0$, $m = 2$

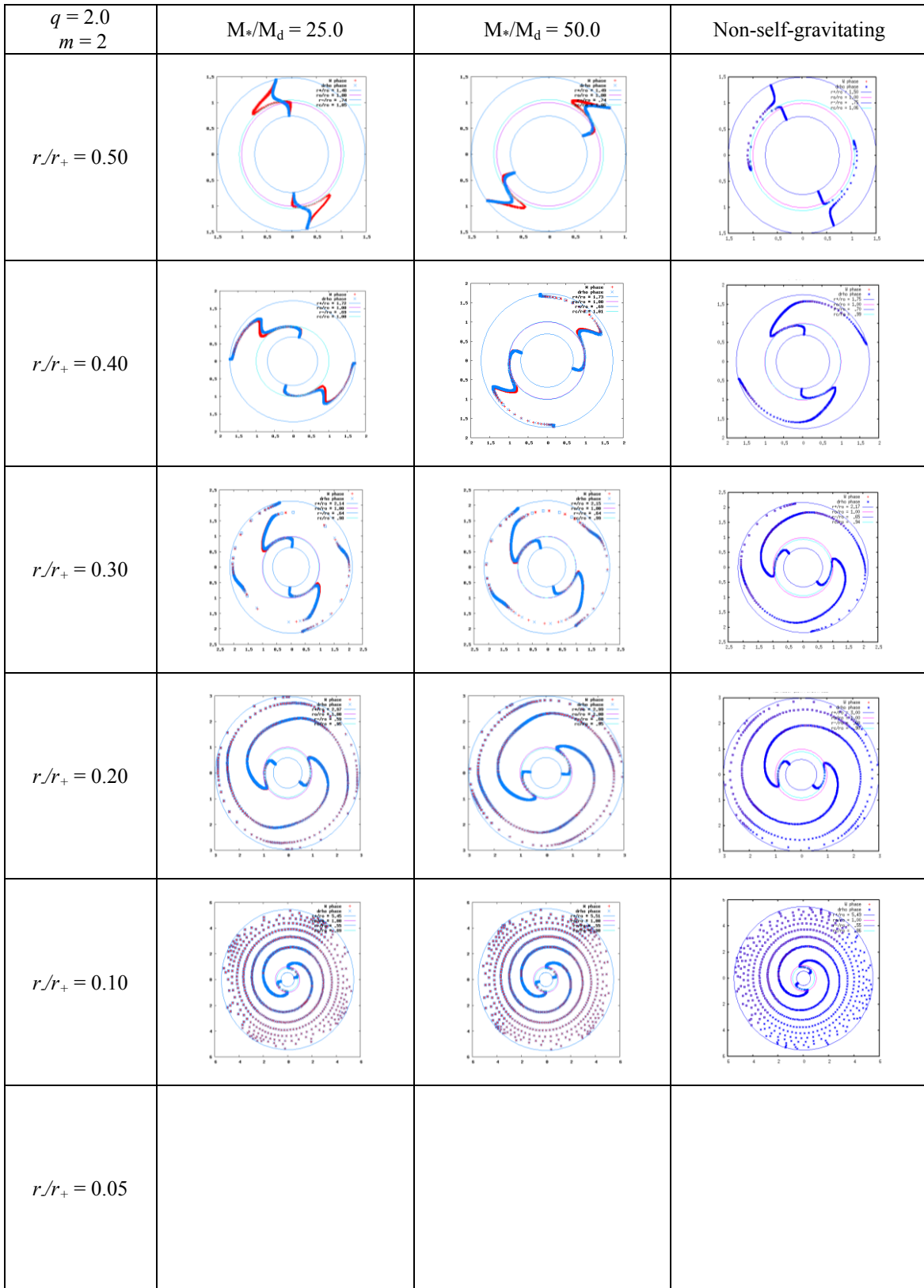


Fig. C.2.1.c. Eigenfunction phases for $q = 2.0$, $m = 2$

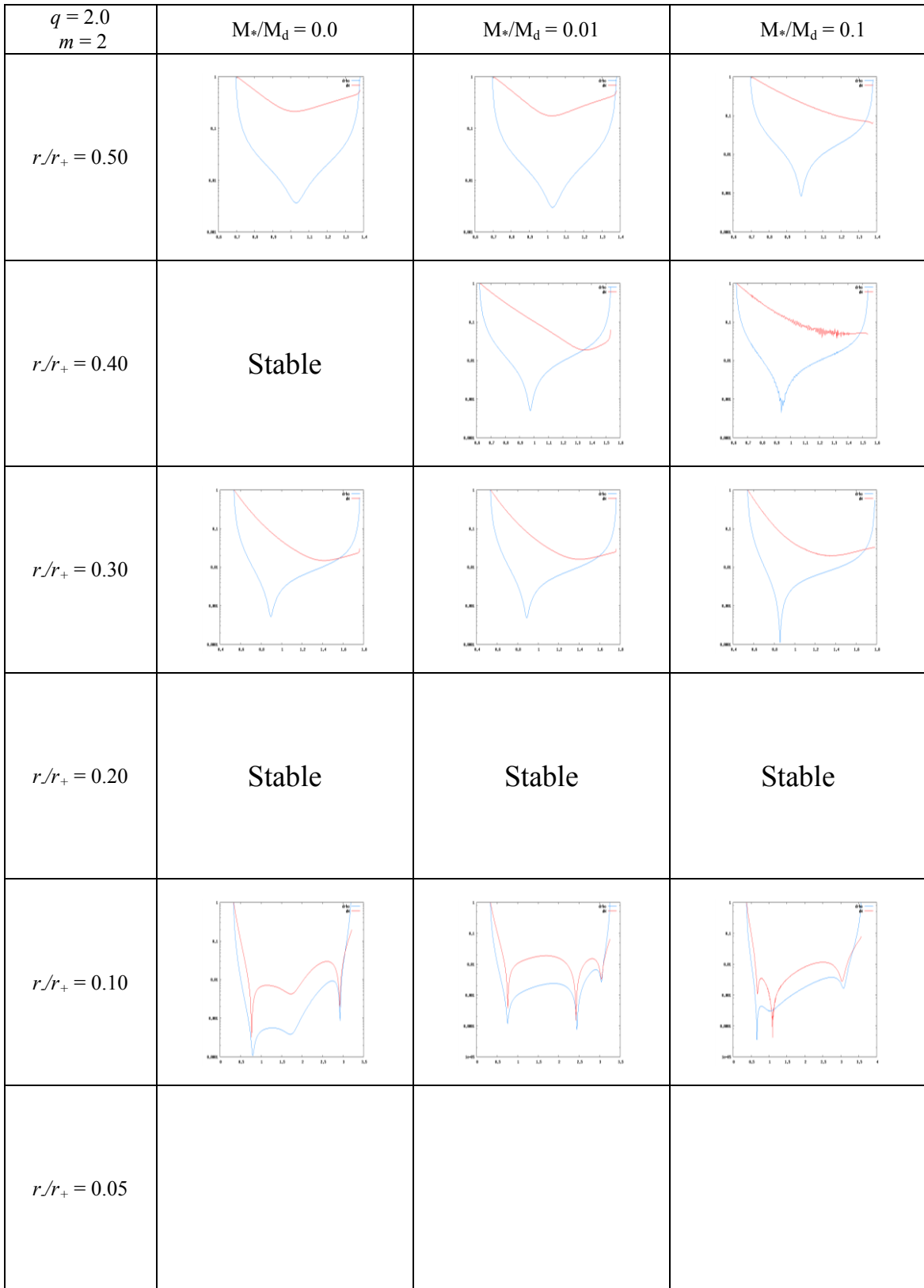


Fig. C.2.2.a. Eigenfunction amplitudes $|\delta\rho|/\rho$ and W for $q = 2.0$, $m = 2$

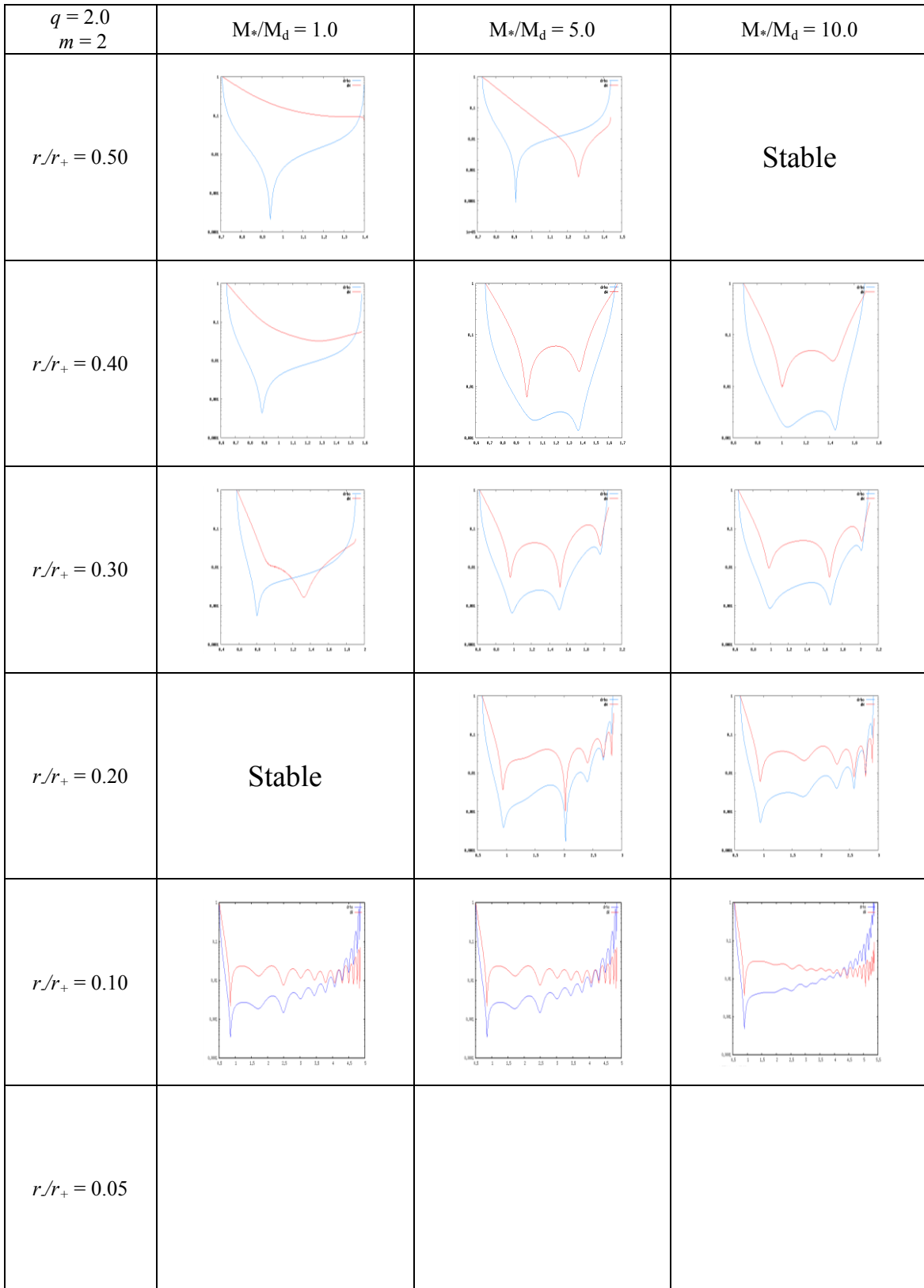


Fig. C.2.2.b. Eigenfunction amplitudes $|\delta\rho|/\rho$ and W for $q = 2.0$, $m = 2$

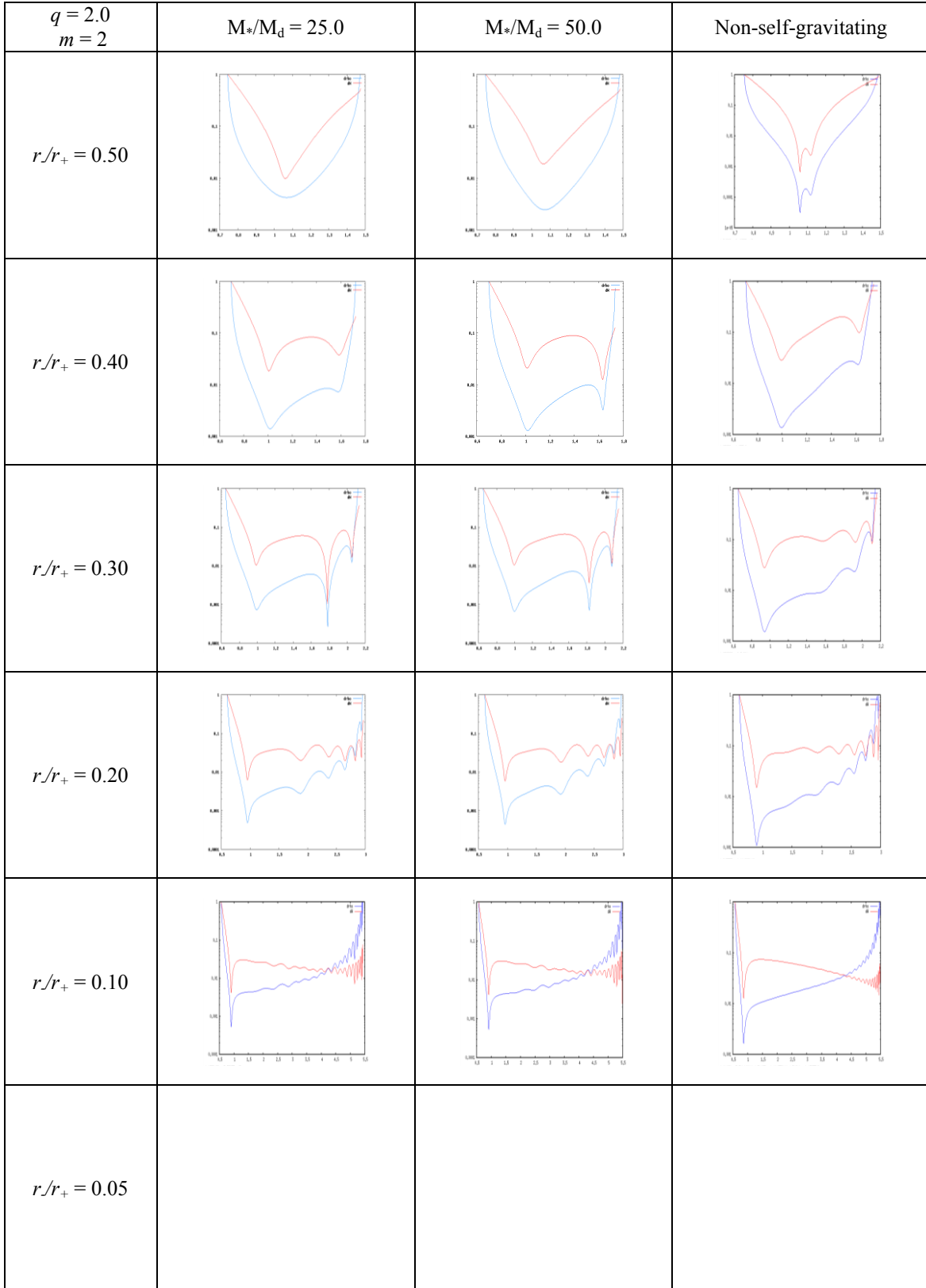


Fig. C.2.2.c. Eigenfunction amplitudes $|\delta\rho|/\rho$ and W for $q = 2.0$, $m = 2$

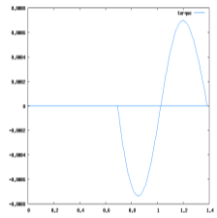
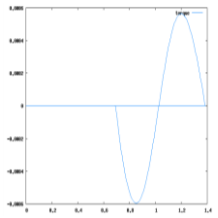
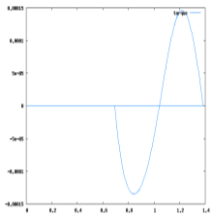
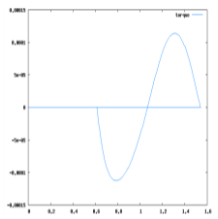
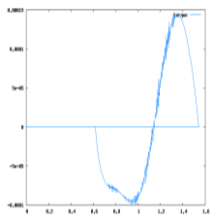
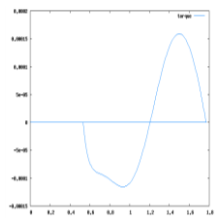
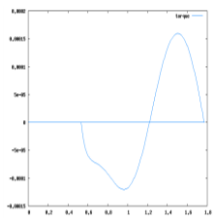
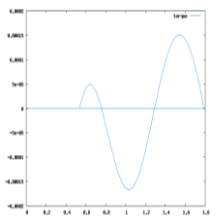
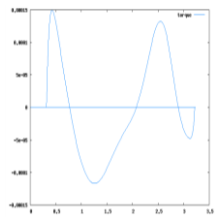
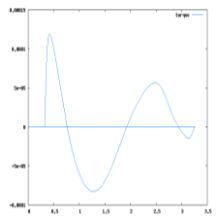
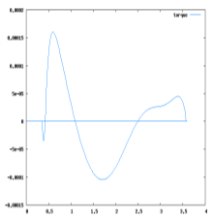
$q = 2.0$ $m = 2$	$M^*/M_d = 0.0$	$M^*/M_d = 0.01$	$M^*/M_d = 0.1$
$r/r_+ = 0.50$			
$r/r_+ = 0.40$	Stable		
$r/r_+ = 0.30$			
$r/r_+ = 0.20$	Stable	Stable	Stable
$r/r_+ = 0.10$			
$r/r_+ = 0.05$			

Fig. C.2.3.a. Self-gravitational torque for $q = 2.0$, $m = 2$

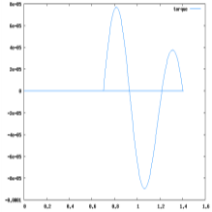
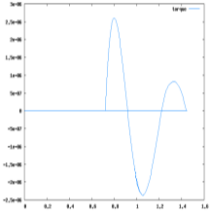
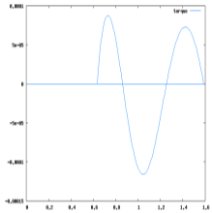
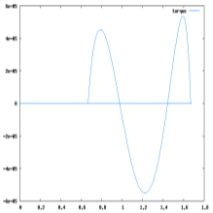
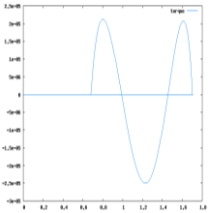
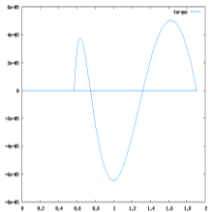
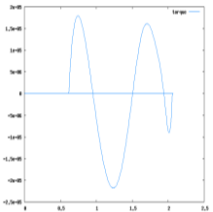
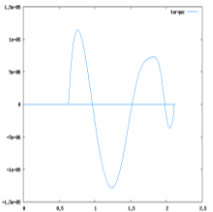
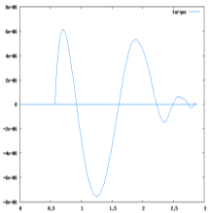
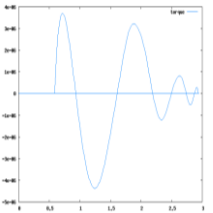
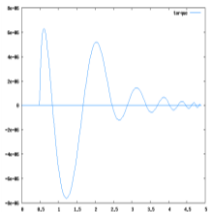
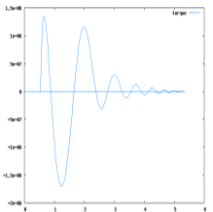
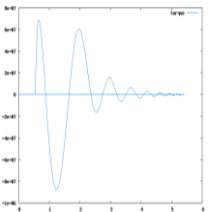
$q = 2.0$ $m = 2$	$M_*/M_d = 1.0$	$M_*/M_d = 5.0$	$M_*/M_d = 10.0$
$r/r_+ = 0.50$			Stable
$r/r_+ = 0.40$			
$r/r_+ = 0.30$			
$r/r_+ = 0.20$	Stable		
$r/r_+ = 0.10$			
$r/r_+ = 0.05$			

Fig. C.2.3.b. Self-gravitational torque for $q = 2.0$, $m = 2$

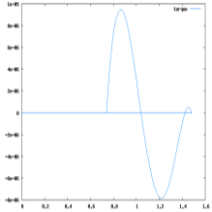
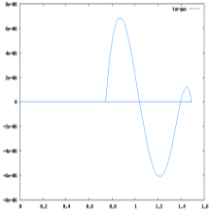
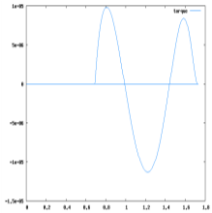
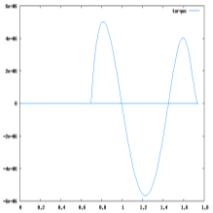
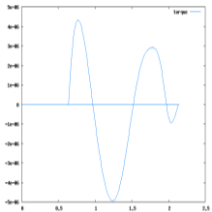
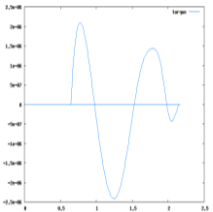
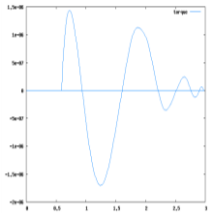
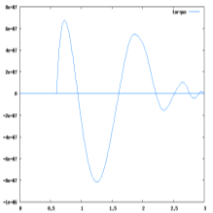
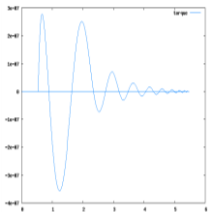
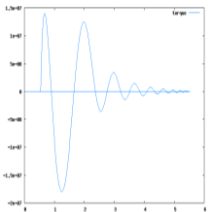
$q = 2.0$ $m = 2$	$M_*/M_d = 25.0$	$M_*/M_d = 50.0$	Non-self-gravitating
$r/r_+ = 0.50$			
$r/r_+ = 0.40$			
$r/r_+ = 0.30$			
$r/r_+ = 0.20$			
$r/r_+ = 0.10$			
$r/r_+ = 0.05$			

Fig. C.2.3.c. Self-gravitational torque for $q = 2.0$, $m = 2$

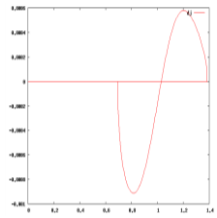
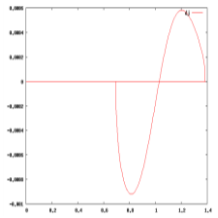
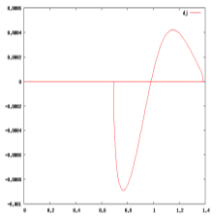
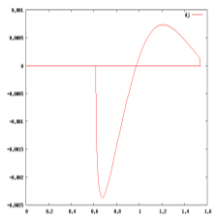
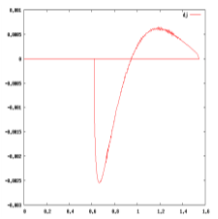
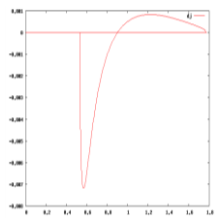
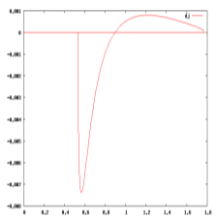
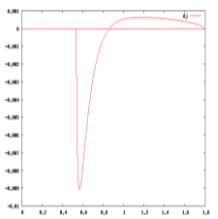
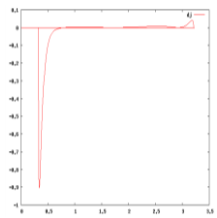
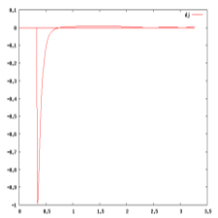
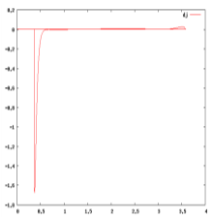
$q = 2.0$ $m = 2$	$M_*/M_d = 0.0$	$M_*/M_d = 0.01$	$M_*/M_d = 0.1$
$r/r_+ = 0.50$			
$r/r_+ = 0.40$	Stable		
$r/r_+ = 0.30$			
$r/r_+ = 0.20$	Stable	Stable	Stable
$r/r_+ = 0.10$			
$r/r_+ = 0.05$			

Fig. C.2.4 a Perturbed angular momentum for $q = 2.0$, $m = 2$

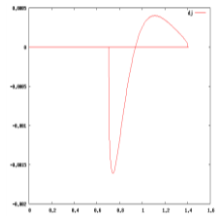
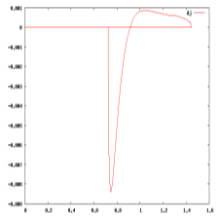
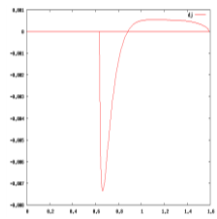
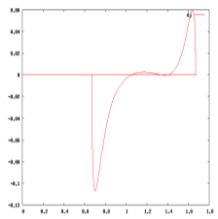
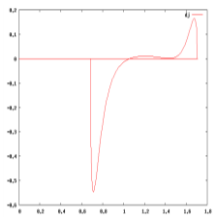
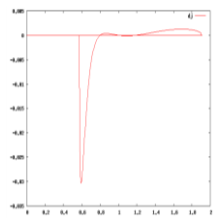
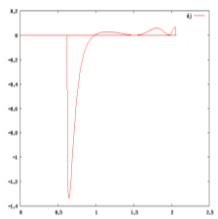
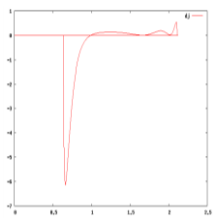
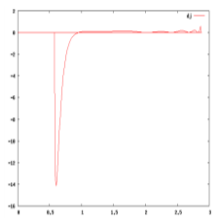
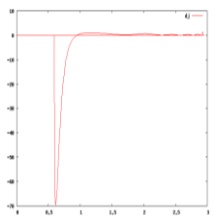
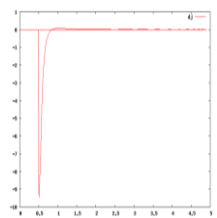
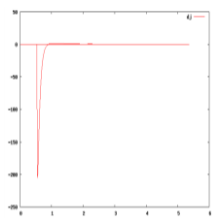
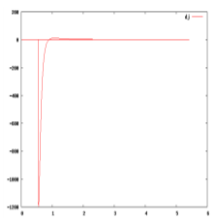
$q = 2.0$ $m = 2$	$M_*/M_d = 1.0$	$M_*/M_d = 5.0$	$M_*/M_d = 10.0$
$r/r_+ = 0.50$			Stable
$r/r_+ = 0.40$			
$r/r_+ = 0.30$			
$r/r_+ = 0.20$	stable		
$r/r_+ = 0.10$			
$r/r_+ = 0.05$			

Fig. C.2.4.b. Perturbed angular momentum for $q = 2.0$, $m = 2$

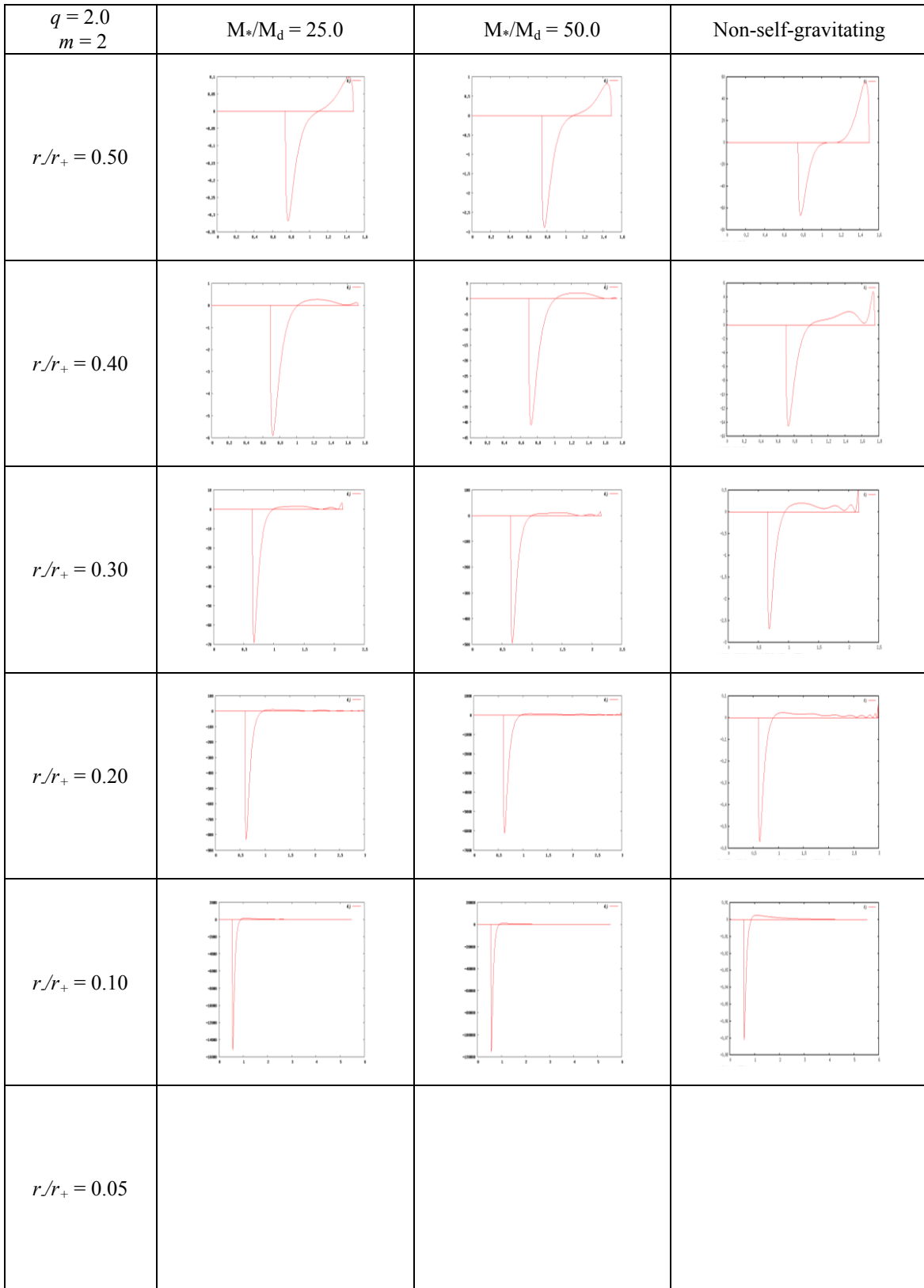


Fig. C.2.4.c. Perturbed angular momentum for $q = 2.0$, $m = 2$

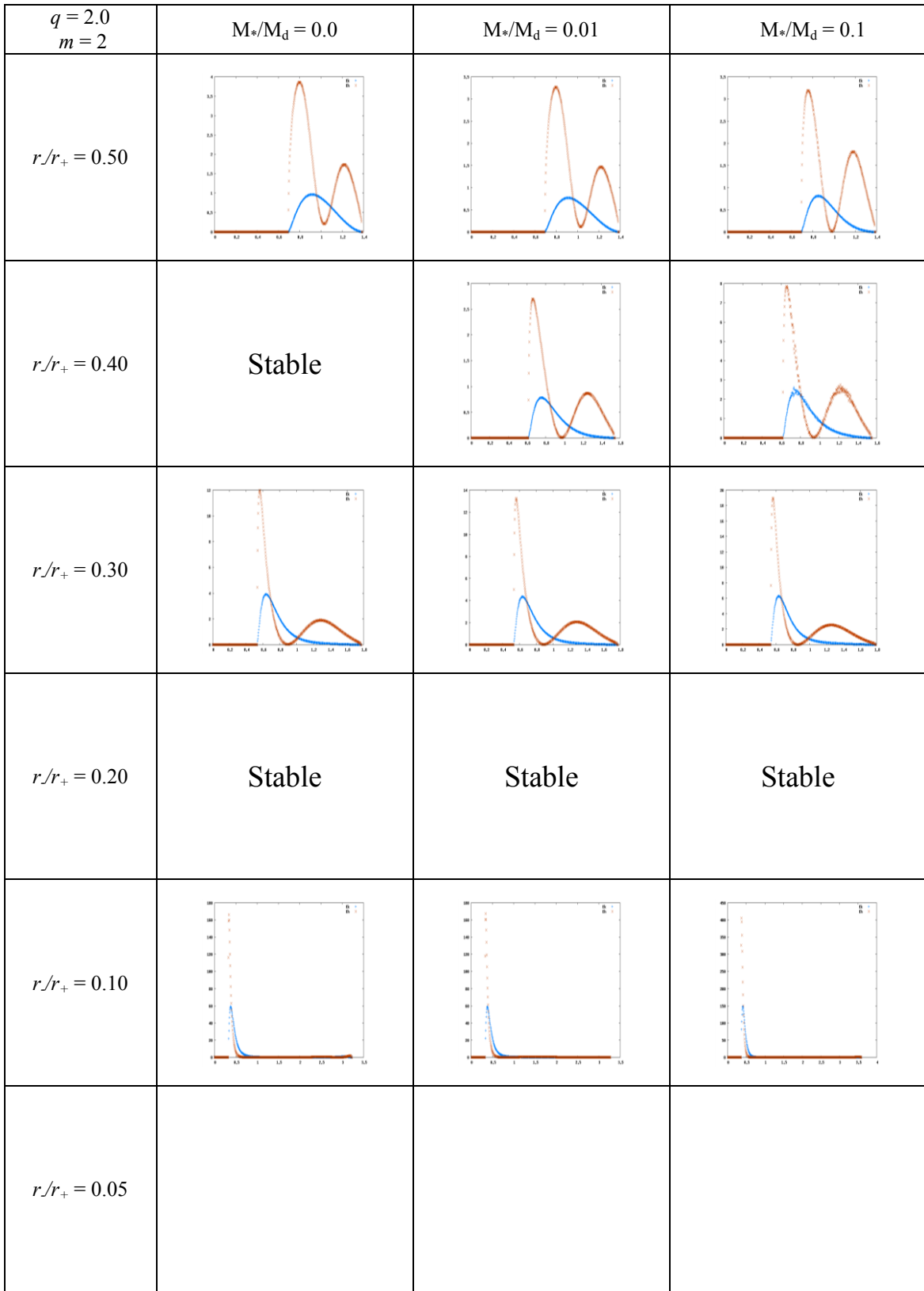


Fig. C.2.5.a. Work integrals for $q = 2.0$, $m = 2$

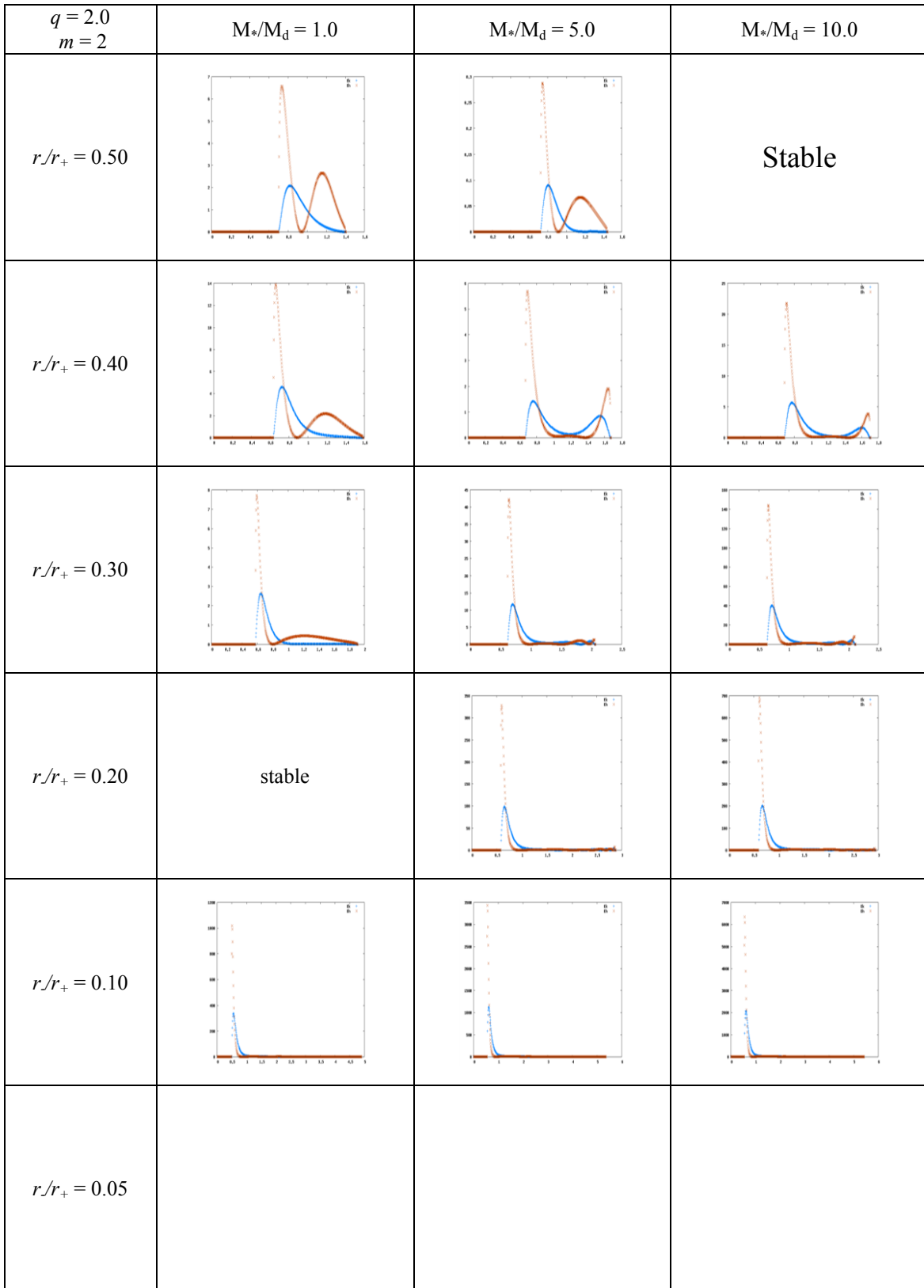


Fig. C.2.5.b. Work integrals for $q = 2.0$, $m = 2$

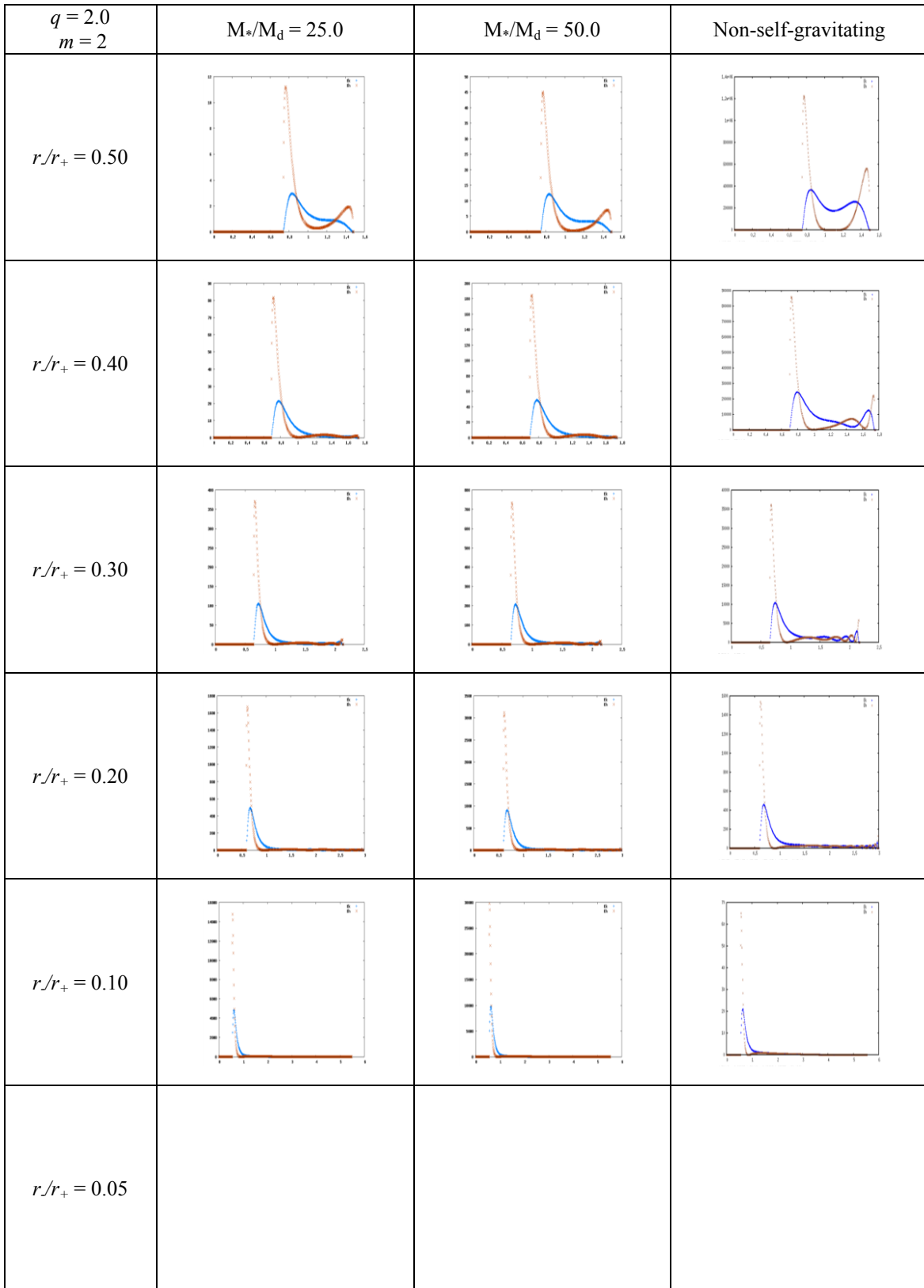


Fig. C.2.5.c. Work integrals for $q = 2.0$, $m = 2$

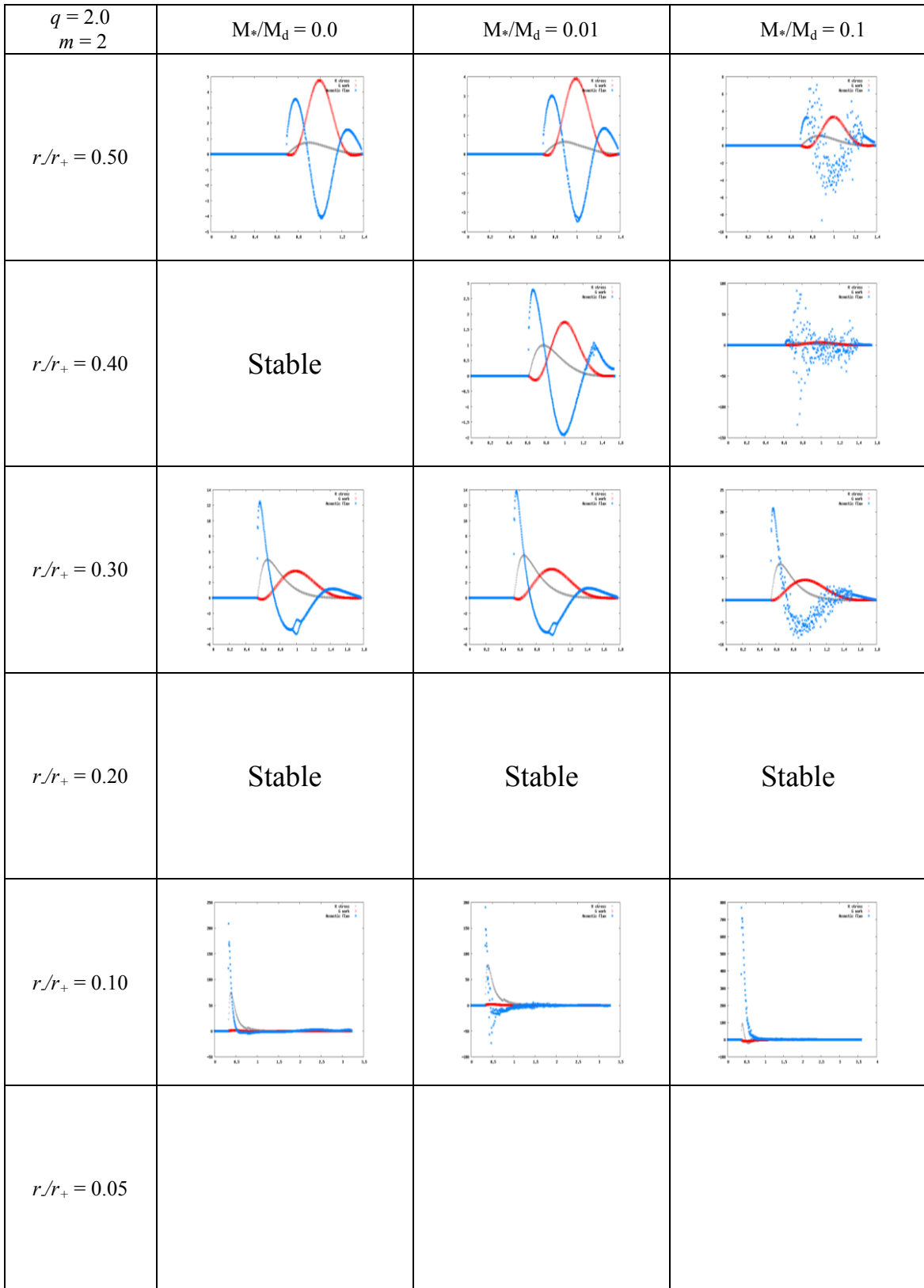


Fig. C.2.6.a. Stresses for $q = 2.0$, $m = 2$

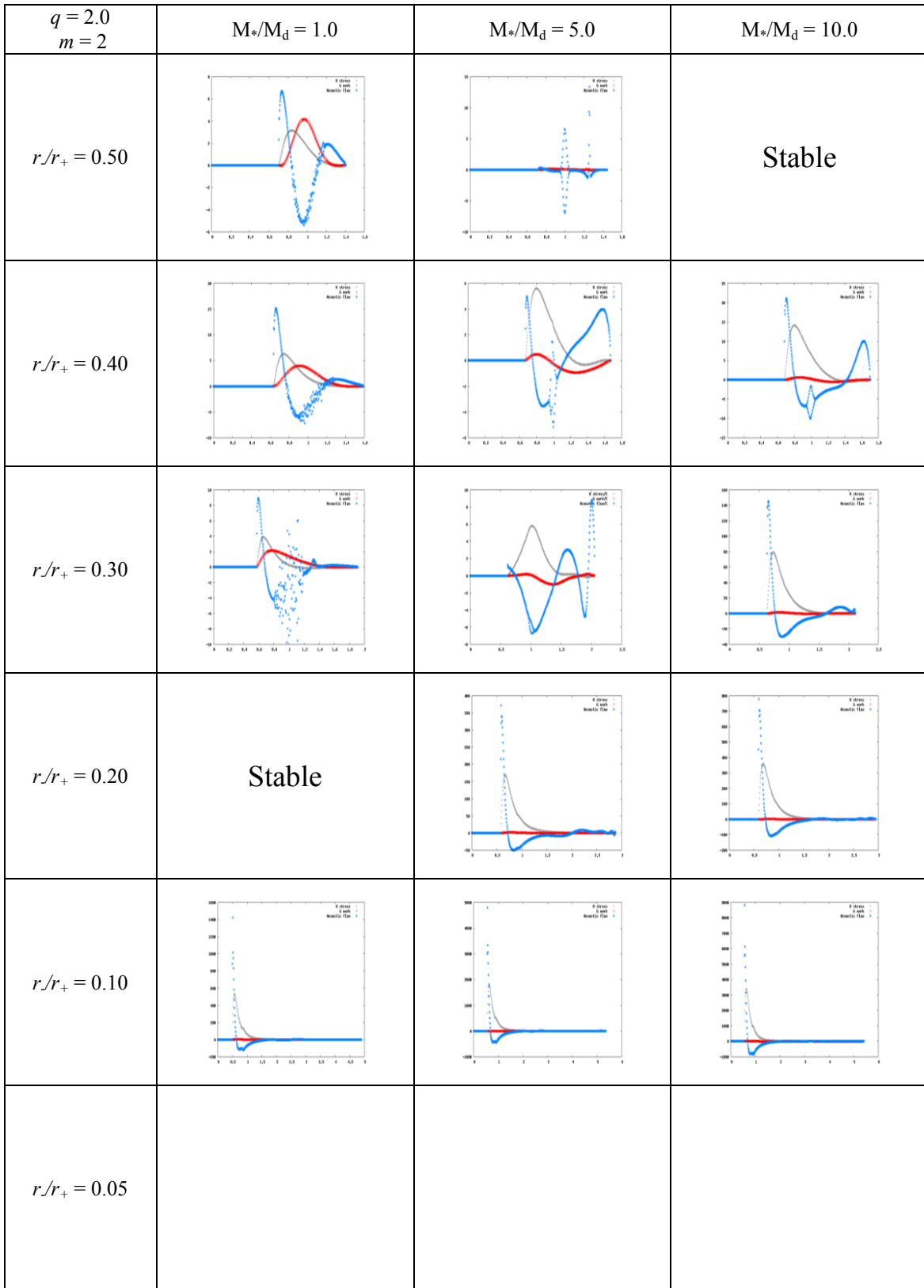


Fig. C.2.6.b. Stresses for $q = 2.0$, $m = 2$

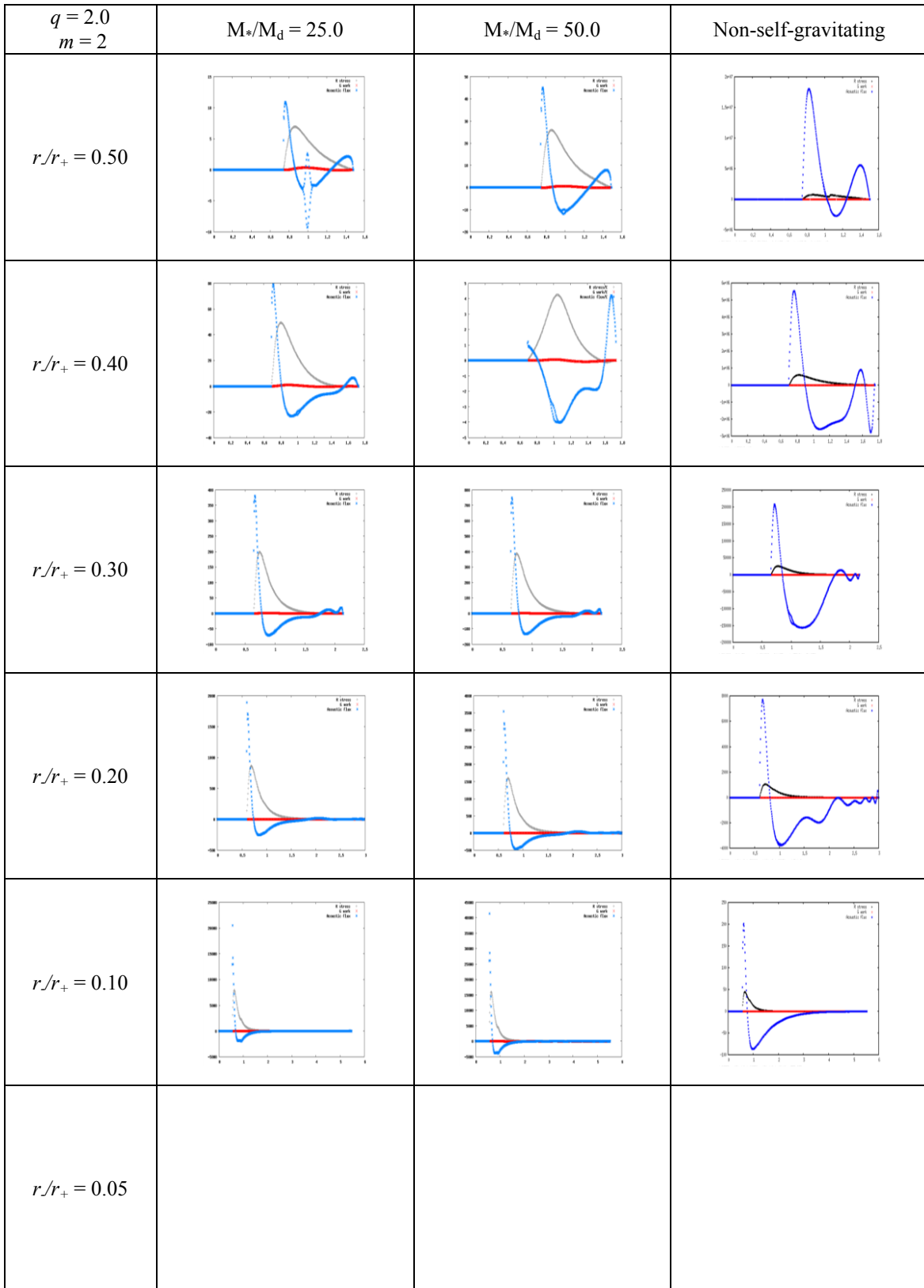


Fig. C.2.6.c. Stresses for $q = 2.0$, $m = 2$

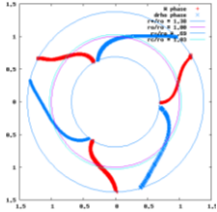
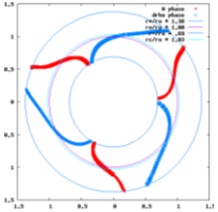
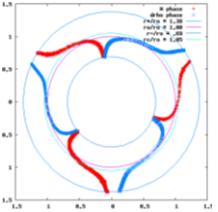
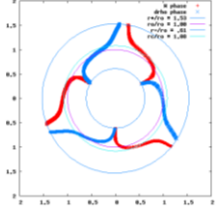
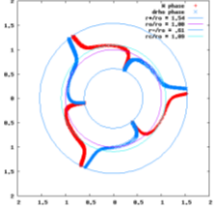
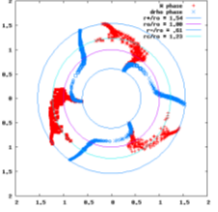
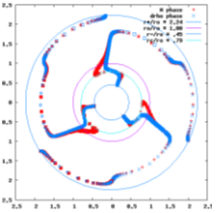
$q = 2.0$ $m = 3$	$M_*/M_d = 0.0$	$M_*/M_d = 0.01$	$M_*/M_d = 0.1$
$r/r_+ = 0.50$			
$r/r_+ = 0.40$			
$r/r_+ = 0.30$	Stable	Stable	Stable
$r/r_+ = 0.20$	Stable	Stable	
$r/r_+ = 0.10$	Stable	Stable	Stable
$r/r_+ = 0.05$			

Fig. C.3.1 a Eigenfunction phases for $q = 2.0$, $m = 3$.

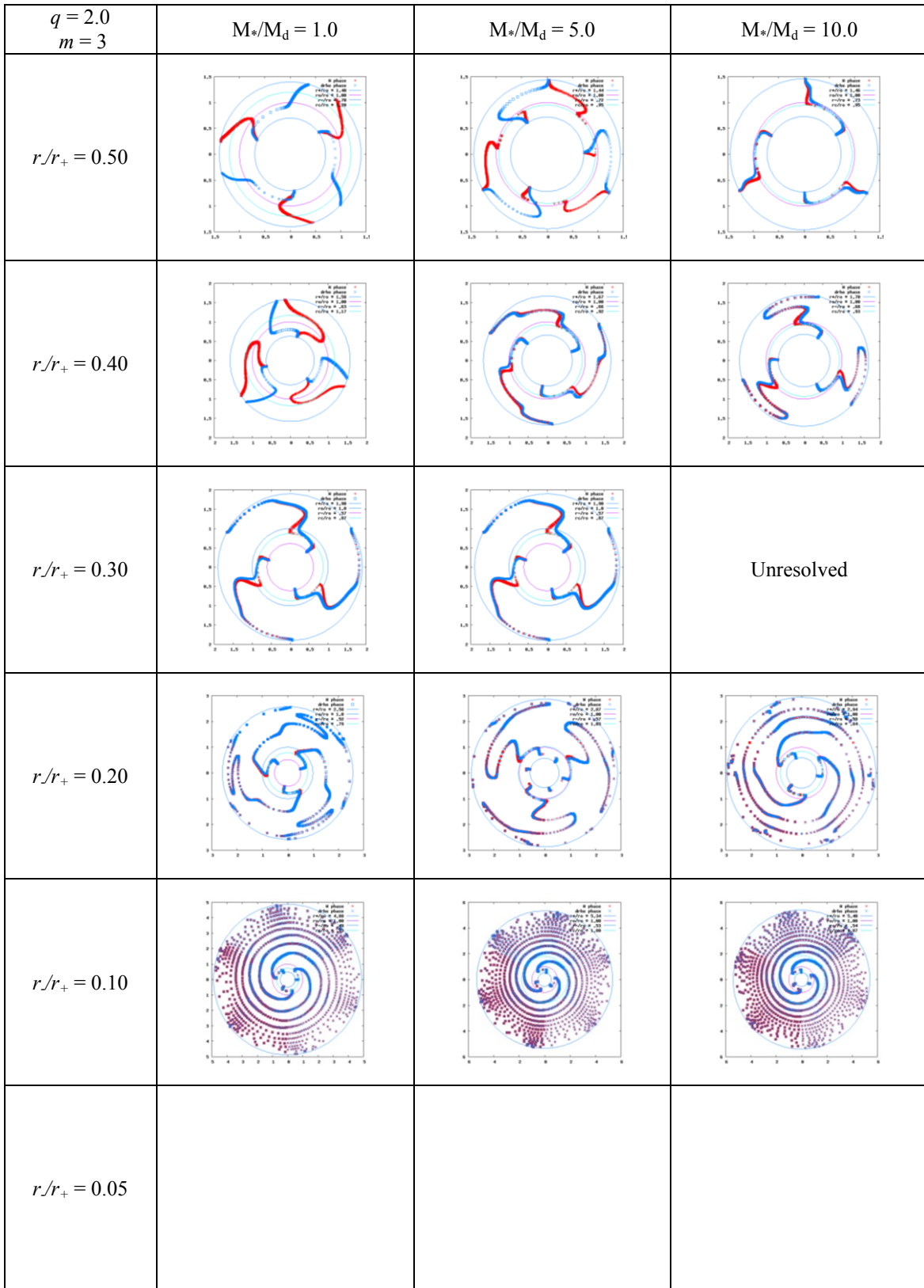


Fig. C.3.1.b. Eigenfunction phases for $q = 2.0$, $m = 3$.

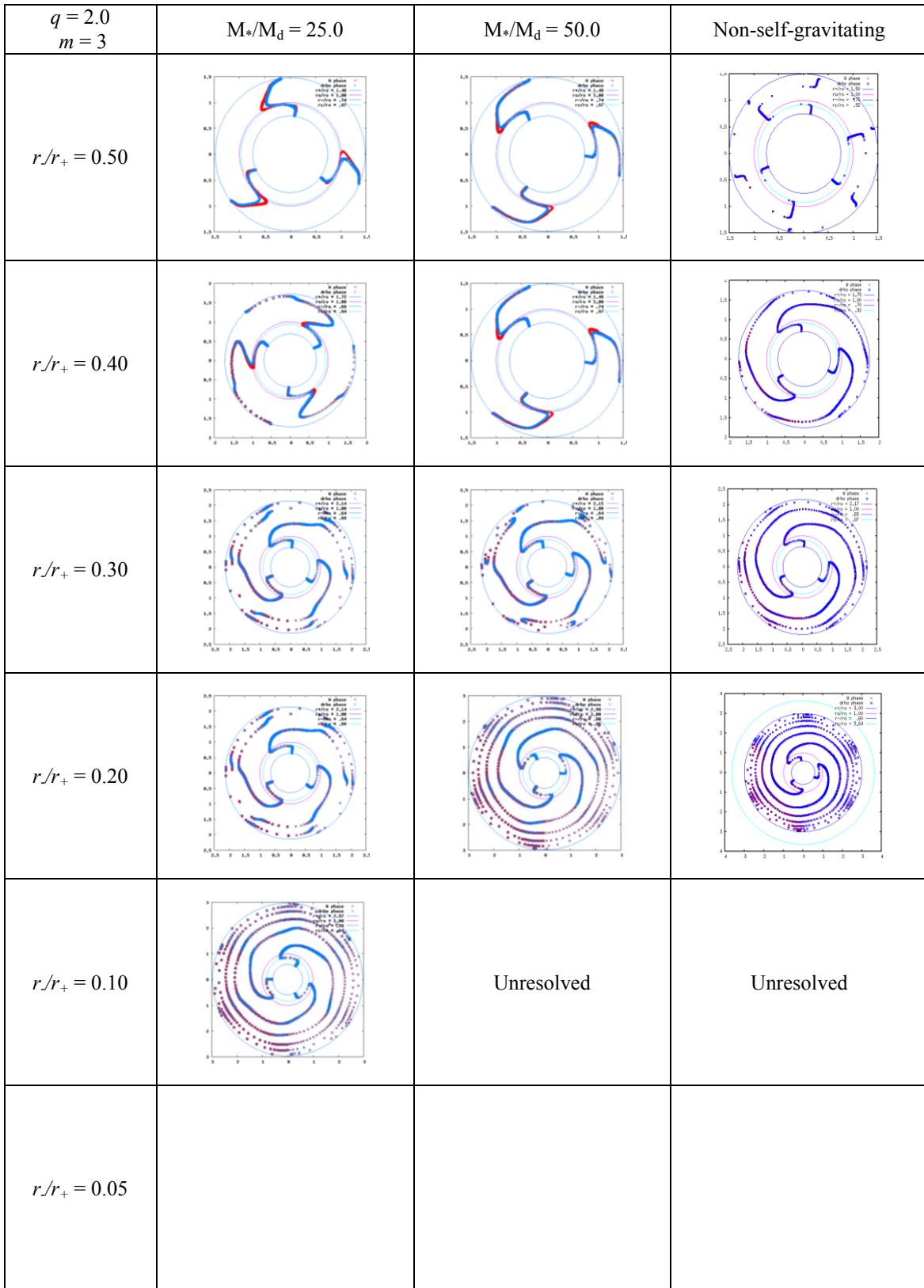


Fig. C.3.1.c. Eigenfunction phases for $q = 2.0$, $m = 3$.

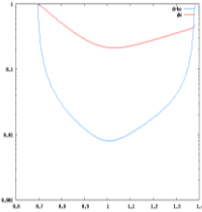
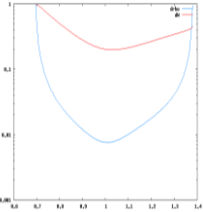
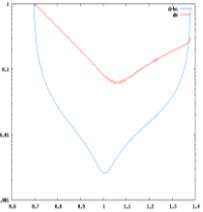
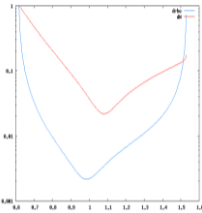
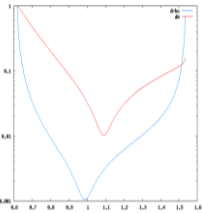
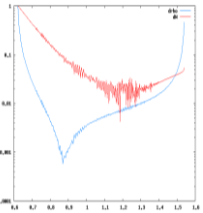
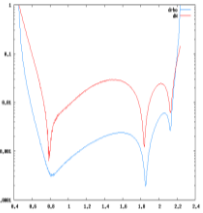
$q = 2.0$ $m = 3$	$M_*/M_d = 0.0$	$M_*/M_d = 0.01$	$M_*/M_d = 0.1$
$r/r_+ = 0.50$			
$r/r_+ = 0.40$			
$r/r_+ = 0.30$	Stable	Stable	Stable
$r/r_+ = 0.20$	Stable	Stable	
$r/r_+ = 0.10$	Stable	Stable	Stable
$r/r_+ = 0.05$			

Fig. C.3.2.a. Eigenfunction amplitudes $|\delta\rho|/\rho$ and W for $q = 2.0$, $m = 3$.

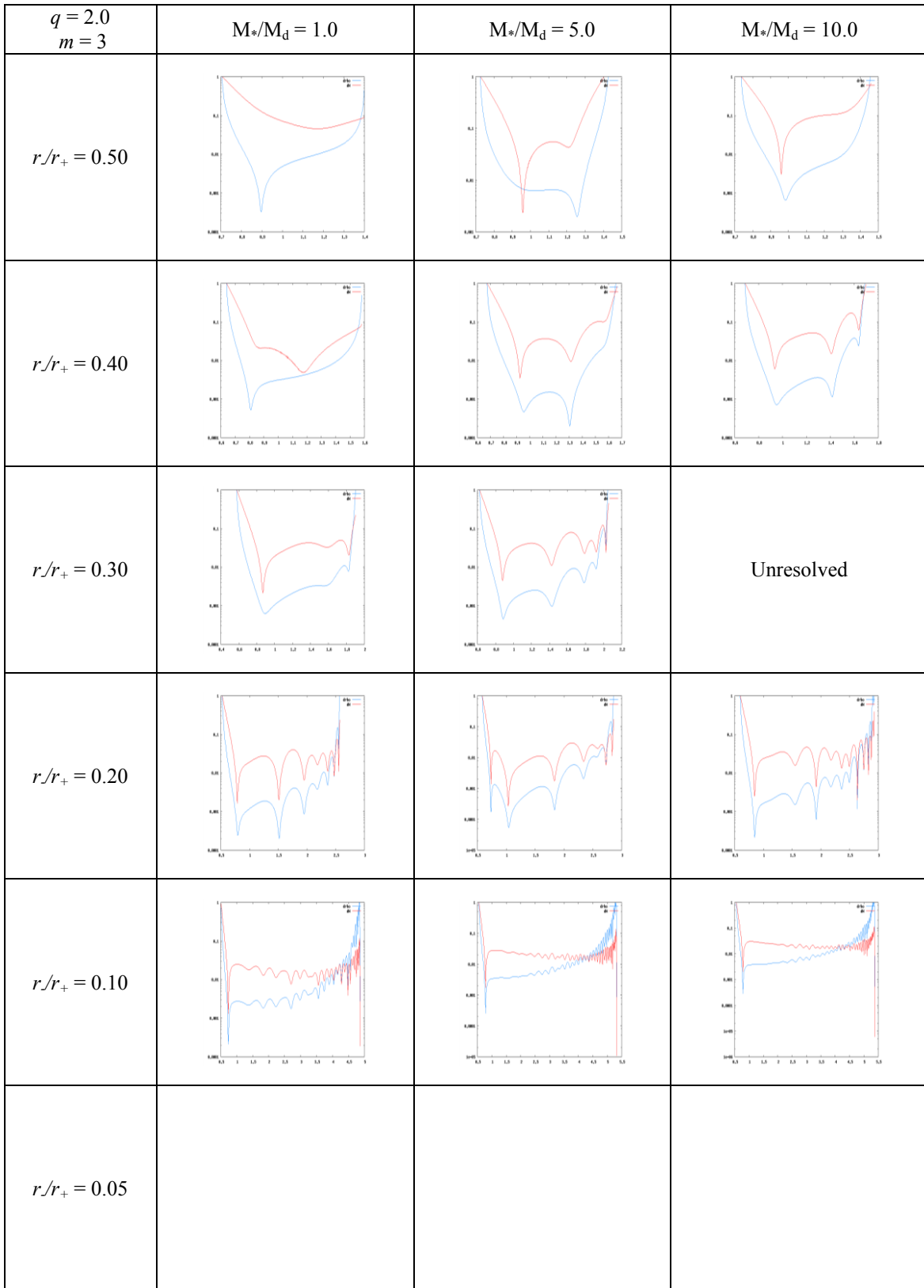


Fig. C.3.2.b. Eigenfunction amplitudes $|\delta\rho|/\rho$ and W for $q = 2.0$, $m = 3$.

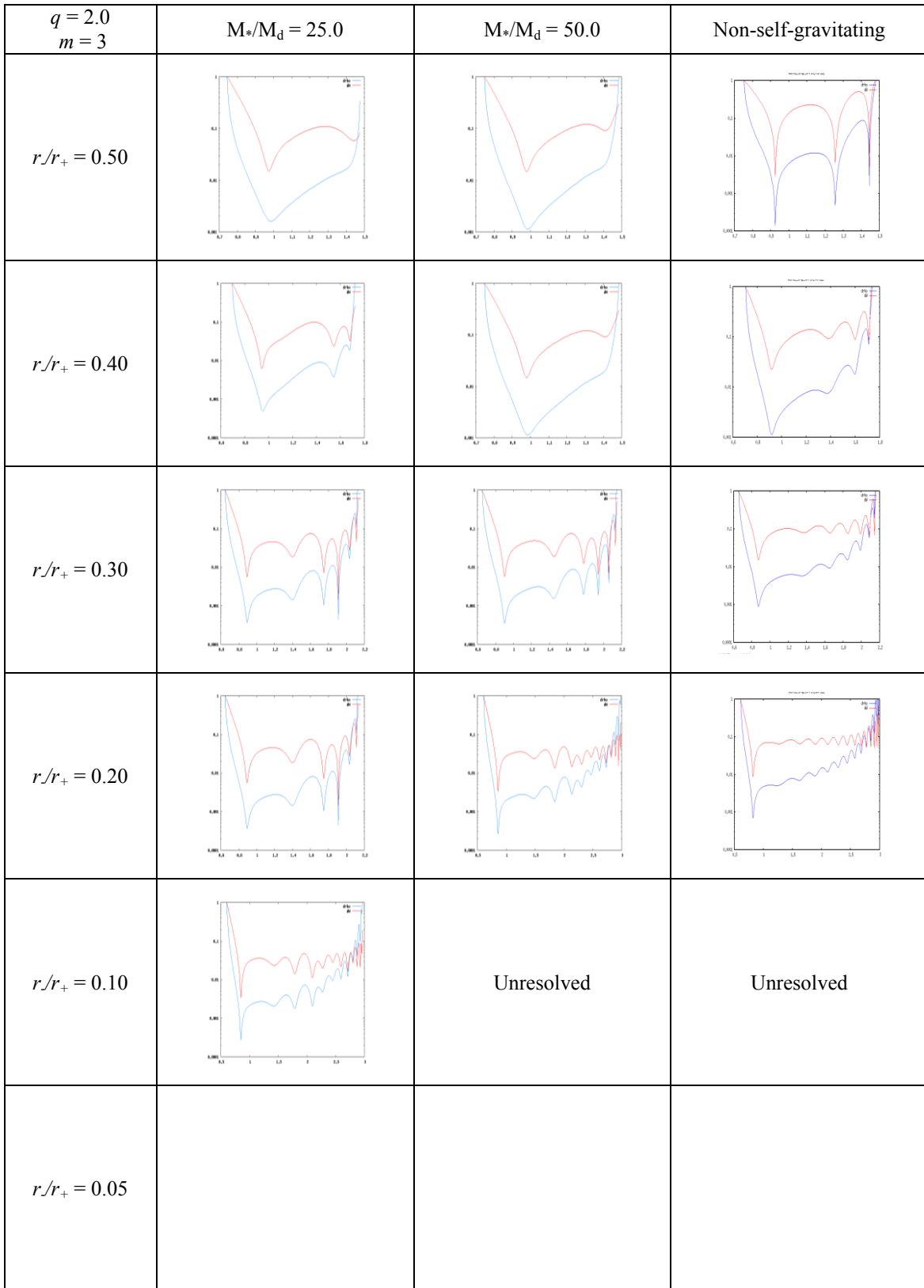


Fig. C.3.2.c. Eigenfunction amplitudes $|\delta\rho|/\rho$ and W for $q = 2.0$, $m = 3$.

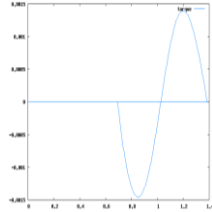
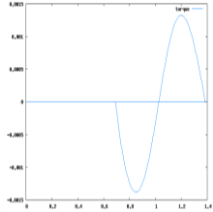
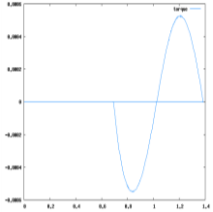
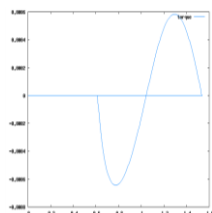
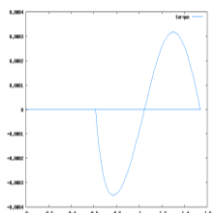
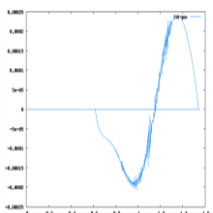
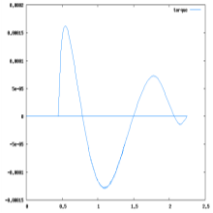
$q = 2.0$ $m = 3$	$M_*/M_d = 0.0$	$M_*/M_d = 0.01$	$M_*/M_d = 0.1$
$r/r_+ = 0.50$			
$r/r_+ = 0.40$			
$r/r_+ = 0.30$	Stable	Stable	Stable
$r/r_+ = 0.20$	Stable	Stable	
$r/r_+ = 0.10$	Stable	Stable	Stable
$r/r_+ = 0.05$			

Fig. C.3.3.a. Self-gravitational torque for $q = 2.0$, $m = 3$.

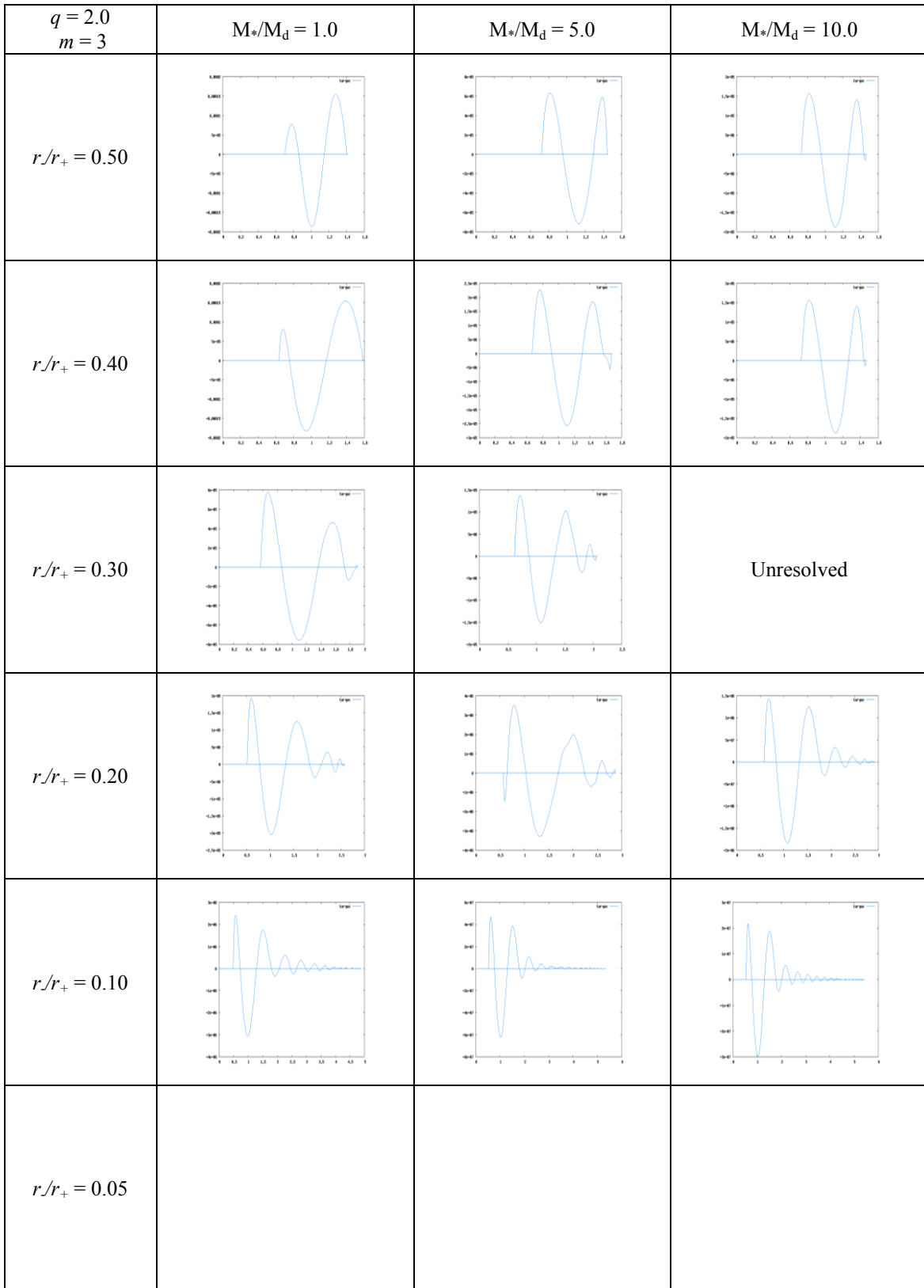


Fig. C.3.3.b. Self-gravitational torque for $q = 2.0$, $m = 3$.

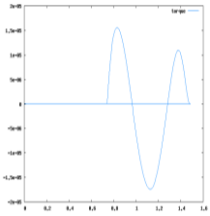
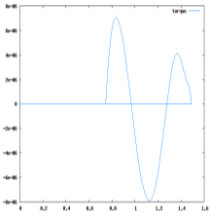
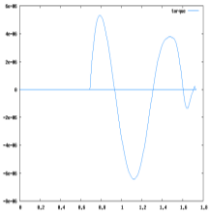
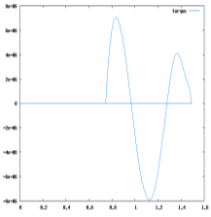
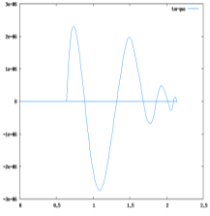
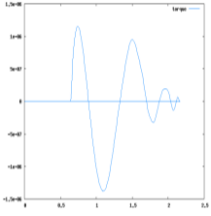
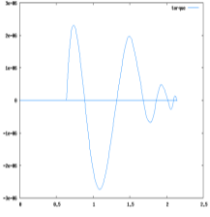
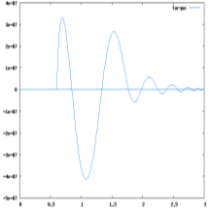
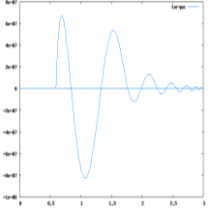
$q = 2.0$ $m = 3$	$M_*/M_d = 25.0$	$M_*/M_d = 50.0$	Non-self-gravitating
$r/r_+ = 0.50$			
$r/r_+ = 0.40$			
$r/r_+ = 0.30$			
$r/r_+ = 0.20$			
$r/r_+ = 0.10$		Unresolved	Unresolved
$r/r_+ = 0.05$			

Fig. C.3.3.c. Self-gravitational torque for $q = 2.0$, $m = 3$.

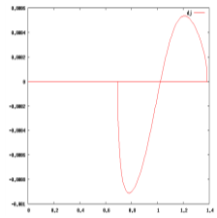
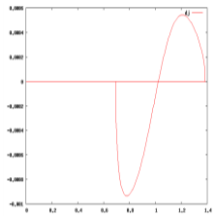
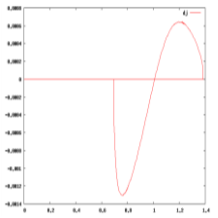
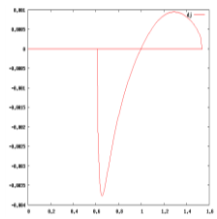
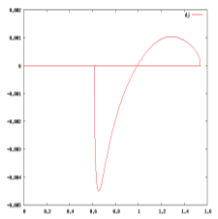
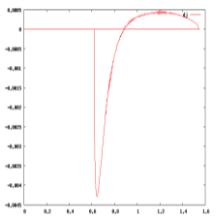
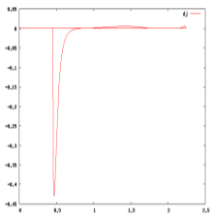
$q = 2.0$ $m = 3.$	$M_*/M_d = 0.0$	$M_*/M_d = 0.01$	$M_*/M_d = 0.1$
$r/r_+ = 0.50$			
$r/r_+ = 0.40$			
$r/r_+ = 0.30$	Stable	Stable	Stable
$r/r_+ = 0.20$	Stable	Stable	
$r/r_+ = 0.10$	Stable	Stable	Stable
$r/r_+ = 0.05$			

Fig. C.3.4 a Perturbed angular momentum for $q = 2.0$, $m = 3$

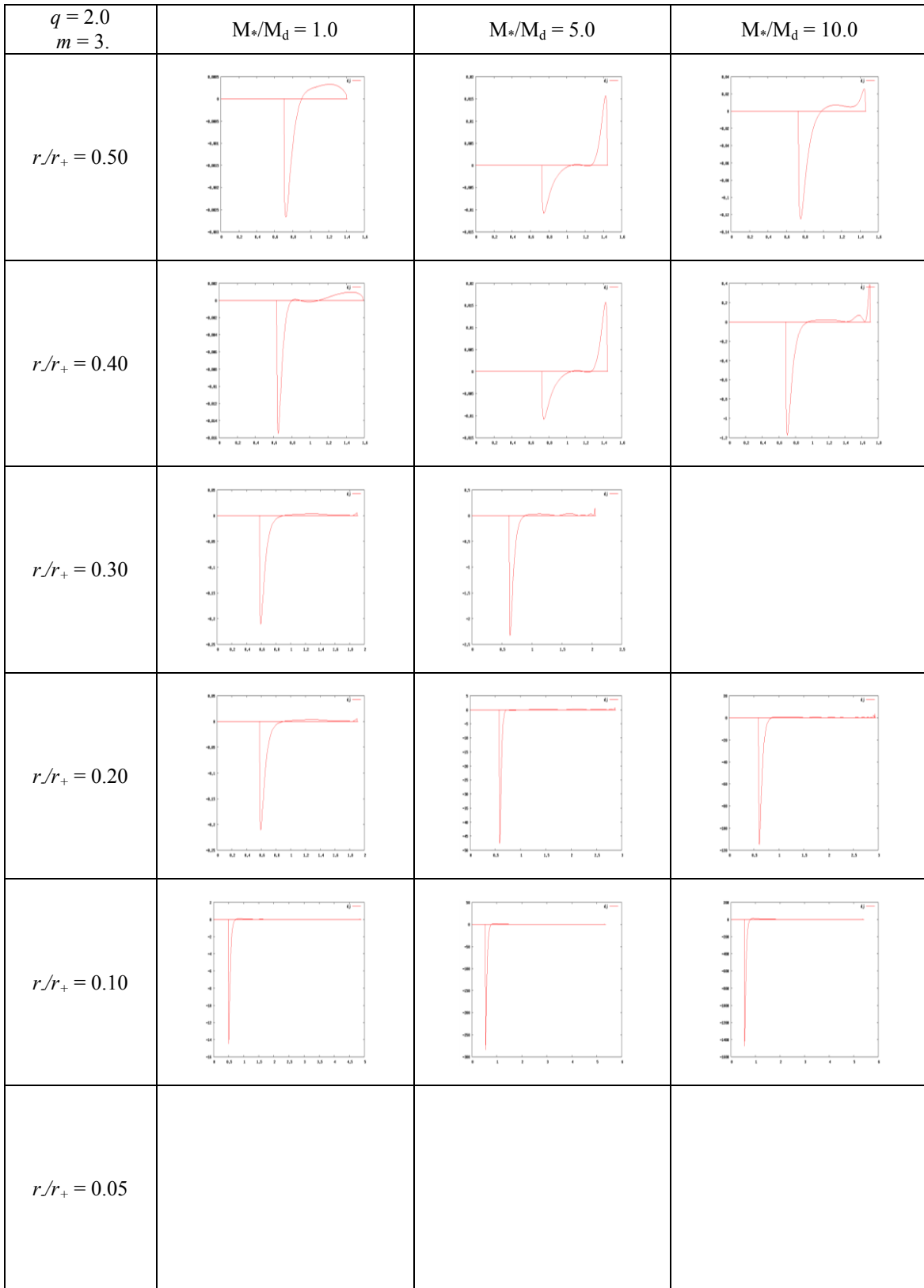


Fig. C.3.4.b. Perturbed angular momentum for $q = 2.0$, $m = 3$

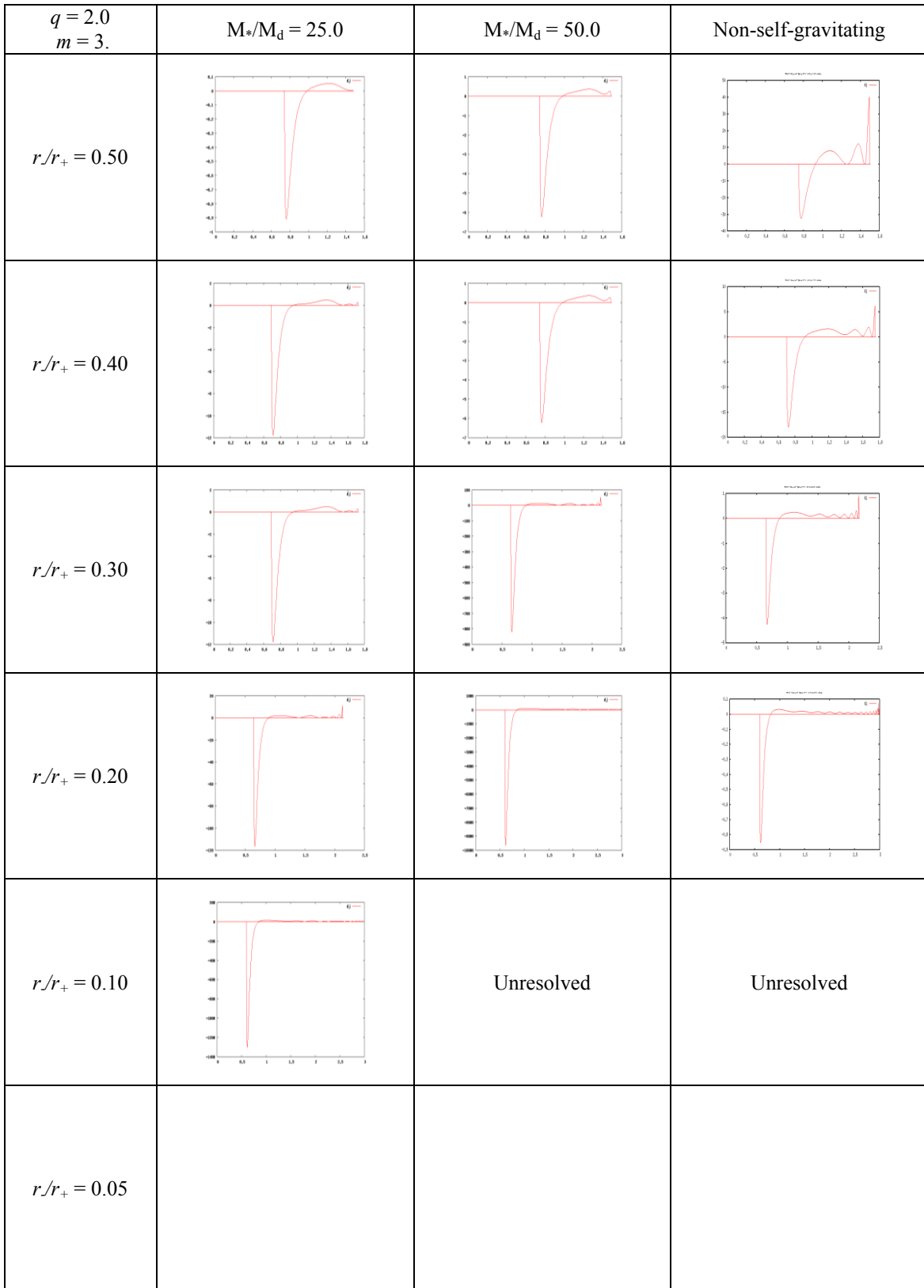


Fig. C.3.4.c. Perturbed angular momentum for $q = 2.0$, $m = 3$

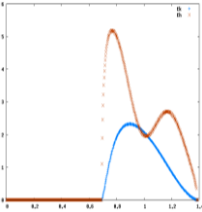
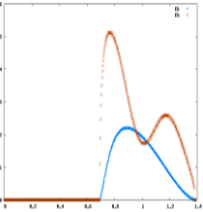
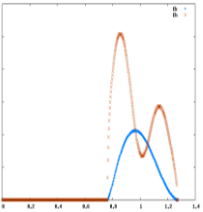
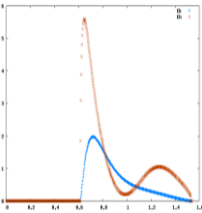
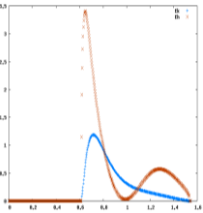
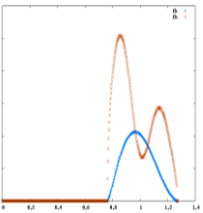
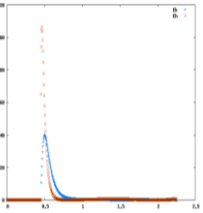
$q = 2.0$ $m = 3.$	$M_*/M_d = 0.0$	$M_*/M_d = 0.01$	$M_*/M_d = 0.1$
$r/r_+ = 0.50$			
$r/r_+ = 0.40$			
$r/r_+ = 0.30$	Stable	Stable	Stable
$r/r_+ = 0.20$	Stable	Stable	
$r/r_+ = 0.10$	Stable	Stable	Stable
$r/r_+ = 0.05$			

Fig. C.3.5.a. Work integrals for $q = 2.0$, $m = 3$

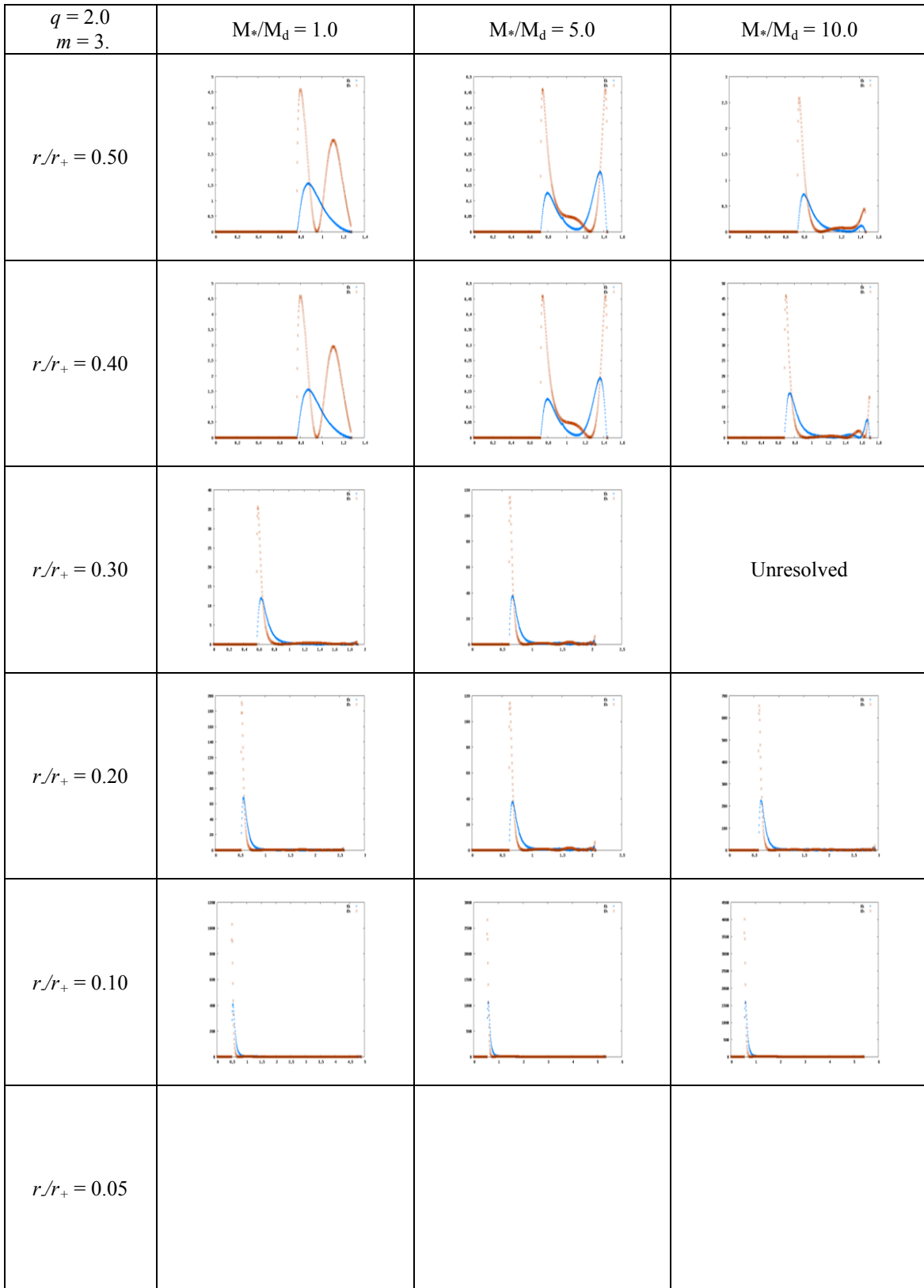


Fig. C.3.5.b. Work integrals for $q = 2.0$, $m = 3$

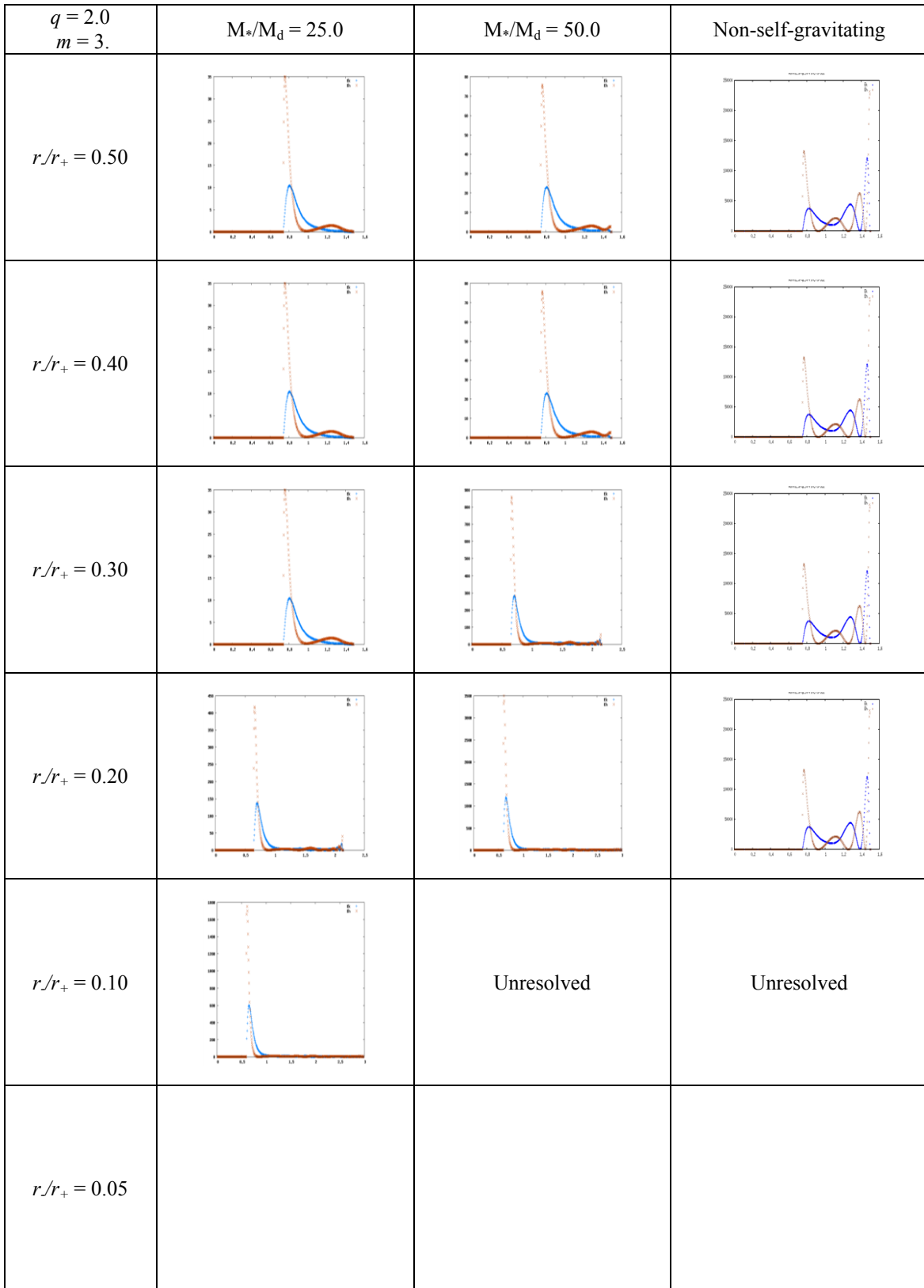


Fig. C.3.5.c. Work integrals for $q = 2.0$, $m = 3$
348

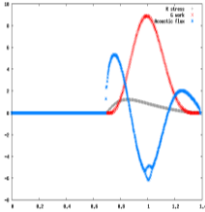
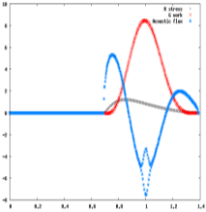
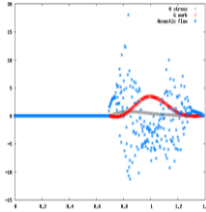
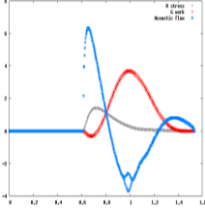
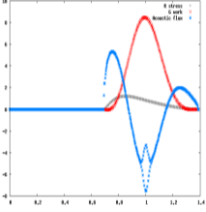
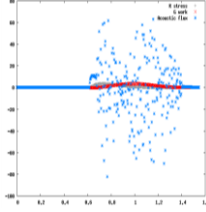
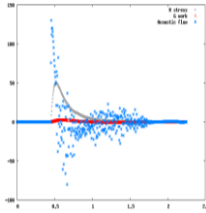
$q = 2.0$ $m = 3$	$M_*/M_d = 0.0$	$M_*/M_d = 0.01$	$M_*/M_d = 0.1$
$r/r_+ = 0.50$			
$r/r_+ = 0.40$			
$r/r_+ = 0.30$	Stable	Stable	Stable
$r/r_+ = 0.20$	Stable	Stable	
$r/r_+ = 0.10$	Stable	Stable	Stable
$r/r_+ = 0.05$			

Fig. C.3.6.a. Stresses for $q = 2.0$, $m = 3$.

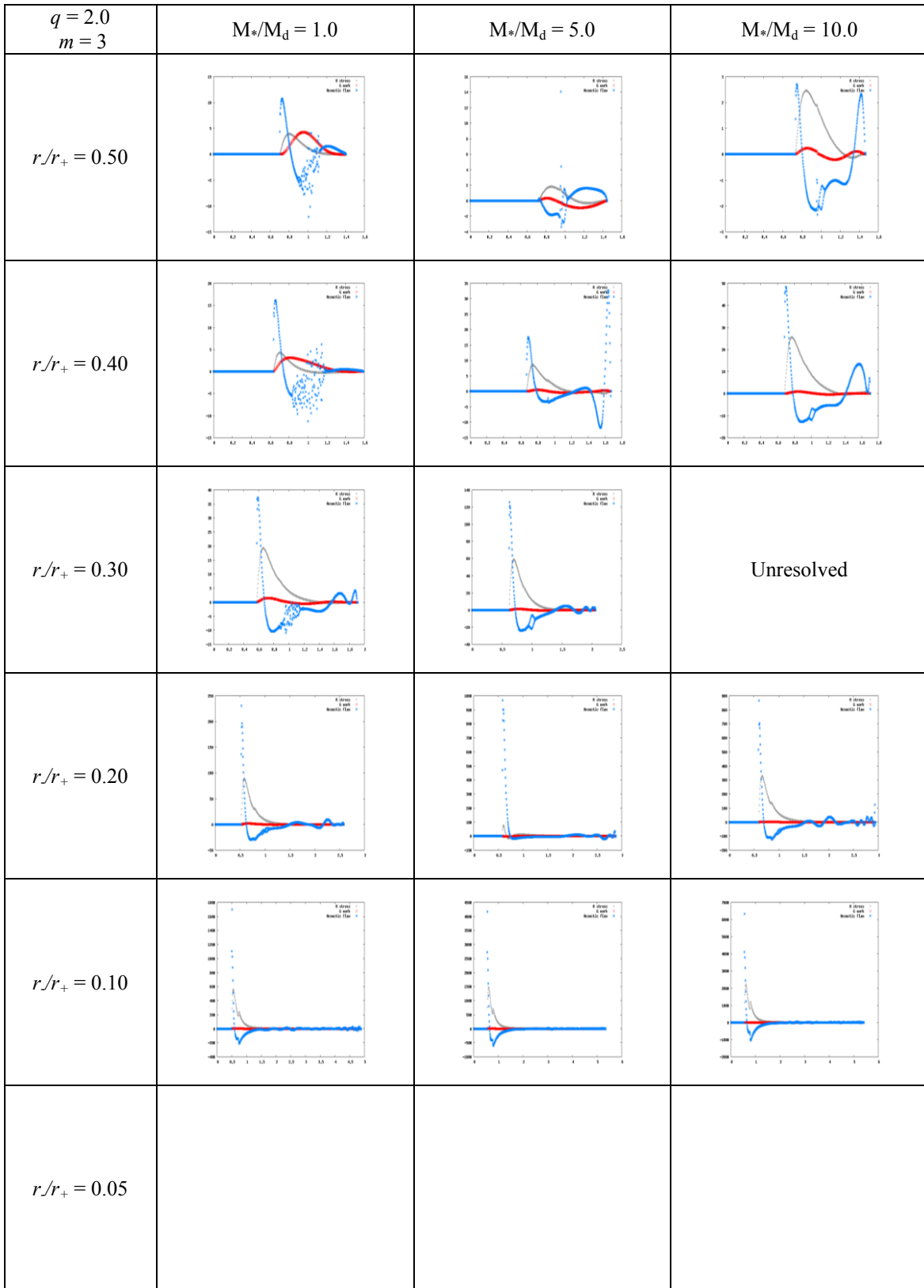


Fig. C.3.6.b. Stresses for $q = 2.0$, $m = 3$.

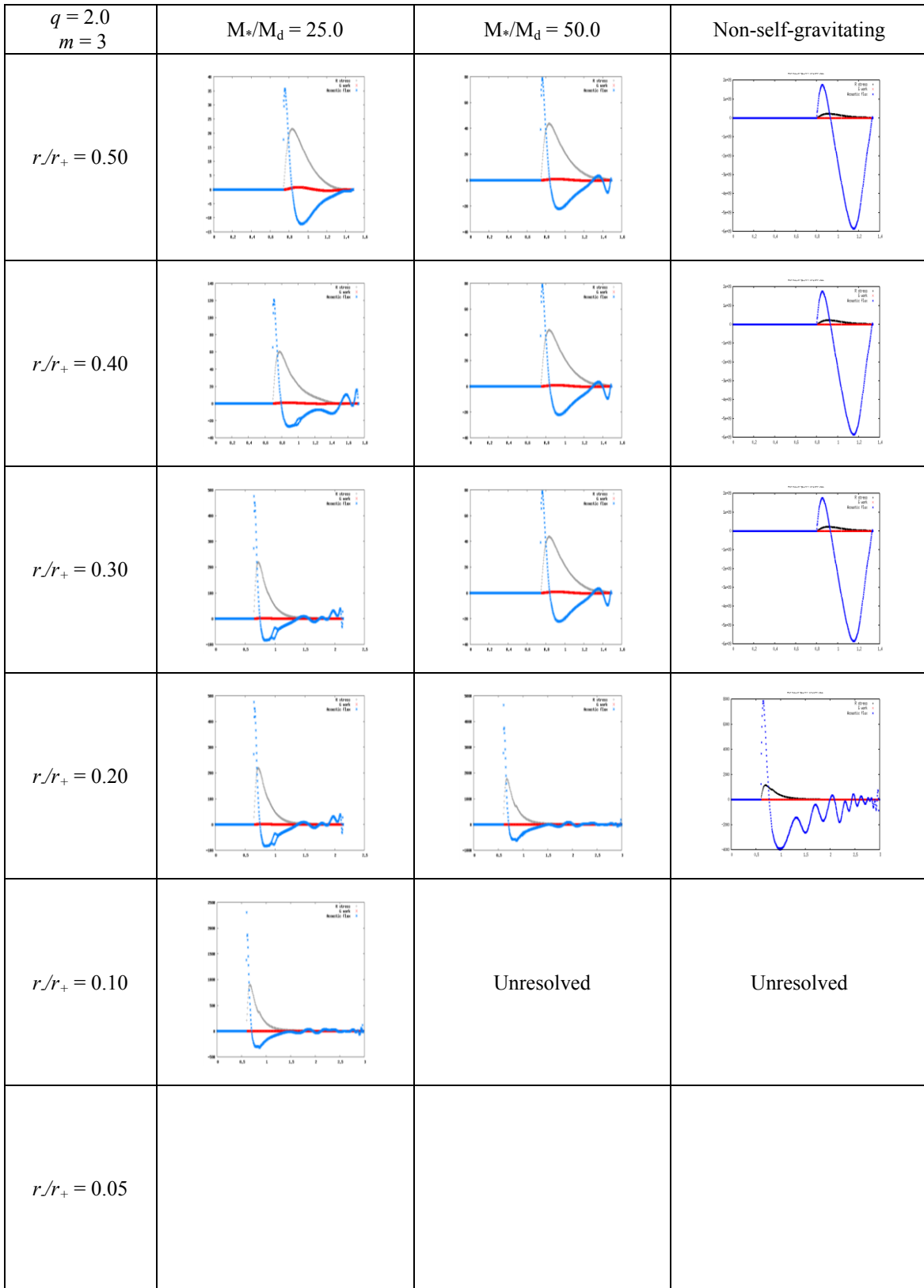


Fig. C.3.6.c. Stresses for $q = 2.0$, $m = 3$.

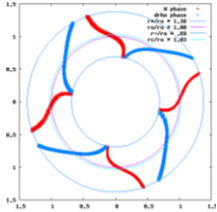
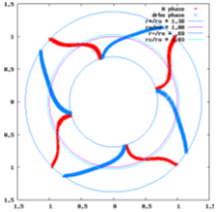
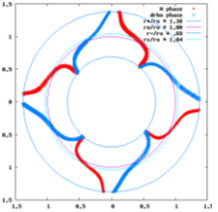
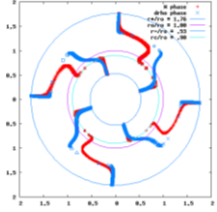
$q = 2.0$ $m = 4$	$M_*/M_d = 0.0$	$M_*/M_d = 0.01$	$M_*/M_d = 0.1$
$r/r_+ = 0.50$			
$r/r_+ = 0.40$	Stable	Stable	Stable
$r/r_+ = 0.30$		Stable	Stable
$r/r_+ = 0.20$	Stable	Stable	Stable
$r/r_+ = 0.10$	Stable	Stable	Stable
$r/r_+ = 0.05$	Stable	Stable	Stable

Fig. C.4.1 a Eigenfunction phases for $q = 2.0$, $m = 4$.

$q = 2.0$ $m = 4$	$M_*/M_d = 1.0$	$M_*/M_d = 5.0$	$M_*/M_d = 10.0$
$r/r_+ = 0.50$			
$r/r_+ = 0.40$	Stable		
$r/r_+ = 0.30$			
$r/r_+ = 0.20$			
$r/r_+ = 0.10$	Stable	Stable	Stable
$r/r_+ = 0.05$	Stable	Stable	Stable

Fig. C.4.1.b. Eigenfunction phases for $q = 2.0$, $m = 4$.

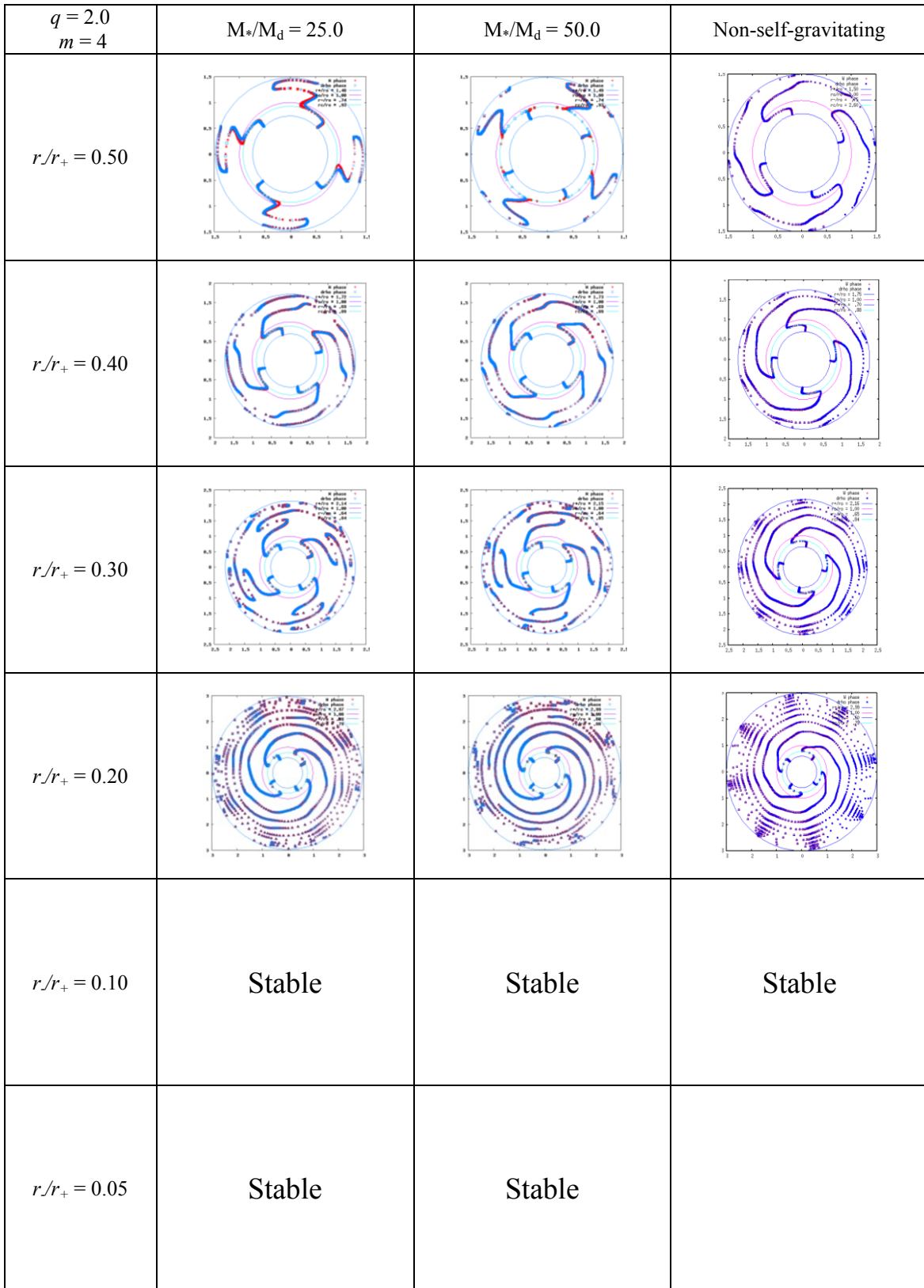


Fig. C.4.1.c. Eigenfunction phases for $q = 2.0$, $m = 4$.

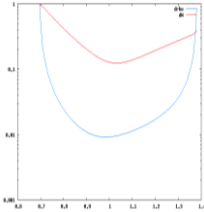
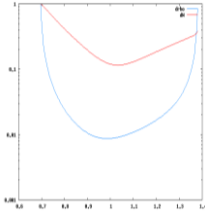
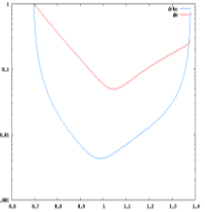
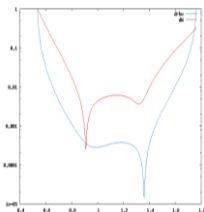
$q = 2.0$ $m = 4$	$M_*/M_d = 0.0$	$M_*/M_d = 0.01$	$M_*/M_d = 0.1$
$r/r_+ = 0.50$			
$r/r_+ = 0.40$	Stable	Stable	Stable
$r/r_+ = 0.30$		Stable	Stable
$r/r_+ = 0.20$	Stable	Stable	Stable
$r/r_+ = 0.10$	Stable	Stable	Stable
$r/r_+ = 0.05$	Stable	Stable	Stable

Fig. C.4.2.a. Eigenfunction amplitudes $|\delta\rho|/\rho$ and W for $q = 2.0$, $m = 4$.

$q = 2.0$ $m = 4$	$M_*/M_d = 1.0$	$M_*/M_d = 5.0$	$M_*/M_d = 10.0$
$r/r_+ = 0.50$			
$r/r_+ = 0.40$	Stable		
$r/r_+ = 0.30$			
$r/r_+ = 0.20$			
$r/r_+ = 0.10$	Stable	Stable	Stable
$r/r_+ = 0.05$	Stable	Stable	Stable

Fig. C.4.2.b. Eigenfunction amplitudes $|\delta\rho|/\rho$ and W for $q = 2.0$, $m = 4$.

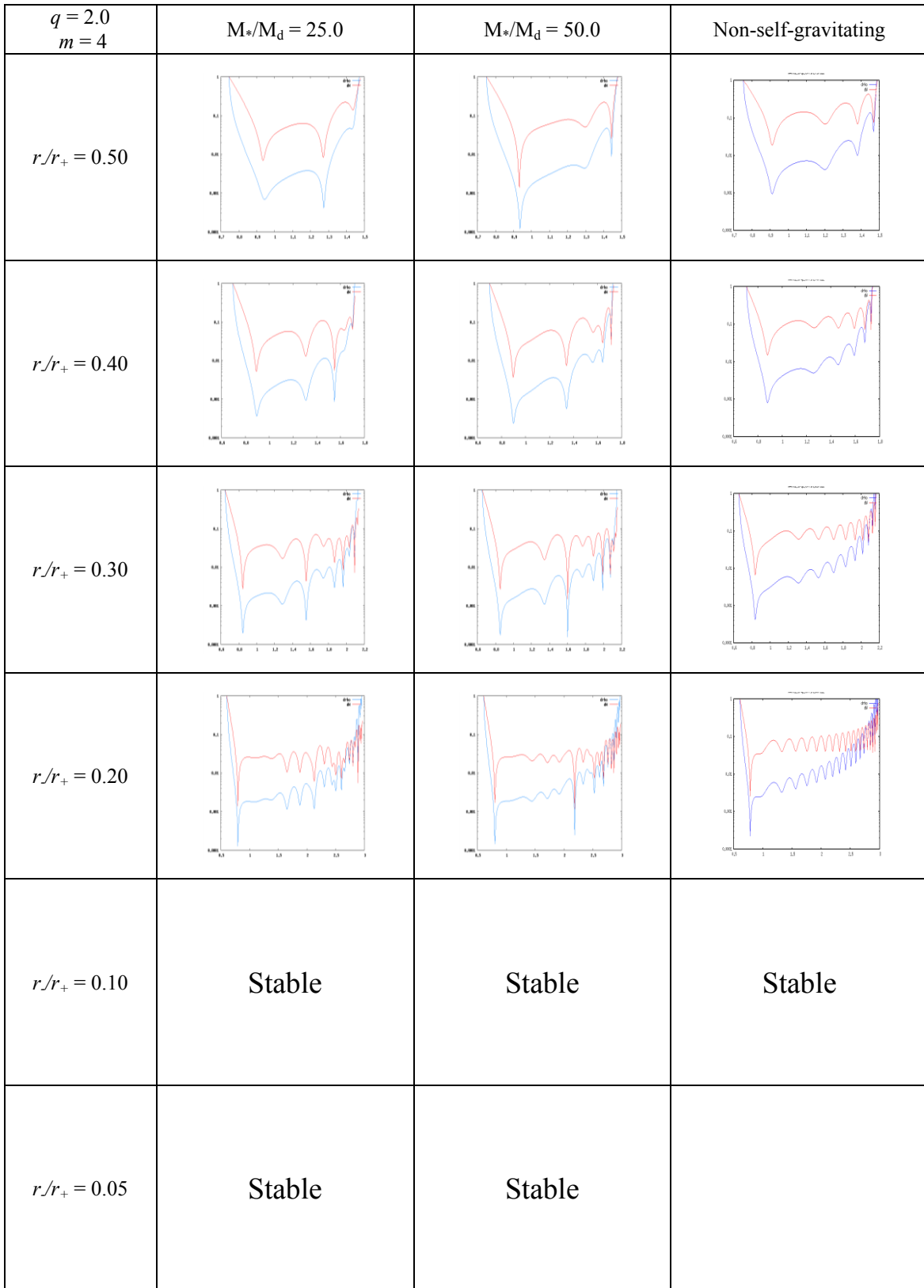


Fig. C.4.2.c. Eigenfunction amplitudes $|\delta\rho|/\rho$ and W for $q = 2.0$, $m = 4$.

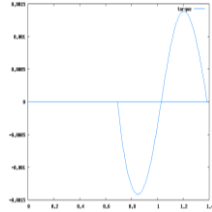
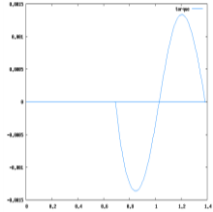
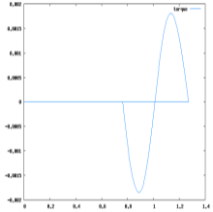
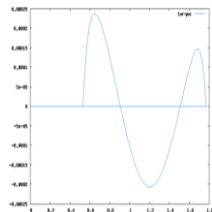
$q = 2.0$ $m = 4$	$M_*/M_d = 0.0$	$M_*/M_d = 0.01$	$M_*/M_d = 0.1$
$r/r_+ = 0.50$			
$r/r_+ = 0.40$	Stable	Stable	Stable
$r/r_+ = 0.30$		Stable	Stable
$r/r_+ = 0.20$	Stable	Stable	Stable
$r/r_+ = 0.10$	Stable	Stable	Stable
$r/r_+ = 0.05$	Stable	Stable	Stable

Fig. C.4.3.a. Self-gravitational torque for $q = 2.0$, $m = 4$.

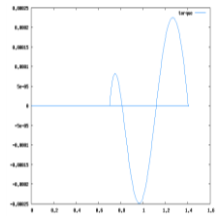
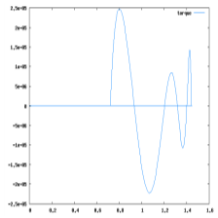
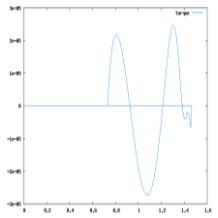
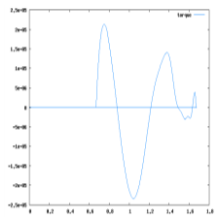
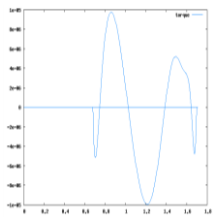
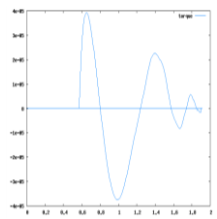
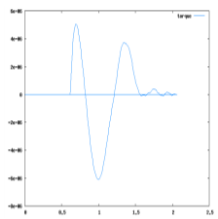
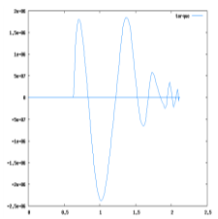
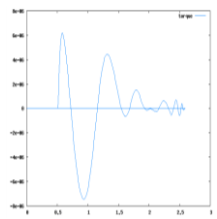
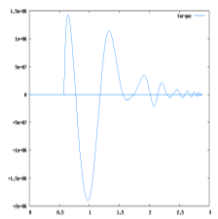
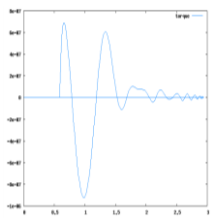
$q = 2.0$ $m = 4$	$M_*/M_d = 1.0$	$M_*/M_d = 5.0$	$M_*/M_d = 10.0$
$r/r_+ = 0.50$			
$r/r_+ = 0.40$	Stable		
$r/r_+ = 0.30$			
$r/r_+ = 0.20$			
$r/r_+ = 0.10$	Stable	Stable	Stable
$r/r_+ = 0.05$	Stable	Stable	Stable

Fig. C.4.3.b. Self-gravitational torque for $q = 2.0$, $m = 4$.

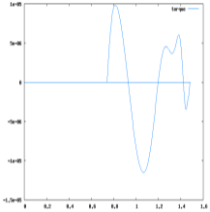
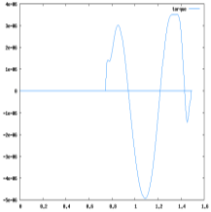
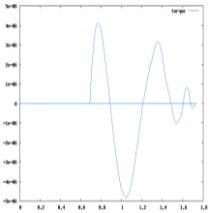
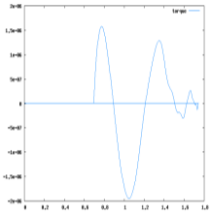
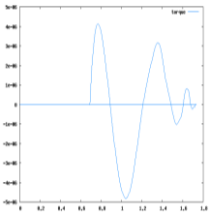
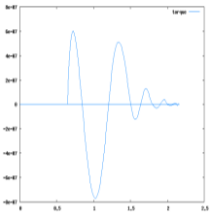
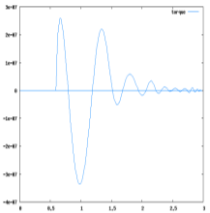
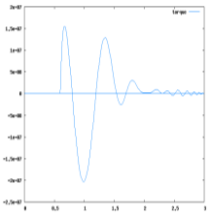
$q = 2.0$ $m = 4$	$M_*/M_d = 25.0$	$M_*/M_d = 50.0$	Non-self-gravitating
$r/r_+ = 0.50$			
$r/r_+ = 0.40$			
$r/r_+ = 0.30$			
$r/r_+ = 0.20$			
$r/r_+ = 0.10$	Stable	Stable	
$r/r_+ = 0.05$	Stable	Stable	

Fig. C.4.3.c. Self-gravitational torque for $q = 2.0$, $m = 4$.

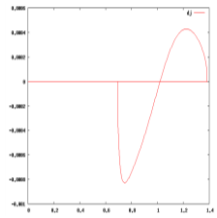
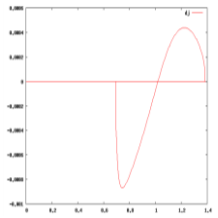
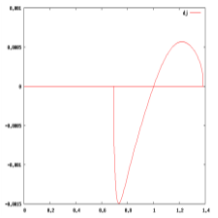
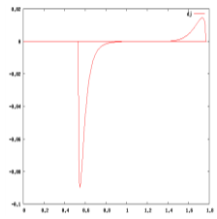
$q = 2.0$ $m = 4$	$M^*/M_d = 0.0$	$M^*/M_d = 0.01$	$M^*/M_d = 0.1$
$r/r_+ = 0.50$			
$r/r_+ = 0.40$	Stable	Stable	Stable
$r/r_+ = 0.30$		Stable	Stable
$r/r_+ = 0.20$	Stable	Stable	Stable
$r/r_+ = 0.10$	Stable	Stable	Stable
$r/r_+ = 0.05$	Stable	Stable	Stable

Fig. C.4.4 a Perturbed angular momentum for $q = 2.0$, $m = 4$.

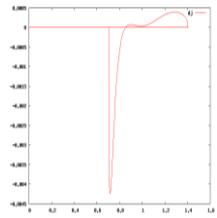
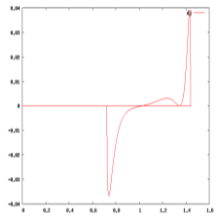
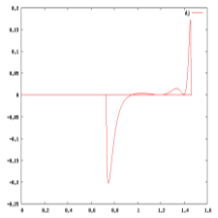
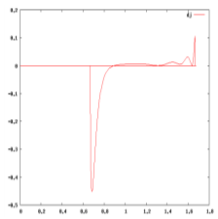
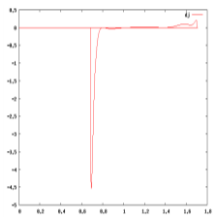
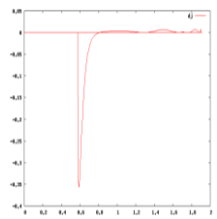
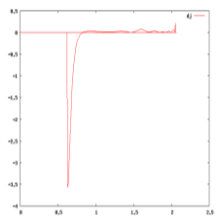
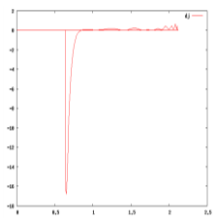
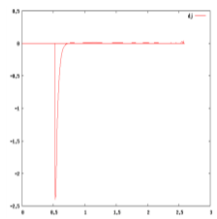
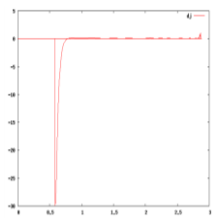
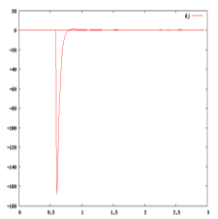
$q = 2.0$ $m = 4$	$M_*/M_d = 1.0$	$M_*/M_d = 5.0$	$M_*/M_d = 10.0$
$r/r_+ = 0.50$			
$r/r_+ = 0.40$	Stable		
$r/r_+ = 0.30$			
$r/r_+ = 0.20$			
$r/r_+ = 0.10$	Stable	Stable	Stable
$r/r_+ = 0.05$	Stable	Stable	Stable

Fig. C.4.4.b. Perturbed angular momentum for $q = 2.0$, $m = 4$.

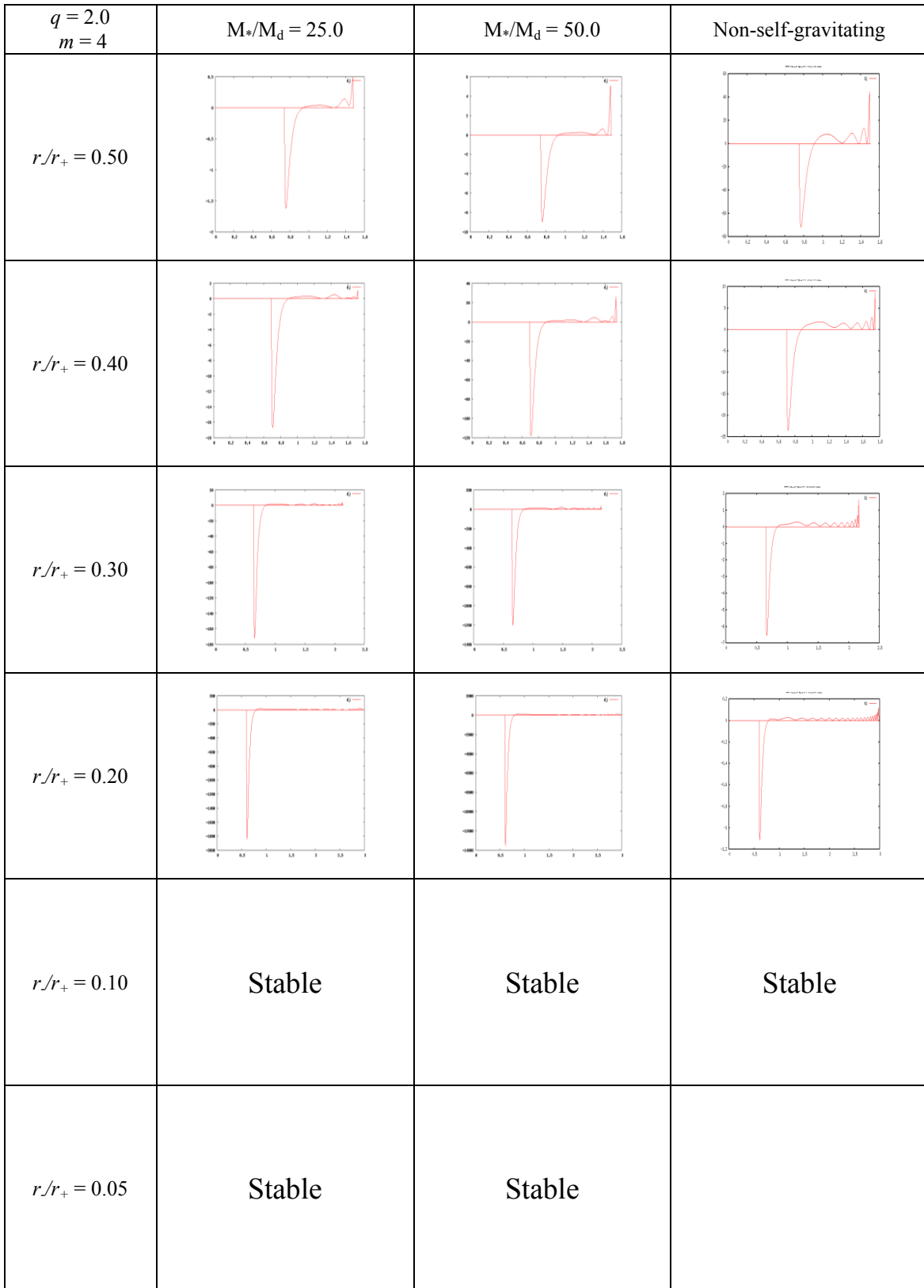


Fig. C.4.4.c. Perturbed angular momentum for $q = 2.0$, $m = 4$.

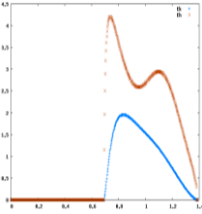
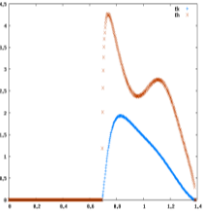
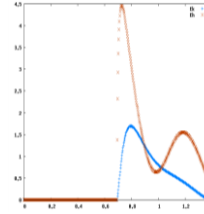
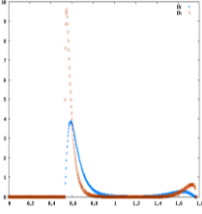
$q = 2.0$ $m = 4$	$M_*/M_d = 0.0$	$M_*/M_d = 0.01$	$M_*/M_d = 0.1$
$r/r_+ = 0.50$			
$r/r_+ = 0.40$	Stable	Stable	Stable
$r/r_+ = 0.30$		Stable	Stable
$r/r_+ = 0.20$	Stable	Stable	Stable
$r/r_+ = 0.10$	Stable	Stable	Stable
$r/r_+ = 0.05$	Stable	Stable	Stable

Fig. C.4.5.a. Work integrals for $q = 2.0$, $m = 4$.

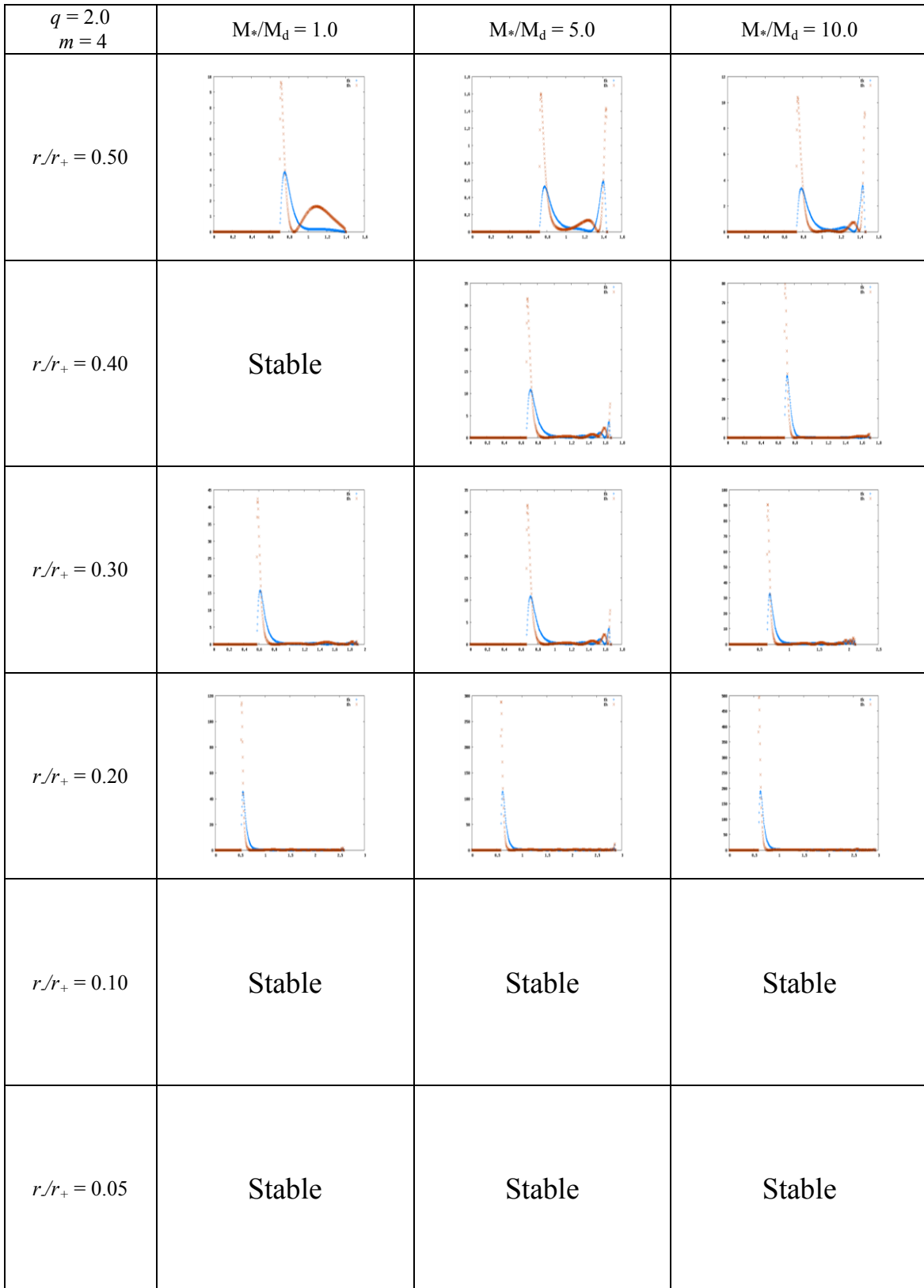


Fig. C.4.5.b. Work integrals for $q = 2.0$, $m = 4$.

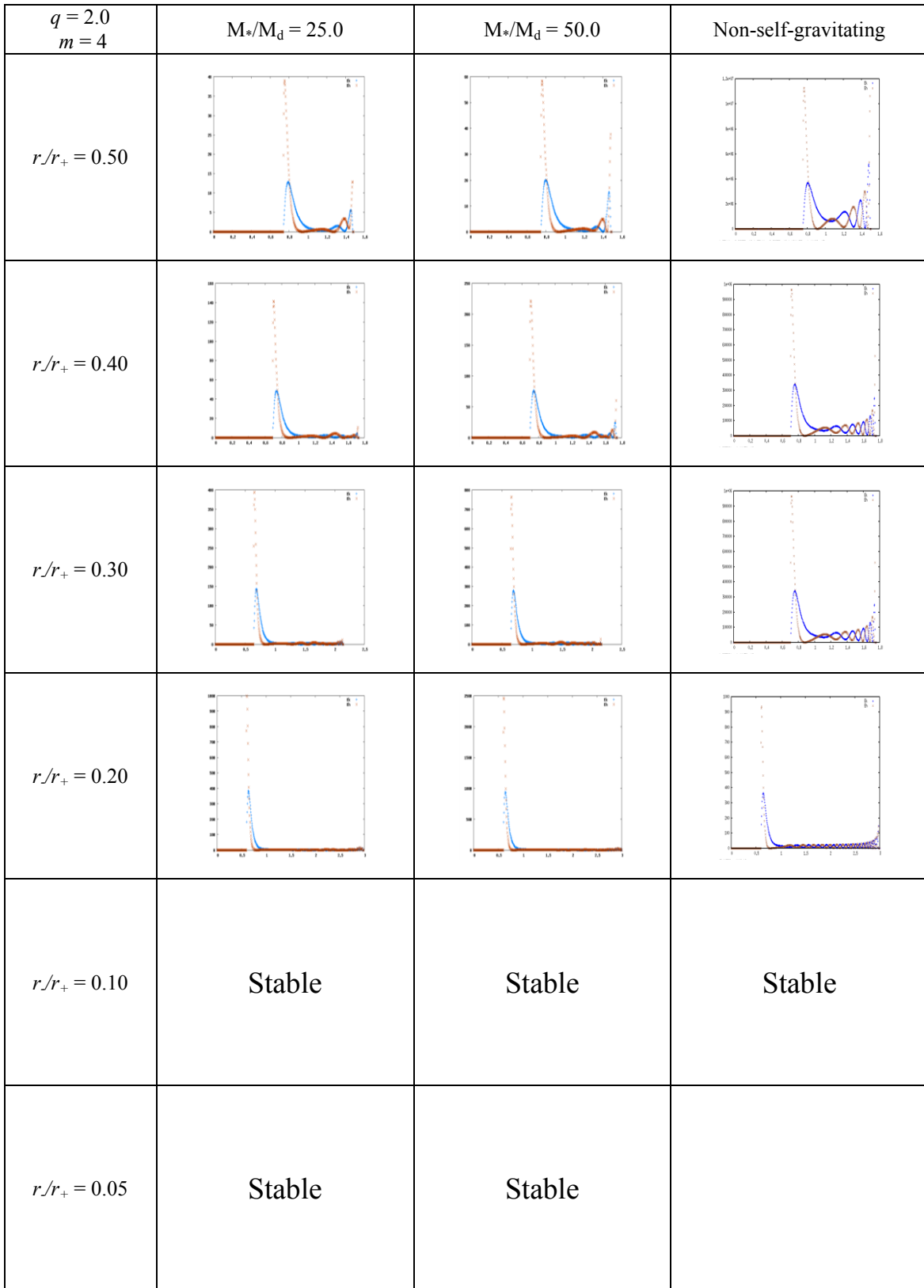


Fig. C.4.5.c. Work integrals for $q = 2.0$, $m = 4$.

$q = 2.0$ $m = 4$	$M_*/M_d = 0.0$	$M_*/M_d = 0.01$	$M_*/M_d = 0.1$
$r/r_+ = 0.50$			
$r/r_+ = 0.40$	Stable	Stable	Stable
$r/r_+ = 0.30$		Stable	Stable
$r/r_+ = 0.20$	Stable	Stable	Stable
$r/r_+ = 0.10$	Stable	Stable	Stable
$r/r_+ = 0.05$	Stable	Stable	Stable

Fig. C.4.6.a. Stresses for $q = 2.0$, $m = 4$.

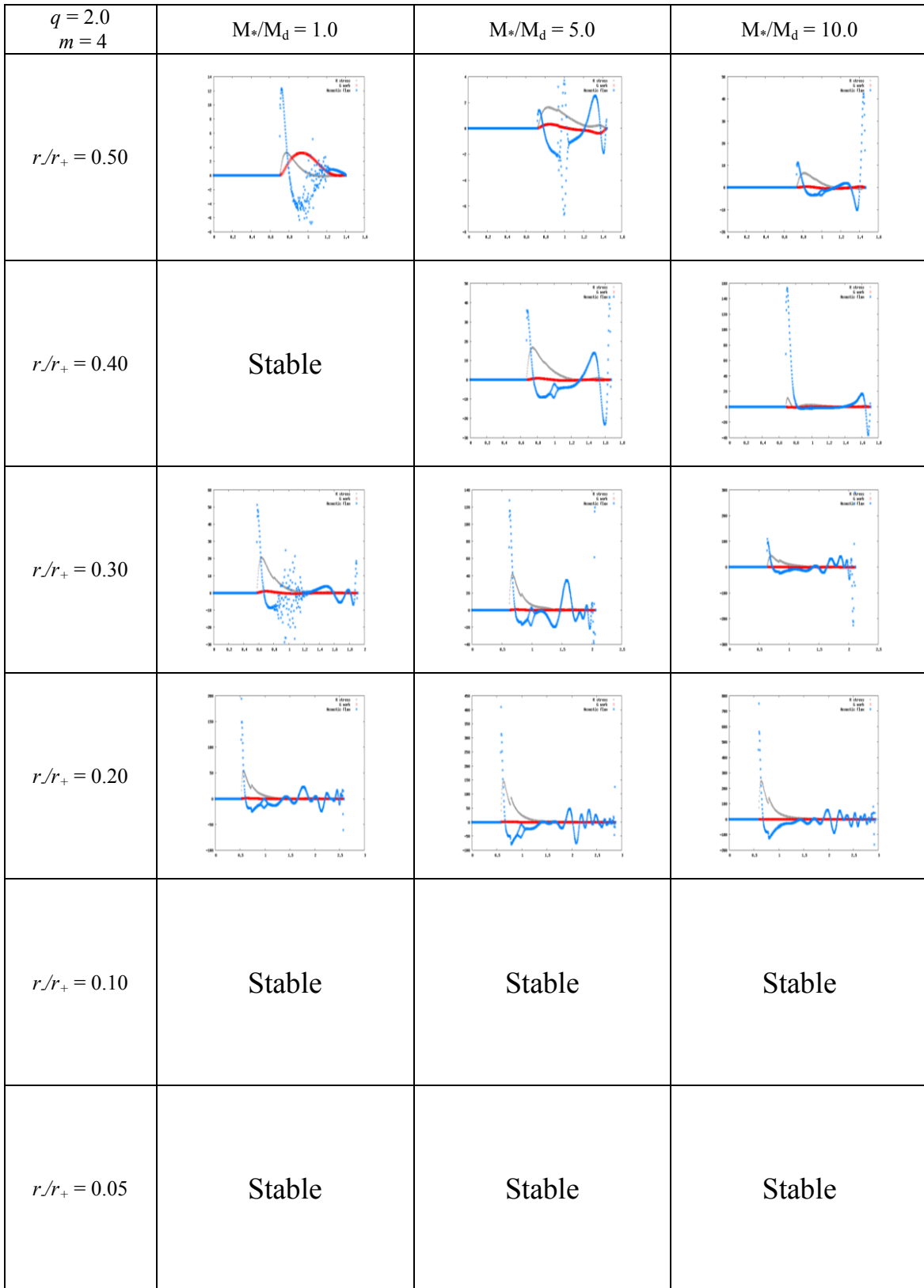


Fig. C.4.6.b. Stresses for $q = 2.0$, $m = 4$.

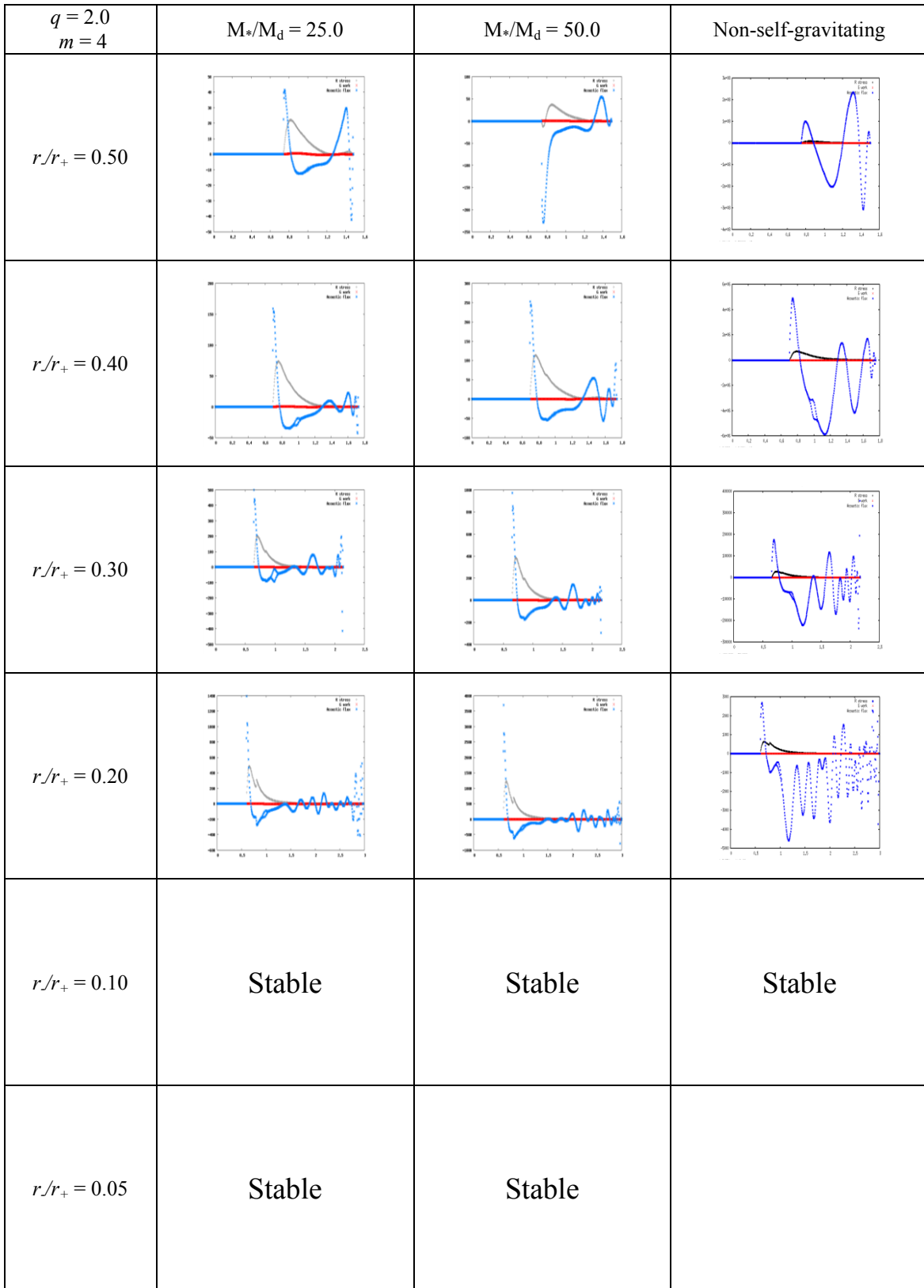


Fig. C.4.6.c. Stresses for $q = 2.0$, $m = 4$.

REFERENCES CITED

- Adams, F.C., Ruden, S.P. & Shu, F.H. 1989, ApJ, 347, 959
- Andalib, S.W., Tohline, J.E., & Christodoulou, D.M. 1997, ApJS, 108, 471
- Binney, J. & Tremaine, S., 1994, Galactic Dynamics (Princeton Univ. Press)
- Balbus, S.A. & Hawley, J.F., 1998, RvMP, 70, 1
- Bodenheimer, P., 1995, ARA&A, 33, 199
- Christodoulou, D.M., & Narayan, R., 1992, ApJ, 388, 451
- Christodoulou, D.M., 1993, ApJ, 412, 719
- Drazin, P.G. & Reid, W.H., 2004, Hydrodynamic Stability (Cambridge: Cambridge Univ. Press)
- Dyson, F. W., 1893, RSPTA, 184, 43
- Eriguchi, Y. & Hachisu, I., 1983, PThPh, 69, 1131
- Goldreich, P., Goodman, J. & Narayan, R., 1986, MNRAS, 221, 339
- Goodman, J., & Narayan, R., 1987, MNRAS, 225, 695
- Goodman, J., & Narayan, R., 1988, MNRAS, 231, 97
- Hunter, J. H., Ball, R., & Gottesman, S. T., 1984, MNRAS, 208, 1
- Hachisu, I., 1986, ApJS, 61, 479
- Hachisu, I., & Eriguchi, Y., 1985, Ap& SS, 99, 71
- Hadley, K., & Imamura, J.N., 2010, Ap&SS, submitted
- Heemskirk, M.H.M, Papaloizou J.C. & Savonije, G.J., 1992, A&A, 260, 161
- Imamura, J.N., Toman, J., Durisen, R.H., Pickett, B.K., & Yang, S., 1995, ApJ, 444, 363
- Kojima, Y., 1986, PThPh, 75, 251
- Kojima, Y., 1989, MNRAS, 236, 589

- Larsen, R.B., 1971, MNRAS, 156, 437
- Lin, D.N.C. & Papaloizou, J.C.B, 1995, ARA&A, 33, 505
- Narayan, R., Goldreich, P., Goodman, J., 1987, MNRAS, 228, 1
- Noh, H., Vishniac, E.T., & Cochran, W.D., 1991, ApJ, 383, 372
- Noh, H., Vishniac, E.T., & Cochran, W.D., 1992, ApJ, 397, 347
- Papaloizou, J.C. & Savonije, G.J., 1991, A&A, 248, 353
- Papaloizou, J.C., & Pringle, J.E., 1984, MNRAS, 208, 702
- Papaloizou, J.C., & Pringle, J.E., 1987, MNRAS, 225, 267
- Rayleigh, Lord, 1916, PMag, 32, 529
- Shapiro, S. L., & Teukolsky, S.A., 1983, Black Holes, White Dwarfs, and Neutron Stars (JohnWiley & Sons)
- Shariff, K., 2008, AnRFM, 41, 283
- Shu, F.H., Adams, F.C., & Lizano, S., 1987, ARA&A, 25, 23
- Stone, J.M., Gammie, C.F., Balbus, S.A., Hawley, J.F., 2000, Protostars and Planets IV (Tucson: U. of Ariz. Press; eds. Mannings, V., Boss, A.P., Russell, S. S.)
- Taga, M. & Iye, M., 1998, MNRAS, 299, 1132
- Tassoul, J.-L., 1978, Theory of Rotating Stars (Princeton Univ. Press)
- Tohline, J.E., 1980, ApJ, 236, 160
- Tohline, J.E., 2002, ARA&A, 40, 349
- Tohline, J.E., & Hachisu, I., 1990, ApJ, 361, 394
- Toomre, A., 1964, ApJ, 139, 1217
- Tsang, D. & Lai, D., 2008, MNRAS, 387, 446
- Woodward, J.W., Tohline, J.E., & Hachisu, I., 1994, ApJ, 420, 247
- Woodward, J.W., 1986, Ph.D. Thesis, Louisiana State University, Baton Rouge